

Copyright
by
Amir Frooqnia
2014

**The Dissertation Committee for Amir Frooqnia Certifies that this is the approved
version of the following dissertation:**

**NUMERICAL SIMULATION AND INTERPRETATION OF
BOREHOLE FLUID-PRODUCTION MEASUREMENTS**

Committee:

Carlos Torres-Verdín, Supervisor

Kamy Sepehrnoori, Co-Supervisor

Matthew Balhoff

Paul Bommer

Roger Bonnecaze

**NUMERICAL SIMULATION AND INTERPRETATION OF
BOREHOLE FLUID-PRODUCTION MEASUREMENTS**

by

Amir Frooqnia, B.E.; M.Sc.

Dissertation

Presented to the Faculty of the Graduate School of

The University of Texas at Austin

in Partial Fulfillment

of the Requirements

for the Degree of

Doctor of Philosophy

The University of Texas at Austin

August 2014

Dedication

To my lovely parents, Fatemeh and GholamHossein, and my sister Sahar, for their
unconditional love, patience, and encouragement

Acknowledgements

During my Ph.D. study at The University of Texas at Austin, I have had the privilege to work with outstanding professors whose support and supervision made this dissertation possible. I would like to express my deepest gratitude to my supervisor, Dr. Carlos Torres-Verdín, for his invaluable advices and all his guidance throughout this project. His scientific intuition with precious technical comments immensely contributed to my academic growth. I am also deeply indebted to my co-supervisor, Dr. Kamy Sepehrnoori, for his priceless input into my research that finely shaped my understanding of the project. In addition, I extend my sincere appreciation to my committee members: Dr. Matthew Balhoff, Dr. Paul Bommer, and Dr. Roger Bonnecaze for reviewing my work, and contributing insightful technical comments.

I would like to acknowledge the staff of Petroleum and Geosystems Engineering Department, Dr. Roger Terzian, Frankie Hart, Joanna Castillo, Glen Baum, and Cheryl Kruzic for their technical and administrative assistance. Special thanks go to Reynaldo Casanova for his patience and day-to-day support that greatly facilitated my academic path at the university.

I would like to specially thank David Itter, Robert Elliott, Jennifer Starck, Adrian Zett, Michael Webster, Ramsey Fisher, Ivan Pinzon, Philippe Marouby, Behrooz Raesi, Alexander Kostin, Jorge Sanchez-Ramirez, Andy Brickell, and Gabriela Schell with whom I worked during my internships. Their professional knowledge and kind mentorship tremendously helped me understand the practical aspects of my Ph.D. project.

I have enjoyed helpful technical discussions with Saeedeh Mohebbinia, Vahid Shabro, Abdolhamid Hadibeik Nishaboori, Mahdy Shirdel, Mohsen Rezaveisi, Zoya

Heidari, Mehdi Haghshenas, and Javad Behseresht for which I am very grateful. A Special note of gratitude goes to Rohollah Abdollah-Pour for his great collaboration in development of the coupled simulator. I am also thankful to my friends from the Formation Evaluation group, Siddharth Misra, Shaina Kelly, Elton Ferreria, Paul Sayar, Kanay Jerath, Ankur Ghandi, Oyinkansola Ajayi, Olabode Ijasan, Haryanto Adiguna, Alberto Mendoza, Renzo Angeles, Abhishek Bansal, Antoine Montaut, Jordan Mimoun, Edwin Ortega, Shan Huang, Robert Mallan, Essi Kwabi, HyungJoo Lee, Rebecca Gao, Andy Popielski, Paul Linden, and Ben Voss for their help and time sharing.

I would like to thank my friends Mehdi Haghshenas, Javad Behseresht, Saeedeh Mohebbinia, Zoya Heidari, Tatyana Torskaya, Chicheng Xu, Ali Moinfar, Seyed Reza Yousefi, Hassan Dehghan-Pour, Ali Afshaar-Pour, Mehran Hosseini, Ehsan Saadat-Pour, Mahdy Shirdel, Ayaz Mehmani, Yashar Mehmani, Saeid Enayat-Pour, Mahdy Haddad, Ahmad Sakhaee-Pour, Shayan Tavassoli, Behzad Eftekhari, Ali Goudarzi, Mohammad Lotfollahi, Hamid Reza Lashgari, Mohsen Taghavifar, Reza Ganjdanesh, Hamed Darabi, Aboulghasem Kazemina, Amir Kianinejad, Mohsen Rezaveisi, Mohammad Javaheri, Ardavan Pedram, Amir Reza Rahmani, Rouzbeh Ghanbarnezhad, Amin Ettehadtavakkol, Abdolhamid Hadibeik Nishaboori, Vahid Shabro, and Rohollah Abdollah-Pour as well as many other friends and classmates whom I did not name explicitly.

The work presented in this dissertation was funded by The University of Texas at Austin's Research Consortium on Formation Evaluation, jointly sponsored by Afren, Anadarko, Apache, Aramco, Baker-Hughes, BG, BHP Billiton, BP, Chevron, China Oilfield Services LTD., ConocoPhillips, Det Norske, ENI, ExxonMobil, Halliburton, Hess, Maersk, Mexican Institute for Petroleum, ONGC, OXY, Petrobras, PTT Exploration and Production, Repsol, RWE, Schlumberger, Shell, Southwestern Energy, Statoil, TOTAL, Weatherford, Wintershall, and Woodside Petroleum Limited.

NUMERICAL SIMULATION AND INTERPRETATION OF BOREHOLE FLUID-PRODUCTION MEASUREMENTS

Amir Frooqnia, Ph.D.

The University of Texas at Austin, 2014

Supervisor: Carlos Torres-Verdín

Co-supervisor: Kamy Sepehrnoori

Downhole production measurements are periodically acquired in hydrocarbon reservoirs to monitor and diagnose fluid movement in the borehole and the near-borehole region. However, because of the complexity involved with physical modeling and numerical implementation of borehole and formation multiphase flow behavior, inference of near-borehole petrophysical properties from production measurements is limited to simplified single-phase reservoir models.

This dissertation develops a new transient coupled borehole-formation fluid flow algorithm to numerically simulate two-phase production logs (PL) acquired across heterogeneous rock formations penetrated by vertical and deviated boreholes. Subsequently, the coupled flow algorithm is used to estimate relevant dynamic petrophysical properties from borehole production measurements.

The developed reservoir-borehole fluid flow model is based on an isothermal, one-dimensional (borehole axis) version of two-fluid formulation that simulates simultaneous flow of two fluid phases in oil-water, oil-gas, and gas-water flowing systems. Linkage of borehole and formation fluid flow models is carried out by introducing additional source terms into borehole mass conservation equations.

Transient simulation of two-phase production measurements indicates the presence of borehole cross-flow when performing a shut-in test across differentially-depleted multilayer reservoirs. In a two-layer synthetic reservoir model penetrated by a vertical borehole, only two hours of through-the-borehole cross-communication of differentially-depleted layers gives rise to more than 14% increase in volume-averaged oil-phase relative permeability of the low-pressure layer. Simulated borehole fluid properties in the presence of cross-flow are used to estimate formation average pressure from two-phase selective-inflow-performance analysis.

A new inversion-based interpretation algorithm is developed to estimate near-borehole absolute permeability and fluid-phase saturation from two-phase production logs. The inversion algorithm integrates production logs acquired in time-lapse mode to construct a near-borehole reservoir model that describes depth variations of skin factor over the elapsed time. Feasibility studies using synthetic reservoir models show that the estimated petrophysical properties are adversely influenced by the large volume of investigation associated with PL measurements. Moreover, undetectable fluid production across low-permeability layers decreases the sensitivity of production logs to layer incremental flow rate, thus increasing estimation uncertainty. Despite these limitations, the estimated fluid saturation and permeability across high-permeability layers are within 25% and 20% of the corresponding actual values, respectively.

Oil-water and oil-gas flowing systems are additionally studied to quantify the added value of remedial workover operations (e.g., water and gas shut-off). Simulation of a gas shut-off performed in a gas-oil field example recommends a minimum bottom-hole pressure to prevent high gas production caused by (i) gas coning effects, and (ii) released gas from oil solution. Maintaining bottom-hole pressure above that limit gives rise to more than 60% reduction of downhole gas production.

Table of Contents

List of Tables	xv
List of Figures	xix
Chapter 1: Introduction	1
1.1 Problem Statement	1
1.2 Review of Relevant Literature	7
1.2.1 Borehole Fluid Flow Modeling	8
1.2.2 Borehole-Formation Coupling	10
1.2.3 Flow-Regime Identification	11
1.2.4 Interpretation of Production Logs	12
1.3 Research Objectives	14
1.4 Review of Chapters	16
Chapter 2: Borehole Fluid Flow Modeling	18
2.1 Introduction	18
2.2 Borehole Fluid Flow Equations	19
2.2.1 Generic Form of the Two-Fluid Model	19
2.2.2 One-Dimensional Form of the Two-Fluid Model	24
2.2.3 Hydrocarbon-Phase Scalar Properties	26
2.2.4 Interfacial Mass Transfer	27
2.3 Flow-Regime Transition	31
2.3.1 Oil-Water Vertical Flowing Systems	32
2.3.1.1 Introduction	33
2.3.1.2 Droplet-Size Modification	35
2.3.2 Oil-Water Deviated Flowing Systems	38
2.3.2.1 Force Balance in Radial Direction	41
2.3.3 Gas-Liquid Vertical Flowing Systems	46
2.3.3.1 Bubbly to Slug Flow-Regime Transition	48

2.3.3.2 Bubbly to Dispersed-Bubbly Flow-Regime Transition	49
2.3.3.3 Dispersed-Bubbly to Slug Flow-Regime Transition.....	50
2.3.3.4 Slug to Annular Flow-Regime Transition.....	51
2.3.3.5 Interfacial Drag Forces	52
2.3.4 Gas-Liquid Deviated Flowing Systems	53
2.3.4.1 Interfacial Drag Forces	54
Chapter 3: Computational Approach	56
3.1 Borehole Discretization	56
3.2 Discretization of Transport Equations	60
3.3 Matrix Form of Discretized Transport Equations.....	63
3.3.1 Component-Based Mass Conservation Equation.....	66
3.3.2 Equation for Fluid-Phase Volume Fraction	68
3.3.3 Conservation Equation for the Overall Mass.....	70
3.3.4 Fluid-Phase Momentum Conservation Equation.....	71
3.4 Borehole Single-Phase Fluid Flow Equations	77
3.5 Solution Algorithm	80
3.5.1 Semi-Implicit Method for Pressure-Linkage Equations, Consistent (SIMPLE-C).....	81
3.5.2 Inter-Phase Slip Algorithm, Coupled (IPSA-C)	85
3.6 Boundary Conditions	90
3.7 Automatic Time-Step Controlling	92
3.8 Borehole-Formation Coupling.....	94
3.8.1 Sequential Coupling Method	95
3.8.2 Differential Depletion	95
3.8.3 Averaging Method	97

Chapter 4: Verification of the Borehole Fluid Flow Model	102
4.1 Introduction.....	102
4.2 Transient Simulations	103
4.2.1 Simulation of Phase Separation	103
4.2.2 Simulation of Shut-In Test.....	104
4.3 Gas Flowing Systems	109
4.4 Oil-Water Flowing Systems.....	112
4.5 Gas-Water Flowing Systems	119
4.6 Gas-Oil Flowing Systems	120
4.7 Field Production Measurements	125
4.8 Computational Time	130
Chapter 5: Steady-State and Transient Simulation of Borehole Production Measurements	131
5.1 Introduction.....	131
5.2 Transient Simulation of Borehole Cross-Flow	132
5.2.1 Model Description	133
5.2.2 Production Measurements Under Shut-In Conditions	137
5.3 Sensitivity Analysis	141
5.3.1 Near-Borehole Formation Damage.....	142
5.3.2 Average Pressure	145
5.3.3 Oil-Phase Density	147
5.3.4 Oil-Phase Viscosity.....	149
5.3.5 Borehole Deviation Angle	151
5.3.6 Cross-Flow Duration.....	153

5.4	Simulation of Selective-Inflow-Performance (SIP) Test.....	156
5.5	Simulation of Water Loading	163
5.6	Summary and Conclusions	169
Chapter 6: Inference of Rock Pressure-Production Properties from Gas-Oil		
	Production Logs.....	173
6.1	Introduction.....	174
6.2	Interpretation Method	176
	6.2.1 General Assumptions	177
	6.2.2 Inverse Problem	177
6.3	Synthetic Example	183
6.4	Field Example	195
	6.4.1 Gas Shut-Off	197
	6.4.2 Sensitivity Analysis	197
6.5	Discussion.....	210
6.6	Summary and Conclusions	211
Chapter 7: Inference of Near-Borehole Permeability and Water Saturation from		
	Time-Lapse Oil-Water Production Measurements	214
7.1	Introduction.....	214
7.2	Permeability Anisotropy	216
7.3	Upscaling of Permeability	222
7.4	Sensitivity of Production Logs to Measurement Noise	227
	7.4.1 Single-Phase Flowing Systems	227
	7.4.2 Two-Phase Flowing Systems	233
7.5	Synthetic Example	242
	7.5.1 General Assumptions	243
	7.5.2 Model Description	244
	7.5.3 Time-Lapse PL Interpretation.....	245

7.6	Field Example	258
7.6.1	General Description	258
7.6.2	Interpretation of Production Logs	260
7.6.3	Sensitivity Analysis	267
7.6.3.1	Formation Pressure	267
7.6.3.2	Permeability Anisotropy	268
7.6.3.3	Radius of Damaged Region	268
7.6.3.4	End Point of Relative Permeability.....	269
7.7	Discussion	271
7.8	Summary and Conclusions	273
Chapter 8: Estimation of Oil-Water Relative Permeability from Inversion of Time-Lapse Production Logs.....		277
8.1	Introduction.....	277
8.2	Interpretation Method	279
8.2.1	General Assumptions	279
8.2.2	Inverse Problem	279
8.2.3	Single-Layer Reservoir Example.....	281

8.3	Uncertainty Analysis.....	289
8.4	Time-Lapse Analysis	294
8.5	Summary and Conclusions	296
Chapter 9: Summary, Conclusions, and Recommendations		303
9.1	Summary	303
9.2	Conclusions.....	307
9.3	Recommendations for Future Studies.....	318
Appendix A: Peng-Robinson’s Equation of State		321
List of Symbols		323
List of Greek Symbols		335
List of Acronyms		339
References.....		341

List of Tables

Table 3.1:	Summary of transport fluid properties (ψ_k), diffusion, and source terms defined in the generic form of transport equation (i.e., Equation 3.1).....	59
Table 3.2:	Summary of coefficients introduced in the discretized component-based mass conservation equation (i.e., Equation 3.23).....	68
Table 3.3:	Summary of coefficients introduced in the discretized mass conservation equation for fluid-phase volume fraction (i.e., Equation 3.25).....	69
Table 3.4:	Summary of coefficients introduced in discretized conservation equation for the overall mass (i.e., Equation 3.26).....	71
Table 3.5:	Summary of the coefficients introduced in fluid-phase momentum conservation equation (i.e., Equation 3.33).....	76
Table 3.6:	Summary of coefficients introduced in the single-phase mass equation.....	78
Table 3.7:	Summary of coefficients introduced in the discretized single-phase momentum conservation equation (i.e., Equation 3.37).....	79
Table 4.1:	Summary of pipe and fluid-phase properties assumed for simulation of the phase separation test.....	105
Table 4.2:	Assumed borehole and gas-phase properties for the simulation of pressure drop in a long pipe reported by Takacs and Guffey (1989).....	110
Table 4.3:	Assumed hydrocarbon component for the simulation of pressure drop in a long pipe reported by Takacs and Guffey (1989).....	110

Table 4.4:	Summary of assumed fluid-phase properties for validation example of the oil-gas flowing system reported by Hasan and Kabir (2002).....	122
Table 4.5:	Summary of assumed hydrocarbon properties for validation example of the oil-gas flowing system reported by Hasan and Kabir (2002).....	122
Table 4.6:	Comparison of the numerically simulated and measured borehole fluid-phase flow rate performed for oil-water field example reported by Schlumberger (1973).	128
Table 4.7:	Computational time obtained for various single- and two-phase fluid flow simulations.....	130
Table 5.1:	Summary of assumed formation petrophysical properties for transient simulation of borehole cross-flow.....	134
Table 5.2:	Summary of the assumed formation, borehole, and fluid-phase properties for the sensitivity analysis of borehole cross-flow in the two-layer reservoir model.....	141
Table 5.3:	Summary of assumed formation petrophysical properties for the simulation of the SIP test.....	159
Table 5.4:	Comparison of the estimated and actual formation average pressure from the SIP analysis in the four-layer reservoir model.....	159
Table 5.5:	Summary of assumed formation, borehole, and fluid-phase properties for simulation of water loading in the two-layer model.....	165
Table 6.1:	Summary of formation, borehole, and fluid-phase properties assumed for PL interpretation of the synthetic multilayer reservoir model.	186

Table 6.2:	Summary of the assumed formation, borehole, and fluid-phase properties for PL interpretation of the sand-shale field example....	199
Table 6.3:	Summary of the assumed hydrocarbon properties for PL interpretation of the sand-shale field example.....	199
Table 6.4:	Comparison of the initial and final estimates of near-borehole permeability and gas saturation obtained for the sand-shale field example. The algorithm progressively refines permeability of near-borehole region to match fluid velocity, pressure, and holdup. During the inversion, gas saturation is assumed to be constant laterally away from the borehole. The final refined model has been shown in Figure 6.21.	202
Table 7.1:	Summary of fluid-phase, formation, and borehole properties assumed for the three-layer reservoir model to quantify directional dependency of PL-derived permeabilities.	218
Table 7.2:	Comparison of PL-derived permeabilities and those computed from the analytical model (i.e., Equation 7.1). Numerical simulation of production measurements is performed under the assumption of isotropic rock formations in the forward reservoir model	218
Table 7.3:	Sensitivity of estimated permeability with respect to Gaussian and skewed-Gaussian noise on single-phase production logs acquired across the four-layer reservoir model. The thinnest layer (i.e., Rock 4) shows more than 170% error involved with the estimates of permeability. On the other hand, the estimated permeability for Rock 1 (with the thickness equal to 30 ft and permeability equal to 800 mD) is within 9% of the actual value.	229

Table 7.4:	Summary of properties assumed for the hydrocarbon component used in PL interpretation of the sand-shale field example.....	260
Table 8.1:	Assumed fluid-phase, formation, and borehole properties for the single-layer reservoir model.	284
Table 8.2:	Assumed formation petrophysical properties for uncertainty analysis of the three-layer reservoir model.....	290

List of Figures

Figure 1.1: Numerically simulated average water holdup as a function of applied pressure drawdown and well inclination. Each step represents the minimum pressure drawdown required to prevent water phase from loading the borehole flow domain. This graph shows that the required pressure drawdown increases with increasing borehole inclination angle.....	7
Figure 2.1: Schematic of the borehole fluid flow model constructed for simulation of two-phase production measurements.....	30
Figure 2.2: Developed workflow to compute interfacial mass transfer rates for simultaneous production of the oil and gas phases.....	31
Figure 2.3: Schematic of the borehole fluid flow model describing flow-regime transition in oil-water vertical flow. Droplet coalescence gives rise to a smooth transition from water-dominant to oil-dominant flow regimes.....	37
Figure 2.4: Schematic of the borehole fluid flow model describing flow-regime transition in oil-water deviated flow. Droplet coalescence gives rise to a smooth transition from water-dominant to oil-dominant flow regimes. In addition, the lighter fluid phase tends to move closer to the upper wall, thus decreasing the contact area shared by two fluid phases.....	40

Figure 2.5: Illustration of the cross-sectional spatial distribution of droplets within (a) uniform bubbly flow, (b) fully-segregated flow, and (c) non-uniform bubbly flow. Drag force associated with Panel (c) is computed based on linear interpolation between drag forces for Panels (a) and (b).41

Figure 2.6: Geometrical description of two-phase fluid flow within a segregated flow regime. The interfacial area shared by two fluid phases (i.e., S^{int}) is numerically computed using Equation 2.65.41

Figure 2.7: Illustration of buoyant, drag, and turbulent forces acting on a single droplet in the radial direction, shown in (a) planar view, and (b) side view.....46

Figure 2.8: Developed workflow for dynamic determination of fluid flow regimes in the borehole. The algorithm dynamically modifies interfacial momentum transfer rates to match the assumed and computed borehole fluid flow regimes.48

Figure 2.9: Schematic of the borehole fluid flow model describing flow-regime transition in gas-liquid deviated flow. Agglomeration of gas bubbles at higher gas holdup leads to occurrence of the annular flow.55

Figure 2.10: Comparison the interpolation weighting factor (W_{sl}) defined in Equation 2.90 for vertical (blue line) and deviated boreholes (red line). Red line biases the interpolation toward the annular flow regime to effectively decrease the interfacial contact area.55

Figure 3.1: Schematic of a finite control volume considered for the discretization of borehole flow domains. Vector properties are defined in the center of the control volume while scalar properties are assigned to n- and s-faces.59

Figure 3.2: Schematic of staggered gridding arrangement used for discretization of the borehole flow domain. Two separate finite control volumes are defined for computation of fluid-phase velocity and pressure. The schematic shows that center of a VCV coincides with face of the preceding SCV.....60

Figure 3.3: Developed iterative workflow to simulate borehole fluid-phase velocity, pressure, volume fraction, density, viscosity, and hydrocarbon molar composition. The algorithm includes two modules: (a) thermodynamics module, and (b) fluid dynamics module. A pressure-correction algorithm is invoked within the fluid dynamics module to compute fluid-phase velocity, pressure, and volume fraction assuming fixed values for fluid-phase density and viscosity. Subsequently, the thermodynamics module computes the overall molar composition, and updates fluid-phase density and viscosity. A detailed description of the equations developed for each module has been presented in Section 3.3.65

Figure 3.4: Developed iterative workflow to simulate borehole single-phase velocity and pressure. The SIMPLE-C algorithm begins with an initial guess for fluid properties. Subsequently, a pressure-correction equation (i.e., Equation 3.51) is constructed to correct the guessed values of pressure and velocity. The guess-and-correction algorithm continues until achieving a satisfactory convergence.....84

Figure 3.5: Developed iterative workflow to simulate borehole two-phase velocity, pressure, and holdup. The IPSA-C algorithm begins with an initial guess for fluid properties. Subsequently, a pressure-correction equation (i.e., Equation 3.82) is constructed to correct the guessed values of pressure and velocity. The guess-and-correction algorithm continues until achieving a satisfactory convergence.....90

Figure 3.6: Developed sequential method to couple separate borehole and formation fluid flow equations. Current time step in the reservoir flow domain is used as the time increment required for the borehole fluid flow simulation. Following the calculation of borehole fluid-phase properties, the developed method updates boundary conditions associated with formation fluid flow equations, and proceeds to the next time step.....99

Figure 3.7: Schematic of the grid arrangement within and around the borehole for (a) vertical and (b) deviated flowing systems. An averaging method has been developed to compute the average values of permeability and porosity associated with grids block shared by the adjacent petrophysical layers.100

Figure 3.8: Geometrical description of a layer bed boundary crossing a grid block in a non-conformal arrangement. Panels (b), (c), and (d) show the projected area of Plane p in r, z, and θ directions, respectively. Panels (e), (f), and (g) show the projected area of the volume occupied by Layer 1 in r, z, and θ directions, respectively. Equations 3.99 through 3.102 use the described shaded areas to compute average permeabilities associated with each grid block.101

Figure 4.1: Transient behavior of borehole (a) oil-phase holdup, (b) water-phase velocity, (c) oil-phase velocity, and (d) fluid pressure, simulated for the phase separation test. Panels (b) and (c) show downward movement of the water and upward movement of the oil that eventually (after 370 seconds) leads to the separation of two fluid phases.....106

Figure 4.2: Transient behavior of borehole fluid-phase volume fraction simulated (a) 10, (b) 170, and (c) 370 seconds after the inception of phase-separation test.106

Figure 4.3: Spatial distributions of borehole production measurements for (a) fluid-phase velocity, (b) fluid-phase holdup, (c) fluid mixture density, and (d) fluid-phase inflow rate, acquired for the simulation of shut-in test. Panel (e) shows borehole and formation pressures at the time of measurement acquisition.107

Figure 4.4: Transient behavior of borehole (a) oil-phase velocity, (b) water-phase velocity, (c) oil-phase holdup, (d) fluid pressure, and (e) fluid mixture density, simulated for the shut-in test.....107

Figure 4.5: Transient behavior of borehole fluid-phase holdup simulated (a) 1, (b) 150, (c) 430, (d) 730, and (e) 1080 seconds after initiating the shut-in test.....108

Figure 4.6: Time required for the water phase to fill the entire borehole domain as a function of fluid-phase density contrast, computed for simulation of the shut-in test.....108

Figure 4.7: Simulated borehole gas-phase (a) velocity, (b) pressure, (c) density, and (d) assumed borehole temperature, for the calculation of pressure drop in a long pipe reported by Takacs and Guffey (1989). Panel (b) compares the numerically simulated and measured pressure drop.111

Figure 4.8: Comparison of the numerically simulated spatial distributions of borehole gas-phase (a) velocity and (b) pressure with those obtained by Shirdel’s (2013) flow model. Panels (c) and (d) show the simulated borehole density, and the assumed borehole temperature, respectively.111

Figure 4.9: Numerically simulated (a) modified superficial velocity (Variable 2), (b) droplet diameter, (c) fluid-phase velocity, and (d) fluid-phase volume fraction, as a function of modified mixture velocity (Variable 1), obtained for the simultaneous flow of oil and water in a vertical pipe. The slope of 1.2 associated with a water-dominant bubbly flow regime is accurately simulated by dynamically modifying the droplet diameter as a function of borehole oil-phase velocity and volume fraction. The unit-slope line shown in Panel (a) is interpreted as the no-slip condition associated with high oil-phase volume fractions (i.e., oil-dominant flow regime).....116

Figure 4.10: Numerically simulated (a) modified superficial velocity (Variable 2), (b) droplet eccentricity factor, (c) fluid-phase velocity, and (d) fluid-phase volume fraction, as a function of modified mixture velocity (Variable 1), obtained for the simultaneous flow of oil and water in a deviated pipe with a deviation angle of 65°. Droplet eccentricity is dynamically modified to account for the excess of slip velocity in deviated pipes.117

Figure 4.11: Comparison of the numerically simulated and measured water holdup in the steady-state conditions for simultaneous flow of oil and water with (a) 1011 and (b) 6038 bfpd total fluid flow rates, simulated for Vigneaux et al.'s (1988) water-oil flowing system. Dash lines describe the no-slip flowing conditions.118

Figure 4.12: Comparison of the numerically simulated and measured water holdup in steady-state conditions for (a) vertical and (b) deviated water-oil flowing systems, reported by Shi et al. (2005). Dash lines describe the no-slip flowing conditions. Error bars quantify uncertainty bounds associated with water holdup estimated from fluid local conductance.118

Figure 4.13: Comparison of numerically simulated (solid curves) and measured water holdup for steady-state conditions simulated in (a) vertical, and (b) deviated water-gas flowing systems (Shi et al., 2005). Dash lines describe no-slip flowing conditions. Error bars quantify uncertainty bounds associated with water holdup estimated from fluid local conductance.120

Figure 4.14: Depth variations of borehole fluid-phase: (a) actual velocity, (b) superficial velocity, (c) holdup, and (d) pressure, simulated for validation example of the oil-gas flowing system (Hasan and Kabir, 2002). Panel (e) shows the assumed borehole fluid temperature. ..123

Figure 4.15: Borehole fluid-phase superficial velocities on the gas-liquid flow-regime map (DB: dispersed-bubbly, BL: bubbly, SL: slug, and AN: annular flow regimes), performed for validation example of the oil-gas flowing system (Hasan and Kabir, 2002).123

Figure 4.16: Borehole (a) gas-phase (b) oil-phase, and (c) overall hydrocarbon molar fractions, simulated for Hasan and Kabir's (2002) validation example.124

Figure 4.17: Borehole (a) gas-phase density, (b) gas-phase viscosity, (c) oil-phase density, and (d) oil-phase viscosity, simulated for Hasan and Kabir’s (2002) validation example.124

Figure 4.18: Comparison of the numerically simulated and measured borehole pressure performed for Hasan and Kabir’s (2002) validation example.125

Figure 4.19: Reconstruction of borehole (a) fluid-phase and mixture velocities, (b) fluid pressure, (c) fluid-phase holdup, and (d) fluid mixture density, for the field example reported by Schlumberger (1973). Panels (c) through (e) compare the numerically simulated and measured fluid holdup, density, and inflow rates.127

Figure 4.20: Numerically simulated and measured fluid-phase superficial velocities on the oil-water flow regime map, reported by Hasan and Kabir (2002). Panel (b) shows the numerically simulated droplet diameter associated with oil- and water-dominant flow regimes. ...128

Figure 4.21: Reconstruction of the borehole fluid-phase (a) inflow rate, and (b) velocity, simulated for the field example reported by Hasan and Kabir (2002). Panel (c) compares the assumed and measured borehole fluid temperature.129

Figure 4.22: Reconstruction of the borehole (a) fluid-phase holdup, (b) fluid mixture density, and (c) fluid pressure, simulated for the field example reported by Hasan and Kabir (2002).129

Figure 5.1: Assumed near-borehole petrophysical properties associated with the cross-flow simulation. Panels (a) and (b) show near-borehole relative permeability and the associated water saturation, respectively. Panel (c) visualizes the spatial distribution of formation pressure prior to measurement acquisition. Rock 1 exhibits a lower average pressure compared to Rock 2 that causes the development of borehole cross-flow. Panels (d) and (e) describe the assumed saturation-dependent relative permeability and capillary pressure curves, respectively. Rock 1 exhibits a lower average pressure compared to Rock 2 that causes the development of borehole cross-flow.135

Figure 5.2: Numerically simulated borehole fluid-phase (a) velocity, (b) holdup, (c) pressure, (d) density, and (e) inflow rate. Because of the fluid-phase density contrast, oil-phase velocity, shown in Panel (a), is higher than that of the water phase. Fluid-phase slippage was simulated by dynamically modifying the spherical droplet sizes associated with the dispersed fluid phase.136

Figure 5.3: Numerically simulated (a) fluid-phase superficial velocities plotted in the oil-water flow-regime map, (b) droplet diameter associated with the dispersed phase, and (c) water-phase holdup. Panel (c) shows unaccounted variations of fluid-phase spillage (i.e., using a no-slip model) causes more than 7% error in the estimates of water holdup.136

Figure 5.4: Numerically simulated spatial distributions of borehole (a) oil-phase velocity, (b) water-phase velocity, (c) oil-phase holdup, (d) fluid mixture velocity, and (e) fluid pressure shown in transient mode. The simulation has been performed for the first 90 seconds after initiation the borehole cross-flow. The negative values of simulated fluid-phase velocity imply the downward movement of fluid phases from high-pressure layer (i.e., Rock 1) to low-pressure layer (i.e., Rock 2).....138

Figure 5.5: Numerically simulated spatial distributions of formation fluid-phase inflow rate (Panels a through d), and borehole fluid-phase holdup (Panels e through h) shown in transient mode. The simulations show downward movement of fluid phases associated with the first 90 seconds after the inception of borehole cross-flow.139

Figure 5.6: Comparison of the numerically simulated spatial distributions of near-borehole (a) oil saturation and fluid-phase relative permeability for (b) initial and (c) final simulation times. Panels (d) and (e) describe variations of oil saturation and pressure over cross-flow time. The development of borehole cross-flow causes an approximately 18% increase in near-borehole fluid-phase saturation, and a 14% increase of relative permeability. Furthermore, fluid injection into the lower layer (i.e., Rock 1) leads to a gradual increase of pressure for that rock. Panel (e) shows that borehole cross-flow continues until achieving hydrodynamic equilibrium between the two layers.....140

Figure 5.7: Sensitivity analysis for the spatial distributions of borehole fluid-phase holdup and fluid-phase inflow rate with respect to the presence of skin in near-borehole region of Rock 1. Panels (c) and (d) show the development of downward cross-flow with respect to only water phase; while for lower skins both fluid phases involve in cross-flow.....143

Figure 5.8: The effect of formation damage associated with Rock 1 on (a) inflow performance of Rock 1, (b) near-borehole oil saturation of Rock 1, and (c) radial distribution of pressure for Rocks 1 and 2. Panel (a) shows that producibility of Rock 1 decreases with increasing skin factor for that rock. Accordingly, higher skins result in lower oil-phase volumes being injected from Rock 2 into Rock 1 (Panel b).....144

Figure 5.9: Sensitivity of near-borehole oil saturation for Rock 1 to the pressure difference between Rock 1 and Rock 2. A higher pressure difference leads to a higher fluid injection rate into Rock 1, thus increasing the near-borehole oil saturation for that rock.145

Figure 5.10: Sensitivity analysis for the spatial distributions of borehole fluid-phase holdup and fluid-phase inflow rate with respect to the pressure difference between Rock 1 and Rock 2. Panels (c) and (d) show that for pressure differences lower than 400 psi the development of downward cross-flow takes place with respect to only the water phase. Increasing layer pressure difference causes both fluid phases to contribute in cross-flow.146

Figure 5.11: Sensitivity of near-borehole oil saturation for Rock 1 with respect to density difference between the oil and water phases. A higher density contrast lowers the volume of oil phase injected into Rock 1, thus decreasing the near-borehole oil saturation for that rock.....147

Figure 5.12: Sensitivity analysis for the spatial distributions of borehole fluid-phase holdup and fluid-phase inflow rate with respect to the density difference between oil and water phases. Panels (a) through (d) show that lowering the density contrast results in injection of larger volumes of the lighter fluid phase (i.e., oil) into Rock 1. Panel (d) shows that for the density contrast equal to 0.35 g/cc the oil volume injected into Rock 1 is approximately 27% lower than that associated with Panel (a) (i.e., density contrast equal to 0.05 g/cc).....148

Figure 5.13: Sensitivity of near-borehole oil saturation for Rock 1 with respect to viscosity ration between the oil and water phases. A higher viscosity ratio lowers producibility of Rock 2 and injectivity of oil-phase into Rock 2. Therefore, at higher viscosity ratios lower volume of oil phase is injected into Rock 1.149

Figure 5.14: Sensitivity analysis for the spatial distributions of borehole fluid-phase holdup and fluid-phase inflow rate with respect to viscosity ratio between the oil and water phases. Panels (a) through (d) show that lowering oil viscosity results in injection of larger volumes of the lighter fluid phase (i.e., oil) into Rock 1. Panel (d) shows that for oil viscosity equal to 3 cp approximately zero volume of oil contributes into borehole cross-flow.....150

Figure 5.15: The effect of borehole deviation angle on development of borehole two-phase cross-flow. Panel (a) shows that oil-phase volume injected into Rock 1 decreases with increasing borehole deviation angle. For deviation angle greater than 15 degrees, zero volume of produced oil contributes into downward borehole cross-flow. Panel (b) shows that inclining the borehole causes oil droplets to agglomerate close to the borehole's upper wall, thus increasing fluid-phase slippage velocity.151

Figure 5.16: Sensitivity analysis for the spatial distributions of borehole fluid-phase holdup and fluid-phase inflow rate with respect to borehole deviation angle. Panels (b) through (d) show no borehole cross-flow with respect to the lighter fluid phase. Inclining the borehole to an angle more than 15 degrees sufficiently increases fluid-phase slip velocity to prevent downward movement of oil phase.152

Figure 5.17: Sensitivity analysis for the spatial distributions of borehole fluid-phase holdup and inflow rate with respect to the duration of cross-flow. Panels (a) through (d) show that the development of downward cross-flow largely depends on the hydrodynamic equilibrium between Rock 1 and Rock 2. At the early stages of cross-flow, a large volume of fluids is injected into Rock 1 while continuous fluid production lowers the pressure difference between the two rocks thereby reducing the two-phase cross-flow.154

Figure 5.18: Transient behavior of (a) formation average pressure and (b) oil volumetric flow rate injected into Rock 1. Fluid production from Rock 1 and fluid injection into Rock 2 lower the pressure differences between the two rocks, thus reducing the volume of oil phase injected into Rock 1. Panel (c) shows the radial distribution of formation average pressure associated with Rocks 1 and 2, 100 minutes after the inception of borehole cross-flow.155

Figure 5.19: Assumed saturation-dependent formation capillary pressure (Panel a) and relative permeability (Panel b) for simulation of the SIP test in the four-layer model.....159

Figure 5.20: Numerically simulated spatial distributions of borehole fluid-phase velocity, holdup, pressure, mixture density, and inflow rate under production conditions (Panels a through e) and shut-in conditions (Panels f through j), obtained for simulation of the SIP test. The low average pressure associated with Rock 2 leads to downward movement of the oil and water phases. Panel (j) shows the injection of oil and water phases into Rock 2 under shut-in conditions giving rise to increase near-borehole oil saturations for that rock.160

Figure 5.21: Numerically simulated spatial distributions of borehole pressure and fluid-phase incremental flow rate associated with production rates equal to (a) 9500, (b) 7500, (c) 3500 bbl/day, and (d) shut-in conditions. Panel (c) shows that water is produced from Rocks 1 and 4, and injected back into Rock 2. Panel (d) shows that under shut-in conditions both oil and water phases contribute in borehole cross-flow.161

Figure 5.22: Numerically simulated IPR curves computed based on (a) total fluid flow rate, (b) water flow rate, and (c) oil flow rate for the SIP analysis of the four-layer model. The lines are plotted based on the interpolation through the points associated with 9500 and 7500 bbl/day production rates. The line intercept with the y-axis represents formation average pressure (see also Table 4). Production performance of Rock 2 (namely, green dots) shows a deviation from the straight line that is associated with the injection of oil into that rock during the shut-in test. Reliable estimation of formation average pressure for Rock 2 requires exclusion of data points influenced by oil injection.162

Figure 5.23: Radial distribution of formation pressure (a) under production conditions and (b) under shut-in conditions obtained for the SIP analysis. Panel (b) shows that fluid injection under shut-in conditions increases the near-borehole pressure of Rock 2.....163

Figure 5.24: Assumed saturation-dependent formation capillary pressure (Panel a) and relative permeability (Panel b) for simulation of water loading in the two-layer reservoir model.....165

Figure 5.25: Numerically simulated spatial distributions of borehole (a) fluid-phase velocity, (b) fluid-phase holdup, (c) pressure, (d) fluid mixture density, and (e) fluid inflow rate for the two-layer reservoir model. Panel (a) quantifies the slippage velocity between the gas and water phases required to lift the produced water and prevent water phase from filling the borehole. The minimum gas velocity required to prevent water loading is a function of pressure drawdown quantified in Figure 5.28.....166

Figure 5.26: Numerically simulated transient behavior of borehole fluid holdup (first row), velocity (second row), and pressure (third row) for water loading example in a vertical borehole. Water velocity exhibits negative values indicating that water moves downward and gradually loads the borehole. Fluid holdup shows a sharp interface between the gas and water phases. Approximately after 42 minutes the borehole is filled with water.167

Figure 5.27: Numerically simulated transient behavior of borehole fluid holdup (first row), velocity (second row), and pressure (third row) for water loading example in a deviated borehole. Fluid holdup shows a sharp interface between gas and water phases; approximately after 71 seconds the borehole becomes filled with water. Deviation angle causes the agglomeration of gas bubble close to the borehole's upper wall that leads to a higher slip velocity.....168

Figure 5.28: Numerically simulated average water holdup as a function of applied pressure drawdown and inclination angle. Each step represents the minimum pressure drawdown required to prevent water phase from loading the borehole flow domain. This graph shows that the required pressure drawdown increases with decreasing borehole inclination angle. The water loading was simulated under the assumption of Darcy flow in the formation.169

Figure 6.1: Iterative algorithm developed in this dissertation to estimate near-borehole fluid-phase saturation (S_p) and permeability (K) from borehole production measurements. The iterative refinement includes three inner loops: Loop 1 assumes fixed values of fluid saturation to estimate permeability. Loop 2 assumes known values of permeability to refine fluid saturation. Following the calculation of the two properties, Loop 3 rescales the entire permeability field to match measurements of borehole pressure.182

Figure 6.2: Schematic of the window-by-window interpretation method adopted in this dissertation to estimate near-borehole fluid-phase saturation and permeability. The algorithm defines several spatial windows in the borehole, and associates each window with the corresponding layer properties. Estimation of near-borehole fluid-phase saturation and permeability is carried out by computing variations of fluid-phase velocity and holdup across each window.183

Figure 6.3: Assumed saturation-dependent relative permeability and capillary pressure for PL interpretation of the synthetic multilayer reservoir model.187

Figure 6.4: Assumed spatial distributions of (a) permeability, and (b) skin factor. Skin factor is computed from Equation 6.2 for a cylindrical region with radius equal to 15 ft around the borehole.187

Figure 6.5: Numerically simulated spatial distributions of formation gas saturation (upper panel) and formation pressure (lower panel) prior to measurement acquisition across the synthetic multilayer reservoir model. Advancement of the gas front causes change of near-borehole gas saturation.188

Figure 6.6: Numerically simulated depth distributions of borehole (a) fluid mixture velocity, (b) pressure, (c) holdup, (d) fluid mixture density, and (d) inflow rate. Borehole measurements correspond to formation gas saturation and pressure plotted in Figure 6.5.....189

Figure 6.7: Numerically simulated depth distributions of near-borehole fluid-phase saturation and relative permeability (a) before, and (b) after gas shut-off performed in the synthetic multilayer reservoir model. Advancement of the gas front decreases oil-phase relative permeability of the top and middle layers.189

Figure 6.8: Comparison of estimated and actual values of near-borehole (a) gas saturation, (b) permeability, and (c) skin factor for the synthetic multilayer reservoir model. Dashed lines in Panel (b) identify the assumed formation far-field permeability. Conditions of immovable gas saturation in Rocks 1 and 2 cause uncertain estimation of gas saturation in those rocks. Uncertainty associated with gas saturations is additionally propagated to estimates of formation permeability, leading to uncertain estimates of skin factor (error bars shown in Panel c). Skin factor is computed based on Hawkins’s formula. Production logging interpretation for Rock 3 yields reliable estimates of formation petrophysical properties.....190

Figure 6.9: Estimated spatial distribution of gas saturation for the synthetic multilayer reservoir model. Because the displacement front associated with Rock 1 and Rock 2 has not reached the borehole, the corresponding gas saturations are interpreted as residual values. However, gas production from Rock 3 makes it possible to estimate an average gas saturation distribution for near-borehole region of that rock.191

Figure 6.10: Comparison of synthetically generated and numerically reproduced (a) fluid mixture velocity, (b) gas holdup, and (c) borehole pressure acquired across the synthetic multilayer reservoir model. The reconstructed production logs are in a good agreement when compared to synthetically generated borehole measurements.....192

Figure 6.11: Simulated formation pressure-production behavior for the synthetic reservoir model (a) before, and (a) after gas shut-off. Rock 3 shows the highest decline in oil producibility caused by the decrease of near-borehole oil-phase relative permeability for that rock. The producibility of Rock 1 remains unaffected before and after gas shut-off.....192

Figure 6.12: Numerically simulated spatial distributions for formation gas saturation (upper panel) and formation pressure (lower panel) after performing gas shut-off in Rock 3 of the synthetic reservoir model. The simulation was carried out by initializing formation gas saturation to that estimated from production logs (shown in Figure 6.9).....193

Figure 6.13: Sensitivity of the produced gas-oil ratio with respect to borehole pressure. The analysis shows that maintaining the bottom-hole pressure above 3600 psia limits gas production to approximately 4 rcf/bbl.....194

Figure 6.14: Numerically simulated depth distributions of borehole: (a) fluid mixture velocity, (b) pressure, (c) holdup, (d) fluid mixture density, and (d) inflow rate after performing the gas shut-off on Rock 3. Borehole measurements correspond to formation gas saturation and pressure plotted in Figure 6.12.194

Figure 6.15: Assumed formation (a) saturation-dependent relative permeability, (b) saturation-dependent capillary pressure, (c) permeability, and (d) total porosity for PL interpretation of the sand-shale field example. Panel (e) shows the capillary-pressure rescaling factor computed from the Leverett-J function (i.e., Equation 6.1). Presence of micropores in the reservoir abnormally increases the irreducible liquid saturation to a value close to 0.43. Error bars quantify uncertainty bounds of well-log-derived formation petrophysical properties.....200

Figure 6.16: Assumed spatial distributions of formation horizontal (upper panel) and vertical (lower panel) permeability for the sand-shale field example. The assumed permeability anisotropy is equal to 0.1. An averaging method described in Chapter 3 computes upscaled values of directional permeability for grid blocks shared by adjacent layers.....201

Figure 6.17: Borehole production measurements acquired for (a) fluid mixture velocity, (b) pressure, (c) holdup, (d) fluid mixture density, and (d) temperature. Abrupt increase of gas holdup across Unit 1 indicates a considerable gas production from that unit.....202

Figure 6.18: Convergence behavior for (a) permeability and (b) gas saturations as a function of iteration number. Panel (c) shows quadratic cost function computed for gas saturation and permeability as a function of iteration number. The refined properties are achieved after 14 iterations.....203

Figure 6.19: Comparison of the numerically simulated (a) fluid mixture velocity, (b) pressure, (c) holdup, (d) fluid mixture density, and (e) temperature with measurements for the sand-shale field model. The reconstructed production logs are in a good agreement with actual measurements. Discrepancies observed below 6360 ft MD are associated with an unaccounted standing column of water in the bottom of the borehole. Panel (f) shows fluid-phase superficial velocities on the developed gas-liquid flow-regime map (DB: dispersed-bubbly, BL: bubbly, SL: slug, and AN: annular flow regimes).204

Figure 6.20: Numerically simulated depth distributions of borehole (a) oil-phase, (b) gas-phase, and (c) overall hydrocarbon composition. Panels (d) and (e) show the associated gas and oil density, respectively. Gas production from Unit 1 decreases the molar composition of the heavy component across that unit (i.e., the brown shaded area in Panel c).205

Figure 6.21: Estimated depth distributions of near-borehole (a) fluid saturation, (b) permeability, and (c) skin factor for the sand-shale field example. Units 1 and 4 were diagnosed as gas-saturated formations with approximately 30% gas saturation. Furthermore, Panel (c) shows that Unit 1 is stimulated (with a negative skin factor equal to -1.1), while Unit 4 is highly damaged. Low fluid production from Unit 4 makes production logs across that unit highly sensitive to measurement noise, thus increasing the uncertainty bound of estimated gas saturation up to 46%. Uncertainty of gas saturation is additionally propagated to the estimated skin factor (Panel c). Furthermore, conditions of immovable gas saturation in Unit 2 cause more than 30% uncertainty for gas saturation of that unit. Interpretation of production logs across Unit 1, with a high value of far-field permeability, yields the lowest uncertainty for near-borehole gas saturation and permeability.....206

Figure 6.22: Numerically simulated (a) fluid mixture velocity, (b) pressure, (c) holdup, (d) mixture density, and (e) temperature after isolating the bottom perforated interval in the sand-shale field example. The reconstructed production logs are in acceptable agreement with actual measurements. Discrepancies observed below depth 6360 ft MD are associated with the unaccounted standing column of water in the bottom of the borehole. Panel (f) shows fluid-phase superficial velocities on the flow-regime map developed in this dissertation (DB: dispersed-bubbly, BL: bubbly, SL: slug, and AN: annular flow regimes).207

Figure 6.23: Simulated pressure-production behavior of the remaining fluid-producing units after performing gas shut-off on Unit 1. Solid lines identify the interpolation through the two data points associated with the largest borehole pressures. The highest oil producibility is associated with Unit 2 with a high permeability and a low gas saturation. Results show that lowering the borehole pressure decreases oil producibility because of the increase of near-borehole gas saturation.208

Figure 6.24: Sensitivity of the estimated near-borehole permeability to formation average pressure. Results show that 200 psi uncertainty in formation average pressure gives rise to underestimation of near-borehole permeability by a factor of 30%.208

Figure 6.25: Sensitivity of the simulated gas-holdup increment across Unit 1 and Unit 4 to the associated formation gas saturation. Because of the low permeability for Unit 4, the simulated gas holdup across that unit exhibits low sensitivity to the associated gas saturation.....209

Figure 6.26: Sensitivity of borehole (a) fluid mixture velocity, (b) gas holdup, and (c) pressure with respect to the slip model assumed for forward simulation of production logs (the simulated slip velocity is approximately 5 ft/s). Panel (d) shows the sensitivity of the estimated near-borehole gas saturation to slip velocity. The no-slip model involves up to 12% error in the estimates of gas saturation.....209

Figure 7.1: Assumed spatial distributions of formation horizontal permeability in the three-layer reservoir model penetrated by boreholes with (a) zero, (b) 45, and (c) 75 degrees of deviation angle. Interpretation of the acquired single-phase production measurements quantifies the sensitivity of PL-derived permeability to permeability anisotropy. The assumed permeability anisotropy (i.e., K_v/K_h) is equal to 0.1 for all cases.219

Figure 7.2: Comparison of the estimated and actual depth distribution of permeability for the anisotropic rock formations shown in Figure 7.1. Panel (a) shows actual horizontal and vertical permeabilities. Panels (b) and (c) compare the estimated and actual permeabilities for 45° and 75° borehole deviation angles, respectively. Inclining the borehole causes the estimates of permeability to become more sensitive to permeabilities in the vertical direction.220

Figure 7.3: Reconstructed depth distributions of oil-phase velocity (Panels a through c) and fluid pressure (Panels d through f) simulated for the anisotropic rock formations shown in Figure 7.1. There is acceptable match between numerically simulated and synthetically measured production logs.221

Figure 7.4: Assumed spatial distribution of permeability in the multilayer reservoir model ($K_v/K_h=1$). The reservoir consists of 23 thin layers penetrated by a vertical borehole. Numerical simulation of production measurements is performed using 1, 8 and, 12 petrophysical layers.223

Figure 7.5: Numerically simulated depth distributions of (a) noise-free, and (b) noisy borehole oil velocity, acquired across the multilayer reservoir model shown in Figure 7.4	224
Figure 7.6: Transient behavior of borehole pressure as a function of time for the multilayer reservoir model shown in Figure 7.4. Equation 7.2 is invoked to compute well-test-derived average permeability of all the fluid-producing layers.....	224
Figure 7.7: Comparison of the estimated and actual depth distributions of permeability for the multilayer reservoir model with (a) 1, (b) 8, and (c) 12 petrophysical layers. The estimated permeability from single-layer reservoir model matches well-test-derived permeability with approximately 4% accuracy. Refining the forward model improves the accuracy of permeability estimation. However, refined petrophysical layers involve larger uncertainty bounds into permeability estimation caused by presence of random noise in production measurements.	225
Figure 7.8: Reconstructed depth distributions of oil velocity (Panels a through c) and fluid pressure (Panels d through f) simulated for the anisotropic rock formations shown in Figure 7.1. There is acceptable match between numerically simulated and synthetically measured borehole production measurements.	226
Figure 7.9: Spatial distributions of (a) permeability ($K_v/K_h=1$), and (b) total porosity assumed for uncertainty analysis of PL interpretation across the flour-layer single-phase reservoir model.	229

Figure 7.10: Numerically simulated spatial distributions of (a) oil velocity, and (b) borehole pressure for the four-layer single-phase reservoir model. Oil velocity shows the lowest variation across Rock 4, thus making PL interpretation of that rock highly sensitive to measurement noise.....230

Figure 7.11: Reconstruction of borehole oil-phase velocity and pressure measurements contaminated with (Panels a and b) Gaussian, and (Panels d and e) skewed Gaussian noise, for the four-layer single-phase reservoir model. Panels (c) and (f) describe the associated estimation uncertainty. Because of a low fluid inflow rate across Rock 4, PL interpretation of that rock involves the largest uncertainty bounds into permeability estimation.....231

Figure 7.12: Sensitivity of the computed quadratic cost function to layer permeability in the four-layer single-phase reservoir model. Rock 1 with a large thickness exhibits a sharp minimum at the corresponding permeability (namely, 800 mD), thus making favorable conditions for permeability estimation. However, the low sensitivity of Rock 4 to its permeability makes that rock largely sensitive to measurement noise.....232

Figure 7.13: Convergence of (a) cost function, (b) 2-norm of data misfit (defined with Equations 6.4 and 6.8), and (c) permeability as a function of iteration number. The final refined properties are achieved after 11 iterations.....233

Figure 7.14: Assumed saturation-dependent (a) relative permeability, and (b) capillary pressure for uncertainty analysis of PL interpretation in the four-layer two-phase reservoir model. Panels (c) and (d) show the assumed spatial distributions of formation water saturation and relative permeability237

Figure 7.15: Numerically simulated depth distributions of borehole (a) fluid mixture velocity, (b) fluid pressure, (c) fluid holdup, (d) fluid mixture density, and (e) fluid inflow rate. Rocks 3 and 4 primarily produce hydrocarbon, while Rock 2 mainly contributes to water production. Fluid velocity, holdup, and pressure are used for the estimation of near-borehole water saturation and permeability.....238

Figure 7.16: Uncertainty bounds for estimated (a) permeability, and (b) water saturation to quantify the effects of Gaussian noise on PL interpretation of the four-layer two-phase reservoir model.239

Figure 7.17: Reconstruction of borehole (a) oil-phase velocity, and (b) pressure in the presence of 8% additive Gaussian noise for the four-layer two-phase reservoir model.239

Figure 7.18: Uncertainty bounds for estimated (a) permeability, and (b) water saturation to quantify the effects of skewed-Gaussian noise on PL interpretation of the four-layer two-phase reservoir model.240

Figure 7.19: Reconstruction of borehole (a) oil-phase velocity, and (b) pressure in the presence of 8% additive skewed-Gaussian noise for the four-layer two-phase reservoir model.....240

Figure 7.20: Quadratic cost function computed based on borehole water holdup as a function of water saturation (namely, Equation 6.5) for rock formations in the four-layer two-phase reservoir model. Conditions of immovable water saturation in Rock 2 cause a low sensitivity of fluid holdup to water saturation of that layer. Identical to single-phase flow, Rock 1 exhibits a sharp minimum at the associated water saturation. The lowest sensitivity corresponds to the thinnest layer with the lowest permeability (i.e., Rock 4).....241

Figure 7.21: Quadratic cost function computed based on borehole fluid velocity and water holdup as a function of permeability (i.e., Equation 6.4) for Rock 1 in the four-layer two-phase reservoir model. The actual near-borehole water saturation of Rock 1 is 0.05. Overestimation of water saturation causes (i) shifting the estimated permeability toward higher values, and (ii) lowering the sensitivity of borehole measurements with respect to permeability.....241

Figure 7.22: Convergence of (a) permeability, (b) water saturation, and (c) 2-norm of data misfit (defined with Equations 6.4, 6.6, and 6.8) in the presence of 8% additive skewed-Gaussian noise. The final refined properties are achieved after 27 iterations242

Figure 7.23: Spatial distributions of (a) permeability, (b) porosity, and (c) fluid-phase relative permeability (upper panel) and capillary pressure (lower panel) assumed for time-lapse interpretation of the synthetic example.....245

Figure 7.24: Assumed spatial distributions of permeability, and the associated skin factor for (Panels a and b) first, (Panels c and d) second, and (Panels e and f) third time lapses. Implementation of near-borehole formation damages is carried out by modifying permeability of a cylindrical region around the borehole with radius equal to 15 ft.....248

Figure 7.25: Spatial distributions of (a) water saturation, (b) near-borehole fluid saturation, and (c) formation pressure numerically simulated for the first time lapse. Advancement of the water front from the aquifer gives rise to a gradual change of near-borehole water saturation. Acquisition and interpretation of two-phase production measurements attempts to estimate near-borehole formation damage and water saturation.....249

Figure 7.26: Spatial distributions of (a) water saturation, (b) near-borehole fluid saturation, and (c) formation pressure numerically simulated for the second time lapse. At this time lapse, the water front within Rocks 1 and 2 has reached the borehole, while Rock 3 still mainly produces oil phase.250

Figure 7.27: Spatial distributions of (a) water saturation, (b) near-borehole fluid saturation, and (c) formation pressure numerically simulated for the third time lapse. At this time lapse, all rock formations are influenced by the immiscible displacement of oil phase.251

Figure 7.28: Spatial distributions of borehole (a) fluid mixture velocity, (b) fluid pressure, (c) fluid mixture density, (d) fluid holdup, (e) droplet diameter, and (f) fluid flow regime, numerically simulated for the first time lapse. Lower layer is mainly producing water where the associated borehole water holdup across that layer is approximately 1. Hydrocarbon production from Rocks 2 and 3 increases oil holdup that changes borehole fluid flow regime.....252

Figure 7.29: Spatial distributions of borehole (a) fluid mixture velocity, (b) fluid pressure, (c) fluid mixture density, (d) fluid holdup, (e) droplet diameter, and (f) fluid flow regime, numerically simulated for the second time lapse. Advancement of the water front causes borehole water holdup to increase from the bottom to the top. Because of higher water holdups, the estimated fluid flow regime is mainly water-dominant bubbly flow regime. Variations of fluid mixture velocity and fluid holdup across each layer correspond to near-borehole water saturation and permeability.....253

Figure 7.30: Spatial distributions of borehole (a) fluid mixture velocity, (b) fluid pressure, (c) fluid mixture density, (d) fluid holdup, (e) droplet diameter, and (f) fluid flow regime, numerically simulated for the third time lapse. Incremental water production results in higher water production. At this time lapse, flow regime for the entire borehole flowing domain is water-dominant bubbly flow regime.254

Figure 7.31: Comparison of the estimated and actual values of (a) permeability, and (b) water saturation for the first time lapse. Panel (c) shows the estimated spatial distribution of formation water saturation. The reconstructed borehole fluid mixture velocity (Panel d), fluid pressure (Panel e), and oil-phase holdup (Panel f) show an acceptable match when compared to the corresponding synthetically acquired logs.255

Figure 7.32: Comparison of the estimated and actual values of (a) permeability, and (b) water saturation for the second time lapse. Panel (c) shows the estimated spatial distribution of formation water saturation. Panel (d) compares the estimated near-borehole formation damage with the corresponding actual values. Formation damage was computed by comparing near-borehole and far-field permeabilities using Equation 7.4. The reconstructed borehole fluid mixture velocity (Panel e), fluid pressure (Panel f), and oil-phase holdup (Panel g) show an acceptable match when compared to the corresponding synthetically acquired logs.256

Figure 7.33: Comparison of the estimated and actual values of (a) permeability, and (b) water saturation for the third time lapse. Panel (c) shows the estimated spatial distribution of formation water saturation. Panel (d) compares the estimated near-borehole formation damage with the corresponding actual values. The interpretation algorithm assumes the availability of far-field permeability from PL interpretation of the first time lapse. The reconstructed borehole fluid mixture velocity (Panel e), fluid pressure (Panel f), and oil-phase holdup (Panel g) show an acceptable match when compared to the corresponding synthetically acquired logs.....257

Figure 7.34: Assumed saturation-dependent (a) capillary pressure, and (b) relative permeabilities for PL interpretation of the sand-shale field example. Panel (c) shows the rescaled values of capillary pressure computed (at the irreducible water saturation) from the Leverett-J function.....259

Figure 7.35: Spatial distributions of formation (a) porosity, and (b) far-field permeability derived from well-log interpretation of the sand-shale field example. The highlighted intervals identify perforations. K_h and K_v are horizontal and vertical permeabilities, respectively, with a permeability anisotropy equal to 0.1.....259

Figure 7.36: Borehole production measurements for (a) fluid mixture velocity, (b) pressure, (c) fluid holdup, (d) temperature, and (e) oil-phase density acquired from the sand-shale reservoir model.....263

Figure 7.37: Comparison of the estimated and actual values of (a) permeability, and (b) water saturation for the sand-shale field example. Panel (c) compares the estimated near-borehole formation damage (computed from Equation 7.4) with the corresponding actual values. Error bars are calculated by adding small perturbation to inverted properties associated with each layer. Presence of measurement noise across Interval C (as a low-permeability layer) widens uncertainty bounds of the associated inverted properties. In addition, Interval A is at immovable fluid saturation that lowers the sensitivity of production logs to fluid-phase relative permeability, thus increasing estimation uncertainty for that layer. However, estimated permeability and skin factor for Interval B (as a high-permeability layer) are within 23% and 21% accuracy.264

Figure 7.38: Spatial distributions of (a) water saturation, and (b) permeability estimated from PL interpretation of the sand-shale field example. Panel (c) shows the simulated formation pressure distribution. Production logging interpretation is performed by assuming six spatial windows for water saturation, and seven for permeability. Coupled flow algorithm assumes that water saturation remains unchanged radially away from the borehole.265

Figure 7.39: Comparison of the actual and reconstructed borehole (a) fluid mixture velocity (b), fluid pressure, and (c) oil-phase holdup for PL interpretation of the sand-shale field example. Panels (d) through (f) show the simulated fluid inflow rate, oil-droplet diameter, and fluid mixture density.266

Figure 7.40: Borehole production measurements for (a) fluid mixture velocity, (b) fluid pressure, (c) fluid holdup, (d) fluid temperature, and (e) oil-phase density after performing water shut-off on the lowermost interval of the sand-shale field example. The remedial operation gives rise to 60 psi decrease of borehole pressure, and a 2.3% decrease of downhole water holdup.....267

Figure 7.41: Sensitivity of the estimated near-borehole permeability to (a) formation average pressure, and (b) permeability anisotropy for PL interpretation of the sand-shale field example. Uncertainty of the assumed formation pressure is one of the most detrimental parameters that decrease the reliability of estimated layer permeability. On the other hand, permeability estimates are nearly independent of the assumed permeability anisotropy.....270

Figure 7.42: Sensitivity of the estimated (a) near-borehole permeability, and (b) skin factor to the assumed radius of damaged region for PL interpretation of the sand-shale field example. When the damaged region becomes thinner, contrasts between near-borehole and far-field permeabilities become larger. On the other hand, a considerable increase of damaged radius lowers the sensitivity of borehole measurements to far-field permeability. However, the estimated skin factor remains independent of the radius of near-borehole region.....270

Figure 7.43: Sensitivity of the estimated (a) permeability, and (b) water saturation to oil-phase end-point relative permeability for PL interpretation of the sand-shale field example. Estimates of permeability and water saturation exhibit the lowest sensitivity to oil-phase end-point relative permeability of the unit with the highest water saturation (i.e., the unit centered at 8150 ft MD).271

Figure 8.1: Developed iterative workflow to estimate near-borehole fluid-phase relative permeability from inversion of borehole production measurements. Within each minimization loop, end-points of fluid-phase relative permeability are estimated by postulating linear interpolation between water saturation and relative permeability ..283

Figure 8.2: Assumed saturation-dependent (a) relative permeability and (b) capillary pressure for the single-layer reservoir model.284

Figure 8.3: Simulated spatial distributions of water saturation (upper panel) and pressure (lower panel) prior to measurement acquisition across the single-layer reservoir model.285

Figure 8.4: Simulated near-borehole fluid-phase (a) saturation, (b) relative permeability, and (c) fluid inflow rate for the single-layer reservoir model.286

Figure 8.5: Simulated borehole (a) fluid mixture velocity, (b) fluid-phase holdup, and (c) fluid pressure for the single-layer reservoir model.....286

Figure 8.6: Reconstructed production measurements for (a) velocity, (b) holdup, and (c) pressure associated with 4-layer forward reservoir model to estimate relative permeability of the single-layer reservoir model.287

Figure 8.7: Reconstructed production measurements for (a) velocity, (b) holdup, and (c) pressure associated with 16-layer forward reservoir model to estimate relative permeability of the single-layer reservoir model.	287
Figure 8.8: Comparison of the estimated fluid-phase relative permeability with the corresponding actual values associated with (a) 4-layer, (b) 8-layer, (c) 16-layer, and (d) 32-layer forward reservoir models for the estimation of relative permeability of the single-layer reservoir model.	288
Figure 8.9: Assumed saturation-dependent (a) relative permeability and (b) capillary pressure for the three-layer reservoir model.	290
Figure 8.10: Simulated spatial distributions of water saturation (upper panel) and pressure (lower panel) prior to measurements acquisition in the three-layer reservoir model.	291
Figure 8.11: Simulated spatial distributions of borehole (a) fluid-phase velocity, (b) fluid-phase holdup, (c) fluid pressure, (d) fluid mixture density, (e) droplet diameter, and (f) fluid-phase inflow rate for the three-layer reservoir model.	292
Figure 8.12: Uncertainty analysis for (a) oil-phase and (b) water-phase relative permeabilities due to the uncertainty associated with porosity of Rock 2.	293
Figure 8.13: Uncertainty analysis for (a) oil-phase and (b) water-phase relative permeabilities due to the uncertainty associated with permeability of Rock 3.	293

Figure 8.14: Uncertainty analysis for (a) oil-phase and (b) water-phase relative permeabilities due to the uncertainty associated with average pressure of Rock 2.	294
Figure 8.15: Assumed relative permeability curves in near-borehole region of the multilayer reservoir model for time-lapse PL analysis.	298
Figure 8.16: Numerically simulated spatial distributions of formation pressure (right column), and water saturation (left column) for time-lapse analysis of the multilayer reservoir model.	299
Figure 8.17: Spatial distributions of borehole (a) fluid mixture velocity, (b) oil-phase holdup, and (c) fluid pressure simulated for time-lapse analysis of the multilayer reservoir model.	300
Figure 8.18: Spatial distributions of formation (a) oil-phase, and (b) water-phase incremental inflow rate simulated for time-lapse analysis of the multilayer reservoir model.	300
Figure 8.19: Comparison of the estimated and actual fluid-phase relative permeability performed for (a) first, (b) second, (c) third, and (d) fifth time lapses for the multilayer reservoir model.	301
Figure 8.20: Uncertainty associated with the estimated fluid-phase relative permeability for first (Panels a and b) and last (Panels c and d) time lapses in time-lapse analysis of the multilayer reservoir model.	302

Chapter 1: Introduction

This chapter describes objectives of the dissertation, briefly reviews the literature related to simulation and interpretation of production logging (PL) measurements, and summarizes all the subsequent chapters.

1.1 PROBLEM STATEMENT

Acquisition of downhole production measurements is increasingly being used to evaluate single- and multi-phase fluid flow conditions in the borehole. Evaluation of downhole flowing conditions enables petrophysicists to (i) infer the type, rate, and direction of fluid phases being produced from (or injected into) various fluid-producing depth intervals (Connolly, 1965), (ii) diagnose fluid movement in vicinity of the borehole, (iii) quantify reservoir performance, and (iv) evaluate workover remedial operations (Hill, 1990). In multiphase flowing conditions, because of density contrast, the lighter fluid phase tends to move at a faster velocity compared to the heavier phase. Discrepancies between fluid-phase velocities give rise to accumulation of the heavier fluid phase, thus resulting in complex fluid flow regimes in the borehole (Hill and Oolman, 1982). In vertical boreholes, the spatial distribution of dispersed fluid phase about the borehole axis is uniform. However, inclining the borehole from the vertical direction causes an eccentric distribution of fluid phases across the borehole where the lighter fluid phase moves closer to the upper wall (Hasan and Kabir, 2002). Reliable evaluation of downhole production measurements requires the development of a method

which accurately simulates fluid-phase properties such as velocity, pressure, and holdup in vertical and deviated flowing systems.

Measurements acquired with borehole production logging tools (PLTs) provide depth distributions of borehole fluid-phase properties (e.g., velocity, pressure, holdup, density, and temperature) across fluid-producing rock formations (Hill, 1990). Properties of interest in production logging interpretation, however, are dynamic petrophysical properties of formations such as near-borehole permeability, saturation-dependent relative permeability, and fluid-phase saturation. Conventionally, formation petrophysical properties were associated with borehole fluid-phase properties via simplified analytical expressions (e.g., simplified Darcy's equation) by neglecting various flow regimes taking place in both borehole and formations. The applicability of traditional production logging interpretation methods is limited to single-phase or homogeneous multiphase flowing systems with vertical boreholes (Sullivan, 2007; Rey et al., 2009). However, inference of formation petrophysical properties in complex multiphase flowing conditions requires simultaneous consideration of fluid flow both in the borehole and porous media. The coupled simulation of borehole and formation fluid flow should enable quantifying the sensitivity of borehole measurements to near-borehole petrophysical properties, diagnosing formation petrophysical properties from production logs, and evaluating reservoir inflow performance.

Conventional methods to simulate and interpret borehole production measurements construct borehole fluid flow models decoupled from the physics of fluid flow in reservoir rocks. Decoupled fluid flow simulation assumes static boundary conditions associated with perforated depth intervals (e.g., static fluid-phase velocity and holdup) to numerically account for productivity (injectivity) of fluid-producing rock formations. Interpretation of borehole measurements in this approach is carried out by

modifying those boundary conditions to progressively match borehole production logs. Even though conventional PL interpretation methods enable the identification of fluid type and quantification of fluid inflow rates, those methods do not quantify formation petrophysical properties. A possible improvement for decoupled PL interpretation is to incorporate available analytical equations (e.g., Darcy's equation) to associate the estimated fluid inflow rates with layer properties (namely, permeability). However, incorporation of analytical equations limits the reliability of estimated petrophysical properties to simplified reservoir models without accounting for variations of formation properties over time (e.g., pressure, permeability, and fluid saturation). A comprehensive approach to interpret borehole production measurements is dynamic linkage of a reservoir flow simulator to borehole fluid flow model that allows inference of formation petrophysical properties by matching production logs. Even though the latter approach involves more computational resources for numerical implementation, its substantial advantage is the simulation of dynamic (two-way) coupling between borehole and formation flowing domains.

An example of two-way coupling arises when simulating water backflow taking place in gas-water producing systems. Because of significant fluid-phase density contrasts, water phase as the heavier fluid phase tends to flow downward, thus loading the borehole domain. Therefore, it is critical for production engineers to maintain the bottom-hole pressure within an optimal range that prevents the water phase from falling downward. Analysis of water loading phenomenon decoupled from the physics of fluid flow in porous media makes it possible to only estimate a minimum gas velocity to lift the produced water, without a quantitative description of borehole and formation pressures. However, when performed in coupled mode, water loading simulation helps to quantify the effects of (*i*) formation properties (e.g., pressure, permeability, and fluid-

phase relative permeability), (ii) borehole properties (e.g., pressure and deviation angle), and (iii) fluid-phase properties (namely, density and viscosity), on the inception and duration of water loading. As shown in Figure 1.1, for a two-layer reservoir model (with water and gas densities equal to 1 and 0.234 g/cc, respectively, water and gas viscosities equal to 1 and 0.031 cp, respectively, and formation permeability equal to 300 mD), coupled fluid flow simulation determines a minimum pressure drawdown (equal to 1100 psi) to maintain gas-phase velocity above the critical (lift) velocity. In addition, results indicate that, because of higher slip velocities in deviated boreholes, pressure drawdowns required to prevent water backflow in deviated systems are higher than those in equivalent vertical flowing systems. This example shows that simplified analytical models can only account for one-way (i.e., formation-to-borehole) coupling in case of no (or slow) variations of formation properties over time. However, rapid variations of formation properties with two-way coupling requires a dynamic borehole-formation fluid flow model to accurately simulate both borehole and near-borehole fluid-phase properties.

Comparison of production logs in time-lapse mode conventionally helps petrophysicists to detect the advancement of fluid contacts in the near-borehole region. Without inclusion of a dynamic reservoir model, conventional time-lapse interpretation remains limited to describing time variations of fluid inflow rates produced from various fluid-producing layers. However, fluid movement in the near-borehole region causes the alteration of formation properties (e.g., permeability and fluid saturation) that eventually changes borehole inflow performance. Analysis of production logs acquired in time-lapse mode, if performed using a coupled fluid flow simulator, should therefore enable the quantification of time variations of near-borehole petrophysical properties. This new time-lapse interpretation approach, integrated with analyses of surface measurements

(e.g., production decline analysis), provides a method to investigate variations of rock pressure-production with time.

Commingle production of several fluid-producing rock formations through a single borehole commonly results in the phenomenon of differential depletion (Cortez and Corbett, 2005). Acquisition of production measurements across a differentially-depleted multilayer reservoir is considerably influenced by fluid cross-flow through the borehole where reservoir fluids flow from high- to low-pressure intervals. Under single-phase conditions, development of borehole cross-flow is governed by borehole pressure, formation near-borehole permeability, and formation average pressure (Frooqnia et al., 2011). However, the presence of a second fluid phase involves interfacial buoyant and drag forces as additional governing factors in developing borehole cross-flow. Under two-phase flowing conditions, borehole cross-flow is regarded as a transient phenomenon where volumetric fraction and relative movement of borehole fluid phases vary with time. Therefore, a comprehensive study of borehole cross-flow requires the development of a model that simulates the transient behavior of borehole and formation fluid flows in a coupled mode. The developed fluid flow model is used to quantify the effects of formation, borehole, and fluid-phase properties on measurements acquired with PLTs in the presence of cross-flow.

From early to late stages of reservoir development, production logging is regarded as one of a few diagnostic methods available to investigate and quantify pressure-production behavior of fluid-producing rock formations. Preceding analyses of PLT measurements (e.g., Sullivan et al., 2006; Rey et al., 2009) were based on the use of idealized reservoir models with the assumption of single-phase vertical flowing systems. However, fluid movement in porous media results in simultaneous production of gas or water throughout the life of the borehole. Neglecting the presence of gas or water in the

borehole and vicinity of the borehole introduces errors to the estimated petrophysical properties from PLT measurements. Reliable estimation of near-borehole petrophysical properties therefore requires (i) developing a coupled borehole-formation multiphase fluid flow model, and (ii) interfacing the developed fluid flow model to an inversion algorithm. The inversion algorithm should estimate near-borehole dynamic petrophysical properties (e.g., near-borehole permeability and fluid-phase saturation) in order to explicitly match borehole production measurements.

The one-dimensional (1D) nature of production measurements (as opposed to conventional pressure-transient measurements) makes it possible to investigate the inflow performance of individual rock formation when producing in commingled mode (Hill, 1990). Therefore, the use of a coupled borehole-formation fluid flow model in PL interpretation can detect and quantify the rock formations exhibiting low productivity or those contributing unwanted fluid production. Furthermore, construction of a near-borehole fluid flow model should enable evaluating and predicting the performance of possible workover remedial operations such as gas or water shut-off.

To the best of the author's knowledge, thus far there has been no attempt to combine the physics of fluid flow in the borehole and the formation in order to numerically simulate and interpret measurements acquired with PLTs. The central objectives of this dissertation are (i) to develop a borehole compositional fluid flow model which accurately simulates 1D spatial distribution of fluid-phase properties across fluid-producing rock formations, (ii) to couple the developed borehole fluid flow model to a three-dimensional (3D), compositional, reservoir simulator (developed by Pour, 2011), and (iii) to develop an inversion algorithm that enables the inference of near-borehole dynamic petrophysical properties from production measurements. The developed method will be invoked to analyze single-phase and two-phase (oil-water, gas-

water, and oil-gas) production measurements acquired in vertical and deviated boreholes. Formation petrophysical properties considered for the interpretation process include permeability, fluid-phase saturation, and fluid-phase relative permeability.

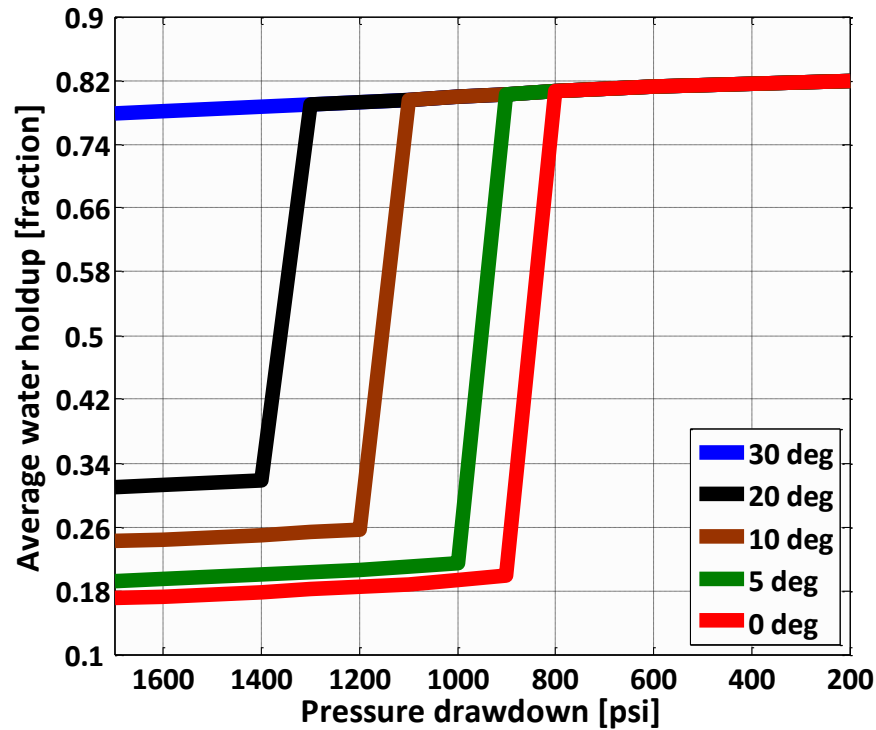


Figure 1.1: Numerically simulated average water holdup as a function of applied pressure drawdown and well inclination. Each step represents the minimum pressure drawdown required to prevent water phase from loading the borehole flow domain. This graph shows that the required pressure drawdown increases with increasing borehole inclination angle.

1.2 REVIEW OF RELEVANT LITERATURE

Estimation of near-borehole petrophysical properties encompasses the following topics: (i) modeling multiphase fluid flow in the borehole, (ii) identifying fluid flow patterns and incorporating flow-pattern transition into the borehole fluid flow model, and

(iii) linking borehole measurements to formation petrophysical properties. This section briefly reviews the relevant theoretical and experimental contributions available in the literature.

1.2.1 Borehole Fluid Flow Modeling

The simplest models to estimate wellbore fluid properties are homogeneous models. Homogeneous models replace multiphase fluid with a single-phase fluid whose properties are represented by effective fluid mixture properties (Sharma et al., 1996; Holmes et al., 1998). Applying single-phase fluid flow equations only to fluid mixture significantly simplifies the numerical implementation of homogeneous models. However, in case of large discrepancies between fluid-phase properties (e.g., density of various fluid phases), fluid homogenization gives rise to inaccurately simulated properties of individual fluid phases. As a modification to homogeneous models, Zuber and Findlay (1965) introduced the drift-flux model. Similar to homogeneous models, the drift-flux models apply single set of the conservation equations to fluid mixture, and neglect interfacial momentum transfer. In contrast, these models make use of empirical correlations to describe fluid-phase slip velocity. Parameters associated with those empirical correlations have been studied by many researches. Among those, through experimental studies of oil-water flowing systems, Hasan and Kabir (1990 and 1999), and Flores et al. (1998) observed a dependency between slip velocity and fluid holdup, and developed holdup-dependent drift-flux parameters. In addition, Shi et al. (2005) formulated flow-regime-dependent drift-flux parameters; they performed extended experimental studies to compute the model parameters valid for both oil-water and gas-liquid systems.

As opposed to the abovementioned models, the two-fluid model, developed by Ishii (1975), applies separate conservation equations to each fluid phase, thereby making it possible to simulate more complex fluid flow behavior in the wellbore. However, two-fluid models require closure relationships to describe mass and momentum transfer between various fluid phases. Truesdell and Toupin (1960), Drew and Lahey (1979), and Drew and Passman (1999) developed general procedures to construct physically-consistent closure relationships that ensure the principles of well-posedness, equipresence, and objectivity (Kleinstreuer, 2003). In addition, because of a larger number of dependent variables involved with two-fluid models compared to homogeneous models, longer computational times are required for convergence, and advanced numerical treatments should be implemented to obtain a reliable solution. Among those, Spalding (1980) developed the inter-phase slip algorithm (IPSA) with the idea that only a few grid blocks require an implicit solution while the remaining ones can be treated explicitly. Kolev (2007) described a segregated algorithm where model equations associated with each fluid phase were solved sequentially by making an explicit assumption for properties of the second fluid phase. In contrast, Prosperetti and Tryggvason (2007) and Yeoh and Tu (2010) documented implicit algorithms to simultaneously compute fluid-phase properties such as velocity, holdup, and pressure.

One-dimensional versions of two-fluid formulation have been applied in the petroleum industry to simulate multiphase fluid flow in boreholes. Bendiksen et al. (1991) developed a dynamic two-fluid model that simulated gas and liquid properties in pipes. Their model assumed simultaneous flow of gas phase, liquid droplets, and a liquid film attached to the borehole wall. They applied separate conservation equations to each fluid phase, and invoked empirical correlations to identify flow-regime transitions. Stone et al. (1989) developed a one-dimensional, black-oil, thermal, two-fluid model to

accurately simulate the process of steam injection in long horizontal wells. Their model assumed the emulsion of oil and water as a single liquid phase, and applied separate conservation equations to each fluid phase. Almehaideb et al. (1989) developed an isothermal, one-dimensional borehole flow model based on the two-fluid method. Their model investigated the effect of phase segregation in simultaneous production of the gas and water phases. Pourafshary (2007) and Pourafshary et al. (2009) solved the one-dimensional two-fluid conservation equations to develop a transient compositional borehole fluid flow model. His model was applied to vertical boreholes to simulate phase segregation, and to quantify the effect of liquid backflow on pressure-transient analyses. Shirdel et al. (2012) and Shirdel (2013) extended Pourafshary's (2007) two-fluid model to deviated and horizontal boreholes. Shirdel's (2013) borehole flow algorithm assumed a one-dimensional compositional thermal model to investigate asphaltene and wax precipitation in the borehole.

1.2.2 Borehole-Formation Coupling

Interfacing borehole and formation fluid flow models has been proposed to (i) enforce a realistic pressure boundary condition for the simulation of formation fluid flow phenomena (Livescu et al., 2009), (ii) accurately simulate the performance of enhanced oil recovery processes such as steam flooding in horizontal boreholes (Stone et al., 1989), (iii) accurately predict borehole and formation fluid-phase properties during the transient stage of fluid production (Shirdel et al., 2012), (vi) account for the effects of phase segregation on pressure-transient measurements (Pourafshary et al., 2009), and (v) accurately simulate measurements acquired with PLTs (Frooqnia et al., 2011).

Sequential and implicit methods have been developed for numerical implementation of borehole-formation coupling. Borehole conservation equations in

sequential methods are solved under an explicit assumption for formation fluid-phase properties. Pourafshary et al. (2009), Shirdel et al. (2012), Frooqnia et al. (2011), and Frooqnia et al. (2013) have adopted various versions of the sequential method where additional source terms are explicitly incorporated into the borehole conservation equations to account for the mass influx from fluid-producing rock formations. By contrast, implicit methods simultaneously solve conservation equations associated with both borehole and formation flowing domains (Winterfeld, 1989; Almehaideb et al., 1989; Stone et al., 1989; Livescu et al., 2009). Because of simultaneous treatment of borehole and formation equations, implicit methods require powerful computational resources and special numerical treatments to ensure stability (Bahonar et al., 2011).

In summary, considering numerical stability, efficiency, and implementation simplicity for the applications addressed in this dissertation, I chose a two-fluid formulation based on the IPSA discretization scheme for borehole modeling. The borehole-formation coupling was subsequently carried out based on the sequential approach.

1.2.3 Flow-Regime Identification

The geometrical configuration of fluid phases in the borehole depends on fluid-phase properties such as velocity and volume fraction. Transition from one flow regime to another takes place when fluid-phase properties change with respect to time or space. Sommerfeld et al. (2003) associated the development of slug flow regime to turbulent-induced random collision of bubbles causing an increase of the local volume fraction of the corresponding fluid phase. In deviated boreholes, because of buoyancy effects, bubbles preferentially move within an eccentric spatial distribution, thus leading to an increase in the rate of bubble random collisions. A reliable identification of fluid flow

regimes requires physically-consistent transition criteria validated against laboratory measurements.

Taitel et al. (1980) modeled physical mechanisms underlying different flow-regime transitions to develop transition criteria in vertical gas-liquid systems. Their method was applicable to a wide range of fluid-phase and borehole properties. Barnea (1985) proposed a method to simulate transition from dispersed-bubbly to bubbly flow regimes. Her approach was based on computing the maximum diameter of stable bubbles in dispersed flow regime that prevented bubbles from agglomeration or deformation. Hasan and Kabir (1988a) developed a mechanistic approach to describe the transition between several flow regimes in vertical boreholes. Their method used drift-flux modeling of gas-liquid flow in vertical boreholes to formulate the transition from bubbly to slug flow regimes. Later, Hasan and Kabir (1988b) adopted a similar approach to mechanistically model the flow-regime transition in deviated boreholes. Ansari et al. (1994) presented a comprehensive mechanistic method to model interfacial momentum transfer associated with several flow regimes for two-phase upward systems. Additionally, Kaya (1999) extended Ansari et al.'s (1994) mechanistic model to deviated boreholes.

In closing, this dissertation applied the flow-regime transition criteria developed by Hasan and Kabir (1988a) for vertical, and Hasan and Kabir (1988b) for deviated boreholes to take advantage of their efficiency and numerical stability.

1.2.4 Interpretation of Production Logs

The majority of documented technical contributions associated with PL interpretation have been focused to estimating borehole flowing conditions with limited attempts to incorporate the physics of fluid flow in porous and permeable rock

formations. Boyle et al. (1996) used PLT measurements to quantify water and gas entry zones in vertical and deviated boreholes. They introduced new PL sensors that accurately measured fluid-phase holdup in the presence of high slip velocity between fluid phases. Elshahawi and Mostafa (2002) showed the application of PLTs in flow profiling of highly-deviated boreholes. Their method accounted for flow-regime change in the borehole and its effects on fluid-phase holdup measurements. Schnorr (1996) documented field examples of successful PL interpretation to estimate formation average pressure and layer productivity index. Zett et al. (2011) applied PLT measurements to assess the performance of a newly-perforated interval in a mature reservoir. By acquiring production logs before and after an add-perforation operation, they verified a successful improvement in oil production via comparing interpreted fluid flow profiles before and after the remedial operation. Gysen et al. (2010) developed a method to combine raw measurements acquired with multiple PL sensors to estimate the flow profile in highly-deviated boreholes. Their probabilistic method reduced uncertainties involved with raw production measurements, thereby improving the reliability of PL interpretation.

There are documented studies that associate PLT measurements acquired from single-phase flowing systems to near-borehole permeability. Under the assumption of stabilized conditions, Rey et al. (2009) related the slope of borehole fluid-phase velocity to fluid-phase inflow rate, and developed a method to estimate formation permeability. Sullivan et al. (2006) described a method to estimate apparent permeability of a multilayer formation. The formation consisted of three main producing layers behaving as three different pressure compartments. They implemented Darcy's equation to separately estimate the apparent permeability of each fluid-producing layer. Estimated permeabilities were subsequently used to improve the reservoir geological model leading to an accurate simulation of pressure responses during inter-well pulse testing (Sullivan,

2007). In a highly heterogeneous reservoir, Abdel-Ghani et al. (2011) conditioned a reservoir dynamic model with respect to PL-derived permeability to successfully match the long-term production history of the reservoir.

Interfacing borehole and formation fluid flow models to specifically simulate production logs was first introduced by Frooqnia et al. (2011). In Frooqnia et al.'s (2011) work, a coupled wellbore-reservoir fluid flow model was developed to estimate near-borehole permeability from numerical simulation and inversion of single-phase production logs. The interpretation method was successfully applied to a field example to estimate depth variations of permeability from flowing PL measurements. Subsequently, the estimated formation permeability was verified by accurately simulating borehole cross-flow observed during shut-in PL passes. Frooqnia et al. (2013) extended their previous work to estimate saturation-dependent formation relative permeability from the integration of production logs acquired in time-lapse mode. They showed that depending on the effective water saturation window monitored in the borehole, reconstruction of a portion or the complete curve of fluid-phase relative permeability was possible.

1.3 RESEARCH OBJECTIVES

The main objective of this dissertation is the development of a compositional coupled borehole-formation fluid flow model to enable the estimation of near-borehole petrophysical properties from measurements acquired with PLTs. The simulator is based on the following assumptions:

- Formation and borehole are modeled under isothermal conditions.
- Borehole fluid phases are modelled as inter-penetrating continua.
- Borehole fluid phases share the same pressure field.

- Local thermodynamic equilibrium is valid.
- All components in a fluid phase flow with the same velocity equal to that of their carrier fluid phase.
- Mass transfer is only permitted between gas and oil phases.
- Mass influx from fluid-producing rock formations transfers no momentum into the borehole.
- Flow regimes identified for fluid flow in pipes are valid for borehole multiphase flow modeling.
- Flow regimes are valid for boreholes with deviation angles equal to or less than 70 degrees.

The developed method should be capable of

- Simulating oil-gas, oil-water, gas-water fluid flow in vertical and deviated boreholes.
- Simulating production measurements in the presence of borehole fluid cross-flow.
- Simulating liquid backflow in the presence of gas.
- Estimating near-borehole permeability and skin factor using borehole production measurements acquired under single-phase conditions.
- Estimating near-borehole permeability and water saturation using borehole production measurements acquired in oil-water flowing systems.
- Estimating near-borehole permeability and gas saturation using borehole production measurements acquired in oil-gas flowing systems.

- Quantifying the performance of water and gas shut-off operations in multilayer reservoirs.
- Estimating fluid-phase relative permeability using oil-water production measurements acquired in time-lapse mode.

1.4 REVIEW OF CHAPTERS

This dissertation describes the development and application of a 1D compositional wellbore fluid flow model coupled with a 3D compositional reservoir fluid flow model.

In Chapter 2, I describe the physical model formulated for simulation of borehole multiphase fluid flow. This chapter describes *(i)* the mass and momentum conservation equations, *(ii)* constitutive equations invoked for computing interfacial mass and momentum transfers, *(iii)* assumptions and method adopted for flow-regime identification, and *(vi)* the sequential method developed for interfacing borehole and formation fluid flow models. Chapter 3 presents *(i)* a detailed description of the discretized mass and momentum conservation equations, *(ii)* numerical implementation of the inter-phase slip algorithm to solve borehole fluid-phase properties, *(vi)* definition of boundary conditions in the borehole flow domain, and *(v)* the method developed for automatic time-step controlling in the borehole flowing domain.

Chapter 4 conducts verification examples using analytical, experimental, and field examples to investigate the accuracy and reliability of the developed borehole fluid flow model. Verification tests include several cases of oil-water, gas-water, and gas-oil fluid flow simulations in vertical and deviated boreholes. Chapter 5 studies the effect of differential depletion on measurements acquired with PLTs. This chapter constructs

several synthetic multilayer reservoir models to quantify the effect of borehole and formation properties on two-phase borehole cross-flow. Chapter 6 describes the development of a PL inversion algorithm to estimate near-borehole formation petrophysical properties. This chapter quantifies the effect of gas production on pressure-production behavior of multilayer rock formations. Production measurements acquired in a laminated sand-shale field example are next analyzed to evaluate the performance of a gas shut-off operation. Chapter 7 discusses the inversion of single-phase and two-phase production logs to estimate near-borehole permeability and fluid-phase saturation. Chapter 8 develops a method to estimate near-borehole fluid-phase relative permeability from inversion of production logs in acquired time-lapse mode. In closing, Chapter 9 summarizes the conclusions stemming from this dissertation, and provides recommendations for future studies.

Chapter 2: Borehole Fluid Flow Modeling

Mathematical model and constitutive equations associated with the development of borehole two-phase fluid flow are formulated in this chapter. I present a detailed description of two-fluid formulation adopted in the dissertation for simulating borehole fluid-phase properties. Flow-regime transitions are next described for cases of liquid-liquid and gas-liquid flowing systems. Additionally, I describe an explicit sequential method to interface separate borehole and formation fluid flow equations.

2.1 INTRODUCTION

The borehole fluid flow model developed in this dissertation simulates time- and spaced-averaged fluid-phase velocity, pressure, density, and holdup across fluid-producing rock formations. I neglect variations of fluid properties in the radial and azimuthal directions to derive a one-dimensional (1D) version of two-fluid formulation in cylindrical coordinates. Dispersed fluid phase is considered as spherical gas bubbles or liquid droplets with variable diameters. When deriving borehole fluid flow equations, fluid phases are assumed to share a single pressure field, thereby neglecting interfacial tension effects. No mass transfer is modeled between the water and hydrocarbon phases, however, mass transfer is permitted between the gas and oil phases. Assuming local thermodynamic equilibrium conditions, an equation-of-state compositional thermodynamic model is invoked to dynamically update density and viscosity of hydrocarbon phases. Even though fluid flow equations are solved under an isothermal assumption, any

a-priori knowledge about borehole temperature can be incorporated into the compositional model to accurately simulate temperature effects on hydrocarbon-phase density and viscosity. In the derivation of momentum conservation equations, continuous fluid phase is assumed to be the only phase in contact with borehole wall, thereby applying wall friction effects only to that phase. In addition, I assume drag and buoyant forces as primary sources for interfacial momentum transfer, and discard negligible interfacial forces such as lift and virtual mass. Moreover, the developed flow model neglects friction effects caused by fluid influx from fluid-producing rock formations. Borehole-formation coupling is next carried out by incorporating additional source terms into the mass conservation equations. The developed sequential coupling method dynamically updates the associated mass source terms to account for variations of fluid producibility from rock formations.

2.2 BOREHOLE FLUID FLOW EQUATIONS

When modeling borehole fluid flow, each fluid phase is considered as a continuum exchanging mass and momentum with both the second phase and the borehole wall (Ishii and Hibiki, 2011). This section describes a general form of two-fluid formulation, and adopts the 1D version of this formulation to simulate borehole fluid-phase properties in vertical and deviated flowing systems.

2.2.1 Generic Form of the Two-Fluid Model

The local instantaneous conservation equations for mass and momentum can be applied for an infinitesimally small volume of multiphase fluid at a given time. This approach results in a complex system of equations describing multiphase fluid dynamics

in microscopic details. However, in most engineering analyses, a macroscopic description of the system adequately characterizes multiphase fluid flow behavior. Macroscopic fluid flow equations are obtained by averaging the local instantaneous conservation equations over time and space. The averaged conservation equations derived for an isothermal system are written as (Ishii, 1975; Kleinstreuer, 2003; Lahey, 2005; Prosperetti and Tryggvason, 2007; Yeoh and Tu, 2010; Ishii and Hibiki, 2011)

$$\frac{\partial}{\partial t}(\alpha_k \rho_k) + \nabla \cdot (\alpha_k \rho_k \vec{V}_k) = \Gamma_k^{\text{int}} + \Gamma_k^{\text{for}}, \quad (2.1)$$

$$\begin{aligned} \frac{\partial}{\partial t}(\alpha_k \rho_k \vec{V}_k) + \nabla \cdot (\alpha_k \rho_k \vec{V}_k \vec{V}_k) = & -\alpha_k \nabla P_k + \nabla \cdot [\alpha_k (\bar{\tau}_k + \bar{\tau}_k^{\text{Re}})] \\ & + \alpha_k \rho_k \vec{g} + (P_k^{\text{int}} - P_k) \nabla \alpha_k + \Gamma_k^{\text{int}} \vec{V}_k^{\text{int}} + \vec{M}_k^{\text{int}}, \quad \text{and} \quad (2.2) \end{aligned}$$

$$\sum_{k=1}^{n_p} \alpha_k = 1. \quad (2.3)$$

In the above equations, subscript "k" identifies k-th fluid phase, and superscripts "int" and "for" denote interface and rock formations, respectively. Remaining variables are described as follows: t is time, α_k is volumetric fraction or holdup, ρ_k is density, \vec{V}_k is velocity, Γ_k^{int} is interphase mass transfer rate per unit volume of fluid mixture, Γ_k^{for} is mass influx, P_k is pressure, $\bar{\tau}_k$ is viscous shear stress tensor, $\bar{\tau}_k^{\text{Re}}$ is turbulent shear stress tensor, P_k^{int} is pressure of k-th fluid phase at the interface, \vec{V}_k^{int} is velocity of k-th fluid phase at the interface, \vec{M}_k^{int} is the summation of interfacial forces acting on k-th fluid phase per unit volume of fluid mixture, n_p is number of fluid phases, and \vec{g} is gravitational acceleration.

The assumption of no mass transfer between the water and hydrocarbon phases leads to vanishing the corresponding terms in Equations 2.1 and 2.2 (Yeoh and Tu, 2010), i.e.,

$$\Gamma_k^{\text{int}} = \Gamma_k^{\text{int}} \vec{V}_k^{\text{int}} = 0. \quad (2.4)$$

The modelling method developed for interfacial mass transfer between the oil and gas phases is described in the next section. The assumption of neglecting interfacial tension effects gives rise to the same local pressure shared by dispersed and continuous fluid phases, namely,

$$P_k = P_k^{\text{int}}. \quad (2.5)$$

The term associated with turbulent shear forces (i.e., $\nabla \cdot \alpha_k \bar{\tau}_k^{\text{Re}}$) is replaced with the borehole wall friction force defined by (Hibiki and Ishii, 1977)

$$\vec{F}_{Wk} = -\frac{\alpha_k}{2} f_k \frac{\rho_k}{D_{hk}} |\vec{V}_k| \vec{V}_k, \quad (2.6)$$

where \vec{F}_{Wk} describes wall friction force acting on k-th fluid phase per unit volume of fluid mixture, f_k is wall friction factor, and D_{hk} is hydraulic diameter computed for k-th fluid phase. Because no contact is assumed between the borehole wall and dispersed phase, D_{hk} is set equal to 0 for dispersed fluid phase, and is given by

$$D_{hk} = \frac{\pi D^2}{\pi D} = D, \quad (2.7)$$

for continuous phase, where D identifies borehole diameter. Wall friction forces based on fluid mixture properties are given by (Kleinstreuer, 2003)

$$\vec{F}_{Wm} = -\frac{1}{2} f_m \frac{\rho_m}{D} |\vec{V}_m| \vec{V}_m, \quad (2.8)$$

where subscript "m" identifies fluid mixture, and ρ_m and \vec{V}_m are density and velocity of fluid mixture, respectively, computed based on a linear volumetric averaging method as

$$\rho_m = \sum_{k=1}^{n_p} \alpha_k \rho_k, \quad (2.9)$$

$$\vec{V}_m = \frac{1}{\rho_m} \sum_{k=1}^{n_p} \alpha_k \rho_k \vec{V}_k, \quad (2.10)$$

and f_m is fluid mixture friction factor calculated by (Colebrook, 1939)

$$\frac{1}{\sqrt{f_m}} = -2 \log_{10} \left(\frac{\varepsilon}{3.7D} + \frac{2.51}{\text{Re}_m \sqrt{f_m}} \right), \quad (2.11)$$

for turbulent flow regimes (i.e., $\text{Re}_m > 2300$), and

$$f_m = \frac{64}{\text{Re}_m}, \quad (2.12)$$

for laminar flow regimes (i.e., $\text{Re}_m \leq 2300$). In the above equations, ε is pipe absolute roughness and Re_m is mixture Reynolds number, given by

$$\text{Re}_m = \frac{\rho_m |\vec{V}_m| D}{\mu_m}, \quad (2.13)$$

where fluid mixture viscosity, μ_m , is computed as (Viswanath et al., 2007)

$$\log_{10} (\mu_m) = \sum_{k=1}^2 \alpha_k \log_{10} (\mu_k). \quad (2.14)$$

An explicit expression for friction factor is derived by Moody (1944), to wit,

$$f_m = 0.0055 \left[1 + \left(2 \times 10^4 \frac{\varepsilon}{D} + 10^6 \frac{1}{\text{Re}_m} \right)^{1/3} \right]. \quad (2.15)$$

In Equation 2.2, viscous shear-stress tensor is related to fluid-phase velocity gradient. Under the assumption of a Newtonian fluid, one obtains (Kleinstreuer, 2003)

$$\bar{\tau}_k = \mu_k \left(\nabla \vec{V}_k + \nabla \vec{V}_k^T \right), \quad (2.16)$$

where "T" defines the matrix transpose operator, and ∇ is the gradient operator.

When continuous phase is in contact with dispersed phase (e.g., within an oil bubbly flow regime), primary component of \bar{M}_k^{int} is defined by interfacial drag forces acting on a single bubble or droplet as (Kleinstreuer, 2003)

$$\vec{F}_D = -\frac{1}{2} C_D \rho_1 A_2 |\vec{V}_2 - \vec{V}_1| (\vec{V}_2 - \vec{V}_1), \quad (2.17)$$

where C_D is drag coefficient defined in Equation 2.20, and A_2 is the projected area of bubbles or droplets perpendicular to direction of fluid flow. Therefore, assuming spherical bubbles or droplets with radius R_d , interfacial drag forces acting on dispersed phase per unit volume of fluid mixture is calculated by

$$\bar{M}_2^{\text{int}} = -\frac{3}{8} \frac{\alpha_2}{R_d} C_D \rho_1 |\vec{V}_2 - \vec{V}_1| (\vec{V}_2 - \vec{V}_1). \quad (2.18)$$

In addition, the continuity of momentum across fluid-phase interface requires that

$$\bar{M}_1^{\text{int}} = -\bar{M}_2^{\text{int}}. \quad (2.19)$$

The drag coefficient in Equation 2.17 is computed as (Kleinstreuer, 2003)

$$C_D = \begin{cases} 24 \frac{(1 + 0.15 \text{Re}_s^{0.687})}{\text{Re}_s}, & \text{Re}_s \leq 1000, \\ 0.44, & \text{Re}_s > 1000 \end{cases}, \quad (2.20)$$

where Re_s is defined as Reynolds number based on fluid-phase slip velocity, i.e.,

$$R_{es} = \frac{2R_d \rho_1 |\vec{V}_2 - \vec{V}_1|}{\mu_1}. \quad (2.21)$$

When two continuous phases flow simultaneously in the borehole, interfacial drag forces are defined as interfacial friction forces, namely,

$$\vec{M}_1^{\text{int}} = -\vec{M}_2^{\text{int}} = -\frac{1}{2D_h^{\text{int}}} f^{\text{int}} \rho_2 |\vec{V}_2 - \vec{V}_1| (\vec{V}_2 - \vec{V}_1), \quad (2.22)$$

where f^{int} is interfacial friction coefficient given by Wallis (1967) as

$$f^{\text{int}} = 0.02[1 + 75\alpha_1], \quad (2.23)$$

for an annular flow regime. In the above equation, D_h^{int} is a shape factor defining the contact area of two fluid phases per unit volume of fluid mixture.

2.2.2 One-Dimensional Form of the Two-Fluid Model

Equations introduced in the previous section simulate fluid-phase properties in three-dimensional flow. However, because of the significant size differences between diameter and length of the borehole, variations of fluid-phase properties in the radial and azimuthal directions are significantly smaller than those in the axial direction. Neglecting radial and azimuthal variations of fluid-phase properties gives rise to a set of one-dimensional partial differential equations that adequately describe borehole multiphase flowing system. This section derives final one-dimensional system of equations that later will be applied for production logging simulation and interpretation.

As shown in Figure 2.1, equations associated with the one-dimensional version of two-fluid model in z direction are derived for a borehole with diameter of D exhibiting a deviation angle θ from vertical; z is defined as the borehole axial distance increasing

downward. In the presence of two fluid phases, the equations of mass conservation are written as (Prosperetti and Tryggvason, 2007)

$$\frac{\partial}{\partial t}(\alpha_1 \rho_1) + \frac{\partial}{\partial z}(\alpha_1 \rho_1 V_1) = \Gamma_{21}^{\text{int}} + \Gamma_1^{\text{for}}, \quad \text{and} \quad (2.24)$$

$$\frac{\partial}{\partial t}(\alpha_2 \rho_2) + \frac{\partial}{\partial z}(\alpha_2 \rho_2 V_2) = \Gamma_{12}^{\text{int}} + \Gamma_2^{\text{for}}, \quad (2.25)$$

and the momentum conservation equations are given by

$$\begin{aligned} \frac{\partial}{\partial t}(\alpha_1 \rho_1 V_1) + \frac{\partial}{\partial z}(\alpha_1 \rho_1 V_1^2) = & -\alpha_1 \frac{\partial P}{\partial z} + 2\mu_1 \frac{\partial}{\partial z} \left(\alpha_1 \frac{\partial V_1}{\partial z} \right) \\ & + \alpha_1 \rho_1 g \cos(\theta) - \frac{K}{2} f_m \frac{\rho_m}{D} |V_m| V_m + F_{D21}, \end{aligned} \quad (2.26)$$

$$\begin{aligned} \frac{\partial}{\partial t}(\alpha_2 \rho_2 V_2) + \frac{\partial}{\partial z}(\alpha_2 \rho_2 V_2^2) = & -\alpha_2 \frac{\partial P}{\partial z} + 2\mu_2 \frac{\partial}{\partial z} \left(\alpha_2 \frac{\partial V_2}{\partial z} \right) \\ & + \alpha_2 \rho_2 g \cos(\theta) - \frac{K}{2} f_m \frac{\rho_m}{D} |V_m| V_m + F_{D12}, \end{aligned} \quad \text{and} \quad (2.27)$$

$$\alpha_1 + \alpha_2 = 1. \quad (2.28)$$

In the above equations, K is zero for dispersed fluid phase, and is set to 1 for continuous phase, F_{D21} and Γ_{21}^{int} are interfacial mass and momentum transfers from the first to the second fluid phase, respectively, and

$$\Gamma_{12}^{\text{int}} = -\Gamma_{21}^{\text{int}}, \quad \text{and} \quad F_{D12} = -F_{D21}. \quad (2.29)$$

Assuming the first fluid phase as a dispersed phase, F_{D21} is given by (Kleinstreuer, 2003),

$$F_{D21} = -\frac{3}{8} \frac{\alpha_1}{R_d} C_D \rho_2 |V_1 - V_2| (V_1 - V_2), \quad (2.30)$$

and assuming two continuous fluid phases flowing simultaneously (i.e., within an annular flow regime),

$$F_{D21} = -\frac{0.01}{D} [1 + 75\alpha_2] \rho_1 |V_1 - V_2| (V_1 - V_2), \quad (2.31)$$

where D is borehole diameter.

2.2.3 Hydrocarbon-Phase Scalar Properties

The presence of various components in the hydrocarbon phase requires a compositional approach that accurately computes hydrocarbon-phase scalar properties (i.e., density and viscosity). I derive a set of component-based mass conservation equations to describe molar composition of hydrocarbon components in the borehole. The mass conservation equations for a single-phase hydrocarbon, under the assumption of identical velocity for all components be equivalent to the velocity of carrier hydrocarbon phase, is written as

$$\frac{\partial}{\partial t} (\alpha_h \hat{\rho}_h \hat{x}_j) + \frac{\partial}{\partial z} (\alpha_h \hat{\rho}_h \hat{x}_j V_h) = \hat{\Gamma}_{jh}^{\text{for}}, \quad \forall j = 1, \dots, n_c, \quad \text{and} \quad (2.32)$$

$$\sum_{j=1}^{n_c} \hat{x}_j = 1, \quad (2.33)$$

where, $\hat{\rho}_h$ is molar density of the hydrocarbon phase, n_c is number of components in hydrocarbon phase, \hat{x}_j is molar fraction of j-th component in the hydrocarbon phase, and $\hat{\Gamma}_{jh}^{\text{for}}$ is molar influx (outflux) of j-th component in the hydrocarbon phase produced from (injected into) the corresponding fluid-producing rock formations.

Hydrocarbon-phase viscosity and mass density as a function of borehole pressure, temperature, and hydrocarbon molar composition are described by the following equations (Smith and Van Ness, 2004):

$$\rho_h = \frac{Mw_h P}{Z_h RT}, \quad \text{and} \quad (2.34)$$

$$\mu_h = \left[\sum_{j=1}^{n_c} \hat{x}_j (\mu_j^{-1/4}) \right]^{-4}, \quad (2.35)$$

where R is the gas universal constant, and Mw_h is hydrocarbon-phase molar weight, given by

$$R = 10.73159 \left[\frac{\text{ft}^3 \text{psi}}{^\circ\text{R lb} - \text{mol}} \right], \quad \text{and} \quad (2.36)$$

$$Mw_h = \sum_{j=1}^{n_c} \hat{x}_j Mw_j. \quad (2.37)$$

In Equations 2.34 and 2.35, P is borehole pressure, T is borehole temperature, and Z_h hydrocarbon-phase compressibility factor calculated from Peng-Robinson's equation of state (Peng and Robinson, 1976). Appendix A presents a detailed formulation of Peng-Robinson's model to describe thermodynamic state of a hydrocarbon flowing system.

2.2.4 Interfacial Mass Transfer

Exchange of hydrocarbon components between the oil and gas phases gives rise to the change of hydrocarbon-phase viscosity and density. I incorporate additional source terms into fluid-phase and component-based mass conservation equations to accurately account for the effects of interfacial mass transfers into borehole fluid-phase properties.

Under the assumption of local thermodynamic equilibrium, the developed compositional model numerically solves separate sets of component-based mass conservation equations for the oil and gas phases as

$$\frac{\partial}{\partial t}(\alpha_o \hat{\rho}_o \hat{x}_j) + \frac{\partial}{\partial z}(\alpha_o \hat{\rho}_o \hat{x}_j V_o) = \hat{\Gamma}_{jo}^g + \hat{\Gamma}_{jo}^{for}, \quad \forall j = 1, \dots, n_c, \quad (2.38)$$

$$\frac{\partial}{\partial t}(\alpha_g \hat{\rho}_g \hat{y}_j) + \frac{\partial}{\partial z}(\alpha_g \hat{\rho}_g \hat{y}_j V_g) = \hat{\Gamma}_{jg}^o + \hat{\Gamma}_{jg}^{for}, \quad \forall j = 1, \dots, n_c, \quad (2.39)$$

$$\sum_{j=1}^{n_c} \hat{x}_j = 1, \quad (2.40)$$

$$\sum_{j=1}^{n_c} \hat{y}_j = 1, \quad (2.41)$$

and because of the continuity of mass across the interface,

$$\hat{\Gamma}_{jg}^o = -\hat{\Gamma}_{jo}^g, \quad \forall j = 1, \dots, n_c, \quad (2.42)$$

where $\hat{\Gamma}_{jg}^o$ is mass transfer rate of j-th component from the oil phase into the gas phase, $\hat{\Gamma}_{jo}^g$ is mass transfer rate of j-th component from the gas phase into the oil phase, $\hat{\rho}_o$ is molar density of the oil phase, $\hat{\rho}_g$ is molar density of the gas phase, \hat{x}_j is molar composition of j-th component in the oil phase, \hat{y}_j is molar composition of j-th component in the gas phase, $\hat{\Gamma}_{jo}^{for}$ is molar influx (outflux) of j-th component into the oil phase, and $\hat{\Gamma}_{jg}^{for}$ is molar influx (outflux) of j-th component into the gas phase.

In Equations 2.38 and 2.39, interphase mass transfer rates implicitly depend on borehole pressure, temperature, and hydrocarbons molar composition. To appropriately address this dependency, I invoke an iterative algorithm that dynamically computes hydrocarbon-phase properties associated with thermodynamic equilibrium conditions. As Figure 2.2 shows, the algorithm begins with solving Equations 2.38 through 2.42 under the assumption of no interfacial mass transfer (i.e., $\hat{\Gamma}_{jo}^g = \hat{\Gamma}_{jg}^o = 0$). The resulting molar

composition of gas and oil phases are subsequently used to calculate the total hydrocarbon-phase composition (i.e., \hat{z}_j) as

$$\hat{z}_j = \frac{\hat{\rho}_o \alpha_o}{\hat{\rho}_o \alpha_o + \hat{\rho}_g \alpha_g} \hat{x}_j + \frac{\hat{\rho}_g \alpha_g}{\hat{\rho}_o \alpha_o + \hat{\rho}_g \alpha_g} \hat{y}_j, \quad \forall j = 1, \dots, n_c. \quad (2.43)$$

Based on the calculated total composition, current borehole pressure and the given temperature, the compositional model computes thermodynamic properties of the oil and gas phases. Consequently, updated hydrocarbon-phase viscosity and mass density are computed by (Chang, 1990; Chang et al., 1990; Firoozabadi, 1999; Rezaveisi et al., 2014a and b)

$$\rho_o = \frac{Mw_o P}{Z_o RT}, \quad \rho_g = \frac{Mw_g P}{Z_g RT}, \quad (2.44)$$

$$\mu_o = \left[\sum_{j=1}^{n_c} \hat{x}_j (\mu_j^{-1/4}) \right]^{-4}, \quad \text{and} \quad \mu_g = \left[\sum_{j=1}^{n_c} \hat{y}_j (\mu_j^{-1/4}) \right]^{-4}, \quad (2.45)$$

where

$$Mw_o = \sum_{j=1}^{n_c} \hat{x}_j Mw_j, \quad \text{and} \quad Mw_g = \sum_{j=1}^{n_c} \hat{y}_j Mw_j. \quad (2.46)$$

The updated interphase mass transfer source for fluid-phase conservation equation is computed using the hydrocarbon properties in thermodynamic equilibrium, namely,

$$\Gamma_{go}^{int} = -\Gamma_{og}^{int} = \frac{[\rho_o \alpha_o - \rho_o^* \alpha_o^*]}{\Delta t}, \quad (2.47)$$

where ρ_o^* , α_o^* and are mass density and volumetric fraction of the oil phase at thermodynamic equilibrium, and Δt is current finite time step. Equation 2.47 determines interfacial mass influx required to achieve borehole thermodynamic equilibrium. The algorithm computes the updated values for fluid-phase density, viscosity, and interfacial

mass transfer, and proceeds to the calculation of borehole fluid-phase velocity, pressure, and holdup from Equation 2.24 through Equation 2.28. A detailed description of the numerical method adopted in this dissertation for computing borehole fluid-phase and component properties is presented in Chapter 3.

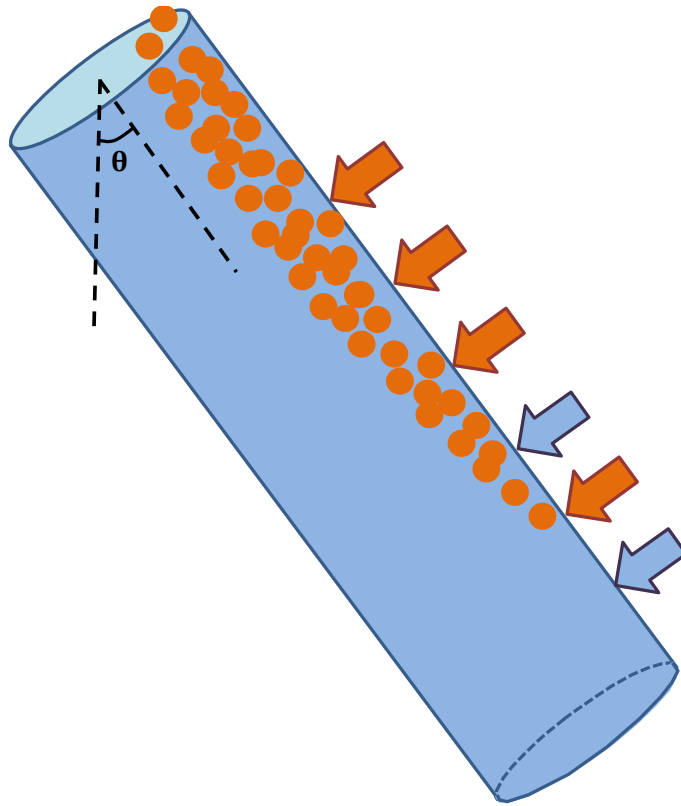


Figure 2.1: Schematic of the borehole fluid flow model constructed for simulation of two-phase production measurements.

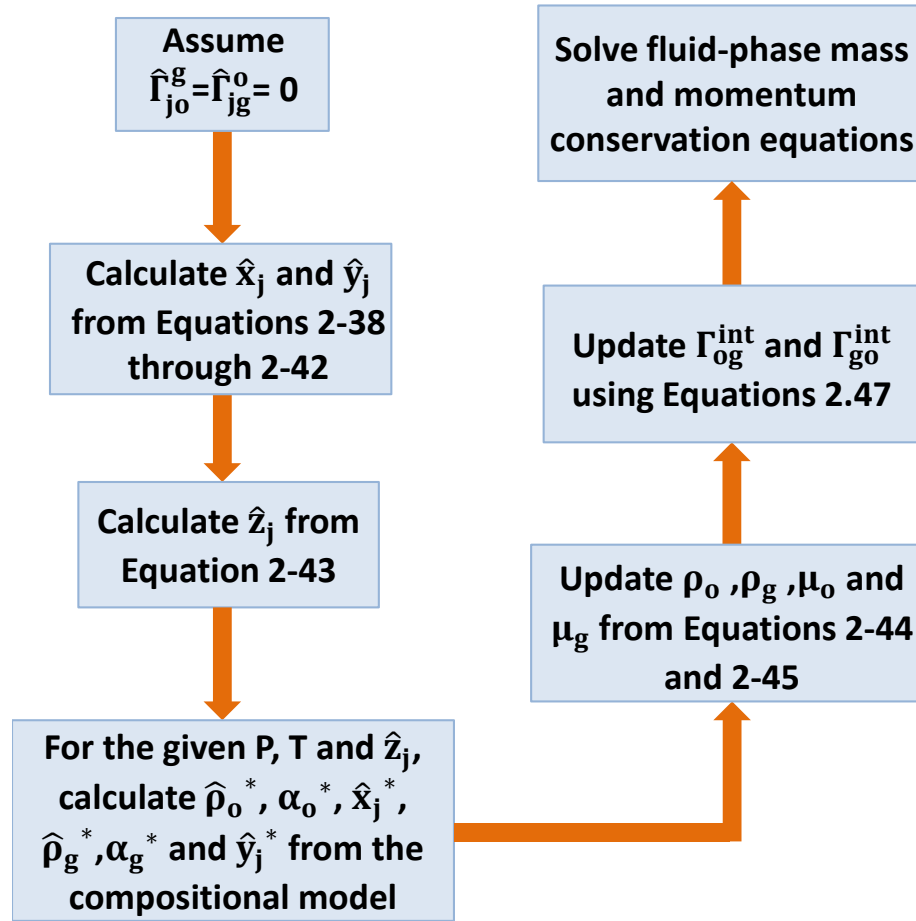


Figure 2.2: Developed workflow to compute interfacial mass transfer rates for simultaneous production of the oil and gas phases.

2.3 FLOW-REGIME TRANSITION

Interactions of fluid phases with each other and the borehole wall depend on fluid-phase flow patterns in the borehole. In a water-dominant oil-water bubbly flow, for instance, oil droplets are subject to drag force applying from the continuous phase of water. Because of random collision of oil droplets, coalescence of droplets takes place, thereby resulting in the formation of larger droplets. As Equation 2.30 suggests, droplet size is inversely proportional to drag force. Because of this inverse proportionality, larger

droplets experience lower drag forces when compared to those with smaller sizes. In addition, borehole deviation angle causes the oil droplets to flow closer to the upper borehole wall, thus lowering the effective interphase drag forces. An accurate estimation of fluid-phase interfacial momentum transfer therefore requires the incorporation of flow-regime transition into the borehole fluid flow model. To do so, I consider two flowing systems, (i) oil-water, and (ii) liquid-gas flows in vertical and deviated boreholes, and describe the method developed for dynamic modification of associated interfacial drag terms.

2.3.1 Oil-Water Vertical Flowing Systems

In the simultaneous production of two immiscible liquid phases, a reliable estimation of formations petrophysical properties from production logs involves a slip model that adequately captures minor yet influential discrepancies between liquid-phase properties. As shown by Vigneaux et al. (1988) for liquid-liquid flowing systems, the surface tension and density contrasts between fluid phases are much lower than those observed between gas and liquid phases. The similarities between fluid-phase properties cause the dispersed phase (e.g., oil or water droplets) to take the form of small droplets rather than large slugs, thus giving rise to slip velocities much lower than those observed in gas-liquid flowing systems.

Flow-regime identification in oil-water flow is conventionally carried out based on the drift-flux model (Flores et al., 1998; Hasan and Kabir, 1999; Flores et al., 1999). This section describes the conventional method, and the approach implemented in this dissertation to simulate flow-regime transition in oil-water flowing systems.

2.3.1.1 Introduction

Experimental studies conducted by Zavareh et al. (1988), Flores et al. (1998), Hasan and Kabir (1999), and Flores et al. (1999) suggest that flow-regime maps developed for gas-liquid flows are not applicable to oil-water flowing systems. Flores et al. (1998) classified oil-water flow regimes into two primary categories: oil-dominant and water-dominant flow regimes. They additionally associated bubbly, dispersed-bubbly, and churn flow regimes with each category. They observed that transition from water-dominant to oil-dominant flow regimes takes place at the oil volume fraction approximately equal to 0.45. Taking a similar approach, Hasan and Kabir (1999) associated three flow regimes with water-dominant flows, i.e., bubbly, pseudoslug, and no-slip flow regimes. Hasan and Kabir (1999) observed that the transition from bubbly to pseudoslug flow regimes takes place at the oil volume fraction equal to 0.25. This observation was similar to gas-liquid systems previously reported by Radovich and Moissis (1962), Taitel et al. (1980), Hasan and Kabir (1988a), and Hasan et al. (1998). Hasan and Kabir (1999) subsequently invoked the drift-flux model to express the transition from bubbly to pseudoslug flow regimes in terms of superficial velocities.

In oil-water vertical systems, interaction of drag and buoyant forces causes the lighter phase (i.e., oil droplets) moves at a faster velocity compared to the water phase. The drift-flux model, introduced by Zuber and Findlay (1965), relates the velocity of oil droplets to fluid mixture velocity by defining a slippage velocity between the lighter and heavier phases, to wit,

$$V_o = C_o V_m + V_d , \quad (2.48)$$

where C_o is distribution parameter (equal 1.2 for turbulent bubbly flows), V_o is oil velocity, V_m is fluid mixture velocity, and V_d is drift velocity. V_d is correlated to oil-

phase volume fraction for vertical upward oil-water systems as follows (Zuber and Findlay, 1965; Wallis, 1969):

$$V_d = V_\infty (1 - \alpha_o)^{n_d}, \quad (2.49)$$

where V_∞ is bubble terminal rise velocity, given by (Harmathy, 1960)

$$V_\infty = 1.53 \left(g \sigma_{ow} \frac{\rho_w - \rho_o}{\rho_w^2} \right)^{1/4}, \quad (2.50)$$

where σ_{ow} is oil-water surface tension, and g is gravitational acceleration. Hasan and Kabir (1999) suggested a value of 2 for exponent n_d in Equation 2.49, and combined Equations 2.48 through 2.50 to derive the following relationship for oil-phase volume fraction:

$$\alpha_o = \frac{V_{os}}{1.2V_m + 1.53 \left(g \sigma_{ow} \frac{\rho_w - \rho_o}{\rho_w^2} \right)^{1/4} (1 - \alpha_o)^2}. \quad (2.51)$$

In the above equation, oil-phase volume fraction was substituted with 0.25 to derive the following expression:

$$V_{os} = 0.43V_{ws} + 0.3060 \left(g \sigma_{ow} \frac{\rho_w - \rho_o}{\rho_w^2} \right)^{1/4}, \quad (2.52)$$

that formulates a criterion for transition from bubbly flow to pseudoslug flow. In Equation 2.52, V_{os} and V_{ws} are oil and water superficial velocities, defined by

$$V_{os} = \alpha_o V_o, \quad \text{and} \quad V_{ws} = \alpha_w V_w. \quad (2.53)$$

Furthermore, Govier and Aziz (1972), Flores et al. (1998), and Hasan and Kabir (1999) reported the occurrence of no-slip conditions for high oil-phase superficial velocities

(namely, oil-dominant flow). Hasan et al. (2007) reported $\alpha_o > 0.7$ as a criterion to differentiate between pseudoslug and no-slip flow conditions. They additionally assumed that the homogeneous model adequately describes the behavior of oil-dominant flowing systems.

The abovementioned experimental and theoretical contributions suggest that in oil-water flowing systems, as opposed to gas-liquid flows, the presence of two continuous liquid phases (e.g., annular and stratified flow regimes) is less likely to take place. Next section describes the method implemented in this dissertation to simulate flow-regime transition in oil-water flowing systems.

2.3.1.2 Droplet-Size Modification

The chaotic nature of fluid flow leads to generating droplets with variable shapes and sizes. Droplets with smaller diameters characterize a larger interfacial area concentration (or a larger surface-to-volume ratio) when compared to the same dispersed-phase volume fraction with large droplets, thus causing them to undergo larger drag forces.

I modify droplet diameters based on the breakup and coalescence of droplets to accurately simulate the associated drag forces. The dependency of droplet diameter on the rate of breakup and coalescence is attributed to turbulence-induced random collisions of droplets (Ishii, 1975; Ishii and Hibiki, 2011). The efficiency of those random collisions and their impact on droplet average diameter is modeled by solving one- or two-group interfacial area transport equations (Hibiki and Ishii, 2002; Sun et al., 2003; Hibiki et al., 2006). Hibiki and Ishii (2002) addressed the mechanism of bubble-bubble and bubble-eddy random collisions to develop a method that incorporated appropriate source and sink terms into a one-group interfacial area transport equation. They conducted

experimental studies in adiabatic air-water bubbly flow conditions, and developed a correlation that associates bubble average diameter to bubble volume fraction, turbulence properties, and surface tension of fluid phases, given by

$$\hat{a}_{ig} = 0.5\hat{L}_p^{-0.283}\alpha_g^{0.847}\hat{\varepsilon}_m^{0.0707}, \quad (2.54)$$

where

$$\hat{\varepsilon}_m = \frac{L_p^4 \rho_g^3}{\mu_g^3} \varepsilon_m, \quad \hat{a}_{ig} = a_{ig} L_p, \quad \text{and} \quad \hat{L}_p = \frac{L_p}{D_h}, \quad (2.55)$$

and \hat{a}_{ig} is dimensionless interfacial area concentration, \hat{L}_p is dimensionless Laplace length (or capillary length), $\hat{\varepsilon}_m$ is dimensionless energy dissipation rate per unit mass of fluid mixture, α_g is gas volume fraction, ρ_g is gas density, and D_h is the hydraulic diameter of pipe. Interfacial area concentration and Laplace length are defined as (Hibiki and Ishii, 2002)

$$L_p = \sqrt{\frac{\sigma_{glq}}{g(\rho_{lq} - \rho_g)}}, \quad \text{and} \quad (2.56)$$

$$a_{ig} = \frac{6\alpha_g}{D_b}, \quad (2.57)$$

respectively, where D_b is bubble diameter, g is gravitational acceleration, σ_{glq} is gas-liquid surface tension, ρ_{lq} is liquid density, and ρ_g is gas density. In turbulent flow, Taitel et al. (1980) showed that ε_m is related to fluid mixture velocity and wall friction as

$$\varepsilon_m = \frac{2f_m V_m^3}{D}, \quad (2.58)$$

where V_m and f_m are defined by Equations 2.10 and 2.11, respectively. The correlation stated in Equation 2.54 was developed for fully-developed steady-state flow conditions in vertical pipes, and is valid for gas volume fractions less than 0.44.

Incorporating the abovementioned correlation into the developed borehole fluid flow model, I dynamically modify droplet diameter according to the local flowing conditions. Depicting in Figure 2.3, dynamic modification of droplet diameter can be viewed as implementing a smooth transition from bubbly flow to pseudoslug flow without a need for any transition criterion. The developed borehole flow model assumes a threshold on oil-phase volume fraction where transition from water-dominant to oil-dominant flows takes place; when $\alpha_o < 0.5$, water phase is assumed as the continuous phase interacting with the borehole wall and oil droplets. $\alpha_o = 0.5$ is defined as the inversion point where oil phase establishes a continuous phase in the borehole interacting with the dispersed phase of water droplets. $\alpha_o > 0.5$ next describes oil-dominant flow regime.

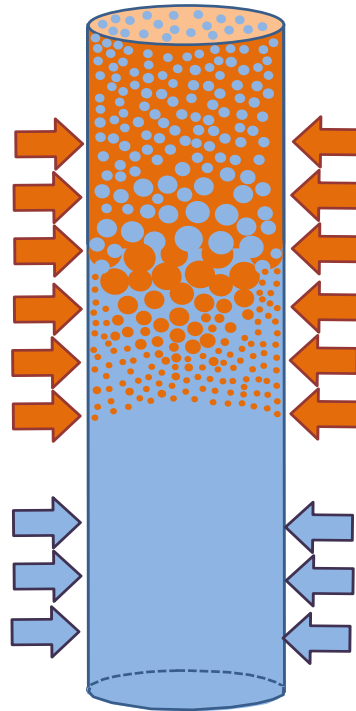


Figure 2.3: Schematic of the borehole fluid flow model describing flow-regime transition in oil-water vertical flow. Droplet coalescence gives rise to a smooth transition from water-dominant to oil-dominant flow regimes.

2.3.2 Oil-Water Deviated Flowing Systems

In vertical boreholes, the cross-sectional distribution of oil or water droplets is determined by random fluctuations of turbulence-induced eddies. The random nature of droplet movements allows one to accurately describe droplet cross-sectional distribution with a uniform distribution. However, in deviated boreholes, as shown in Figure 2.4, droplets experience asymmetric forces in the radial direction resulting in a non-uniform cross-sectional distribution. The non-uniform cross-sectional distribution of droplets has also been observed through the experimental studies conducted by Davarzani and Miller (1983), Flores et al. (1998), and Shi et al. (2005). Experimental studies on deviated flowing systems performed by Zavareh et al. (1988) showed counter-current fluid flow in pipes where the heavier phase moves in opposite direction with reference to the main direction of flow. Hasan and Kabir (1999) observed that independent of the borehole diameter, the lighter phase exhibits a tendency to move closer to the upper wall. They reported significantly higher slip velocities compared to equivalent flowing conditions in vertical systems. To account for higher slip velocity, Hasan and Kabir's (1999) work suggested the following modification on bubble terminal rise velocity introduced in Equation 2.50:

$$V_{\infty\theta} = V_{\infty} \sqrt{\cos \theta} (1 + \sin \theta)^2, \quad (2.59)$$

where $V_{\infty\theta}$ is modified bubble terminal rise velocity, and θ is pipe inclination angle from the vertical direction.

Lower slip velocities reported from experimental studies in deviated systems are associated to the reduction of interfacial area concentration compared to equivalent vertical systems. As Figure 2.5 shows, in deviated boreholes, agglomeration of droplets toward the upper wall decreases the effective contact area between the two fluid phases,

thereby lowering interfacial drag forces. The following two-phase flowing systems are used to describe the upper and lower bounds for effective two-phase contact area: (i) a flowing system with uniformly-distributed droplets (as shown in Figure 2.5a), defining the upper bound, and (ii) simultaneous flow of two fluid phases within a completely-segregated flow pattern (as shown in Figure 2.5b), characterizing the lower value of interfacial contact area. The developed borehole flow model calculates interfacial drag forces associated with the upper and lower bounds. Subsequently, the effective interfacial drag force is computed by linear interpolation between the two bounds as

$$F_D = W_e F_{Du} + (1 - W_e) F_{Ds}, \quad (2.60)$$

where F_{Du} is drag forces associated with the uniformly-distributed flow regime given by Equation (2.30), W_e is weighting factor of interpolation yet to be defined, and F_{Ds} is interfacial drag forces associated with segregated flow regimes, described by (Bonizzi and Issa, 2003)

$$F_{Ds} = -\frac{1}{2D_h^{\text{int}}} f^{\text{int}} \rho_o |V_o - V_w| (V_o - V_w), \quad (2.61)$$

where D_h^{int} is interfacial area concentration, and f^{int} is interfacial friction factor. Furthermore, following the recommendation of Taitel et al. (1995), Khor et al. (1997), and Bonizzi and Issa (2003),

$$f^{\text{int}} = 0.014. \quad (2.62)$$

In Equation (2.61), D_h^{int} is defined by (Bird et al., 2002)

$$D_h^{\text{int}} = \frac{A}{S^{\text{int}}}, \quad (2.63)$$

where S^{int} is the area shared by two fluid phases. As Figure 2.6 illustrates, S^{int} is estimated by

$$A_{B'oA'} = A\alpha_o + \frac{S^{\text{int}}H}{2}. \quad (2.64)$$

Parameters of the above equation have been described in Figure 2.6. Rearranging Equation 2.64 yields the following equation:

$$\sin^{-1}\left(\frac{S^{\text{int}}}{D}\right) - \left(\frac{S^{\text{int}}}{D}\right)\sqrt{1 - \left(\frac{S^{\text{int}}}{D}\right)^2} - \pi\alpha_o = 0, \quad \forall \alpha_o < 0.5, \quad (2.65)$$

that is numerically solved to compute S^{int} .

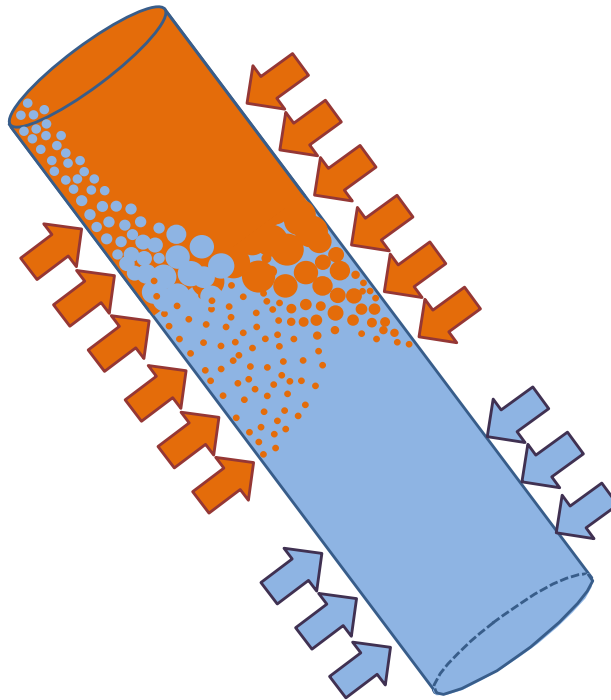


Figure 2.4: Schematic of the borehole fluid flow model describing flow-regime transition in oil-water deviated flow. Droplet coalescence gives rise to a smooth transition from water-dominant to oil-dominant flow regimes. In addition, the lighter fluid phase tends to move closer to the upper wall, thus decreasing the contact area shared by two fluid phases.

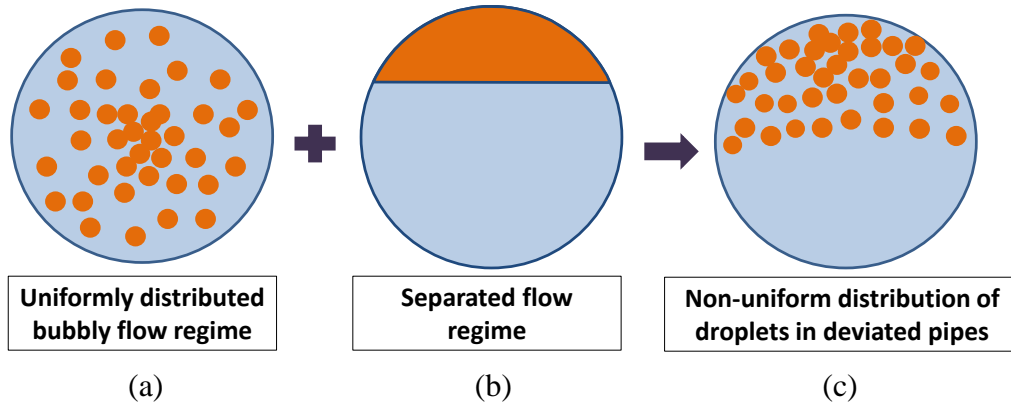


Figure 2.5: Illustration of the cross-sectional spatial distribution of droplets within (a) uniform bubbly flow, (b) fully-segregated flow, and (c) non-uniform bubbly flow. Drag force associated with Panel (c) is computed based on linear interpolation between drag forces for Panels (a) and (b).

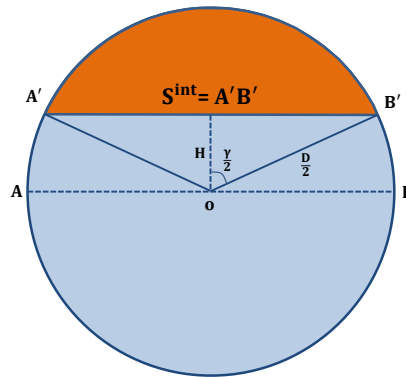


Figure 2.6: Geometrical description of two-phase fluid flow within a segregated flow regime. The interfacial area shared by two fluid phases (i.e., S^{int}) is numerically computed using Equation 2.65.

2.3.2.1 Force Balance in Radial Direction

The weighting factor of interpolation in Equation 2.60, namely W_e , depends on forces acting on the dispersed fluid phase perpendicular to the direction of flow. Taitel and Dukler (1976), Barnea (1985), and Barnea (1987) showed that the balance between

turbulence-induced and buoyant forces acting on the dispersed phase governs the migration of droplets toward the upper wall. Later, Ouyang and Aziz (1999) included a third force (i.e., drag force in the radial direction) to account for the presence of fluid influx from (outflux into) the borehole wall. This section simulates buoyant, drag and turbulence-induced forces acting on a single droplet to solve a force-balance equation perpendicular to the direction of flow. The derived force-balance equation effectively estimates the deviation of droplet cross-sectional distribution from uniform distribution.

Because of a zero average fluid-phase velocity in the radial and azimuthal directions, forces acting on a droplet from all directions perpendicular to the borehole axis counterbalance each other. Therefore, the associated force-balance equation is written as

$$F_{B,r}(r) + F_{D,r}(r) + F_{T,r}(r) = 0, \quad (2.66)$$

where subscript "r" identifies forces in the radial direction (as shown in Figure 2.7), F_B is the radial component of buoyant forces acting on a droplet with radius R_d , namely,

$$F_{B,r}(r) = \frac{4}{3}\pi R_d^3(\rho_w - \rho_o)g \sin \theta, \quad (2.67)$$

and $F_{D,r}$ is drag forces in the radial direction, computed based on Equation 2.17 (Prosperetti and Tryggvason, 2007), i.e.,

$$F_{D,r}(r) = -\frac{1}{2}\pi R_d^2 C_D \rho_w |V_{m,r}(r)|V_{m,r}(r), \quad (2.68)$$

where $V_{m,r}$ is fluid mixture velocity in the radial direction that depends on productivity index of the corresponding fluid-producing rock formations, and C_D is drag coefficient given by Equation 2.20 with the Reynolds number based on $V_{m,r}$. In proximity of the

borehole wall, $V_{m,r}$ is calculated based on the total inflow (outflow) rate produced from (injected into) the formation, given by

$$V_{m,r}|_{r=\frac{D}{2}} = \frac{Q_t}{A_{\text{perf}}\phi}, \quad (2.69)$$

where Q_t is total fluid flow rate (defined positive for production, and negative during injecting), ϕ is formation porosity, and A_{perf} is the available area for fluid phases to flow into the borehole, given by

$$A_{\text{perf}} = C_{\text{perf}}\pi D\Delta z, \quad (2.70)$$

where D is borehole diameter, Δz is length of a grid block constructed for the numerical simulation of fluid flow in porous media, and C_{perf} is a correction factor (between 0 and 1) that accounts for the flow restriction imposed by perforations.

In Equation 2.66, $F_{T,r}$ is the force due to turbulent fluctuations. Levich (1962) and Barnea (1985) defined an average value of that force as

$$\bar{F}_{T,r} = -\frac{1}{2}\pi R_d^2 \rho_w v'^2, \quad (2.71)$$

where v' is radial velocity fluctuations whose root mean square is approximated by (Barnea, 1985)

$$\overline{v'^2} = \frac{f_m}{2} V_m^2, \quad (2.72)$$

where V_m and f_m are fluid mixture velocity and friction factor, respectively, given by Equations 2.10 and 2.11. I combine Equations 2.71 and 2.72 to obtain the following expression for average turbulent-induced forces:

$$\bar{F}_{T,r} = -\frac{1}{4}\pi R_d^2 f_m \rho_w V_m^2. \quad (2.73)$$

Force-balance equation derived in the radial direction is applied to estimate W_e in Equation 2.60. While buoyant forces are independent of the radial distance from borehole centerline, the estimation of W_e requires drag and turbulent-induced forces to be described as appropriate functions of radial distance. Experimental studies reported by Kim et al. (1987), Hughes and Brighton (1991), and Satta et al. (2006) suggest that root mean square of radial velocity fluctuations approximately varies linearly with the radial position. Root mean square of radial velocity fluctuations reaches a maximum in close proximity of the borehole wall, and abruptly reduces to zero due to the wall boundary-layer effects (Kim et al., 1987). Neglecting the boundary-layer effects, I invoke the following linear interpolation to describe dependency between turbulent-induced forces and the dimensionless radial distance:

$$F_{T,r}(r) = F_{T,r}|_{r=\frac{D}{2}} \times \left(\frac{2r}{D}\right)^2 + F_{T,r}|_{r=0}. \quad (2.74)$$

Turbulent-induced forces in the borehole centerline are assumed equivalent in all radial directions, implying that

$$F_{T,r}|_{r=0} = 0. \quad (2.75)$$

Accordingly, the following integration along the borehole radial axis is carried out to compute $F_{T,r}|_{r=\frac{D}{2}}$:

$$-\frac{1}{4}\pi R_d^2 f_m \rho_w V_m^2 = \frac{2}{D} \int_0^{\frac{D}{2}} F_{T,r}|_{r=\frac{D}{2}} \left(\frac{2r}{D}\right)^2 dr = \left(\frac{2}{D}\right)^3 F_{T,r}|_{r=\frac{D}{2}} \left[\frac{r^3}{3}\right]_0^{\frac{D}{2}} = \frac{1}{3} F_{T,r}|_{r=\frac{D}{2}}. \quad (2.76)$$

The above equation is simplified to

$$F_{T,r}|_{r=\frac{D}{2}} = -\frac{3}{4}\pi R_d^2 f_m \rho_w V_m^2, \quad (2.77)$$

therefore,

$$F_{T,r}(r) = -3\pi R_d^2 f_m \rho_w V_m^2 \left(\frac{r}{D}\right)^2. \quad (2.78)$$

To express $V_{m,r}$ in Equation 2.69 as a function of borehole radial position, I assume that radial component of drag forces behaves similar to fluid axial-velocity profile within a fully-developed turbulent flow (Bird et al., 2002). Subsequently, I invoke Equation 2.69 to derive the following expression for fluid mixture velocity in the radial direction:

$$V_{m,r}(r) = \frac{Q_t}{A_{\text{perf}}\Phi} \left[1 - \left(1 - \frac{2r}{D}\right)^{\frac{1}{7}} \right]. \quad (2.79)$$

The above equation is substituted into Equation 2.68 to yield a description for radial drag forces as

$$F_{D,r}(r) = -\frac{1}{2} \pi R_d^2 C_D \rho_w \frac{|Q_t|Q_t}{(A_{\text{perf}}\Phi)^2} \left[1 - \left(1 - \frac{2r}{D}\right)^{\frac{1}{7}} \right]^2. \quad (2.80)$$

Combining Equations 2.66, 2.67, 2.78, and 2.80 gives rise to a relationship that determines the position of a droplet experiencing buoyant, drag, and turbulence-induced forces under steady-state conditions, namely,

$$\begin{aligned} \frac{4}{3} \pi R_d^3 (\rho_w - \rho_o) g \sin \theta = & \frac{1}{2} \pi R_d^2 C_D \rho_w \frac{|Q_t|Q_t}{(A_{\text{perf}}\Phi)^2} \left[1 - \left(1 - \frac{2r}{D}\right)^{\frac{1}{7}} \right]^2 \\ & + 3\pi R_d^2 f_m \rho_w V_m^2 \left(\frac{r}{D}\right)^2, \end{aligned} \quad (2.81)$$

where r describes the degree of deviation or eccentricity of droplets from a uniform cross-sectional distribution, and will be used as the interpolation weighting factor in Equation 2.60 (i.e., W_e).

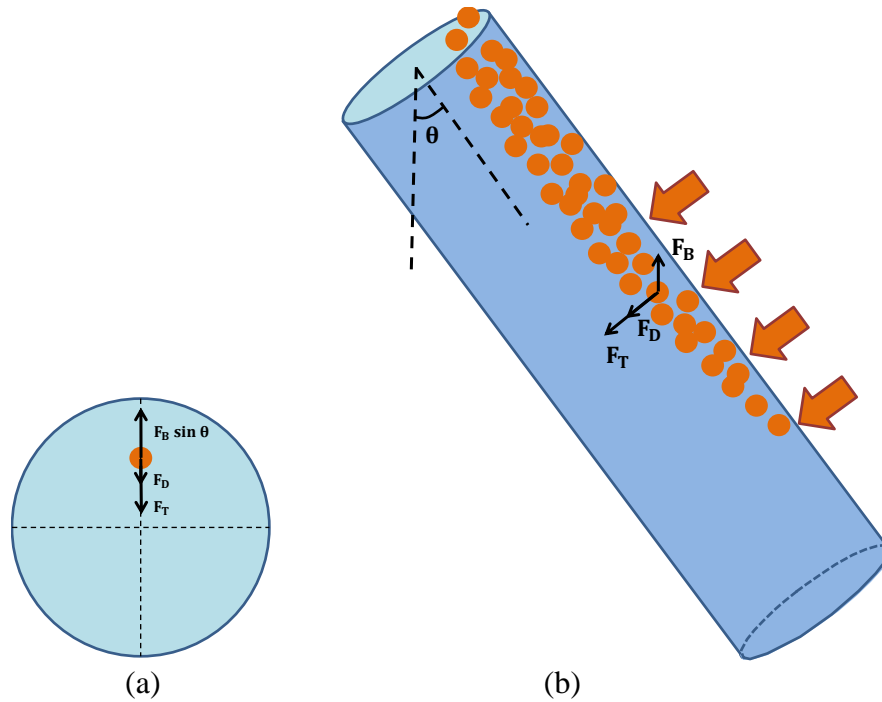


Figure 2.7: Illustration of buoyant, drag, and turbulent forces acting on a single droplet in the radial direction, shown in (a) planar view, and (b) side view.

2.3.3 Gas-Liquid Vertical Flowing Systems

Significant discrepancy between gas and liquid properties gives rise to complex flow regimes in gas-liquid flowing systems. At low gas volume fractions, bubbly flow regime is established where small gas bubbles flow through the continuous phase of liquid. However, increasing gas volume fraction causes gas bubbles to agglomerate about the center of borehole, thereby resulting in the formation of larger bubbles. Large bubbles

experience lower drag force compared to those within bubbly flow regimes, thus forcing them to flow at velocities significantly larger than liquid-phase velocities. Additional increasing of gas volume fraction establishes a cylindrical gas core moving in the center portion of borehole accompanied with a thin liquid film moving attached to the borehole wall. A variety of theoretical and experimental studies has been documented to describe the mechanism of flow-regime transition in gas-liquid systems. Challenge in flow-regime description is to develop transition criteria that accurately simulates the occurrence of a specific flow regime associated with the given borehole and fluid-phase properties.

The borehole fluid flow model developed in this dissertation applies appropriate flow-regime maps to determine the occurrence of each flow regime. I assume the presence of four flow regimes, namely, bubbly, dispersed-bubbly, slug, and annular flow regimes. As Figure 2.8 describes, flow-regime determination begins with solving borehole fluid flow equations under the assumption of bubbly flow for the entire borehole flow domain. According to flow-regime transition criteria, yet to be formulated, the interfacial and wall drag forces are modified in order to update the borehole flow regimes. Flow-regime identification algorithm proceeds to the next time step when the predicted and assumed flow regimes for all numerical grid blocks become identical.

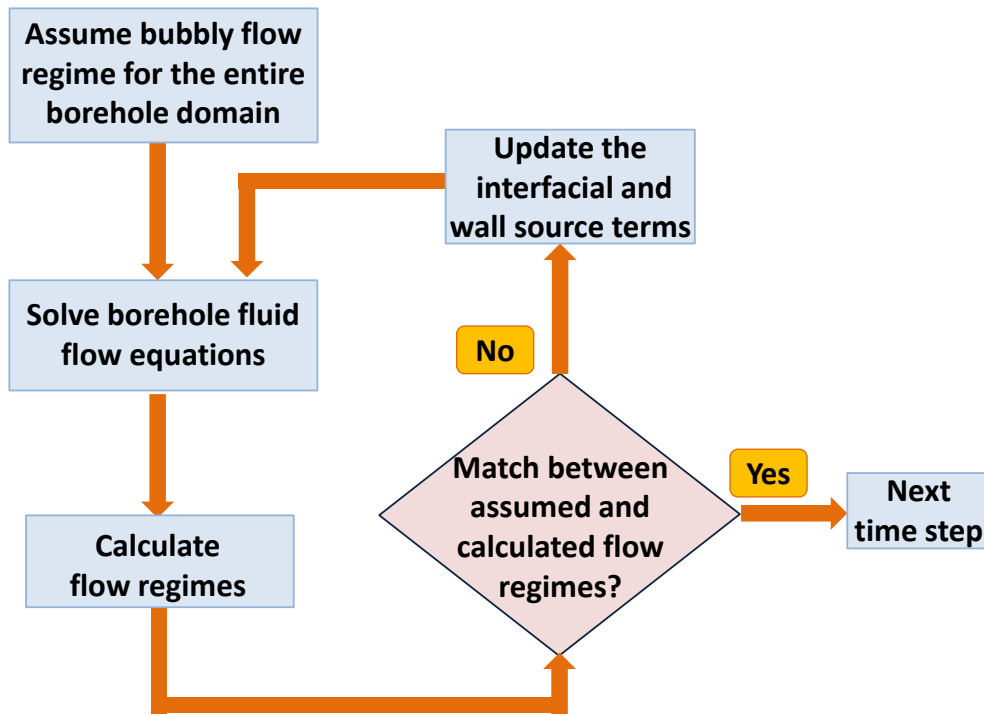


Figure 2.8: Developed workflow for dynamic determination of fluid flow regimes in the borehole. The algorithm dynamically modifies interfacial momentum transfer rates to match the assumed and computed borehole fluid flow regimes.

2.3.3.1 Bubbly to Slug Flow-Regime Transition

Transition from gas bubbly flow to slug flow is governed by the coalescence of small gas bubbles. In turbulent flow, random fluctuations of gas bubbles give rise to bubble-bubble collision. As shown by Radovich and Mossis (1962) and Hibiki et al. (2001), the frequency of bubble-bubble collision depends on fluid-phase velocity and volume fraction. Radovich and Mossis (1962) investigated the behavior of fluctuating bubbles in a cubic lattice, and showed that at gas volume fraction approximately equal to 0.3, the frequency of bubble-bubble collision becomes high enough to initiate the transition from bubbly to slug flow regime. Through experimental observations, Hasan

and Kabir (1988a) reported gas volume fraction of 0.25 as bubbly-to-slug transition criterion. The transition criterion was associated to gas and liquid superficial velocities by applying the drift-flux model as (Hasan and Kabir, 1988a)

$$\frac{V_{gs}}{\alpha_g} = 1.2V_m + V_\infty = 1.2(V_{lqs} + V_{gs}) + V_\infty, \quad (2.82)$$

substituting $\alpha_g = 0.25$ yields

$$V_{gs} = 0.429V_{lqs} + 0.357V_\infty, \quad (2.83)$$

where V_m is fluid mixture velocity, V_∞ is bubble terminal rise velocity given by Equation 2.50, V_{gs} and V_{lqs} are gas and liquid superficial velocities, respectively, defined in Equation 2.53. Moreover, Taitel et al. (1980) reported that the development of bubbly flow regime requires an additional criterion for minimum pipe diameter (D_{min}). The additional transition criterion was formulated as follow:

$$D_{min} = 19.01 \left[\frac{\sigma_{glq} (\rho_{lq} - \rho_g)}{\rho_{lq}^2 g} \right], \quad (2.84)$$

where σ_{glq} is gas-liquid surface tension, ρ_g and ρ_l are gas and liquid densities, respectively, and g is gravitational acceleration.

The developed borehole fluid flow model applies the criteria stated in Equations 2.83 and 2.84 to determine the occurrence of bubbly flow regime.

2.3.3.2 Bubbly to Dispersed-Bubbly Flow-Regime Transition

At high liquid or gas velocities, turbulent-induced forces overcome forces associated with interfacial tension causing the breakage of gas bubbles (Taitel et al., 1980; Barnea et al., 1982). Barnea et al. (1982) showed that bubble breakup requires a

stable bubble diameter for gas bubbles to remain dispersed in the continuous phase. The stable bubble diameter was attributed to gas-liquid surface tension, gas volume fraction, and mixture turbulent conditions, to wit,

$$d_{\text{stable}} = \left(0.725 + 4.15\alpha_g^{\frac{1}{2}}\right) \left(\frac{\sigma_{\text{glq}}}{\rho_{\text{lq}}}\right)^{\frac{3}{5}} \varepsilon_m^{-\frac{2}{5}}, \quad (2.85)$$

where σ_{glq} is gas-liquid surface tension, and ε_m is the rate of energy dissipation per unit mass of fluid mixture defined by Equation 2.58. In addition, Barnea et al. (1982) estimated the following critical bubble diameter (d_{CD}) beyond which bubble deformation and agglomeration takes place, thereby resulting in a flow-regime transition:

$$d_{\text{CD}} = 2 \left[\frac{0.4\sigma_{\text{glq}}}{(\rho_{\text{lq}} - \rho_g)g} \right]^{\frac{1}{2}}. \quad (2.86)$$

They combined Equations 2.85 and 2.86 to derive bubbly to dispersed-bubbly transition criterion as

$$2 \left[\frac{0.4\sigma_{\text{glq}}}{(\rho_{\text{lq}} - \rho_g)g} \right]^{\frac{1}{2}} = \left(0.725 + 4.15\alpha_g^{\frac{1}{2}}\right) \left(\frac{\sigma_{\text{glq}}}{\rho_{\text{lq}}}\right)^{\frac{3}{5}} \varepsilon_m^{-\frac{2}{5}}, \quad (2.87)$$

This dissertation implements Equation 2.87 as the criterion for transition from bubbly to dispersed-bubbly flow regimes.

2.3.3.3 Dispersed-Bubbly to Slug Flow-Regime Transition

In a dispersed-bubbly flow regime, stability of small bubbles prevents the deformation or agglomeration of bubbles. However, as volume fraction of gas phase increases, frequent bubble-bubble collisions result in the formation of larger bubbles.

Taitel et al. (1980) showed that $\alpha_g = 0.52$ is approximately the maximum gas volume fraction for which dispersed-bubbly flow regime remains stable. At higher gas volume fractions, transition to slug flow regime takes place. The transition criterion was subsequently achieved under the assumption of no-slip conditions, namely,

$$V_{gs} = 1.08V_{lqs}, \quad (2.88)$$

The above equation is implemented to describe the transition from dispersed-bubbly to slug flow regimes.

2.3.3.4 Slug to Annular Flow-Regime Transition

At extremely high gas velocities, shear stresses between gas and liquid phases force the liquid phase to move closer to the borehole wall. The interaction of shear forces generates a gas core in the center portion of borehole surrounded by a thin film of liquid. Taitel et al. (1980) showed that independent of liquid-film velocity, the minimum gas velocity, given by

$$V_{gs} = 3.1 \left[\frac{\sigma_{glq} g (\rho_{lq} - \rho_g)}{\rho_g^2} \right]^{0.25}, \quad (2.89)$$

is required to prevent the liquid film from falling backward. In addition, Hasan et al. (2007) suggested a minimum gas volume fraction equal to 0.7 as a requirement to prevent the liquid film from bridging the borehole cross section. I apply the abovementioned criteria to predict the transition from slug to annular flow regimes.

2.3.3.5 Interfacial Drag Forces

When modeling borehole fluid flow using two-fluid method, incorporation of flow-regime maps is performed by modifying interfacial drag forces according to the identified flow regimes. When a dispersed fluid phase is established in the borehole (i.e., bubbly or dispersed-bubbly flow regimes), the developed borehole fluid flow model computes drag forces for spherical bubbles according to the associated drag-force term (i.e., Equation 2.30). The bubble diameter is estimated from Hibiki and Ishii's (2002) correlation described with Equations 2.54 through 2.58. As an alternative method for dispersed-bubbly flow regime, bubble diameter can be estimated from Barnea et al.'s (1982) relationship (namely, Equation 2.85). Simulation results show that both methods estimate approximately identical values for gas bubble diameter.

In the occurrence of annular flow regime, drag forces are implemented as friction between the two continuous fluid phases. I apply friction-force term formulated with Equation 2.31 to accurately compute fluid-phase properties within the annular flow. Furthermore, computing interfacial drag forces within the slug flow regime is carried out by a linear interpolation between drag forces associated with the adjacent flow-regime boundaries, i.e.,

$$F_{Dsl} = W_{sl}F_{Da} + (1 - W_{sl})F_{Db}, \quad (2.90)$$

where F_{Dsl} , F_{Db} , and F_{Da} are interfacial drag forces associated with slug, bubbly, and annular flow regimes, respectively. The weighting factor of interpolation, namely W_{sl} , is defined based on the associated gas volume fractions as

$$W_{sl} = \frac{\alpha_g - \alpha_{gb}}{\alpha_{ga} - \alpha_{gb}}, \quad (2.91)$$

where α_{ga} and α_{gb} are gas volume fractions for slug-to-annular and bubbly-to-slug transition criteria, respectively. It should be noted that when a transition takes place from dispersed-bubbly to slug flow regime, the calculation of W_{sl} requires gas volume fraction associated with dispersed-bubbly-to-slug transition criterion (i.e., $\alpha_{gb} = 0.52$).

2.3.4 Gas-Liquid Deviated Flowing Systems

Flow regimes observed in deviated flowing systems with slight to moderate deviation angles are identical to those observed in vertical flowing systems (Taitel et al., 1980; Barnea, 1985; Hasan and Kabir, 1988b; Ansari et al., 1994). However, because of the agglomeration of gas bubbles toward the upper borehole wall, transition from bubbly to slug flow regimes takes place at lower gas volume fractions compared to equivalent vertical systems. To account for the borehole inclination effects, Hasan and Kabir (1988b) showed that the actual cross-sectional area available for gas bubbles to flow is the projection of cross-sectional area on a horizontal plane. Subsequently, they applied the drift-flux model, and derived the following criterion for transition from bubbly to slug flow regimes in deviated boreholes:

$$V_{gs} = \left(0.429V_{lqs} + 0.357V_{\infty} \right) \cos \theta, \quad (2.92)$$

where θ is borehole deviation angle from vertical.

The transition criteria associated with dispersed-bubbly and annular flow regimes are identical to those applied for vertical flowing systems (i.e., Equations 2.84 through 2.89).

2.3.4.1 Interfacial Drag Forces

The modification of interfacial drag forces implemented for vertical flowing systems are applicable to deviated systems. However, in deviated systems, slip velocities observed in slug flow regime are considerably larger than those in equivalent vertical following systems. As Figure 2.9 describes, the coalescence of gas bubbles in deviated flow, significantly decreases local interfacial area concentration. Reduction of interfacial area concentration is modeled by replacing the field of gas bubbles with a cylindrical gas core exhibiting the equivalent volume fraction. The modeling is carried out by modifying the interpolation weighting factor of Equation 2.91 as

$$W_{sl} = \left(\frac{\alpha_g - \alpha_{gb}}{\alpha_{ga} - \alpha_{gb}} \right)^{\frac{1}{7}}. \quad (2.93)$$

As shown in Figure 2.10, the modified interpolation coefficient, biases the interpolation toward the annular flow regime to numerically increase the presence of a gas core at low gas volume fractions yet maintaining the continuity of drag forces at flow-regime boundaries.

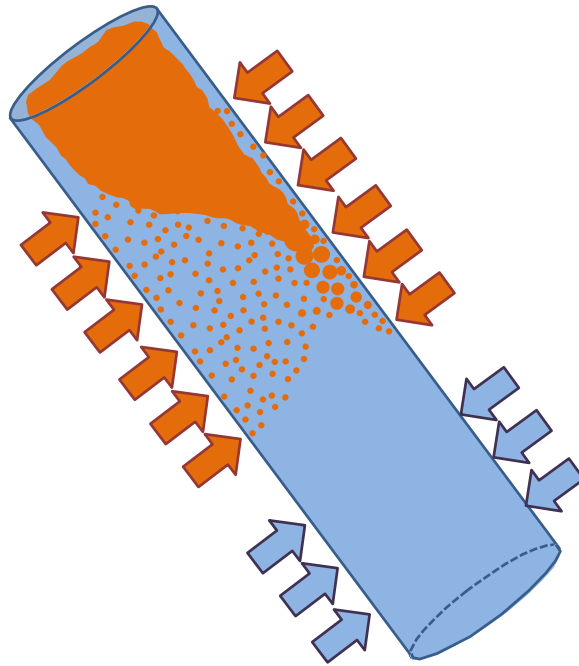


Figure 2.9: Schematic of the borehole fluid flow model describing flow-regime transition in gas-liquid deviated flow. Agglomeration of gas bubbles at higher gas holdup leads to occurrence of the annular flow.

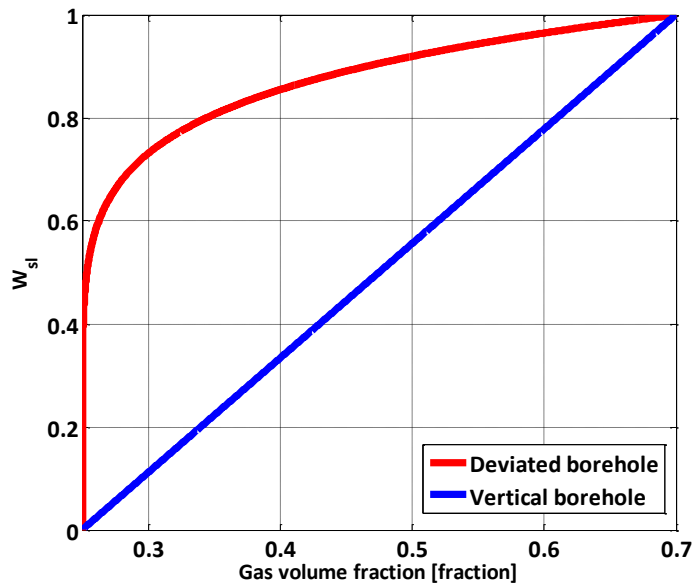


Figure 2.10: Comparison the interpolation weighting factor (W_{sl}) defined in Equation 2.90 for vertical (blue line) and deviated boreholes (red line). Red line biases the interpolation toward the annular flow regime to effectively decrease the interfacial contact area.

Chapter 3: Computational Approach

This chapter describes discretization of the mass and momentum conservation equations using the finite-volume method. Discretization is performed in one-dimensional (1D) cylindrical coordinates to take advantage of the geometrical conformity with reservoir fluid flow simulator. I develop an inter-phase slip algorithm (i.e., IPSA-C) that constructs a pressure equation based on conservation of the overall mass (Spalding, 1980). Following the calculation of pressure, fluid-phase velocities are computed from the momentum conservation equations in an implicit form. Subsequently, fluid-phase volume fractions are computed by solving the mass conservation equations. In this chapter, I describe the discretized equations and the numerical method developed to solve borehole fluid-phase velocity, pressure, and volume fraction.

3.1 BOREHOLE DISCRETIZATION

Borehole two-phase fluid flow equations developed in this dissertation consist of fluid-phase mass and momentum conservation equations formulated with Equations 2.24 through 2.28. In the presence of hydrocarbon phases, a set of component-based mass conservation equations is numerically solved to describe the phase behavior of flowing system. The developed equations are written in the following conservative form:

$$\frac{\partial}{\partial t}(\alpha_k \rho_k \psi_k) + \frac{\partial}{\partial z}(\alpha_k \rho_k \psi_k V_k) = \frac{\partial}{\partial z} \left(\alpha_k \eta_{\psi_k} \frac{\partial \psi_k}{\partial z} \right) + \Gamma_{\psi_k}, \quad (3.1)$$

where subscript "k" identifies a fluid phase, α is holdup, ρ is density, V is velocity, t is time, z is borehole axial position, ψ_k is a transport variable (e.g., fluid-phase velocity), and η_{ψ_k} and Γ_{ψ_k} are diffusion coefficient and source terms associated with the transport variable, respectively. Coefficients introduced in the above equation have been specified in Table 3.1 for the mass and momentum conservation equations. This dissertation develops a 1D finite-volume method to numerically solve the conservative form of transport equations. As a starting point, the finite-volume method takes the integral form of generic transport equations over a finite control volume, to wit,

$$\int_v \frac{\partial}{\partial t} (\alpha_k \rho_k \psi_k) dv + \int_v \frac{\partial}{\partial z} (\alpha_k \rho_k \psi_k V_k) dv = \int_v \frac{\partial}{\partial z} \left(\alpha_k \eta_{\psi_k} \frac{\partial \psi_k}{\partial z} \right) dv + \int_v \Gamma_{\psi_k} dv. \quad (3.2)$$

The volume integrals of advection and diffusion terms are transformed to surface integrals by applying Gauss's divergence theorem as (Stewart, 2008)

$$\int_v \frac{\partial}{\partial t} (\alpha_k \rho_k \psi_k) dv + \int_{A_{cv}} (\alpha_k \rho_k \psi_k V_k) \hat{n} \cdot dA = \int_{A_{cv}} \left(\alpha_k \eta_{\psi_k} \frac{\partial \psi_k}{\partial z} \right) \hat{n} \cdot dA + \int_v \Gamma_{\psi_k} dv, \quad (3.3)$$

where \hat{n} is unit vector perpendicular to the surface of a control volume, namely, A_{cv} . This dissertation assumes cylindrical stationary control volumes where variations of fluid properties take place along the axis of cylinder. This assumption yields

$$\begin{aligned} \frac{\partial}{\partial t} \int_s^n \alpha_k \rho_k \psi_k dz + (\alpha_k \rho_k \psi_k V_k)_n - (\alpha_k \rho_k \psi_k V_k)_s = \\ \left(\alpha_k \eta_{\psi_k} \frac{\partial \psi_k}{\partial z} \right)_n - \left(\alpha_k \eta_{\psi_k} \frac{\partial \psi_k}{\partial z} \right)_s + \int_s^n \Gamma_{\psi_k} dz, \end{aligned} \quad (3.4)$$

where "s" and "n" identify two faces of a control volume along the z axis, as shown in Figure 3.1. Equation 3.4 represents a set of nonlinear and coupled partial differential equations describing transport of fluid property ψ_k .

When considered transport equation for fluid velocity (i.e., $\psi_k = V_k$), interfacial drag effects cause fluid-phase velocity to become coupled to that of the second fluid phase. Furthermore, borehole fluid pressure is coupled to fluid-phase velocity and density through the momentum conservation equation. However, none of the available partial differential equations directly describe borehole pressure. I implement an effective numerical method that addresses the nonlinearity and strong coupling between dependent variables (i.e., fluid-phases velocity, holdup, density, and pressure).

The developed method discretizes fluid flow domain and the relevant transport equations in a staggered gridding arrangement. In this arrangement, scalar variables such as pressure and density are stored at the center of an ordinary control volume. While a separate control volume, associated with faces of the ordinary control volume, is defined to compute fluid-phase velocities. Figure 3.2 shows the discretized borehole domain with the associated staggered grids. In this figure, SCV identifies the control volume of scalar properties, and VCV denotes velocity control volume. The center of a VCV, defined based on the location of a velocity vector, coincides with faces of the corresponding SCV. Storing velocity vectors at locations different from those for pressure prevents the pressure field from unrealistic oscillations, thus improving stability of the developed numerical method. Furthermore, in this arrangement, the computation of flux terms in Equation 3.4 requires no interpolation at SCV faces, thereby securing a more accurate solution compared to a regular gridding arrangement.

ψ_k	η_{ψ_k}	Γ_{ψ_k}
1	0	$\Gamma_k^{\text{for}} + \Gamma_k^{\text{int}}$
x_{jk}	0	Γ_{jk}^{for}
V_k	$2\mu_k$	$-\alpha_k \frac{\partial P}{\partial z} + \alpha_k \rho_k g \cos \theta - F_{Wk} + F_{Dk}$

Table 3.1: Summary of transport fluid properties (ψ_k), diffusion, and source terms defined in the generic form of transport equation (i.e., Equation 3.1).

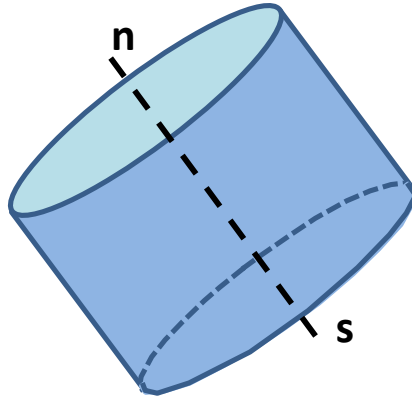


Figure 3.1: Schematic of a finite control volume considered for the discretization of borehole flow domains. Vector properties are defined in the center of the control volume while scalar properties are assigned to n- and s-faces.

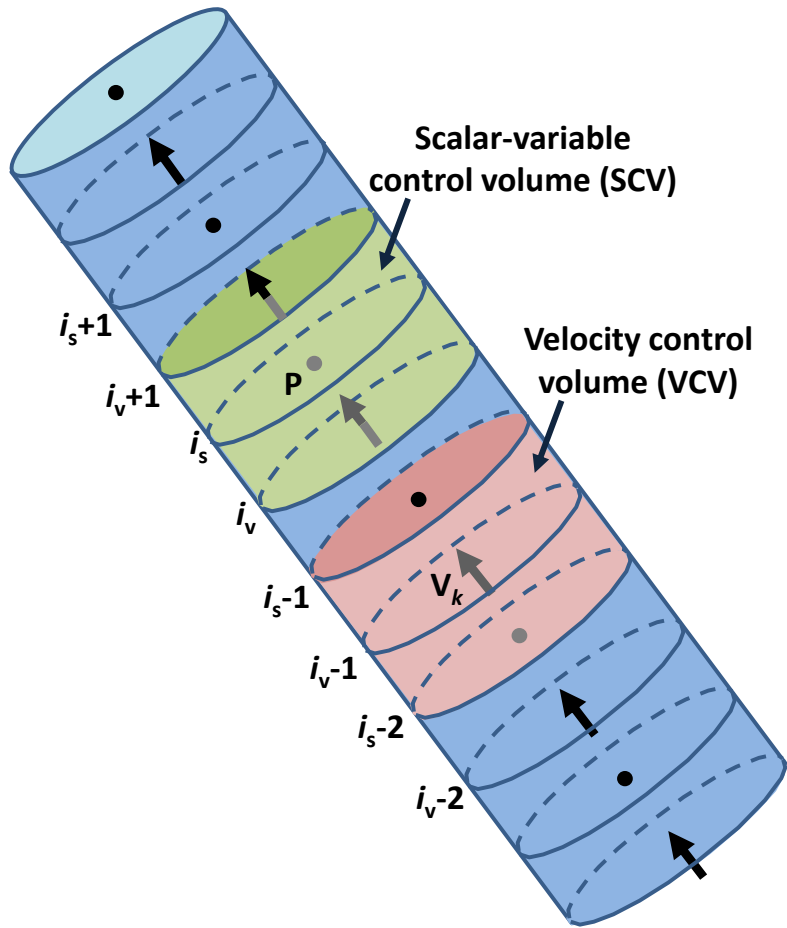


Figure 3.2: Schematic of staggered gridding arrangement used for discretization of the borehole flow domain. Two separate finite control volumes are defined for computation of fluid-phase velocity and pressure. The schematic shows that center of a VCV coincides with face of the preceding SCV.

3.2 DISCRETIZATION OF TRANSPORT EQUATIONS

Staggered gridding method is applied to Equation 3.4 to yield two sets of discretized transport equations: one for fluid-phase scalar properties (i.e., mass conservation equations), and the other for fluid-phase velocity (i.e., momentum conservation equations). Integral form of the mass conservation equations over a SCV is discretized as

$$\frac{\partial}{\partial t}(\alpha_k \rho_k \psi_k)_{i_s} + \frac{1}{\Delta z_{i_s}}(\alpha_k \rho_k \psi_k V_k)_{i_v+1} - \frac{1}{\Delta z_{i_s}}(\alpha_k \rho_k \psi_k V_k)_{i_v} = (\Gamma_{\psi_k})_{i_s}, \quad (3.5)$$

where $\psi_k = 1$ describes fluid-phase mass conservation equations, and $\psi_k = x_{jk}$ identifies component-based mass conservation equations. In the above equation, subscripts "i_s" and "i_v" are indices for scalar and velocity control volumes, respectively, Δz_{i_s} is the length of a scalar control volume in z direction, and Γ_{ψ_k} is volumetric average of mass source terms. I invoke a first-order upwind-weighting scheme to define scalar variables associated with convective flux terms. This scheme assigns the value of ψ_k equivalent to the associated convected value from upstream face of the control volume (Versteeg and Malalasekera, 1995), i.e.,

$$(\alpha_k \rho_k \psi_k V_k)_{i_v+1} = \begin{cases} (\alpha_k \rho_k \psi_k)_{i_s+1} (V_k)_{i_v+1}, & (V_k)_{i_v+1} < 0 \\ (\alpha_k \rho_k \psi_k)_{i_s} (V_k)_{i_v+1}, & (V_k)_{i_v+1} \geq 0 \end{cases}, \quad \text{and} \quad (3.6)$$

$$(\alpha_k \rho_k \psi_k V_k)_{i_v} = \begin{cases} (\alpha_k \rho_k \psi_k)_{i_s} (V_k)_{i_v}, & (V_k)_{i_v} < 0 \\ (\alpha_k \rho_k \psi_k)_{i_s-1} (V_k)_{i_v}, & (V_k)_{i_v} \geq 0 \end{cases}. \quad (3.7)$$

Space discretization of momentum equations over a finite VCV yields

$$\begin{aligned} \frac{\partial}{\partial t}(\alpha_k \rho_k V_k)_{i_v} + \frac{1}{\Delta z_{i_v}}(\alpha_k \rho_k V_k V_k)_{i_s} - \frac{1}{\Delta z_{i_v}}(\alpha_k \rho_k V_k V_k)_{i_s-1} = \\ \frac{1}{\Delta z_{i_v}} \left(\alpha_k 2\mu_k \frac{\partial V_k}{\partial z} \right)_{i_s} - \frac{1}{\Delta z_{i_v}} \left(\alpha_k 2\mu_k \frac{\partial V_k}{\partial z} \right)_{i_s-1} + (\Gamma_{V_k})_{i_v}, \end{aligned} \quad (3.8)$$

where Δz_{i_v} is the length of VCV in z direction, and $(\Gamma_{V_k})_{i_v}$ is volumetric average of momentum source terms. Scalar variables associated with the accumulation term are evaluated by invoking linear interpolations, given by (Hoffmann and Chiang, 2000)

$$(\alpha_k \rho_k V_k)_{i_v} = \left[\frac{z_{i_s} - z_{i_v}}{\Delta z_{i_v}} (\alpha_k \rho_k)_{i_s-1} + \frac{z_{i_v} - z_{i_s-1}}{\Delta z_{i_v}} (\alpha_k \rho_k)_{i_s} \right] (V_k)_{i_v}. \quad (3.9)$$

A combination of linear interpolation and upwind weighting is additionally applied to evaluate variables associated with convection flux terms. The linear interpolation first computes convective fluxes at the locations of velocity vector as follows:

$$(\alpha_k \rho_k V_k V_k)_{i_s} = \frac{z_{i_v+1} - z_{i_s}}{\Delta z_{i_s}} (\alpha_k \rho_k V_k V_k)_{i_v} + \frac{z_{i_s} - z_{i_v}}{\Delta z_{i_s}} (\alpha_k \rho_k V_k V_k)_{i_v+1}, \quad \text{and} \quad (3.10)$$

$$(\alpha_k \rho_k V_k V_k)_{i_{s-1}} = \frac{z_{i_v} - z_{i_{s-1}}}{\Delta z_{i_{s-1}}} (\alpha_k \rho_k V_k V_k)_{i_{v-1}} + \frac{z_{i_{s-1}} - z_{i_{v-1}}}{\Delta z_{i_{s-1}}} (\alpha_k \rho_k V_k V_k)_{i_v}, \quad (3.11)$$

subsequently, scalar variables are evaluated via the upwind-weighting method as

$$(\alpha_k \rho_k V_k V_k)_{i_v+1} = \begin{cases} (\alpha_k \rho_k)_{i_{s+1}} (V_k V_k)_{i_v+1}, & (V_k)_{i_v+1} < 0 \\ (\alpha_k \rho_k)_{i_s} (V_k V_k)_{i_v+1}, & (V_k)_{i_v+1} \geq 0 \end{cases}, \quad (3.12)$$

$$(\alpha_k \rho_k V_k V_k)_{i_v} = \begin{cases} (\alpha_k \rho_k)_{i_s} (V_k V_k)_{i_v}, & (V_k)_{i_v} < 0 \\ (\alpha_k \rho_k)_{i_{s-1}} (V_k V_k)_{i_v}, & (V_k)_{i_v} \geq 0 \end{cases}, \quad \text{and} \quad (3.13)$$

$$(\alpha_k \rho_k V_k V_k)_{i_{v-1}} = \begin{cases} (\alpha_k \rho_k)_{i_{s-1}} (V_k V_k)_{i_{v-1}}, & (V_k)_{i_{v-1}} < 0 \\ (\alpha_k \rho_k)_{i_{s-2}} (V_k V_k)_{i_{v-1}}, & (V_k)_{i_{v-1}} \geq 0 \end{cases}. \quad (3.14)$$

Diffusive flux terms in Equation (3.8) are discretized by applying a central differencing method to yield

$$\left(2\alpha_k \mu_k \frac{\partial V_k}{\partial z} \right)_{i_s} = 2(\alpha_k \mu_k)_{i_s} \frac{(V_k)_{i_v+1} - (V_k)_{i_v}}{\Delta z_{i_s}}, \quad \text{and} \quad (3.15)$$

$$\left(2\alpha_k \mu_k \frac{\partial V_k}{\partial z} \right)_{i_{s-1}} = 2(\alpha_k \mu_k)_{i_{s-1}} \frac{(V_k)_{i_v} - (V_k)_{i_{v-1}}}{\Delta z_{i_{s-1}}}. \quad (3.16)$$

Momentum source terms in Equation 3.8 contain forces associated with pressure, gravity, wall friction, and interfacial frictions. Space discretization of the source term is performed as

$$\begin{aligned}
(\Gamma_{V_k})_{i_v} = & \left(-\alpha_k \frac{\partial P}{\partial z} + \alpha_k \rho_k g \cos \theta - F_{Wk} + F_{Dk} \right)_{i_v} = -(\alpha_k)_{i_v} \frac{(P)_{i_s} - (P)_{i_{s-1}}}{\Delta z_{i_v}} \\
& + (\alpha_k \rho_k)_{i_v} g \cos \theta - (f_{Wk})_{i_v} |V_k|_{i_v} (V_k)_{i_v} \\
& + (f_{Dk})_{i_v} |V_k - V_l|_{i_v} (V_k - V_l)_{i_v}, \tag{3.17}
\end{aligned}$$

where subscript "l" identifies the second fluid phase flowing in the borehole, f_{Wk} is borehole wall friction coefficient described with Equation 2.6, and f_{Dkl} indicates the coefficients associated with interfacial drag forces defined by Equations 2.18 and 2.22. The required fluid-phase scalar properties in the center of VCVs are obtained by performing appropriate linear interpolations; the linear interpolation for fluid-phase volume fraction, for instance, is given by

$$(\alpha_k)_{i_v} = \frac{z_{i_s} - z_{i_v}}{\Delta z_{i_v}} (\alpha_k)_{i_{s-1}} + \frac{z_{i_v} - z_{i_{s-1}}}{\Delta z_{i_v}} (\alpha_k)_{i_s}. \tag{3.18}$$

3.3 MATRIX FORM OF DISCRETIZED TRANSPORT EQUATIONS

The numerical method developed in this dissertation consists of two parts: (i) a thermodynamics module, and (ii) a fluid dynamics module. As illustrated in Figure 3.3, the thermodynamics module solves $2 \times (n_c - 1)$ convective transport equations to iteratively update fluid-phase composition, density, and viscosity. Following the calculation of fluid-phase density and viscosity, the developed fluid dynamics module assumes known values for those properties to iteratively update fluid-phase velocity, pressure, and volume fraction. The solution algorithm adopted in this module is based on a guess-and-correct procedure originally pioneered by Patankar and Spalding (1972). Semi-implicit-method-for-pressure-linkage-equations (SIMPLE) algorithm was introduced for single-phase fluid flows. This algorithm constructs a pressure-correction

equation from the continuity equation. Subsequently, the algorithm iteratively corrects pressure and velocity fields to guarantee conservation of the overall mass. I implement two variants of SIMPLE algorithm, namely, (i) SIMPLE-consistent (SIMPLE-C) algorithm, introduced by Van Doormal and Raithby (1984) for single-phase fluid flow, and (ii) inter-phase-slip-algorithm-coupled (IPSA-C) introduced by Spalding (1980) for two-phase fluid flows. This section develops the discretized transport equations in time and space suitable for SIMPLE-C and IPSA-C algorithms. Details of those algorithms will be discussed in Section 3.5.

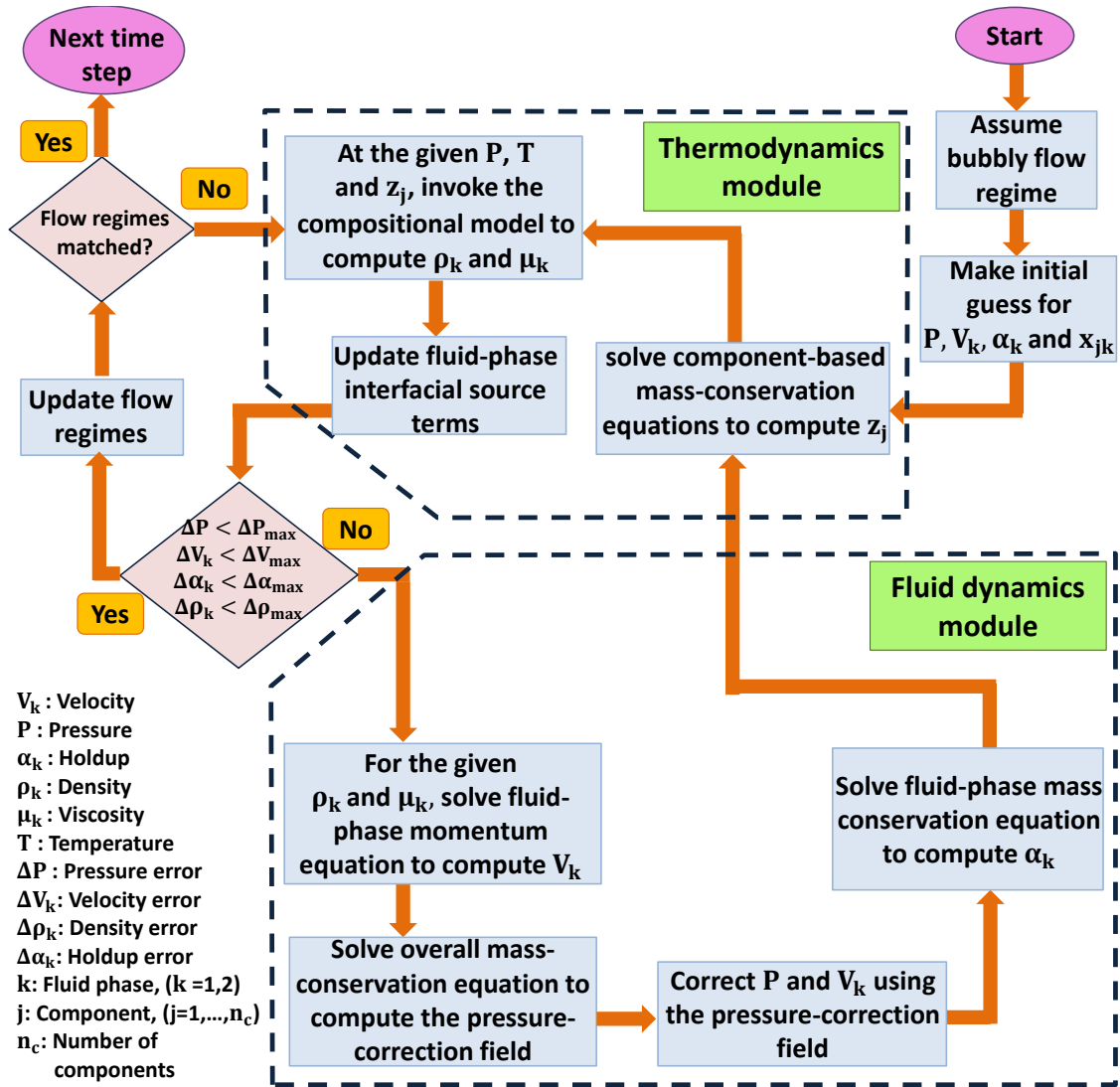


Figure 3.3: Developed iterative workflow to simulate borehole fluid-phase velocity, pressure, volume fraction, density, viscosity, and hydrocarbon molar composition. The algorithm includes two modules: (a) thermodynamics module, and (b) fluid dynamics module. A pressure-correction algorithm is invoked within the fluid dynamics module to compute fluid-phase velocity, pressure, and volume fraction assuming fixed values for fluid-phase density and viscosity. Subsequently, the thermodynamics module computes the overall molar composition, and updates fluid-phase density and viscosity. A detailed description of the equations developed for each module has been presented in Section 3.3.

3.3.1 Component-Based Mass Conservation Equation

Integration of the component transport equation over a finite time step (namely, Δt_n) yields

$$\begin{aligned}
& \int_{t_n}^{t_n+\Delta t_n} \frac{\partial}{\partial t} (\alpha_k \rho_k x_{jk})_{i_s} dt \\
& + \int_{t_n}^{t_n+\Delta t_n} \frac{1}{2\Delta z_{i_s}} [1 - \text{sign}(V_k)_{i_{v+1}}] (\alpha_k \rho_k x_{jk})_{i_{s+1}} (V_k)_{i_{v+1}} dt \\
& + \int_{t_n}^{t_n+\Delta t_n} \frac{1}{2\Delta z_{i_s}} [1 + \text{sign}(V_k)_{i_{v+1}}] (\alpha_k \rho_k x_{jk})_{i_s} (V_k)_{i_{v+1}} dt \\
& - \int_{t_n}^{t_n+\Delta t_n} \frac{1}{2\Delta z_{i_s}} [1 - \text{sign}(V_k)_{i_v}] (\alpha_k \rho_k x_{jk})_{i_s} (V_k)_{i_v} dt \\
& - \int_{t_n}^{t_n+\Delta t_n} \frac{1}{2\Delta z_{i_s}} [1 + \text{sign}(V_k)_{i_v}] (\alpha_k \rho_k x_{jk})_{i_{s-1}} (V_k)_{i_v} dt \\
& = \int_{t_n}^{t_n+\Delta t_n} (\Gamma_{jk}^{\text{for}})_{i_s} dt, \tag{3.19}
\end{aligned}$$

where

$$\text{sign}(x) = \begin{cases} 1, & x > 0 \\ 0, & x = 0 \\ -1, & x < 0 \end{cases}. \tag{3.20}$$

The developed algorithm decouples the abovementioned set of equations from the equations associated with fluid-phase mass and momentum conservation to solve for component mass (or molar) fraction. Decoupling is carried out by replacing fluid-phase velocity, density, and volume fraction with the most updated values computed from fluid-phase mass and momentum conservation equations. These intermediary fluid-phase properties are denoted with superscript "c_p". In this notation, $(\alpha_k)^{c_p}$, $(P)^{c_p}$, and $(V_k)^{c_p}$ describes previous solution computed with the fluid dynamics module, and $(\rho_k)^{c_p}$, $(\mu_k)^{c_p}$ and $(x_{jk})^{c_p}$ identify previous solution calculated by the thermodynamics module.

Furthermore, superscripts "c_n" and "c_n^{*}" are used to represent new and previous trial solutions within each module, respectively. When convergence criteria are achieved, the associated "c_p" values are substituted with the newly-computed "c_n" values. Applying the introduced notation, integration described with Equation 3.19 is carried out as

$$\begin{aligned}
& \frac{1}{\Delta t_n} \left[(\alpha_k \rho_k)_{i_s}^{c_p} (x_{jk})_{i_s}^{c_n} - (\alpha_k \rho_k x_{jk})_{i_s}^n \right] \\
& + \frac{1}{2\Delta z_{i_s}} \left[1 - \text{sign}(V_k)_{i_{v+1}}^{c_p} \right] (\alpha_k \rho_k)_{i_{s+1}}^{c_p} (V_k)_{i_{v+1}}^{c_p} (x_{jk})_{i_{s+1}}^{c_n} \\
& + \frac{1}{2\Delta z_{i_s}} \left[1 + \text{sign}(V_k)_{i_{v+1}}^{c_p} \right] (\alpha_k \rho_k)_{i_s}^{c_p} (V_k)_{i_{v+1}}^{c_p} (x_{jk})_{i_s}^{c_n} \\
& - \frac{1}{2\Delta z_{i_s}} \left[1 - \text{sign}(V_k)_{i_v}^{c_p} \right] (\alpha_k \rho_k)_{i_s}^{c_p} (V_k)_{i_v}^{c_p} (x_{jk})_{i_s}^{c_n} \\
& - \frac{1}{2\Delta z_{i_s}} \left[1 + \text{sign}(V_k)_{i_v}^{c_p} \right] (\alpha_k \rho_k)_{i_{s-1}}^{c_p} (V_k)_{i_v}^{c_p} (x_{jk})_{i_{s-1}}^{c_n} \\
& = \left(\Gamma_{jk}^{\text{for}} \right)_{i_s}^n.
\end{aligned} \tag{3.21}$$

Rearranging Equation 3.21 simplifies that equation to

$$\begin{aligned}
& \left\{ \frac{1}{\Delta t_n} (\alpha_k \rho_k)_{i_s}^{c_p} + \frac{1}{2\Delta z_{i_s}} \left[1 + \text{sign}(V_k)_{i_{v+1}}^{c_p} \right] (\alpha_k \rho_k)_{i_s}^{c_p} (V_k)_{i_{v+1}}^{c_p} \right. \\
& \quad \left. - \frac{1}{2\Delta z_{i_s}} \left[1 - \text{sign}(V_k)_{i_v}^{c_p} \right] (\alpha_k \rho_k)_{i_s}^{c_p} (V_k)_{i_v}^{c_p} \right\} (x_{jk})_{i_s}^{c_n} \\
& = \frac{1}{2\Delta z_{i_s}} \left[1 + \text{sign}(V_k)_{i_v}^{c_p} \right] (\alpha_k \rho_k)_{i_{s-1}}^{c_p} (V_k)_{i_v}^{c_p} (x_{jk})_{i_{s-1}}^{c_n} \\
& - \frac{1}{2\Delta z_{i_s}} \left[1 - \text{sign}(V_k)_{i_{v+1}}^{c_p} \right] (\alpha_k \rho_k)_{i_{s+1}}^{c_p} (V_k)_{i_{v+1}}^{c_p} (x_{jk})_{i_{s+1}}^{c_n} \\
& + \frac{1}{\Delta t_n} (\alpha_k \rho_k x_{jk})_{i_s}^n + \left(\Gamma_{jk}^{\text{for}} \right)_{i_s}^n,
\end{aligned} \tag{3.22}$$

and a compact form of discretized component-based mass conservation equation is next written as

$$A_{i_s, x_{jk}} (x_{jk})_{i_s}^{c_n} = A_{i_s-1, x_{jk}} (x_{jk})_{i_s-1}^{c_n} + A_{i_s+1, x_{jk}} (x_{jk})_{i_s+1}^{c_n} + B_{i_s, x_{jk}}, \quad (3.23)$$

where coefficients of the above equation have been summarized in Table 3.2.

Coefficient	Value
$A_{i_s, x_{jk}}$	$\frac{1}{\Delta t_n} (\alpha_k \rho_k)_{i_s}^{c_p} + \frac{1}{2\Delta z_{i_s}} \left[1 + \text{sign}(V_k)_{i_v+1}^{c_p} \right] (\alpha_k \rho_k)_{i_s}^{c_p} (V_k)_{i_v+1}^{c_p}$ $- \frac{1}{2\Delta z_{i_s}} \left[1 - \text{sign}(V_k)_{i_v}^{c_p} \right] (\alpha_k \rho_k)_{i_s}^{c_p} (V_k)_{i_v}^{c_p}$
$A_{i_s-1, x_{jk}}$	$\frac{1}{2\Delta z_{i_s}} \left[1 + \text{sign}(V_k)_{i_v}^{c_p} \right] (\alpha_k \rho_k)_{i_s-1}^{c_p} (V_k)_{i_v}^{c_p}$
$A_{i_s+1, x_{jk}}$	$- \frac{1}{2\Delta z_{i_s}} \left[1 - \text{sign}(V_k)_{i_v+1}^{c_p} \right] (\alpha_k \rho_k)_{i_s+1}^{c_p} (V_k)_{i_v+1}^{c_p}$
$B_{i_s, x_{jk}}$	$\frac{1}{\Delta t_n} (\alpha_k \rho_k x_{jk})_{i_s}^n + (\Gamma_{jk}^{\text{for}})_{i_s}^n$

Table 3.2: Summary of coefficients introduced in the discretized component-based mass conservation equation (i.e., Equation 3.23).

3.3.2 Equation for Fluid-Phase Volume Fraction

I apply the integration procedure introduced in Equation 3.19 to fluid-phase mass conservation equation to derive the following discretized equation for fluid holdup:

$$\begin{aligned} & \frac{1}{\Delta t_n} \left[(\rho_k)_{i_s}^{c_p} (\alpha_k)_{i_s}^{c_n} - (\alpha_k \rho_k)_{i_s}^n \right] \\ & + \frac{1}{2\Delta z_{i_s}} \left[1 - \text{sign}(V_k)_{i_v+1}^{c_n} \right] (\rho_k)_{i_s+1}^{c_p} (V_k)_{i_v+1}^{c_n} (\alpha_k)_{i_s+1}^{c_n} \\ & + \frac{1}{2\Delta z_{i_s}} \left[1 + \text{sign}(V_k)_{i_v+1}^{c_n} \right] (\rho_k)_{i_s}^{c_p} (V_k)_{i_v+1}^{c_n} (\alpha_k)_{i_s}^{c_n} \end{aligned}$$

$$\begin{aligned}
& -\frac{1}{2\Delta z_{i_s}} \left[1 - \text{sign}(V_k)_{i_v}^{c_n^*} \right] (\rho_k)_{i_s}^{c_p} (V_k)_{i_v}^{c_n^*} (\alpha_k)_{i_s}^{c_n} \\
& -\frac{1}{2\Delta z_{i_s}} \left[1 + \text{sign}(V_k)_{i_v}^{c_n^*} \right] (\rho_k)_{i_{s-1}}^{c_p} (V_k)_{i_v}^{c_n^*} (\alpha_k)_{i_{s-1}}^{c_n} \\
& = (\Gamma_k^{\text{for}})_{i_s}^n + (\Gamma_k^{\text{int}})_{i_s}^{c_p},
\end{aligned} \tag{3.24}$$

where in a compact notation is written as

$$A_{i_s, \alpha_k} (\alpha_k)_{i_s}^{c_n} = A_{i_{s-1}, \alpha_k} (\alpha_k)_{i_{s-1}}^{c_n} + A_{i_{s+1}, \alpha_k} (\alpha_k)_{i_{s+1}}^{c_n} + B_{i_s, \alpha_k}, \tag{3.25}$$

and Table 3.3 describes coefficients of the above equation.

Coefficient	Value
A_{i_s, α_k}	$\frac{1}{\Delta t_n} (\rho_k)_{i_s}^{c_n} + \frac{1}{2\Delta z_{i_s}} \left[1 + \text{sign}(V_k)_{i_{v+1}}^{c_n^*} \right] (\rho_k)_{i_s}^{c_p} (V_k)_{i_{v+1}}^{c_n^*}$ $- \frac{1}{2\Delta z_{i_s}} \left[1 - \text{sign}(V_k)_{i_v}^{c_n^*} \right] (\rho_k)_{i_s}^{c_p} (V_k)_{i_v}^{c_n^*}$
A_{i_{s-1}, α_k}	$\frac{1}{2\Delta z_{i_s}} \left[1 + \text{sign}(V_k)_{i_v}^{c_n^*} \right] (\rho_k)_{i_{s-1}}^{c_p} (V_k)_{i_v}^{c_n^*}$
A_{i_{s+1}, α_k}	$- \frac{1}{2\Delta z_{i_s}} \left[1 - \text{sign}(V_k)_{i_{v+1}}^{c_n^*} \right] (\rho_k)_{i_{s+1}}^{c_p} (V_k)_{i_{v+1}}^{c_n^*}$
B_{i_s, α_k}	$\frac{1}{\Delta t_n} (\alpha_k \rho_k)_{i_s}^n + (\Gamma_k^{\text{for}})_{i_s}^n + (\Gamma_k^{\text{int}})_{i_s}^{c_p}$

Table 3.3: Summary of coefficients introduced in the discretized mass conservation equation for fluid-phase volume fraction (i.e., Equation 3.25).

3.3.3 Conservation Equation for the Overall Mass

Numerical method developed in this dissertation combines the mass conservation equations for two fluid phases to obtain an equation describing the overall mass conservation. This method first normalizes the mass conservation equation by fluid-phase density, and next rearranges the equation in terms of fluid-phase velocity. The resulting velocity equation in a compact form is written as

$$A_{i_v, \rho_k} (V_k)_{i_v}^{c_n} + A_{i_v+1, \rho_k} (V_k)_{i_v+1}^{c_n} = B_{i_v, \rho_k}, \quad (3.26)$$

with coefficients summarized in Table 3.4. Subsequently, a summation is performed over the two fluid phases to yield

$$\begin{aligned} A_{i_v, \rho_1} (V_1)_{i_v}^{c_n} + A_{i_v+1, \rho_1} (V_1)_{i_v+1}^{c_n} + A_{i_v, \rho_2} (V_2)_{i_v}^{c_n} + A_{i_v+1, \rho_2} (V_2)_{i_v+1}^{c_n} \\ = B_{i_v, \rho_1} + B_{i_v, \rho_2}, \end{aligned} \quad (3.27)$$

Section 3.5 will describe the developed algorithm to obtain pressure-correction equation from Equation 3.27.

Coefficient	Value
A_{i_v, ρ_k}	$-\frac{1}{(\rho_k)_{i_s}^n} \frac{1}{2\Delta z_{i_s}} \left[1 - \text{sign}(V_k)_{i_v}^{c_n^*} \right] (\alpha_k)_{i_s}^{c_n^*} (\rho_k)_{i_s}^{c_p}$ $-\frac{1}{(\rho_k)_{i_s}^n} \frac{1}{2\Delta z_{i_s}} \left[1 + \text{sign}(V_k)_{i_v}^{c_n^*} \right] (\alpha_k)_{i_{s-1}}^{c_n^*} (\rho_k)_{i_{s-1}}^{c_p}$
A_{i_{v+1}, ρ_k}	$\frac{1}{(\rho_k)_{i_s}^n} \frac{1}{2\Delta z_{i_s}} \left[1 - \text{sign}(V_k)_{i_{v+1}}^{c_n^*} \right] (\alpha_k)_{i_{s+1}}^{c_n^*} (\rho_k)_{i_{s+1}}^{c_p}$ $+\frac{1}{(\rho_k)_{i_s}^n} \frac{1}{2\Delta z_{i_s}} \left[1 + \text{sign}(V_k)_{i_{v+1}}^{c_n^*} \right] (\alpha_k)_{i_s}^{c_n^*} (\rho_k)_{i_s}^{c_p}$
B_{i_v, ρ_k}	$\frac{1}{(\rho_k)_{i_s}^n} (\Gamma_k^{\text{for}})_{i_s}^n - \frac{1}{(\rho_k)_{i_s}^n} \frac{1}{\Delta t_n} \left[(\rho_k)_{i_s}^{c_p} (\alpha_k)_{i_s}^{c_n^*} - (\alpha_k \rho_k)_{i_s}^n \right]$

Table 3.4: Summary of coefficients introduced in discretized conservation equation for the overall mass (i.e., Equation 3.26).

3.3.4 Fluid-Phase Momentum Conservation Equation

I integrate momentum conservation equations described with Equation 3.8 over a finite time step to perform time discretization as

$$\begin{aligned}
& \int_{t_n}^{t_n + \Delta t_n} \frac{\partial}{\partial t} \left\{ \left[\frac{z_{i_s} - z_{i_v}}{\Delta z_{i_v}} (\alpha_k \rho_k)_{i_{s-1}} + \frac{z_{i_v} - z_{i_{s-1}}}{\Delta z_{i_v}} (\alpha_k \rho_k)_{i_s} \right] (V_k)_{i_v} \right\} dt \\
& + \int_{t_n}^{t_n + \Delta t_n} \frac{z_{i_{v+1}} - z_{i_s}}{2\Delta z_{i_v} \Delta z_{i_s}} [1 + \text{sign}(V_k)_{i_v}] (\alpha_k \rho_k)_{i_{s-1}} (V_k V_k)_{i_v} dt \\
& + \int_{t_n}^{t_n + \Delta t_n} \frac{z_{i_{v+1}} - z_{i_s}}{2\Delta z_{i_v} \Delta z_{i_s}} [1 - \text{sign}(V_k)_{i_v}] (\alpha_k \rho_k)_{i_s} (V_k V_k)_{i_v} dt \\
& + \int_{t_n}^{t_n + \Delta t_n} \frac{z_{i_s} - z_{i_v}}{2\Delta z_{i_v} \Delta z_{i_s}} [1 + \text{sign}(V_k)_{i_{v+1}}] (\alpha_k \rho_k)_{i_s} (V_k V_k)_{i_{v+1}} dt
\end{aligned}$$

$$\begin{aligned}
& + \int_{t_n}^{t_n+\Delta t_n} \frac{z_{i_s} - z_{i_v}}{2\Delta z_{i_v} \Delta z_{i_s}} [1 - \text{sign}(V_k)_{i_v+1}] (\alpha_k \rho_k)_{i_s+1} (V_k V_k)_{i_v+1} dt \\
& - \int_{t_n}^{t_n+\Delta t_n} \frac{z_{i_v} - z_{i_s-1}}{2\Delta z_{i_v} \Delta z_{i_s-1}} [1 + \text{sign}(V_k)_{i_v-1}] (\alpha_k \rho_k)_{i_s-2} (V_k V_k)_{i_v-1} dt \\
& - \int_{t_n}^{t_n+\Delta t_n} \frac{z_{i_v} - z_{i_s-1}}{2\Delta z_{i_v} \Delta z_{i_s-1}} [1 - \text{sign}(V_k)_{i_v-1}] (\alpha_k \rho_k)_{i_s-1} (V_k V_k)_{i_v-1} dt \\
& - \int_{t_n}^{t_n+\Delta t_n} \frac{z_{i_s-1} - z_{i_v-1}}{2\Delta z_{i_v} \Delta z_{i_s-1}} [1 + \text{sign}(V_k)_{i_v}] (\alpha_k \rho_k)_{i_s-1} (V_k V_k)_{i_v} dt \\
& - \int_{t_n}^{t_n+\Delta t_n} \frac{z_{i_s-1} - z_{i_v-1}}{2\Delta z_{i_v} \Delta z_{i_s-1}} [1 - \text{sign}(V_k)_{i_v}] (\alpha_k \rho_k)_{i_s} (V_k V_k)_{i_v} dt \\
& = \int_{t_n}^{t_n+\Delta t_n} \frac{2}{\Delta z_{i_v} \Delta z_{i_s}} (\alpha_k \mu_k)_{i_s} [(V_k)_{i_v+1} - (V_k)_{i_v}] dt \\
& - \int_{t_n}^{t_n+\Delta t_n} \frac{2}{\Delta z_{i_v} \Delta z_{i_s-1}} (\alpha_k \mu_k)_{i_s-1} [(V_k)_{i_v} - (V_k)_{i_v-1}] dt \\
& - \int_{t_n}^{t_n+\Delta t_n} \frac{1}{\Delta z_{i_v}} \left\{ \frac{z_{i_s} - z_{i_v}}{\Delta z_{i_v}} (\alpha_k)_{i_s-1} + \frac{z_{i_v} - z_{i_s-1}}{\Delta z_{i_v}} (\alpha_k)_{i_s} \right\} [(P)_{i_s} \\
& - (P)_{i_s-1}] dt \\
& + \int_{t_n}^{t_n+\Delta t_n} \left\{ \frac{z_{i_s} - z_{i_v}}{\Delta z_{i_v}} (\alpha_k \rho_k)_{i_s-1} + \frac{z_{i_v} - z_{i_s-1}}{\Delta z_{i_v}} (\alpha_k \rho_k)_{i_s} \right\} g \cos \theta dt \\
& - \int_{t_n}^{t_n+\Delta t_n} (f_{wk})_{i_v} |V_k|_{i_v} (V_k)_{i_v} dt \\
& + \int_{t_n}^{t_n+\Delta t_n} (f_{Dlk})_{i_v} |V_k - V_l|_{i_v} (V_k - V_l)_{i_v} dt. \tag{3.28}
\end{aligned}$$

Time discretization of the above equation requires the nonlinear terms to be linearized around time $t_n + \Delta t_n$. Linearization of the nonlinear terms is performed by applying Taylor series expansion, to wit,

$$(V_k V_k)_{i_v}^{c_n} = (V_k V_k)_{i_v}^{c_n^*} + \frac{1}{2} (2V_k)_{i_v}^{c_n^*} [(V_k)_{i_v}^{n+1} - (V_k)_{i_v}^{c_n^*}] + \text{H. O. T.}$$

$$\approx (V_k)_{i_v}^{c_n^*} (V_k)_{i_v}^{c_n}. \quad (3.29)$$

Furthermore, linearization of the nonlinear momentum source terms is carried out as (Prosperetti and Tryggvason, 2007)

$$(|V_k - V_l|(V_k - V_l))_{i_v}^{c_n} \approx (|V_k - V_l|)_{i_v}^{c_n^*} (V_k - V_l)_{i_v}^{c_n}. \quad (3.30)$$

The discretized form of momentum transport equations replaces fluid-phase density and viscosity with their corresponding "c_p" values (i.e., the most updated solution of thermodynamics module). In addition, when explicit values for fluid-phase velocity and volume fraction are required, the developed algorithm assigns the corresponding "c_n^{*}" values. Accordingly, combining Equations 3.28 through 3.30 yields

$$\begin{aligned} & \frac{1}{\Delta t_n} \left\{ \left[\frac{z_{i_s} - z_{i_v}}{\Delta z_{i_v}} (\alpha_k)_{i_{s-1}}^{c_n^*} (\rho_k)_{i_{s-1}}^{c_p} + \frac{z_{i_v} - z_{i_{s-1}}}{\Delta z_{i_v}} (\alpha_k)_{i_s}^{c_n^*} (\rho_k)_{i_s}^{c_p} \right] (V_k)_{i_v}^{c_n} \right. \\ & - \left. \left[\frac{z_{i_s} - z_{i_v}}{\Delta z_{i_v}} (\alpha_k \rho_k)_{i_{s-1}}^n + \frac{z_{i_v} - z_{i_{s-1}}}{\Delta z_{i_v}} (\alpha_k \rho_k)_{i_s}^n \right] (V_k)_{i_v}^n \right\} \\ & + \frac{z_{i_{v+1}} - z_{i_s}}{2\Delta z_{i_v} \Delta z_{i_s}} \left[1 + \text{sign}(V_k)_{i_v}^{c_n^*} \right] (\alpha_k)_{i_{s-1}}^{c_n^*} (\rho_k)_{i_{s-1}}^{c_p} (V_k)_{i_v}^{c_n^*} (V_k)_{i_v}^{c_n} \\ & + \frac{z_{i_{v+1}} - z_{i_s}}{2\Delta z_{i_v} \Delta z_{i_s}} \left[1 - \text{sign}(V_k)_{i_v}^{c_n^*} \right] (\alpha_k)_{i_s}^{c_n^*} (\rho_k)_{i_s}^{c_p} (V_k)_{i_v}^{c_n^*} (V_k)_{i_v}^{c_n} \\ & + \frac{z_{i_s} - z_{i_v}}{2\Delta z_{i_v} \Delta z_{i_s}} \left[1 + \text{sign}(V_k)_{i_{v+1}}^{c_n^*} \right] (\alpha_k)_{i_s}^{c_n^*} (\rho_k)_{i_s}^{c_p} (V_k)_{i_{v+1}}^{c_n^*} (V_k)_{i_{v+1}}^{c_n} \\ & + \frac{z_{i_s} - z_{i_v}}{2\Delta z_{i_v} \Delta z_{i_s}} \left[1 - \text{sign}(V_k)_{i_{v+1}}^{c_n^*} \right] (\alpha_k)_{i_{s+1}}^{c_n^*} (\rho_k)_{i_{s+1}}^{c_p} (V_k)_{i_{v+1}}^{c_n^*} (V_k)_{i_{v+1}}^{c_n} \\ & - \frac{z_{i_v} - z_{i_{s-1}}}{2\Delta z_{i_v} \Delta z_{i_{s-1}}} \left[1 + \text{sign}(V_k)_{i_{v-1}}^{c_n^*} \right] (\alpha_k)_{i_{s-2}}^{c_n^*} (\rho_k)_{i_{s-2}}^{c_p} (V_k)_{i_{v-1}}^{c_n^*} (V_k)_{i_{v-1}}^{c_n} \\ & - \frac{z_{i_v} - z_{i_{s-1}}}{2\Delta z_{i_v} \Delta z_{i_{s-1}}} \left[1 - \text{sign}(V_k)_{i_{v-1}}^{c_n^*} \right] (\alpha_k)_{i_{s-1}}^{c_n^*} (\rho_k)_{i_{s-1}}^{c_p} (V_k)_{i_{v-1}}^{c_n^*} (V_k)_{i_{v-1}}^{c_n} \\ & - \frac{z_{i_{s-1}} - z_{i_{v-1}}}{2\Delta z_{i_v} \Delta z_{i_{s-1}}} \left[1 + \text{sign}(V_k)_{i_v}^{c_n^*} \right] (\alpha_k)_{i_{s-1}}^{c_n^*} (\rho_k)_{i_{s-1}}^{c_p} (V_k)_{i_v}^{c_n^*} (V_k)_{i_v}^{c_n} \end{aligned}$$

$$\begin{aligned}
& -\frac{z_{i_s-1} - z_{i_v-1}}{2\Delta z_{i_v}\Delta z_{i_s-1}} \left[1 - \text{sign}(V_k)_{i_v}^{c_n^*} \right] (\alpha_k)_{i_s}^{c_n^*} (\rho_k)_{i_s}^{c_p} (V_k)_{i_v}^{c_n^*} (V_k)_{i_v}^{c_n} \\
& = \frac{2}{\Delta z_{i_v}\Delta z_{i_s}} (\alpha_k)_{i_s}^{c_n^*} (\mu_k)_{i_s}^{c_p} \left[(V_k)_{i_v+1}^{c_n} - (V_k)_{i_v}^{c_n} \right] \\
& - \frac{2}{\Delta z_{i_v}\Delta z_{i_s-1}} (\alpha_k)_{i_s-1}^{c_n^*} (\mu_k)_{i_s-1}^{c_p} \left[(V_k)_{i_v}^{c_n} - (V_k)_{i_v-1}^{c_n} \right] \\
& - \frac{1}{\Delta z_{i_v}} \left\{ \frac{z_{i_s} - z_{i_v}}{\Delta z_{i_v}} (\alpha_k)_{i_s-1}^{c_n^*} + \frac{z_{i_v} - z_{i_s-1}}{\Delta z_{i_v}} (\alpha_k)_{i_s}^{c_n^*} \right\} \left[(P)_{i_s}^{c_n} - (P)_{i_s-1}^{c_n} \right] \\
& + \left\{ \frac{z_{i_s} - z_{i_v}}{\Delta z_{i_v}} (\alpha_k)_{i_s-1}^{c_n^*} (\rho_k)_{i_s-1}^{c_p} + \frac{z_{i_v} - z_{i_s-1}}{\Delta z_{i_v}} (\alpha_k)_{i_s}^{c_n^*} (\rho_k)_{i_s}^{c_p} \right\} g \cos \theta \\
& - (f_{Wk})_{i_v}^{c_n^*} (|V_k|)_{i_v}^{c_n^*} (V_k)_{i_v}^{c_n} \\
& + (f_{Dlk})_{i_v}^{c_n^*} (|V_k - V_l|)_{i_v}^{c_n^*} (V_k - V_l)_{i_v}^{c_n}. \tag{3.31}
\end{aligned}$$

Rearranging the above equation obtains the following discretized equation:

$$\begin{aligned}
& \left\{ \frac{1}{\Delta t_n} \left[\frac{z_{i_s} - z_{i_v}}{\Delta z_{i_v}} (\alpha_k)_{i_s-1}^{c_n^*} (\rho_k)_{i_s-1}^{c_p} + \frac{z_{i_v} - z_{i_s-1}}{\Delta z_{i_v}} (\alpha_k)_{i_s}^{c_n^*} (\rho_k)_{i_s}^{c_p} \right] \right. \\
& \quad + \frac{1}{\Delta z_{i_v}} \left[\frac{z_{i_v+1} - z_{i_s}}{\Delta z_{i_s}} - \frac{z_{i_s-1} - z_{i_v-1}}{\Delta z_{i_s-1}} \right] \left[1 + \text{sign}(V_k)_{i_v}^{c_n^*} \right] \\
& \quad \times (\alpha_k)_{i_s-1}^{c_n^*} (\rho_k)_{i_s-1}^{c_p} (V_k)_{i_v}^{c_n^*} \\
& \quad + \frac{2}{\Delta z_{i_v}} \left[\frac{1}{\Delta z_{i_s}} (\alpha_k)_{i_s}^{c_n^*} (\mu_k)_{i_s}^{c_p} + \frac{1}{\Delta z_{i_s-1}} (\alpha_k)_{i_s-1}^{c_n^*} (\mu_k)_{i_s-1}^{c_p} \right] \\
& \quad \left. + (f_{Wk})_{i_v}^{c_n^*} (|V_k|)_{i_v}^{c_n^*} \right\} (V_k)_{i_v}^{c_n} \\
& = \left\{ \frac{z_{i_v} - z_{i_s-1}}{2\Delta z_{i_v}\Delta z_{i_s-1}} \left[1 + \text{sign}(V_k)_{i_v-1}^{c_n^*} \right] (\alpha_k)_{i_s-2}^{c_n^*} (\rho_k)_{i_s-2}^{c_p} (V_k)_{i_v-1}^{c_n^*} \right. \\
& \quad + \frac{z_{i_v} - z_{i_s-1}}{2\Delta z_{i_v}\Delta z_{i_s-1}} \left[1 - \text{sign}(V_k)_{i_v-1}^{c_n^*} \right] (\alpha_k)_{i_s-1}^{c_n^*} (\rho_k)_{i_s-1}^{c_p} (V_k)_{i_v-1}^{c_n^*} \\
& \quad \left. + \frac{2}{\Delta z_{i_v}\Delta z_{i_s-1}} (\alpha_k)_{i_s-1}^{c_n^*} (\mu_k)_{i_s-1}^{c_p} \right\} (V_k)_{i_v-1}^{c_n}
\end{aligned}$$

$$\begin{aligned}
& + \left\{ \frac{z_{i_s} - z_{i_v}}{2\Delta z_{i_v} \Delta z_{i_s}} \left[1 + \text{sign}(V_k)_{i_v+1}^{c_n^*} \right] (\alpha_k)_{i_s}^{c_n^*} (\rho_k)_{i_s}^{c_p} (V_k)_{i_v+1}^{c_n} \right. \\
& \quad + \frac{z_{i_s} - z_{i_v}}{2\Delta z_{i_v} \Delta z_{i_s}} \left[1 - \text{sign}(V_k)_{i_v+1}^{c_n^*} \right] (\alpha_k)_{i_s+1}^{c_n^*} (\rho_k)_{i_s+1}^{c_p} (V_k)_{i_v+1}^{c_n^*} \\
& \quad \left. + \frac{2}{\Delta z_{i_v} \Delta z_{i_s}} (\alpha_k)_{i_s}^{c_n^*} (\mu_k)_{i_s}^{c_p} \right\} (V_k)_{i_v+1}^{c_n} \\
& - \frac{1}{\Delta z_{i_v}} \left\{ \frac{z_{i_s} - z_{i_v}}{\Delta z_{i_v}} (\alpha_k)_{i_s-1}^{c_n^*} + \frac{z_{i_v} - z_{i_s-1}}{\Delta z_{i_v}} (\alpha_k)_{i_s}^{c_n^*} \right\} \left[(P)_{i_s}^{c_n} - (P)_{i_s-1}^{c_n} \right] \\
& + (f_{Dlk})_{i_v}^{c_n^*} (|V_k - V_l|)_{i_v}^{c_n^*} (V_k - V_l)_{i_v}^{c_n} \\
& + \frac{1}{\Delta t_n} \left[\frac{z_{i_s} - z_{i_v}}{\Delta z_{i_v}} (\alpha_k \rho_k)_{i_s-1}^n + \frac{z_{i_v} - z_{i_s-1}}{\Delta z_{i_v}} (\alpha_k \rho_k)_{i_s}^n \right] (V_k)_{i_v}^n \\
& + \left[\frac{z_{i_s} - z_{i_v}}{\Delta z_{i_v}} (\alpha_k)_{i_s-1}^{c_n^*} (\rho_k)_{i_s-1}^{c_p} + \frac{z_{i_v} - z_{i_s-1}}{\Delta z_{i_v}} (\alpha_k)_{i_s}^{c_n^*} (\rho_k)_{i_s}^{c_p} \right] g \cos \theta . \quad 3.32
\end{aligned}$$

The above equation is expressed in a compact form as

$$\begin{aligned}
A_{i_v, V_k} (V_k)_{i_v}^{c_n} & = A_{i_v-1, V_k} (V_k)_{i_v-1}^{c_n} + A_{i_v+1, V_k} (V_k)_{i_v+1}^{c_n} \\
& \quad - A_{i_v, P_k} \left[(P)_{i_s}^{c_n} - (P)_{i_s-1}^{c_n} \right] + A_{i_v, V_{lk}} (V_k - V_l)_{i_v}^{c_n} + B_{i_v, V_k}, \quad (3.33)
\end{aligned}$$

where coefficients of Equation 3.33 are summarized in Table 3.5.

Coefficient	Value
A_{i_v, V_k}	$\frac{1}{\Delta t_n} \left[\frac{z_{i_s} - z_{i_v}}{\Delta z_{i_v}} (\alpha_k)_{i_{s-1}}^{c_n^*} (\rho_k)_{i_{s-1}}^{c_p} + \frac{z_{i_v} - z_{i_{s-1}}}{\Delta z_{i_v}} (\alpha_k)_{i_s}^{c_n^*} (\rho_k)_{i_s}^{c_p} \right]$ $+ \frac{1}{\Delta z_{i_v}} \left[\frac{z_{i_{v+1}} - z_{i_s}}{\Delta z_{i_s}} - \frac{z_{i_{s-1}} - z_{i_{v-1}}}{\Delta z_{i_{s-1}}} \right] \left[1 + \text{sign}(V_k)_{i_v}^{c_n^*} \right]$ $\times (\alpha_k)_{i_{s-1}}^{c_n^*} (\rho_k)_{i_{s-1}}^{c_p} (V_k)_{i_v}^{c_n^*}$ $+ \frac{2}{\Delta z_{i_v}} \left[\frac{1}{\Delta z_{i_s}} (\alpha_k)_{i_s}^{c_n^*} (\mu_k)_{i_s}^{c_p} + \frac{1}{\Delta z_{i_{s-1}}} (\alpha_k)_{i_{s-1}}^{c_n^*} (\mu_k)_{i_{s-1}}^{c_p} \right]$ $+ (f_{Wk})_{i_v}^{c_n^*} (V_k)_{i_v}^{c_n^*}$
A_{i_v-1, V_k}	$\frac{z_{i_v} - z_{i_{s-1}}}{2\Delta z_{i_v} \Delta z_{i_{s-1}}} \left[1 + \text{sign}(V_k)_{i_{v-1}}^{c_n^*} \right] (\alpha_k)_{i_{s-2}}^{c_n^*} (\rho_k)_{i_{s-2}}^{c_p} (V_k)_{i_{v-1}}^{c_n^*}$ $+ \frac{z_{i_v} - z_{i_{s-1}}}{2\Delta z_{i_v} \Delta z_{i_{s-1}}} \left[1 - \text{sign}(V_k)_{i_{v-1}}^{c_n^*} \right] (\alpha_k)_{i_{s-1}}^{c_n^*} (\rho_k)_{i_{s-1}}^{c_p} (V_k)_{i_{v-1}}^{c_n^*}$ $+ \frac{2}{\Delta z_{i_v} \Delta z_{i_{s-1}}} (\alpha_k)_{i_{s-1}}^{c_n^*} (\mu_k)_{i_{s-1}}^{c_p}$
A_{i_v+1, V_k}	$\frac{z_{i_s} - z_{i_v}}{2\Delta z_{i_v} \Delta z_{i_s}} \left[1 + \text{sign}(V_k)_{i_{v+1}}^{c_n^*} \right] (\alpha_k)_{i_s}^{c_n^*} (\rho_k)_{i_s}^{c_p} (V_k)_{i_{v+1}}^{c_n^*}$ $+ \frac{z_{i_s} - z_{i_v}}{2\Delta z_{i_v} \Delta z_{i_s}} \left[1 - \text{sign}(V_k)_{i_{v+1}}^{c_n^*} \right] (\alpha_k)_{i_{s+1}}^{c_n^*} (\rho_k)_{i_{s+1}}^{c_p} (V_k)_{i_{v+1}}^{c_n^*}$ $+ \frac{2}{\Delta z_{i_v} \Delta z_{i_s}} (\alpha_k)_{i_s}^{c_n^*} (\mu_k)_{i_s}^{c_p}$
A_{i_v, P_k}	$\frac{1}{\Delta z_{i_v}} \left[\frac{z_{i_s} - z_{i_v}}{\Delta z_{i_v}} (\alpha_k)_{i_{s-1}}^{c_n^*} + \frac{z_{i_v} - z_{i_{s-1}}}{\Delta z_{i_v}} (\alpha_k)_{i_s}^{c_n^*} \right]$
$A_{i_v, V_{lk}}$	$(f_{Dlk})_{i_v}^{c_n^*} (V_k - V_l)_{i_v}^{c_n^*}$
B_{i_v, V_k}	$+ \frac{1}{\Delta t_n} \left[\frac{z_{i_s} - z_{i_v}}{\Delta z_{i_v}} (\alpha_k \rho_k)_{i_{s-1}}^n + \frac{z_{i_v} - z_{i_{s-1}}}{\Delta z_{i_v}} (\alpha_k \rho_k)_{i_s}^n \right] (V_k)_{i_v}^n$ $+ \left[\frac{z_{i_s} - z_{i_v}}{\Delta z_{i_v}} (\alpha_k)_{i_{s-1}}^{c_n^*} (\rho_k)_{i_{s-1}}^{c_p} + \frac{z_{i_v} - z_{i_{s-1}}}{\Delta z_{i_v}} (\alpha_k)_{i_s}^{c_n^*} (\rho_k)_{i_s}^{c_p} \right] g \cos \theta$

Table 3.5: Summary of the coefficients introduced in fluid-phase momentum conservation equation (i.e., Equation 3.33).

3.4 BOREHOLE SINGLE-PHASE FLUID FLOW EQUATIONS

A special form of two-fluid formulation is obtained when fluid-phase volume fraction reaches its maximum value (namely, $\alpha_k = 1$). Single-phase borehole fluid flow equations are derived from Equations 3.23 for fluid mass conservation, namely,

$$\begin{aligned}
& \frac{1}{\Delta t_n} \left[(\rho)_{i_s}^{c_p} - (\rho)_{i_s}^n \right] \\
& + \frac{1}{2\Delta z_{i_s}} \left[1 - \text{sign}(V)_{i_{v+1}}^{c_n} \right] (\rho)_{i_{s+1}}^{c_p} (V)_{i_{v+1}}^{c_n} \\
& + \frac{1}{2\Delta z_{i_s}} \left[1 + \text{sign}(V)_{i_{v+1}}^{c_n} \right] (\rho)_{i_s}^{c_p} (V)_{i_{v+1}}^{c_n} \\
& - \frac{1}{2\Delta z_{i_s}} \left[1 - \text{sign}(V)_{i_v}^{c_n} \right] (\rho)_{i_s}^{c_p} (V)_{i_v}^{c_n} \\
& - \frac{1}{2\Delta z_{i_s}} \left[1 + \text{sign}(V)_{i_v}^{c_n} \right] (\rho)_{i_{s-1}}^{c_p} (V)_{i_v}^{c_n} \\
& = (\Gamma^{\text{for}})_{i_s}^n,
\end{aligned} \tag{3.34}$$

and from Equation 3.32 for fluid momentum conservation, i.e.,

$$\begin{aligned}
& \left\{ \frac{1}{\Delta t_n} \left[\frac{z_{i_s} - z_{i_v}}{\Delta z_{i_v}} (\rho)_{i_{s-1}}^{c_p} + \frac{z_{i_v} - z_{i_{s-1}}}{\Delta z_{i_v}} (\rho)_{i_s}^{c_p} \right] \right. \\
& + \frac{1}{\Delta z_{i_v}} \left[\frac{z_{i_{v+1}} - z_{i_s}}{\Delta z_{i_s}} - \frac{z_{i_{s-1}} - z_{i_{v-1}}}{\Delta z_{i_{s-1}}} \right] \left[1 + \text{sign}(V)_{i_v}^{c_n^*} \right] (\rho)_{i_{s-1}}^{c_p} (V)_{i_v}^{c_n^*} \\
& + \frac{2}{\Delta z_{i_v}} \left[\frac{1}{\Delta z_{i_s}} (\mu)_{i_s}^{c_p} + \frac{1}{\Delta z_{i_{s-1}}} (\mu)_{i_{s-1}}^{c_p} \right] + (f_w)_{i_v}^{c_n^*} (|V|)_{i_v}^{c_n^*} \left. \right\} (V)_{i_v}^{c_n} \\
& = \left\{ \frac{z_{i_v} - z_{i_{s-1}}}{2\Delta z_{i_v} \Delta z_{i_{s-1}}} \left[1 + \text{sign}(V)_{i_{v-1}}^{c_n^*} \right] (\rho)_{i_{s-2}}^{c_p} (V)_{i_{v-1}}^{c_n^*} \right. \\
& + \frac{z_{i_v} - z_{i_{s-1}}}{2\Delta z_{i_v} \Delta z_{i_{s-1}}} \left[1 - \text{sign}(V)_{i_{v-1}}^{c_n^*} \right] (\rho)_{i_{s-1}}^{c_p} (V)_{i_{v-1}}^{c_n^*} \\
& \left. + \frac{2}{\Delta z_{i_v}} \left[\frac{1}{\Delta z_{i_s}} (\mu)_{i_s}^{c_p} + \frac{1}{\Delta z_{i_{s-1}}} (\mu)_{i_{s-1}}^{c_p} \right] \right\} (V)_{i_{v-1}}^{c_n}
\end{aligned}$$

$$\begin{aligned}
& + \left\{ \frac{z_{i_s} - z_{i_v}}{2\Delta z_{i_v}\Delta z_{i_s}} \left[1 + \text{sign}(V)_{i_v+1}^{c_n^*} \right] (\rho)_{i_s}^{c_p} (V)_{i_v+1}^{c_n} \right. \\
& + \frac{z_{i_s} - z_{i_v}}{2\Delta z_{i_v}\Delta z_{i_s}} \left[1 - \text{sign}(V)_{i_v+1}^{c_n^*} \right] (\rho)_{i_s+1}^{c_p} (V)_{i_v+1}^{c_n} \\
& + \frac{2}{\Delta z_{i_v}\Delta z_{i_s}} (\mu)_{i_s}^{c_p} \left. \right\} (V)_{i_v+1}^{c_n} \\
& - \frac{1}{\Delta z_{i_v}} \left[(P)_{i_s}^{c_n} - (P)_{i_s-1}^{c_n} \right] \\
& + \frac{1}{\Delta t_n} \left[\frac{z_{i_s} - z_{i_v}}{\Delta z_{i_v}} (\rho)_{i_s-1}^n + \frac{z_{i_v} - z_{i_s-1}}{\Delta z_{i_v}} (\rho)_{i_s}^n \right] (V)_{i_v}^n \\
& + \left[\frac{z_{i_s} - z_{i_v}}{\Delta z_{i_v}} (\rho)_{i_s-1}^{c_p} + \frac{z_{i_v} - z_{i_s-1}}{\Delta z_{i_v}} (\rho)_{i_s}^{c_p} \right] g \cos \theta . \tag{3.35}
\end{aligned}$$

The abovementioned equations are written in the following compact notation to enable implementation of SIMPLE-C algorithm:

$$A_{i_v,\rho} (V)_{i_v}^{c_n} + A_{i_v+1,\rho} (V)_{i_v+1}^{c_n} = B_{i_v,\rho}, \quad \text{and} \tag{3.36}$$

$$\begin{aligned}
A_{i_v,V} (V)_{i_v}^{c_n} &= A_{i_v-1,V} (V)_{i_v-1}^{c_n} + A_{i_v+1,V} (V)_{i_v+1}^{c_n} \\
&\quad - A_{i_v,P} \left[(P)_{i_s}^{c_n} - (P)_{i_s-1}^{c_n} \right] + B_{i_v,V}, \tag{3.37}
\end{aligned}$$

where Tables 3.6 and 3.7 describe coefficients of the above equations.

Coefficient	Value
$A_{i_v,\rho}$	$-\frac{1}{2\Delta z_{i_s}} \left[1 - \text{sign}(V)_{i_v}^{c_n^*} \right] (\rho)_{i_s}^{c_p} - \frac{1}{2\Delta z_{i_s}} \left[1 + \text{sign}(V)_{i_v}^{c_n^*} \right] (\rho)_{i_s-1}^{c_p}$
$A_{i_v+1,\rho}$	$\frac{1}{2\Delta z_{i_s}} \left[1 - \text{sign}(V)_{i_v+1}^{c_n^*} \right] (\rho)_{i_s+1}^{c_p} + \frac{1}{2\Delta z_{i_s}} \left[1 + \text{sign}(V)_{i_v+1}^{c_n^*} \right] (\rho)_{i_s}^{c_p}$
$B_{i_v,\rho}$	$(\Gamma^{\text{for}})_{i_s}^n - \frac{1}{\Delta t_n} \left[(\rho)_{i_s}^{c_p} - (\rho)_{i_s}^n \right]$

Table 3.6: Summary of coefficients introduced in the single-phase mass equation.

Coefficient	Value
$A_{i_v, V}$	$\frac{1}{\Delta t_n} \left[\frac{z_{i_s} - z_{i_v}}{\Delta z_{i_v}} (\rho)_{i_s-1}^{c_p} + \frac{z_{i_v} - z_{i_s-1}}{\Delta z_{i_v}} (\rho)_{i_s}^{c_p} \right]$ $+ \frac{1}{\Delta z_{i_v}} \left[\frac{z_{i_v+1} - z_{i_s}}{\Delta z_{i_s}} - \frac{z_{i_s-1} - z_{i_v-1}}{\Delta z_{i_s-1}} \right] \left[1 + \text{sign}(V)_{i_v}^{c_n^*} \right] (\rho)_{i_s-1}^{c_p} (V)_{i_v}^{c_n^*}$ $+ \frac{2}{\Delta z_{i_v}} \left[\frac{1}{\Delta z_{i_s}} (\mu)_{i_s}^{c_p} + \frac{1}{\Delta z_{i_s-1}} (\mu)_{i_s-1}^{c_p} \right] + (f_w)_{i_v}^{c_n^*} (V)_{i_v}^{c_n^*}$
$A_{i_v-1, V}$	$\frac{z_{i_v} - z_{i_s-1}}{2\Delta z_{i_v} \Delta z_{i_s-1}} \left[1 + \text{sign}(V)_{i_v-1}^{c_n^*} \right] (\rho)_{i_s-2}^{c_p} (V)_{i_v-1}^{c_n^*}$ $+ \frac{z_{i_v} - z_{i_s-1}}{2\Delta z_{i_v} \Delta z_{i_s-1}} \left[1 - \text{sign}(V)_{i_v-1}^{c_n^*} \right] (\rho)_{i_s-1}^{c_p} (V)_{i_v-1}^{c_n^*}$ $+ \frac{2}{\Delta z_{i_v} \Delta z_{i_s-1}} (\mu)_{i_s-1}^{c_p}$
$A_{i_v+1, V}$	$\frac{z_{i_s} - z_{i_v}}{2\Delta z_{i_v} \Delta z_{i_s}} \left[1 + \text{sign}(V)_{i_v+1}^{c_n^*} \right] (\rho)_{i_s}^{c_p} (V)_{i_v+1}^{c_n^*}$ $+ \frac{z_{i_s} - z_{i_v}}{2\Delta z_{i_v} \Delta z_{i_s}} \left[1 - \text{sign}(V_k)_{i_v+1}^{c_n^*} \right] (\alpha_k)_{i_s+1}^{c_n^*} (\rho_k)_{i_s+1}^{c_p} (V_k)_{i_v+1}^{c_n^*}$
$A_{i_v, P}$	$\frac{1}{\Delta z_{i_v}}$
$B_{i_v, V}$	$+ \frac{1}{\Delta t_n} \left[\frac{z_{i_s} - z_{i_v}}{\Delta z_{i_v}} (\rho)_{i_s-1}^n + \frac{z_{i_v} - z_{i_s-1}}{\Delta z_{i_v}} (\rho)_{i_s}^n \right] (V)_{i_v}^n$ $+ \left[\frac{z_{i_s} - z_{i_v}}{\Delta z_{i_v}} (\rho)_{i_s-1}^{c_p} + \frac{z_{i_v} - z_{i_s-1}}{\Delta z_{i_v}} (\rho)_{i_s}^{c_p} \right] g \cos \theta$

Table 3.7: Summary of coefficients introduced in the discretized single-phase momentum conservation equation (i.e., Equation 3.37).

3.5 SOLUTION ALGORITHM

The fluid-dynamics part of the developed fluid flow model applies an iterative algorithm to compute borehole fluid-phase properties. The developed iterative algorithm numerically solves the following discretized equations in order to obtain a solution vector consisting of 5 unknowns for each control volume, i.e., fluid-phase velocities, fluid-phase volume fractions, and borehole pressure:

$$A_{i_s, \alpha_k} (\alpha_k)_{i_s}^{c_n} = A_{i_s-1, \alpha_k} (\alpha_k)_{i_s-1}^{c_n} + A_{i_s+1, \alpha_k} (\alpha_k)_{i_s+1}^{c_n} + B_{i_s, \alpha_k}, \quad (3.25)$$

$$A_{i_v, V_k} (V_k)_{i_v}^{c_n} = A_{i_v-1, V_k} (V_k)_{i_v-1}^{c_n} + A_{i_v+1, V_k} (V_k)_{i_v+1}^{c_n} - A_{i_v, P_k} [(P)_{i_s}^{c_n} - (P)_{i_s-1}^{c_n}] + A_{i_v, V_{lk}} (V_k - V_l)_{i_v}^{c_n} + B_{i_v, V_k}, \quad (3.33)$$

and

$$\sum_{k=1}^2 (\alpha_k)_{i_s}^{c_n} = 1. \quad (3.38)$$

As mentioned earlier, superscript "c_n" denotes a tentative solution vector that satisfies fluid-phase mass and momentum conservation equations. However, this solution does not necessarily result in a thermodynamic equilibrium. The final solution vector emerges as the result of an iterative procedure performed between thermodynamics and fluid-dynamics modules. As formulated in Equation 3.33, borehole fluid-phase velocity is coupled to borehole pressure and interfacial slippage velocity. Robustness and stability of any numerical method developed to solve the abovementioned system of equations is considerably influenced by interfacial and pressure-velocity couplings. In this dissertation, velocity-velocity and pressure-velocity couplings are effectively addressed by implementing SIMPLE-C algorithm for single-phase fluid flows, and IPSA-C algorithm for two-phase fluid flows. Both algorithms invoke the mass conservation equation to construct an explicit equation that formulates pressure-velocity linkage. In

addition, as an intermediary step, IPSA-C constructs a set of linear equations that specifically relates fluid-phase velocity to interfacial slip velocity, and addresses velocity-velocity coupling (Yeoh and Tu, 2010). This section presents a detailed description of the developed SIMPLE-C and IPSA-C methods.

3.5.1 Semi-Implicit Method for Pressure-Linkage Equations, Consistent (SIMPLE-C)

The developed iterative procedure begins with an initial guess for pressure field. The algorithm subsequently constructs a pressure-correction equation to progressively correct the guessed pressure. Let assume $(P)_{i_s}^n$ and $(V)_{i_v}^n$ are solutions of borehole single-phase fluid flow equations at time t_n , $(P)_{i_s}^{c_n^*}$ and $(V)_{i_v}^{c_n^*}$ are current trial solutions, and $(P)_{i_s}^{c_n}$ and $(V)_{i_v}^{c_n}$ are corrected solutions for time $t_n + \Delta t_n$. The guessed pressure, denoted by $(P)_{i_s}^{c_n^{**}}$, therefore, is equal to $(P)_{i_s}^{c_n^*}$, and is related to corrected pressure $(P)_{i_s}^{c_n}$ by (Versteeg and Malalasekera, 1995; Cebeci et al., 2005)

$$(P)_{i_s}^{c_n} = (P)_{i_s}^{c_n^{**}} + (P)_{i_s}^{c_n'}, \quad (3.39)$$

where $(P)_{i_s}^{c_n'}$ is defined as a correction to be applied to the guessed pressure. Subsequently, fluid momentum equation, described by Equation 3.37, is solved to compute the guessed velocity as

$$A_{i_v, V} (V)_{i_v}^{c_n^{**}} = A_{i_v-1, V} (V)_{i_v-1}^{c_n^{**}} + A_{i_v+1, V} (V)_{i_v+1}^{c_n^{**}} - A_{i_v, P} \left[(P)_{i_s}^{c_n^{**}} - (P)_{i_s-1}^{c_n^{**}} \right] + B_{i_v, V}. \quad (3.40)$$

Similarly, the guessed and corrected velocities are related through a velocity-correction field denoted by $(V)_{i_v}^{c_n'}$, as follows (Versteeg and Malalasekera, 1995; Cebeci et al., 2005):

$$(V)_{i_v}^{c_n} = (V)_{i_v}^{c_n^{**}} + (V)_{i_v}^{c_n'}. \quad (3.41)$$

Subtraction of Equation 3.40 from Equation 3.37 yields

$$\begin{aligned} A_{i_v, V} \left[(V)_{i_v}^{c_n} - (V)_{i_v}^{c_n^{**}} \right] &= A_{i_{v-1}, V} \left[(V)_{i_{v-1}}^{c_n} - (V)_{i_{v-1}}^{c_n^{**}} \right] \\ &+ A_{i_{v+1}, V} \left[(V)_{i_{v+1}}^{c_n} - (V)_{i_{v+1}}^{c_n^{**}} \right] \\ &- A_{i_v, P} \left\{ \left[(P)_{i_s}^{c_n} - (P)_{i_s}^{c_n^{**}} \right] - \left[(P)_{i_{s-1}}^{c_n} - (P)_{i_{s-1}}^{c_n^{**}} \right] \right\}. \end{aligned} \quad (3.42)$$

Applying the correction formula (i.e., Equation 3.41) to the above equation leads to

$$A_{i_v, V} (V)_{i_v}^{c_n'} = A_{i_{v-1}, V} (V)_{i_{v-1}}^{c_n'} + A_{i_{v+1}, V} (V)_{i_{v+1}}^{c_n'} - A_{i_v, P} \left[(P)_{i_s}^{c_n'} - (P)_{i_{s-1}}^{c_n'} \right], \quad (3.43)$$

that directly relates velocity correction to pressure correction. I assume velocity corrections associated with neighboring nodes are approximately equivalent to that of the central node (Versteeg and Malalasekera, 1995), therefore, I simplify velocity correction as

$$(V)_{i_{v-1}}^{c_n'} \approx (V)_{i_{v+1}}^{c_n'} \approx (V)_{i_v}^{c_n'}. \quad (3.44)$$

The above assumption results in the following equation that explicitly formulates velocity correction in terms of pressure correction:

$$\begin{aligned} (V)_{i_v}^{c_n'} &= -\frac{A_{i_v, P}}{A_{i_v, V} - A_{i_{v-1}, V} - A_{i_{v+1}, V}} \left[(P)_{i_s}^{c_n'} - (P)_{i_{s-1}}^{c_n'} \right] \\ &= -H_{i_v, P} \left[(P)_{i_s}^{c_n'} - (P)_{i_{s-1}}^{c_n'} \right], \end{aligned} \quad (3.45)$$

where

$$H_{i_v, P} = \frac{A_{i_v, P}}{A_{i_v, V} - A_{i_{v-1}, V} - A_{i_{v+1}, V}}. \quad (3.46)$$

Corrected velocity is therefore related to pressure correction via

$$(V)_{i_v}^{c_n} = (V)_{i_v}^{c_n^{**}} - H_{i_v,P} \left[(P)_{i_s}^{c'_n} - (P)_{i_{s-1}}^{c'_n} \right]. \quad (3.47)$$

A similar expression associates the corrected velocity of neighboring node to pressure correction as

$$(V)_{i_{v+1}}^{c_n} = (V)_{i_{v+1}}^{c_n^{**}} - H_{i_{v+1},P} \left[(P)_{i_{s+1}}^{c'_n} - (P)_{i_s}^{c'_n} \right]. \quad (3.48)$$

Algorithm next substitutes the mass conservation equation described with Equation 3.36 into Equations 3.47 and 3.48 to construct the pressure-correction equation as follows:

$$A_{i_v,\rho} \left\{ (V)_{i_v}^{c_n^{**}} - H_{i_v,P} \left[(P)_{i_s}^{c'_n} - (P)_{i_{s-1}}^{c'_n} \right] \right\} \\ A_{i_{v+1},\rho} \left\{ (V)_{i_{v+1}}^{c_n^{**}} - H_{i_{v+1},P} \left[(P)_{i_{s+1}}^{c'_n} - (P)_{i_s}^{c'_n} \right] \right\} = B_{i_v,\rho}. \quad (3.49)$$

Equation 3.49 is rearranged to

$$\left[A_{i_v,\rho} H_{i_v,P} - A_{i_{v+1},\rho} H_{i_{v+1},P} \right] (P)_{i_s}^{c'_n} = A_{i_v,\rho} H_{i_v,P} (P)_{i_{s-1}}^{c'_n} \\ - A_{i_{v+1},\rho} H_{i_{v+1},P} (P)_{i_{s+1}}^{c'_n} + A_{i_v,\rho} (V)_{i_v}^{c_n^{**}} \\ + A_{i_{v+1},\rho} (V)_{i_{v+1}}^{c_n^{**}} - B_{i_v,\rho}, \quad (3.50)$$

and in a compact notation, is written as

$$A_{i_s,PC}^S (P)_{i_s}^{c'_n} = A_{i_{s-1},PC}^S (P)_{i_{s-1}}^{c'_n} + A_{i_{s+1},PC}^S (P)_{i_{s+1}}^{c'_n} + B_{i_s,PC}^S, \quad (3.51)$$

where

$$A_{i_s,PC}^S = A_{i_v,\rho} H_{i_v,P} - A_{i_{v+1},\rho} H_{i_{v+1},P}, \quad (3.52)$$

$$A_{i_{s-1},PC}^S = A_{i_v,\rho} H_{i_v,P}, \quad (3.53)$$

$$A_{i_{s+1},PC}^S = -A_{i_{v+1},\rho} H_{i_{v+1},P}, \quad \text{and} \quad (3.54)$$

$$B_{i_s,PC}^s = A_{i_v,\rho} (V)_{i_v}^{c_n^{**}} + A_{i_v+1,\rho} (V)_{i_v+1}^{c_n^{**}} - B_{i_v,\rho}. \quad (3.55)$$

As Figure 3.4 shows, SIMPLE-C algorithm computes pressure correction from Equation 3.51, and accordingly corrects fluid pressure and velocity. Subsequently, the trial solutions (i.e., $(P)_{i_s}^{c_n^*}$ and $(V)_{i_v}^{c_n^*}$) are replaced with the corrected pressure and velocity iteration continues until the solution vector satisfies both mass and momentum conservation equations.

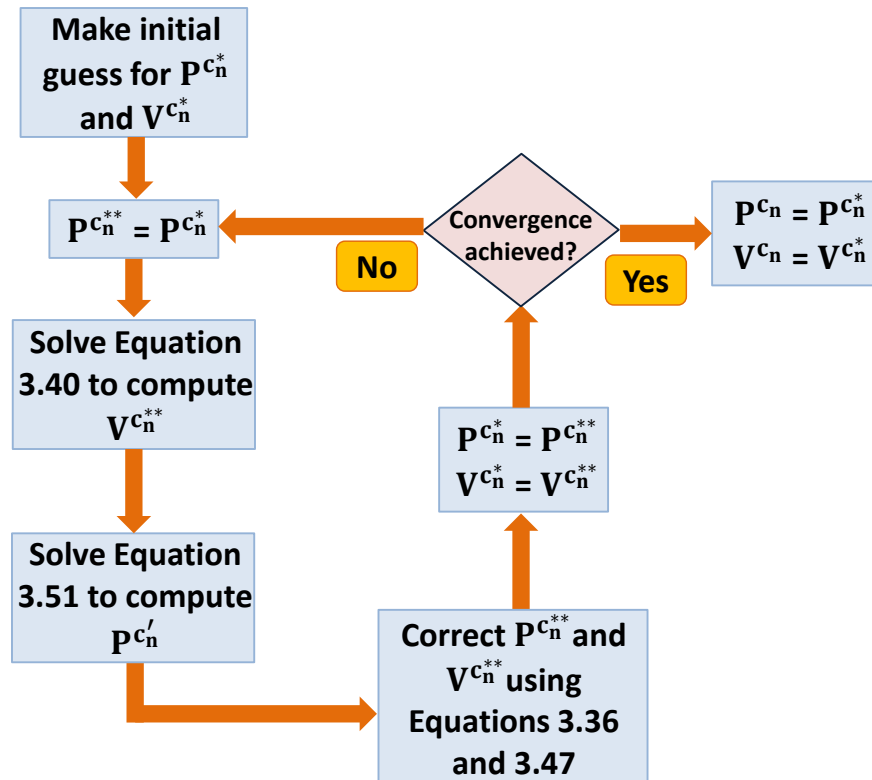


Figure 3.4: Developed iterative workflow to simulate borehole single-phase velocity and pressure. The SIMPLE-C algorithm begins with an initial guess for fluid properties. Subsequently, a pressure-correction equation (i.e., Equation 3.51) is constructed to correct the guessed values of pressure and velocity. The guess-and-correction algorithm continues until achieving a satisfactory convergence.

3.5.2 Inter-Phase Slip Algorithm, Coupled (IPSA-C)

In the presence of a strong interfacial coupling, explicit treatment of drag terms in momentum equations gives rise to an inaccurate simulation of fluid-phase properties. As formulated in Equation 3.33, a more robust and numerically-stable approach, is to include the interfacial drag term as a part of solution vector. I invoke a variant of SIMPLE-C algorithm for two-phase flow to improve the performance of pressure-correction step by a semi-implicit inclusion of interfacial drag terms in the computation of velocity-correction equation. This algorithm assumes the same local pressure shared by both fluid phases, and adds fluid-phase mass conservation equations to construct the pressure-correction equation.

Let $(P)_{i_s}^n$, $(V_k)_{i_v}^n$, and $(\alpha_k)_{i_v}^n$ be solution vector for borehole two-phase fluid flow equations at time t_n . Therefore, $(P)_{i_s}^{c_n}$, $(V_k)_{i_v}^{c_n}$, and $(\alpha_k)_{i_v}^{c_n}$ are current trial solutions, and $(P)_{i_s}^{c_n}$, $(V_k)_{i_v}^{c_n}$, and $(\alpha_k)_{i_v}^{c_n}$ are corrected solutions for time $t_n + \Delta t_n$. Identical to SIMPLE-C algorithm, guessed and corrected fluid-phase properties are defined as (Prosperetti and Tryggvason, 2007; Yeoh and Tu, 2010)

$$(P)_{i_s}^{c_n} = (P)_{i_s}^{c_n^{**}} + (P)_{i_s}^{c_n'}, \quad \text{and} \quad (3.56)$$

$$(V_k)_{i_s}^{c_n} = (V_k)_{i_s}^{c_n^{**}} + (V_k)_{i_s}^{c_n'}, \quad (3.57)$$

where superscript " c_n " identifies correction to be applied to the guessed properties. Fluid-phase momentum conservation equations (i.e., Equation 3.33) is next invoked to compute the guessed fluid-phase velocity as

$$A_{i_v, V_k} (V_k)_{i_v}^{c_n^{**}} = A_{i_v-1, V_k} (V_k)_{i_v-1}^{c_n^{**}} + A_{i_v+1, V_k} (V_k)_{i_v+1}^{c_n^{**}} - A_{i_v, P_k} \left[(P)_{i_s}^{c_n^{**}} - (P)_{i_s-1}^{c_n^{**}} \right] + A_{i_v, V_{1k}} (V_k - V_1)_{i_v}^{c_n^{**}} + B_{i_v, V_k} \cdot \quad (3.58)$$

Subtracting equation 3.58 from Equation 3.33 yields the following velocity-correction equation:

$$A_{i_v, V_k} (V_k)_{i_v}^{c'_n} = A_{i_v-1, V_k} (V_k)_{i_v-1}^{c'_n} + A_{i_v+1, V_k} (V_k)_{i_v+1}^{c'_n} - A_{i_v, P_k} \left[(P)_{i_s}^{c'_n} - (P)_{i_s-1}^{c'_n} \right] + A_{i_v, V_{lk}} (V_k - V_l)_{i_v}^{c'_n}. \quad (3.59)$$

Identical to SIMPLE-C, IPSA-C algorithm assumes an equivalent velocity correction for all neighboring control volumes (Yeoh and Tu, 2010), leading to

$$(V_k)_{i_v-1}^{c'_n} \approx (V_k)_{i_v+1}^{c'_n} \approx (V_k)_{i_v}^{c'_n}, \quad (3.60)$$

that simplifies Equation 3.59 to

$$\begin{aligned} (V_k)_{i_v}^{c'_n} &= -\frac{A_{i_v, P_k}}{A_{i_v, V_k} - A_{i_v-1, V_k} - A_{i_v+1, V_k}} \left[(P)_{i_s}^{c'_n} - (P)_{i_s-1}^{c'_n} \right] \\ &+ \frac{A_{i_v, V_{lk}}}{A_{i_v, V_k} - A_{i_v-1, V_k} - A_{i_v+1, V_k}} (V_k - V_l)_{i_v}^{c'_n} \\ &= -H_{i_v, P_k} \left[(P)_{i_s}^{c'_n} - (P)_{i_s-1}^{c'_n} \right] + H_{i_v, V_{lk}} (V_k - V_l)_{i_v}^{c'_n}, \end{aligned} \quad (3.61)$$

where

$$H_{i_v, P_k} = \frac{A_{i_v, P_k}}{A_{i_v, V_k} - A_{i_v-1, V_k} - A_{i_v+1, V_k}}, \quad \text{and} \quad (3.62)$$

$$H_{i_v, V_{lk}} = \frac{A_{i_v, V_{lk}}}{A_{i_v, V_k} - A_{i_v-1, V_k} - A_{i_v+1, V_k}}. \quad (3.63)$$

The set of linear equations that explicitly relates velocity correction to pressure correction is obtained by applying the following change of variable:

$$(\Psi_k)_{i_v}^{c'_n} = \frac{(V_k)_{i_v}^{c'_n}}{\left[(P)_{i_s}^{c'_n} - (P)_{i_s-1}^{c'_n} \right]}. \quad (3.64)$$

Assuming $k = 1$ and $l = 2$, Equation 3.64 is combined with Equation 3.61, to wit,

$$(\Psi_1)_{i_v}^{c'_n} = -H_{i_v, P_1} + H_{i_v, V_{21}} (\Psi_1 - \Psi_2)_{i_v}^{c'_n}, \quad \text{and} \quad (3.65)$$

$$(\Psi_2)_{i_v}^{c'_n} = -H_{i_v, P_2} + H_{i_v, V_{12}} (\Psi_2 - \Psi_1)_{i_v}^{c'_n}. \quad (3.66)$$

The above equations is rearranged to a matrix form as

$$\begin{bmatrix} 1 - H_{i_v, V_{21}} & H_{i_v, V_{21}} \\ H_{i_v, V_{12}} & 1 - H_{i_v, V_{12}} \end{bmatrix} \begin{bmatrix} (\Psi_1)_{i_v}^{c'_n} \\ (\Psi_2)_{i_v}^{c'_n} \end{bmatrix} = \begin{bmatrix} -H_{i_v, P_1} \\ -H_{i_v, P_2} \end{bmatrix}. \quad (3.67)$$

Solution of the above system of equations is obtained as

$$(\Psi_1)_{i_v}^{c'_n} = -\frac{H_{i_v, P_1} - H_{i_v, P_1} H_{i_v, V_{12}} - H_{i_v, P_2} H_{i_v, V_{21}}}{1 - H_{i_v, V_{12}} - H_{i_v, V_{21}}}, \quad \text{and} \quad (3.68)$$

$$(\Psi_2)_{i_v}^{c'_n} = -\frac{H_{i_v, P_2} - H_{i_v, P_1} H_{i_v, V_{12}} - H_{i_v, P_2} H_{i_v, V_{21}}}{1 - H_{i_v, V_{21}} - H_{i_v, V_{12}}}. \quad (3.69)$$

Substituting Equation 3.64 into the above equations leads to the following equations for fluid-phase velocity correction as an explicit function of pressure correction:

$$(V_1)_{i_v}^{c'_n} = -\frac{H_{i_v, P_1} - H_{i_v, P_1} H_{i_v, V_{12}} - H_{i_v, P_2} H_{i_v, V_{21}}}{1 - H_{i_v, V_{12}} - H_{i_v, V_{21}}} \left[(P)_{i_s}^{c'_n} - (P)_{i_s-1}^{c'_n} \right], \quad \text{and} \quad (3.70)$$

$$(V_2)_{i_v}^{c'_n} = -\frac{H_{i_v, P_2} - H_{i_v, P_1} H_{i_v, V_{12}} - H_{i_v, P_2} H_{i_v, V_{21}}}{1 - H_{i_v, V_{21}} - H_{i_v, V_{12}}} \left[(P)_{i_s}^{c'_n} - (P)_{i_s-1}^{c'_n} \right]. \quad (3.71)$$

In a compact notation, one obtains

$$(V_1)_{i_v}^{c'_n} = -G_{i_v, P_1} \left[(P)_{i_s}^{c'_n} - (P)_{i_{s-1}}^{c'_n} \right], \quad \text{and} \quad (3.72)$$

$$(V_2)_{i_v}^{c'_n} = -G_{i_v, P_2} \left[(P)_{i_s}^{c'_n} - (P)_{i_{s-1}}^{c'_n} \right], \quad (3.73)$$

where

$$G_{i_v, P_1} = \frac{H_{i_v, P_1} - H_{i_v, P_1} H_{i_v, V_{12}} - H_{i_v, P_2} H_{i_v, V_{21}}}{1 - H_{i_v, V_{21}} - H_{i_v, V_{12}}}, \quad \text{and} \quad (3.74)$$

$$G_{i_v, P_2} = \frac{H_{i_v, P_2} - H_{i_v, P_1} H_{i_v, V_{12}} - H_{i_v, P_2} H_{i_v, V_{21}}}{1 - H_{i_v, V_{21}} - H_{i_v, V_{12}}}. \quad (3.75)$$

Corrected fluid-phase velocities are subsequently computed as

$$(V_1)_{i_v}^{c_n} = (V_1)_{i_v}^{c_n^{**}} - G_{i_v, P_1} \left[(P)_{i_s}^{c'_n} - (P)_{i_{s-1}}^{c'_n} \right], \quad (3.76)$$

$$(V_2)_{i_v}^{c_n} = (V_2)_{i_v}^{c_n^{**}} - G_{i_v, P_2} \left[(P)_{i_s}^{c'_n} - (P)_{i_{s-1}}^{c'_n} \right], \quad (3.77)$$

$$(V_1)_{i_{v+1}}^{c_n} = (V_1)_{i_{v+1}}^{c_n^{**}} - G_{i_{v+1}, P_1} \left[(P)_{i_{s+1}}^{c'_n} - (P)_{i_s}^{c'_n} \right], \quad \text{and} \quad (3.78)$$

$$(V_2)_{i_{v+1}}^{c_n} = (V_2)_{i_{v+1}}^{c_n^{**}} - G_{i_{v+1}, P_2} \left[(P)_{i_{s+1}}^{c'_n} - (P)_{i_s}^{c'_n} \right]. \quad (3.79)$$

The overall mass conservation equation, described by Equation 3.27, is next invoked to construct the pressure-correction equation as

$$\begin{aligned} & A_{i_v, \rho_1} \left\{ (V_1)_{i_v}^{c_n^{**}} - G_{i_v, P_1} \left[(P)_{i_s}^{c'_n} - (P)_{i_{s-1}}^{c'_n} \right] \right\} \\ & + A_{i_{v+1}, \rho_1} \left\{ (V_1)_{i_{v+1}}^{c_n^{**}} - G_{i_{v+1}, P_1} \left[(P)_{i_s}^{c'_n} - (P)_{i_{s-1}}^{c'_n} \right] \right\} \\ & + A_{i_v, \rho_2} \left\{ (V_2)_{i_v}^{c_n^{**}} - G_{i_v, P_2} \left[(P)_{i_{s+1}}^{c'_n} - (P)_{i_s}^{c'_n} \right] \right\} \\ & + A_{i_{v+1}, \rho_2} \left\{ (V_2)_{i_{v+1}}^{c_n^{**}} - G_{i_{v+1}, P_2} \left[(P)_{i_{s+1}}^{c'_n} - (P)_{i_s}^{c'_n} \right] \right\} \\ & = B_{i_v, \rho_1} + B_{i_v, \rho_2}. \end{aligned} \quad (3.80)$$

The above equation is rearranged to

$$\begin{aligned}
& \left\{ A_{i_v, \rho_1} G_{i_v, P_1} + A_{i_v+1, \rho_1} G_{i_v+1, P_1} - A_{i_v, \rho_2} G_{i_v, P_2} - A_{i_v+1, \rho_2} G_{i_v+1, P_2} \right\} (P)_{i_s}^{c'_n} \\
&= \left\{ A_{i_v, \rho_1} G_{i_v, P_1} + A_{i_v+1, \rho_1} G_{i_v+1, P_1} \right\} (P)_{i_s-1}^{c'_n} \\
&- \left\{ A_{i_v, \rho_2} G_{i_v, P_2} + A_{i_v+1, \rho_2} G_{i_v+1, P_2} \right\} (P)_{i_s+1}^{c'_n} \\
&+ A_{i_v, \rho_1} (V_1)_{i_v}^{c_n^{**}} + A_{i_v+1, \rho_1} (V_1)_{i_v+1}^{c_n^{**}} \\
&+ A_{i_v, \rho_2} (V_2)_{i_v}^{c_n^{**}} + A_{i_v+1, \rho_2} (V_2)_{i_v+1}^{c_n^{**}} - B_{i_v, \rho_1} - B_{i_v, \rho_2}. \tag{3.81}
\end{aligned}$$

Rewriting the above equation in a compact form yields

$$A_{i_s, PC} (P)_{i_s}^{c'_n} = A_{i_s-1, PC} (P)_{i_s-1}^{c'_n} + A_{i_s+1, PC} (P)_{i_s+1}^{c'_n} + B_{i_s, PC}, \tag{3.82}$$

where

$$A_{i_s, PC} = A_{i_v, \rho_1} G_{i_v, P_1} + A_{i_v+1, \rho_1} G_{i_v+1, P_1} - A_{i_v, \rho_2} G_{i_v, P_2} - A_{i_v+1, \rho_2} G_{i_v+1, P_2}, \tag{3.83}$$

$$A_{i_s-1, PC} = A_{i_v, \rho_1} G_{i_v, P_1} + A_{i_v+1, \rho_1} G_{i_v+1, P_1}, \tag{3.84}$$

$$A_{i_s+1, PC} = -A_{i_v, \rho_2} G_{i_v, P_2} - A_{i_v+1, \rho_2} G_{i_v+1, P_2}, \quad \text{and} \tag{3.85}$$

$$\begin{aligned}
B_{i_s, PC} = & A_{i_v, \rho_1} (V_1)_{i_v}^{c_n^{**}} + A_{i_v+1, \rho_1} (V_1)_{i_v+1}^{c_n^{**}} \\
& + A_{i_v, \rho_2} (V_2)_{i_v}^{c_n^{**}} + A_{i_v+1, \rho_2} (V_2)_{i_v+1}^{c_n^{**}} - B_{i_v, \rho_1} - B_{i_v, \rho_2}. \tag{3.86}
\end{aligned}$$

The iterative algorithm computes pressure correction vector from Equation 3.82, and corrects fluid-phase pressure and velocity vectors using Equations 3.56 and 3.72. Subsequently, the algorithm applies fluid-phase mass conservation equation described with Equation 3.25 to compute fluid-phase volume fraction. As Figure 3.5 describes, the iterative procedure continues until trial solutions satisfy both fluid-phase mass and momentum conservation equations.

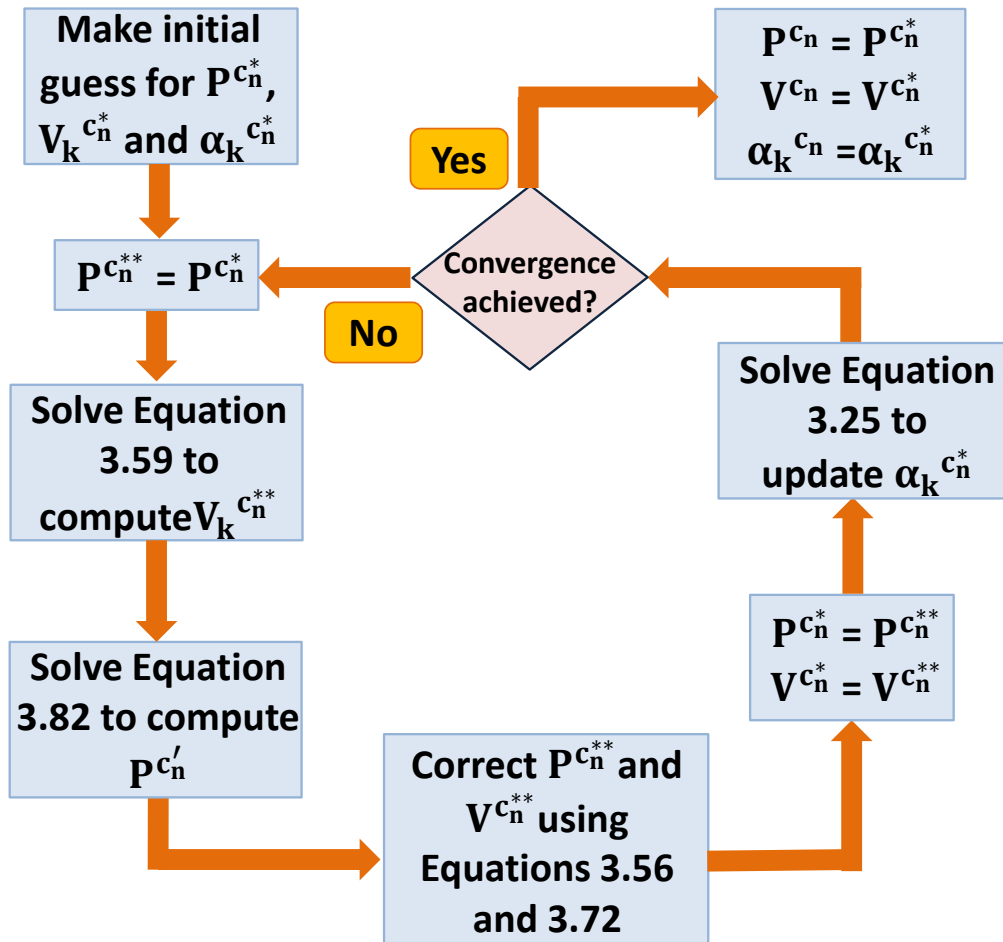


Figure 3.5: Developed iterative workflow to simulate borehole two-phase velocity, pressure, and holdup. The IPISA-C algorithm begins with an initial guess for fluid properties. Subsequently, a pressure-correction equation (i.e., Equation 3.82) is constructed to correct the guessed values of pressure and velocity. The guess-and-correction algorithm continues until achieving a satisfactory convergence.

3.6 BOUNDARY CONDITIONS

A physically-realistic solution for the abovementioned system of two-phase fluid flow equations requires a proper description of fluid-phase properties associated with the borehole boundaries. The developed fluid flow model assumes constant fluid-phase

velocity and volume fraction at the inlet. Furthermore, under the assumption of a constant molar fraction at the inlet, the compositional model is invoked to compute fluid-phase molar composition, density, and viscosity:

$$\varphi|_{\text{inlet}} = \text{Constant}, \quad \varphi: V_k, \alpha_k, \rho_k, x_{jk}, y_{jk} \quad (3.87)$$

Because the location of fluid-phase velocities (i.e., SCV faces) in staggered gridding arrangement coincide with the borehole physical boundaries, implementation of constant-velocity conditions is carried out by omitting the corresponding discretized terms in fluid-phase momentum equations. However, fluid-phase scalar variables are stored at the center of SCVs that requires an additional node to be introduced outside the borehole flow domain to store the corresponding inlet values.

In the outlet of fluid flow, a zero-gradient boundary condition is implemented to associate fluid-phase properties to the corresponding nodal values at immediate vicinity of the outlet, i.e.,

$$\frac{d\varphi}{dz} \Big|_{\text{outlet}} = 0, \quad \varphi: V_k, \alpha_k, \rho_k, x_{jk}, y_{jk} \quad (3.88)$$

Solution of the pressure-correction equation describes the correction terms for fluid-phase velocity and pressure without computing the absolute values for pressure. A constant-pressure boundary condition is therefore implemented in the outlet to specify the absolute value of borehole pressure. Constant-pressure boundary conditions imply that no correction is required to be applied to the outlet pressure. Therefore, a zero-pressure-correction boundary condition is implemented at the outlet for the pressure-correction equation. Similarly, because the inlet fluid-phase velocity is known, a zero-pressure-correction boundary condition is also applicable for the borehole inlet, therefore,

$$P'|_{\text{inlet}} = P'|_{\text{outlet}} = 0, \quad \text{and} \quad (3.89)$$

$$P|_{\text{outlet}} = \text{Constant}, \quad (3.90)$$

3.7 AUTOMATIC TIME-STEP CONTROLLING

Numerical stability of the developed algorithm is enhanced by adopting an automatic time-step controlling. The automatic time-step controlling is performed by calculating error associated with the overall mass. The mass conservation error is examined by calculating root mean square of the pressure-correction vector computed for time t_n , namely,

$$\text{PCE} = \sqrt{\sum_{i_s=1}^{N_s} [(P)_{i_s}^{n'}]^2}. \quad (3.91)$$

where N_s identifies number of scalar-variable control volumes. Moreover, I compute the maximum changes in fluid mixture velocity and pressure from time t_n to time $t_n + \Delta t_n$ to impose a constraint on time step as

$$\Delta P_{\max} = \max \left(\frac{(P)_{i_s}^{n+1} - (P)_{i_s}^n}{(P)_{i_s}^{n+1}}, \quad \forall i_s = 1, \dots, N_s, \quad \text{and} \quad (3.92)$$

$$\Delta V_{\max} = \max \left(\frac{(V_m)_{i_v}^{n+1} - (V_m)_{i_v}^n}{(V_m)_{i_v}^{n+1}}, \quad \forall i_v = 1, \dots, N_v, \quad (3.93)$$

where N_v denotes number of velocity control volumes, and V_m is computed from Equation 2.10. The following procedure is subsequently implemented to update the time step:

1. Obtain initial time step, upper and lower bounds for mass conservation error, maximum acceptable variations of pressure and velocity, and time step associated with the current solution of formation domain.
2. Calculate PCE from Equation 3.91,

$$\Delta t_p = \Delta t_n \frac{\Delta P_{lim}}{\Delta P_{max}}, \quad \forall i_s = 1, \dots, N_s, \quad (3.94)$$

$$\Delta t_v = \Delta t_n \frac{\Delta V_{lim}}{\Delta V_{max}}, \quad \forall i_v = 1, \dots, N_v, \quad \text{and} \quad (3.95)$$

$$\Delta t_{pv} = \min(\Delta t_p, \Delta t_v), \quad (3.96)$$

where subscript "lim" identifies maximum acceptable variations of pressure and velocity.

3. Update time step as

$$\text{if PCE} > \text{MBEUB} \quad \Delta t^{\text{new}} = \frac{1}{2} \times \Delta t^{\text{old}},$$

$$\text{if MBELB} < \text{PCE} < \text{MBEUB} \quad \Delta t^{\text{new}} = \Delta t^{\text{old}},$$

$$\text{if PCE} < \text{MBELB} \quad \Delta t^{\text{new}} = 2 \times \Delta t^{\text{old}},$$

where MBEUB and MBELB indicate upper and lower acceptable bounds for mass conservation error, respectively.

4. Limit the updated time step by

$$\Delta t^{\text{new}} < \Delta t_{pv}. \quad (3.97)$$

5. Limit the updated time step by time step associated with Courant-Friedrichs-Lewy (CFL) condition, namely,

$$\Delta t_{\text{CFL}} = \min \left(C \frac{\Delta z_{i_v}}{\max \left[(V_1)_{i_v}^n, (V_2)_{i_v}^n \right]} \right), \quad \forall i_v = 1, \dots, N_v, \quad (3.98)$$

where C is the Courant number (Courant et al., 1967) defined between 0 and 1. A default value of 0.5 is chosen for C to ensure stability of the developed method.

6. Limit time step by the time step associated with current solution of formation flowing domain.

3.8 BOREHOLE-FORMATION COUPLING

The borehole fluid flow model developed in this dissertation is coupled to a reservoir fluid flow model to enable the association of formation petrophysical properties to borehole production measurements (Frooqnia et al., 2011; Hadibeik et al., 2012a; Hadibeik et al., 2012b; Frooqnia et al., 2013). Borehole-reservoir coupling is performed by dynamically modifying source terms associated with fluid-phase and component-based mass conservation equations (i.e., Γ_{jk}^{for} and Γ_k^{for} in Equations 3.23 and 3.25, respectively). At a given time, the equations associated with reservoir fluid flow are numerically solved to compute fluid-phase and component molar influx transferred into the borehole. The compositional model is next invoked to modify the values of molar influx according to current borehole pressure and temperature. Subsequently, borehole fluid flow simulator modifies source terms in the mass conservation equations, and numerically solves equations associated with borehole fluid flow. The calculated borehole pressure is applied as a new boundary condition for reservoir fluid flow domain, and simulation proceeds to next time step.

3.8.1 Sequential Coupling Method

Larger fluid-phase velocity in the borehole compared to that in the formation requires significantly smaller time steps for solving borehole fluid flow equations to ensure numerical stability. Figure 3.6 indicates that proper borehole-formation synchronization is achieved by defining the current time step associated with formation flow domain as the time increment required for solving borehole fluid flow equations. The developed coupled fluid flow model modifies source terms associated with borehole mass conservation equations from the most updated formation properties. Subsequently, an automatic time-step controlling method determines borehole time steps to numerically solve borehole flow equations. Following the computation of borehole fluid-phase properties, the developed borehole fluid flow model updates the corresponding boundary conditions associated with formation flow domain. The succession of borehole and formation fluid flow simulations continues to ensure an accurate coupling between separate borehole and formation fluid flow equations.

3.8.2 Differential Depletion

When producing from a multilayer fluid-producing system, those layers with initially-high production rates become depleted at faster rates compared to those with lower producing flow rates. In commingled systems, depending on the production mechanisms (e.g., solution-gas drive), and the hydraulic connectivity of fluid-producing layers, differential depletion takes place that alters the producibility of various fluid-producing rock formations. Because of differential depletion, production logs acquired from multilayer fluid-producing rock formations exhibit a cross-flow through the borehole where borehole fluids are produced from the layers with high productivity index, and injected back into layers with lower productivity index. I implement the

following procedure to simulate simultaneous fluid injection and production in the presence of differential depletion:

1. Simulate borehole fluid-phase properties.
2. Obtain formation pressure in the immediate vicinity of the borehole.
3. Define formation grid blocks attached to the wellbore as follows:
 - if $P_{\text{borehole}} > P_{\text{reservoir}}$, The formation grid block is an injector,
 - if $P_{\text{borehole}} \leq P_{\text{reservoir}}$, The formation grid block is a producer.
4. Use the current wellbore fluid-phase properties to determine type and volume fraction of injected fluids associated with each injector.
5. Update formation boundary conditions.
6. Solve formation fluid flow equations.

The developed fluid flow model discretizes the coupled fluid flow domain into cylindrical grid blocks with variable sizes to adequately capture the geometry of borehole and fluid-producing rock formations. Figure 3.7 shows the schematic of grid arrangement developed for the coupled borehole-formation fluid flow domain. In this arrangement, because of a mismatch between formation and borehole grid-block boundaries, a distributor function is defined to properly distribute the mass flow rates produced from a formation grid block over the corresponding borehole grid blocks. Under the assumption of uniform production across a formation grid block, mass distribution is carried out by computing the overlapping intervals between the neighboring borehole and formation grid blocks.

3.8.3 Averaging Method

When a layer crosses the borehole with an angle, formation grid blocks do not coincide with layer boundary lines. An averaging method is therefore implemented to compute the petrophysical properties of grid blocks associated with layer boundaries. Figure 3.7b describes the schematic of a formation grid block in cylindrical coordinates with a crossing petrophysical boundary. The following planes are defined to determine the arrangement of adjacent layers within each grid block (namely, Layer 1 and Layer 2 in Figure 3.8a):

1. Plane p: The boundary of adjacent layers.
2. Plane r: A reference plane located at center of grid the block and perpendicular to r direction.
3. Plane θ : A reference plane located at center of the grid block and perpendicular to θ direction.
4. Plane z: A reference plane located at center of the grid block and perpendicular to z direction.

The developed averaging method computes averaged permeability in r direction as (Peters, 2012)

$$K_r = \left(1 - \frac{A_{p,r}}{A_{v,r}}\right) K_{r,Parallel} + \frac{A_{p,r}}{A_{v,r}} K_{r,Series}, \quad (3.99)$$

where K_r is averaged permeability of grid block in the radial direction, $A_{p,r}$ is projected area of Plane p on Plane r (Figure 3.8b), $A_{v,r}$ is projected area of the volume occupied by Layer 1 on Plane r (Figure 3.8e), $K_{r,Parallel}$ is averaged radial permeability of grid block when the same volume of Layer 1 is arranged in parallel to Layer 2, and $K_{r,Series}$ is

averaged radial permeability when the same volume of Layer 1 is arranged in series with respect to Layer 2.

Similarly, averaged permeabilities in the vertical and azimuthal directions are defined as

$$K_z = \left(1 - \frac{A_{p,z}}{A_{v,z}}\right) K_{z,Parallel} + \frac{A_{p,z}}{A_{v,z}} K_{z,Series}, \quad \text{and} \quad (3.100)$$

$$K_\theta = \left(1 - \frac{A_{p,\theta}}{A_{v,\theta}}\right) K_{\theta,Parallel} + \frac{A_{p,\theta}}{A_{v,\theta}} K_{\theta,Series}, \quad (3.101)$$

where K_z and K_θ are averaged permeability in the vertical and azimuthal directions, respectively, $A_{v,z}$ and $A_{v,\theta}$ are projected areas of the volume occupied by Layer 1 on Plane z and Plane θ , respectively, $A_{p,z}$ and $A_{p,\theta}$ are projected areas of Plane p on Plane z and Plane θ , respectively, $K_{z,Parallel}$ and $K_{\theta,Parallel}$ are averaged permeability in the vertical and azimuthal directions, respectively, when the same volume of Layer 1 is arranged in parallel to Layer 2, and $K_{z,Series}$ and $K_{\theta,Series}$ are averaged permeability in the vertical and azimuthal directions, respectively, when the same volume of Layer 1 is arranged in series with respect to Layer 2.

Porosity of a formation grid block is computed by applying linear volumetric-averaging method as

$$\phi = \frac{v_{b1}}{v_b} \phi_1 + \frac{v_{b2}}{v_b} \phi_2, \quad (3.102)$$

where ϕ_1 is porosity of Layer 1, ϕ_2 is porosity of Layer 2, v_{b1} is volume of the grid block occupied by Layer 1, v_{b2} is volume of the grid block occupied by Layer 2, and v_b is total volume of the grid block.

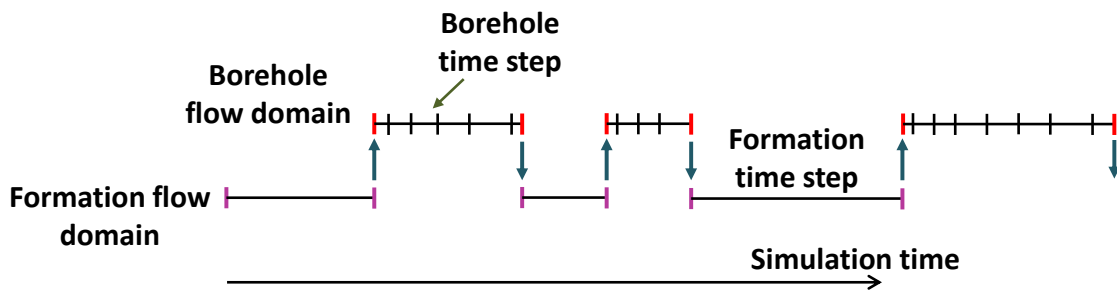
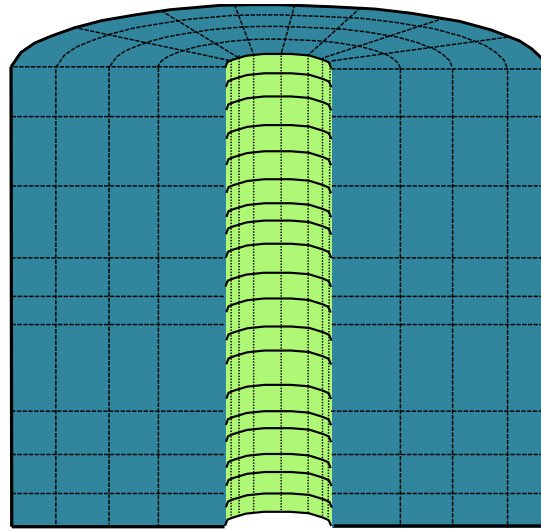
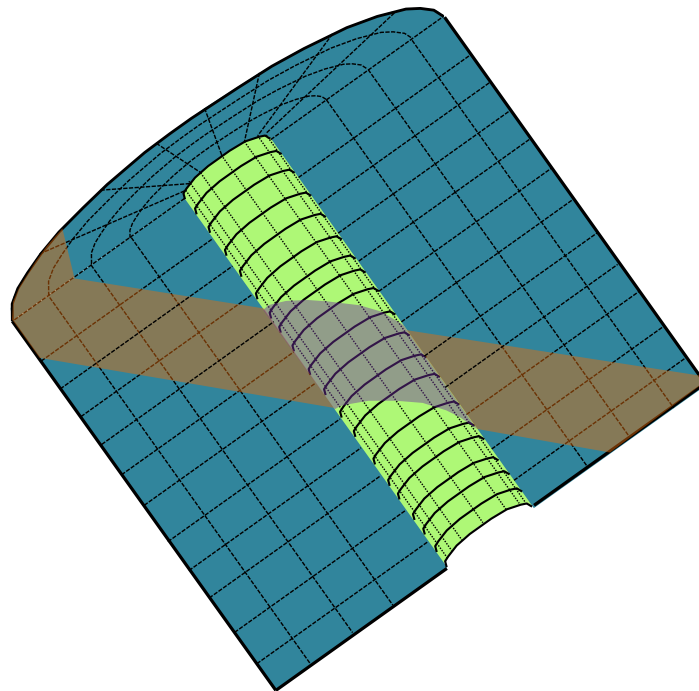


Figure 3.6: Developed sequential method to couple separate borehole and formation fluid flow equations. Current time step in the reservoir flow domain is used as the time increment required for the borehole fluid flow simulation. Following the calculation of borehole fluid-phase properties, the developed method updates boundary conditions associated with formation fluid flow equations, and proceeds to the next time step.



(a)



(b)

Figure 3.7: Schematic of the grid arrangement within and around the borehole for (a) vertical and (b) deviated flowing systems. An averaging method has been developed to compute the average values of permeability and porosity associated with grids block shared by the adjacent petrophysical layers.

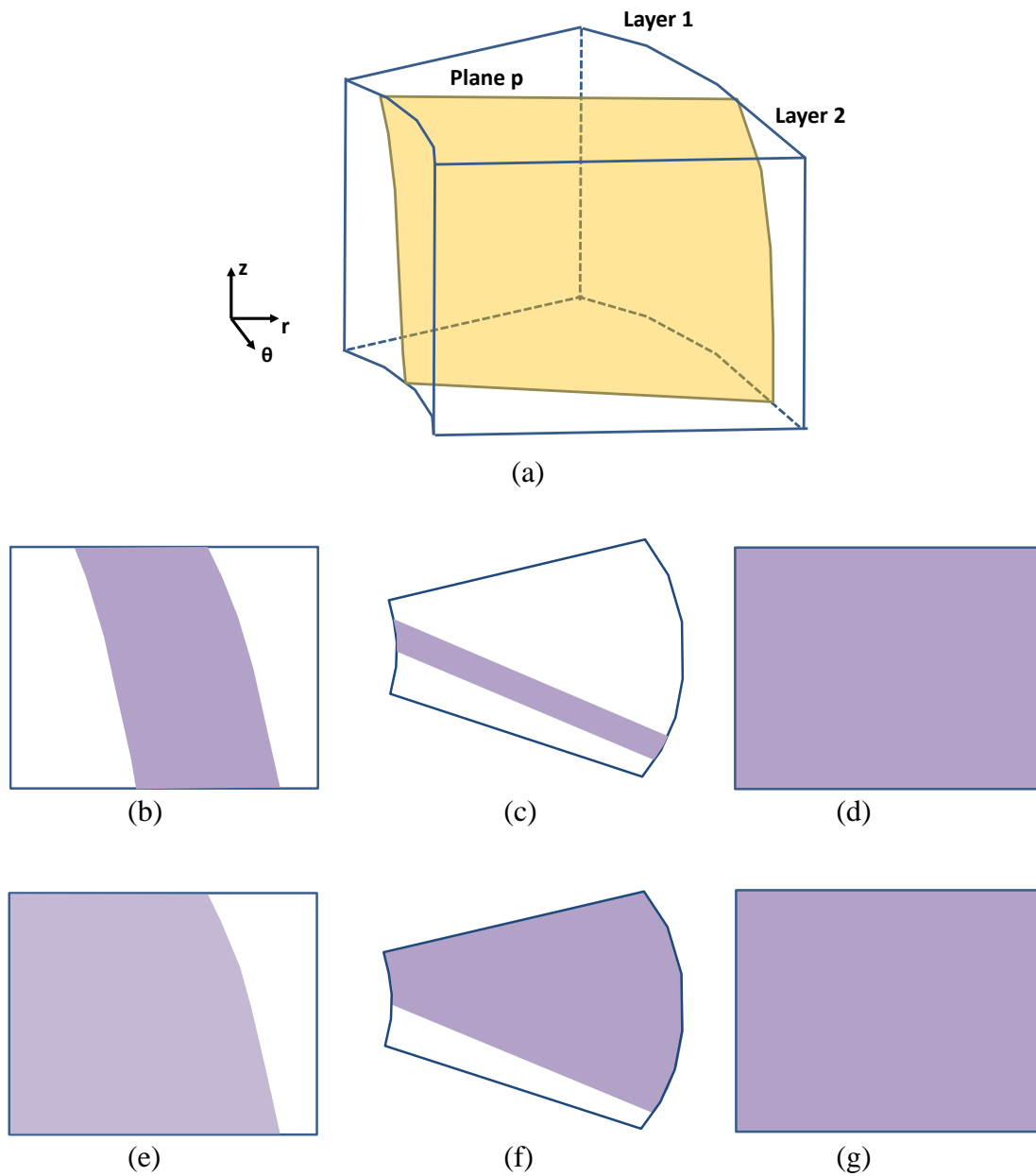


Figure 3.8: Geometrical description of a layer bed boundary crossing a grid block in a non-conformal arrangement. Panels (b), (c), and (d) show the projected area of Plane p in r, z, and θ directions, respectively. Panels (e), (f), and (g) show the projected area of the volume occupied by Layer 1 in r, z, and θ directions, respectively. Equations 3.99 through 3.102 use the described shaded areas to compute average permeabilities associated with each grid block.

Chapter 4: Verification of the Borehole Fluid Flow Model

Reliable estimation of formation petrophysical properties from production measurements requires an accurate simulation of borehole fluid-phase properties across fluid-producing depth intervals. The developed borehole fluid flow model is based on a new two-fluid formulation that enables accurate simulation of fluid-phase slip velocity, borehole fluid pressure, and fluid flow regimes. This chapter conducts verification tests to investigate accuracy and reliability of the developed borehole fluid flow model in simulating steady-state and transient behaviors of borehole fluid-phase properties.

4.1 INTRODUCTION

Transient behavior of the developed borehole fluid flow model is verified against analytical solutions available for a phase-separation test. Furthermore, synthetic and field examples of gas flowing systems are studied to investigate accuracy of the developed borehole fluid flow model to simulate borehole wall friction and fluid-phase compressibility effects. Prediction of fluid-phase slip velocity is next examined against published experimental studies for oil-water and gas-water flowing systems. I invoke the developed borehole model to reconstruct experimental results available for both vertical and deviated flowing systems. An oil-gas vertical flowing system is examined to verify the implemented interfacial mass and momentum source terms. In addition, oil-water field production measurements are used to investigate accuracy of the developed fluid flow model in simulating fluid flow rates produced from individual rock formations. I

show that the implemented algorithm successfully reconstructs borehole measurements, and accurately estimates incremental fluid flow rates associated with various fluid-producing depth intervals.

4.2 TRANSIENT SIMULATIONS

I perform verification tests to investigate reliability and accuracy of the developed borehole fluid flow model in simulating transient behaviors of (i) a phase-separation test, and (ii) a shut-in test with no borehole cross-flow.

4.2.1 Simulation of Phase Separation

The first example is a gravity-induced phase separation case that examines the capability of the developed model to quantify counter-current flow conditions commonly observed in borehole production measurements. Phase-separation test considers a vertical pipe with height equal to 300 ft and diameter equal to 3 in. The pipe is initially filled with a homogeneous mixture of hydrocarbon and water phases with a volume fraction of $\alpha_o = 0.5$. Specific challenge is to simulate counter-current movements of two void fronts from the top and bottom ends of the pipe. An analytical model exists for describing the quasi-steady-state flow conditions in the undisturbed middle section of the pipe where upward and downward volumetric fluxes of two fluid phases compensate each other. Assuming gravity and interfacial drag forces as primary components for fluid-phase momentum source terms, fluid-phase velocity in the middle section of the pipe is given by (Stadtke, 2006)

$$V_o = \alpha_o \Delta V \quad \text{and} \quad V_w = -\alpha_w \Delta V, \quad (4.1)$$

where ΔV is fluid-phase slip velocity, written as (Stadtke, 2006)

$$\Delta V = V_o - V_w = \sqrt{\frac{8(\rho_w - \rho_o)R_d g}{3C_D \rho_m}}, \quad (4.2)$$

where ρ_w , ρ_o and ρ_m are water, hydrocarbon and fluid mixture densities, respectively, R_d is droplet diameter, C_D is drag coefficient, and g is gravitational acceleration. I apply the fluid-phase properties listed in Table 4.1 to compute water and hydrocarbon velocities as

$$V_w = -0.28 \text{ ft/s} \quad \text{and} \quad V_o = 0.28 \text{ ft/s} . \quad (4.3)$$

The simulation of phase separation is performed using the developed borehole flow model under the assumption of no-flow boundary conditions at the pipe top and bottom ends. Furthermore, pressure at the top is assumed to be constant, equal to 2200 psia. Numerical results, shown in Figures 4.1 and 4.2, show acceptable agreements with the analytical solution computed for the location of void fronts and fluid-phase velocity. After 370 seconds, the two void fronts meet at the middle section of the pipe, and establish a sharp interface. Because of the zero mass influx and constant top pressure, pressure at the bottom end for various times remains constant. In addition, the hydrocarbon as the lighter fluid phase is moving upward in the opposite direction of water movement. Eventually, when the phase separation is complete velocity of both fluid phases reduces to zero.

4.2.2 Simulation of Shut-In Test

The developed borehole fluid flow model is applied to simulate the transient behavior of borehole fluid flow during a shut-in test. Simulation of shut-in test is performed by initializing borehole flow model with the simulated production logs

acquired under production conditions (shown in Figure 4.3). Borehole pressure (i.e., pressure at 5000 ft MD) is subsequently changed to the corresponding shut-in pressure to initiate the shut-in test. When shut-in is initiated, gravity-induced force causes the lighter fluid phase to separate itself from the heavier phase. The rate at which fluid-phase separation takes place primarily depends on fluid-phase density and volume fraction. As shown in Figures 4.4 and 4.5, upward movement of the oil phase and downward movement of the water phase result in fluid-phase separation when after approximately 16 minutes the entire borehole flow domain becomes filled with water. Because of the assumption of constant pressure at depth 5000 ft MD, replacing the lighter fluid phase with the heavier one continuously increases the pressure at 5100 ft MD. As shown in Figure 4.6, because of lower buoyant forces, decreasing fluid-phase density contrast gives rise to longer times required for the water phase to entirely fill the borehole domain.

Property	Unit	Value
Water density	lb _m /ft ³	62.4
Oil density	lb _m /ft ³	53
Initial pressure	psia	2200
Drag coefficient	-	0.44
Droplet diameter	in	0.2
Pipe diameter	in	3
Pipe height	ft	300

Table 4.1: Summary of pipe and fluid-phase properties assumed for simulation of the phase separation test.

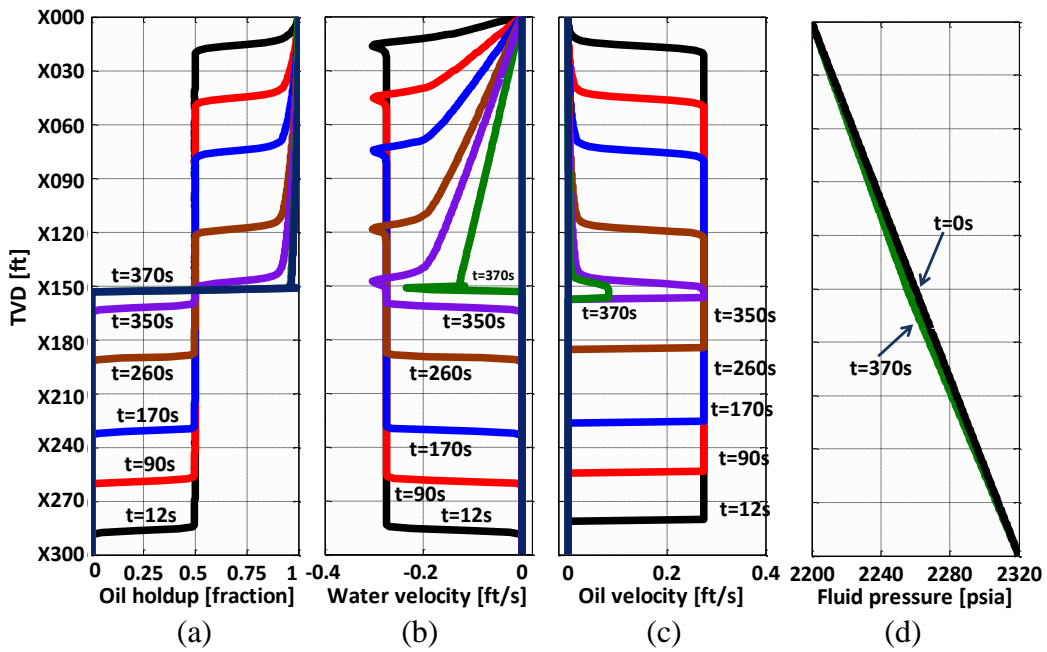


Figure 4.1: Transient behavior of borehole (a) oil-phase holdup, (b) water-phase velocity, (c) oil-phase velocity, and (d) fluid pressure, simulated for the phase separation test. Panels (b) and (c) show downward movement of the water and upward movement of the oil that eventually (after 370 seconds) leads to the separation of two fluid phases.

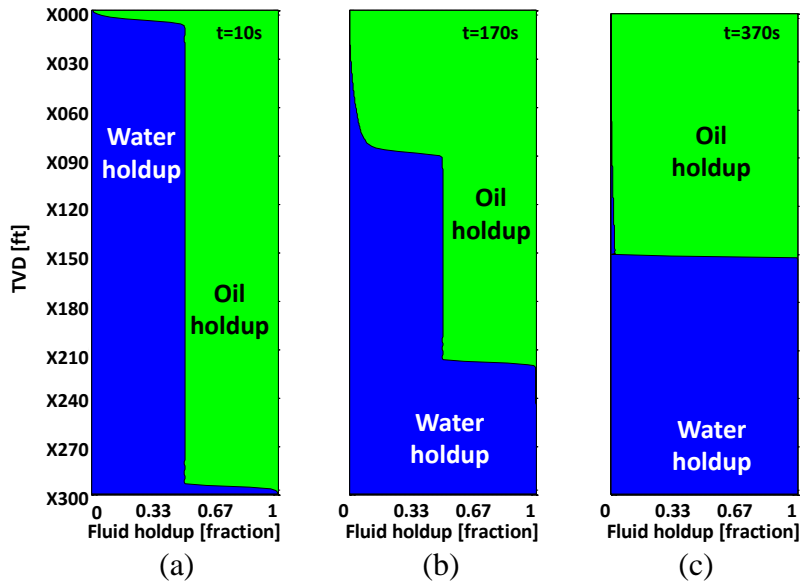


Figure 4.2: Transient behavior of borehole fluid-phase volume fraction simulated (a) 10, (b) 170, and (c) 370 seconds after the inception of phase-separation test.

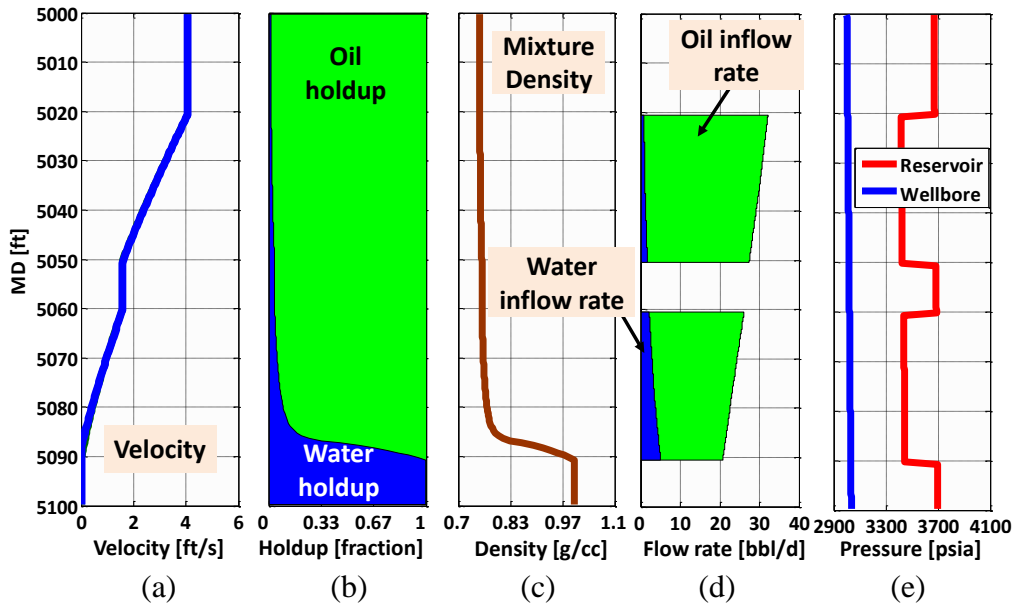


Figure 4.3: Spatial distributions of borehole production measurements for (a) fluid-phase velocity, (b) fluid-phase holdup, (c) fluid mixture density, and (d) fluid-phase inflow rate, acquired for the simulation of shut-in test. Panel (e) shows borehole and formation pressures at the time of measurement acquisition.

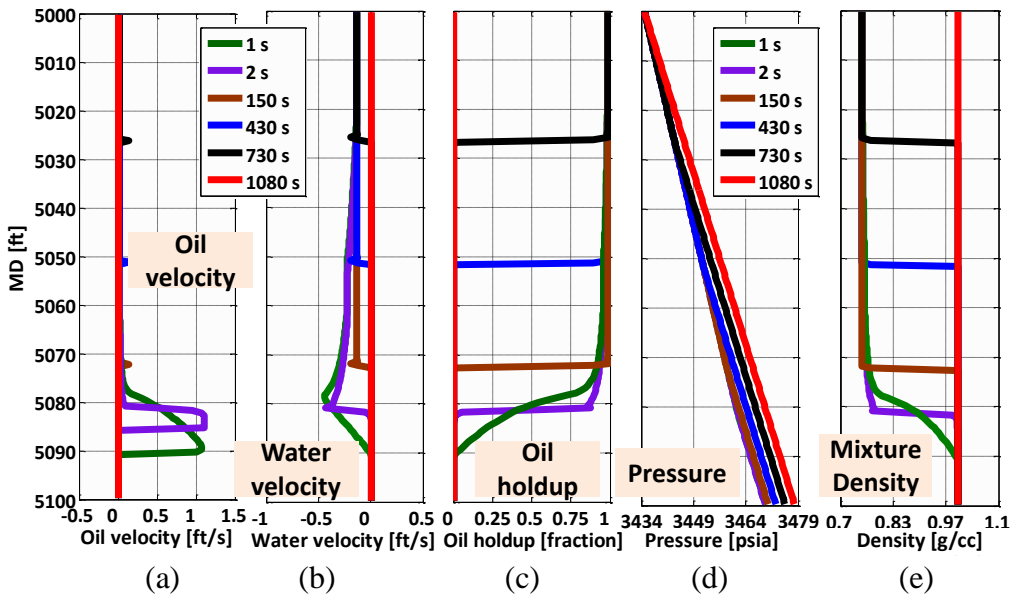


Figure 4.4: Transient behavior of borehole (a) oil-phase velocity, (b) water-phase velocity, (c) oil-phase holdup, (d) fluid pressure, and (e) fluid mixture density, simulated for the shut-in test.

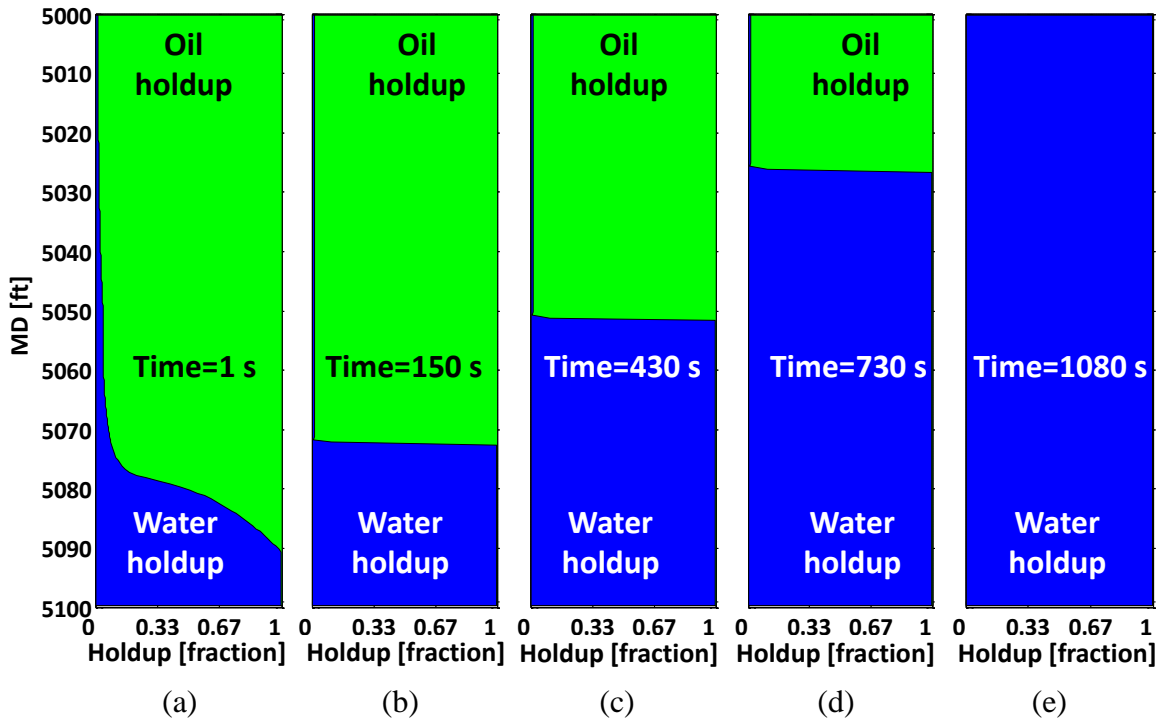


Figure 4.5: Transient behavior of borehole fluid-phase holdup simulated (a) 1, (b) 150, (c) 430, (d) 730, and (e) 1080 seconds after initiating the shut-in test.

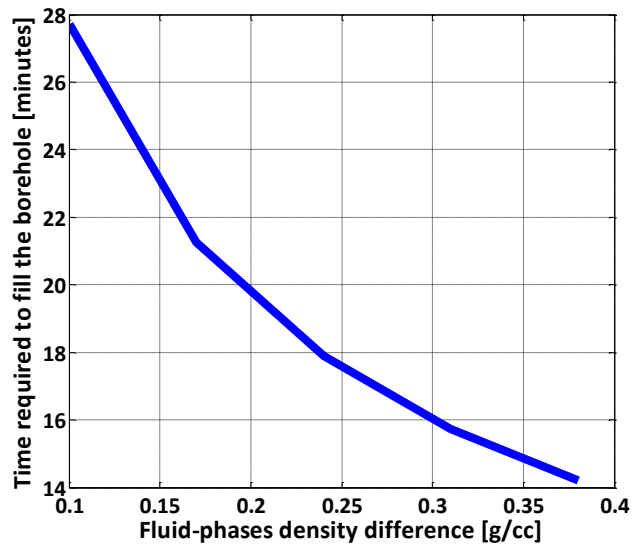


Figure 4.6: Time required for the water phase to fill the entire borehole domain as a function of fluid-phase density contrast, computed for simulation of the shut-in test.

4.3 GAS FLOWING SYSTEMS

In single-phase flowing systems, borehole pressure is primarily influenced by fluid compressibility and the pressure loss originating from the borehole wall friction. This section simulates the flow of single-phase gas through a long pipe to investigate accuracy of the developed fluid flow model in simulating borehole pressure drop. Two verification examples are studied: (i) field measurements of pressure drop in a 3100-ft long pipe reported by Takacs and Guffey (1989), and (ii) a synthetic example of the spatial distributions for gas pressure and velocity in a 2000-ft long pipe reported by Shirdel (2013).

Takacs and Guffey (1989) reported a vertical borehole with length equal to 3100 ft and radius equal to 1.75 in. The borehole produces gas at single-phase conditions with gas flow rate equal to 6.13 MMSCFPD. Available gas properties at wellhead conditions with remaining borehole properties are summarized in Table 4.2. A pseudo-component with properties listed in Table 4.3 is created to honor gas PVT behavior at the given wellhead conditions. I simulate borehole pressure, and compare the estimated bottom-hole pressure with the measured value. As Figure 4.7 shows, the simulated bottom-hole pressure is within 1% of the measured pressure value.

Synthetic example reported by Shirdel (2013) is used to verify accuracy of the developed borehole fluid flow model to simulate the spatial distributions of pressure and velocity in a long pipe. Shirdel's (2013) example simulates production of single-phase gas (i.e., methane) at gas flow rate equal to 243 RCFPD from a borehole with length, radius, and roughness equal to 2000 ft, 1.374 in, and 0.005 in, respectively. Comparison of the borehole fluid properties shows that simulated properties closely match those obtained with Shirdel's (2013) borehole flow model (Figure 4.8).

Property	Unit	Value
ρ_g	g/cc	0.050
μ_g	cp	0.035
Q_g	MMSCFPD	6.13
r_w	in	1.75
L	ft	3100
ε	in	0.0024
T_{wellhead}	$^{\circ}\text{F}$	85
$T_{\text{bottomhole}}$	$^{\circ}\text{F}$	155
P_{wellhead}	psia	919.5
$P_{\text{bottomhole}}$	psia	992

Table 4.2: Assumed borehole and gas-phase properties for the simulation of pressure drop in a long pipe reported by Takacs and Guffey (1989).

Property	Unit	Component
T_{crit}	$^{\circ}\text{K}$	275.5
P_{crit}	atm	322.6
A_c	-	0.33
V_{crit}	$\frac{\text{m}^3}{\text{kgmole}}$	0.099
MW	$\frac{\text{lb}_m}{\text{lb}_m \text{mole}}$	19.07

Table 4.3: Assumed hydrocarbon component for the simulation of pressure drop in a long pipe reported by Takacs and Guffey (1989).

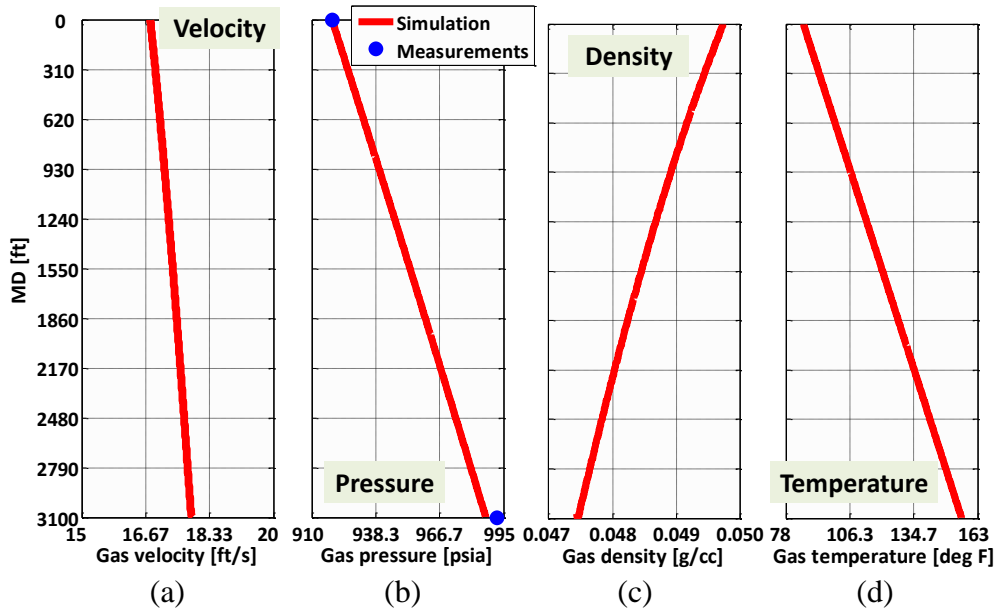


Figure 4.7: Simulated borehole gas-phase (a) velocity, (b) pressure, (c) density, and (d) assumed borehole temperature, for the calculation of pressure drop in a long pipe reported by Takacs and Guffey (1989). Panel (b) compares the numerically simulated and measured pressure drop.

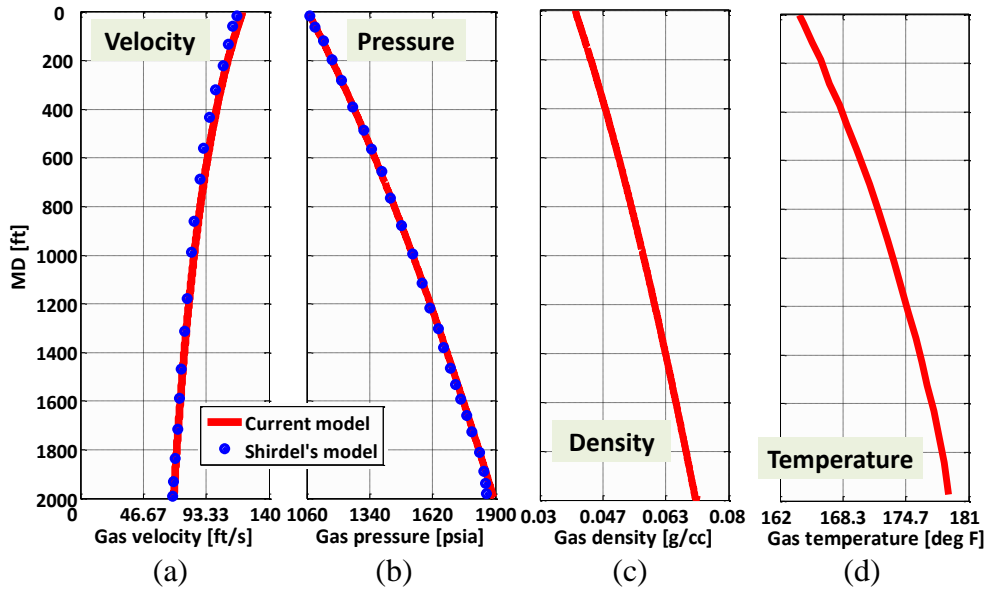


Figure 4.8: Comparison of the numerically simulated spatial distributions of borehole gas-phase (a) velocity and (b) pressure with those obtained by Shirdel's (2013) flow model. Panels (c) and (d) show the simulated borehole density, and the assumed borehole temperature, respectively.

4.4 OIL-WATER FLOWING SYSTEMS

In two-phase flowing systems with significant fluid-phase density contrast, the heavier phase flows at slower velocities compared to the lighter phase, thereby causing the accumulation of heavier phase in the borehole. Unaccounted fluid-phase slip velocity results in unreliable estimates of near-borehole petrophysical properties. This section studies several laboratory examples to investigate accuracy of the developed fluid flow model in simulating slip velocity. The first case compares oil-water slip velocities simulated with the borehole flow model developed in this dissertation and those obtained from the drift-flux model (Hasan and Kabir, 1999). This verification example considers simultaneous flow of the hydrocarbon and water phases in a pipe with two deviation angles. Fluid phases at various flow rates are injected from the bottom end of the pipe. Subsequently, the steady-state values for fluid-phase velocity and volume fraction are computed at the top end. Hasan and Kabir (1999) showed that in drift-flux modeling of borehole oil-water flow, oil-phase volume fraction is related to superficial velocities by

$$\frac{V_{os}}{\alpha_o(1 - \alpha_o)^2} = 1.2 \frac{V_m}{(1 - \alpha_o)^2} + V_{\infty\theta}, \quad (4.4)$$

where V_{os} is oil-phase superficial velocity, α_o is oil-phase volume fraction, V_m is fluid mixture velocity, and $V_{\infty\theta}$ is oil droplet terminal rise velocity given by (Harmathy, 1960)

$$V_{\infty\theta} = 1.53 \left(g \sigma_{ow} \frac{\rho_w - \rho_o}{\rho_w^2} \right)^{1/4} \sqrt{\cos \theta (1 + \sin \theta)^2}, \quad (4.5)$$

where θ is pipe deviation angle from the vertical, σ_{ow} is oil-water surface tension, and g is gravitational acceleration. Equations 4.4 and 4.5 were shown to be valid for oil volume fractions less than 0.7, and pipe deviation angles less than 70° . Through experimental studies, Hasan and Kabir (1999) showed that a graph of $\frac{V_{os}}{\alpha_o(1 - \alpha_o)^2}$ versus

$\frac{V_m}{(1-\alpha_o)^2}$ exhibits a linear relationship where the slope is unaffected by the pipe diameter and deviation angle.

Comparison of the developed borehole flow model against the drift-flux model is carried out by reconstructing the graph suggested by Equations 4.4 and 4.5. Fluid flow simulation is performed by applying the following borehole and fluid-phase properties: oil-phase density: 0.801 g/cc, water-phase density: 1.0 g/cc, oil-phase viscosity: 1.5 cp, water-phase viscosity: 1 cp, and borehole diameter: 2.45 in. As shown in Figure 4.9, numerical results favorably confirm slip velocity simulated with Hasan and Kabir's (1999) drift-flux model. The slope of 1.2 associated with a water-dominant bubbly flow regime is accurately simulated by dynamically modifying the droplet diameter as a function of borehole oil-phase velocity and volume fraction. Increasing the size of oil droplets decreases oil-water interfacial drag forces, thereby increasing fluid-phase slip velocity. The largest slip velocity is obtained at the oil-phase volume fraction equal to $\alpha_o = 0.5$ where transition from water-dominant to oil-dominant flow regimes takes place. Subsequently, the breakage of water droplets associated with oil-dominant flow regime causes the reduction of fluid-phase slip velocity. No-slip conditions established at high oil-phase volume fractions is interpreted as the unit slop shown in Figure 4.9a.

In deviated pipes, because of gravity effects, the lighter phase exhibit a tendency to move closer to the upper wall. Asymmetric conditions of fluid flow in deviated boreholes lead to larger slip velocities compared to equivalent vertical following systems. The capability of the developed borehole model to simulate slip velocity in deviated systems is verified by simultaneous injection of the water and hydrocarbon phases into a pipe with deviation angle equal to 65° from the vertical. Assuming identical droplet diameter compared to the equivalent vertical system, the developed borehole model dynamically modifies droplet eccentricity to effectively account for the excess of slip

velocity in deviated pipes. Figure 4.10 confirms that the developed borehole model accurately simulate the slope of 1.2 associated with water-dominant flow regime. Furthermore, the unit slope associated with no-slip conditions is accurately simulated for high oil-phase volume fractions.

In the presence of two fluid phases with considerable density contrasts, fluid-phase slip velocity results in accumulation of the heavier phase, thereby increasing the corresponding volume fraction in the borehole. Accuracy of the developed borehole fluid flow model to compute water volume fraction in an oil-water flowing system is verified against experimental results conducted and reported by Vigneaux et al. (1988). Vigneaux et al.'s (1988) experimental study included an inclinable 14-m long pipe with internal diameter equal to 20 cm. Oil phase (density=0.801 g/cc and viscosity=1.5 cp) and water phase (density=1 g/cc and viscosity=1 cp) were simultaneously injected into the pipe at various total fluid flow rates. Subsequently, the steady-state fluid-phase volume fractions were measured using a small high frequency impedance probe (Kobori and Terada, 1978).

Figure 4.11 compares the simulated water volume fraction with the measured values associated with two total fluid flow rates (i.e., 1011 and 6038 bfpd), and three inclination angles (namely, 5, 25, and 65 degrees). At low fluid flow rates and low deviations, the simulated water volume fractions are within less than 5% of those associated with no-slip conditions (i.e., red dash lines). Increasing pipe inclination angle results in considerable slip velocity where causes the water phase to accumulate in the pipe. Figure 4.11 shows that numerical results obtained from the developed borehole fluid flow model closely match those reported from laboratory measurements.

Shi et al. (2005) conducted a similar experiment to measure water volume fraction at various oil-water flowing conditions. Shi et al.'s (2005) experiments included an

inclined flow loop with length and diameter equal to 36 ft and 6 in, respectively. Oil (density=0.801 g/cc and viscosity=1.5 cp) and water (density=1 g/cc and viscosity=1 cp) were simultaneously injected at three different oil flow rates (i.e., 301, 1509, and 6038 bopd), and two deviation angles (i.e., 0 and 70 degrees). They used ten electric probes installed at various pipe locations to measure fluid local conductance. Probe measurements were subsequently inverted to estimate steady-state water holdup with approximately 5% uncertainty bounds (error bars shown in 4.12). As Figure 4.12 compares, the developed borehole fluid flow model reliably simulates the deviation of water volume fraction from input water volume fraction mainly caused by presence of slippage between fluid phases.

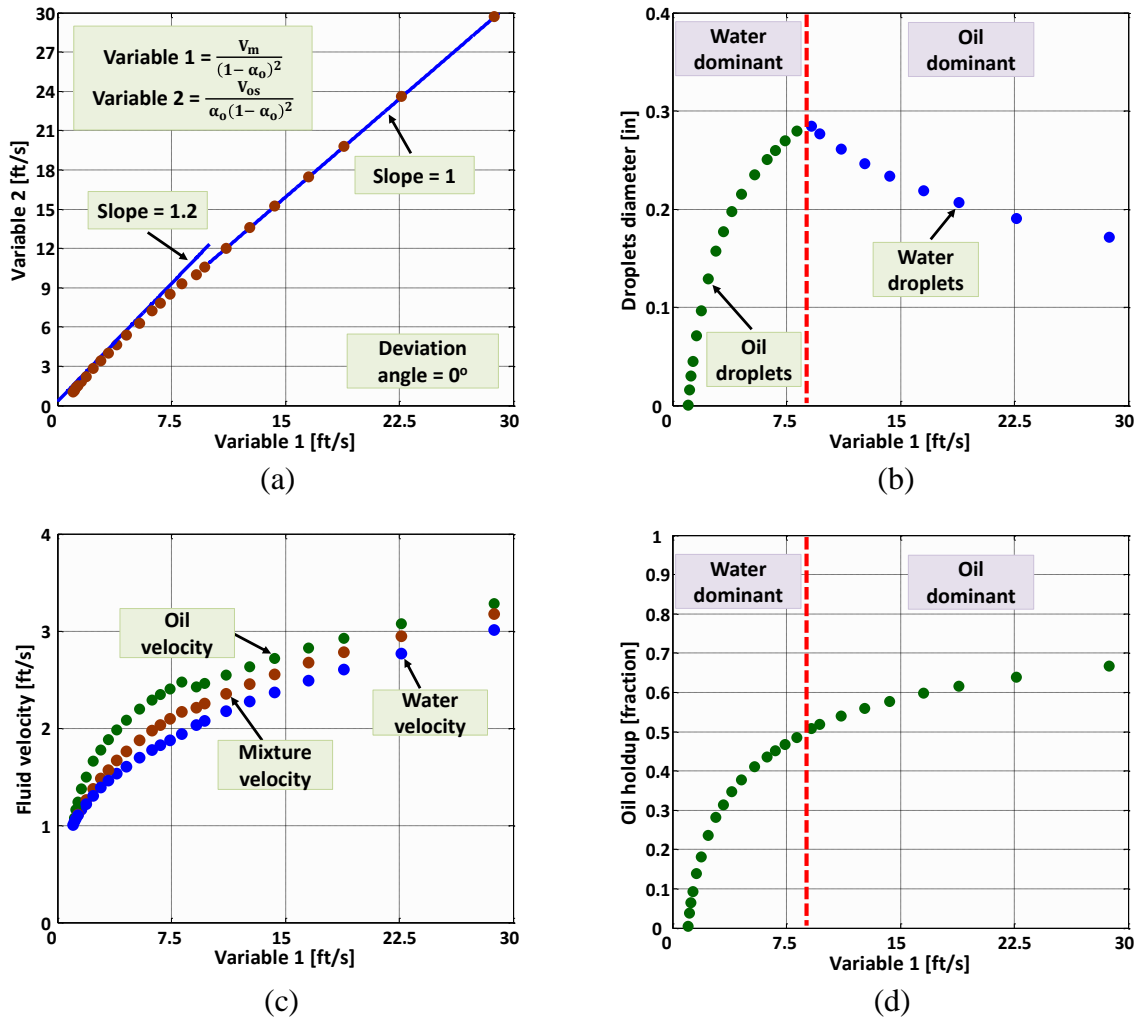
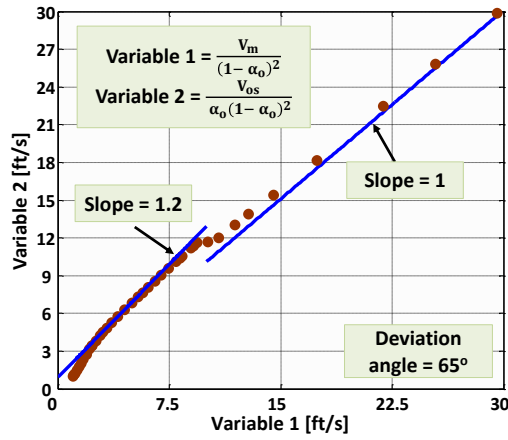
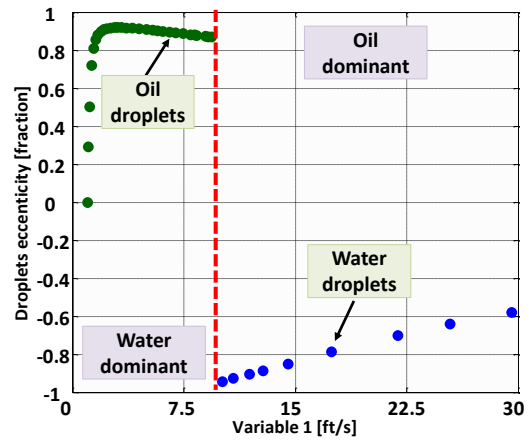


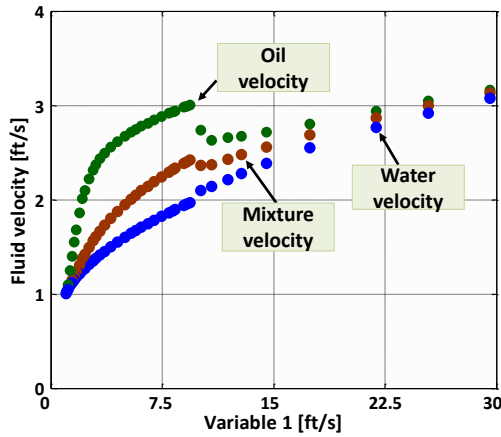
Figure 4.9: Numerically simulated (a) modified superficial velocity (Variable 2), (b) droplet diameter, (c) fluid-phase velocity, and (d) fluid-phase volume fraction, as a function of modified mixture velocity (Variable 1), obtained for the simultaneous flow of oil and water in a vertical pipe. The slope of 1.2 associated with a water-dominant bubbly flow regime is accurately simulated by dynamically modifying the droplet diameter as a function of borehole oil-phase velocity and volume fraction. The unit-slope line shown in Panel (a) is interpreted as the no-slip condition associated with high oil-phase volume fractions (i.e., oil-dominant flow regime).



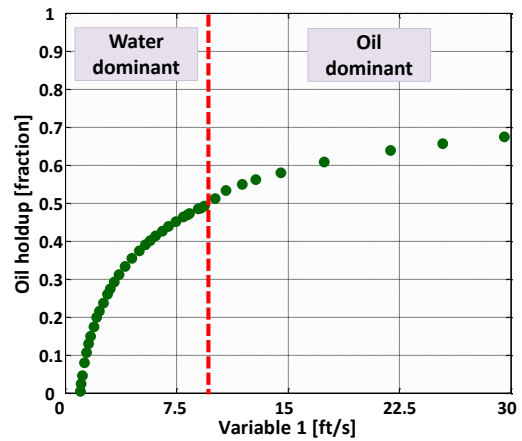
(a)



(b)



(c)



(d)

Figure 4.10: Numerically simulated (a) modified superficial velocity (Variable 2), (b) droplet eccentricity factor, (c) fluid-phase velocity, and (d) fluid-phase volume fraction, as a function of modified mixture velocity (Variable 1), obtained for the simultaneous flow of oil and water in a deviated pipe with a deviation angle of 65°. Droplet eccentricity is dynamically modified to account for the excess of slip velocity in deviated pipes.

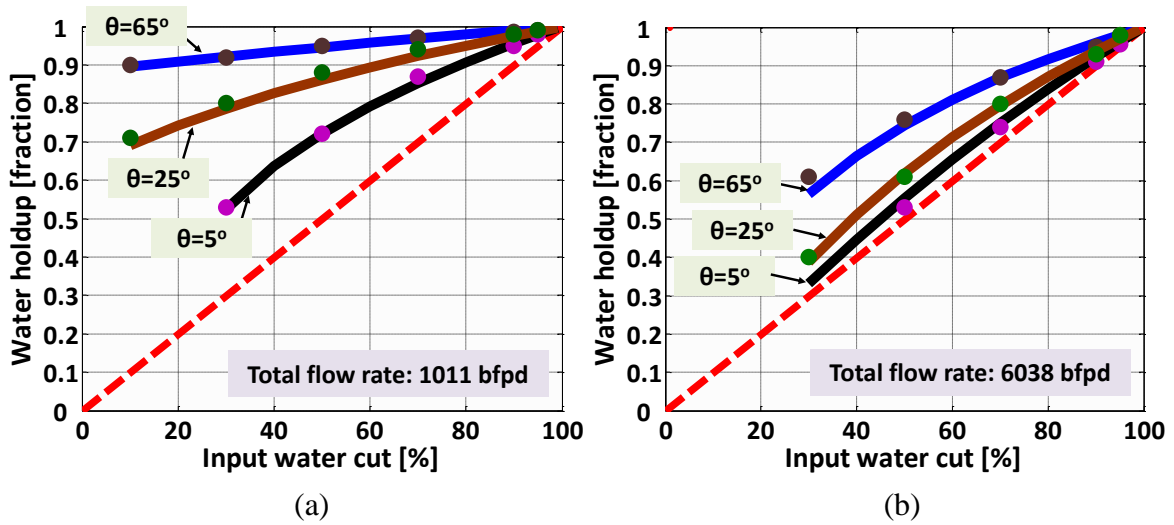


Figure 4.11: Comparison of the numerically simulated and measured water holdup in the steady-state conditions for simultaneous flow of oil and water with (a) 1011 and (b) 6038 bfpd total fluid flow rates, simulated for Vigneaux et al.'s (1988) water-oil flowing system. Dash lines describe the no-slip flowing conditions.

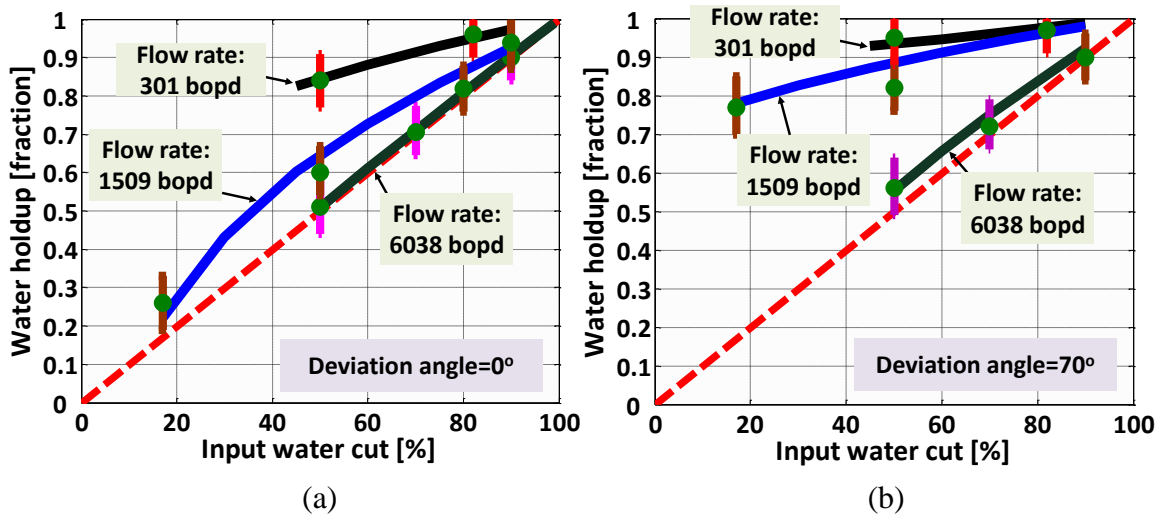


Figure 4.12: Comparison of the numerically simulated and measured water holdup in steady-state conditions for (a) vertical and (b) deviated water-oil flowing systems, reported by Shi et al. (2005). Dash lines describe the no-slip flowing conditions. Error bars quantify uncertainty bounds associated with water holdup estimated from fluid local conductance.

4.5 GAS-WATER FLOWING SYSTEMS

The developed borehole fluid flow model invokes flow-regime maps specified for vertical and deviated boreholes to simulate fluid-phase slip velocity across fluid-producing depth intervals. The accuracy of slippage simulation is validated against experimental results reported by Shi et al. (2005). Shi et al.'s (2005) experimental study included simultaneous injection of water ($\rho_w=1$ g/cc and $\mu_w=1$ cp) and nitrogen ($\rho_g=0.00125$ g/cc and $\mu_g=0.0173$ cp) into an inclinable flow loop with length and diameter equal to 36 ft and 6 in, respectively. Identical to oil-water flowing systems, comparison between steady-state water holdup and input water volume fraction (input water cut) is carried out to quantify slip velocity at various inclinations and fluid flow rates. The deviation of measured water holdup from input water volume fraction indicates velocity contrast between the two fluid phases.

Cases of validation include injection of water and gas into the flow loop at two inclination angles (namely, 0 and 45 degrees) and two input gas flow rates (i.e., 1812 and 9212 bbl/day). Input water flow rate is changed accordingly to investigate the slip velocity associated with various flowing conditions. As shown in Figure 4.13, the numerically simulated water holdups are within an acceptable range of accuracy in comparison to the corresponding measured values. Because of flow-regime change, increasing input gas flow rates lowers the steady-state water holdups. Furthermore, inclining the pipe from the vertical direction causes the accumulation of lighter phase close to the upper wall thereby increasing the steady-state water holdup.

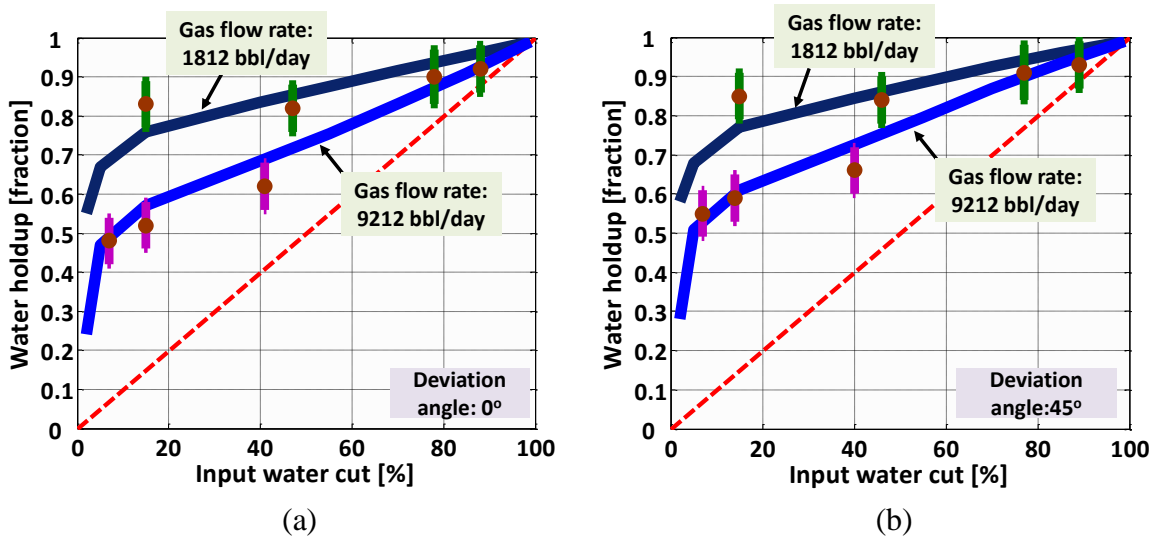


Figure 4.13: Comparison of numerically simulated (solid curves) and measured water holdup for steady-state conditions simulated in (a) vertical, and (b) deviated water-gas flowing systems (Shi et al., 2005). Dash lines describe no-slip flowing conditions. Error bars quantify uncertainty bounds associated with water holdup estimated from fluid local conductance.

4.6 GAS-OIL FLOWING SYSTEMS

Accuracy of the developed borehole fluid flow model to simulate pressure drop in a long pipe is verified against a field example documented by Hasan and Kabir (2002). The field example includes a vertical gas-oil producing well with length, diameter, and roughness equal to 5151 ft, 2.99 in, and 0.003 in, respectively. Available gas and liquid properties at standard and wellhead conditions are summarized in Table 4.4. Four hydrocarbon components, with properties listed in Table 4.5, are generated to honor phase behavior of the producing system. The given oil and gas superficial velocities are used to simulate borehole fluid-phase properties, and to compare the numerically simulated borehole pressure with measured values.

Figure 4.14 shows the simulated spatial distributions of fluid velocity, holdup, temperature, and pressure. Linear interpolation has been assumed to construct the

distribution of borehole temperature. Because of gas expansion, borehole gas holdup exhibits a nonlinear spatial distribution with respect to depth. In addition, gas expansion gives rise to a flow-regime transition in the borehole that accordingly increases fluid-phase slip velocity. As Figure 4.15 shows, bubbly and slug flow regimes have been identified with a transition taking place at approximately 2060 ft MD. The simulated flow regime in the wellhead conditions is in agreement with the flow regime reported by Hasan and Kabir (2002). Furthermore, the comparison of measured and simulated borehole pressure shows an acceptable match.

Figure 4.16 shows the numerically simulated gas and oil compositions. Because of interfacial mass transfer, the molar fraction of heavier components in the oil phase (i.e., FC_{16} and C_{17}^+) increases from the bottom to top of the pipe. In addition, simulated oil-phase density, shown in Figure 4.17, confirms a heavier oil phase at wellhead conditions when compared to that in bottom-hole conditions. On the other hand, depth variations of pressure, temperature, and composition cause the decrease of gas-phase density from bottom-hole to wellhead. As shown in Figure 4.18, the developed borehole fluid flow model accurately simulates measured borehole pressure.

Property	Unit	Wellhead	Standard
ρ_o	g/cc	0.8821	0.9159
ρ_g	g/cc	0.0351	0.000964
μ_o	cp	13.9	-
μ_g	cp	0.019	-
σ_{og}	dynes/cm	31.6	-
V_{so}	ft/s	1.601	-
V_{sg}	ft/s	2.824	-
Q_o	STBPD	-	1140
GOR	scf/STB	-	450

Table 4.4: Summary of assumed fluid-phase properties for validation example of the oil-gas flowing system reported by Hasan and Kabir (2002).

Property	Unit	Methane	Ethane	FC ₁₆	C ₁₇ ⁺
T_{crit}	°K	190.60	305.4	734.5	989.1
P_{ritc}	atm	45.4	48.2	17.15	5.98
A_c	-	0.008	0.098	0.683	1.39
V_{crit}	$\frac{m^3}{kgmole}$	0.099	0.148	0.835	4.38
MW	$\frac{lb_m}{lb_m mole}$	16.04	30.07	222	954

Table 4.5: Summary of assumed hydrocarbon properties for validation example of the oil-gas flowing system reported by Hasan and Kabir (2002).

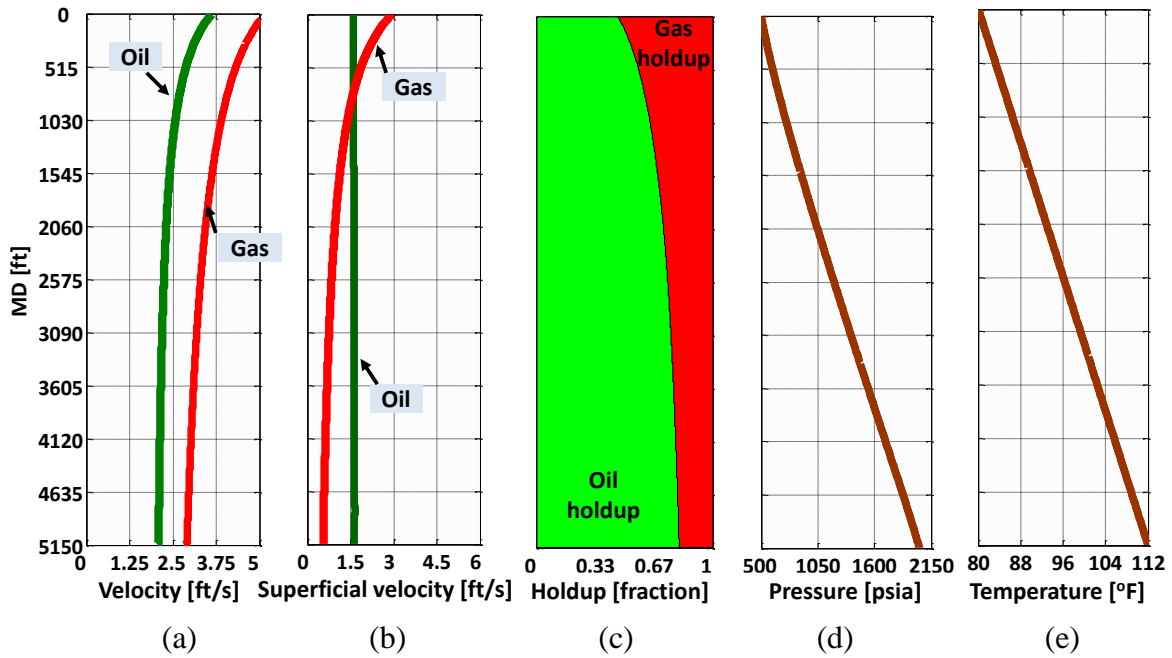


Figure 4.14: Depth variations of borehole fluid-phase: (a) actual velocity, (b) superficial velocity, (c) holdup, and (d) pressure, simulated for validation example of the oil-gas flowing system (Hasan and Kabir, 2002). Panel (e) shows the assumed borehole fluid temperature.

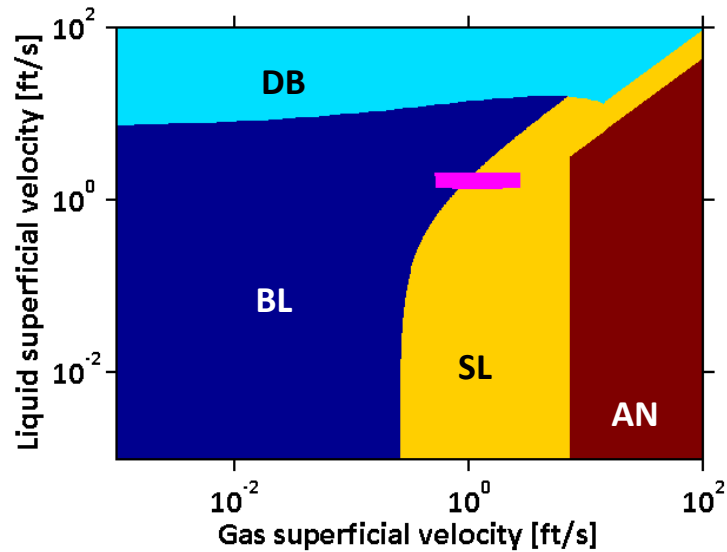


Figure 4.15: Borehole fluid-phase superficial velocities on the gas-liquid flow-regime map (DB: dispersed-bubbly, BL: bubbly, SL: slug, and AN: annular flow regimes), performed for validation example of the oil-gas flowing system (Hasan and Kabir, 2002).

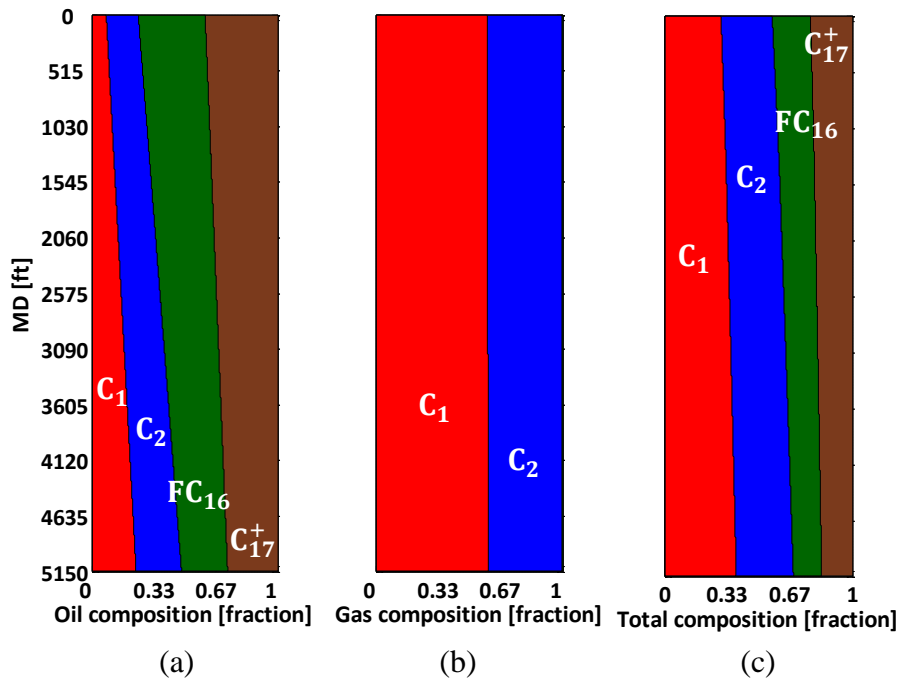


Figure 4.16: Borehole (a) gas-phase (b) oil-phase, and (c) overall hydrocarbon molar fractions, simulated for Hasan and Kabir's (2002) validation example.

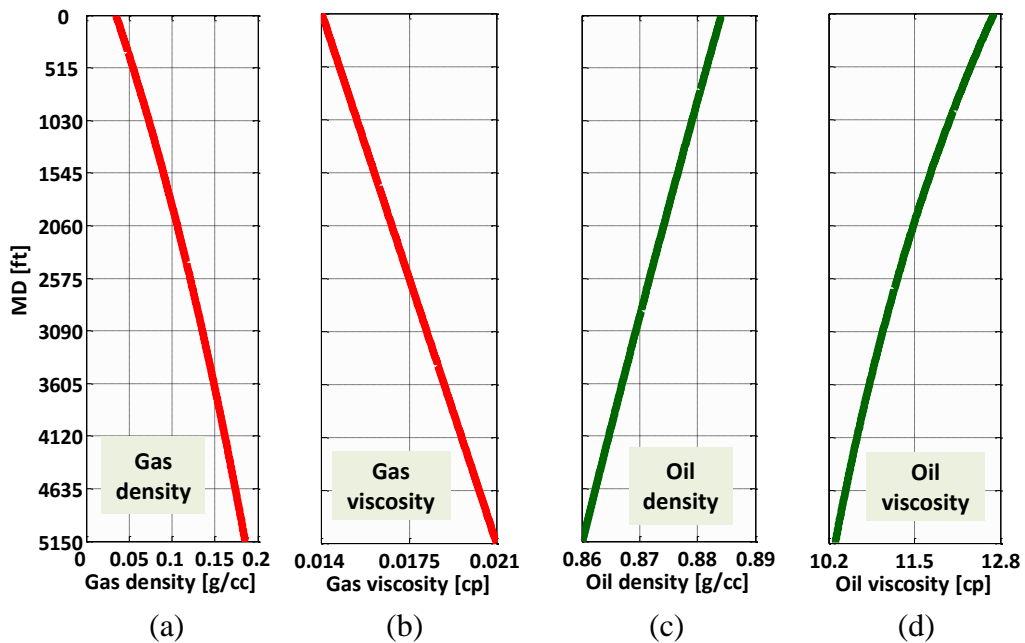


Figure 4.17: Borehole (a) gas-phase density, (b) gas-phase viscosity, (c) oil-phase density, and (d) oil-phase viscosity, simulated for Hasan and Kabir's (2002) validation example.

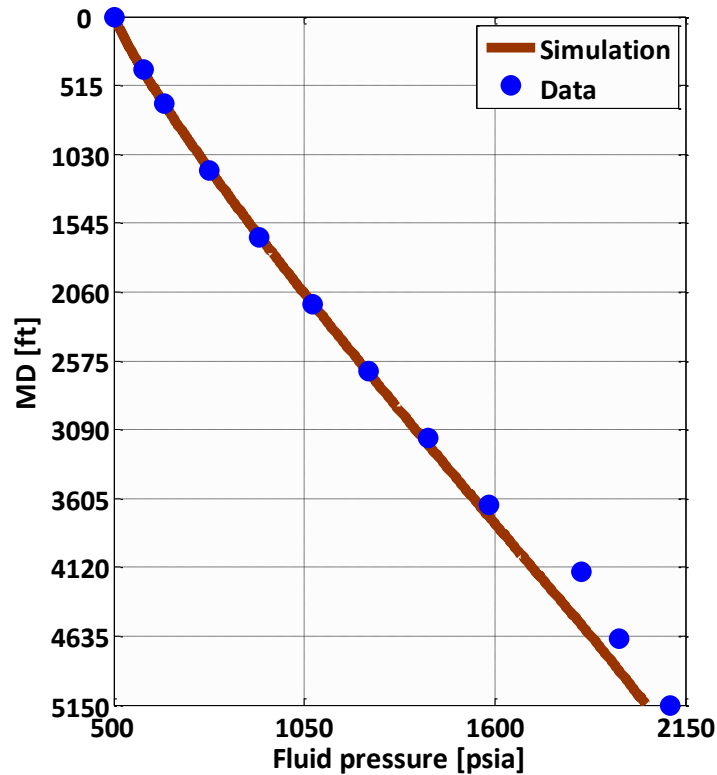


Figure 4.18: Comparison of the numerically simulated and measured borehole pressure performed for Hasan and Kabir’s (2002) validation example.

4.7 FIELD PRODUCTION MEASUREMENTS

Borehole production measurements are conventionally used to quantify the type and rate of fluids produced from (injected into) various fluid-producing rock formations. Under conditions of zero slip velocity, a linear relationship adequately describes measured borehole fluid-phase holdup as a function of the corresponding fluid flow rates. However, slippage between fluid phases causes the heavier phase to accumulate in the borehole, thereby leading to a nonlinear behavior of borehole fluid-phase holdup with respect to the volumetric fluid flow rates. In the presence of a significant slip velocity, concomitant measurements of fluid-phase velocity and holdup are required to enable the

quantification of fluid-phase flow rates associated with individual fluid-producing depth interval.

Reliability of the developed borehole flow model to simulate fluid flow rates is validated against a field example reported by Schlumberger (1973). The field example under consideration includes simultaneous production of oil (density=0.78 g/cc and viscosity=0.8 cp) and water (density=1.03 g/cc and viscosity=1 cp) from a reservoir consisting of four producing layers. Borehole measurements are acquired from six positions to provide a detailed description of borehole fluid-phase properties above each fluid-producing layer. Production logging simulation is subsequently performed under explicit assumptions for fluid-phase density, holdup, and fluid mixture velocity to reconstruct fluid inflow rates across each layer. As Figure 4.19 shows, comparison between numerically simulated and measured fluid flow rates indicate acceptable match. Table 4.6 additionally quantifies that the estimation error is less than 10.2% of the corresponding measured flow rates.

The developed borehole flow model is validated against production measurements acquired in an oil-water producing borehole documented by Hasan and Kabir (2002). The validation is performed by reconstructing water-phase volume fraction associated with the known distributions of fluid flow rates, fluid-phase density, and borehole temperature. Assumed borehole and fluid-phase properties are summarized as follows: oil-phase density: 0.7848 g/cc, water-phase density: 1.13 g/cc, oil-phase viscosity: 1.5 cp, water-phase viscosity: 1 cp, and borehole diameter: 3 in. Figure 4.20 shows fluid-phase superficial velocities in a flow-regime map adopted by Flores et al. (1998). The corresponding simulated droplet diameter shows a sharp transition from water-dominant to oil-dominant flow regimes across the top set of perforations. As compared in Figures 4.21 and 4.22, simulated values for water-phase volume fraction and fluid mixture

density show acceptable agreement with the corresponding measured values. However, a discrepancy is observed close to the bottom set of perforations which is associated with unreliable production measurements across that interval. Furthermore, the estimated borehole pressure distribution confirms the measured values within an acceptable range of accuracy.

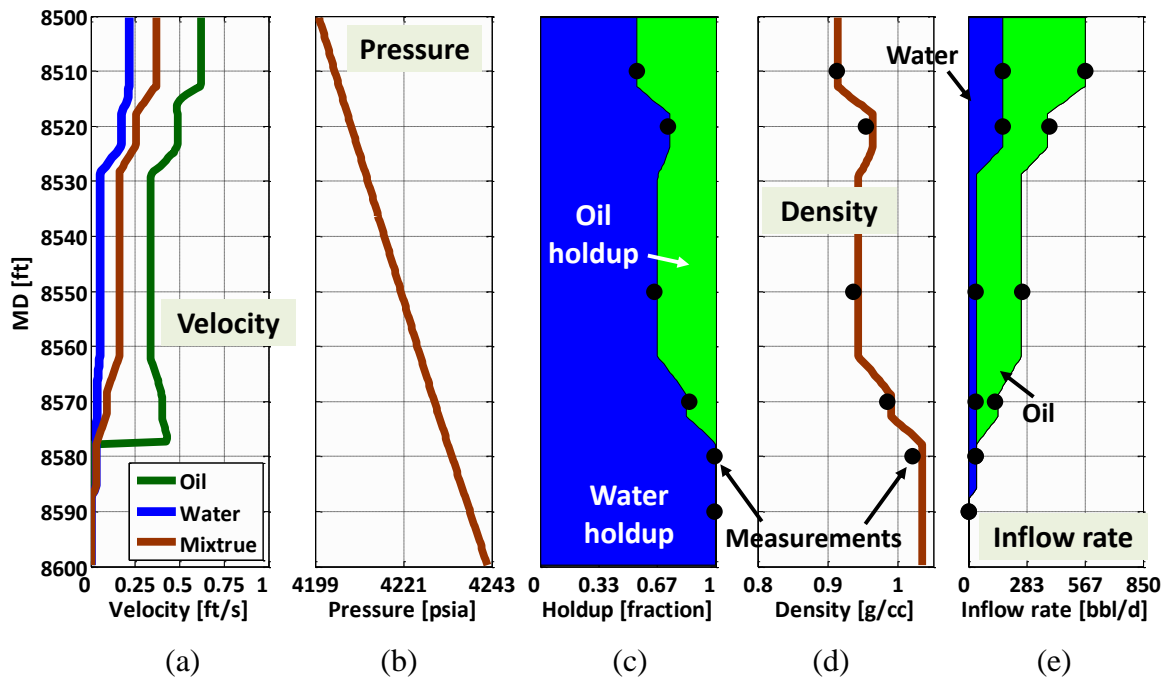


Figure 4.19: Reconstruction of borehole (a) fluid-phase and mixture velocities, (b) fluid pressure, (c) fluid-phase holdup, and (d) fluid mixture density, for the field example reported by Schlumberger (1973). Panels (c) through (e) compare the numerically simulated and measured fluid holdup, density, and inflow rates.

Position [ft]	Measured oil flow rate [bbl/d]	Simulated oil flow rate [bbl/d]	Measured water flow rate [bbl/d]	Simulated water flow rate [bbl/d]
8590	400	398.2	167	168.6
8580	225	218.6	167	168.6
8570	225	218.6	35	39.9
8550	95	104.7	35	39.9
8520	0	0	35	39.9
8510	0	0	0	0

Table 4.6: Comparison of the numerically simulated and measured borehole fluid-phase flow rate performed for oil-water field example reported by Schlumberger (1973).

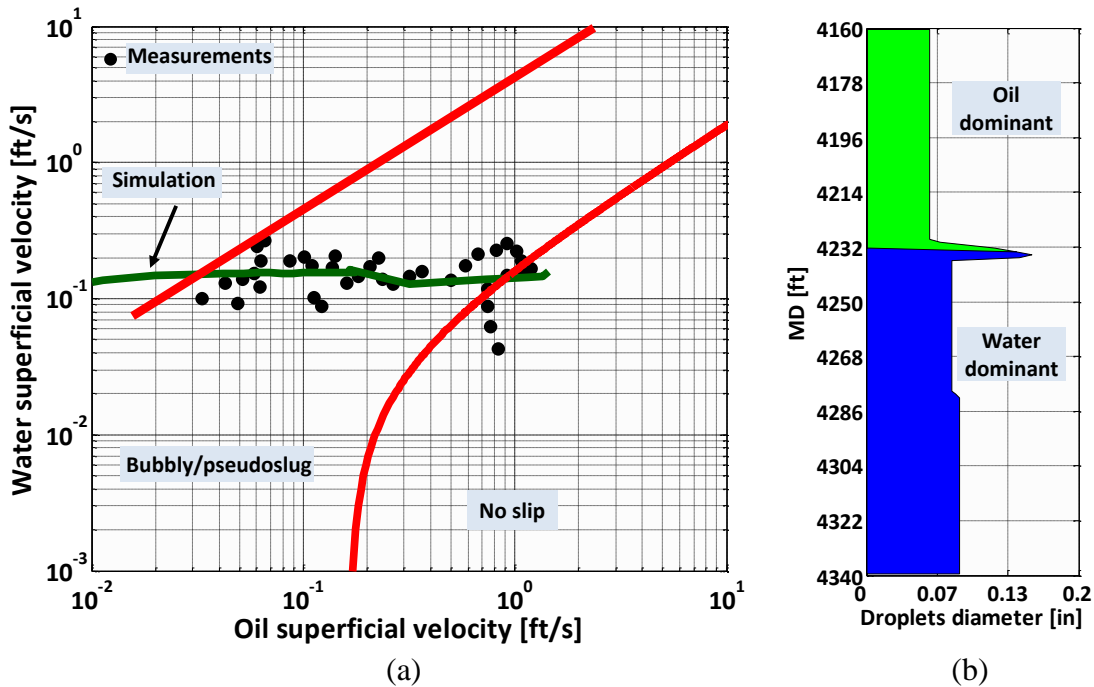


Figure 4.20: Numerically simulated and measured fluid-phase superficial velocities on the oil-water flow regime map, reported by Hasan and Kabir (2002). Panel (b) shows the numerically simulated droplet diameter associated with oil- and water-dominant flow regimes.

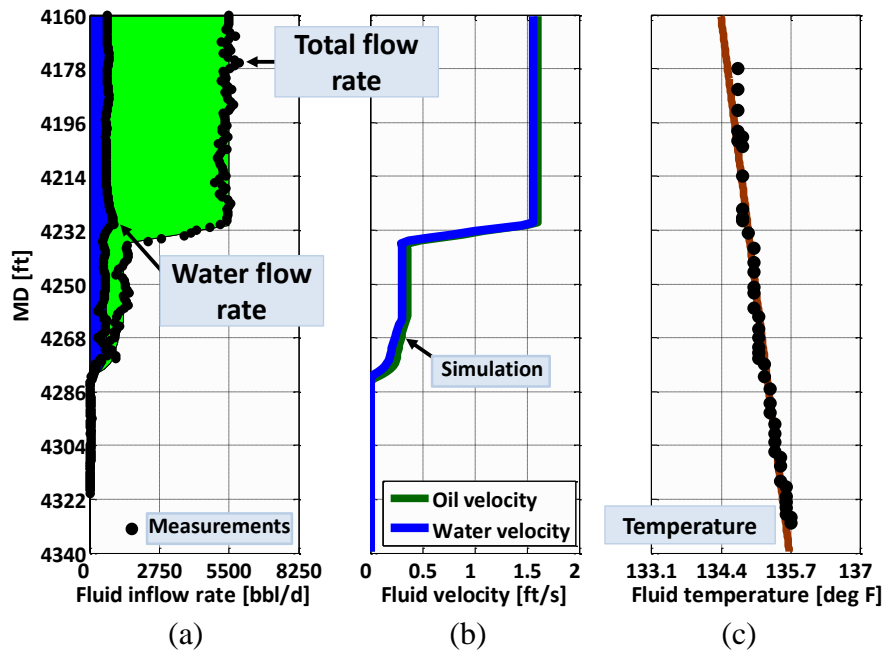


Figure 4.21: Reconstruction of the borehole fluid-phase (a) inflow rate, and (b) velocity, simulated for the field example reported by Hasan and Kabir (2002). Panel (c) compares the assumed and measured borehole fluid temperature.

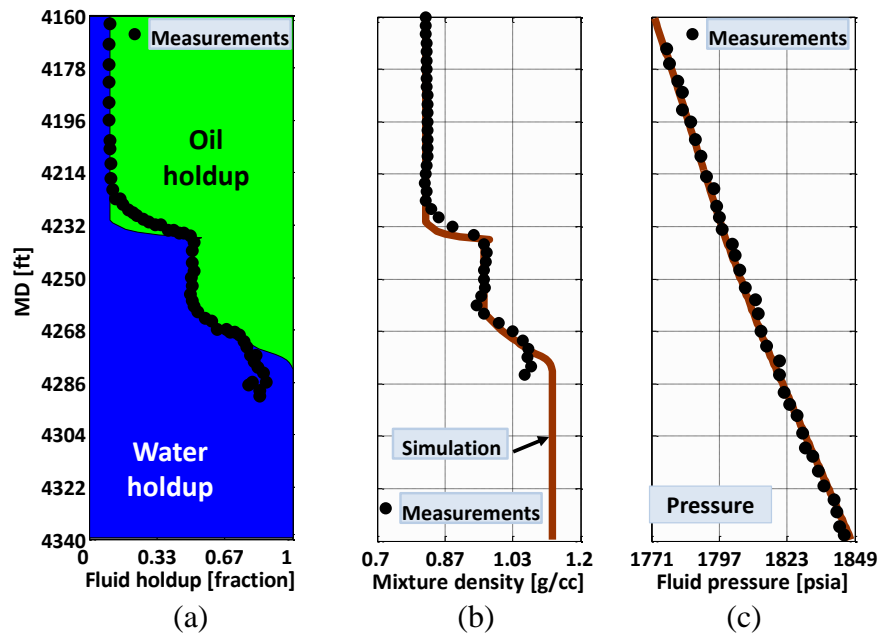


Figure 4.22: Reconstruction of the borehole (a) fluid-phase holdup, (b) fluid mixture density, and (c) fluid pressure, simulated for the field example reported by Hasan and Kabir (2002).

4.8 COMPUTATIONAL TIME

Simulated borehole fluid properties are ultimately used to estimate formation relevant properties by minimizing of a cost function to progressively match production logs. Because minimization process involves multiple cost function evolutions, solution algorithm for borehole fluid flow equations should be fast enough to obtain a reasonably low computational speed for PL interpretation. Results show that computational time is highly dependent on density and velocity contrasts (i.e., slippage) between two fluid phases. When simulating oil-gas flow, additional (component-based) mass conservation equations should be solved to compute (i) hydrocarbon density, (ii) hydrocarbon viscosity, (iv) and interfacial mass transfer rate that additionally decreases the simulation speed. As compared in Table 4.7, assuming identical number of numerical control volumes (namely, 200), on a computer with 8.00 GB (giga byte) of RAM (random access memory) and 3.4 GHz (giga hertz) of CPU (central processing unit), one day of oil-water flow simulation requires approximately three minutes, while presence of gas phase increases the computational time up to ten minutes. However, explicit assumption for hydrocarbon density and viscosity lowers the computational time to approximately 5 minutes.

Case	Density [g/cc]			Velocity [ft/s]			Time [minute]
	Water	Oil	Gas	Water	Oil	Gas	
Water	1.0	-	-	5	-	-	0.45
Gas	-	-	0.15	-	-	25	1.0
Oil-water	1.0	0.85	-	7	7.5	-	3.0
Gas-water	1.0	-	0.12	4	-	20	4.0
Gas-oil (with no mass transfer)	-	0.9	0.18	-	8.0	16	5.0
Gas-oil (with mass transfer)	-	0.9	0.18	-	7.5	15	10.0

Table 4.7: Computational time obtained for various single- and two-phase fluid flow simulations.

Chapter 5: Steady-State and Transient Simulation of Borehole Production Measurements

The main objective of this chapter is to show the advantages of using a coupled borehole-formation fluid flow model in simulation and interpretation of production measurements. I study synthetic cases of commingled two-phase fluid production to exemplify how borehole fluid flow behavior influences near-borehole formation petrophysical properties.

5.1 INTRODUCTION

Interpretation of two-phase production logs (PL) traditionally constructs borehole fluid flow models decoupled from the physics of reservoir rocks. Decoupled PL interpretation achieves valuable information about borehole flowing conditions. However, quantifying formation dynamic petrophysical properties from production logs requires simultaneous modeling of both borehole and formation fluid flow phenomena. This chapter applies the developed coupled wellbore-reservoir fluid flow model to (i) simulate transient behavior of cross-flow taking place in differentially-depleted rock formations, (ii) simulate a selective-inflow-performance (SIP) test to quantify the inflow performance of fluid-producing rock formations from dynamic and static PL passes, and (iii) estimate minimum pressure drawdowns required to prevent water loading phenomenon in gas-water producing systems.

The new iterative coupling method integrated with the developed borehole fluid flow model allows dynamic modification of reservoir boundary conditions to accurately simulate transient behavior of borehole cross-flow taking place across differentially-depleted rock formations. In the case of rapid variations of near-borehole properties, frequent borehole-formation communication inevitably increases the computational time required for fluid flow simulation. Despite this limitation, in a two-layer reservoir model penetrated by a vertical borehole, the coupling method accurately quantifies a 14% increase of volume-averaged oil-phase relative permeability of the low-pressure layer caused by through-the-borehole cross-communication of differentially-depleted layers. Sensitivity analyses indicate that the alteration of near-borehole petrophysical properties primarily depends on formation average pressure, fluid-phase density contrast, and borehole deviation angle. A practical application of the new coupled fluid flow model is numerical simulation of borehole production measurements to estimate formation average pressure from two-phase selective-inflow-performance (SIP) analysis. This study suggests that incorporating static (shut-in) PL passes into the SIP analysis could result in misleading estimation of formation average pressure.

5.2 TRANSIENT SIMULATION OF BOREHOLE CROSS-FLOW

In multilayer reservoirs saturated with a single fluid phase, borehole fluid flow associated with differential depletion is primarily controlled by near-borehole permeability and the average pressure of layers. Because of single-phase conditions, the borehole fluid is produced from formations exhibiting high productivity index, and is injected back into low-pressure formations. However, the simultaneous production of two fluid phases from multilayer reservoirs introduces fluid-phase buoyant and interfacial drag forces as additional controlling parameters associated with borehole cross-flow. In

the reservoir flowing domain, on the other hand, fluid-phase mobility associated with various fluid-producing rock formations dynamically determines the formation productivity index thus influencing borehole cross-flow behavior. Moreover, the deviation of the borehole from the vertical changes the borehole fluid flow regimes thereby involving an additional level of complexity into the cross-flow phenomenon. The synthetic example examined in this section attempts to quantify the sensitivity of borehole fluid properties to relevant formation and borehole properties.

5.2.1 Model Description

Simulation of borehole cross-flow in a two-phase producing system is carried out by constructing a coupled borehole-reservoir flow model consisting of two rock formations. Figure 5.1 shows the dynamic petrophysical properties associated with the two-layer model. The average pressure of Rock 1 (namely, the lower layer) is equal to 3250 psia that is 700 psia lower than that of the top layer (i.e., Rock 2). Both rocks belong to the same rock type shown in Figures 5.1d and 5.1e, with permeability and porosity equal to 300 mD and 18 pu, respectively. Production logs numerically simulated with the coupled system under production conditions are shown in Figure 5.2. Because of a lower average pressure, Rock 1 exhibits a lower productivity index compared to Rock 2. In addition, low water saturations associated with Rock 2 cause that rock to mainly produce hydrocarbon.

Figure 5.3 shows fluid-phase superficial velocity on the oil-water flow-regime map plotted with the estimated spatial distribution of droplet diameter. Droplet coalescence across Rock 2 gives rise to the formation of larger droplets thus increasing fluid-phase slip velocity. At depth 8035 ft MD, the transition of water-dominant flow regime to oil-dominant flow regime takes place when water droplets start to break up.

Droplet breakup consequently establishes no-slip flow regime associated with high hydrocarbon volume fractions. Moreover, as shown in Figure 5.3c, if no-slip conditions were assumed for the entire borehole flow domain the simulation of water-phase volume fraction would involve more than 7% error compared to the variable-droplet-diameter model.

Property	Unit	Rock1	Rock 2
ϕ	pu	18	18
K	mD	300	300
S_w	fraction	0.35	0.60
P_{avg}	psia	3250	3950

Table 5.1: Summary of assumed formation petrophysical properties for transient simulation of borehole cross-flow.

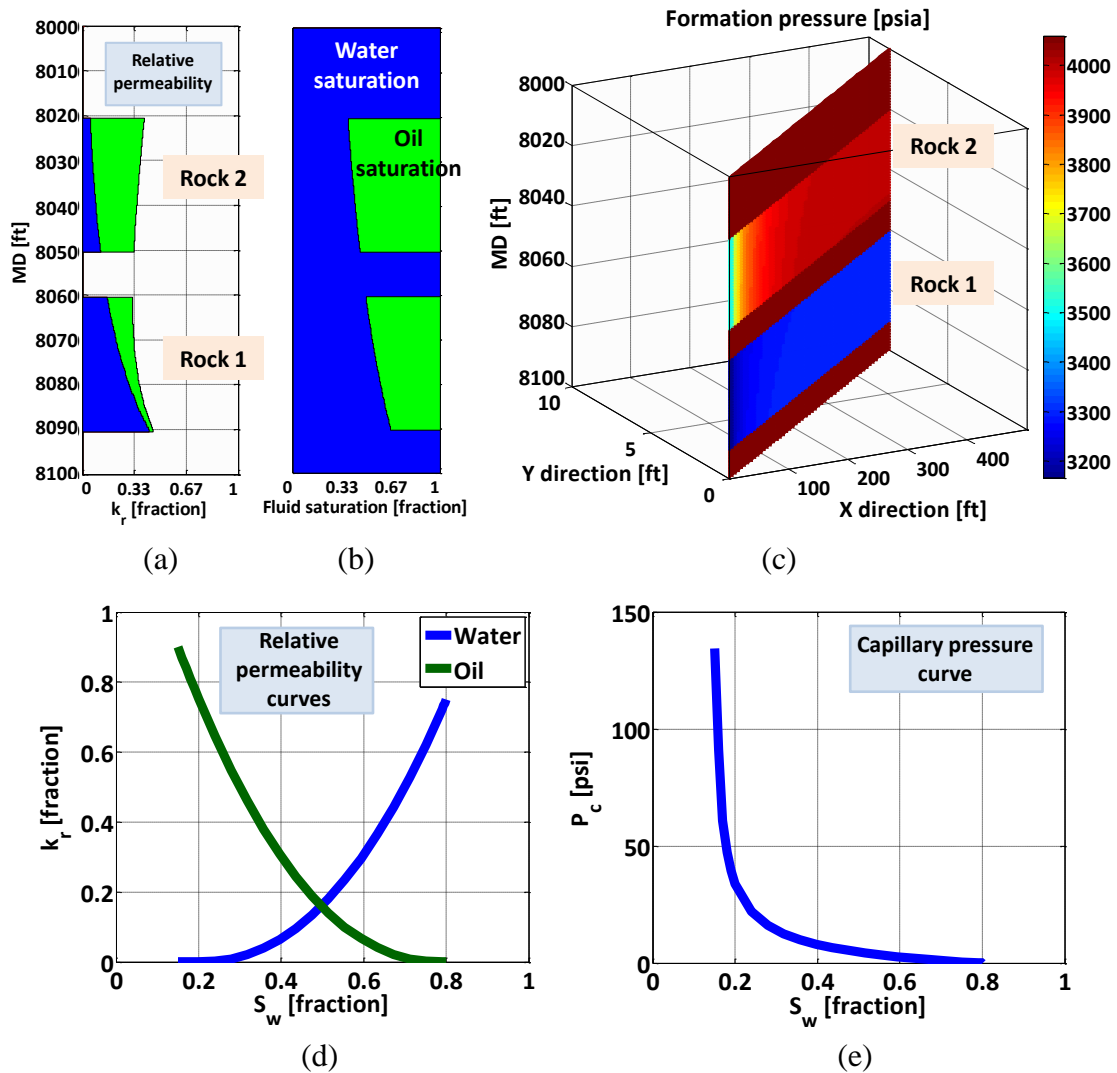


Figure 5.1: Assumed near-borehole petrophysical properties associated with the cross-flow simulation. Panels (a) and (b) show near-borehole relative permeability and the associated water saturation, respectively. Panel (c) visualizes the spatial distribution of formation pressure prior to measurement acquisition. Rock 1 exhibits a lower average pressure compared to Rock 2 that causes the development of borehole cross-flow. Panels (d) and (e) describe the assumed saturation-dependent relative permeability and capillary pressure curves, respectively. Rock 1 exhibits a lower average pressure compared to Rock 2 that causes the development of borehole cross-flow.

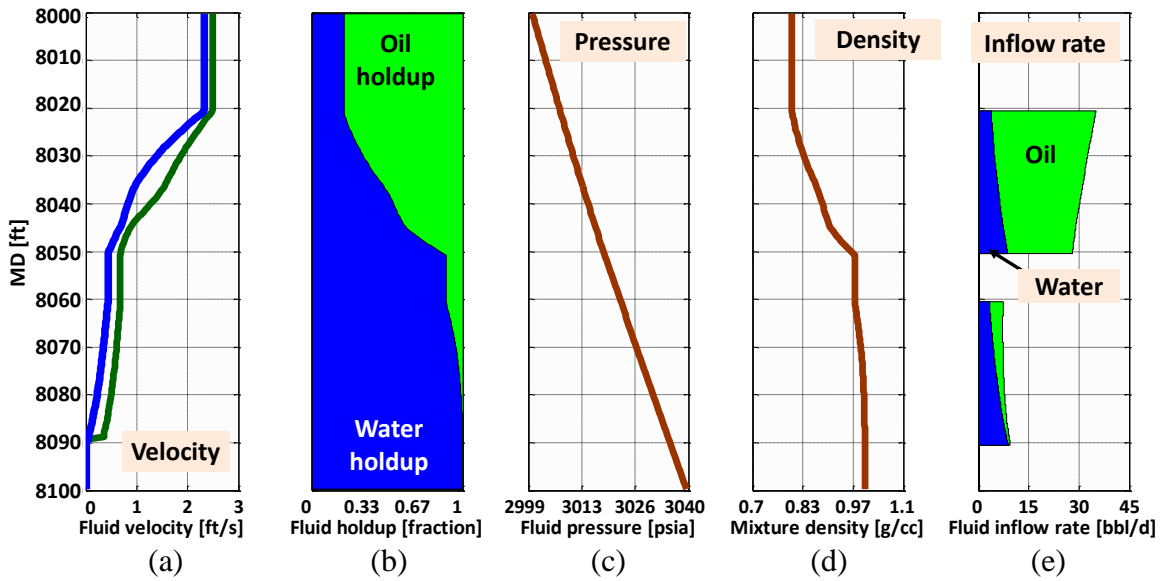


Figure 5.2: Numerically simulated borehole fluid-phase (a) velocity, (b) holdup, (c) pressure, (d) density, and (e) inflow rate. Because of the fluid-phase density contrast, oil-phase velocity, shown in Panel (a), is higher than that of the water phase. Fluid-phase slippage was simulated by dynamically modifying the spherical droplet sizes associated with the dispersed fluid phase.

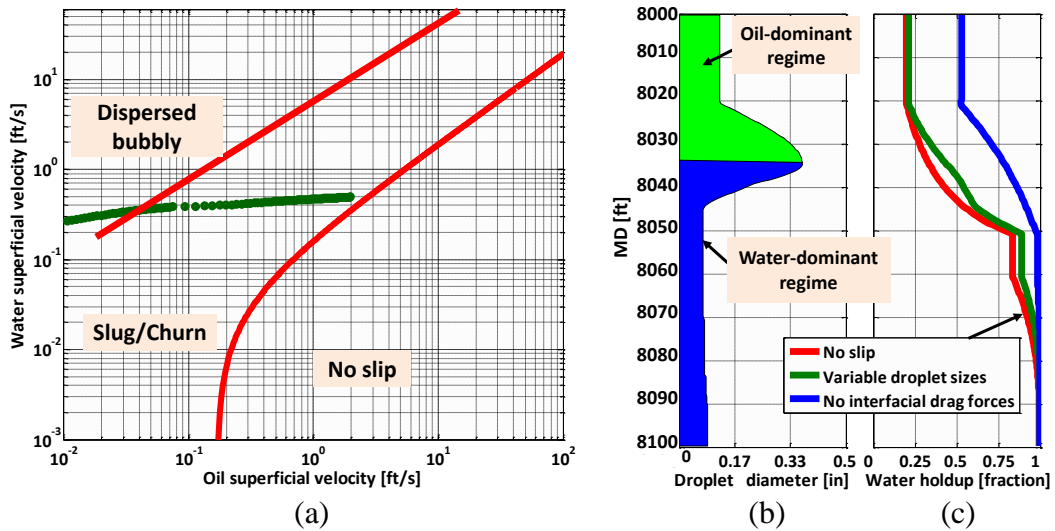


Figure 5.3: Numerically simulated (a) fluid-phase superficial velocities plotted in the oil-water flow-regime map, (b) droplet diameter associated with the dispersed phase, and (c) water-phase holdup. Panel (c) shows unaccounted variations of fluid-phase spillage (i.e., using a no-slip model) causes more than 7% error in the estimates of water holdup.

5.2.2 Production Measurements Under Shut-In Conditions

The coupled fluid flow model is initialized with the simulated fluid-phase properties obtained under production conditions. Subsequently, a shut-in test is performed to investigate the effects of borehole cross-flow on the producing behavior of coupled flowing system. Pressure at the top end of the borehole domain (i.e., depth 8000 ft MD) is set to 3550 psia to secure through-the-borehole cross-communication of Rocks 1 and 2 during shut-in time. Furthermore, zero-gradient boundary conditions associated with fluid-phase velocity and volume fraction at the top end ensure that sufficient fluid is available to replace the injected fluids. As shown in Figure 5.4, initiating shut-in causes both oil and water phases to flow downward to the low- pressure interval. Because of fluid-phase density contrast, oil phase flows at a lower velocity compared to that of the water phase. After 90 seconds, borehole hydrodynamic equilibrium is achieved when the water phase becomes segregated from the oil phase. Water-phase velocity associated with hydrodynamic equilibrium is negative, implying that water is produced from Rock 1 and is injected back into Rock 2. Accordingly, the oil phase, produced from Rock 1, is partially injected into the lower layer. Oil-phase velocities associated with the depth interval above 8025 ft MD exhibit positive values, indicating an upward movement of that phase.

Injection of multiphase fluid caused by borehole cross-flow, results in the alteration of near-borehole petrophysical properties of Rock 1. Figure 5.5 shows transient behavior of the coupled flowing system associated with the first 90 seconds of shut-in test. During this time interval, the spatial distribution of injected fluids into Rock 1 is dynamically determined by the borehole fluid-phase volume fraction. When borehole hydrodynamic equilibrium is achieved, water as the heavier fluid phase is injected from the lower part of Rock 1 while upper parts are mainly invaded by the oil phase. After 90

seconds, transient behavior of the coupled flowing system is governed by formation petrophysical properties. I invoke the coupled borehole-formation fluid flow model to estimate the variations of near-borehole fluid-phase saturation and relative permeability with time. Figure 5.6 indicates that, for a cylindrical region with radius equal to 10 ft around the borehole, the injection of oil phase into Rock 1 causes up to 18% increase in volume-averaged oil saturation associated with that layer. Furthermore, as indicated by Figure 5.6b and Figure 5.6c, the spatial distribution of oil-phase relative permeability exhibits a 14% increase caused by fluid injection into Rock 1. Because of no fluid invasion into Rock 2, fluid-phase relative permeability and saturation associated with that rock remain unaffected.

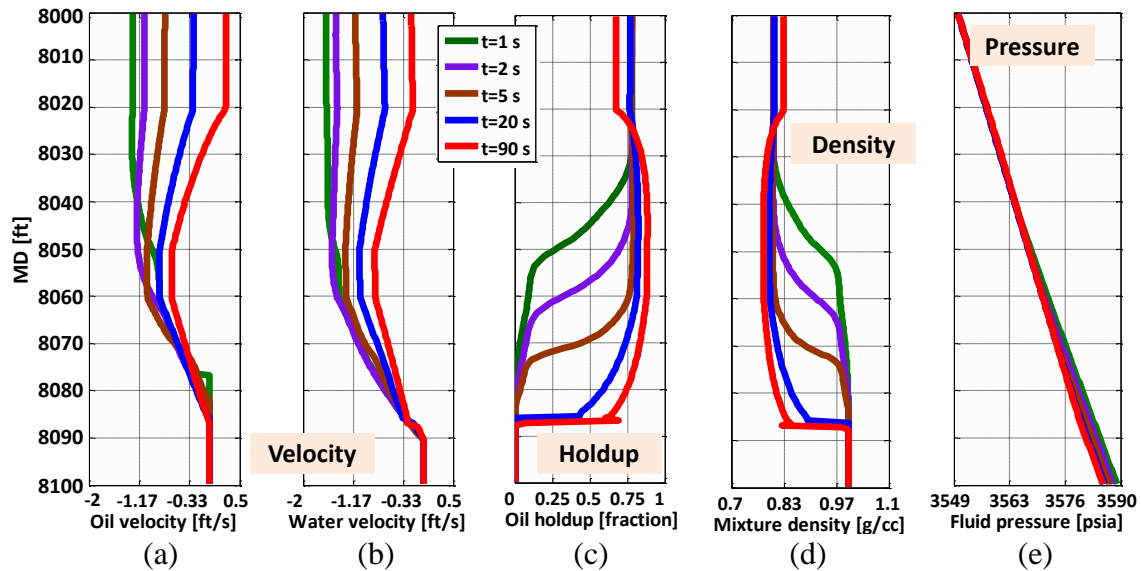


Figure 5.4: Numerically simulated spatial distributions of borehole (a) oil-phase velocity, (b) water-phase velocity, (c) oil-phase holdup, (d) fluid mixture velocity, and (e) fluid pressure shown in transient mode. The simulation has been performed for the first 90 seconds after initiation the borehole cross-flow. The negative values of simulated fluid-phase velocity imply the downward movement of fluid phases from high-pressure layer (i.e., Rock 1) to low-pressure layer (i.e., Rock 2).

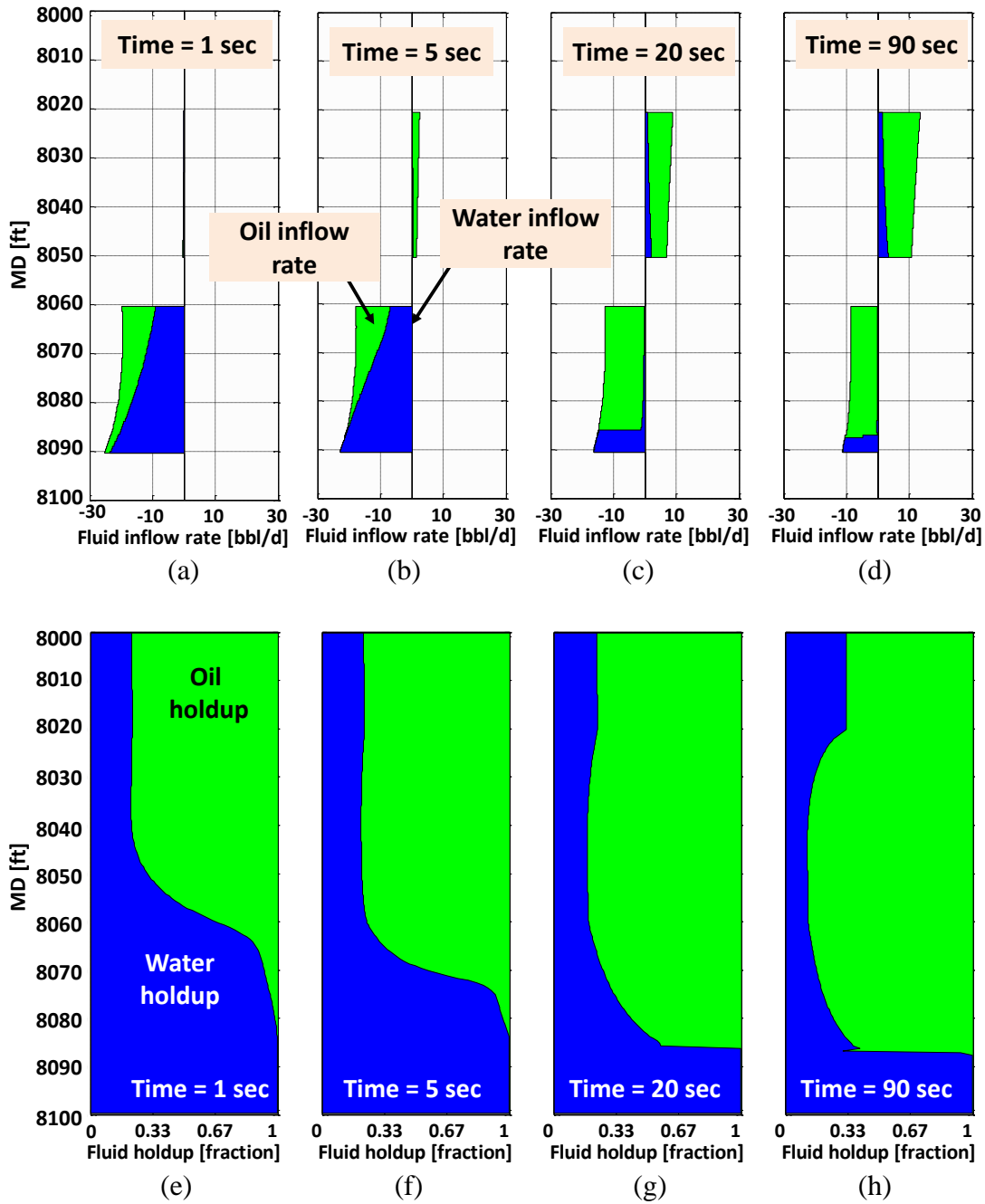


Figure 5.5: Numerically simulated spatial distributions of formation fluid-phase inflow rate (Panels a through d), and borehole fluid-phase holdup (Panels e through h) shown in transient mode. The simulations show downward movement of fluid phases associated with the first 90 seconds after the inception of borehole cross-flow.

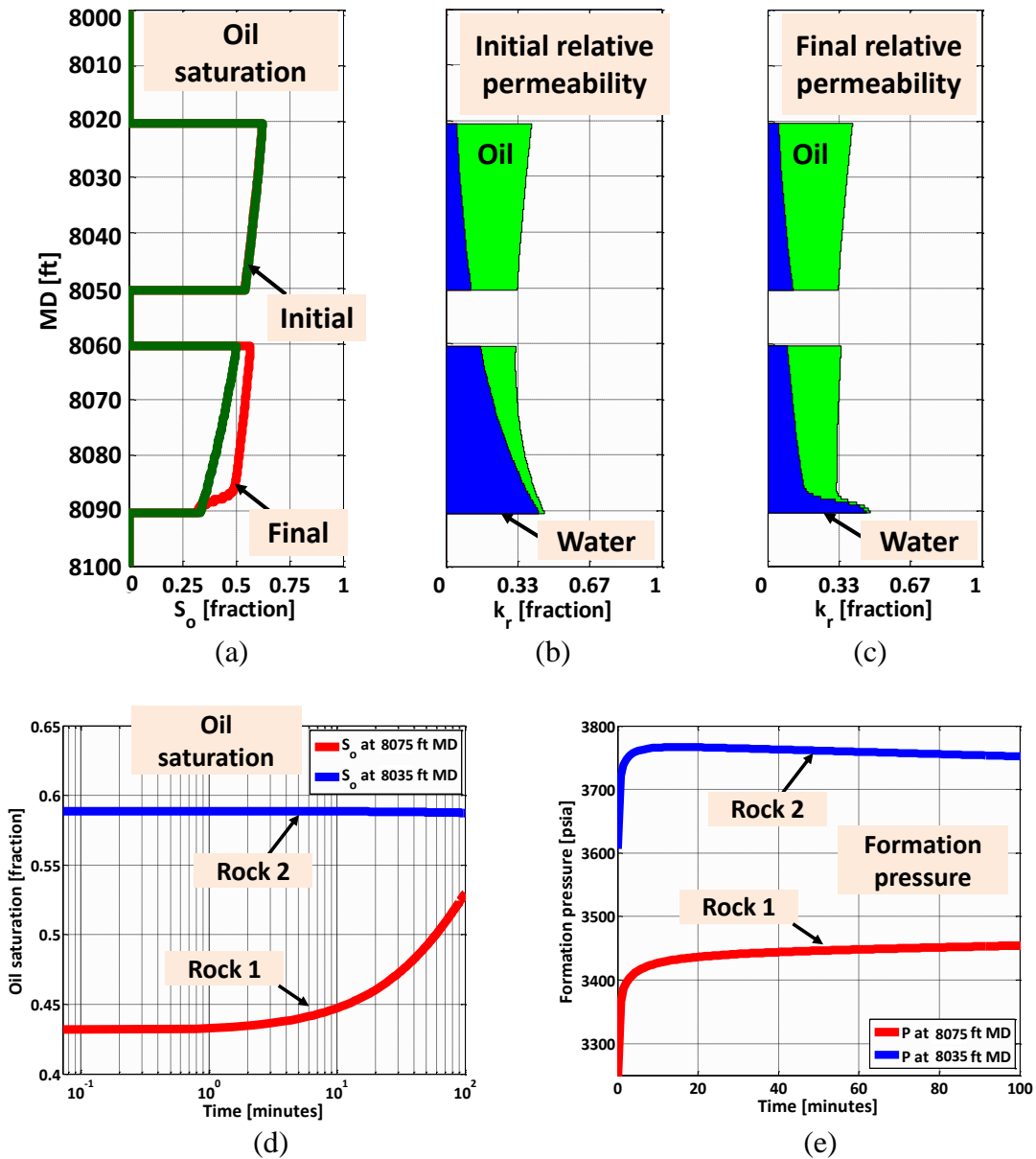


Figure 5.6: Comparison of the numerically simulated spatial distributions of near-borehole (a) oil saturation and fluid-phase relative permeability for (b) initial and (c) final simulation times. Panels (d) and (e) describe variations of oil saturation and pressure over cross-flow time. The development of borehole cross-flow causes an approximately 18% increase in near-borehole fluid-phase saturation, and a 14% increase of relative permeability. Furthermore, fluid injection into the lower layer (i.e., Rock 1) leads to a gradual increase of pressure for that rock. Panel (e) shows that borehole cross-flow continues until achieving hydrodynamic equilibrium between the two layers.

5.3 SENSITIVITY ANALYSIS

The two-layer system constructed in the previous section is additionally studied to quantify the effects of borehole and fluid-phase properties, and formation petrophysical properties on borehole cross-flow. Table 5.2 summarizes properties associated with the base case. The high permeability and low pressure associated with Rock 1 are favorable for the development of downward cross-flow. In addition, Rock 1 is fully saturated with water that makes it possible to quantify the effects of oil-phase invasion into that layer. The following section investigates the sensitivity of two-phase borehole cross-flow with respect to (i) near-borehole skin, (ii) the average pressure of Rock 1, (iii) oil-phase density, (iv) oil-phase viscosity, (v) borehole deviation angle, and (vi) cross-flow duration.

Formation	Unit	Rock1	Rock 2	Borehole	Unit	Value	Fluid phase	Unit	Oil	water
ϕ	pu	25	15	D	in	3	ρ	g/cc	0.85	1
P_{avg}	psia	5200	5900	L	ft	100	μ	cp	0.835	1
S	-	0	0	θ	deg.	0	C	μ siP	10	3
K	mD	640	320	ε	in	0.003	σ_{ow}	dyne/cm	40	-
S_w	fraction	0.9	0.45	P_{bh}	psia	5550				

Table 5.2: Summary of the assumed formation, borehole, and fluid-phase properties for the sensitivity analysis of borehole cross-flow in the two-layer reservoir model.

5.3.1 Near-Borehole Formation Damage

Formation permeability associated with a cylindrical region around the borehole with radius equal to 15 ft is modified to implement the skin caused by formation damage. I invoke the following formula to compute the associated skin factor:

$$S = \left(\frac{k}{k_s} - 1 \right) \text{Ln} \left(\frac{r_s}{r_w} \right), \quad (5.1)$$

where k is formation permeability, k_s is near-borehole permeability, r_s is the radius associated with near-borehole region, and r_w is borehole radius. Reduction of near-borehole permeability requires a larger pressure drawdown to maintain the same fluid inflow rate when compared to an undamaged rock. Figure 5.7 illustrates cross-flow behavior in the presence of near-borehole skin. Reduction of injection rates associated with skin factors larger than 4 are adequate to prevent the oil phase from moving downward thus resulting in the development of cross-flow with respect to only water phase. As Figure 5.8 shows, simulated IPR curves associated with Rock 1 show larger slopes with increasing skin factor. The larger slopes imply lower formation productivity indices. On the other hand, all curves exhibit an identical intercept with y-axis being interpreted as the static pressure of Rock 1 (namely, 5200 psia). Furthermore, because of a lower injection rate compared to an undamaged rock, near-borehole fluid-phase relative permeability of Rock 1 is less influenced by borehole cross-flow leading to IPR curves with negligible deviation from a straight line.

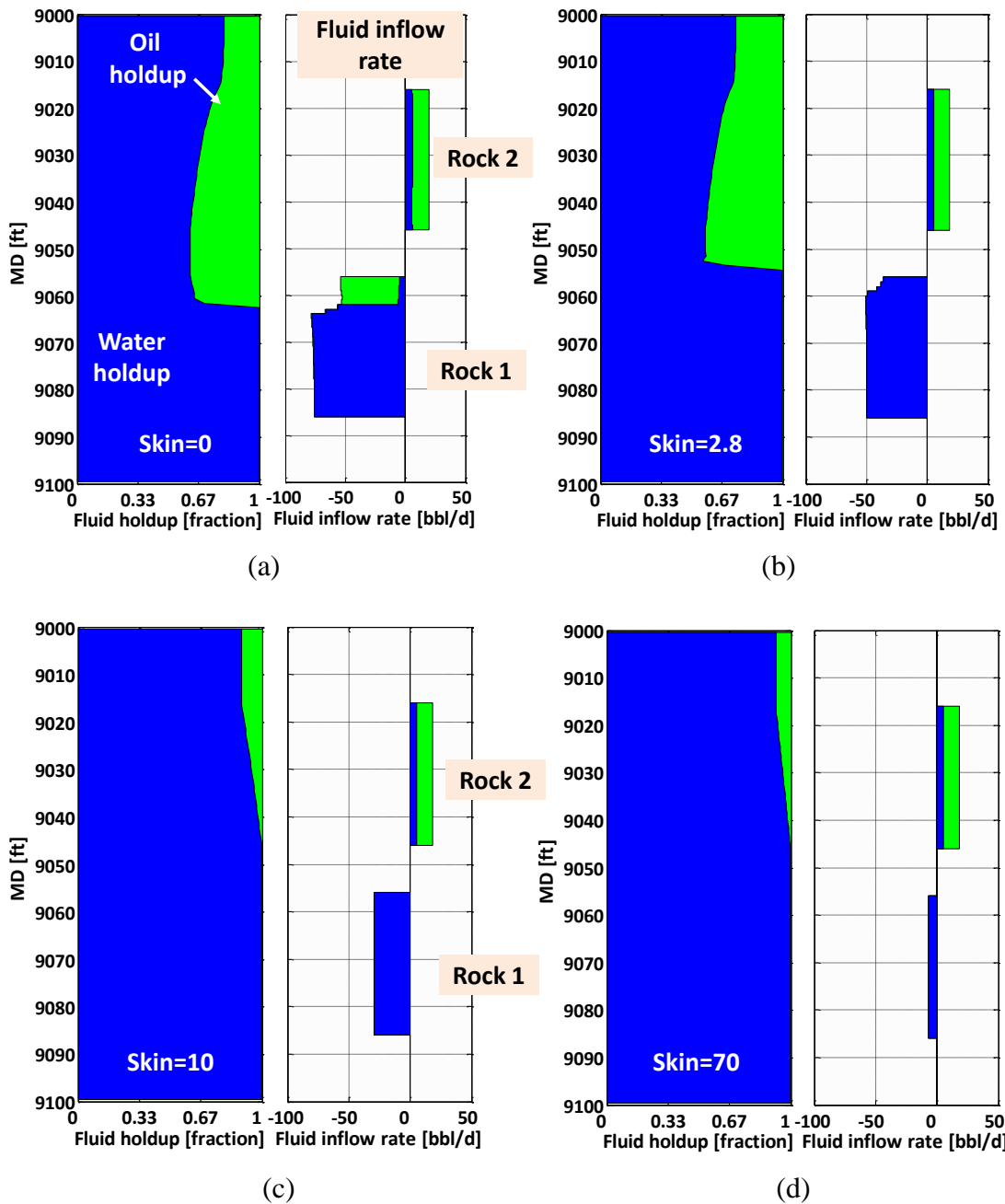


Figure 5.7: Sensitivity analysis for the spatial distributions of borehole fluid-phase holdup and fluid-phase inflow rate with respect to the presence of skin in near-borehole region of Rock 1. Panels (c) and (d) show the development of downward cross-flow with respect to only water phase; while for lower skins both fluid phases involve in cross-flow.

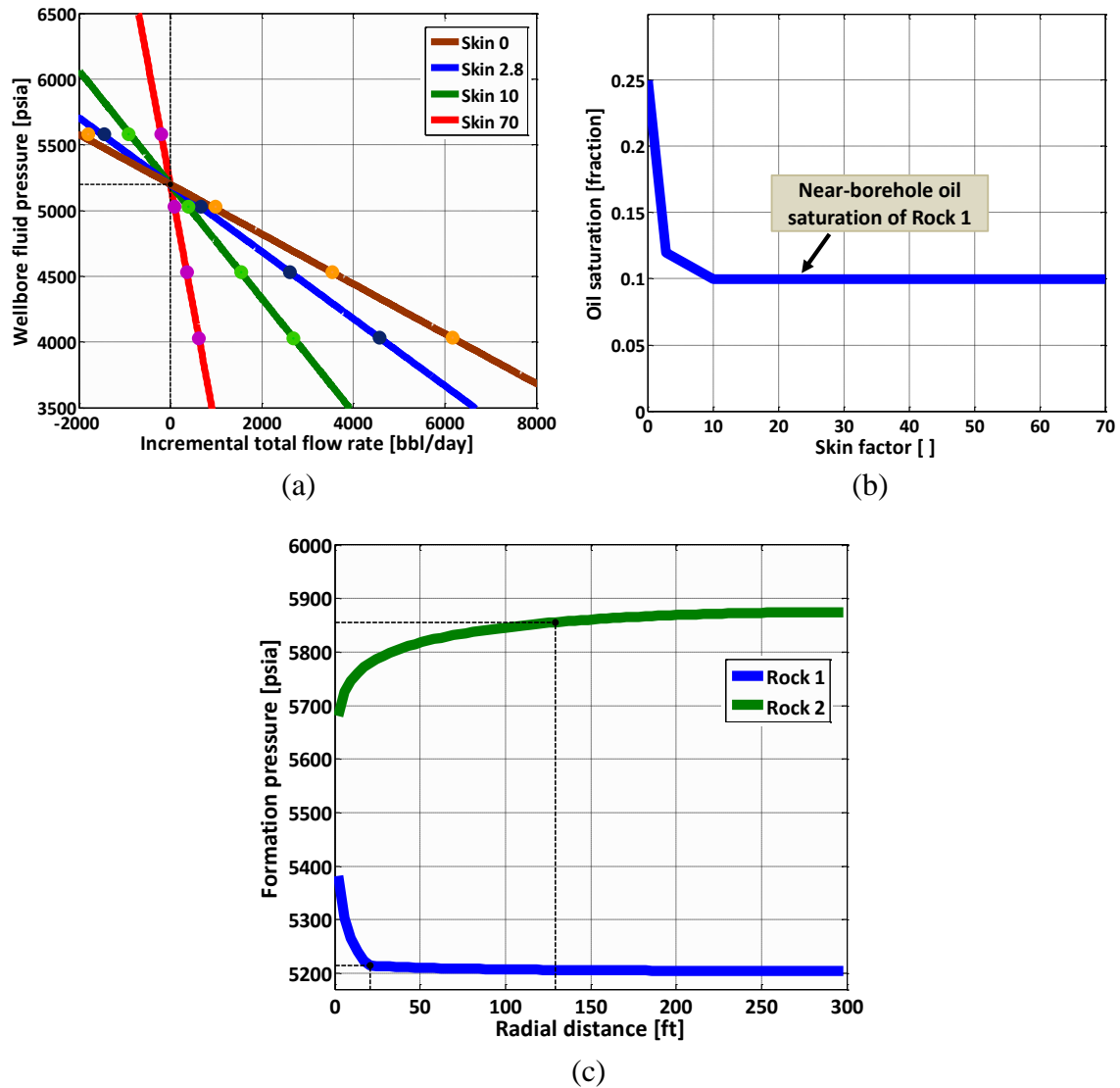


Figure 5.8: The effect of formation damage associated with Rock 1 on (a) inflow performance of Rock 1, (b) near-borehole oil saturation of Rock 1, and (c) radial distribution of pressure for Rocks 1 and 2. Panel (a) shows that producibility of Rock 1 decreases with increasing skin factor for that rock. Accordingly, higher skins result in lower oil-phase volumes being injected from Rock 2 into Rock 1 (Panel b).

5.3.2 Average Pressure

The coupled simulation of borehole fluid cross-flow suggests that initiating cross-flow with respect to the lighter fluid phase considerably depends on the pressure differences between the corresponding fluid-producing rock formations. A minimum pressure drawdown is required to prevent the lighter fluid phase from migrating upward. I invoke the coupled borehole-formation fluid flow model to quantify the sensitivity of borehole cross-flow to the average pressure of the depleted rock formation (namely, Rock 1). As shown in Figures 5.9 and 5.10, increasing the average pressure of Rock 1 shifts the coupled system toward hydrodynamic equilibrium, thus reducing fluid-phase inflow rates. When differences between the average pressure of Rocks 1 and 2 are lower than 400 psi, water is the only fluid phase that is injected into the lower layer. Figures 5.9 shows that the depletion of Rock 1 results in more than a three-fold increase of near-borehole oil saturation of that rock when compared to the associated initial oil saturation.

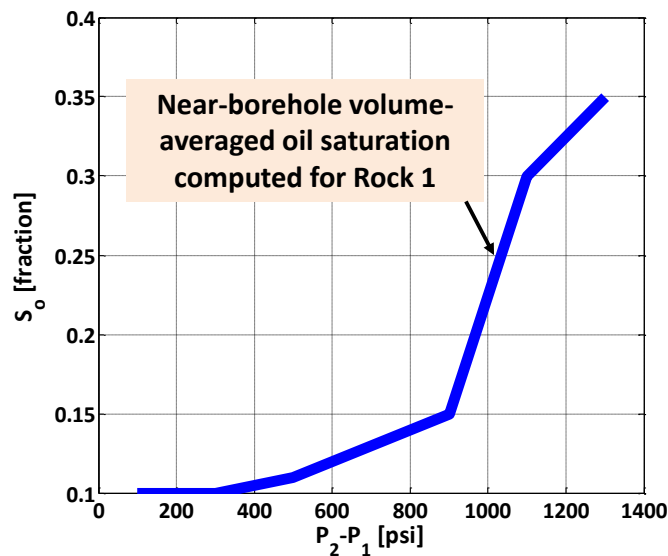


Figure 5.9: Sensitivity of near-borehole oil saturation for Rock 1 to the pressure difference between Rock 1 and Rock 2. A higher pressure difference leads to a higher fluid injection rate into Rock 1, thus increasing the near-borehole oil saturation for that rock.

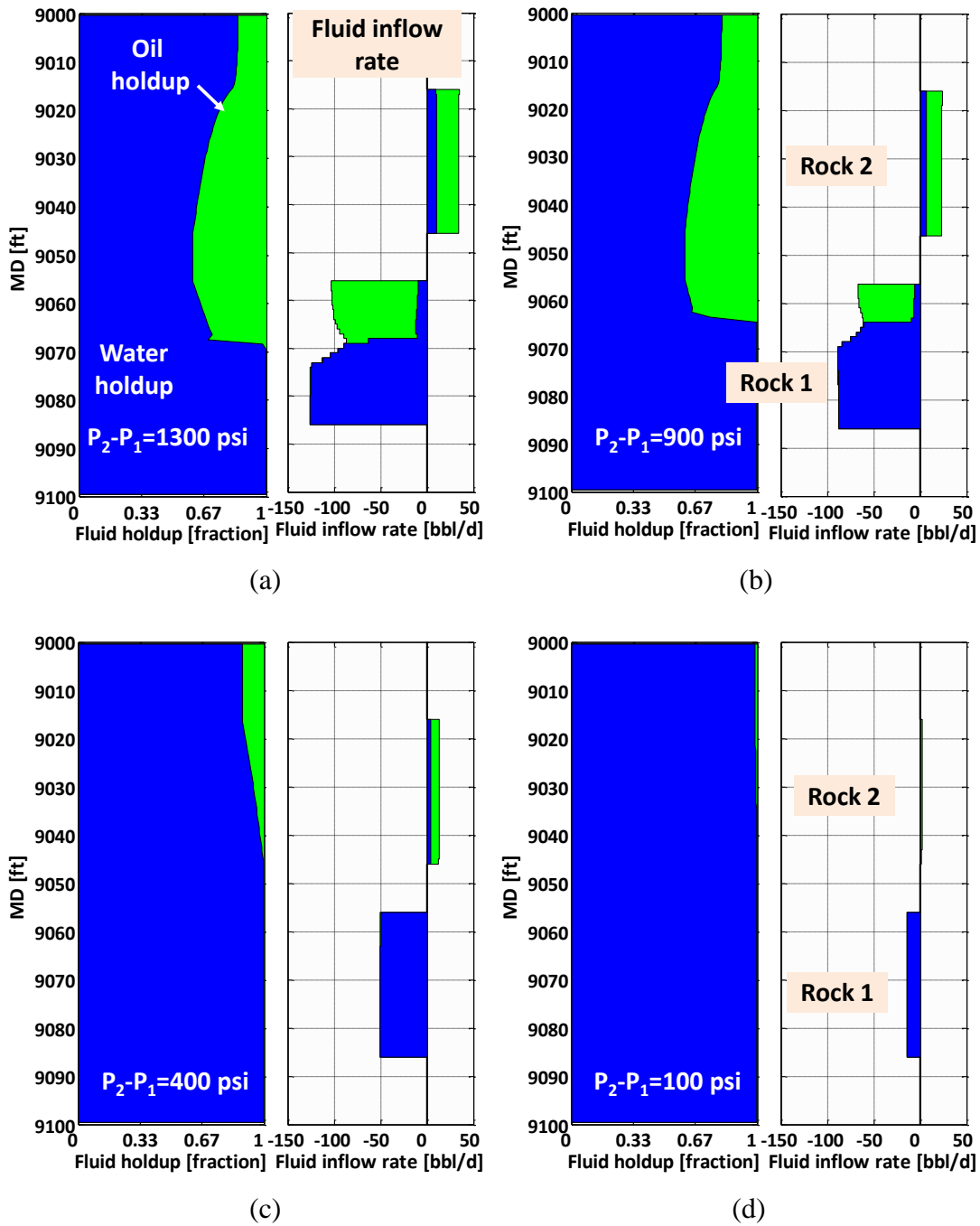


Figure 5.10: Sensitivity analysis for the spatial distributions of borehole fluid-phase holdup and fluid-phase inflow rate with respect to the pressure difference between Rock 1 and Rock 2. Panels (c) and (d) show that for pressure differences lower than 400 psi the development of downward cross-flow takes place with respect to only the water phase. Increasing layer pressure difference causes both fluid phases to contribute in cross-flow.

5.3.3 Oil-Phase Density

The magnitude of buoyant forces is influenced by differences in fluid-phase density. As shown in Figures 5.11 and 5.12, a low density contrast provides a favorable condition for developing two-phase cross-flow.

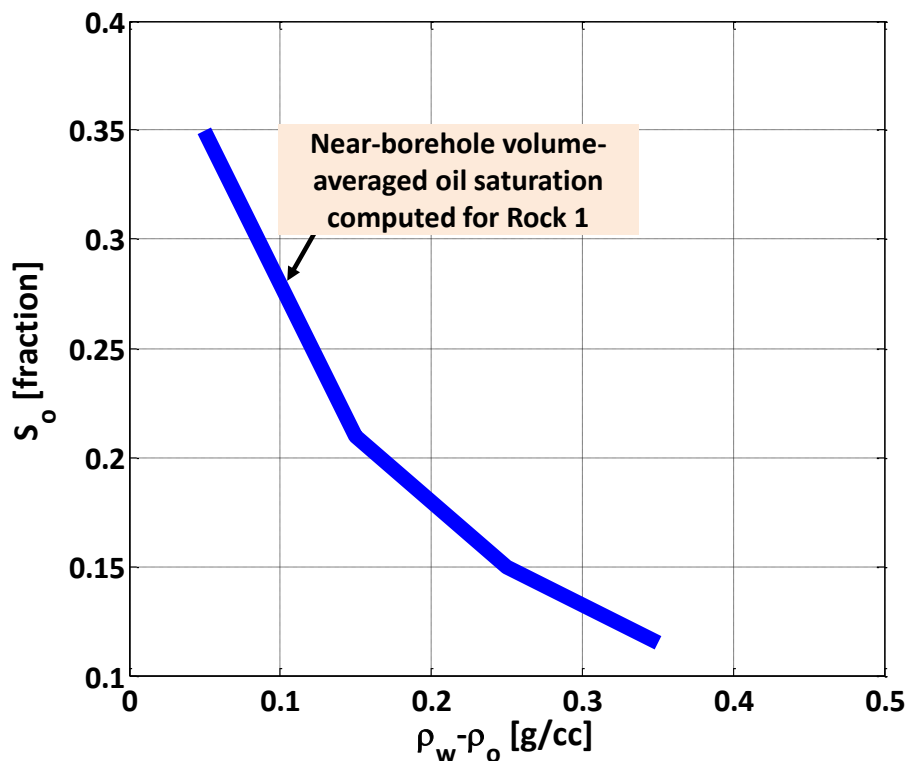


Figure 5.11: Sensitivity of near-borehole oil saturation for Rock 1 with respect to density difference between the oil and water phases. A higher density contrast lowers the volume of oil phase injected into Rock 1, thus decreasing the near-borehole oil saturation for that rock.

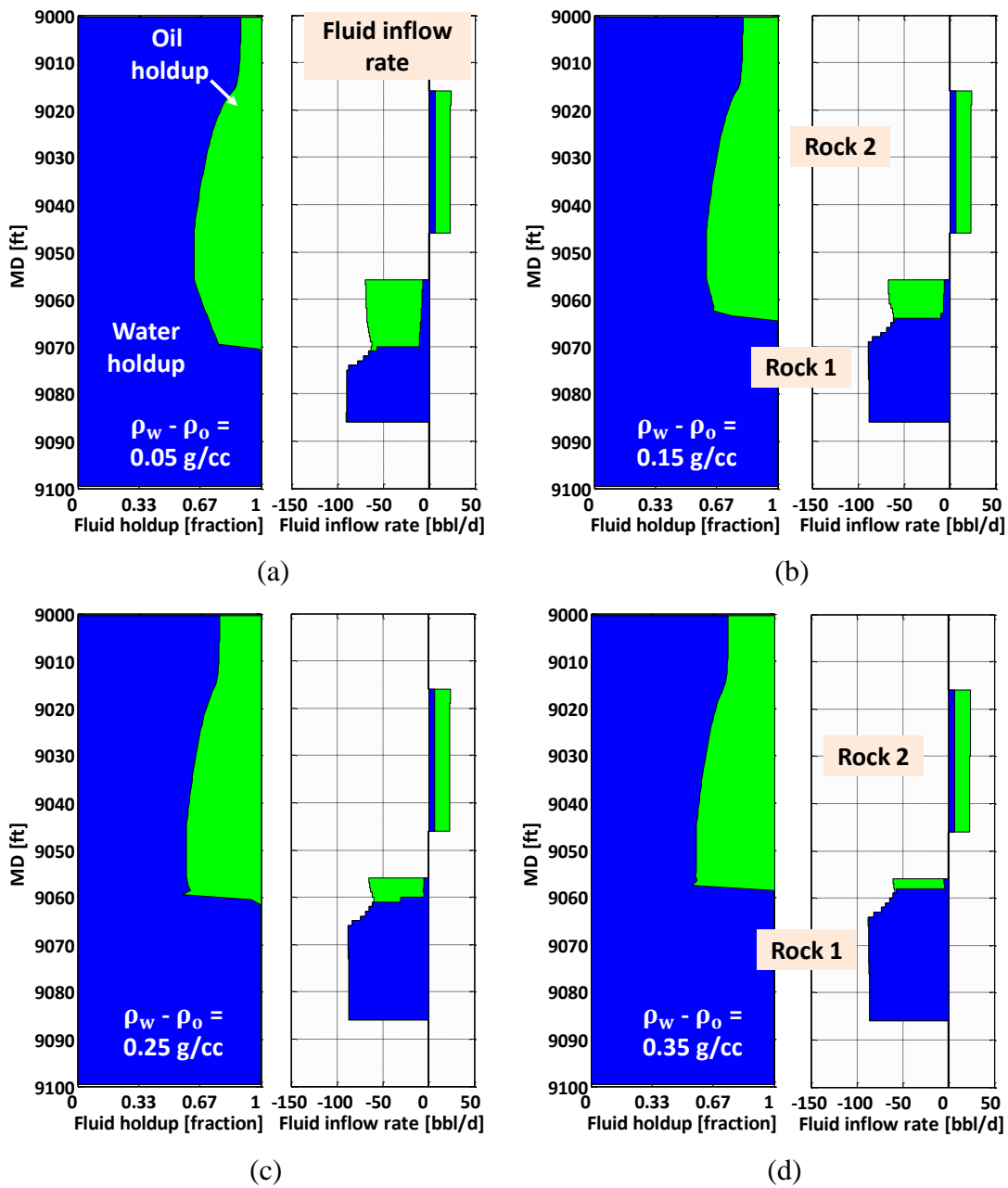


Figure 5.12: Sensitivity analysis for the spatial distributions of borehole fluid-phase holdup and fluid-phase inflow rate with respect to the density difference between oil and water phases. Panels (a) through (d) show that lowering the density contrast results in injection of larger volumes of the lighter fluid phase (i.e., oil) into Rock 1. Panel (d) shows that for the density contrast equal to 0.35 g/cc the oil volume injected into Rock 1 is approximately 27% lower than that associated with Panel (a) (i.e., density contrast equal to 0.05 g/cc).

5.3.4 Oil-Phase Viscosity

Increasing oil-phase viscosity decreases formation productivity index with respect to the oil phase (Figure 5.13). Because of lower production rates associated with viscous oil, the corresponding volume fraction in the borehole is lower compared to oil phase with a lower viscosity. However, as shown in Figure 5.14, development of borehole cross-flow is independent of oil-phase viscosity.

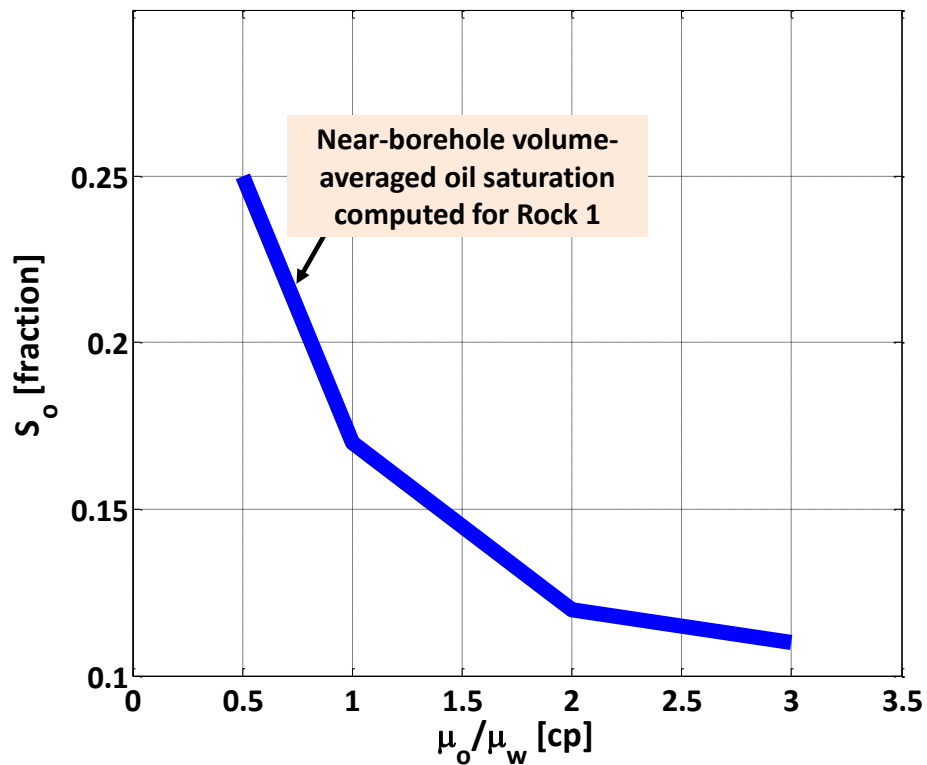


Figure 5.13: Sensitivity of near-borehole oil saturation for Rock 1 with respect to viscosity ratio between the oil and water phases. A higher viscosity ratio lowers producibility of Rock 2 and injectivity of oil-phase into Rock 2. Therefore, at higher viscosity ratios lower volume of oil phase is injected into Rock 1.

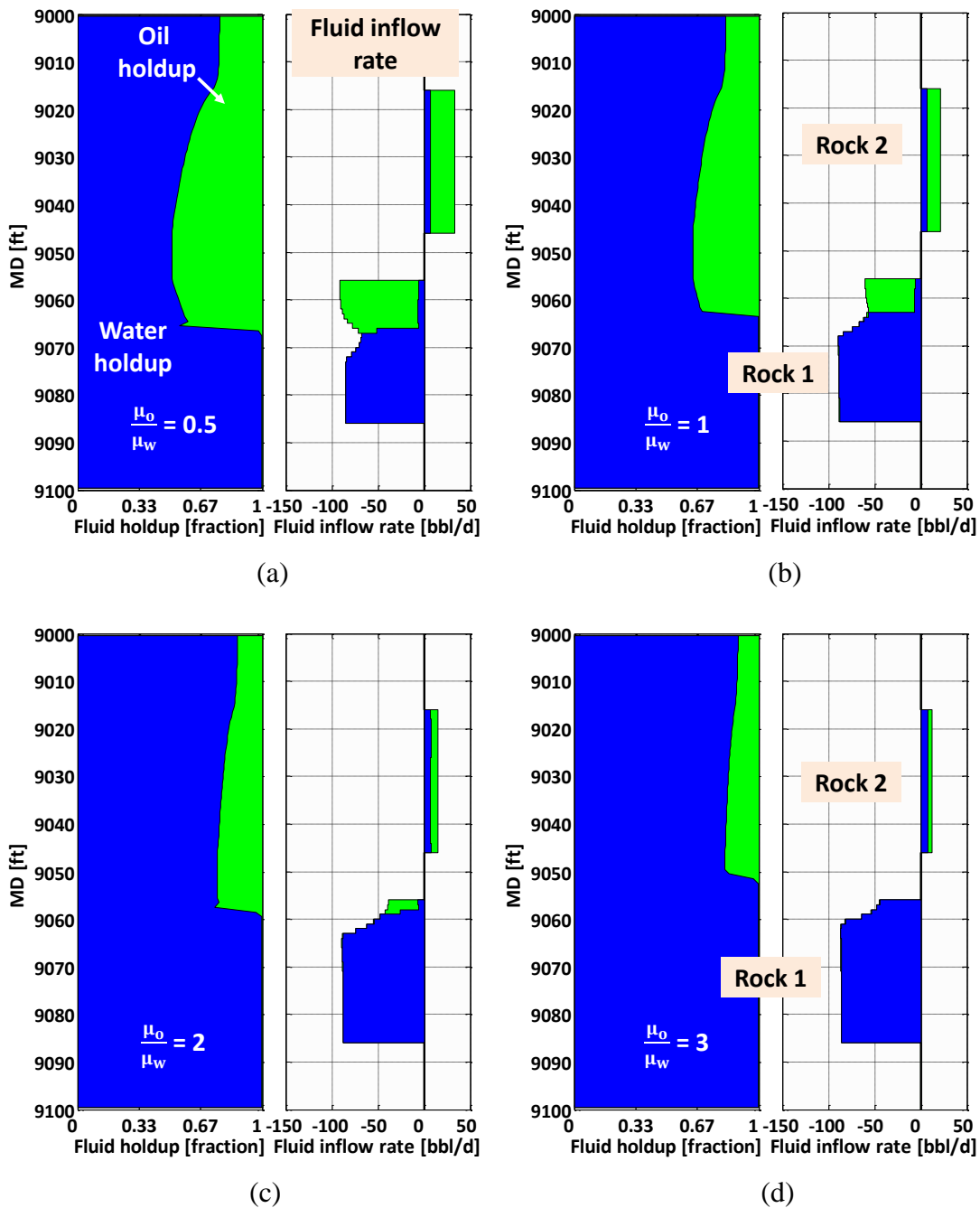


Figure 5.14: Sensitivity analysis for the spatial distributions of borehole fluid-phase holdup and fluid-phase inflow rate with respect to viscosity ratio between the oil and water phases. Panels (a) through (d) show that lowering oil viscosity results in injection of larger volumes of the lighter fluid phase (i.e., oil) into Rock 1. Panel (d) shows that for oil viscosity equal to 3 cp approximately zero volume of oil contributes into borehole cross-flow.

5.3.5 Borehole Deviation Angle

In deviated boreholes, buoyant and turbulent-induced forces in the radial direction initiate the migration of droplets toward the borehole wall thereby reducing the contact area between the two fluid phases. The lower interfacial area concentration allows the lighter fluid phase to flow at considerably faster velocities compared to those in equivalent vertical systems. As shown in Figures 5.15 and 5.16, a slight inclination of the borehole from the vertical direction (e.g., 15°) is sufficient to separate the two fluid phases, and to vanish borehole cross-flow with respect to the oil phase. In a borehole with only 4° of inclination angle, the simulated droplet eccentricity factor shows more than 70% deviation from a uniform cross-sectional distribution (Figures 5.15b).

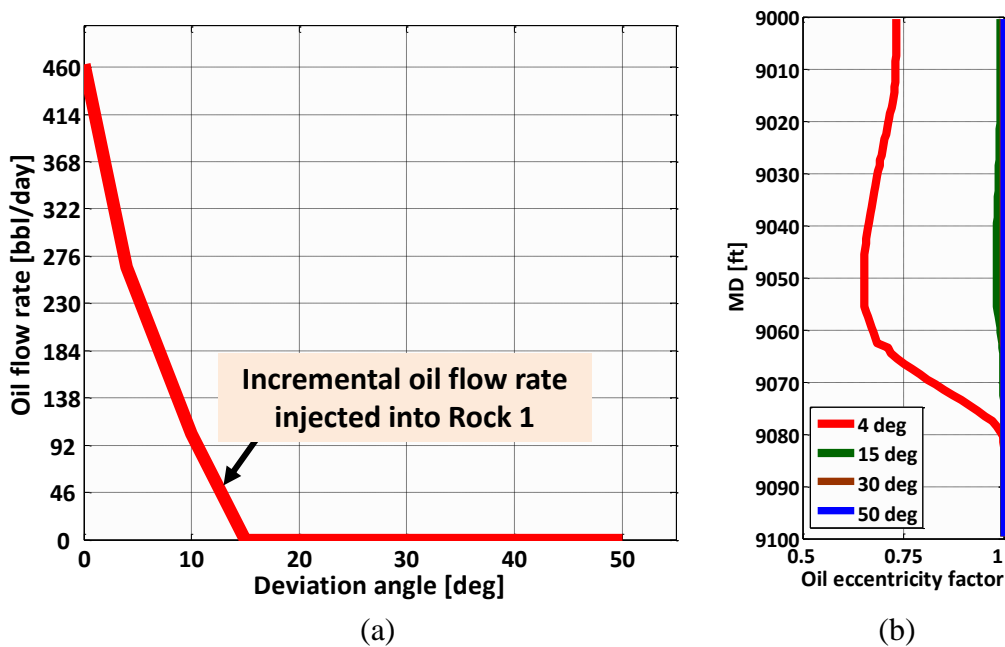


Figure 5.15: The effect of borehole deviation angle on development of borehole two-phase cross-flow. Panel (a) shows that oil-phase volume injected into Rock 1 decreases with increasing borehole deviation angle. For deviation angle greater than 15 degrees, zero volume of produced oil contributes into downward borehole cross-flow. Panel (b) shows that inclining the borehole causes oil droplets to agglomerate close to the borehole's upper wall, thus increasing fluid-phase slippage velocity.

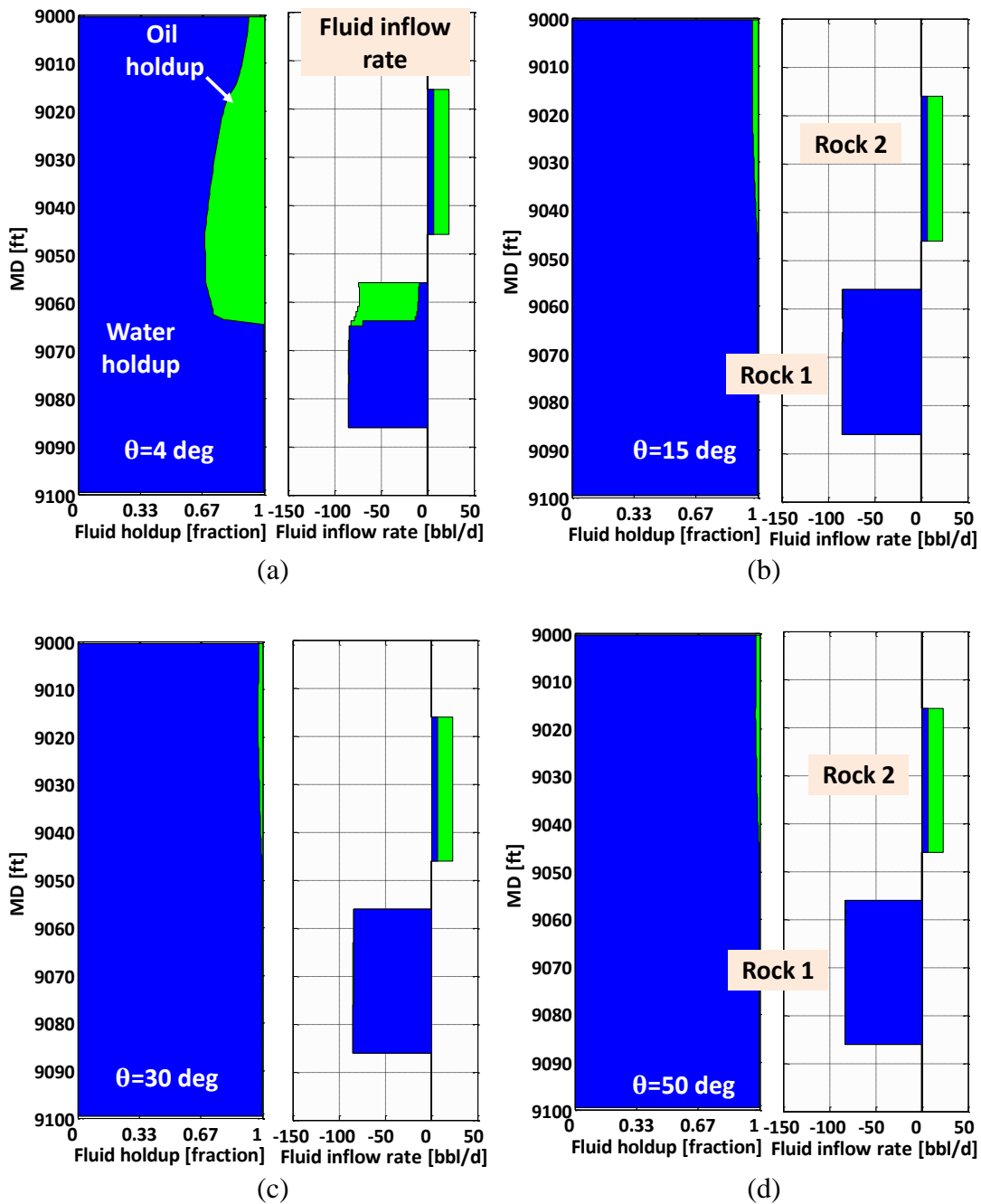


Figure 5.16: Sensitivity analysis for the spatial distributions of borehole fluid-phase holdup and fluid-phase inflow rate with respect to borehole deviation angle. Panels (b) through (d) show no borehole cross-flow with respect to the lighter fluid phase. Inclining the borehole to an angle more than 15 degrees sufficiently increases fluid-phase slip velocity to prevent downward movement of oil phase.

5.3.6 Cross-Flow Duration

The transient behavior of borehole fluid-phase cross-flow involves two different time scales: one associated with borehole fluids, and another associated with porous media. As borehole cross-flow is initiated, the properties of borehole fluids continue to change until establishing hydrodynamic equilibrium. As shown in the previous section, the time scale required to reach borehole hydrodynamic equilibrium is of the order of seconds. However, fluid flow in porous media introduces another time scale that is primarily determined by the variations of formation petrophysical properties. The developed coupled fluid flow model enables the simulation of the transient behavior of coupled producing systems associated with both borehole and formation time scales.

Figure 5.17 shows the numerically simulated fluid-phase holdup and inflow rates associated with 100 minutes of borehole cross-flow. At early times, large pressure differences between Rock 1 and Rock 2 cause downward movement of the oil phase, thus initiating borehole cross-flow. However, continuous fluid production from Rock 1 and fluid injection into Rock 2 gives rise to a gradual reduction of the pressure difference between the two rocks, thus decreasing fluid-phase cross-flow. As shown in Figure 5.18, after 100 minutes, cross-communication of Rock 1 and Rock 2 results in reduction of the pressure difference between the two rocks by a factor of two compared to the initial value.

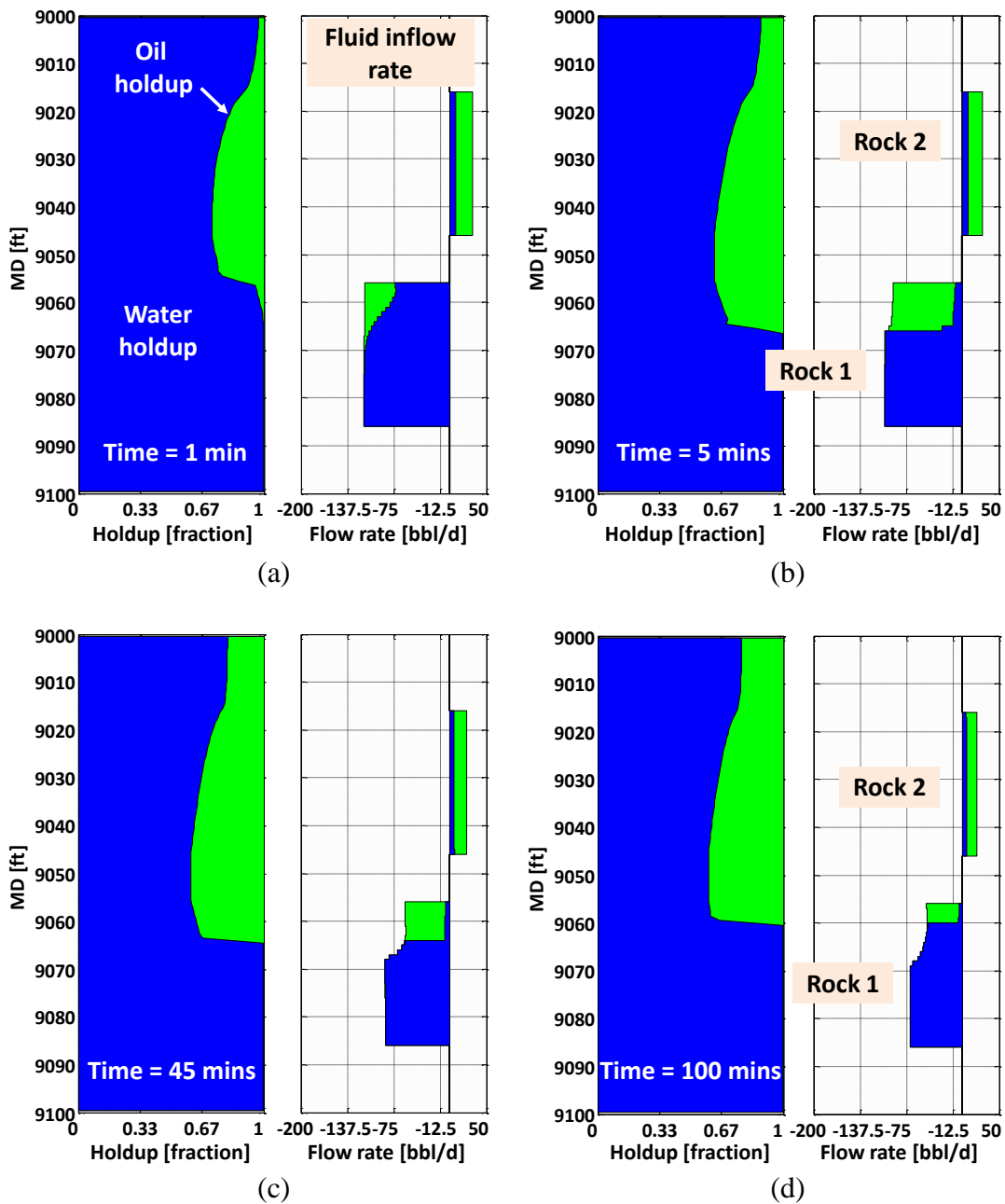


Figure 5.17: Sensitivity analysis for the spatial distributions of borehole fluid-phase holdup and inflow rate with respect to the duration of cross-flow. Panels (a) through (d) show that the development of downward cross-flow largely depends on the hydrodynamic equilibrium between Rock 1 and Rock 2. At the early stages of cross-flow, a large volume of fluids is injected into Rock 1 while continuous fluid production lowers the pressure difference between the two rocks thereby reducing the two-phase cross-flow.

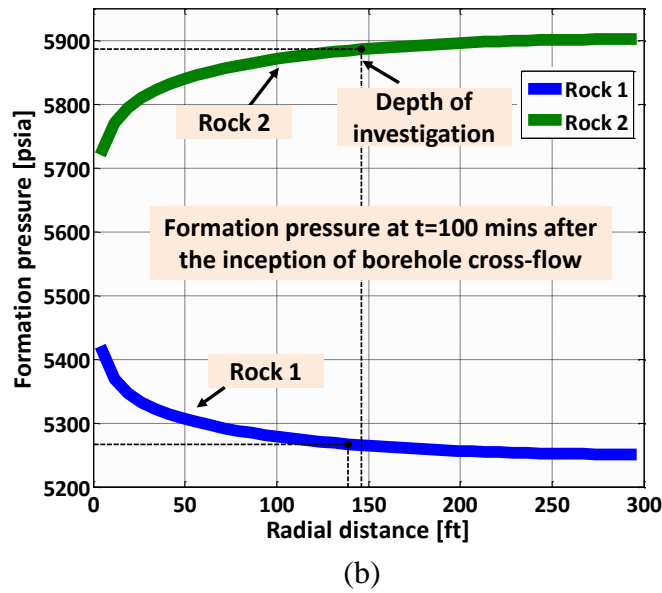
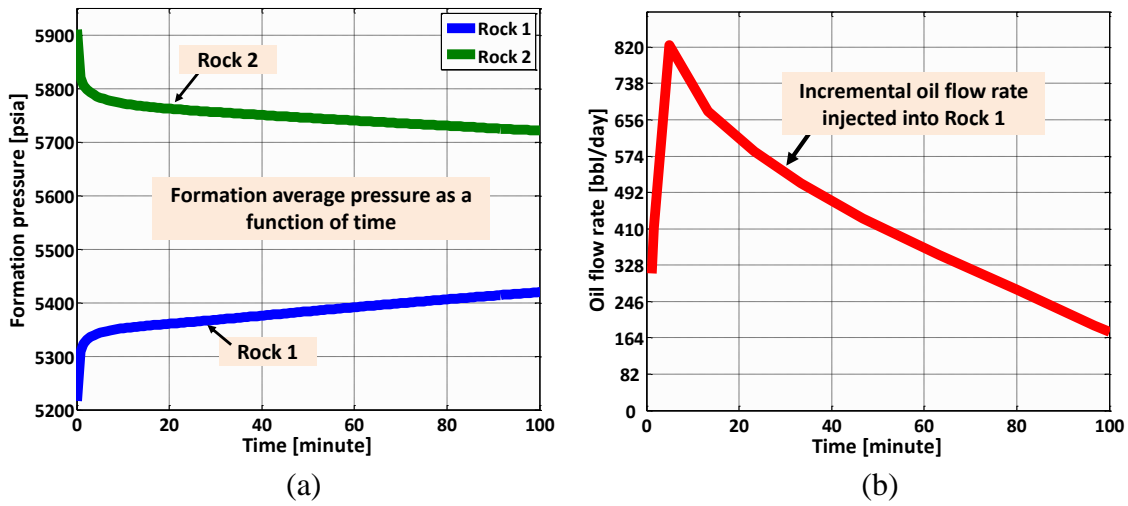


Figure 5.18: Transient behavior of (a) formation average pressure and (b) oil volumetric flow rate injected into Rock 1. Fluid production from Rock 1 and fluid injection into Rock 2 lower the pressure differences between the two rocks, thus reducing the volume of oil phase injected into Rock 1. Panel (c) shows the radial distribution of formation average pressure associated with Rocks 1 and 2, 100 minutes after the inception of borehole cross-flow.

5.4 SIMULATION OF SELECTIVE-INFLOW-PERFORMANCE (SIP) TEST

In multilayer reservoirs consisting of hydraulically-isolated fluid-producing rock formations, SIP analysis is an effective method to estimate layer average pressure. A SIP test acquires downhole production measurements at multiple production rates to estimate the inflow performance relationship (IPR) associated with each fluid-producing layer. I numerically simulate a multiphase SIP analysis for a differentially-depleted multilayer reservoir to quantify the effects of cross-flow on the estimation of formation average pressure. Simulation of SIP test is carried out by scheduling a stepwise fluid-production scheme which includes 3 different production rates, i.e., 9500, 7500, 3500 bbl/day, followed by a shut-in test. Production measurements associated with each production rate are acquired after the fluid-producing system reaches steady-state conditions. Consequently, IPR curves are constructed by plotting borehole pressure versus incremental fluid flow rate associated with each fluid-producing depth interval. The pressure at which formation incremental fluid flow rate decreases to zero is interpreted as the formation average pressure.

The multilayer reservoir constructed for this study is composed of four fluid-producing rock formations with the associated petrophysical properties summarized in Table 5.3. Rock 1, as shown in Figure 5.19, belongs to a low-permeability, high-capillary-pressure rock type, while Rock 3 exhibits the highest permeability and lowest capillary pressure. Figure 5.20 shows simulated production logs associated with the total fluid production rate equal to 9500 bbl/day and those associated with shut-in test, respectively. Because of low average pressure, Rock 2 exhibits the fluid inflow rate compared to the remaining fluid-producing rock formations. The low fluid-phase velocity gradient across Rock 2 is interpreted as the low productivity index associated with that rock. Rock 3, on the other hand, exhibits a moderate average pressure (i.e., 4400 psia),

and is considered as the main hydrocarbon producer of the sequence. However, when the borehole is under shut-in conditions, negligible pressure drawdown across Rock 3 considerably decrease the fluid production associated with that rock. In the borehole, water as the heavier fluid phase segregates itself from the hydrocarbon phase thereby giving rise to a sharp interface at 7108 ft MD. Accordingly, the sharp fluid-phase interface influences the type of fluids being injected into the corresponding rock formation (i.e., Rock 2).

The spatial distribution of formation incremental inflow rate depends on pressure drawdown across each fluid-producing rock formation (Figure 5.21). I quantify the pressure-inflow-rate dependency by constructing the IPR curve for each fluid-producing rock formation. As shown in Figure 5.22, IPR curves for each rock exhibits a unique slope which depends on the formation permeability, fluid-phase relative permeability, fluid-phase viscosity, and near-borehole skin. Specifically for Rock 2, invasion of fluid phases into that rock has altered the near-borehole fluid-phase relative permeability of that rock, hence resulting in the deviation of IPR curve from a straight line. The invasion effect is emphasized when borehole pressure is plotted versus incremental inflow rates associated with each fluid phase (Figures 5.22b and 5.22c). Because of the alteration of near-borehole relative permeability, water-phase and oil-phase IPR curves associated with Rock 2 exhibit two distinct slopes. When producing from Rock 2, the initial fluid saturation associated with that rock primarily determines the slope of fluid-phase IPR curve. However, the injection of fluid phases into that rock alters the near-borehole water saturation, thereby changing the corresponding slope of fluid-phase IPR curves.

Table 5.4 compares the estimated and actual values of formations average pressure. Estimation of formation average pressure is performed by computing the borehole pressure associated with a zero incremental fluid flow rate. Both total and fluid-

phase IPR curves suggest that incorporating production measurements acquired under shut-in conditions into SIP analysis gives rise to an unreliable estimate of average pressure associated with Rock 2.

SIP analyses for total and oil-phase IPR curves of Rock 2 (after neglecting shut-in production logs) yield reliable estimates of average pressure. However, due to volume of investigation, average pressures associated with Rock 1, 3 and 4, are underestimated when compared to the corresponding actual values. Figure 5.23 compares near-borehole and far-field formation pressure computed for two sets of production measurements namely, production logs acquired at flow rate equal to 9500 bbl/day (Figure 5.23a), and those acquired at shut-in conditions (Figure 5.23b). The estimates of formation average pressure are limited by volume of investigation associated with various production measurements. Furthermore, depletion of fluid-producing rock formations (e.g., Rock 3) during PL acquisition causes lower estimates of formation average pressure compared to the corresponding initial values.

Property	Unit	Rock 1	Rock 2	Rock 3	Rock 4
Effective porosity	pu	15	22	20	17
Permeability	mD	120	480	360	200
Average pressure	psia	4800	3800	4400	4600
Average water saturation fraction		0.93	0.45	0.05	0.7

Table 5.3: Summary of assumed formation petrophysical properties for the simulation of the SIP test.

Average pressure	Unit	Total IPR curve	Oil-phase IPR curve	Water-phase IPR curve	Actual value
Rock 1	psia	4735	-	4737	4800
Rock 2	psia	3795	3801	3769	3800
Rock 3	psia	4335	4339	-	4400
Rock 4	psia	4528	-	4531	4600

Table 5.4: Comparison of the estimated and actual formation average pressure from the SIP analysis in the four-layer reservoir model.

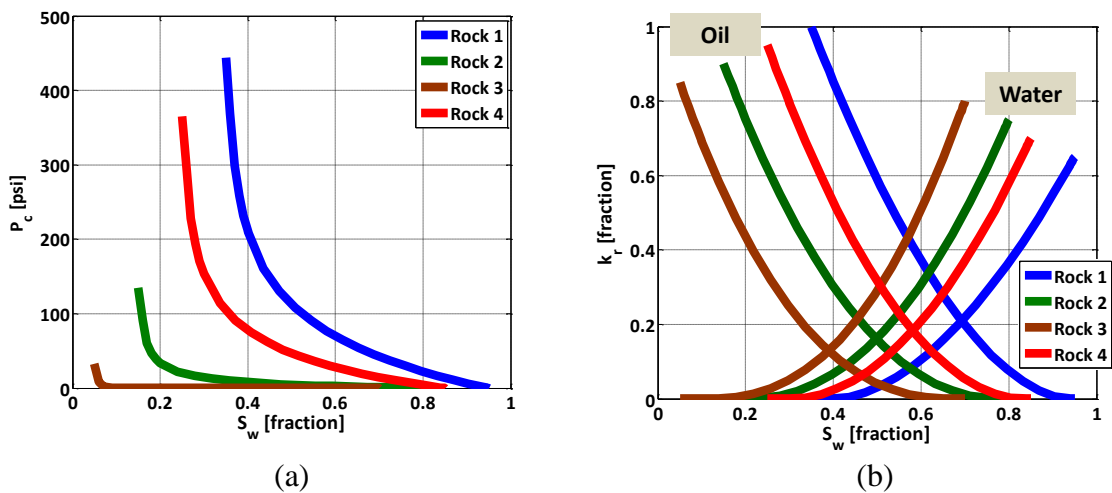


Figure 5.19: Assumed saturation-dependent formation capillary pressure (Panel a) and relative permeability (Panel b) for simulation of the SIP test in the four-layer model.

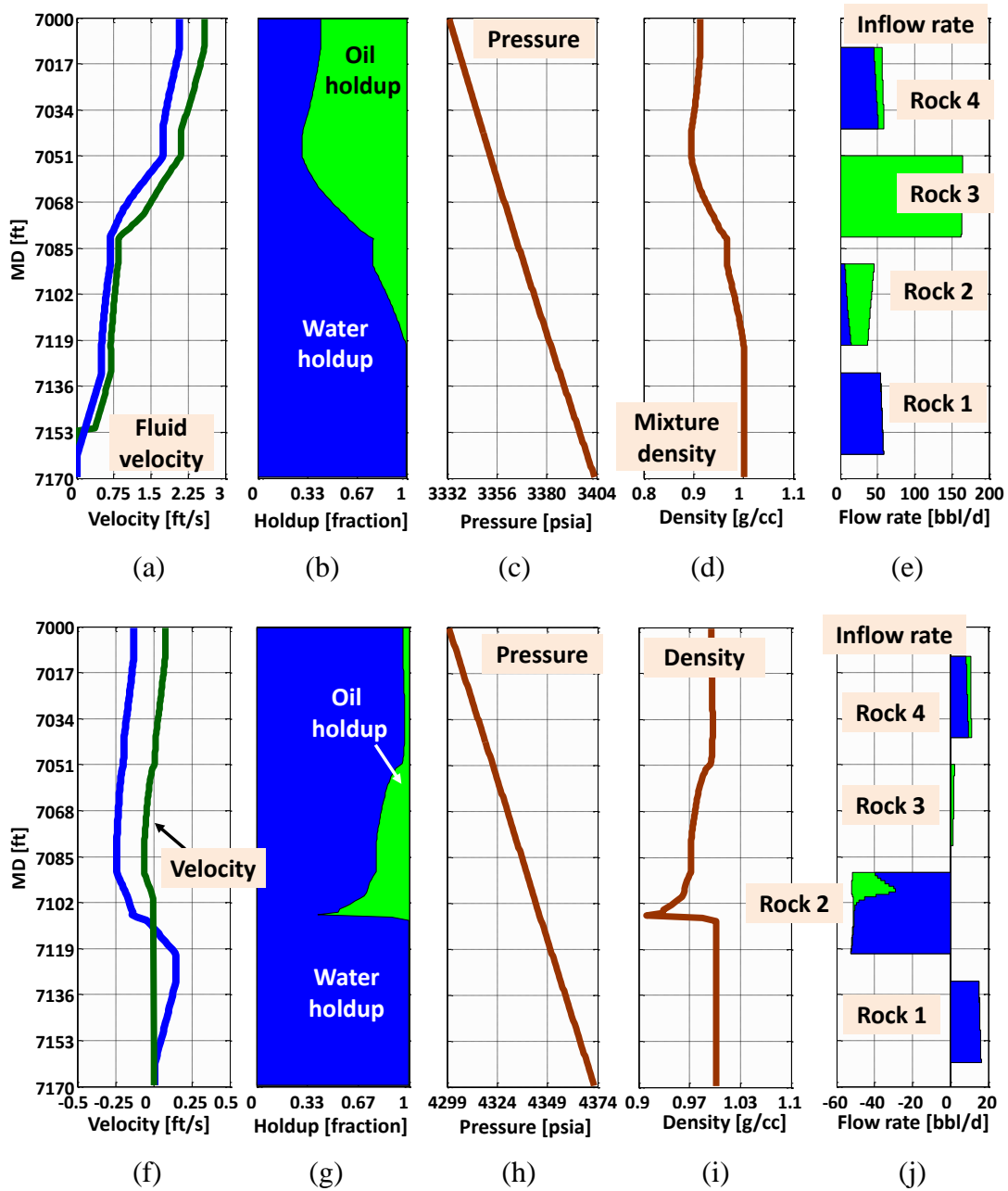


Figure 5.20: Numerically simulated spatial distributions of borehole fluid-phase velocity, holdup, pressure, mixture density, and inflow rate under production conditions (Panels a through e) and shut-in conditions (Panels f through j), obtained for simulation of the SIP test. The low average pressure associated with Rock 2 leads to downward movement of the oil and water phases. Panel (j) shows the injection of oil and water phases into Rock 2 under shut-in conditions giving rise to increase near-borehole oil saturations for that rock.

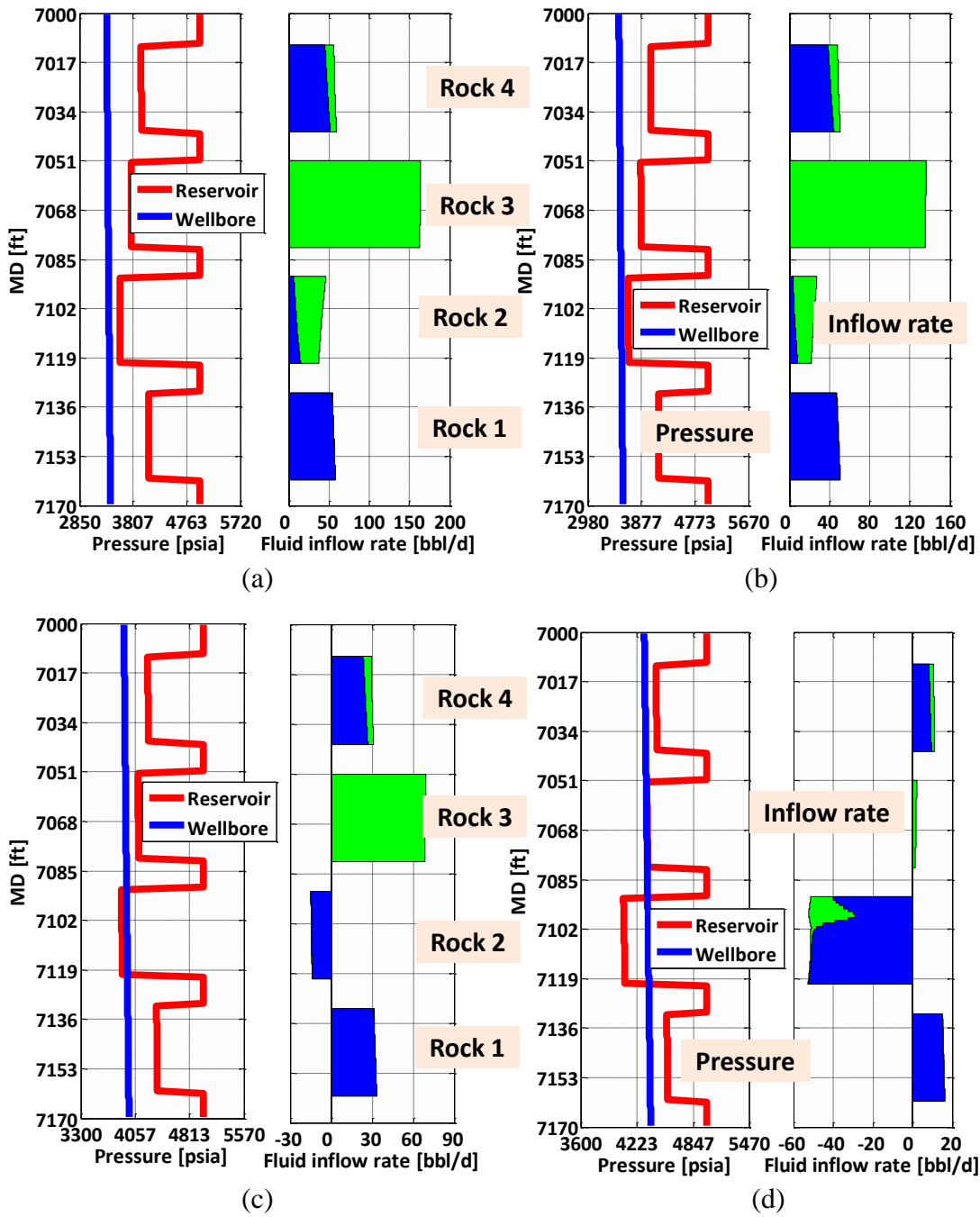


Figure 5.21: Numerically simulated spatial distributions of borehole pressure and fluid-phase incremental flow rate associated with production rates equal to (a) 9500, (b) 7500, (c) 3500 bbl/day, and (d) shut-in conditions. Panel (c) shows that water is produced from Rocks 1 and 4, and injected back into Rock 2. Panel (d) shows that under shut-in conditions both oil and water phases contribute in borehole cross-flow.

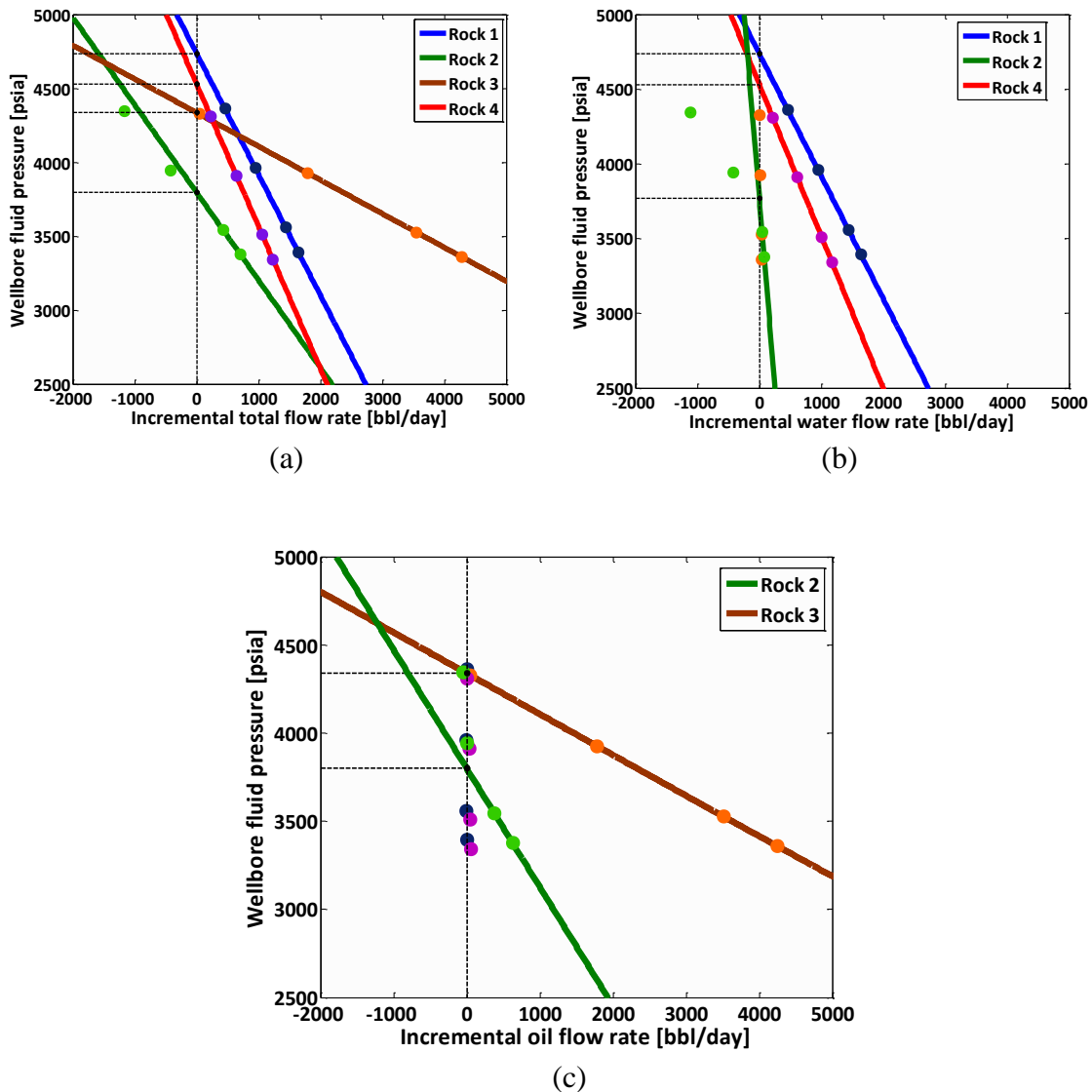


Figure 5.22: Numerically simulated IPR curves computed based on (a) total fluid flow rate, (b) water flow rate, and (c) oil flow rate for the SIP analysis of the four-layer model. The lines are plotted based on the interpolation through the points associated with 9500 and 7500 bbl/day production rates. The line intercept with the y-axis represents formation average pressure (see also Table 4). Production performance of Rock 2 (namely, green dots) shows a deviation from the straight line that is associated with the injection of oil into that rock during the shut-in test. Reliable estimation of formation average pressure for Rock 2 requires exclusion of data points influenced by oil injection.

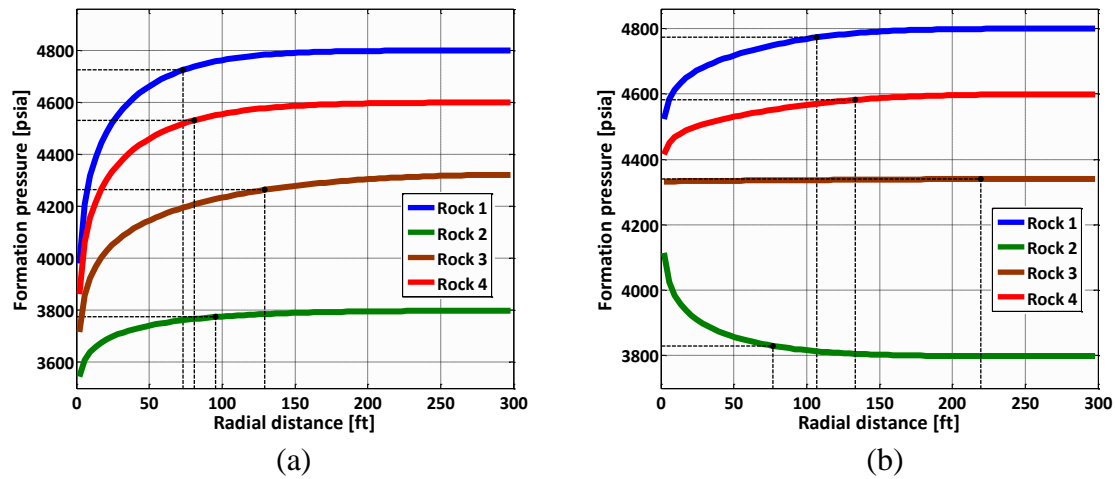


Figure 5.23: Radial distribution of formation pressure (a) under production conditions and (b) under shut-in conditions obtained for the SIP analysis. Panel (b) shows that fluid injection under shut-in conditions increases the near-borehole pressure of Rock 2.

5.5 SIMULATION OF WATER LOADING

In gas-water producing systems, if velocity of gas phase is inadequate to lift water droplets, water phase starts to accumulate in the borehole. The accumulated water increases bottom-hole pressure, thereby decreasing the available pressure drawdown to be imposed on the formation. A minimum gas-phase velocity is therefore required to ensure removal of produced water phase from the borehole. I invoke the developed borehole-formation model to construct a two-layer gas-water producing system, and to simulate transient behavior of water loading phenomenon. Formation and borehole properties are summarized in Table 5.5 and Figure 5.24. Rock 1 is entirely saturated with gas phase while Rock 2 is at residual gas saturation. The spatial distribution of formation fluid phases makes a favorable condition for the water phase to flow backward and fill the borehole. However, if pressure drawdown exceeds a critical limit the produced water will be lifted upward, thus preventing water loading problem (Figure 5.25). The

numerically simulated spatial distribution of borehole fluid-phase properties associated with a vertical system and a pressure drawdown equal to 1300 psi are shown in Figure 5.25. A high gas production rate from Rock 1 increases gas-phase velocity up to 9.7 ft/s leading to lifting the produced water. However, as illustrated in Figure 5.26, low gas velocities associated with a low pressure drawdown (i.e., 600 psi) give rise to water loading where after 42 minutes borehole flowing domain is entirely filled with the water phase. At early time, water-phase velocity exhibits negative values indicating water backflow. As water phase reaches the bottom of borehole, the associated volume fraction increases to 1, and water-phase velocity decreases to zero to achieve borehole hydrodynamic equilibrium.

In case of an inclined borehole, the lighter fluid phase agglomerates close to the borehole's upper wall that changes borehole fluid flow regimes. As shown in Figure 5.27, for a borehole with a deviation angle equal to 30 degrees, fluid-phase slip velocity considerably increases, thus causing the water phase to fill the borehole in less than a minute. Neglecting non-Darcy effects, Figure 5.28 estimates minimum pressure drawdowns associated with various deviation angles required for preventing water backflow. This figure shows the development of water loading for deviation angles greater than 24 degrees independent of pressure drawdown on the formations. Furthermore, inclining the borehole decreases fluid-phase interfacial area concentration thus increasing borehole water-phase volume fraction.

Formation	Unit	Rock1	Rock 2	Borehole	Unit	Value	Fluid phase	Unit	Gas	Water
ϕ	pu	16	9	D	in	3.18	ρ	g/cc	0.234	1
P_{avg}	psia	6800	6800	L	ft	100	μ	cp	0.031	1
K	mD	3	300	θ	deg.	0	C	μsip	10	3
S_w	su	0.1	0.85	ε	in	0.003	σ_{gw}	dyne/cm	72.4	-

Table 5.5: Summary of assumed formation, borehole, and fluid-phase properties for simulation of water loading in the two-layer model.

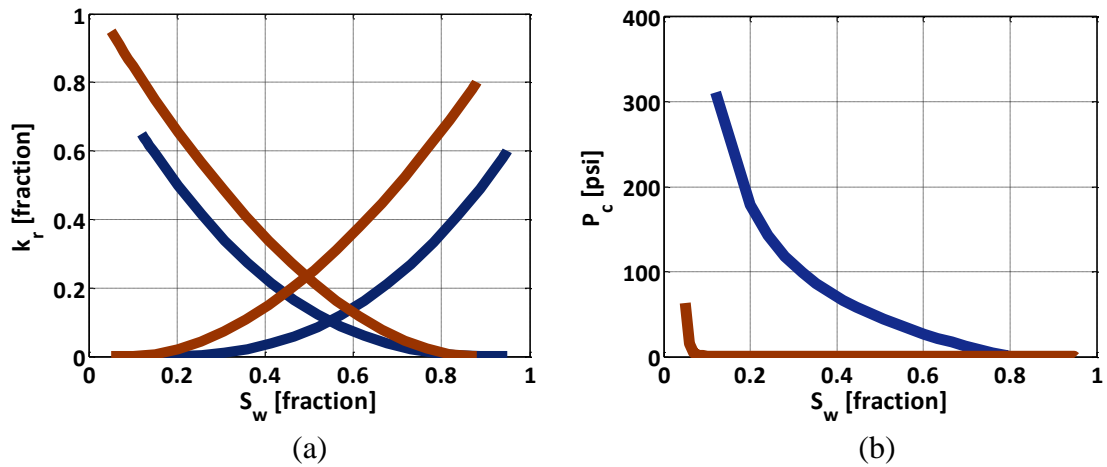


Figure 5.24: Assumed saturation-dependent formation capillary pressure (Panel a) and relative permeability (Panel b) for simulation of water loading in the two-layer reservoir model.

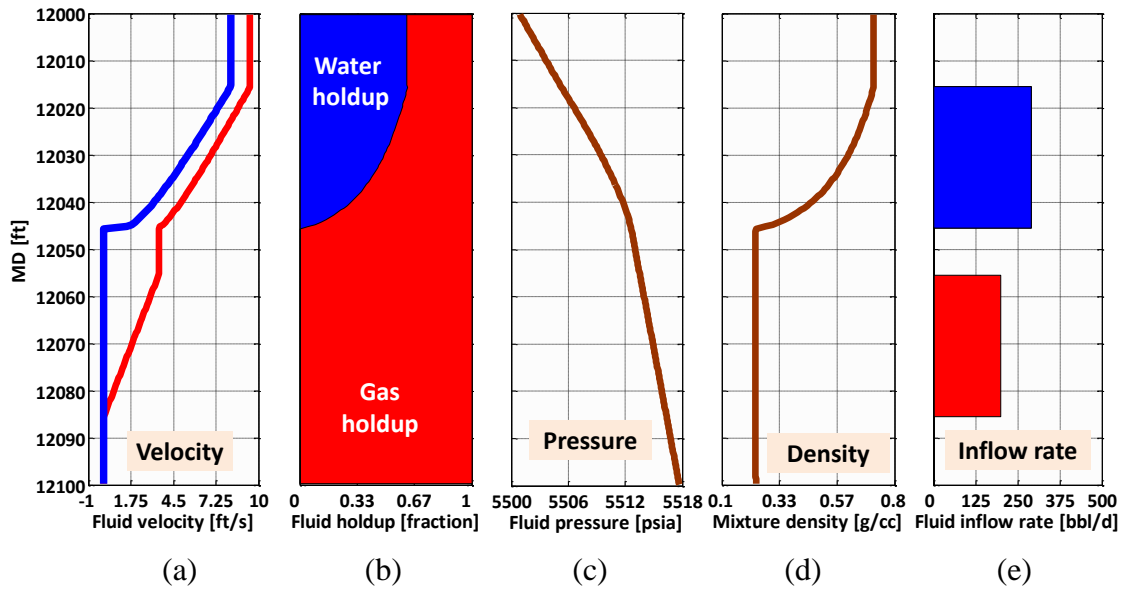


Figure 5.25: Numerically simulated spatial distributions of borehole (a) fluid-phase velocity, (b) fluid-phase holdup, (c) pressure, (d) fluid mixture density, and (e) fluid inflow rate for the two-layer reservoir model. Panel (a) quantifies the slippage velocity between the gas and water phases required to lift the produced water and prevent water phase from filling the borehole. The minimum gas velocity required to prevent water loading is a function of pressure drawdown quantified in Figure 5.28.

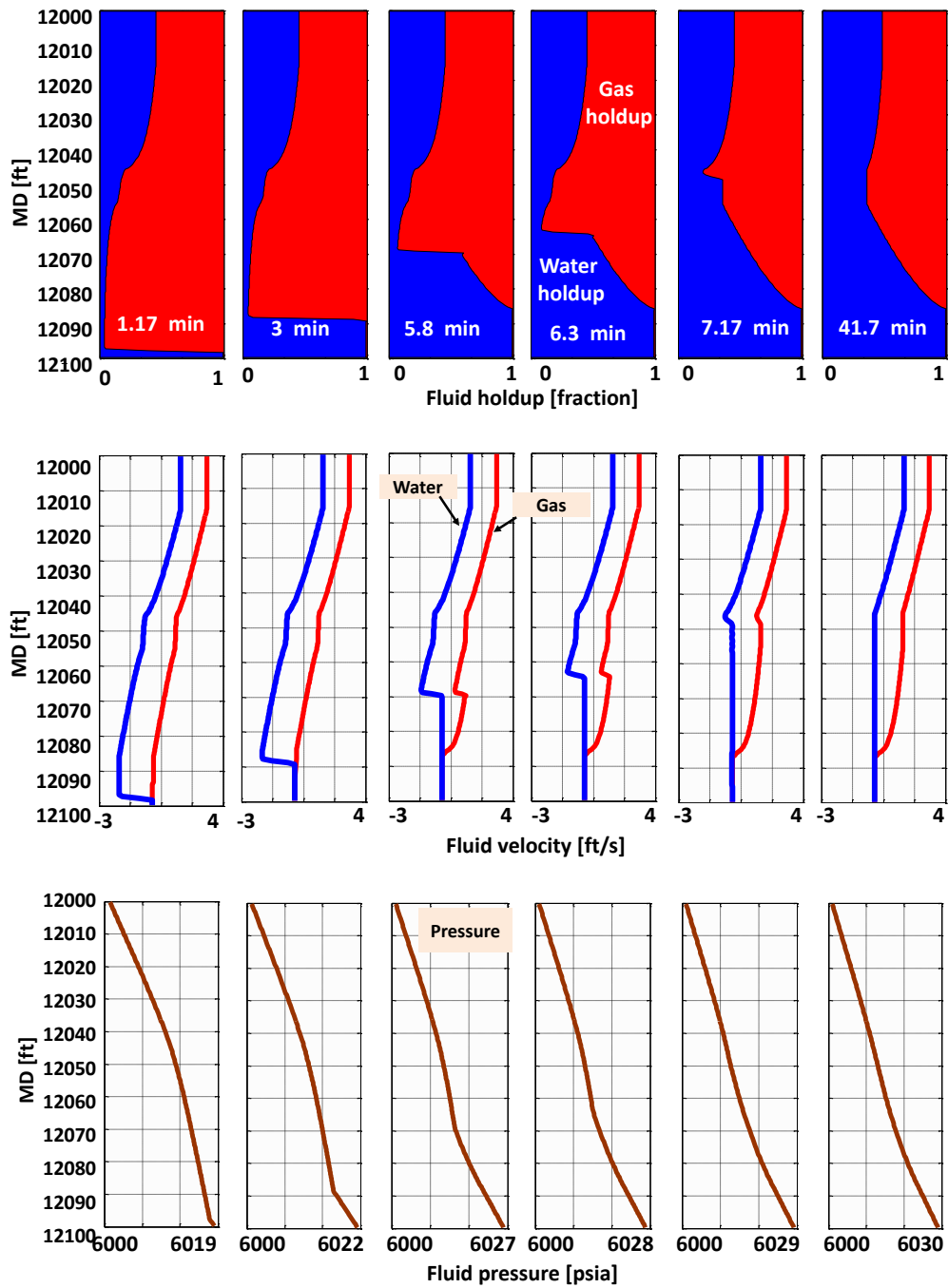


Figure 5.26: Numerically simulated transient behavior of borehole fluid holdup (first row), velocity (second row), and pressure (third row) for water loading example in a vertical borehole. Water velocity exhibits negative values indicating that water moves downward and gradually loads the borehole. Fluid holdup shows a sharp interface between the gas and water phases. Approximately after 42 minutes the borehole is filled with water.

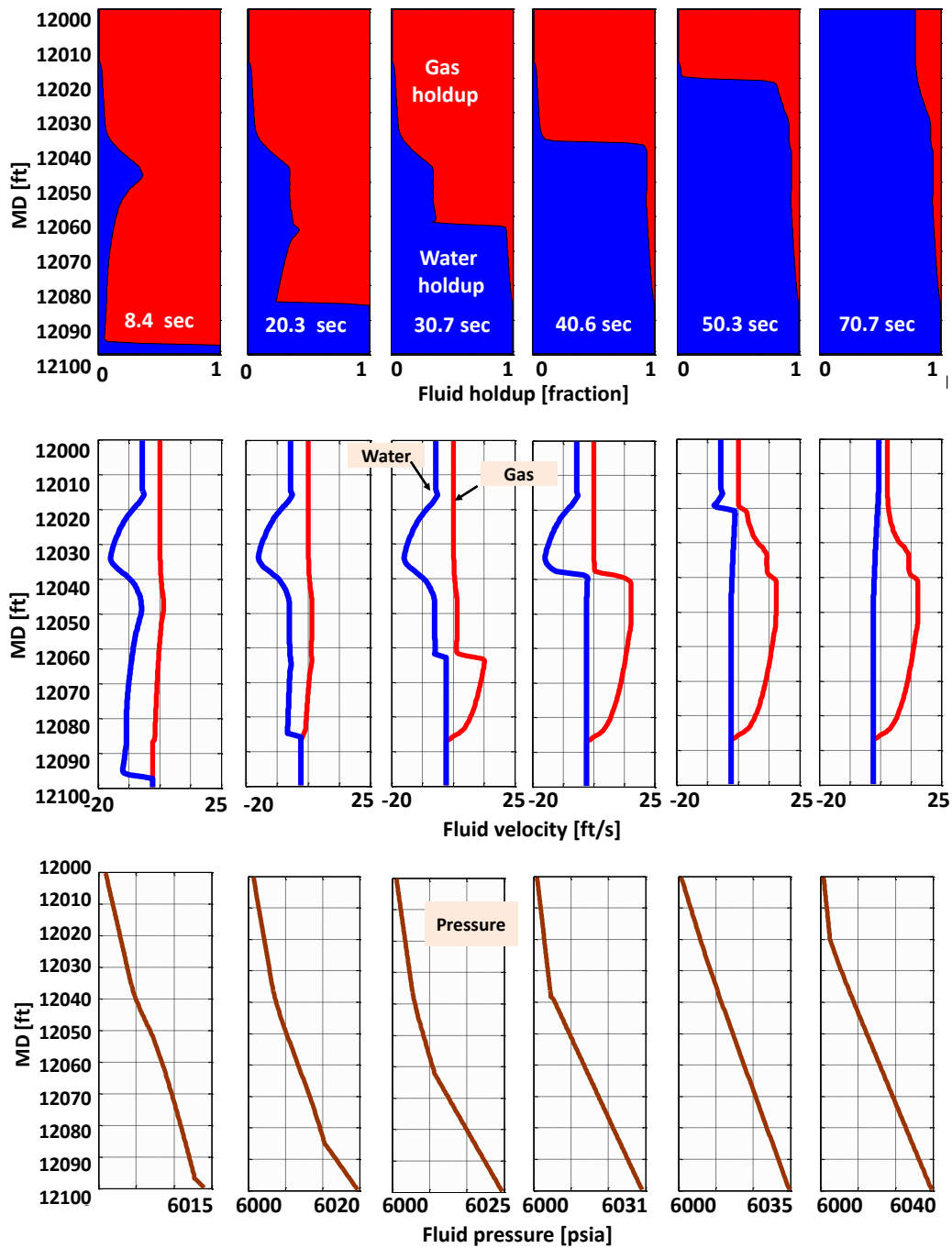


Figure 5.27: Numerically simulated transient behavior of borehole fluid holdup (first row), velocity (second row), and pressure (third row) for water loading example in a deviated borehole. Fluid holdup shows a sharp interface between gas and water phases; approximately after 71 seconds the borehole becomes filled with water. Deviation angle causes the agglomeration of gas bubble close to the borehole's upper wall that leads to a higher slip velocity.

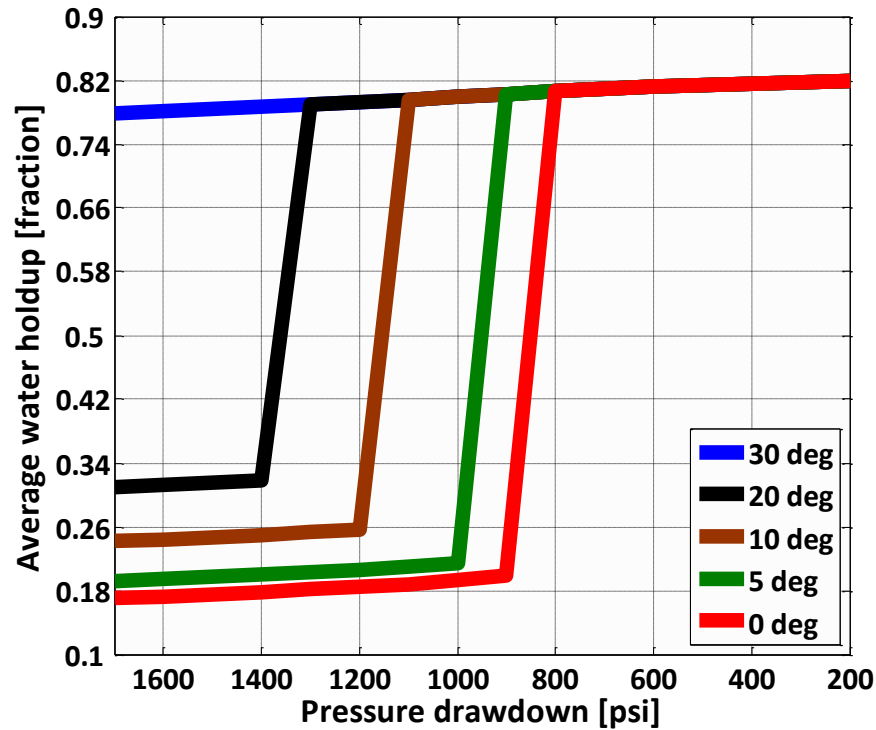


Figure 5.28: Numerically simulated average water holdup as a function of applied pressure drawdown and inclination angle. Each step represents the minimum pressure drawdown required to prevent water phase from loading the borehole flow domain. This graph shows that the required pressure drawdown increases with decreasing borehole inclination angle. The water loading was simulated under the assumption of Darcy flow in the formation.

5.6 SUMMARY AND CONCLUSIONS

An isothermal transient two-fluid model is implemented to simulate average fluid-phase velocity, pressure, volume fraction, and density along the borehole axial direction. Assuming commingled production of two fluid phases, the developed borehole fluid flow model numerically solves separate sets of mass and momentum conservation equations associated with each fluid phase. Drag and buoyant forces are assumed as the primary source of fluid-phase interfacial momentum transfer in solving fluid-phase

momentum conservation equations. Drag forces between the continuous and dispersed fluid phases are modeled by assuming a uniform cross-sectional droplet-size distribution associated with the dispersed fluid phase. I dynamically modify the droplet sizes along the borehole axis to account for mass influx from the borehole wall, and to accurately simulate fluid-phase slip velocity. The developed borehole fluid flow model is subsequently interfaced with a formation fluid flow model to quantitatively relate borehole fluid-phase properties with near-borehole formation petrophysical properties.

Numerical simulation of borehole production measurements acquired in an oil-water producing system indicated that unaccounted fluid-phase slip velocity could generate more than 7% error in the simulation of the borehole fluid-phase volume fraction. The error involved in the simulated borehole fluid-phase properties arose from neglecting the flow-regime change associated with fluid-phase influx from the borehole wall. Correlating droplet sizes to fluid-phase local holdup and velocity was an effective method to account for the variable slip velocity associated with various borehole flow regimes. The developed slip model was verified against experimental results reported by Hasan and Kabir (1999) for vertical and deviated oil-water flowing systems. I showed that the slope of 1.2 associated with churn-slug water-dominant flow regimes was simulated within an acceptable range of accuracy.

Simulation of cross-flow could be performed by imposing static boundary conditions on the reservoir to represent borehole flowing conditions without intervention of a borehole fluid flow model. However, the alteration of near-borehole formation properties required effective coupling of separate borehole and formation fluid flow models to enable dynamic modification of pressure and fluid flow-rate boundary conditions over time. When near-borehole formation properties rapidly changed with time, the sequential coupling method developed in this dissertation required frequent

updates of formation boundary conditions to accurately simulate productivity of fluid-producing layers. Frequent iterations between borehole and formation flow domains increased the computational time required for simulation of the coupled producing system. Despite this limitation, the developed coupling method allowed separate time-step controlling for borehole and formation fluid flow equations to ensure numerical stability of the solution algorithm. In addition, separate treatment of borehole and formation fluid flow equations allowed implementation of different numerical methods suitable for each set of fluid flow equations.

Transient simulation of borehole cross-flow associated with differentially-depleted rock formations identified two different time scales: (i) an early transient time required for borehole fluid phases to achieve hydrodynamic equilibrium, and (ii) a longer time scale associated with multiphase fluid flow in porous media. The latter time scale (referred to as late transient time) was required to achieve pressure equilibrium between differentially-depleted rock formations. In a two-layer rock formation model with borehole length equal to 100 ft, the time required for borehole fluid equilibrium was estimated to be approximately 90 seconds. However, depending on the petrophysical properties of the rock formations, considerably larger time windows (e.g., hours or days) were required to achieve formation hydrodynamic equilibrium. Formation pressure, fluid-phase density difference, and borehole deviation angle were found to be the primary factors controlling the early and late transient behavior of borehole cross-flow. For the specified two-layer formation model, I found that a minimum pressure difference equal to 400 psi between the two rocks was required to initiate downward movement of the lighter fluid phase. Because the flowing system monotonically shifts toward pressure equilibrium conditions, at late transient time, the lighter fluid phase started to move

upward, and eventually the heavier fluid phase was the only phase contributing to borehole cross-flow.

The alteration of near-borehole fluid-phase relative permeability was quantified by constructing IPR curves associated with individual fluid-producing rock formations. In a four-layer reservoir model, injection of fluid phases into low-pressure formations caused up to 50% deviation of IPR curves from the straight line. I next excluded data points associated with fluid-phase injection to accurately investigate the estimation of formation average pressure from SIP analysis. Estimates of pressure were found within 10% of actual values. However, the final estimates were influenced by the volume of investigation of PLT measurements and possible depletion of rock formations during production measurements acquisition.

The coupled borehole-formation fluid flow model was invoked to simulate water loading phenomenon commonly observed in gas-water producing systems. I showed that depending on formation and fluid-phase properties a minimum pressure drawdown is required to prevent the heavier fluid phase from falling backward. In addition, inclining the borehole caused higher fluid-phase slip velocities, thus leading to shorter time required for water loading compared to equivalent vertical producing systems. Because of higher slippage in deviated producing systems, larger pressure drawdowns were required to entirely lift the heavier fluid phase when compared to equivalent vertical systems.

Chapter 6: Inference of Rock Pressure-Production Properties from Gas-Oil Production Logs

Conventional interpretation of production logs (PL) numerically accounts for fluid productivity (or injectivity) of reservoir rocks by constructing simplified reservoir flow models. They describe the contribution of various fluid-producing rock formations into borehole fluid flow without quantitatively estimating formation dynamic properties. This chapter interfaces borehole and formation fluid flow models to link formation petrophysical properties to borehole production logs. A new interpretation method is subsequently developed to diagnose and quantify formation near-borehole permeability and gas saturation from gas-oil production measurements acquired in deviated boreholes. The specific application considered in this study invokes a new coupled flow algorithm to simulate pressure-production behavior of individual rock formations in multilayer reservoirs with/without cross-flow.

The developed coupled fluid flow model is interfaced to a nonlinear inversion-based algorithm that minimizes quadratic differences between production logs and their corresponding numerical simulations. The inversion process consists of estimating near-borehole permeability and gas saturation to explicitly match measurements of borehole fluid-phase velocity, volume fraction, and pressure.

In a synthetic multilayer reservoir model with a gas cap, PL interpretation recommends a critical bottom-hole pressure to prevent high gas production because of *(i)* downward advancement of the gas displacement front, and *(ii)* released gas from oil

solution. The estimation error is less than 20% for near-borehole gas saturation, and less than 25% for near-borehole permeability. However, the reliability of estimation is adversely influenced by conditions of immovable gas saturation in rock formations. Additionally, I examine a field example consisting of a gas-oil sand-shale laminated system where PL interpretation is carried out to quantitatively investigate the inflow performance relationship of individual flowing units. The interpretation method integrates well-log-derived and PL-derived permeabilities to quantify the depth distributions of near-borehole skin factor and gas saturation. The estimated near-borehole reservoir model subsequently quantifies more than 60% reduction of unwanted gas production caused by a gas shut-off remedial operation.

6.1 INTRODUCTION

Pressure-production behavior of multilayer rock formations is commonly estimated from surface well-test measurements. This method constructs a curve of fluid flow rates versus the corresponding (bottom-hole or surface) flowing pressures to describe average inflow performance of the reservoir. Measurements acquired with well tests provide no information about depth variations of formation properties, thus only enabling the estimation of an average performance relationship associated with the set of fluid-producing rock formations. However, in complex heterogeneous rocks, proper production management requires quantifying inflow performance of individual rock formations. In addition, because of the change of near-borehole dynamic petrophysical properties over time (e.g., absolute permeability and fluid saturation), a method is deemed necessary to update pressure-production relationships associated with individual fluid-producing rock formations.

As opposed to surface well tests, downhole measurements acquired with production logging tools (PLTs) provide one-dimensional (1D) spatial distributions of borehole fluid-phase properties across fluid-producing depth intervals. Primary application of PLTs is flow profiling where borehole fluid-phase properties (e.g., fluid velocity and holdup) is interpreted to determine fluid-phase inflow rate across fluid-producing depth intervals. Without the incorporation of a formation fluid flow model, interpretation of production logs remains limited to describing borehole fluid flow conditions.

The main objective of this chapter is to investigate the possibility of quantifying formation dynamic petrophysical properties based on a coupled borehole-formation fluid flow model that explicitly honors production logs. To that end, three key steps are followed: (i) developing a borehole compositional multiphase fluid flow model, (ii) coupling the developed borehole fluid flow model to a formation fluid flow model specified for near-borehole applications, and (iii) developing an interpretation method to estimate near-borehole formation petrophysical properties.

Interpretation of production logs is carried out by developing an inversion algorithm to estimate relevant formation petrophysical properties by reconstructing borehole fluid-phase measurements. Petrophysical properties considered for inversion in this chapter include near-borehole permeability and fluid-phase saturation. The developed inversion method consists of an iterative loop that minimizes quadratic differences between borehole fluid-phase measurements (i.e., fluid-phase volume fraction, fluid mixture velocity, and borehole pressure), and the corresponding numerical simulations. Within the main iterative loop, I define three inner minimization loops to selectively increase the sensitivity of borehole fluid-phase properties to a specific formation property. The inner loops consist of (i) a loop to estimate formation fluid-phase saturation

from the inversion of fluid-phase holdup, (ii) estimation of formation permeability by minimizing a quadratic cost function computed based on fluid mixture velocity and fluid-phase holdup, and (iii) a minimization loop that matches borehole fluid pressure by rescaling the entire permeability distribution.

Unwanted production of gas or water requires the acquisition of downhole production measurements to identify depth intervals accountable for gas or water production. Gas shut-off and water shut-off operations are consequently performed to prevent gas or water production. The specific application considered in this chapter quantifies the performance of gas shut-off operations. I construct a near-borehole formation fluid flow model based on matching production logs acquired before performing the shut-off operation. Quantitative evaluation of the shut-off operation is carried out by simulating pressure-production behavior of fluid-producing rock formations after performing shut-off.

This chapter studies synthetic and field examples to investigate the estimation of near-borehole permeability and fluid-phase saturation from inversion of production logs. Cases of consideration include gas-oil flowing systems with and without gas coning effects.

6.2 INTERPRETATION METHOD

This section describes the developed iterative refinement algorithm to estimate near-borehole petrophysical properties from inversion of production measurements.

6.2.1 General Assumptions

Unknown petrophysical properties considered in this chapter for PL interpretation include formation's near-borehole permeability and fluid-phase saturation. The developed interpretation algorithm makes explicit assumptions for formation pressure and temperature, layer bed boundaries and dip, fluid-phase density and viscosity, rock capillary pressure, porosity, and relative permeability. In multilayer rock formations belonging to the same rock type, saturation-dependent capillary pressure associated with each layer is rescaled via the Leverett-J function, to wit,

$$P_c = P_c^{\text{ref}} \sqrt{\left(\frac{\phi}{K}\right) \left(\frac{K^{\text{ref}}}{\phi^{\text{ref}}}\right)}, \quad (6.1)$$

where superscript "ref" identifies reference values for porosity (ϕ), permeability (K), and capillary pressure (P_c). Implementation of near-borehole formation damage is carried out by assuming a cylindrical region of altered permeability around the borehole. Hawkins's (1956) equation, namely,

$$S = \left(\frac{k}{k_s} - 1\right) \text{Ln} \left(\frac{r_s}{r_w}\right), \quad (6.2)$$

is next invoked to express near-borehole permeability in terms of skin factor (i.e., S). In Equation 6.2, k_s is near-borehole permeability, k is far-field permeability, r_s is radius of near-borehole region, and r_w is borehole radius.

6.2.2 Inverse Problem

Estimation of formation petrophysical properties from production logs requires an inversion method that progressively refines unknown petrophysical properties to improve the agreement between measurements, and their numerical simulation. Production

measurements considered for inversion in this dissertation include borehole fluid-phase volume fraction, borehole fluid mixture velocity, and borehole fluid pressure. The developed inversion method defines a representative number of spatial windows in the borehole flowing domain where variations of borehole fluid-phase properties across each window are computed for inversion of the corresponding petrophysical properties (Figure 6.1). Computing variations of borehole fluid-phase properties across a specific depth window (instead of the entire borehole flowing domain) selectively increases the sensitivity of borehole fluid measurements to a certain unknown petrophysical property. Specifically, separate depth windows are defined to (i) associate formation near-borehole permeability to the slope of borehole fluid mixture velocity, and (ii) associate formation fluid-phase saturation to the slope of borehole fluid-phase volume fraction. Furthermore, a global multiplier (i.e., γ) rescales the entire near-borehole permeability to progressively match borehole pressure measurements.

Implementation of the abovementioned inversion method is carried out in three separate iterative inner loops. Figure 6.1 describes the workflow adopted in this dissertation to adjust near-borehole permeability and fluid-phase saturation until securing an acceptable match with measured production logs. The inversion method begins with specifying formation petrophysical layers and the corresponding spatial windows defined in the borehole. An initial guess of formation petrophysical properties is made to start the simulation of borehole fluid-phase properties. The first loop (Loop 1) estimates layer near-borehole permeability assuming fixed values of fluid-phase saturation. Subsequently, Loop 2 is invoked to estimate near-borehole fluid-phase saturation, while assuming fixed values for layer permeability. Rescaling layer permeability distribution is next performed within Loop 3 by estimating the global multiplier, γ . Refinement

iterations continue until achieving an acceptable match for borehole fluid velocity, holdup, and pressure.

Quadratic cost function minimized in Loop 1 is based on variations of borehole fluid-phase volume fraction and fluid mixture velocity across a depth window, given by

$$C_1(\mathbf{K}) = \frac{1}{2} [\|\mathbf{W}_1 \cdot \mathbf{e}_1(\mathbf{K})\|^2 + \lambda_1 \|\mathbf{K}\|^2], \quad (6.3)$$

where \mathbf{K} is unknown permeability vector, $\mathbf{e}_1(\mathbf{K})$ is vector of data residuals, and \mathbf{W}_1 is a data weighing matrix that specifies the subset of borehole fluid measurements used for the inversion of an individual layer permeability. The second term in Equation 6.3 is a regularization (stabilization) term that is included in the cost function to improve numerical stability of the method in case of non-unique solutions or noisy measurements. The regularization multiplier λ_1 defines the relative importance of the regularization term compared to the first additive term; λ_1 is determined via Hansen's L-curve criterion (Aster et al., 2005). The vector of data residuals, $\mathbf{e}_1(\mathbf{K})$, describes data misfit as

$$\mathbf{e}_1(\mathbf{K}) = \left[\left(\frac{S_v^s(\mathbf{K}) - S_v^m}{S_v^m} \right)_1, \dots, \left(\frac{S_v^s(\mathbf{K}) - S_v^m}{S_v^m} \right)_{N_{wp}}, \right. \\ \left. \left(\frac{S_\alpha^s(\mathbf{K}) - S_\alpha^m}{S_\alpha^m} \right)_1, \dots, \left(\frac{S_\alpha^s(\mathbf{K}) - S_\alpha^m}{S_\alpha^m} \right)_{N_{wp}} \right]^T, \quad (6.4)$$

where S identifies the slope of borehole fluid-phase properties as shown in Figure 6.2, subscripts "v" and " α " indicate borehole fluid mixture velocity and fluid-phase volume fraction, respectively, N_{wp} is number of depth windows generated in the borehole domain to estimate permeability, superscripts "s" and "m" denote simulated and measured production logs, respectively, and superscript "T" defines the transpose operator.

Loop 2 estimates fluid-phase saturation assuming fixed values of layer permeability. The cost function associated with Loop 2 is written as

$$C_2(\mathbf{S}_k) = \frac{1}{2} [\|\mathbf{W}_2 \cdot \mathbf{e}_2(\mathbf{S}_k)\|^2 + \lambda_2 \|\mathbf{S}_k\|^2], \quad (6.5)$$

where \mathbf{S}_k is unknown fluid-phase saturation vector, \mathbf{W}_2 is data weighing matrix, λ_2 is regularization multiplier, and $\mathbf{e}_2(\mathbf{S}_k)$ is data misfit vector, given by

$$\mathbf{e}_2(\mathbf{S}_k) = \left[\left(\frac{S_\alpha^s(\mathbf{S}_k) - S_\alpha^m}{S_\alpha^m} \right)_1, \dots, \left(\frac{S_\alpha^s(\mathbf{S}_k) - S_\alpha^m}{S_\alpha^m} \right)_{N_{ws}} \right]^T, \quad (6.6)$$

where N_{ws} is number of windows considered in the borehole to estimate fluid-phase saturation.

Loop 3 calculates the following cost function to match measurements of borehole pressure:

$$C_3(\gamma) = \frac{1}{2} \|\mathbf{e}_3(\gamma)\|^2, \quad (6.7)$$

where γ is permeability rescaling coefficient, and $\mathbf{e}_3(\gamma)$ is vector of data residual, defined by

$$\mathbf{e}_3(\gamma) = \left[\left(\frac{P^s(\gamma) - P^m}{P^m} \right)_1, \dots, \left(\frac{P^s(\gamma) - P^m}{P^m} \right)_{N_{mp}} \right]^T, \quad (6.8)$$

where P is borehole pressure, N_{mp} identifies number of borehole pressure measurements, and superscripts "s" and "m" denote simulated and measured production logs, respectively.

Minimization of the quadratic cost functions described by Equations 6.3, 6.5, and 6.7 is iteratively performed using the Gauss-Newton method. This method begins with an initial guess of unknown properties to construct the Jacobian matrix. Unknown petrophysical properties are subsequently refined to obtain the minimum of the cost function. Let \mathbf{x}^c be the vector of unknown properties at c-th iteration. The solution of unknown properties for the next iteration is computed by solving the following system of linear equations:

$$\mathbf{x}^{c+1} = \mathbf{x}^c - [\mathbf{J}(\mathbf{x}^c, \mathbf{d})^T \cdot \mathbf{J}(\mathbf{x}^c, \mathbf{d}) + \lambda^c \mathbf{I}]^{-1} \mathbf{J}(\mathbf{x}^c, \mathbf{d})^T \cdot \mathbf{e}(\mathbf{x}^c), \quad (6.9)$$

where \mathbf{d} is data vector, $\mathbf{e}(\mathbf{x}^c)$ is vector of residuals, \mathbf{I} is the identity matrix, and $\mathbf{J}(\mathbf{x}^c, \mathbf{d})$ is the Jacobian (data substitution) matrix whose entries are given by

$$J_{i_m i_p}^c = \frac{\partial e_{i_m}}{\partial x_{i_p}^k}, \quad \forall i_m = 1, 2, \dots, N_m, \quad i_p = 1, 2, \dots, N_p, \quad (6.10)$$

where N_m is number of measurements, and N_p is number of unknown properties.

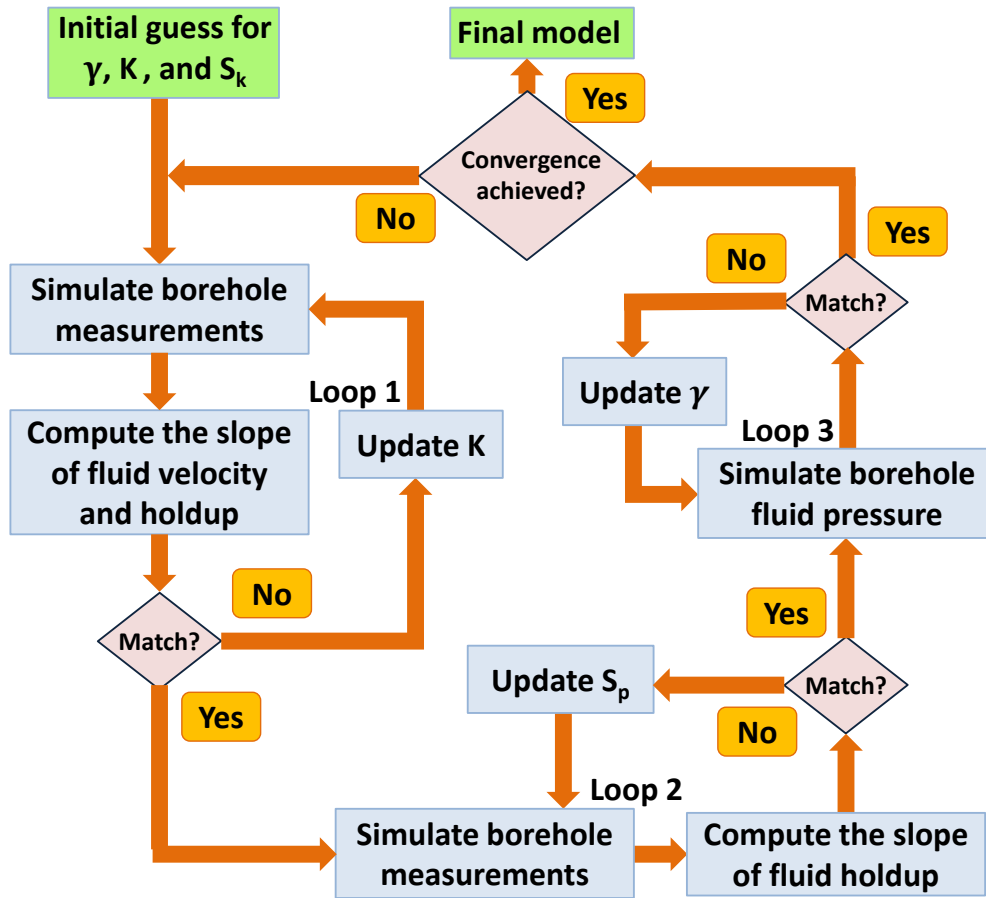


Figure 6.1: Iterative algorithm developed in this dissertation to estimate near-borehole fluid-phase saturation (S_p) and permeability (K) from borehole production measurements. The iterative refinement includes three inner loops: Loop 1 assumes fixed values of fluid saturation to estimate permeability. Loop 2 assumes known values of permeability to refine fluid saturation. Following the calculation of the two properties, Loop 3 rescales the entire permeability field to match measurements of borehole pressure.

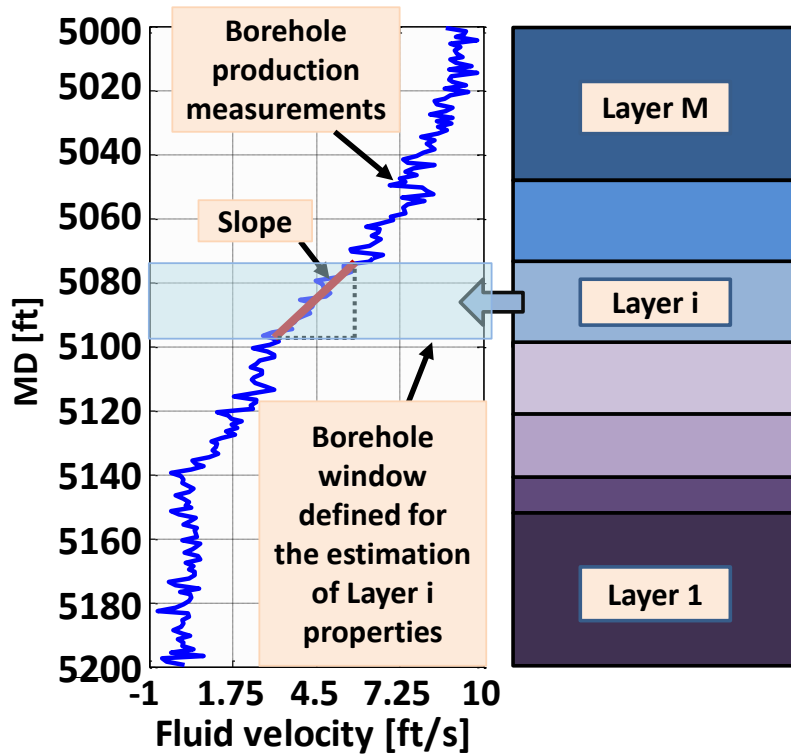


Figure 6.2: Schematic of the window-by-window interpretation method adopted in this dissertation to estimate near-borehole fluid-phase saturation and permeability. The algorithm defines several spatial windows in the borehole, and associates each window with the corresponding layer properties. Estimation of near-borehole fluid-phase saturation and permeability is carried out by computing variations of fluid-phase velocity and holdup across each window.

6.3 SYNTHETIC EXAMPLE

A multilayer reservoir model is constructed to exemplify the PL interpretation process and simulation of a gas shut-off operation. The synthetic model simulates gas coning phenomenon taking place in a gas-oil reservoir consisting of three fluid-producing rock formations with a 45-degree dip penetrated by a vertical borehole (Figures 6.3 and 6.4). Remaining formation, fluid, and borehole properties are summarized in Table 6.1.

Assuming a known forward model, simulation of gas-oil miscible displacement is performed to investigate pressure-production behavior of fluid-producing rock formations in the presence of gas coning. After the occurrence of gas breakthrough, borehole production measurements are synthetically measured and contaminated with 5% additive Gaussian noise to account for uncertainty involved with production measurements. Production logs are subsequently inverted to estimate near-borehole permeability and gas saturation. Based on PL interpretation results, a gas-shut off operation is simulated to quantify pressure-production behavior of the multilayer reservoir system after performing the remedial operation.

To simulate gas-oil miscible displacement, I locate the gas-oil-contact at depth equal to 7000 ft MD (i.e., top of the reservoir). Subsequently, fluid withdrawal starts at a constant bottom-hole fluid flow rate equal to 1000 bopd. Figure 6.5 shows the spatial distributions of formation pressure and gas saturation after 3 months of constant-flow-rate production. Because of low capillary pressure and high permeability associated with Rock 3, the miscible displacement front associated with that rock is the first one to reach the borehole. Production logs acquired after gas breakthrough at a production rate equal to 2300 bopd are shown in Figure 6.6. The slope of borehole fluid mixture velocity across Rock 3 considerably increases, indicating the production of gas. Furthermore, borehole pressure exhibits a lower slope across Rock 3, implying the presence of a lighter fluid in the borehole. The sensitivity of borehole production measurements to near-borehole formation permeability and gas saturation is quantified by constructing a near-borehole fluid flow model that matches numerically simulated production logs.

Figure 6.7 through Figure 6.9 show the estimated distributions of near-borehole properties. Because the displacement front associated with Rock 1 and Rock 2 has not reached the borehole, the corresponding gas saturations are interpreted as residual values.

However, gas production from Rock 3 makes it possible to estimate an average gas saturation distribution for the near-borehole region of that rock. The interpretation algorithm makes explicit assumption for far-field permeability, and estimates the permeability of the near-borehole region. Figure 6.10 indicates an acceptable agreement between synthetically generated production logs and their numerical simulations.

The estimated petrophysical properties are within 25% of their corresponding actual values. However, presence of noise in production measurements does not permit refining the depth windows of PL inversion below a certain length. Refining petrophysical layers below that length scale gives rise to a significant influence of noise that decreases the reliability of estimated gas saturation and permeability. Furthermore, when the formation is at residual gas saturation (i.e., in Rocks 1 and 2), there is uncertainty involved with the estimates of immovable gas saturations that additionally propagates to the estimates of near-borehole permeability (error bars shown in Figure 6.8). These results suggest that a-priori knowledge for residual hydrocarbon saturation is required to secure a reliable interpretation from production measurements.

Pressure-production behavior of individual rock formations is quantified by constructing plots of borehole pressure as a function of oil inflow rate associated with each layer. Figure 6.11 shows that Rock 3 exhibits the highest productivity at low values of pressure drawdown. However, decreasing the borehole pressure leads to considerable gas production, thereby lowering the productivity of Rock 3 compared to Rocks 1 and 2. Based on the high values of near-borehole gas saturation and permeability estimated for Rock 3, it is decided to isolate the corresponding perforated interval. The estimated near-borehole fluid flow model is invoked to simulate the performance of gas shut-off. As shown in Figure 6.12, continuing fluid production with the remaining set of perforations causes advancement of the gas front from Rock 3 into Rock 2. Pressure-production

behavior of rock formations shows that gas coning into Rock 2 can decrease the productivity of that rock up to 50%. However, sensitivity analysis of the produced gas-oil ratio suggests that maintaining the bottom-hole pressure above 3600 psia limits the gas-oil ratio to approximately 4 rcf/bbl (Figure 6.13).

I simulate borehole production measurements after performing the gas shut-off under the assumption of a constant bottom-hole pressure (equal to 3760 psia). The results, shown in Figure 6.14, quantify 58% reduction of borehole gas volume fraction due to gas shut-off. The reduction of gas production is caused by lowering near-borehole relative permeability of gas phase after shutting the gas-saturated rock formation (Figure 6.7).

Formation	Unit	Rock 1	Rock 2	Rock 3	Borehole	Unit	Value	Fluid	Unit	Gas	Oil
ϕ	pu	0.23	0.2	0.27	D	in	2.95	ρ	g/cc	0.16	0.7
P_{avg}	psia	4200	4200	4200	L	ft	150	μ	cp	0.02	0.8
K_{ff}	mD	400	80	900	θ	deg.	0	C	μ si	150	10
K_{nw}	mD	250	70	600	ε	in	0.004	Methane	%	99	51
Dip	deg.	45	45	45	T	$^{\circ}$ F	160	C_{22}	%	1	49

Table 6.1: Summary of formation, borehole, and fluid-phase properties assumed for PL interpretation of the synthetic multilayer reservoir model.

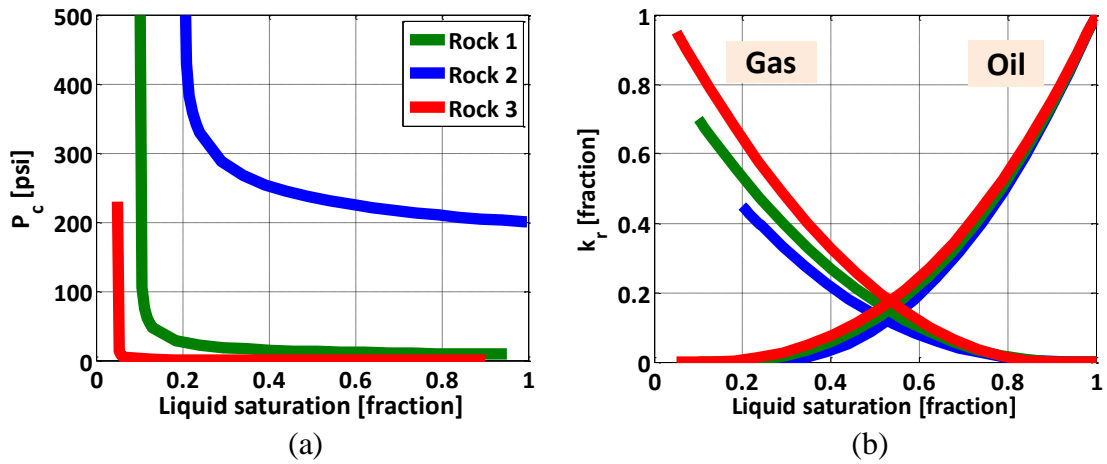


Figure 6.3: Assumed saturation-dependent relative permeability and capillary pressure for PL interpretation of the synthetic multilayer reservoir model.

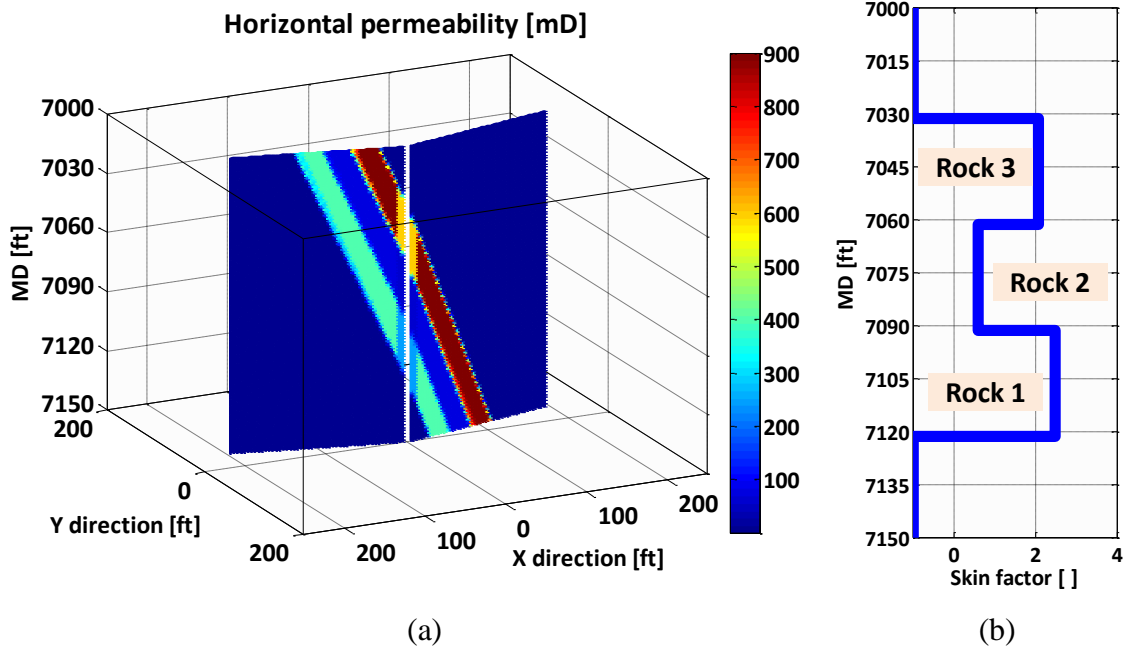


Figure 6.4: Assumed spatial distributions of (a) permeability, and (b) skin factor. Skin factor is computed from Equation 6.2 for a cylindrical region with radius equal to 15 ft around the borehole.

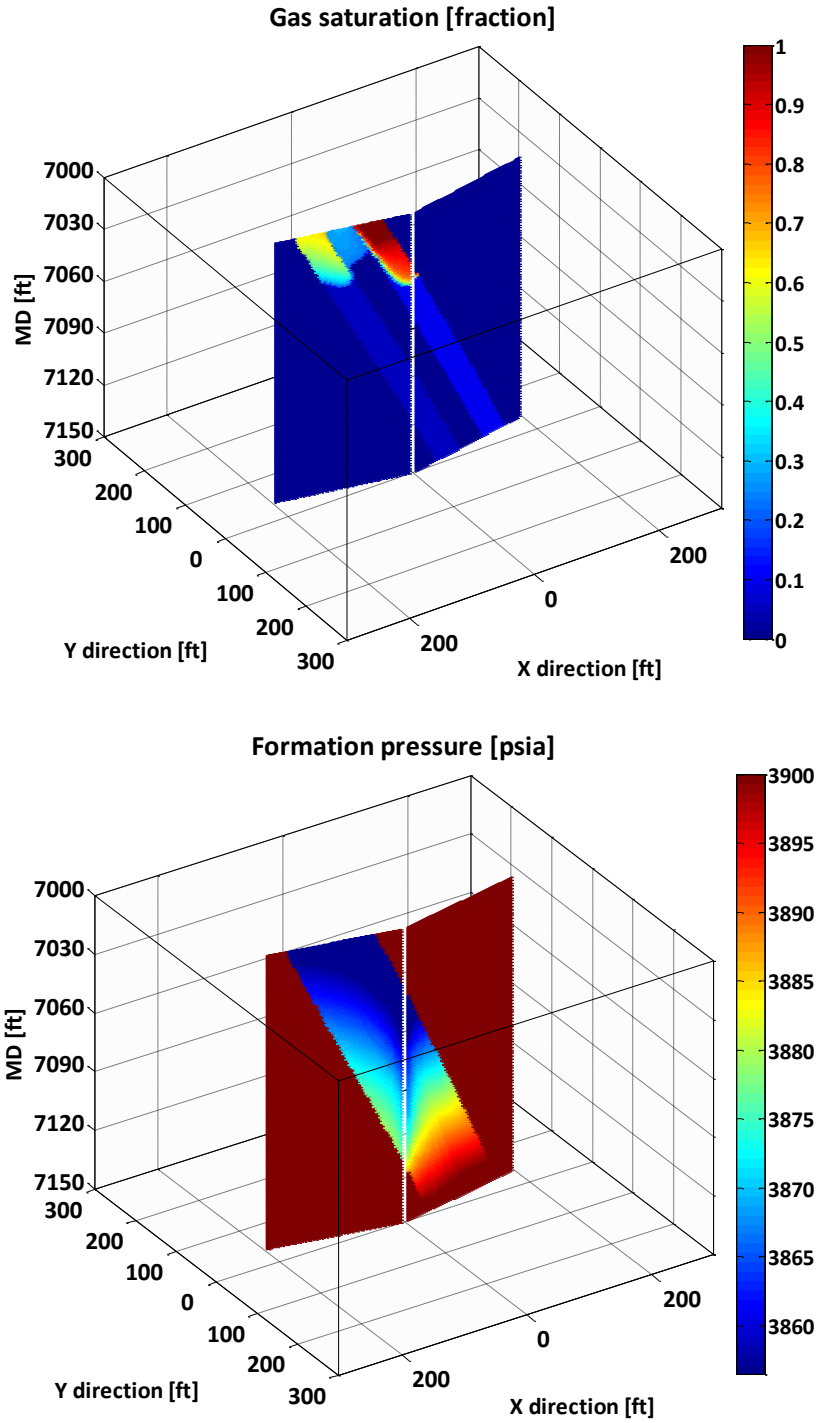


Figure 6.5: Numerically simulated spatial distributions of formation gas saturation (upper panel) and formation pressure (lower panel) prior to measurement acquisition across the synthetic multilayer reservoir model. Advancement of the gas front causes change of near-borehole gas saturation.

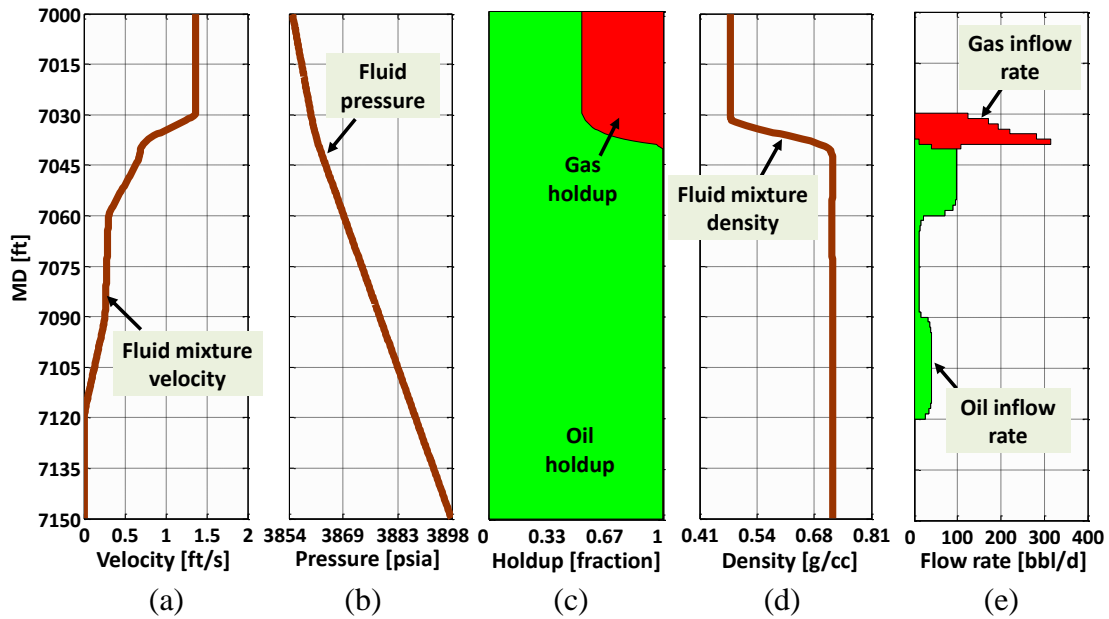


Figure 6.6: Numerically simulated depth distributions of borehole (a) fluid mixture velocity, (b) pressure, (c) holdup, (d) fluid mixture density, and (d) inflow rate. Borehole measurements correspond to formation gas saturation and pressure plotted in Figure 6.5.

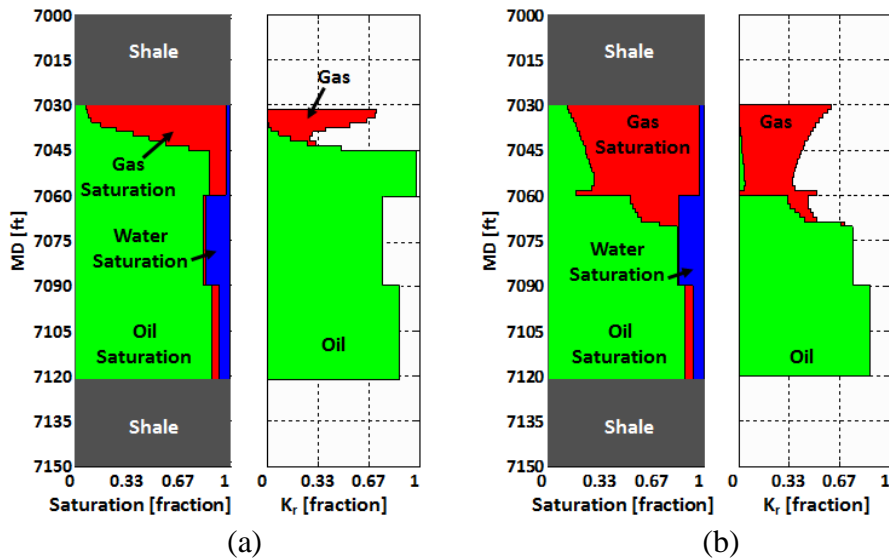


Figure 6.7: Numerically simulated depth distributions of near-borehole fluid-phase saturation and relative permeability (a) before, and (b) after gas shut-off performed in the synthetic multilayer reservoir model. Advancement of the gas front decreases oil-phase relative permeability of the top and middle layers.

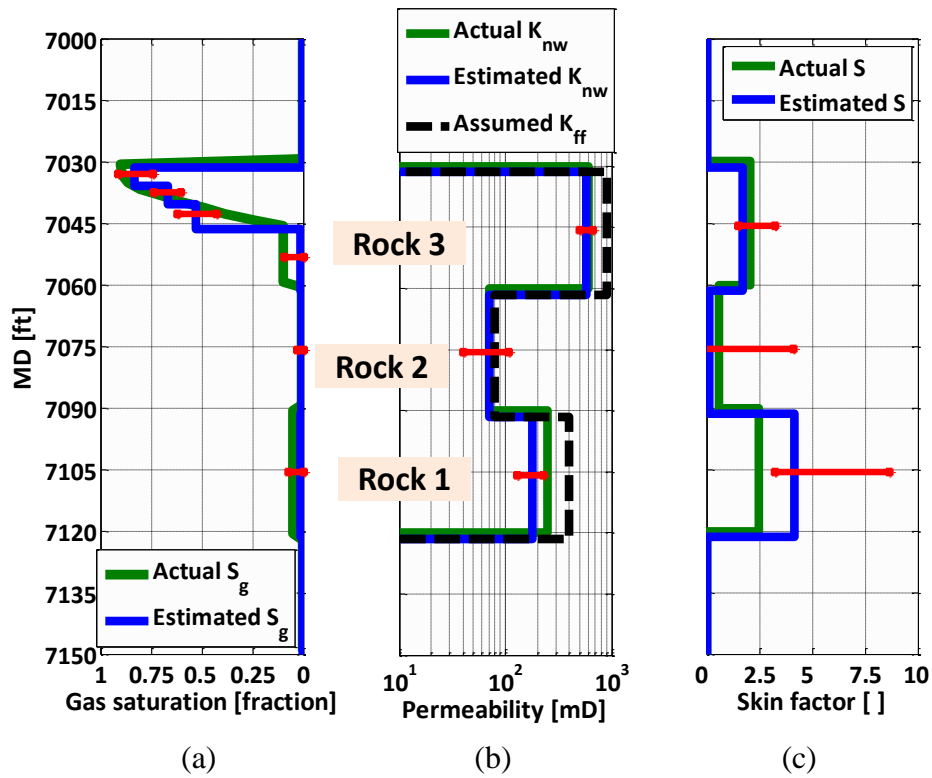


Figure 6.8: Comparison of estimated and actual values of near-borehole (a) gas saturation, (b) permeability, and (c) skin factor for the synthetic multilayer reservoir model. Dashed lines in Panel (b) identify the assumed formation far-field permeability. Conditions of immovable gas saturation in Rocks 1 and 2 cause uncertain estimation of gas saturation in those rocks. Uncertainty associated with gas saturations is additionally propagated to estimates of formation permeability, leading to uncertain estimates of skin factor (error bars shown in Panel c). Skin factor is computed based on Hawkins's formula. Production logging interpretation for Rock 3 yields reliable estimates of formation petrophysical properties.

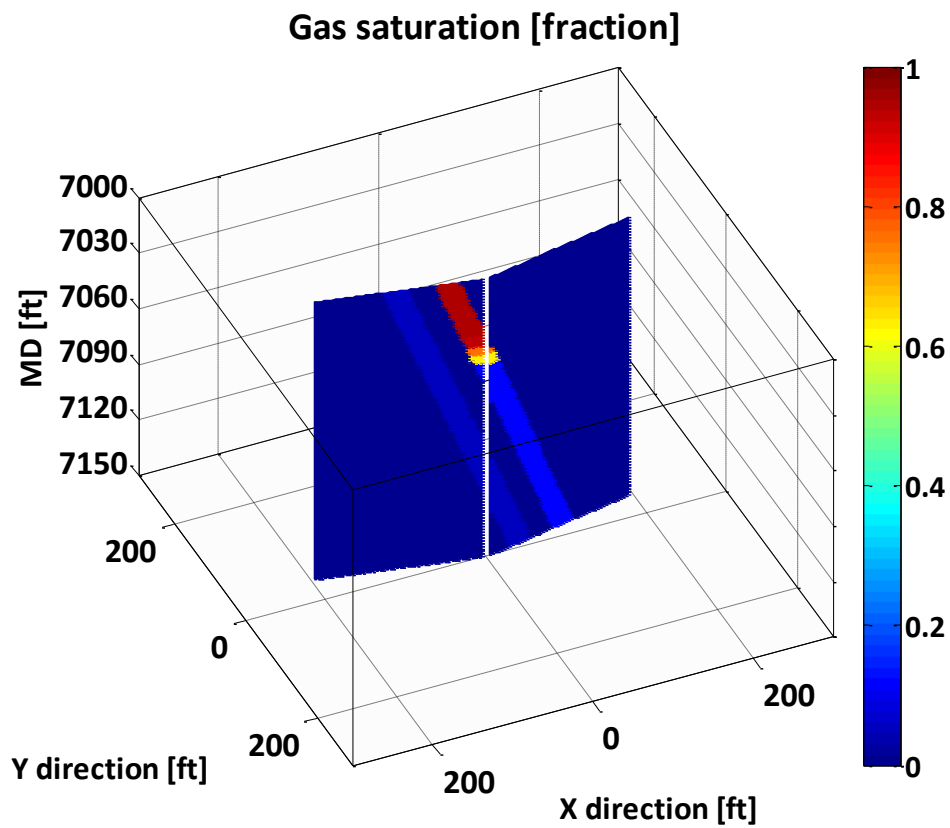


Figure 6.9: Estimated spatial distribution of gas saturation for the synthetic multilayer reservoir model. Because the displacement front associated with Rock 1 and Rock 2 has not reached the borehole, the corresponding gas saturations are interpreted as residual values. However, gas production from Rock 3 makes it possible to estimate an average gas saturation distribution for near-borehole region of that rock.

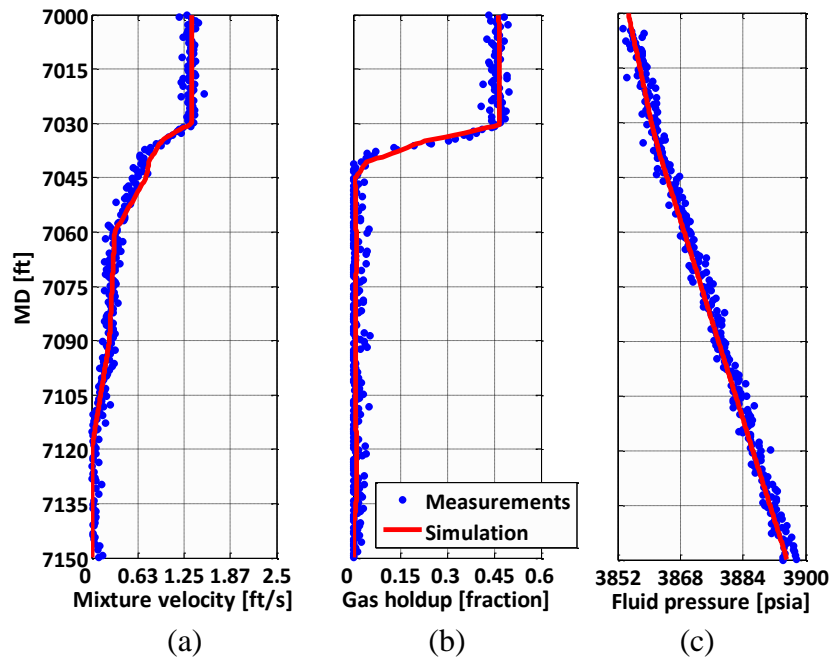


Figure 6.10: Comparison of synthetically generated and numerically reproduced (a) fluid mixture velocity, (b) gas holdup, and (c) borehole pressure acquired across the synthetic multilayer reservoir model. The reconstructed production logs are in a good agreement when compared to synthetically generated borehole measurements.

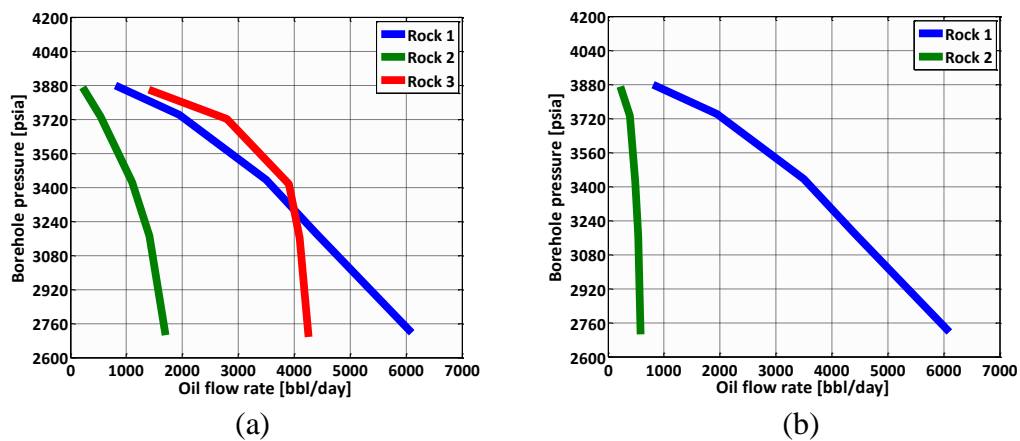


Figure 6.11: Simulated formation pressure-production behavior for the synthetic reservoir model (a) before, and (a) after gas shut-off. Rock 3 shows the highest decline in oil producibility caused by the decrease of near-borehole oil-phase relative permeability for that rock. The producibility of Rock 1 remains unaffected before and after gas shut-off.

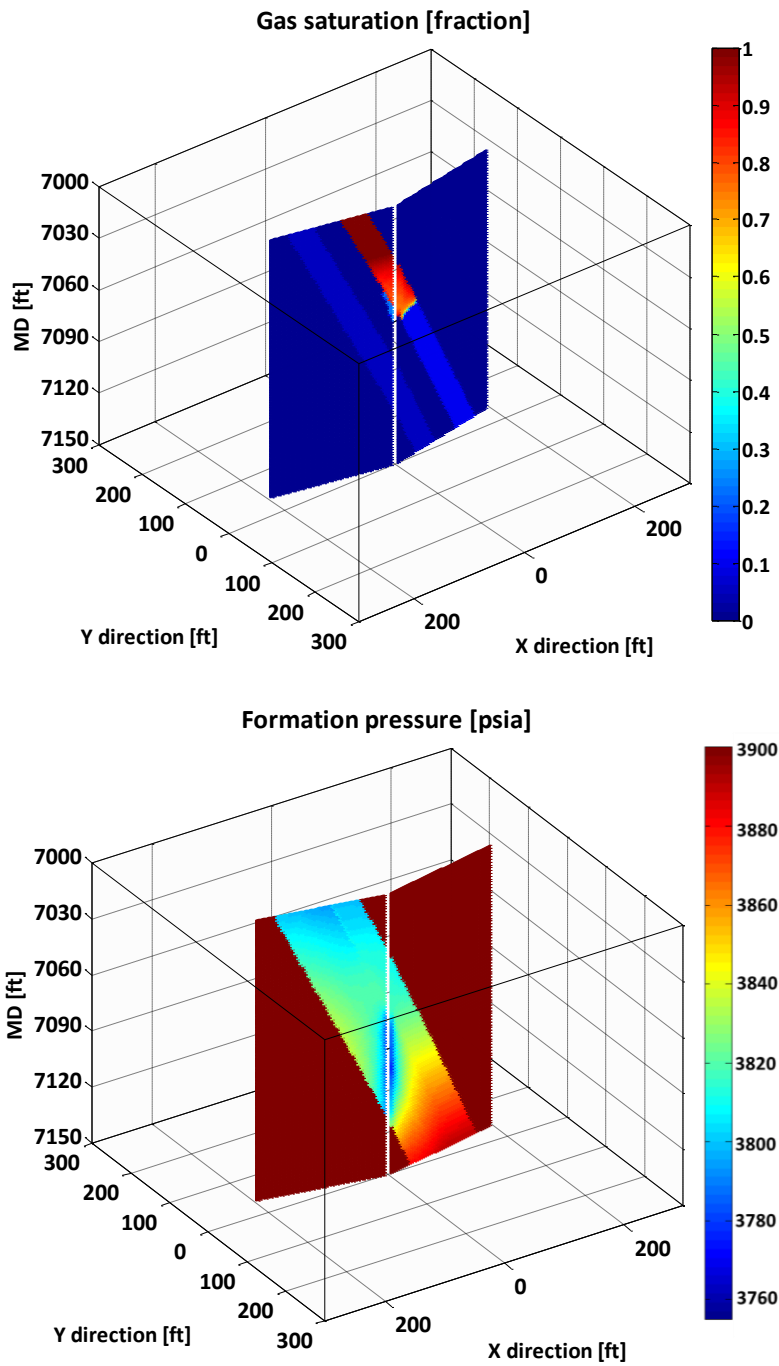


Figure 6.12: Numerically simulated spatial distributions for formation gas saturation (upper panel) and formation pressure (lower panel) after performing gas shut-off in Rock 3 of the synthetic reservoir model. The simulation was carried out by initializing formation gas saturation to that estimated from production logs (shown in Figure 6.9).

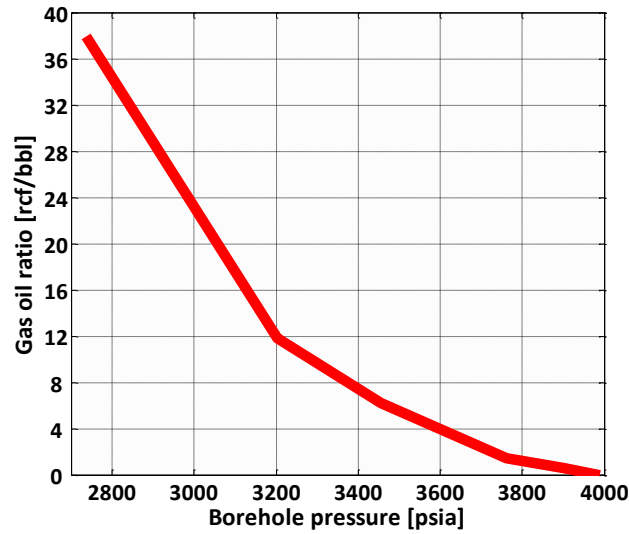


Figure 6.13: Sensitivity of the produced gas-oil ratio with respect to borehole pressure. The analysis shows that maintaining the bottom-hole pressure above 3600 psia limits gas production to approximately 4 rcf/bbl.

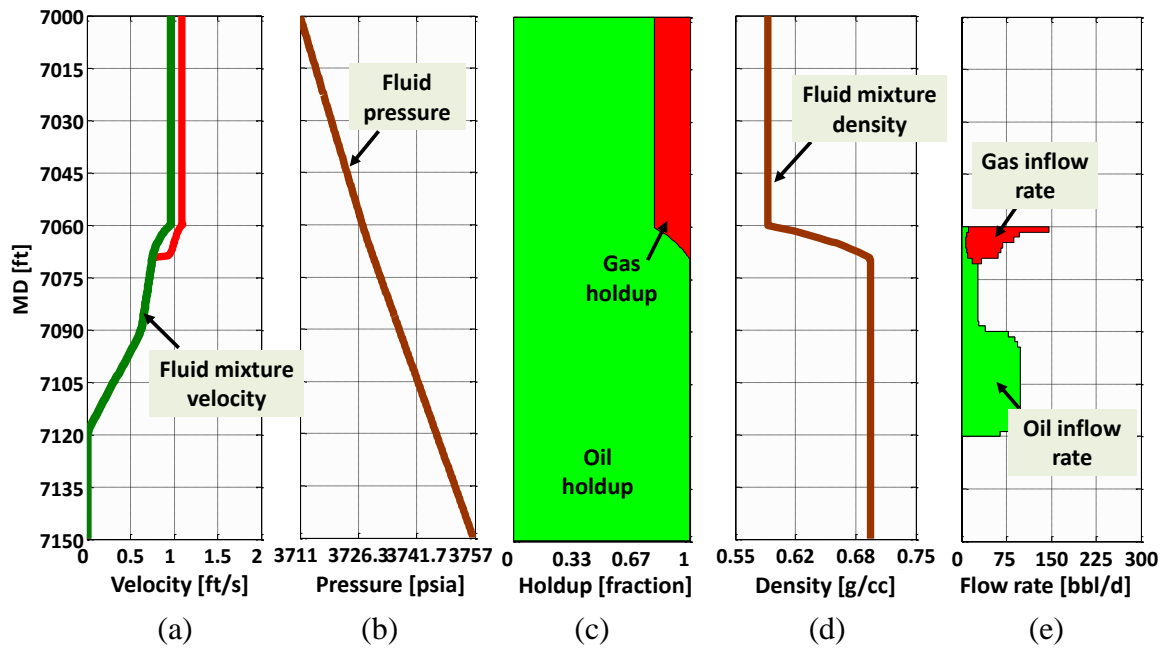


Figure 6.14: Numerically simulated depth distributions of borehole: (a) fluid mixture velocity, (b) pressure, (c) holdup, (d) fluid mixture density, and (d) inflow rate after performing the gas shut-off on Rock 3. Borehole measurements correspond to formation gas saturation and pressure plotted in Figure 6.12.

6.4 FIELD EXAMPLE

The developed PL interpretation method is invoked to diagnose and quantify near-borehole gas saturation and permeability of a multilayer laminated sand-shale system. Formations under consideration originating from a deltaic depositional environment with a bimodal grain size distribution. The sedimentary rock contains coarse to medium grains with poor sorting and a significant portion of micropores. The presence of micropores abnormally increases formation irreducible liquid saturation as shown in Figure 6.15. The plotted capillary pressure curve is associated with a reference porosity and permeability equal to 22 pu and 200 mD, respectively. Assuming a constant irreducible liquid saturation, the Leverett-J function is invoked to rescale capillary pressure with respect to porosity and permeability of each layer. Furthermore, Figure 6.16 shows that the spatial distributions of horizontal and vertical permeabilities are generated from well-log-derived permeability. Because layer boundaries do not coincide with grid blocks in cylindrical coordinates, I use an upscaling method (described in Chapter 3) to compute average horizontal and vertical permeabilities for the grid blocks shared by adjacent layers.

The multilayer reservoir is penetrated by a borehole exhibiting a 32-degree deviation angle with perforated intervals highlighted in Figure 6.15. Table 6.2 summarizes borehole, formation, and fluid properties assumed for simulation and interpretation of production logs. At the time of PL acquisition, the multilayer system was producing oil and gas with negligible water production. Three hydrocarbon components, listed in Table 6.3, are used to simulate PVT properties of the oil and gas phases. Figure 6.17 shows the acquired fluid velocity, pressure, holdup, density, and temperature. The bottom set of perforated intervals is a main gas producer that is interpreted from the high gas holdup and low fluid mixture density above that fluid-

producing depth interval. Furthermore, depth variations of borehole temperature and pressure across that depth interval clearly indicate a gas entry. I iteratively refine near-borehole gas saturation and permeability to reconstruct the measurements of borehole fluid mixture velocity, pressure, and gas holdup.

The interpretation process begins with specifying four spatial windows in the borehole flowing domain each associated with four fluid-producing depth intervals. I identify four flowing units in the formation being separated by impermeable shale layers. However, presence of a pressure-supporting gas cap suggests an identical formation average pressure associated with all the fluid-producing layers. Far-field permeabilities are assumed identical to those estimated from well logs to initiate the iterative refinement process. Table 6.4 and Figure 6.18 compare initial and final estimates of near-borehole permeability and gas saturation obtained with the iterative refinement. Comparison of measured production logs and their numerical simulation (Figure 6.19) shows an average quadratic difference less than 9% for fluid mixture velocity, 2% for fluid pressure, and 3% for gas holdup.

Figure 6.20 shows the final estimated depth distributions of the overall, gas, and oil compositions, and the corresponding fluid densities. Although fluid mixture density was not included in the estimation, the reconstructed fluid mixture density (Figure 6.19d) shows an acceptable match compared to measured values. A mismatch is observed for depths below 6362 ft MD because of unaccounted standing column of water in the borehole. Figure 6.21 shows the final refined model; Unit 1 exhibits the largest near-borehole average gas saturation and permeability with the lowest estimation uncertainties (error bars in Figure 6.21b) However, average gas saturation estimated for Unit 4 involves more than 46% uncertainty due to low fluid production associated with that flowing unit.

6.4.1 Gas Shut-Off

Based on production-log interpretation, I isolate the perforated interval associated with Unit 4 to achieve a lower gas production rate. Figure 6.22 shows the simulated borehole fluid-phase properties after performing the operation. Downhole pressure has been assumed equal to that before gas shut-off. Borehole gas holdup simulated at 6170 ft MD has decreased from 0.63 (before gas shut-off) to approximately 0.17 after the operation. Figure 6.23 additionally describes the pressure-production behavior of formation with the remaining perforated intervals. Because of a high permeability and a low gas saturation diagnosed for Unit 2, that flowing unit exhibits the highest oil productivity. However, lowering the borehole pressure increases near-borehole gas saturation, thereby resulting in a decrease of oil production from that unit. On the other hand, the lowest oil productivity is associated with Unit 4 which had been previously diagnosed as a highly-damaged formation.

6.4.2 Sensitivity Analysis

The coupled borehole-formation fluid flow model allows quantifying sensitivity of the estimated unknown properties to uncertainties associated with formation properties (e.g., average pressure). Figure 6.24 shows that assuming a formation average pressure 200 psi greater than the actual value results in underestimation of near-borehole absolute permeability by a factor of 30%. However, the sensitivity analysis shows negligible effects of formation average pressure on the final estimates of near-borehole gas saturation. Figure 6.25 describes the sensitivity of gas holdup increment with respect to the corresponding formation gas saturation, computed across Unit 1 and Unit 4. Because of a high permeability, variations of gas saturation in Unit 1 considerably influence borehole gas volume fraction, thus decreasing the sensitivity to noise. However, the flat

response associated with Unit 4 (green curve) makes the estimate of gas saturation highly sensitive to presence of noise in the measurements.

I investigate the effect of slip velocity on estimates of near-borehole gas saturation by assuming no-slip conditions for borehole fluid flow simulation. As Figure 6.26 shows, considerable discrepancy between gas and oil velocities causes the accumulation of the heavier fluid phase in the borehole, thereby increasing the corresponding fluid-phase holdup. In addition, lifting the heavier fluid phase by the gas phase increases the simulated fluid mixture velocity associated with no-slip conditions. This exercise, therefore, shows that unaccounting fluid-phase slip velocity gives rise to an underestimation of formation gas saturation. Specifically, it is quantified that more than 12% error would be involved with the estimates of near-borehole gas saturation if PL interpretation were performed with the assumption of no-slip conditions in the forward model.

Property	P_{avg}	Dip	D	L	θ	ϵ	T	ρ_o	ρ_g	μ_o	μ_g	C_o	C_g
Unit	psia	deg.	in	ft	deg.	in	$^{\circ}$ F	g/cc	g/cc	cp	cp	μ slip	μ slip
Value	4200	2	4.8	240	32	0.005	130	0.75	0.15	0.9	0.02	10	150

Table 6.2: Summary of the assumed formation, borehole, and fluid-phase properties for PL interpretation of the sand-shale field example.

Property	Unit	Methane	Propane	C_4^+
T_{crit}	$^{\circ}$ K	190.60	369.8	998.21
P_{crit}	atm	45.4	41.9	8.43
A_c	-	0.008	0.152	1.24
V_{crit}	$\frac{m^3}{kgmol}$	0.099	0.203	1.74
MW	$\frac{lb_m}{lb_m mole}$	16.04	44.1	600

Table 6.3: Summary of the assumed hydrocarbon properties for PL interpretation of the sand-shale field example.

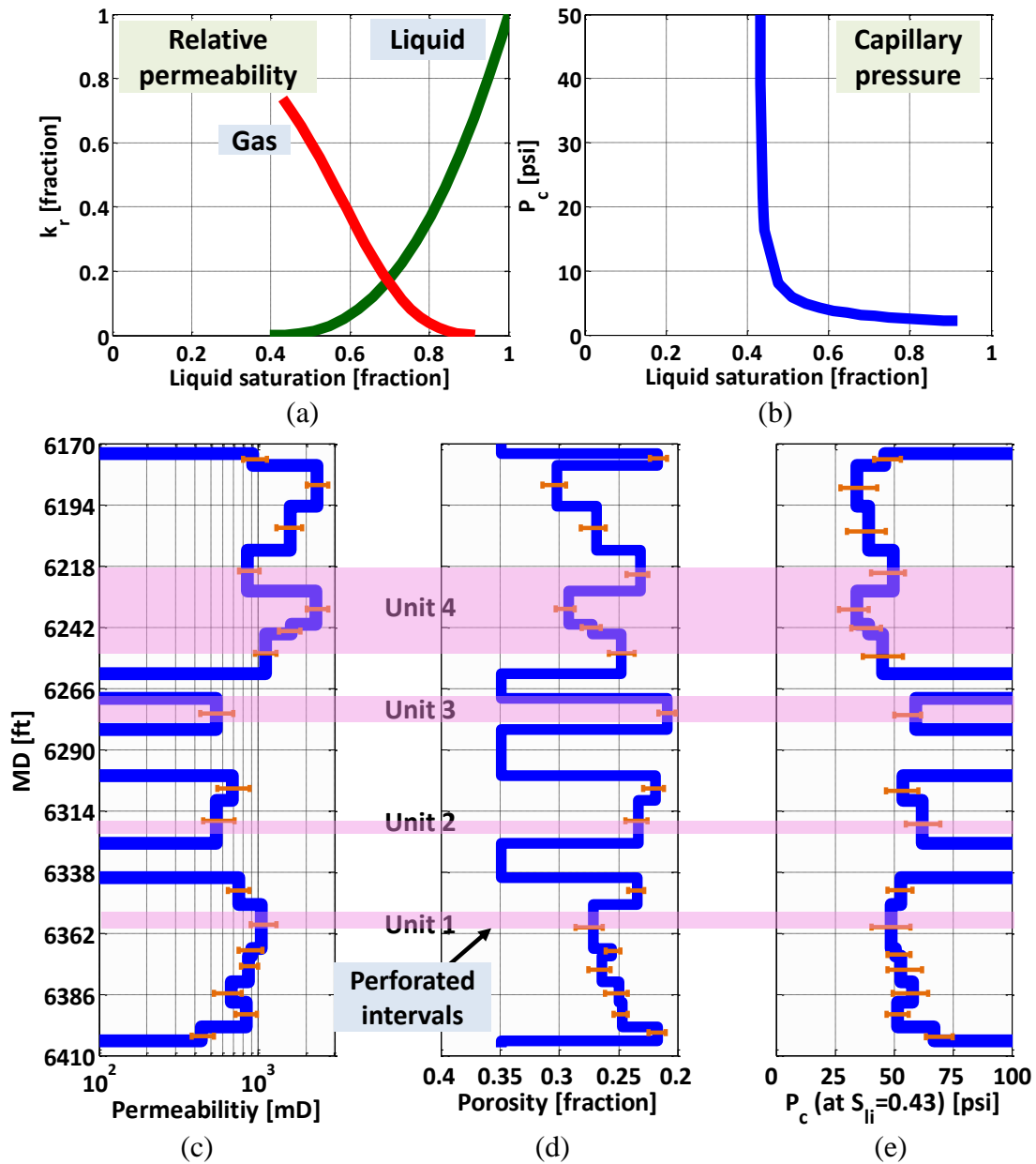


Figure 6.15: Assumed formation (a) saturation-dependent relative permeability, (b) saturation-dependent capillary pressure, (c) permeability, and (d) total porosity for PL interpretation of the sand-shale field example. Panel (e) shows the capillary-pressure rescaling factor computed from the Leverett-J function (i.e., Equation 6.1). Presence of micropores in the reservoir abnormally increases the irreducible liquid saturation to a value close to 0.43. Error bars quantify uncertainty bounds of well-log-derived formation petrophysical properties.

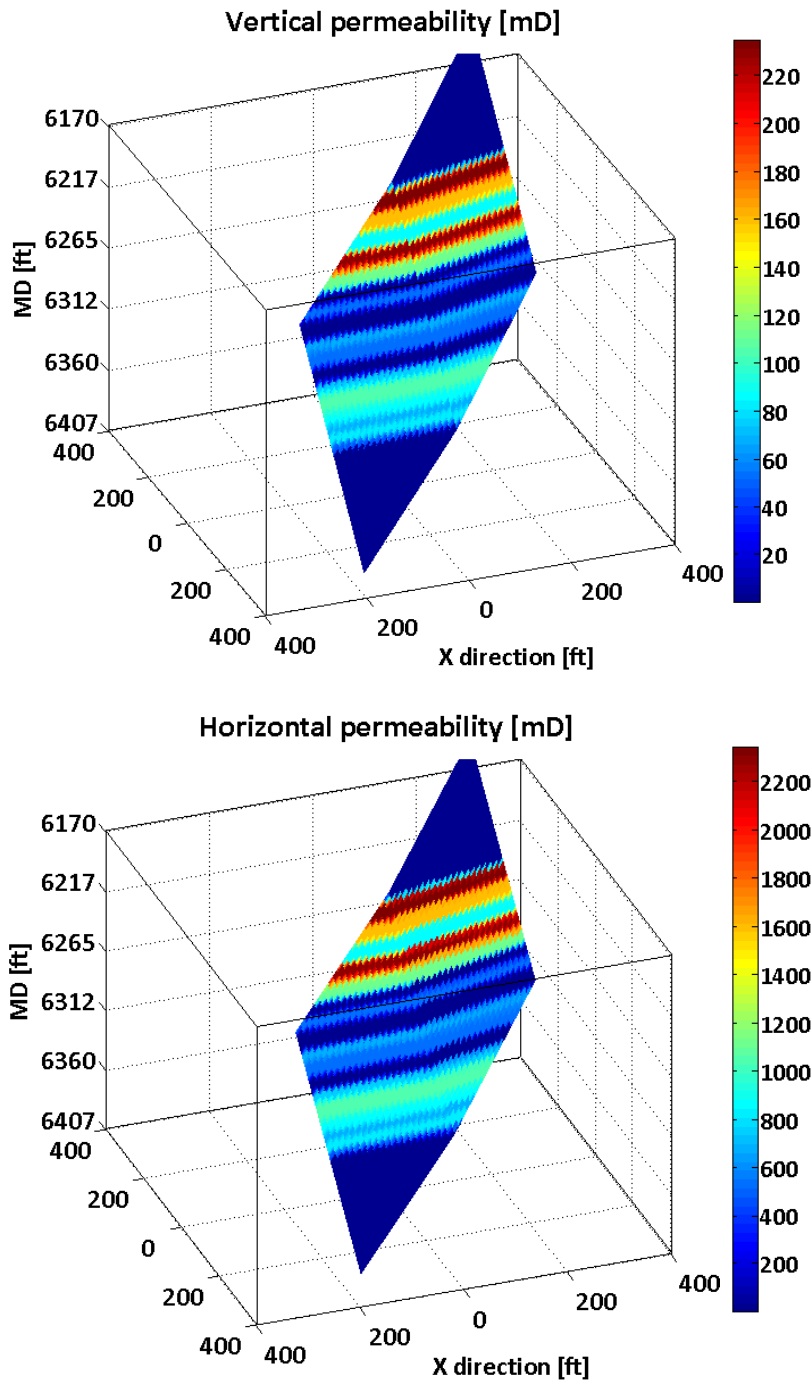


Figure 6.16: Assumed spatial distributions of formation horizontal (upper panel) and vertical (lower panel) permeability for the sand-shale field example. The assumed permeability anisotropy is equal to 0.1. An averaging method described in Chapter 3 computes upscaled values of directional permeability for grid blocks shared by adjacent layers.

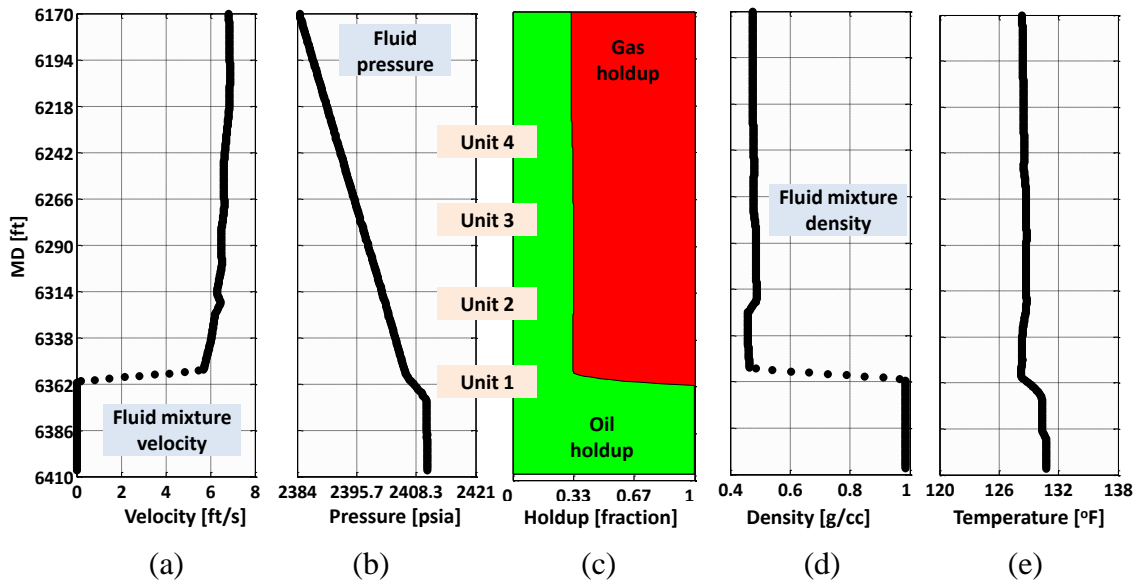


Figure 6.17: Borehole production measurements acquired for (a) fluid mixture velocity, (b) pressure, (c) holdup, (d) fluid mixture density, and (e) temperature. Abrupt increase of gas holdup across Unit 1 indicates a considerable gas production from that unit.

Property	Near-borehole permeability [mD]				Near-borehole gas saturation			
	Unit 1	Unit 2	Unit 3	Unit 4	Unit 1	Unit 2	Unit 3	Unit 4
Initial	200	200	200	200	0.5	0.5	0.5	0.5
Final	2296	2154	257	49	0.32	0.09	0.21	0.27

Table 6.4: Comparison of the initial and final estimates of near-borehole permeability and gas saturation obtained for the sand-shale field example. The algorithm progressively refines permeability of near-borehole region to match fluid velocity, pressure, and holdup. During the inversion, gas saturation is assumed to be constant laterally away from the borehole. The final refined model has been shown in Figure 6.21.

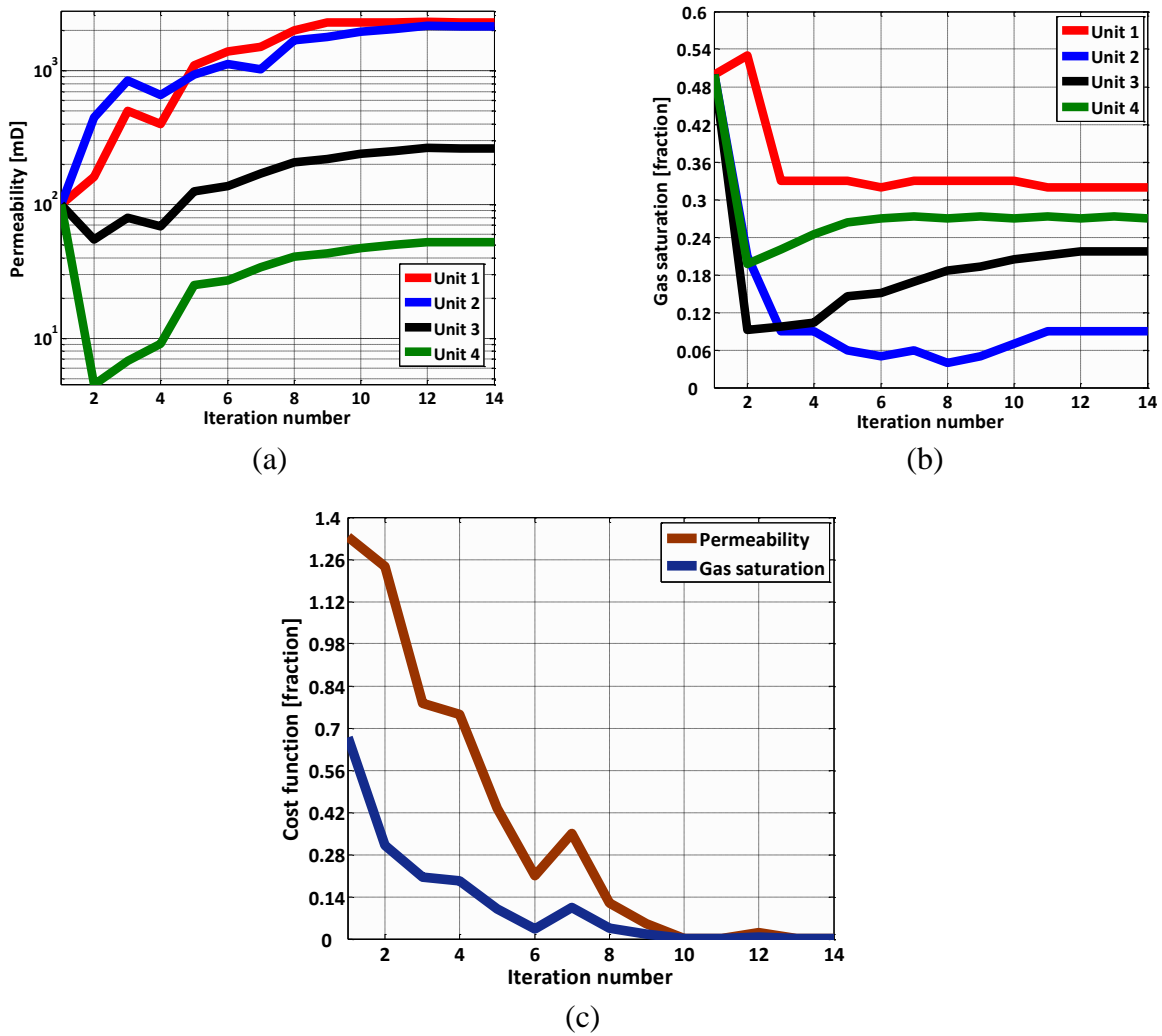


Figure 6.18: Convergence behavior for (a) permeability and (b) gas saturations as a function of iteration number. Panel (c) shows quadratic cost function computed for gas saturation and permeability as a function of iteration number. The refined properties are achieved after 14 iterations.

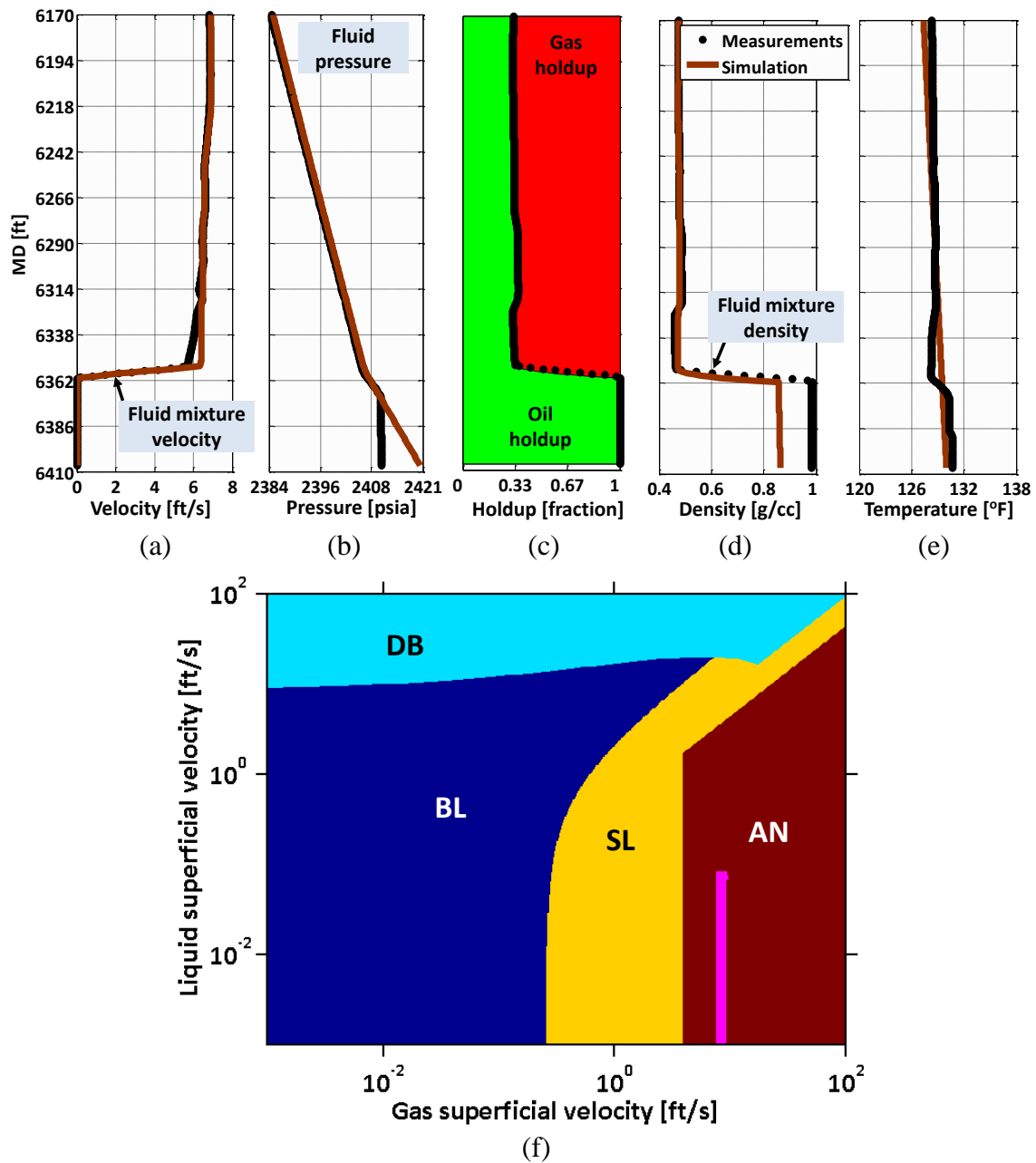


Figure 6.19: Comparison of the numerically simulated (a) fluid mixture velocity, (b) pressure, (c) holdup, (d) fluid mixture density, and (e) temperature with measurements for the sand-shale field model. The reconstructed production logs are in a good agreement with actual measurements. Discrepancies observed below 6360 ft MD are associated with an unaccounted standing column of water in the bottom of the borehole. Panel (f) shows fluid-phase superficial velocities on the developed gas-liquid flow-regime map (DB: dispersed-bubbly, BL: bubbly, SL: slug, and AN: annular flow regimes).

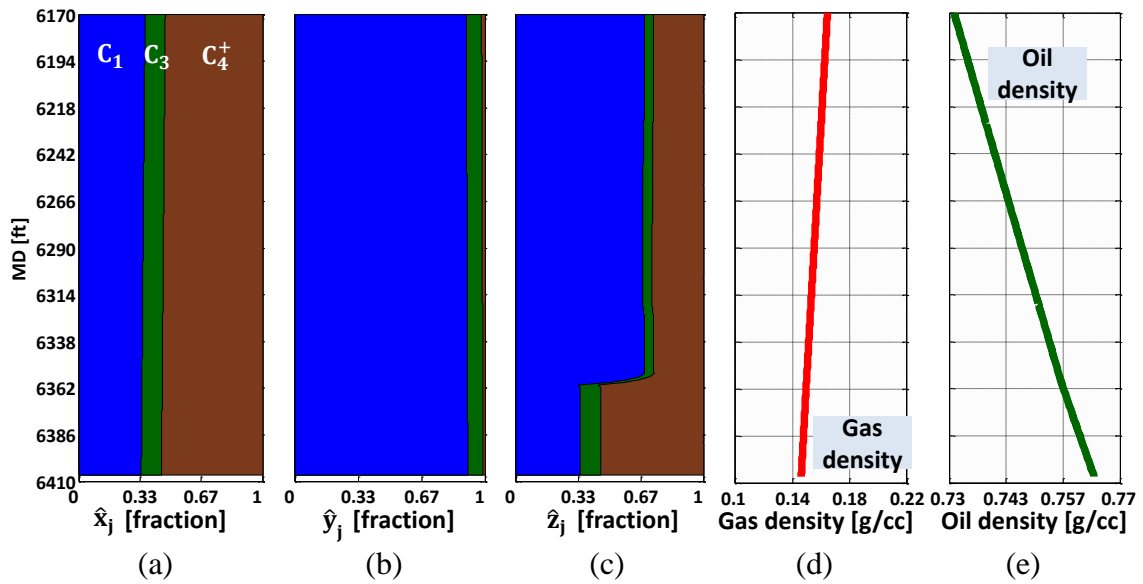


Figure 6.20: Numerically simulated depth distributions of borehole (a) oil-phase, (b) gas-phase, and (c) overall hydrocarbon composition. Panels (d) and (e) show the associated gas and oil density, respectively. Gas production from Unit 1 decreases the molar composition of the heavy component across that unit (i.e., the brown shaded area in Panel c).

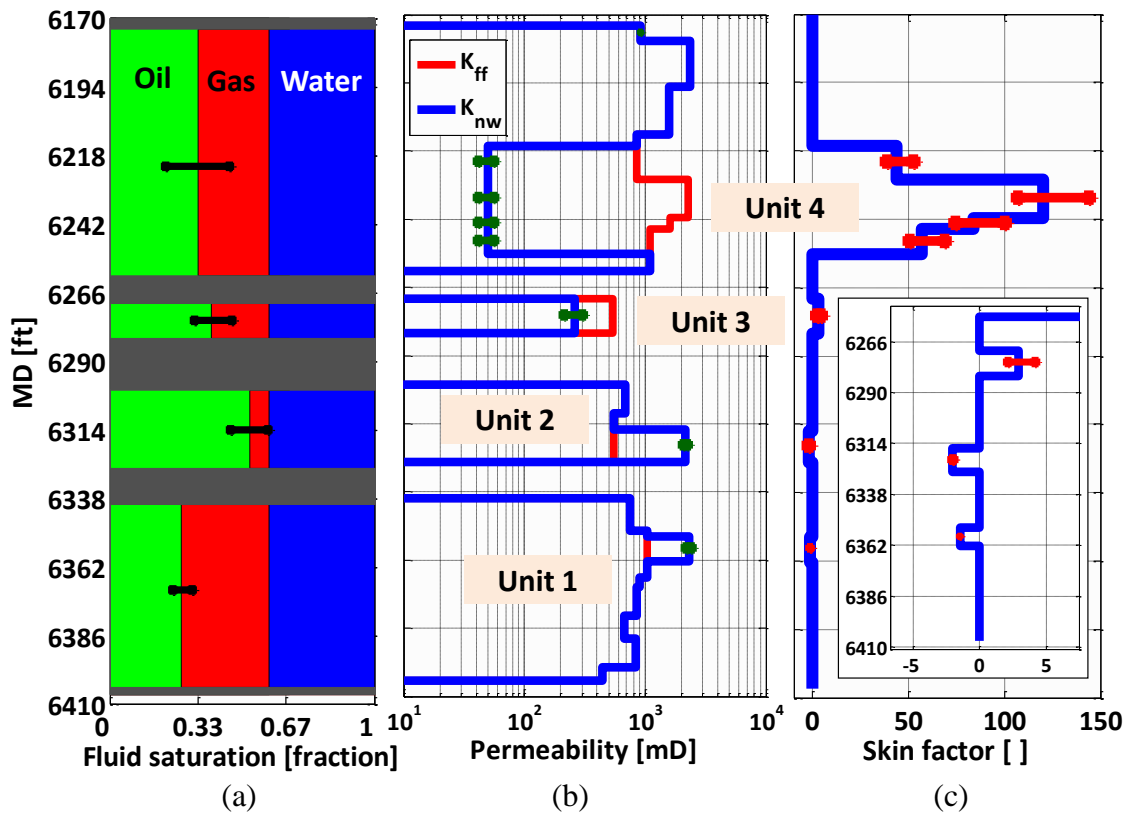


Figure 6.21: Estimated depth distributions of near-borehole (a) fluid saturation, (b) permeability, and (c) skin factor for the sand-shale field example. Units 1 and 4 were diagnosed as gas-saturated formations with approximately 30% gas saturation. Furthermore, Panel (c) shows that Unit 1 is stimulated (with a negative skin factor equal to -1.1), while Unit 4 is highly damaged. Low fluid production from Unit 4 makes production logs across that unit highly sensitive to measurement noise, thus increasing the uncertainty bound of estimated gas saturation up to 46%. Uncertainty of gas saturation is additionally propagated to the estimated skin factor (Panel c). Furthermore, conditions of immovable gas saturation in Unit 2 cause more than 30% uncertainty for gas saturation of that unit. Interpretation of production logs across Unit 1, with a high value of far-field permeability, yields the lowest uncertainty for near-borehole gas saturation and permeability.

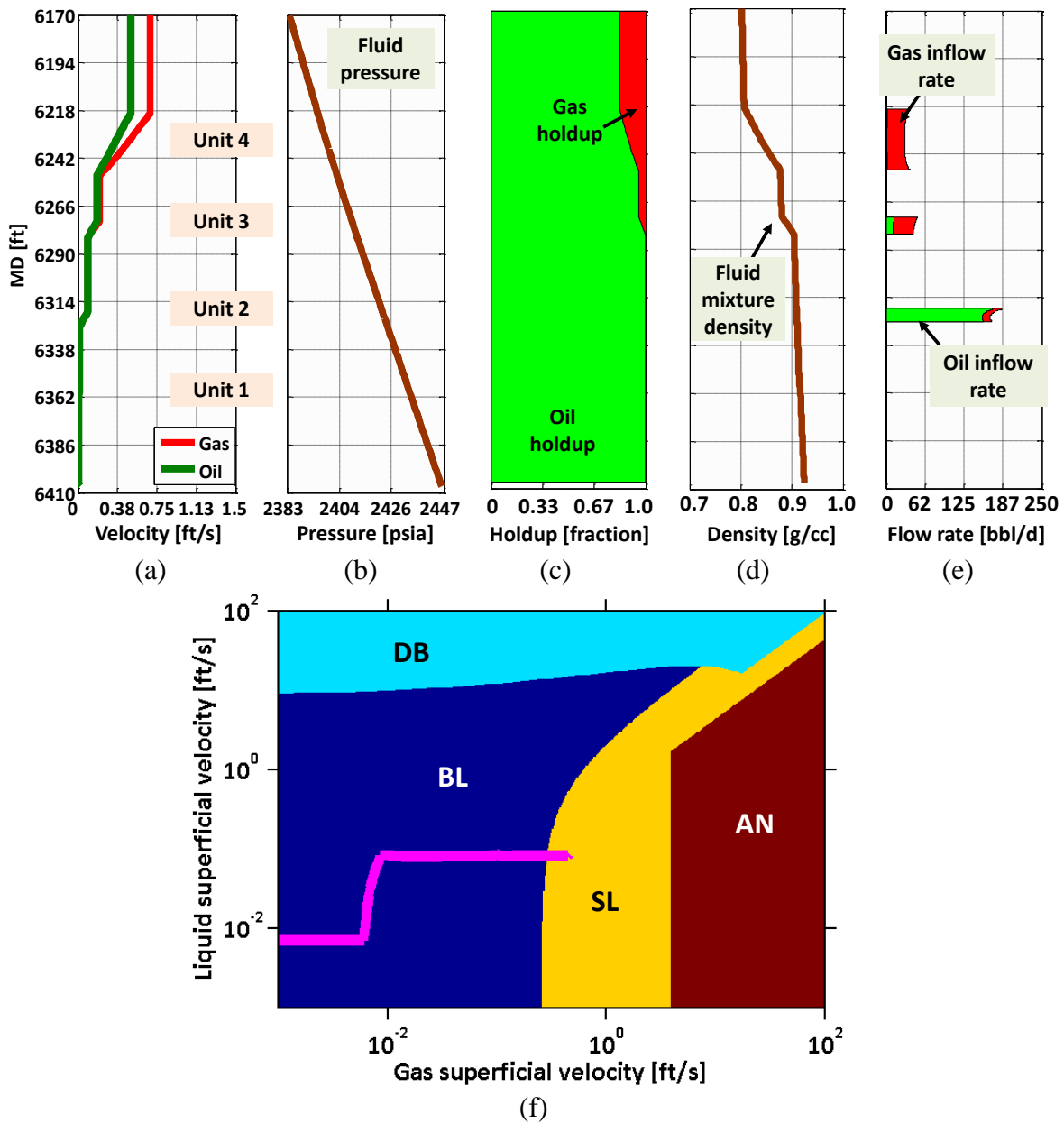


Figure 6.22: Numerically simulated (a) fluid mixture velocity, (b) pressure, (c) holdup, (d) mixture density, and (e) temperature after isolating the bottom perforated interval in the sand-shale field example. The reconstructed production logs are in acceptable agreement with actual measurements. Discrepancies observed below depth 6360 ft MD are associated with the unaccounted standing column of water in the bottom of the borehole. Panel (f) shows fluid-phase superficial velocities on the flow-regime map developed in this dissertation (DB: dispersed-bubbly, BL: bubbly, SL: slug, and AN: annular flow regimes).

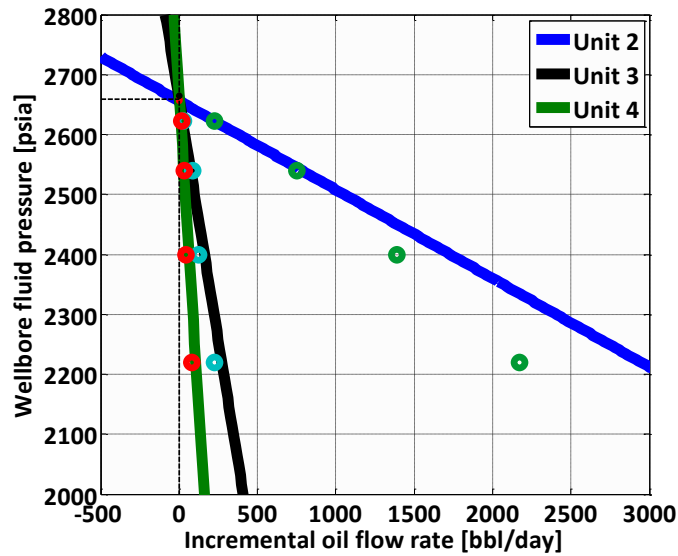


Figure 6.23: Simulated pressure-production behavior of the remaining fluid-producing units after performing gas shut-off on Unit 1. Solid lines identify the interpolation through the two data points associated with the largest borehole pressures. The highest oil producibility is associated with Unit 2 with a high permeability and a low gas saturation. Results show that lowering the borehole pressure decreases oil producibility because of the increase of near-borehole gas saturation.

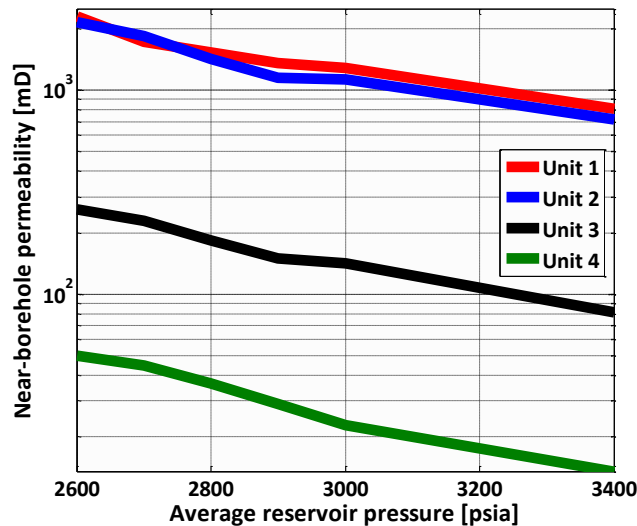


Figure 6.24: Sensitivity of the estimated near-borehole permeability to formation average pressure. Results show that 200 psi uncertainty in formation average pressure gives rise to underestimation of near-borehole permeability by a factor of 30%.

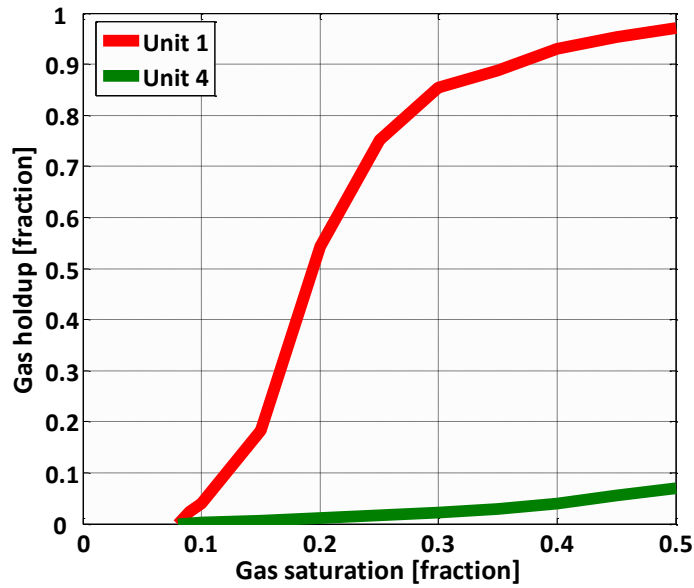


Figure 6.25: Sensitivity of the simulated gas-holdup increment across Unit 1 and Unit 4 to the associated formation gas saturation. Because of the low permeability for Unit 4, the simulated gas holdup across that unit exhibits low sensitivity to the associated gas saturation.

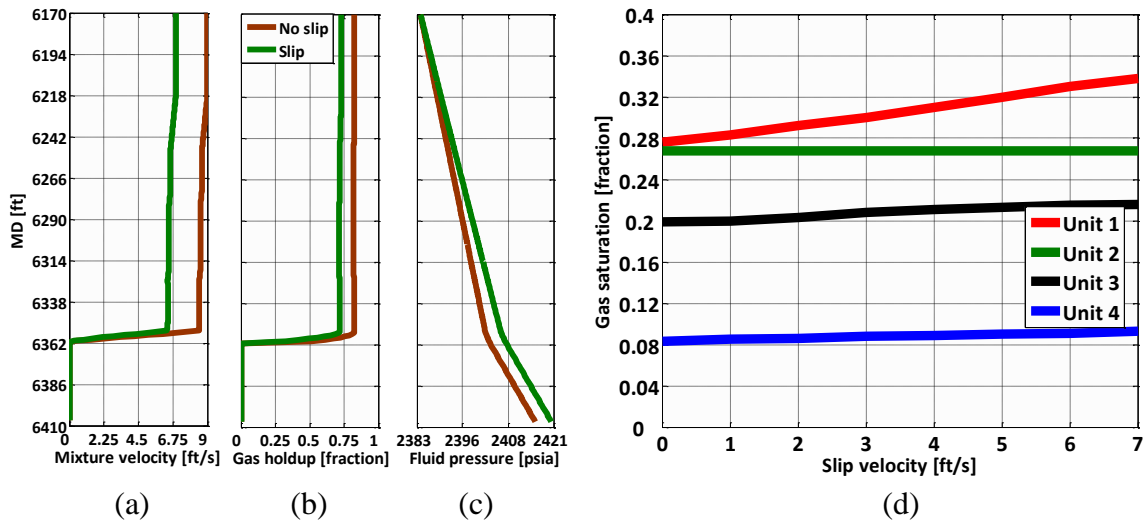


Figure 6.26: Sensitivity of borehole (a) fluid mixture velocity, (b) gas holdup, and (c) pressure with respect to the slip model assumed for forward simulation of production logs (the simulated slip velocity is approximately 5 ft/s). Panel (d) shows the sensitivity of the estimated near-borehole gas saturation to slip velocity. The no-slip model involves up to 12% error in the estimates of gas saturation.

6.5 DISCUSSION

The developed interpretation method is based on the use of a 3D multiphase reservoir fluid flow model that enables differentiating the skin factor associated with formation damage from that associated with partial perforation and presence of a second fluid phase. Quantifying near-borehole damage of individual rock formations is a substantial advantage of the developed coupled fluid flow model over conventional PL interpretation methods. Estimated near-borehole petrophysical properties can be used to update available dynamic reservoir flow models. One limitation arises from the validity of assumptions made on the formation petrophysical properties laterally away from the borehole. Specifically, this study assumed that far-field permeabilities were equivalent to those estimated from well logs. However, in highly heterogeneous rocks, discrepancies between well-log-derived and field-scale permeability can cause unrealistic estimation of near-borehole petrophysical properties.

In multilayer reservoirs, the developed interpretation method effectively accounts for cross-flow taking place between hydraulically-connected fluid-producing units. Detailed simulation of the near-borehole fluid flow regimes makes it possible to reliably quantify the flow performance of individual rock formations. However, a limitation is the vertical resolution of estimated near-borehole properties. Measurable sensitivity of production logs to near-borehole petrophysical properties is only available across perforated intervals. Because of a low sensitivity, extending unknown parameters to petrophysical properties beyond perforated intervals considerably increases the non-uniqueness of PL interpretation. Furthermore, the presence of noise in production measurements imposes a limit on the minimum representative length scale permitted for defining the thickness of petrophysical layers. Refining the petrophysical layers below

that representative length yields uncertain estimates of near-borehole permeability and fluid saturation.

The developed interpretation method defines a data-weighting matrix to exclusively associate variations of borehole fluid properties to corresponding layer properties. From a mathematical point of view, window-by-window inversion of production logs enhances the diagonal dominance of the Jacobian matrix, thereby improving the numerical stability of PL interpretation. Furthermore, the diagnostic algorithm computes variations of production logs across each petrophysical layer that prevents the propagation of error originated from possible unreliable properties of adjacent layers. On the other hand, constructing the Jacobian matrix based on variations of production logs (instead of using their absolute values) increases sensitivity of the inversion method to non-physical variations of production measurements (e.g., due to tool movements). It is therefore highly recommended to perform preliminary processing on production logs to reduce deleterious noise effects before using them in the inversion algorithm.

6.6 SUMMARY AND CONCLUSIONS

This study a coupled borehole-formation fluid flow model to simulate borehole fluid measurements acquired with PLTs in vertical and deviated flowing systems. Coupling the physics of fluid flow in the borehole and porous media enabled the quantification of near-borehole permeability and fluid saturation. A practical application of the new coupled model was to reconstruct near-borehole dynamic reservoir models to infer pressure-production properties of reservoir rocks. In addition, production logs and well logs were integrated to diagnose and quantify depth distribution of skin factor. The PL-calibrated near-borehole reservoir model was additionally invoked to simulate and

quantify the decrease of unwanted gas production caused by performing gas shut-off remedial operations.

In the synthetic reservoir example, the estimation error was less than 20% for near-borehole gas saturation, and within 25% of actual permeability values. When a layer was at conditions of immovable gas saturation, because of no gas production, the interpretation method was unable to accurately estimate the corresponding gas saturation. The uncertainty involved with estimation of gas saturation was additionally propagated to the estimates of near-borehole permeability. I concluded that a-priori knowledge about immovable fluid saturation is required to reliably estimate near-borehole petrophysical properties from production logs. A gas shut-off operation was synthetically performed to isolate the gas-producing layer, and to simulate gas-oil miscible displacement within the remaining fluid-producing layers. The coupled fluid flow model quantified a critical borehole pressure (equal to 3700 pisa) to maintain the producing gas-oil ratio (below 4 rcf/bbl). Lowering the borehole pressure below that critical value resulted in considerable gas production because of gas coning.

The field example indicated that it was possible to reliably estimate average values of near-borehole gas saturation and permeability associated with high-permeability layers. However, sensitivity analysis of production logs across flowing units with relatively low near-borehole permeability (e.g., 48 mD) showed that near-borehole gas saturation exhibited almost no sensitivity to corresponding gas saturation. Such behavior was associated with low fluid influx from those flowing units. In the presence of noise, the estimated gas saturation of low-permeability layers was highly sensitive to measurements noise. I next quantified sensitivity of inverted properties to assumptions made on borehole and formation properties. Among those, formation average pressure was shown to considerably influence the estimates of near-borehole permeability.

Specifically, a 200-psi higher-than-actual formation pressure involved more than 30% error into the estimates of near-borehole permeability.

The estimated near-borehole reservoir flow model was used to investigate the inflow performance relationship of individual fluid-producing units. Incremental fluid flow rate for each flowing unit was a function of borehole pressure, skin factor, and gas saturation. A highly-damaged formation (with a low near-borehole permeability equal 48 mD) exhibited the steepest slope in the graph of borehole pressure versus incremental oil flow rate. Such behavior implied that low borehole pressures (or high pressure drawdowns) are required for fluid withdraw from highly-damaged formations. Additionally, it was found that decreasing borehole pressure increases free gas released from oil solution, thereby decreasing the incremental flow rate from fluid-producing rock formations. In fact, released gas in the near-borehole region decreased the relative permeability of oil phase, thus causing the associated inflow performance curves to deviate from the expected linear behavior. The inferred pressure-production properties can be incorporated into dynamic field-scale reservoir models to calibrate those models with respect to borehole production measurements.

Chapter 7: Inference of Near-Borehole Permeability and Water Saturation from Time-Lapse Oil-Water Production Measurements

Interpretation of production logs (PL) acquired in time-lapse mode conventionally helps petrophysicists to detect the advancement of fluid contacts in the near-borehole region. Without inclusion of a dynamic reservoir model, conventional time-lapse interpretation remains limited to describing time variations of fluid inflow rates produced from various fluid-producing rock formations. However, a proper reservoir management requires quantifying depth variations of near-borehole properties (e.g., formation damage and fluid saturation) over time to construct reliable field-scale reservoir models.

This chapter studies several synthetic and field examples to investigate a new application of production logging to estimate near-borehole permeability and water saturation. I invoke the coupled fluid flow model developed in Chapter 2 to simulate and interpret single-phase and two-phase production measurements. I additionally quantify the sensitivity of the estimated properties to uncertainty associated with measurements and formation petrophysical properties (e.g., permeability anisotropy and layer thickness). The new application is next extended to the interpretation of production measurements in time-lapse mode to quantify near-borehole formation damage.

7.1 INTRODUCTION

Borehole production logs are sensitive to the volumetric average of near-borehole petrophysical properties within the volume of investigation of PL measurements. Because

of a large volume of investigation associated with production logs, anisotropy and heterogeneity laterally away from the borehole give rise to discrepancies between PL-derived and well-log-derived petrophysical properties. Large volumes of rock investigated by production logging tools (PLTs) considerably increases shoulder-bed effect, thus decreasing the vertical resolution of inverted properties. This section synthetically acquires production logs across multilayer reservoir models to (i) quantify effects of permeability anisotropy on the estimated permeabilities from production logs, (ii) upscale near-borehole permeability of heterogeneous rocks, (iii) analyze uncertainty involved with the inverted petrophysical properties (i.e., permeability and fluid saturation) originating from variable layer thickness, and (iv) estimate near-borehole formation damage from the integration of production measurements acquired in time-lapse mode.

Fluid withdrawal from a hydrocarbon reservoir usually starts under single-phase conditions. However, over time, fluid movement in the reservoir gives rise to production of multiphase fluid. In oil-water flowing systems, aquifer encroachment, or advancement of the water from injector wells incrementally change near-borehole water saturation. The alteration of near-borehole water saturation, accompanied with near-borehole formation damage, considerably decreases the inflow performance of the borehole. An established method to quantify borehole productivity is the analysis of surface measurements that estimates an average skin factor associated with the set of fluid-producing rock formations. Despite its reliability, interpretation of surface production measurements does not quantify depth variations of skin factor. To circumvent this limitation, downhole production logs should be acquired and interpreted to quantify highly-damaged rock formations, and to identify layers accountable for high water production. The latter

method enables production engineers to design and evaluate adequate remedial workover operations (e.g., water shut-off) to enhance borehole inflow performance.

The coupled flow algorithm integrates production logs acquired in time-lapse mode to construct a near-borehole reservoir model that describes depth variations of skin factor over the elapsed time. In a synthetic reservoir model supported by an infinite-acting aquifer, the estimated fluid saturation and permeability across high-permeability layers are within 15% and 20% of the corresponding actual values, respectively. The interpretation algorithm additionally integrates well logs and production logs acquired in an oil-water field example to construct a PL-calibrated near-borehole reservoir model. Results enable (i) the differentiation of low-permeability layers from highly-damaged formations, (ii) the identification of layers accountable for high water production, and (iii) the quantification of the added value of remedial workover operations to isolate water-producing layers.

7.2 PERMEABILITY ANISOTROPY

Production measurements acquired across anisotropic porous and permeable rock formations are primarily sensitive to rock effective permeability in the direction of fluid flow. For horizontal layers penetrated by a vertical borehole, the estimated permeability from production logs corresponds to layer permeability in the horizontal direction. However, inclining the borehole from the vertical direction causes production measurements to become sensitive to vertical permeability of rock formations. I construct a single-phase multilayer reservoir model to quantify the relationship between actual and estimated permeabilities in an anisotropic porous media. As Figure 7.1 shows, the reservoir under consideration is penetrated by boreholes with 0-, 45-, and 75-degree deviation angles. All layers exhibit permeability anisotropy which vertical permeabilities

lower than horizontal permeabilities by a factor of 10. Table 7.1 summarizes relevant borehole, fluid, and formation properties.

The diagnostic iterative process is performed under the assumption of isotropic rock formations in forward reservoir model. Figure 7.2 shows the estimated permeability from the inversion of production logs. When production logs are acquired from the borehole with 45-degree deviation angle, the estimated permeabilities are nearly identical to horizontal permeabilities. However, production logs associated with 75-degree inclined borehole primarily diagnose layer permeability in the vertical direction. Furthermore, because of shoulder-bed effects, permeabilities estimated in the vicinity of bed boundaries correspond to the average permeability associated with the two adjacent layers.

I invoke the following formula to analytically calculate directional permeability in a direction perpendicular to borehole axial direction (Peters, 2012):

$$\frac{1}{\left(\frac{1}{K_d}\right)} = \frac{\cos^2 \theta}{\left(\frac{1}{K_v}\right)} + \frac{\sin^2 \theta}{\left(\frac{1}{K_h}\right)}, \quad (7.1)$$

where θ is borehole deviation angle, K_d is directional permeability, and K_v and K_h are horizontal and vertical permeabilities, respectively. A comparison is next performed between K_d and the permeability estimated from production measurements. Table 7.2 quantifies that estimated permeabilities associated with the middle point of each layer are within 10% of those estimated with Equation 7.1. Moreover, reconstructed borehole fluid measurements, shown in Figure 7.3, closely match the synthetically acquired production measurements.

Fluid	Unit	Value	Formation	Unit	Rock 1	Rock 2	Rock 3	Borehole	Unit	Value
ρ_o	g/cc	0.75	ϕ	pu	0.23	0.25	0.26	D	in	3
μ_o	cp	0.8	P_{avg}	psia	4100	4100	4100	L	ft	150
C_o	μsip	10	K_h	mD	800	200	500	ε	in	0.003
ρ_w	g/cc	1.0	K_v	mD	80	20	50	T	$^{\circ}\text{F}$	135
μ_w	cp	1.0	Dip	deg.	0	0	0			
C_w	μsip	3.6								

Table 7.1: Summary of fluid-phase, formation, and borehole properties assumed for the three-layer reservoir model to quantify directional dependency of PL-derived permeabilities.

Permeability [mD]	Rock 1		Rock 2		Rock 3	
	$\theta=45^{\circ}$	$\theta=75^{\circ}$	$\theta=45^{\circ}$	$\theta=75^{\circ}$	$\theta=45^{\circ}$	$\theta=75^{\circ}$
Estimated	474.6	137.1	119.8	34.6	296.3	85.5
Analytical model	440.0	128.2	110.0	32.0	275.0	80.1

Table 7.2: Comparison of PL-derived permeabilities and those computed from the analytical model (i.e., Equation 7.1). Numerical simulation of production measurements is performed under the assumption of isotropic rock formations in the forward reservoir model.

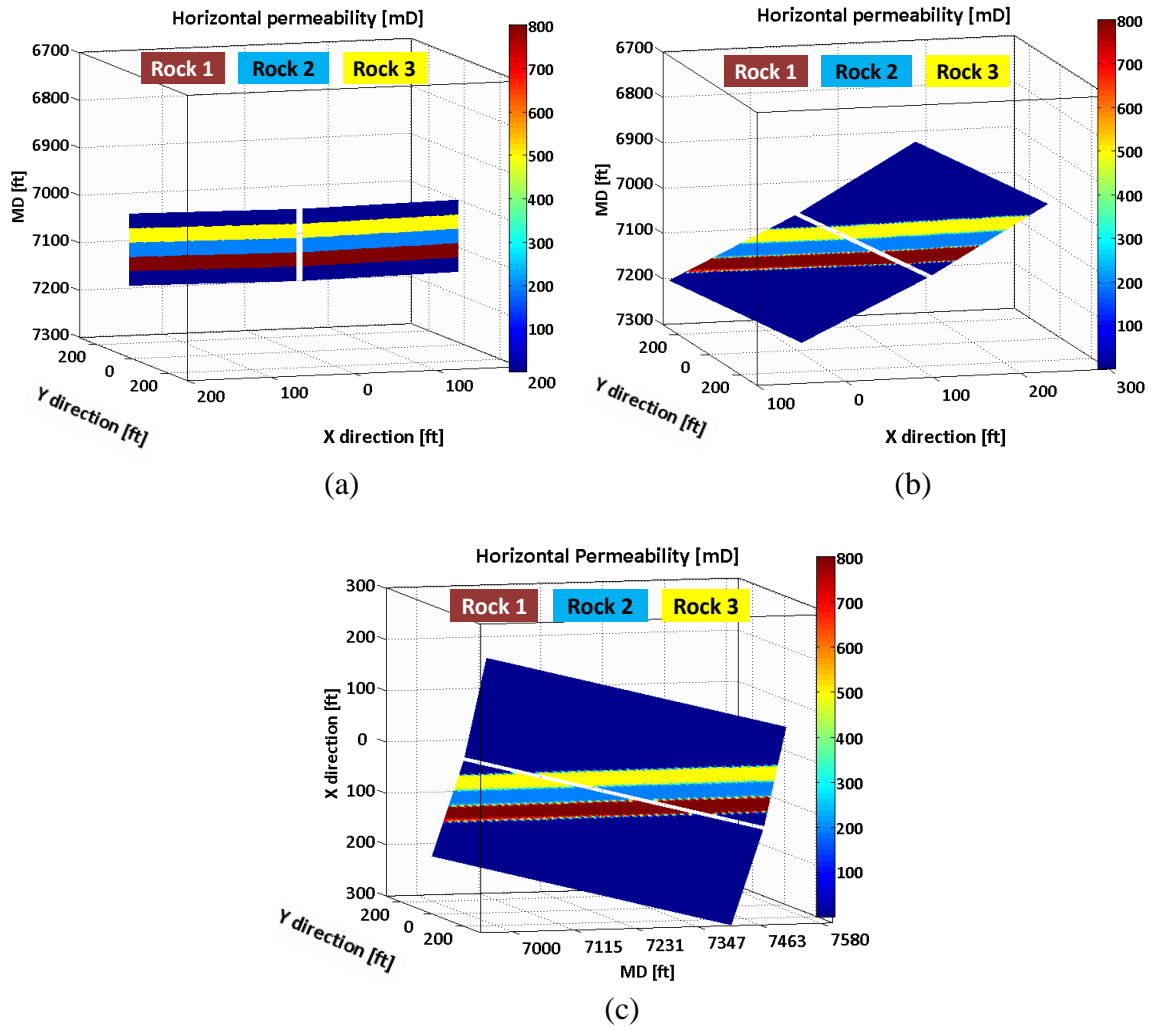


Figure 7.1: Assumed spatial distributions of formation horizontal permeability in the three-layer reservoir model penetrated by boreholes with (a) zero, (b) 45, and (c) 75 degrees of deviation angle. Interpretation of the acquired single-phase production measurements quantifies the sensitivity of PL-derived permeability to permeability anisotropy. The assumed permeability anisotropy (i.e., K_v/K_h) is equal to 0.1 for all cases.

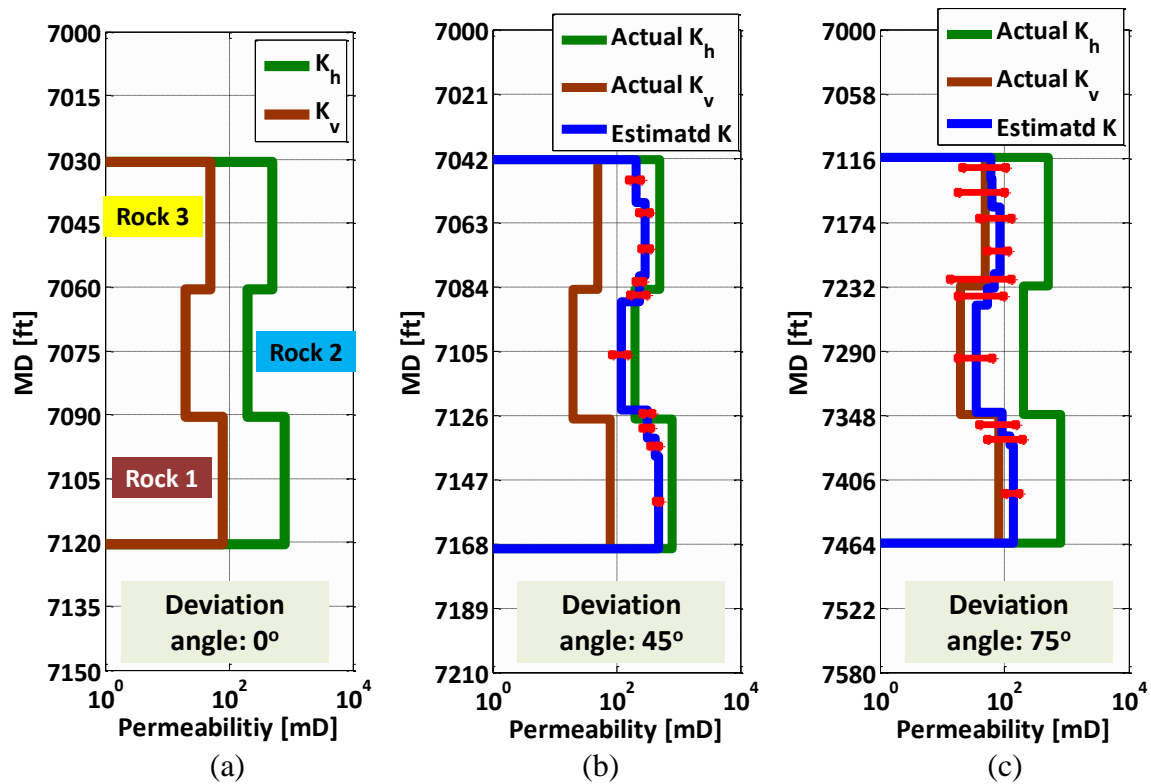


Figure 7.2: Comparison of the estimated and actual depth distribution of permeability for the anisotropic rock formations shown in Figure 7.1. Panel (a) shows actual horizontal and vertical permeabilities. Panels (b) and (c) compare the estimated and actual permeabilities for 45° and 75° borehole deviation angles, respectively. Inclining the borehole causes the estimates of permeability to become more sensitive to permeabilities in the vertical direction.

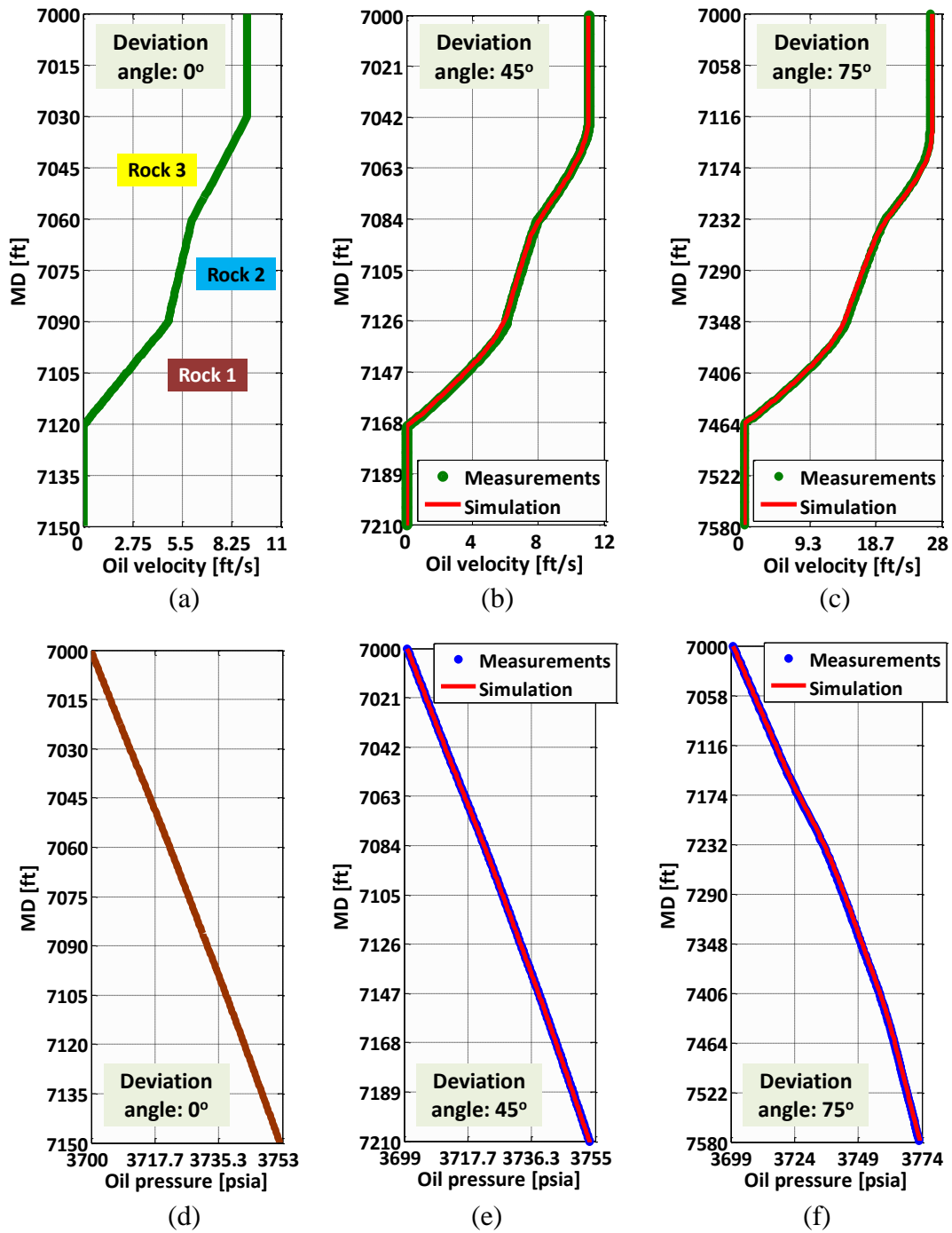


Figure 7.3: Reconstructed depth distributions of oil-phase velocity (Panels a through c) and fluid pressure (Panels d through f) simulated for the anisotropic rock formations shown in Figure 7.1. There is acceptable match between numerically simulated and synthetically measured production logs.

7.3 UPSCALING OF PERMEABILITY

Interpretation of production measurements estimates an average value of permeability associated with thin layers. This section constructs a multilayer reservoir model including several thin layers to quantify the upscaled permeability estimated from production logs. As shown in Figure 7.4, the reservoir consists of 23 layers producing single-phase oil from a vertical borehole. Fluid and borehole properties are identical to those assumed in Table 7.1. Figure 7.5 compares noise-free and noisy measurements of borehole fluid-phase velocity synthetically acquired with PLTs at a downhole flow rate equal to 3100 bopd. The presence of 8% Gaussian random noise masks fine variations of fluid-phase velocity, and thus decreasing the vertical resolution of borehole fluid measurements. The diagnostic process is carried out under the assumption of 1, 8, and 12 petrophysical layers in the forward reservoir model.

When PL interpretation is performed using a single petrophysical layer, the estimated permeability yields an average permeability associated with all the fluid-producing rock formations. Therefore, it is expected to obtain identical well-test- and PL-derived permeabilities. Therefore, downhole pressure-transient measurements are synthetically acquired to estimate average permeability of the reservoir. Figure 7.6 shows the semi-log plot of borehole fluid pressure as a function of time. The slope of borehole pressure associated with early times (equal to -60 psi/log cycle) is used to compute formation average permeability from the following formula (Peters, 2012):

$$K_{\text{avg}} = -\frac{162.6Q_o\mu_o}{mh}, \quad (7.2)$$

where K_{avg} is average permeability, Q_o is oil flow rate, μ_o is oil viscosity, h is formation thickness, and m is the slope of borehole pressure in the semi-log plot. Substituting the corresponding values in Equation 7.2 yields

$$K_{\text{avg}} = -\frac{162.6 \times 3100 \times 0.8}{(-60) \times 11.5} = 584.4 \text{ mD} . \quad (7.3)$$

The estimated permeability from production logs (Figure 7.7a) is equal to 564.7 mD indicating a relative error less than 4% when compared to well-test-derived permeability. Figure 7.7 describes depth variations of the estimated permeability when 1, 8 and 12 petrophysical layers are assumed in the forward reservoir model. Refining the petrophysical layers gives rise to more accurate permeability estimates compared to that estimated with the single-layer model. However, the presence of noise increases non-uniqueness of PL inversion, thereby decreasing the estimation reliability.. This exercise concludes that there is an optimum length scale to refine petrophysical layer that depends on the presence of measurement noise across thin layers.

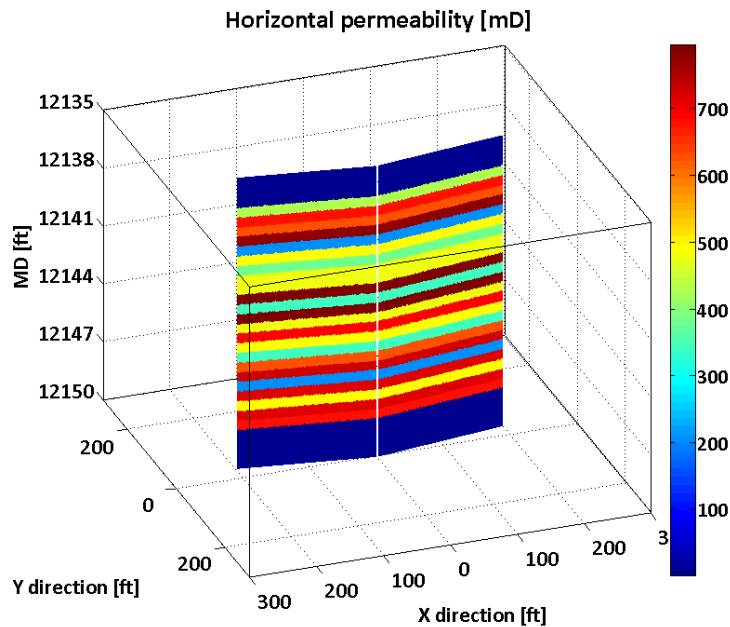


Figure 7.4: Assumed spatial distribution of permeability in the multilayer reservoir model ($K_v/K_h=1$). The reservoir consists of 23 thin layers penetrated by a vertical borehole. Numerical simulation of production measurements is performed using 1, 8 and, 12 petrophysical layers.

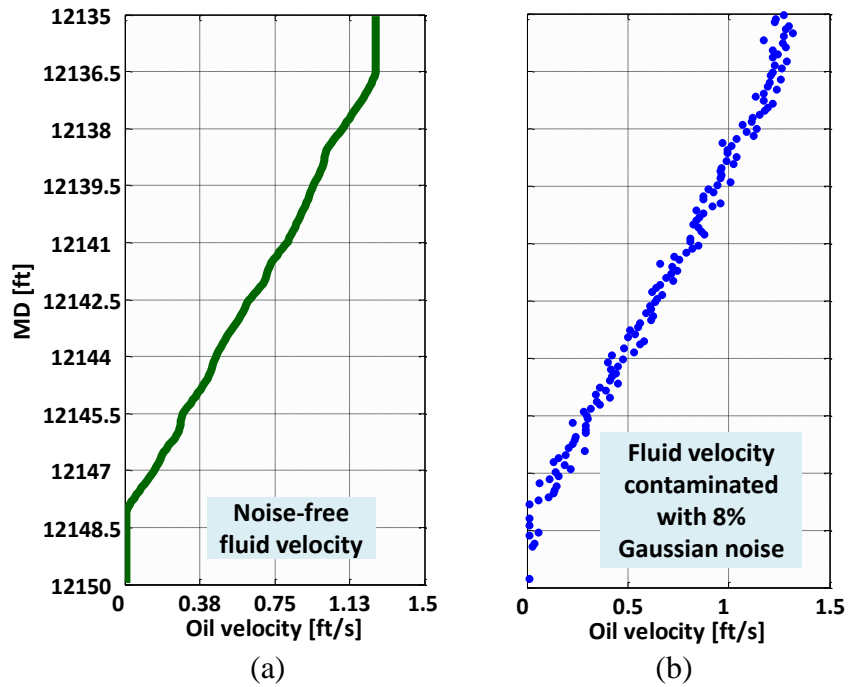


Figure 7.5: Numerically simulated depth distributions of (a) noise-free, and (b) noisy borehole oil velocity, acquired across the multilayer reservoir model shown in Figure 7.4.

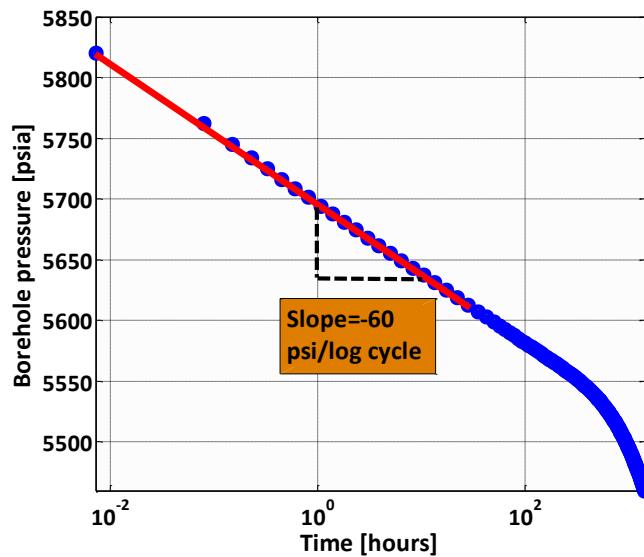


Figure 7.6: Transient behavior of borehole pressure as a function of time for the multilayer reservoir model shown in Figure 7.4. Equation 7.2 is invoked to compute well-test-derived average permeability of all the fluid-producing layers.

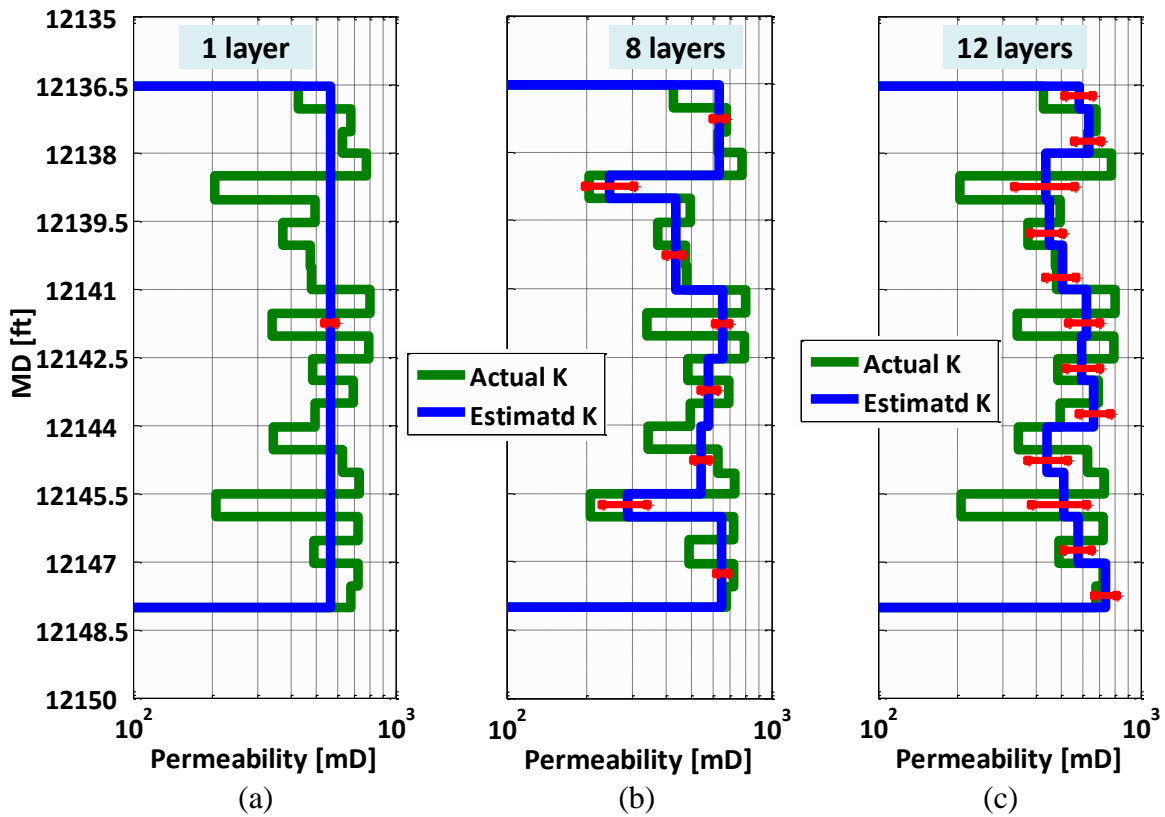


Figure 7.7: Comparison of the estimated and actual depth distributions of permeability for the multilayer reservoir model with (a) 1, (b) 8, and (c) 12 petrophysical layers. The estimated permeability from single-layer reservoir model matches well-test-derived permeability with approximately 4% accuracy. Refining the forward model improves the accuracy of permeability estimation. However, refined petrophysical layers involve larger uncertainty bounds into permeability estimation caused by presence of random noise in production measurements.

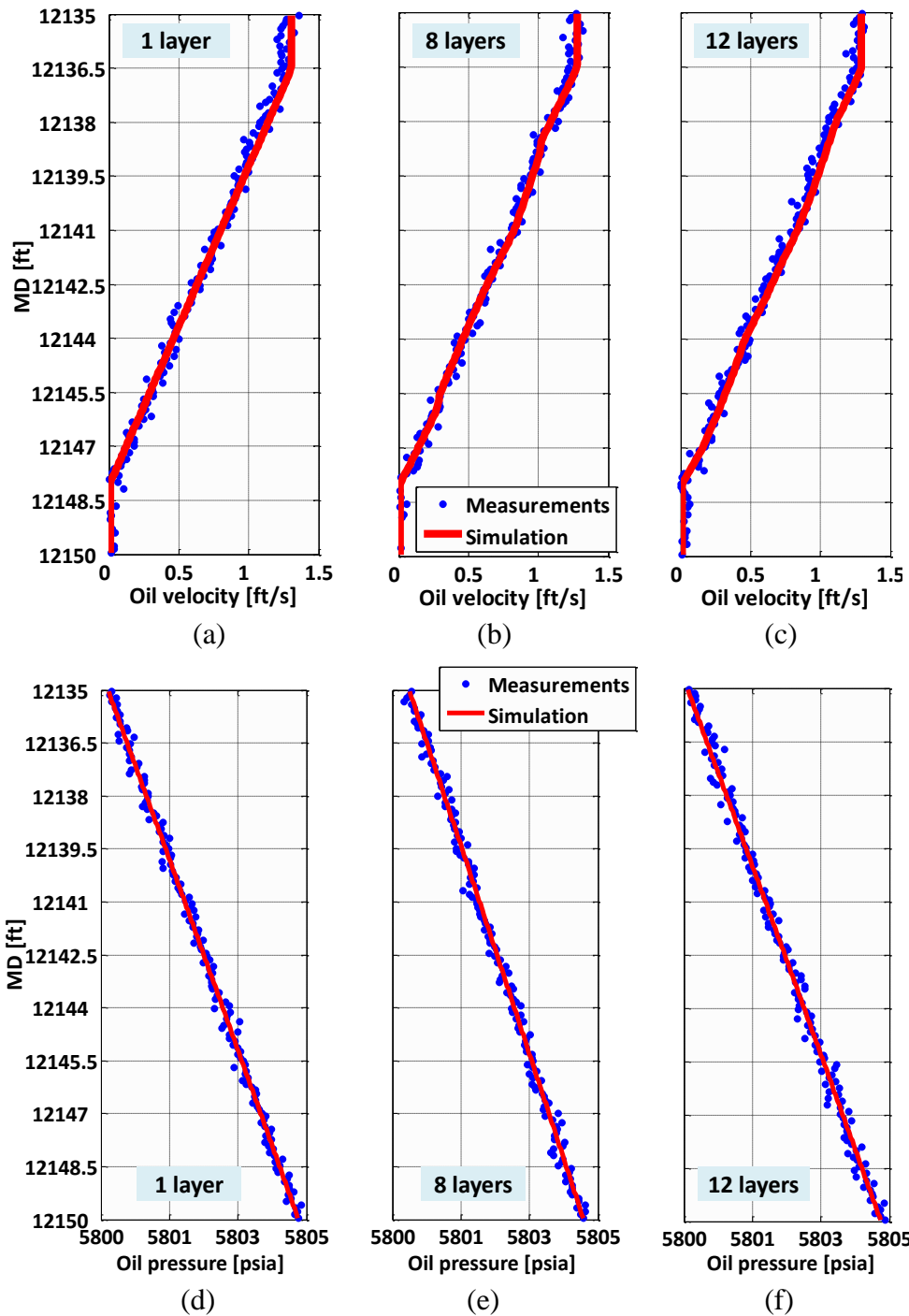


Figure 7.8: Reconstructed depth distributions of oil velocity (Panels a through c) and fluid pressure (Panels d through f) simulated for the anisotropic rock formations shown in Figure 7.1. There is acceptable match between numerically simulated and synthetically measured borehole production measurements.

7.4 SENSITIVITY OF PRODUCTION LOGS TO MEASUREMENT NOISE

Conditions of turbulent flow in the borehole cause random movements of production logging tools that introduce random noise to production measurements. Non-physical variations of borehole measurements originating from measurement noise lower the reliability of estimated petrophysical properties. To quantify noise effects, I construct a synthetic multilayer reservoir model consisting of 4 petrophysical layers with variable layer thicknesses. Subsequently, single-phase and two-phase production logs are synthetically acquired and analyzed to quantify the sensitivity of PL interpretation to the presence of Gaussian and non-Gaussian noise in measurements. As Figure 7.9 shows, the multilayer reservoir under consideration consists of four rock formations with different permeabilities, porosities and thicknesses. Fluid and borehole properties are identical to those described with Table 7.1.

7.4.1 Single-Phase Flowing Systems

In single-phase flowing systems, non-physical fluctuations of borehole fluid-phase velocity adversely influence the physical variations of fluid velocity caused by layer fluid production. In addition, fluid-producing layers with low permeability (and low thickness) inherently generate low variations on fluid velocity that can be entirely masked by measurement noise. Figure 7.10 describes the synthetically acquired borehole measurements across the single-phase reservoir model. The lowest slope on fluid velocity curve is associated with Rock 4 that is classified as a thin layer with a low permeability (i.e., 50 mD). On the other hand, Rock 1 with a high value of permeability (i.e., 800 mD) gives rise to the largest variation of borehole fluid velocity. Production measurements are contaminated with 5% Gaussian and skewed Gaussian noises. Subsequently, the iterative diagnostic process is invoked to estimate permeability from PL inversion.

As shown in Figures 7.11 and 7.12, uncertainty involved with the estimated layer permeability increases with decreasing layer thickness. Furthermore, the presence of skewed Gaussian noise in borehole measurements gives rise to an overestimation of formation permeability. Table 7.3 quantifies that interpretation of noisy production logs associated with Rock 4 involves more than 170% error when compared to the actual permeability for that rock. However, the estimated permeability associated with Rock1 is quantified within 9% of the corresponding actual value. Significant uncertainty involved with estimated permeability of thin layers is associated with non-uniqueness of inversion procedure in the presence of noise. Figure 7.12 shows that the cost function associated with Rock 4 (i.e., slope of fluid velocity across that rock) exhibits the lowest sensitivity to formation permeability among all fluid-producing rock formations. However, increasing layer thickness results in a measurable sensitivity of fluid velocity to layer permeability, thus lowering the uncertainty involved with permeability estimates.

Permeability [mD]	Rock 1		Rock 2		Rock 3		Rock 4	
	Gaussian	Skewed	Gaussian	Skewed	Gaussian	Skewed	Gaussian	Skewed
Lower bound	737.8	775.5	343.7	369.6	154.2	168.4	5.1	18.2
Upper bound	858.3	869.9	462.5	478.2	245.8	278.5	128.3	138.4
Mean	809.2	835.2	398.4	427.7	197.6	226.4	62.3	85.8
Actual	800.0		400.0		200.0		50.0	

Table 7.3: Sensitivity of estimated permeability with respect to Gaussian and skewed-Gaussian noise on single-phase production logs acquired across the four-layer reservoir model. The thinnest layer (i.e., Rock 4) shows more than 170% error involved with the estimates of permeability. On the other hand, the estimated permeability for Rock 1 (with the thickness equal to 30 ft and permeability equal to 800 mD) is within 9% of the actual value.

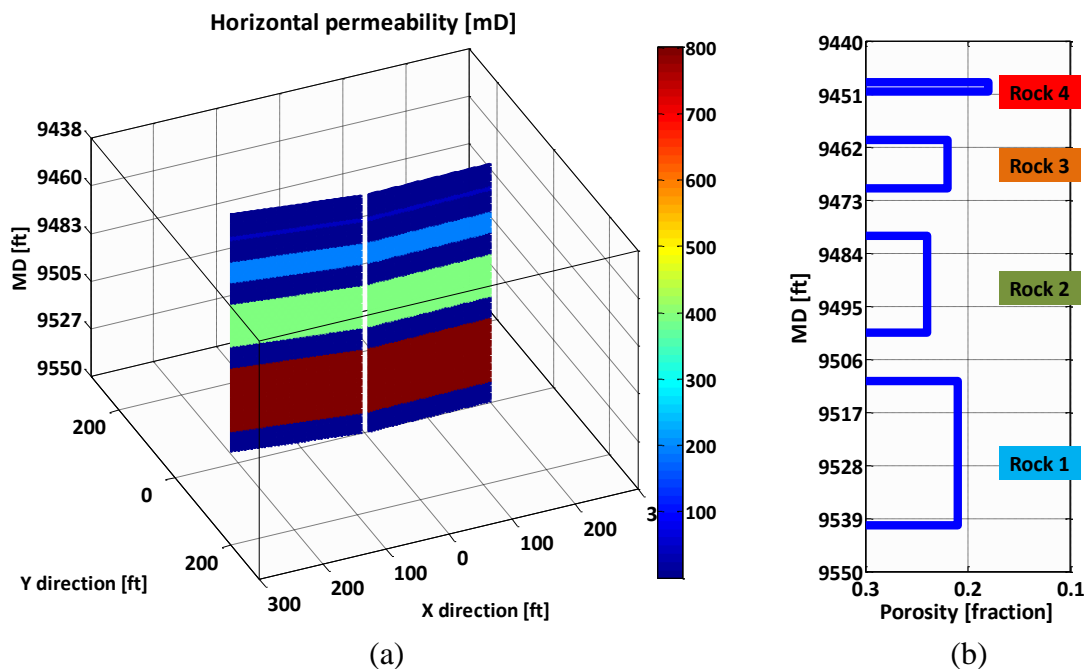


Figure 7.9: Spatial distributions of (a) permeability ($K_v/K_h=1$), and (b) total porosity assumed for uncertainty analysis of PL interpretation across the four-layer single-phase reservoir model.

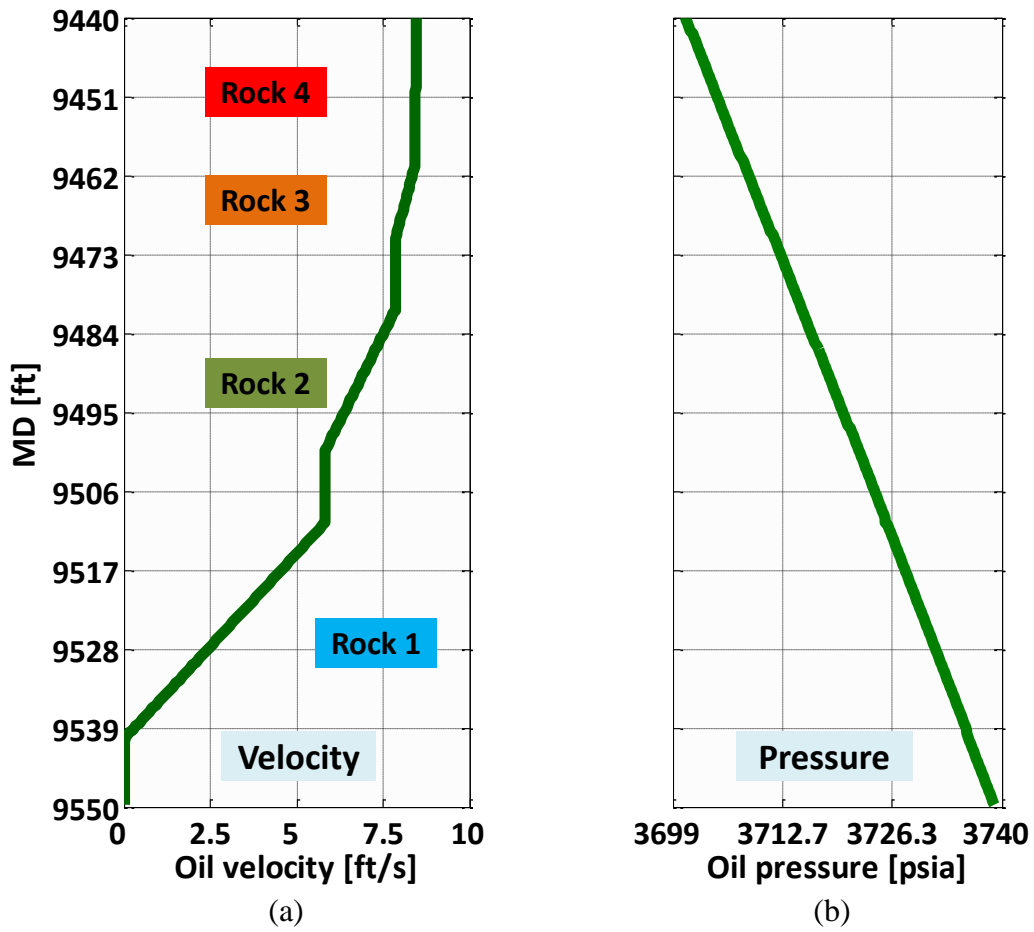


Figure 7.10: Numerically simulated spatial distributions of (a) oil velocity, and (b) borehole pressure for the four-layer single-phase reservoir model. Oil velocity shows the lowest variation across Rock 4, thus making PL interpretation of that rock highly sensitive to measurement noise.

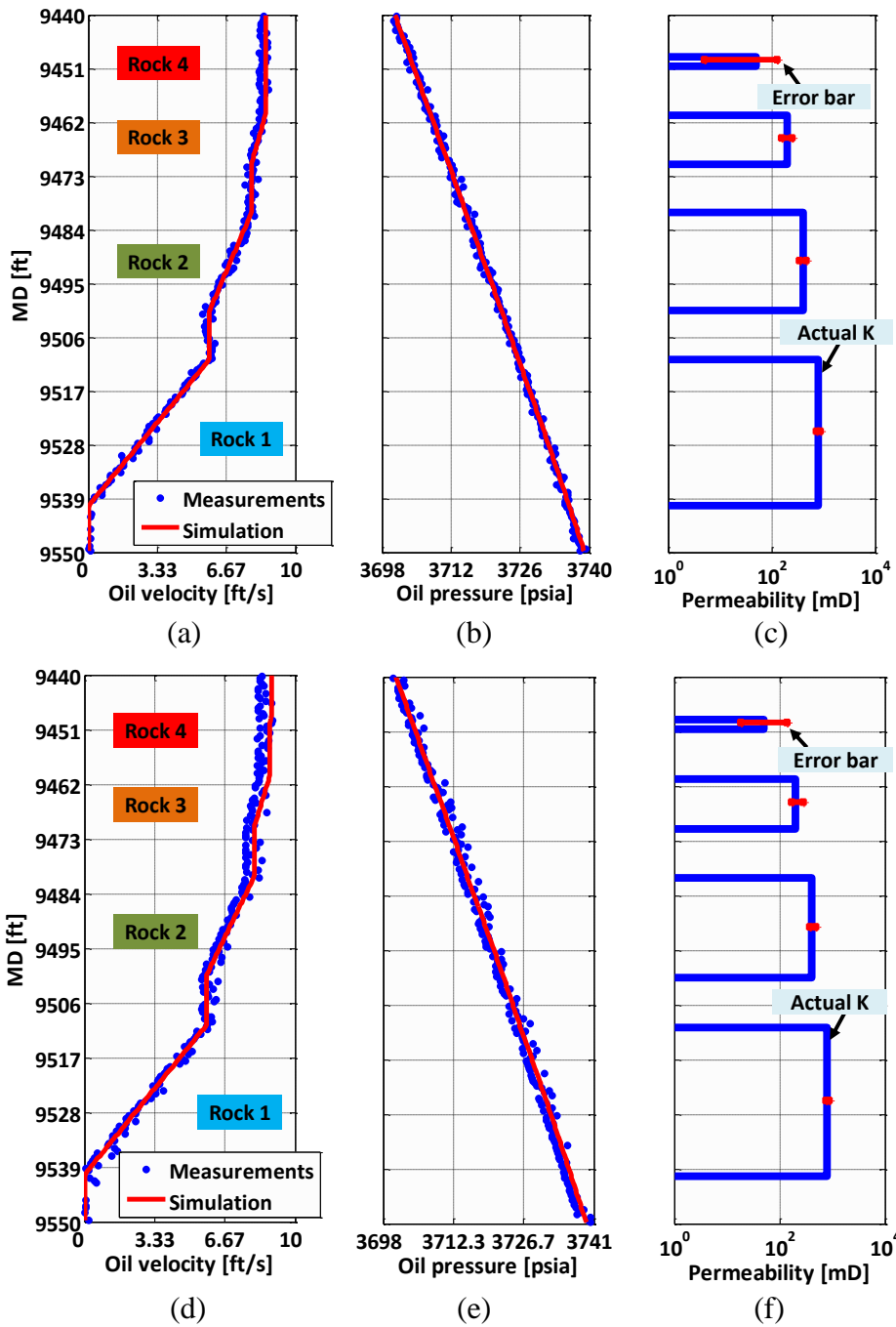


Figure 7.11: Reconstruction of borehole oil-phase velocity and pressure measurements contaminated with (Panels a and b) Gaussian, and (Panels d and e) skewed Gaussian noise, for the four-layer single-phase reservoir model. Panels (c) and (f) describe the associated estimation uncertainty. Because of a low fluid inflow rate across Rock 4, PL interpretation of that rock involves the largest uncertainty bounds into permeability estimation.

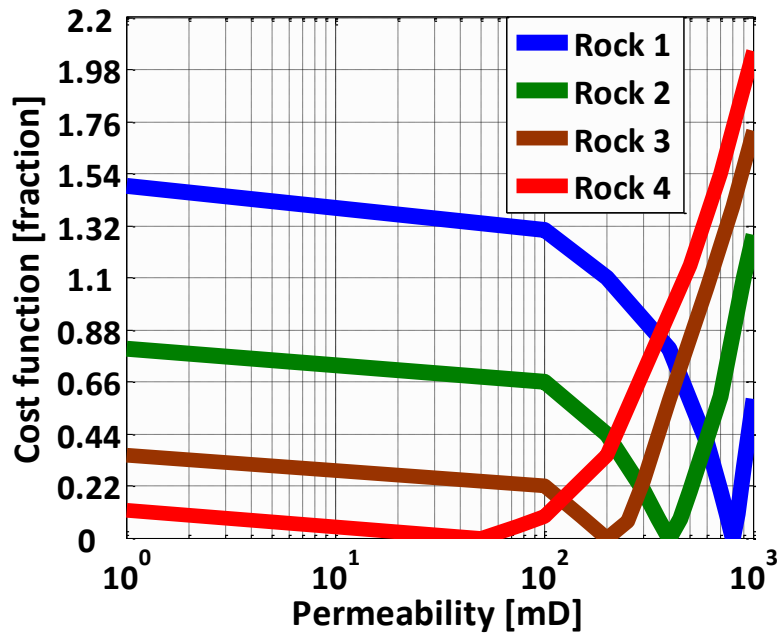


Figure 7.12: Sensitivity of the computed quadratic cost function to layer permeability in the four-layer single-phase reservoir model. Rock 1 with a large thickness exhibits a sharp minimum at the corresponding permeability (namely, 800 mD), thus making favorable conditions for permeability estimation. However, the low sensitivity of Rock 4 to its permeability makes that rock largely sensitive to measurement noise.

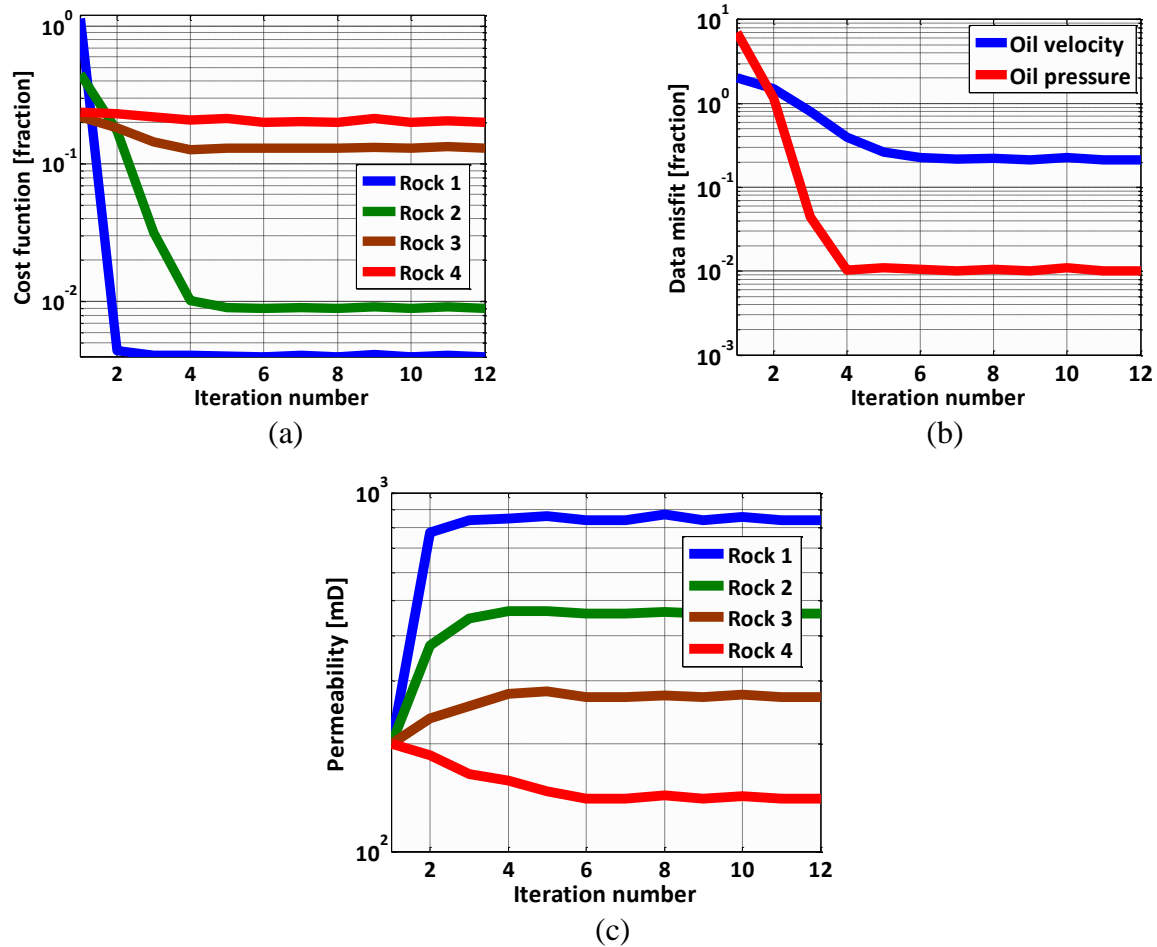


Figure 7.13: Convergence of (a) cost function, (b) 2-norm of data misfit (defined with Equations 6.4 and 6.8), and (c) permeability as a function of iteration number. The final refined properties are achieved after 11 iterations.

7.4.2 Two-Phase Flowing Systems

Interpretation of two-phase production logs requires simultaneous estimation of near-borehole formation permeability and fluid-phase saturation. Because of a larger number of unknown formation properties compared to equivalent single-phase flowing systems, diagnostic process of two-phase production logs involves more uncertainty into the inverted petrophysical properties. As described in Section 6.2, this dissertation

develops a new PL inversion algorithm that defines separate cost functions for inversion of permeability and fluid-phase saturation. In addition, reconstruction of borehole production measurements is carried out by dividing the borehole flowing domain into a representative number of depth windows. The window-by-window reconstruction of production logs selectively increases sensitivity of formation petrophysical properties to borehole fluid measurements, thereby improving reliability of the inverted petrophysical properties.

The multilayer reservoir model constructed in Section 7.4.1 is additionally studied to investigate the accuracy and reliability of PL inversion in presence of two fluid phases. I simulate simultaneous production of the water and oil phases with properties summarized in Table 7.1. Figures 7.14a and b describe the assumed saturation-dependent relative permeability and capillary pressure. Spatial distribution of near-borehole water saturation (Figure 7.14c) shows that Rock 2 is nearly entirely saturated with water phase, while Rock 3 is mainly an oil-bearing layer. On the other hand, Rock 1 and Rock 4 are partially saturated with the two fluid phases, thus yielding measureable oil and water production across those layers (Figures 7.14d and 7.15a). Synthetically acquired production measurements are shown in Figure 7.15. Fluid mixture velocity, oil-phase holdup, and fluid pressure are contaminated with 8% Gaussian and non-Gaussian noise to perform the estimation.

Interpretation of two-phase production logs shows that uncertainty involved with the inverted petrophysical properties originates from (i) presence of noise in measurements, and (ii) conditions of immovable fluid saturation in rock formations. As shown in Figure 7.16, the estimated water saturation in Rock 4 (namely, rock with the lowest thickness) contains approximately 15% error when compared to the corresponding actual water saturation. Uncertainty associated with the estimated water saturation for

Rock 4 mainly originates from the presence of Gaussian noise in measurements of oil holdup that is additionally propagated to the estimated permeability of that rock. Furthermore, conditions of immovable water saturation in Rock 2 leads to approximately 11% error in the estimate of water saturation, and 17% error in the estimate of permeability. On the other hand, measurable oil and water production from Rock 1 makes it possible to estimate water saturation and permeability within 8% and 7% accuracy, respectively. Figure 7.17 indicates less than 11% error for fluid mixture velocity, 4% error for fluid pressure, and 7% error for oil-phase holdup when compared to the corresponding synthetically acquired values.

Figure 7.18 and 7.19 describe the effect of skewed Gaussian noise on the estimated petrophysical properties. Results show that additive skewed-Gaussian noise causes an overestimation of formation water saturations and permeabilities. In particular, mean values of estimated water saturation and permeability, in the presence of 8% skewed Gaussian noise for Rock 4, are approximately 18% and 165% larger than the corresponding actual values, respectively. The high uncertainty for permeability of Rock 4 is associated with the low sensitivity of borehole production measurements with respect to petrophysical properties across that rock. As Figure 7.20 quantifies, the cost function computed for water saturation of Rock 4 exhibits nearly zero sensitivity around its water saturation (i.e., $S_w = 0.6$). The low sensitivity of borehole measurements to water saturation gives rise to a significant influence of noise, thus yielding uncertain estimates of petrophysical properties.

In two-phase flowing systems, uncertainty associated with the estimated water saturation additionally propagates to estimates of permeability. The propagation of error results in a larger uncertainty for estimated petrophysical properties in contrary to equivalent single-phase flowing systems. The interpretation algorithm developed in this

dissertation progressively refines formation water saturation and permeability of rock formations to minimize the propagation of error in the presence of two fluid phases. Figure 7.21 compares the cost function calculated for permeability of Rock 1 when a-priori assumptions are made for the value of water saturation in that rock. Results show that presence of a second fluid phase decreases reliability and accuracy of PL inversion process by (i) shifting the estimated permeability toward higher values, and (ii) lowering the sensitivity of borehole measurements with respect to permeability. Specifically, (wrong) assumption of water saturation equal to $S_w = 0.2$ (instead of 0.05) in Rock 1 results in overestimation of the permeability of that rock up to 20.8%.

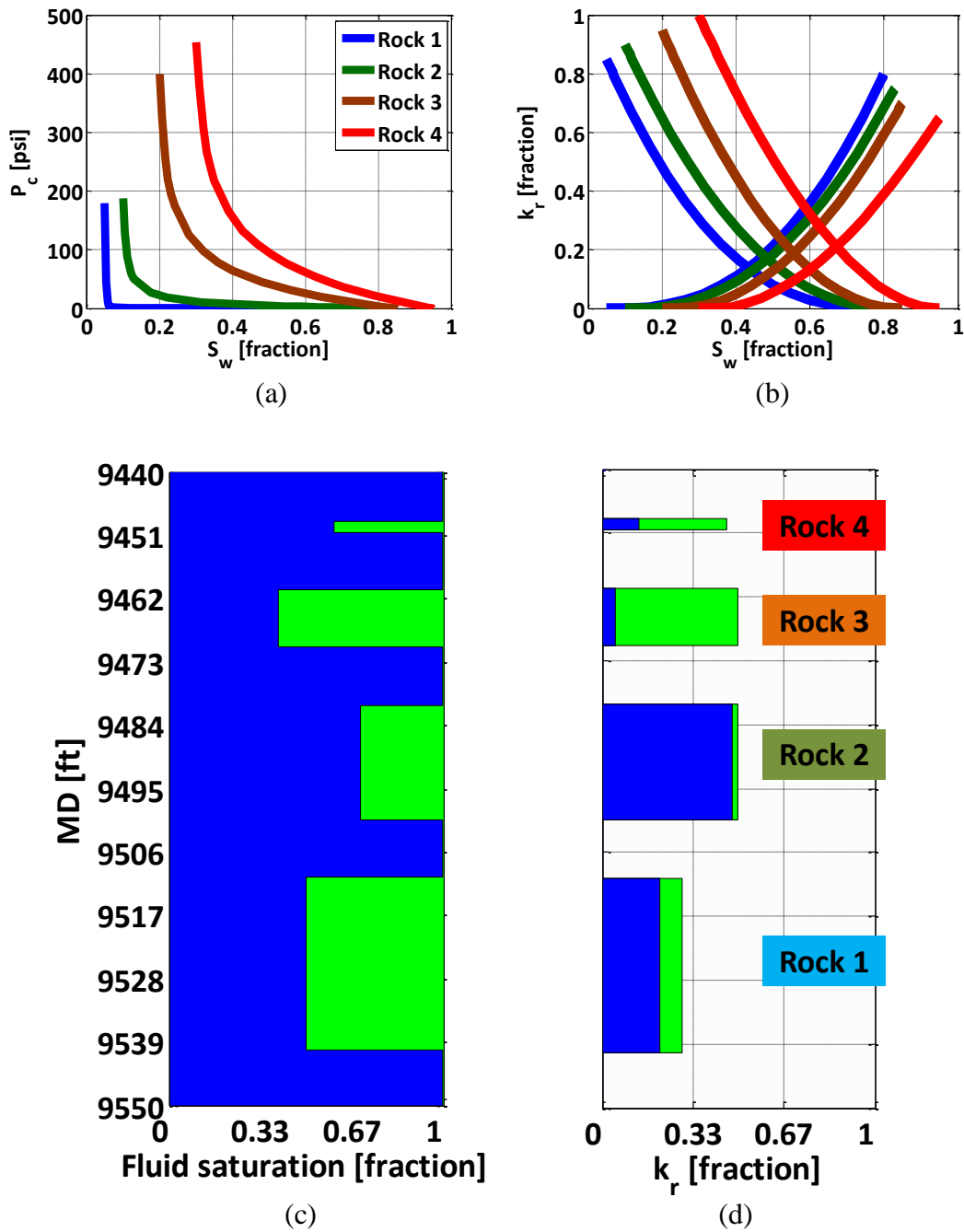


Figure 7.14: Assumed saturation-dependent (a) relative permeability, and (b) capillary pressure for uncertainty analysis of PL interpretation in the four-layer two-phase reservoir model. Panels (c) and (d) show the assumed spatial distributions of formation water saturation and relative permeability.

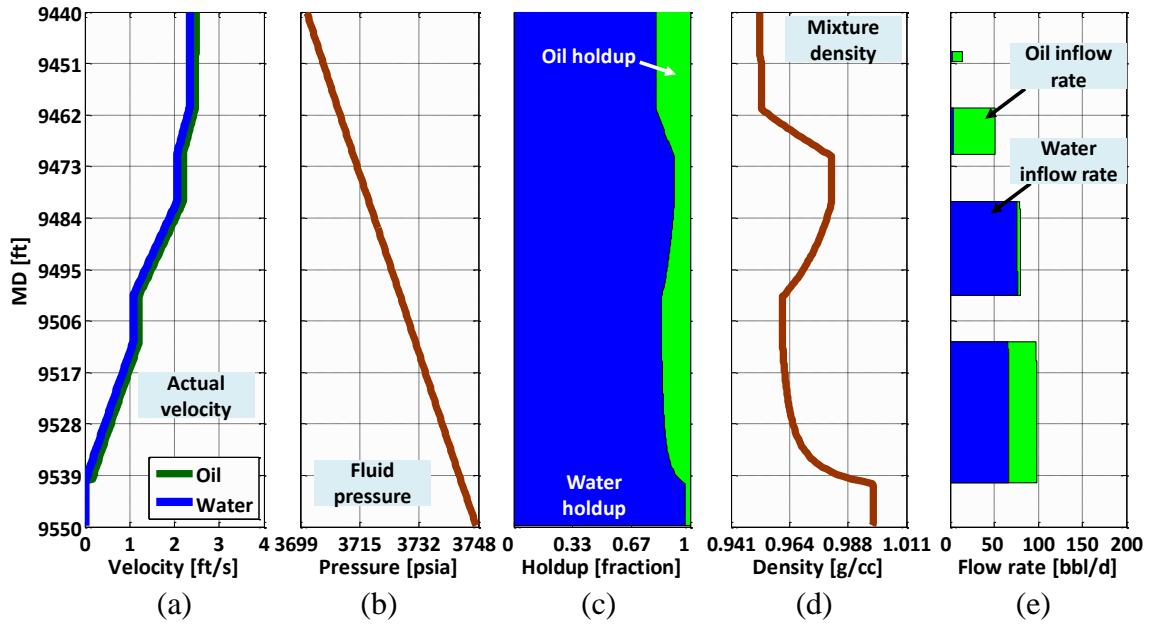


Figure 7.15: Numerically simulated depth distributions of borehole (a) fluid mixture velocity, (b) fluid pressure, (c) fluid holdup, (d) fluid mixture density, and (e) fluid inflow rate. Rocks 3 and 4 primarily produce hydrocarbon, while Rock 2 mainly contributes to water production. Fluid velocity, holdup, and pressure are used for the estimation of near-borehole water saturation and permeability.

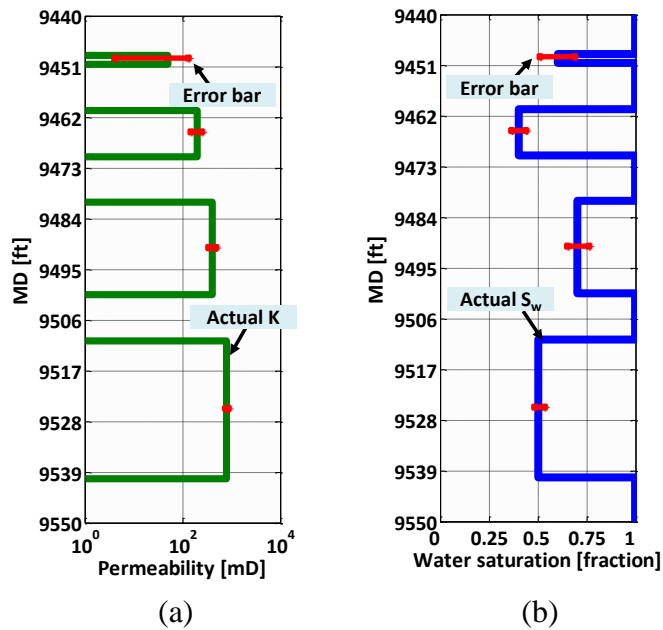


Figure 7.16: Uncertainty bounds for estimated (a) permeability, and (b) water saturation to quantify the effects of Gaussian noise on PL interpretation of the four-layer two-phase reservoir model.

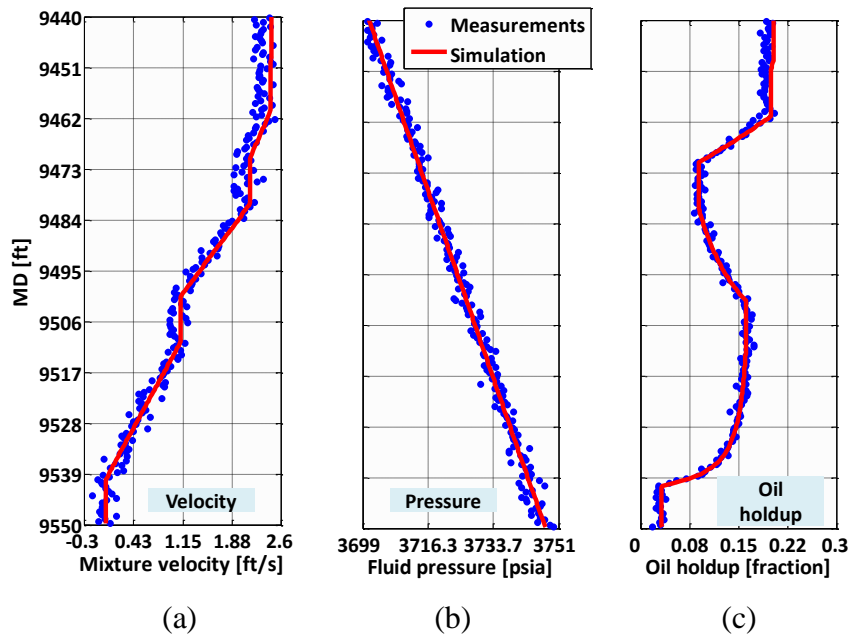


Figure 7.17: Reconstruction of borehole (a) oil-phase velocity, and (b) pressure in the presence of 8% additive Gaussian noise for the four-layer two-phase reservoir model.

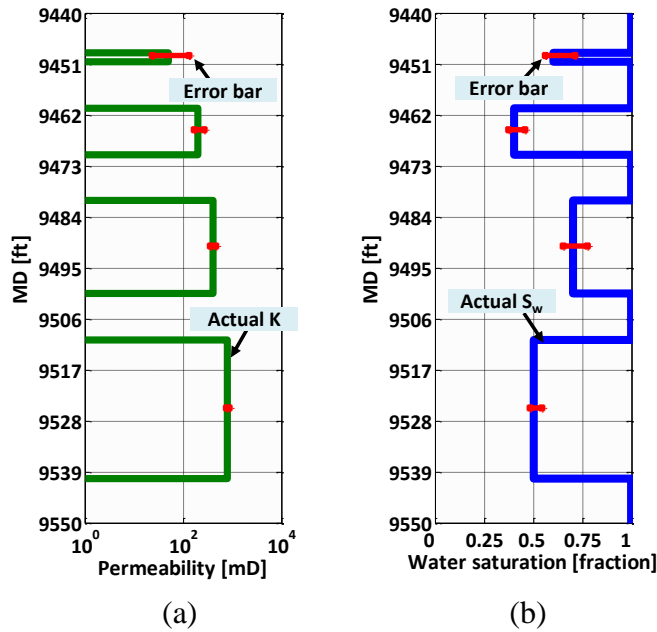


Figure 7.18: Uncertainty bounds for estimated (a) permeability, and (b) water saturation to quantify the effects of skewed-Gaussian noise on PL interpretation of the four-layer two-phase reservoir model.

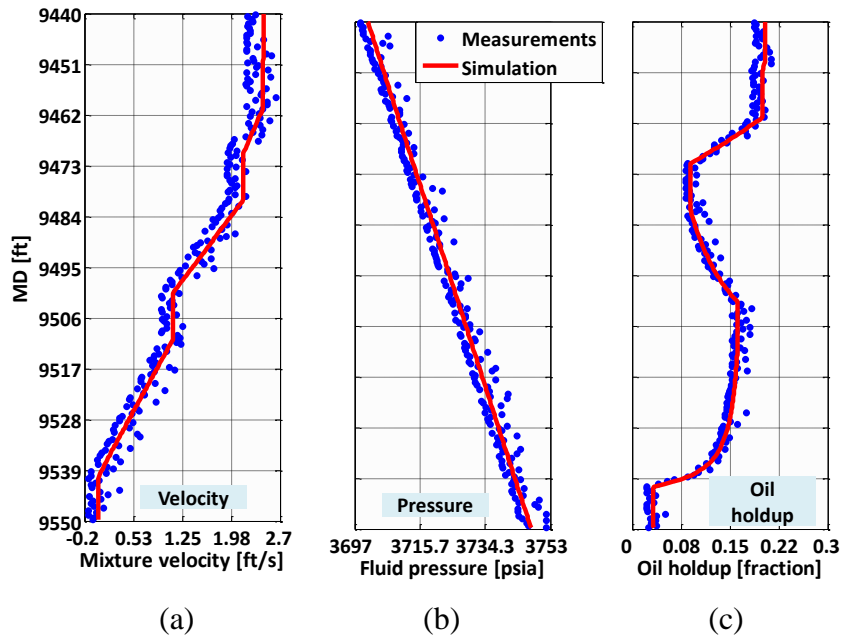


Figure 7.19: Reconstruction of borehole (a) oil-phase velocity, and (b) pressure in the presence of 8% additive skewed-Gaussian noise for the four-layer two-phase reservoir model.

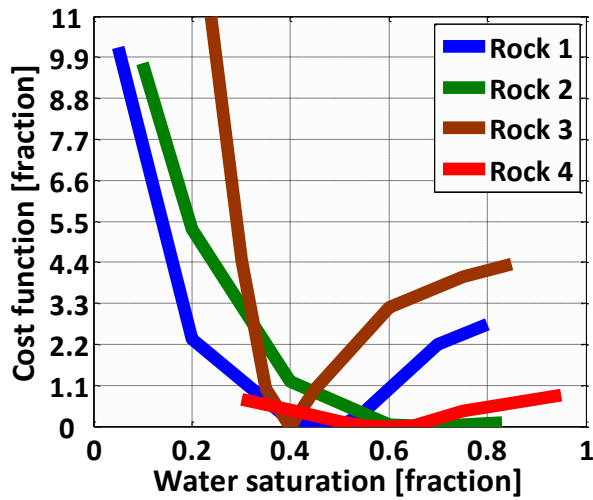


Figure 7.20: Quadratic cost function computed based on borehole water holdup as a function of water saturation (namely, Equation 6.5) for rock formations in the four-layer two-phase reservoir model. Conditions of immovable water saturation in Rock 2 cause a low sensitivity of fluid holdup to water saturation of that layer. Identical to single-phase flow, Rock 1 exhibits a sharp minimum at the associated water saturation. The lowest sensitivity corresponds to the thinnest layer with the lowest permeability (i.e., Rock 4).

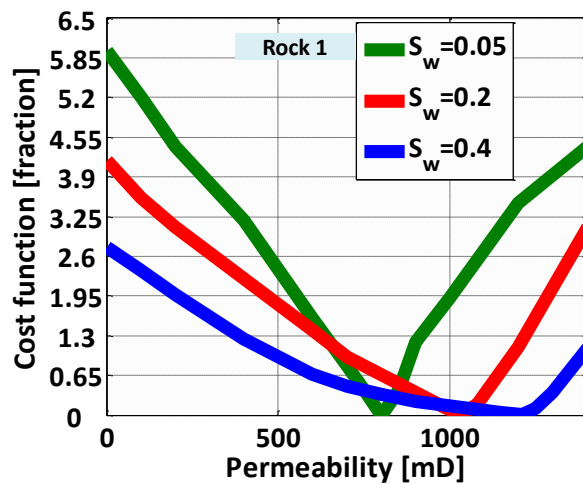


Figure 7.21: Quadratic cost function computed based on borehole fluid velocity and water holdup as a function of permeability (i.e., Equation 6.3) for Rock 1 in the four-layer two-phase reservoir model. The actual near-borehole water saturation of Rock 1 is 0.05. Overestimation of water saturation causes (i) shifting the estimated permeability toward higher values, and (ii) lowering the sensitivity of borehole measurements with respect to permeability.

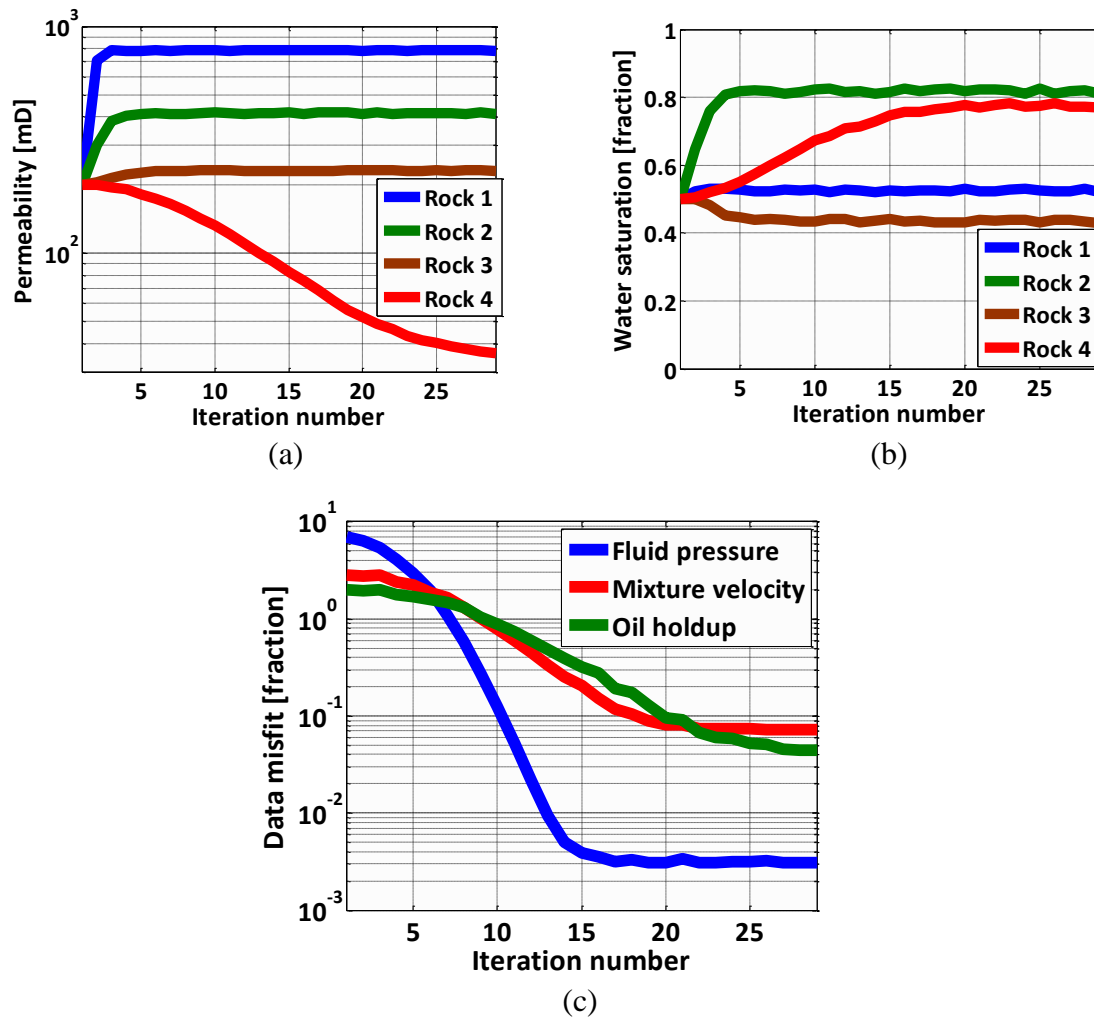


Figure 7.22: Convergence of (a) permeability, (b) water saturation, and (c) 2-norm of data misfit (defined with Equations 6.4, 6.6, and 6.8) in the presence of 8% additive skewed-Gaussian noise. The final refined properties are achieved after 27 iterations.

7.5 SYNTHETIC EXAMPLE

Discrepancies between borehole fluid-production measurements acquired at different time lapses are associated with the alteration of near-borehole petrophysical properties. Borehole production measurements acquired from one time lapse can be compared to those from a preceding lapse to quantify variations of near-borehole

petrophysical properties over the elapsed time. The synthetic example constructed in this section investigates the possibility of quantifying near-borehole formation permeability and fluid saturation by simulating and integrating oil-water production logs acquired in time-lapse mode.

7.5.1 General Assumptions

Unknown petrophysical properties considered for PL inversion include near-borehole permeability and water saturation. The interpretation algorithm assumes availability of formation average pressure, temperature, porosity, capillary pressure, relative permeability, bed boundary depths, bed dips, fluid-phase density, and fluid-phase viscosity. To minimize uncertainty of formation pressure, (synthetic) acquisition of borehole measurements at each time lapse is performed when the reservoir reaches its average pressure. This assumption requires an adequate duration of shut-in prior to measurement acquisition.

The synthetic example integrates production logs acquired in time-lapse mode to quantify near-borehole formation damage. In this interpretation method, average permeability estimated from a preceding time lapse is defined as formation far-field permeability required for interpretation of the next time lapse. The inversion algorithm is subsequently invoked to estimate formation near-borehole permeability. Comparison between near-borehole and far-field permeabilities is next performed to quantify the developed formation damage in vicinity of the borehole over the elapsed time.

Implementation of near-borehole permeability is carried out by constructing a cylindrical region of altered permeability in vicinity of the borehole. I subsequently apply Hawkin's (1956) relationship to quantify formation damage (stimulation) as

$$S = \left(\frac{K_{ff}}{K_{nw}} - 1 \right) \text{Ln} \left(\frac{r_s}{r_w} \right), \quad (7.4)$$

where S is total skin factor, k_{nw} is near-borehole permeability, k_{ff} is far-field permeability, r_s is radius of near-borehole region, and r_w is borehole radius. A layer-by-layer method is additionally used to populate water saturation in the three-dimensional reservoir model. This method constructs layers with constant water saturation radially away from the borehole to estimate depth variations of water saturation along the borehole axial direction.

7.5.2 Model Description

The synthetic example under consideration consists of three hydraulically-connected rock formations saturated with oil ($\rho_o=0.85$ g/cc, $\mu_o=0.835$ cp, and $C_o=10$ μ sip) and water ($\rho_w=1$ g/cc, $\mu_w=1$ cp, and $C_w=3$ μ sip). Figure 7.23 describes the petrophysical properties assumed for various fluid-producing rock formations. Rock 1 is a low-permeability layer exhibiting high capillary pressures and high initial water saturations. By contrast, Rock 2 is nearly entirely saturated with the oil phase with a high permeability. All layers exhibit a 25-degree dip penetrated by a vertical borehole with a radius equal to 4.2 inches. An infinite-acting aquifer is located at the bottom of the reservoir (i.e., 22500 ft MD) to maintain the reservoir pressure. Fluid production causes the aquifer to displace the hydrocarbon phase, thereby changing the spatial distribution of formation water saturation over time. The objective of this example is to estimate variations of near-borehole water saturation and skin factor using measurements acquired with PLTs.

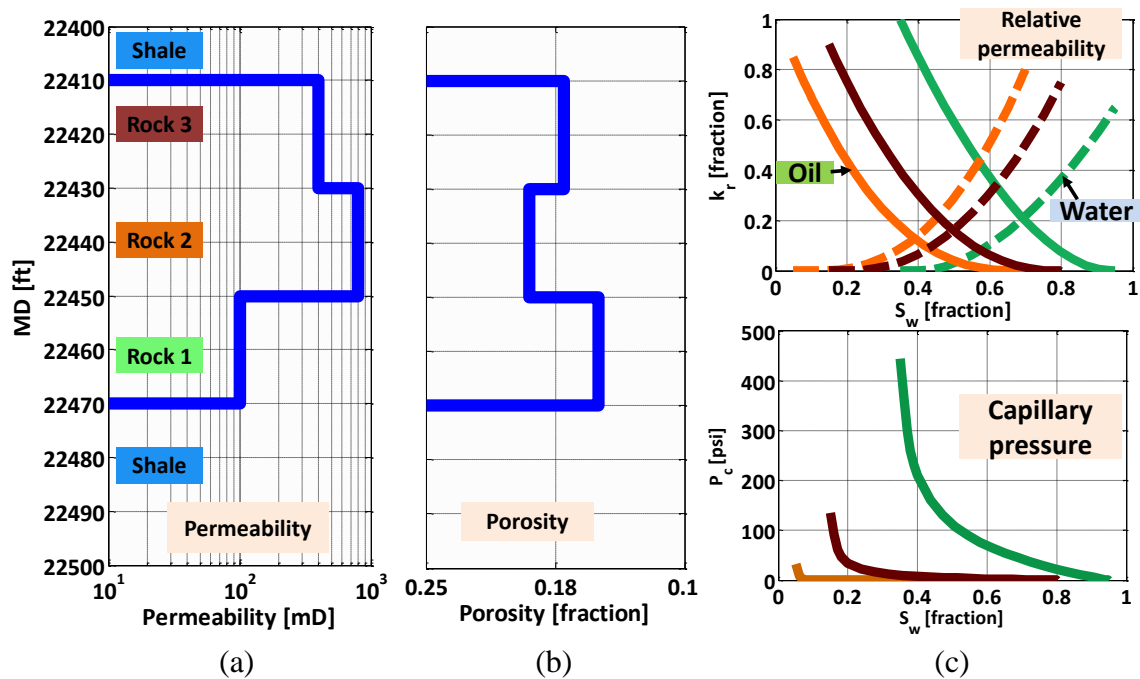


Figure 7.23: Spatial distributions of (a) permeability, (b) porosity, and (c) fluid-phase relative permeability (upper panel) and capillary pressure (lower panel) assumed for time-lapse interpretation of the synthetic example.

7.5.3 Time-Lapse PL Interpretation

The synthetic example considers three time lapses for acquisition and interpretation of borehole production measurements. The spatial distribution of near-borehole permeability associated with each time lapse is synthetically modified to enforce a known distribution of formation damage, while far-field permeabilities remain unchanged over time (Figure 7.24, left panels). Figures 7.25 through 7.27 show spatial distributions of water saturation and formation pressure associated with various time lapses. Because of aquifer encroachment, the immiscible displacement front gradually advances toward the borehole, thus changing near-borehole water saturation. Rock 2 (with a low capillary pressure) exhibits a sharp immiscible displacement front. By

contrast, the displacement front observed in Rock 3 tends to be more smooth and spread out, indicating a higher capillary pressure compared to that of Rock 1. Shape of the immiscible displacement front determines the number of petrophysical layers required to accurately reconstruct near-borehole water saturation.

Figures 7.28 through 7.30 describe borehole fluid-phase velocity, pressure, holdup, density, droplet diameter, and flow patterns simulated for different time lapses. Visual comparison between water holdups shows a gradual increase of water production caused by the continuous advancement of oil-water displacement front. Furthermore, simultaneous production of oil and water results in the development of oil- and water-dominant bubbly flow patterns with a flow-regime inversion taking place at 22440 ft MD (Figure 7.28f). Below that depth, oil-phase behaves as the dispersed fluid phase where droplet coalescence (from bottom to top) leads to the formation of larger (oil) droplets. At 22440 ft MD, flow-regime inversion results in the generation of water droplets whose diameters start to decrease upward. A similar behavior is observed for simulated droplets in second and third time lapses. However, because of higher water productions, inversion points associated with second and third time lapses take place at lower measured depths compared to that of the first time lapse.

The developed interpretation algorithm is invoked to estimate formation near-borehole permeability and water saturation (Figures 7.31 through 7.33). Fluid mixture velocity, pressure, and oil holdup, contaminated with 5% Gaussian noise, are used to perform the inversion. To estimate near-borehole petrophysical properties, I divide the region in vicinity of the borehole into several depth windows. As Figure 7.31 shows for the first time lapse, three spatial windows are specified for the estimation of formation permeability, while 13 windows are used to estimate near-borehole water saturation. Because of null water production from Rock 3, the algorithm makes an explicit

assumption for near-borehole water saturation associated with that rock. This assumption decreases the uncertainty associated with conditions of immovable water saturation in Rock 3, thereby enhancing the numerical stability of PL inversion.

Interpretation of production logs performed for the first time lapse indicates errors lower than 12% and 23% for water saturation and permeability, respectively. Because of a large volume of investigation associated with production logs, inverted water saturation across bed boundaries tends to be the volume-averaged water saturation of the adjacent layers. On the other hand, the reconstructed borehole production measurements show an acceptable match when compared to the actual (synthetic) measurements. Figures 7.31 through 7.33 additionally show the layer-by-layer method adopted in this dissertation to populate formation water saturation.

Inversion of production logs acquired in the second and third time lapses is carried out under the assumption of far-field permeabilities equal to those estimated from the first time lapse. This assumption enables the quantification of formation damage developed over the elapsed time. Figures 7.32d and 7.33d compares the estimated and actual near-borehole skin factors computed from Equation 7.4. Discrepancies between assumed and actual far-field permeabilities are propagated to the estimates of skin factor, thus decreasing accuracy of skin estimation. However, the estimated near-borehole permeability and water saturation show an acceptable agreement when compared to the corresponding actual values. In addition, reconstructed borehole measurements favorably match the corresponding measured values.

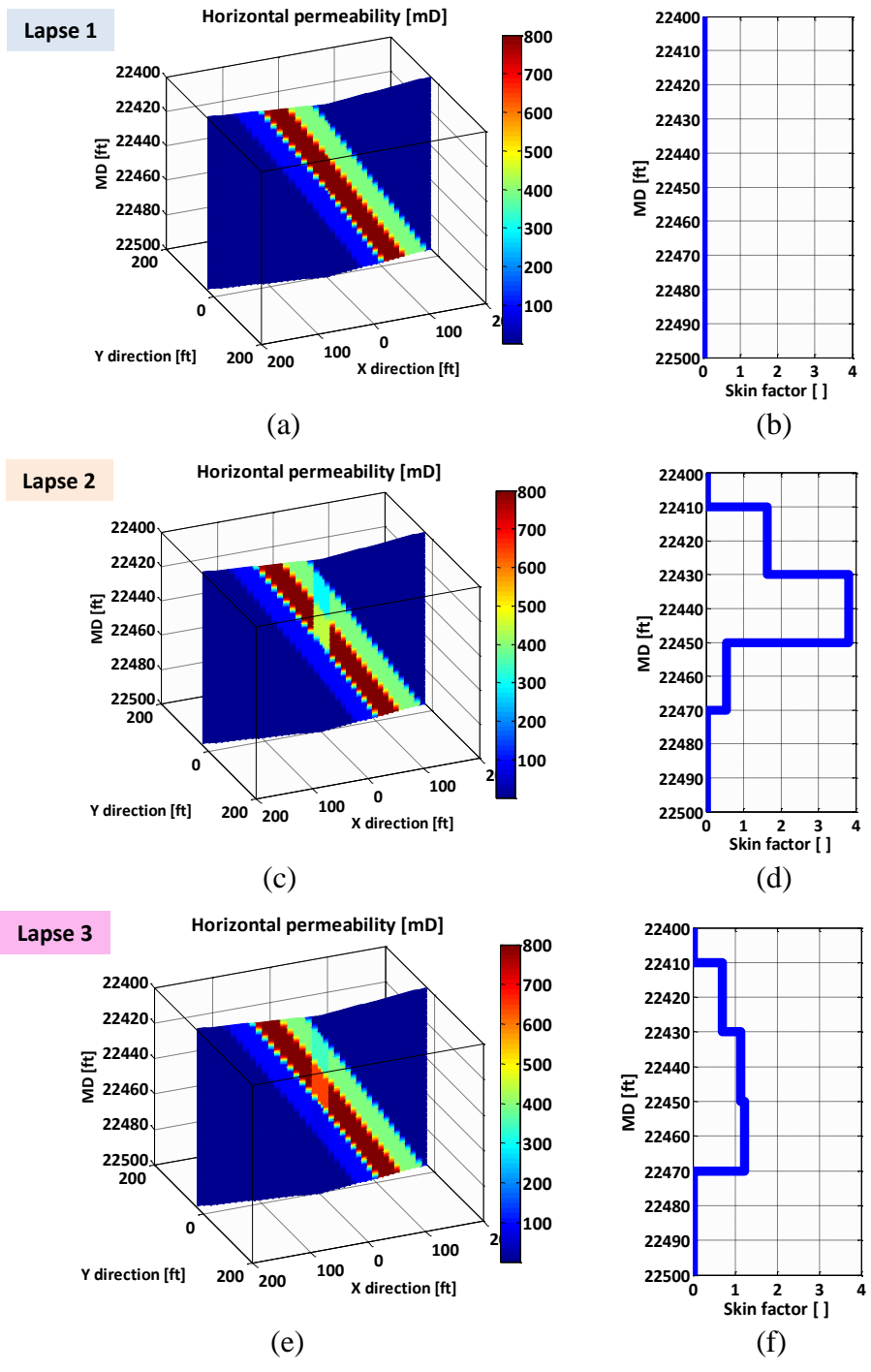


Figure 7.24: Assumed spatial distributions of permeability, and the associated skin factor for (Panels a and b) first, (Panels c and d) second, and (Panels e and f) third time lapses. Implementation of near-borehole formation damages is carried out by modifying permeability of a cylindrical region around the borehole with radius equal to 15 ft.

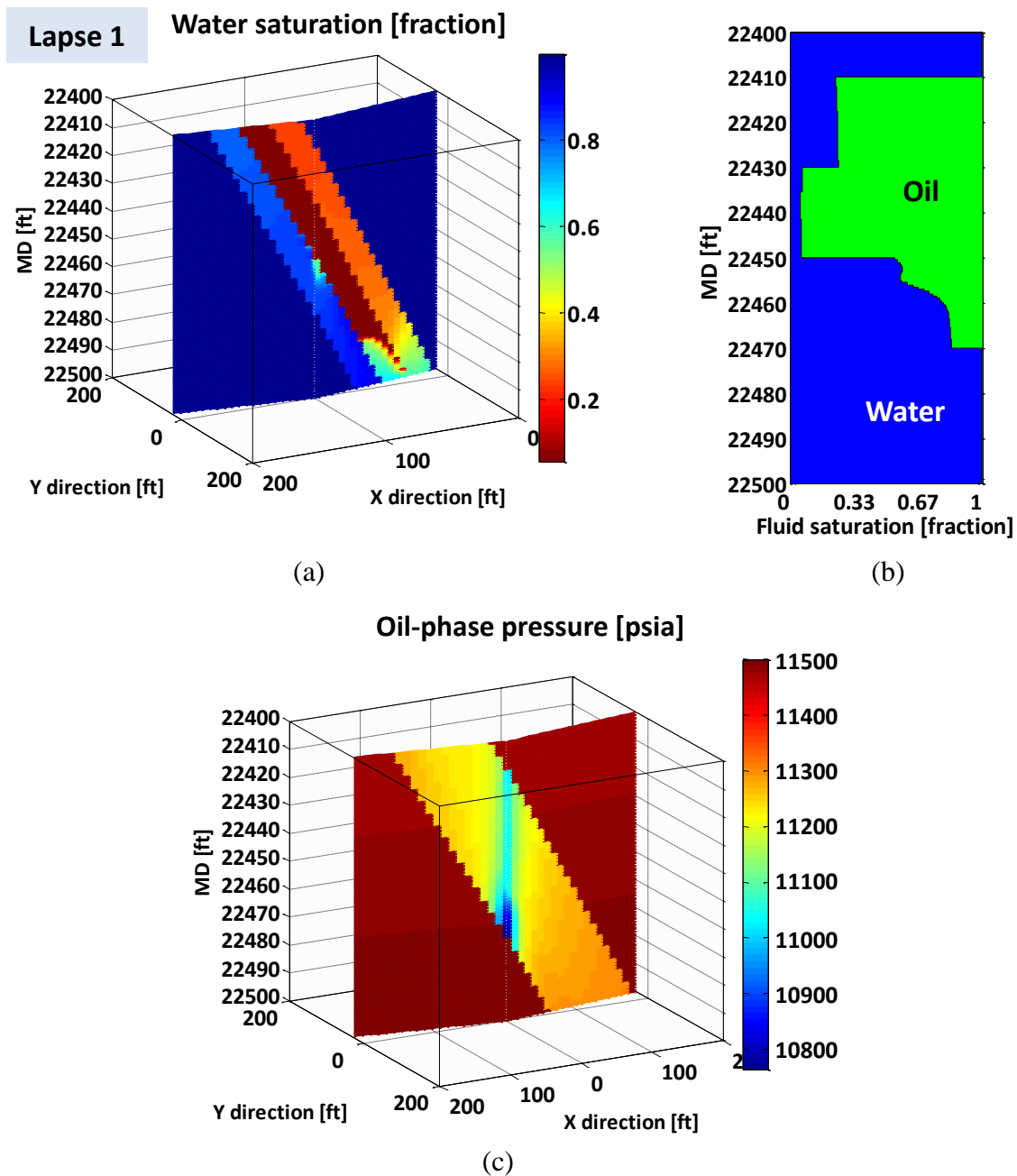


Figure 7.25: Spatial distributions of (a) water saturation, (b) near-borehole fluid saturation, and (c) formation pressure numerically simulated for the first time lapse. Advancement of the water front from the aquifer gives rise to a gradual change of near-borehole water saturation. Acquisition and interpretation of two-phase production measurements attempts to estimate near-borehole formation damage and water saturation.

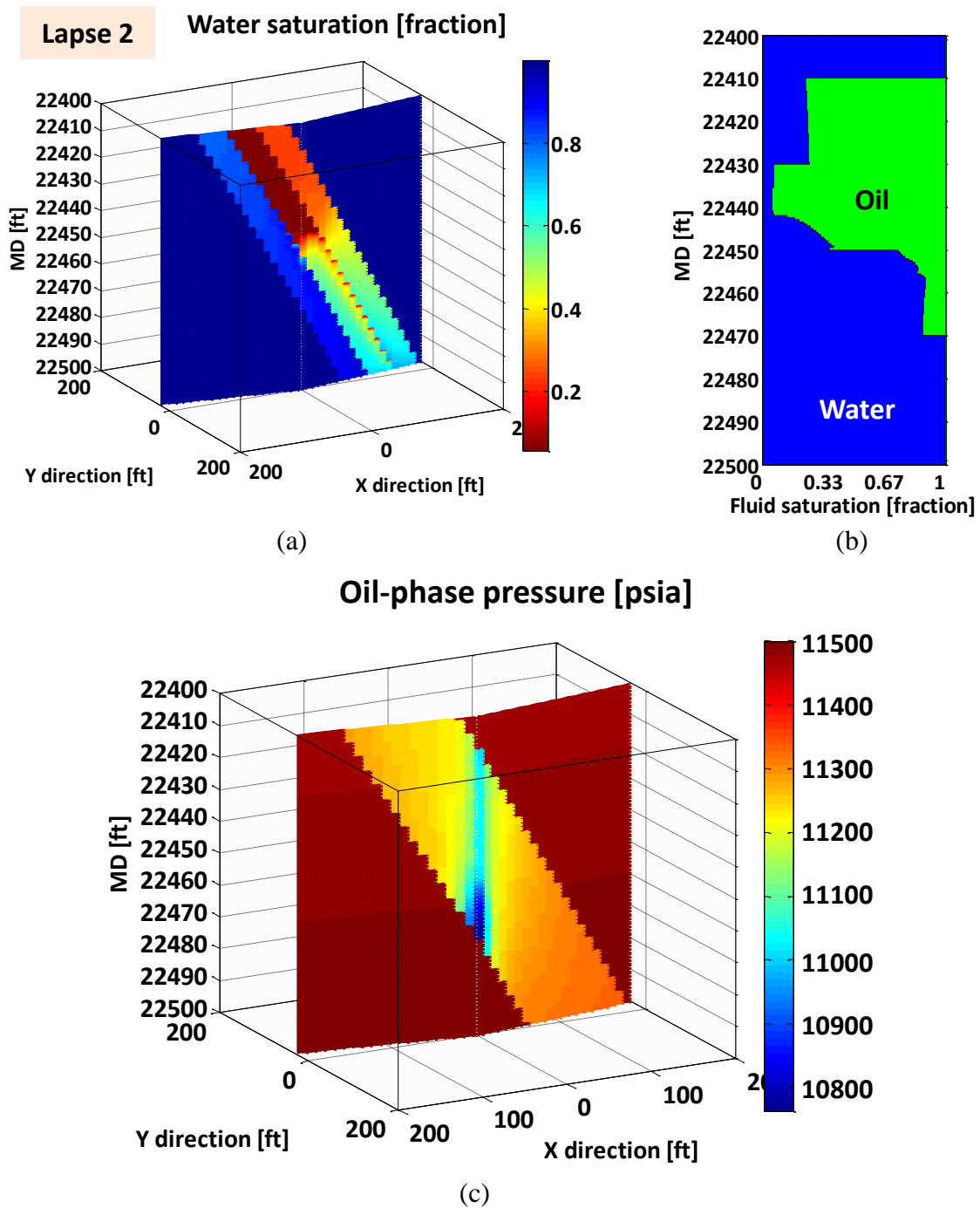


Figure 7.26: Spatial distributions of (a) water saturation, (b) near-borehole fluid saturation, and (c) formation pressure numerically simulated for the second time lapse. At this time lapse, the water front within Rocks 1 and 2 has reached the borehole, while Rock 3 still mainly produces oil phase.

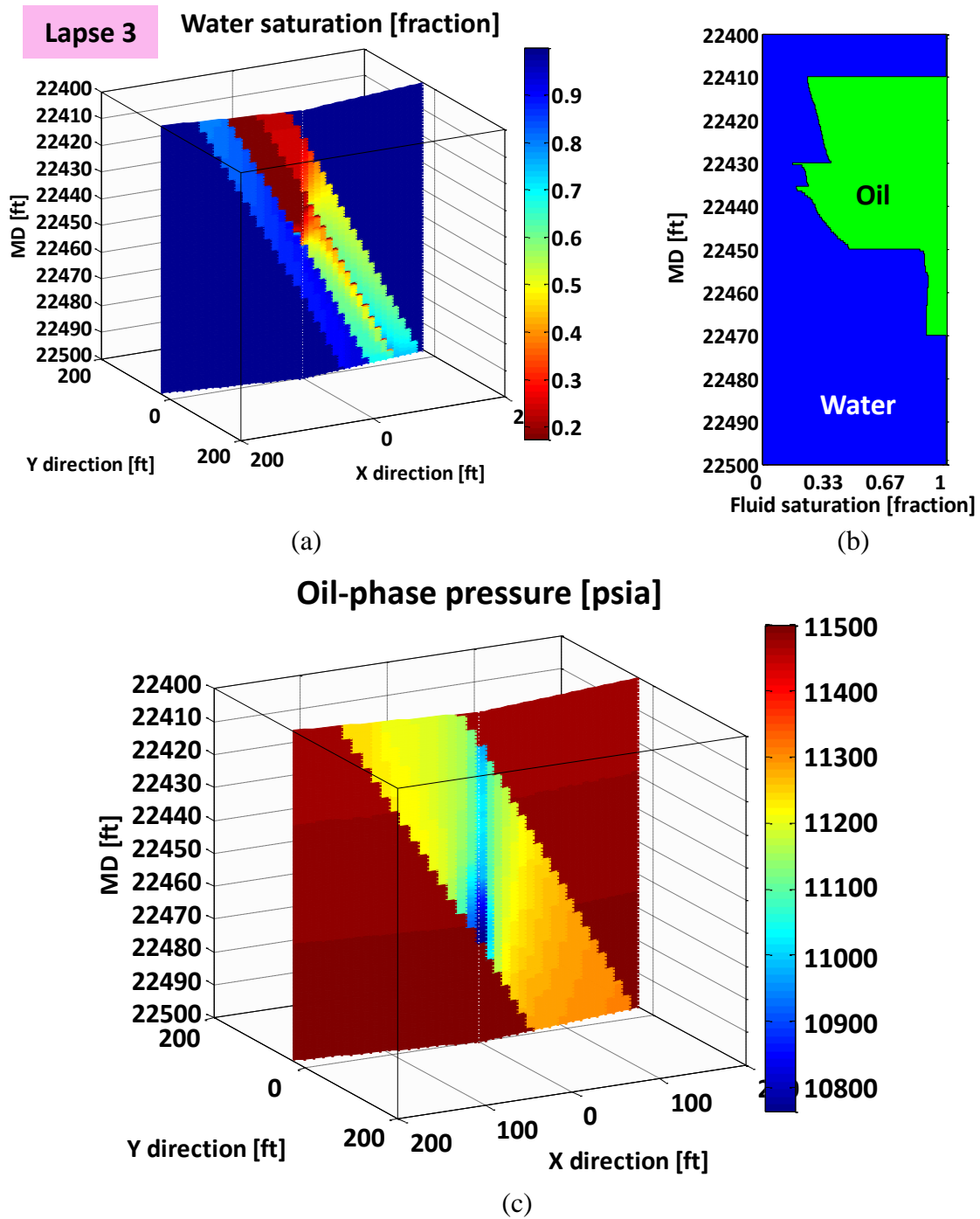


Figure 7.27: Spatial distributions of (a) water saturation, (b) near-borehole fluid saturation, and (c) formation pressure numerically simulated for the third time lapse. At this time lapse, all rock formations are influenced by the immiscible displacement of oil phase.

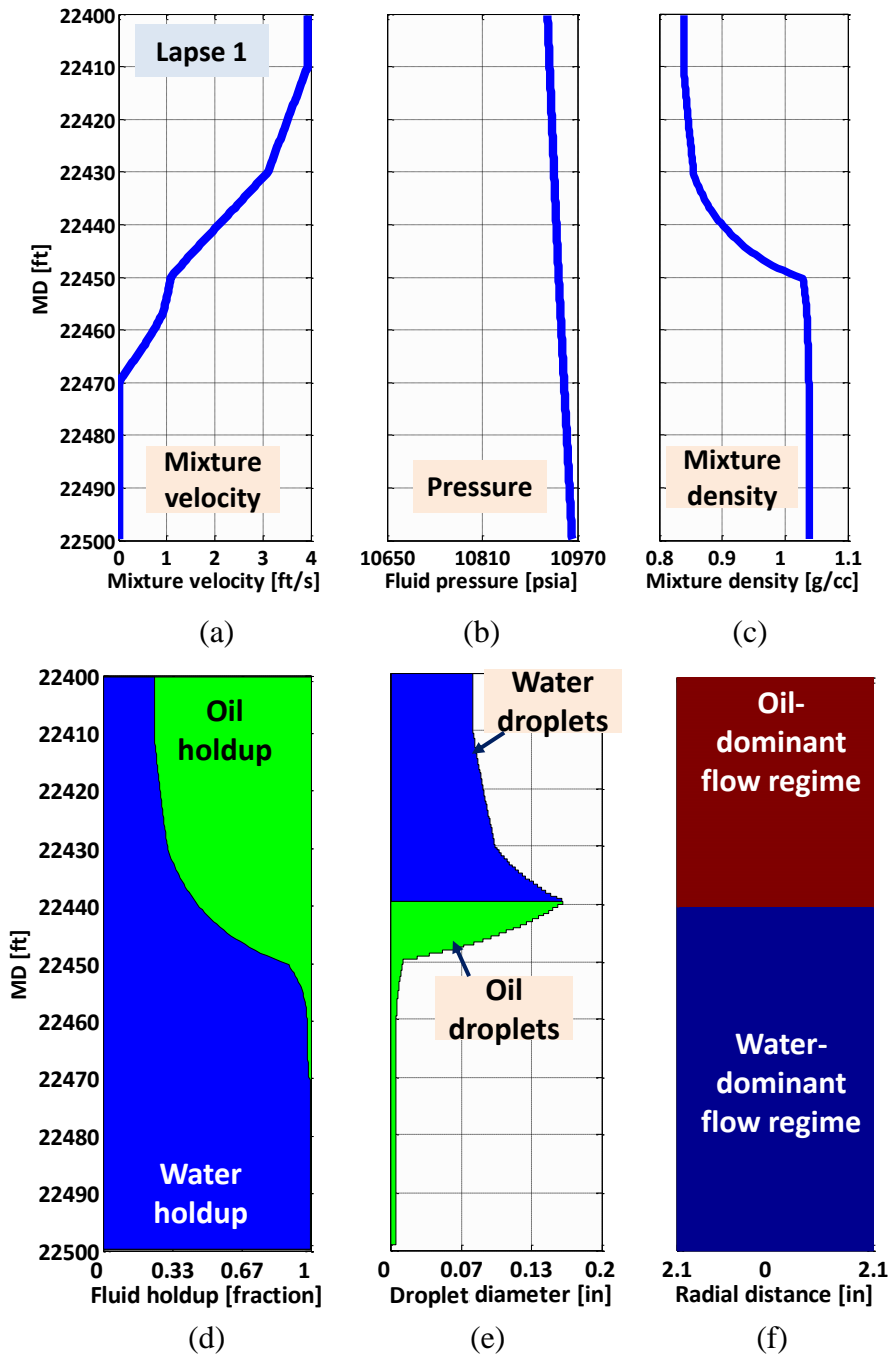


Figure 7.28: Spatial distributions of borehole (a) fluid mixture velocity, (b) fluid pressure, (c) fluid mixture density, (d) fluid holdup, (e) droplet diameter, and (f) fluid flow regime, numerically simulated for the first time lapse. Lower layer is mainly producing water where the associated borehole water holdup across that layer is approximately 1. Hydrocarbon production from Rocks 2 and 3 increases oil holdup that changes borehole fluid flow regime.

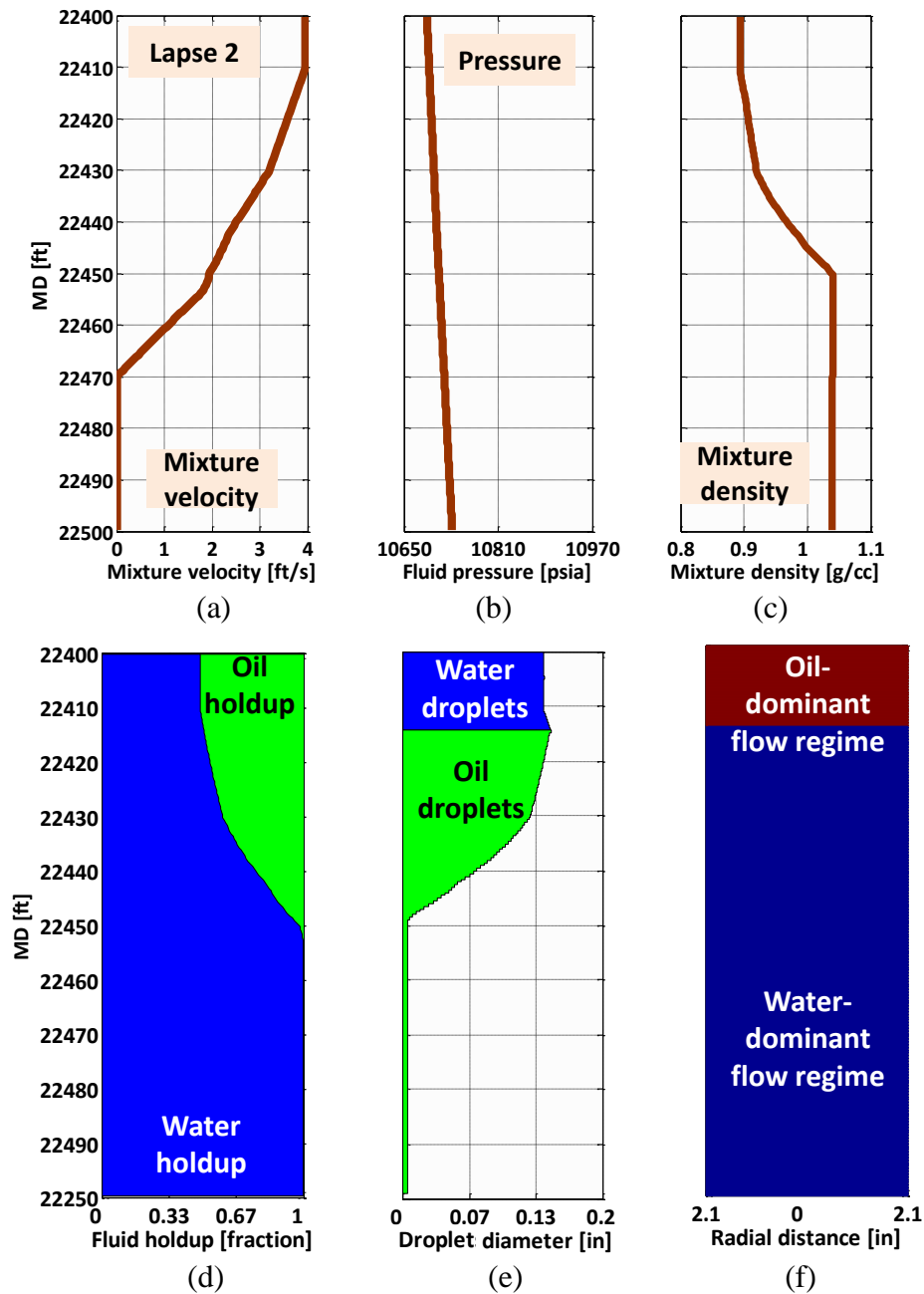


Figure 7.29: Spatial distributions of borehole (a) fluid mixture velocity, (b) fluid pressure, (c) fluid mixture density, (d) fluid holdup, (e) droplet diameter, and (f) fluid flow regime, numerically simulated for the second time lapse. Advancement of the water front causes borehole water holdup to increase from the bottom to the top. Because of higher water holdups, the estimated fluid flow regime is mainly water-dominant bubbly flow regime. Variations of fluid mixture velocity and fluid holdup across each layer correspond to near-borehole water saturation and permeability.

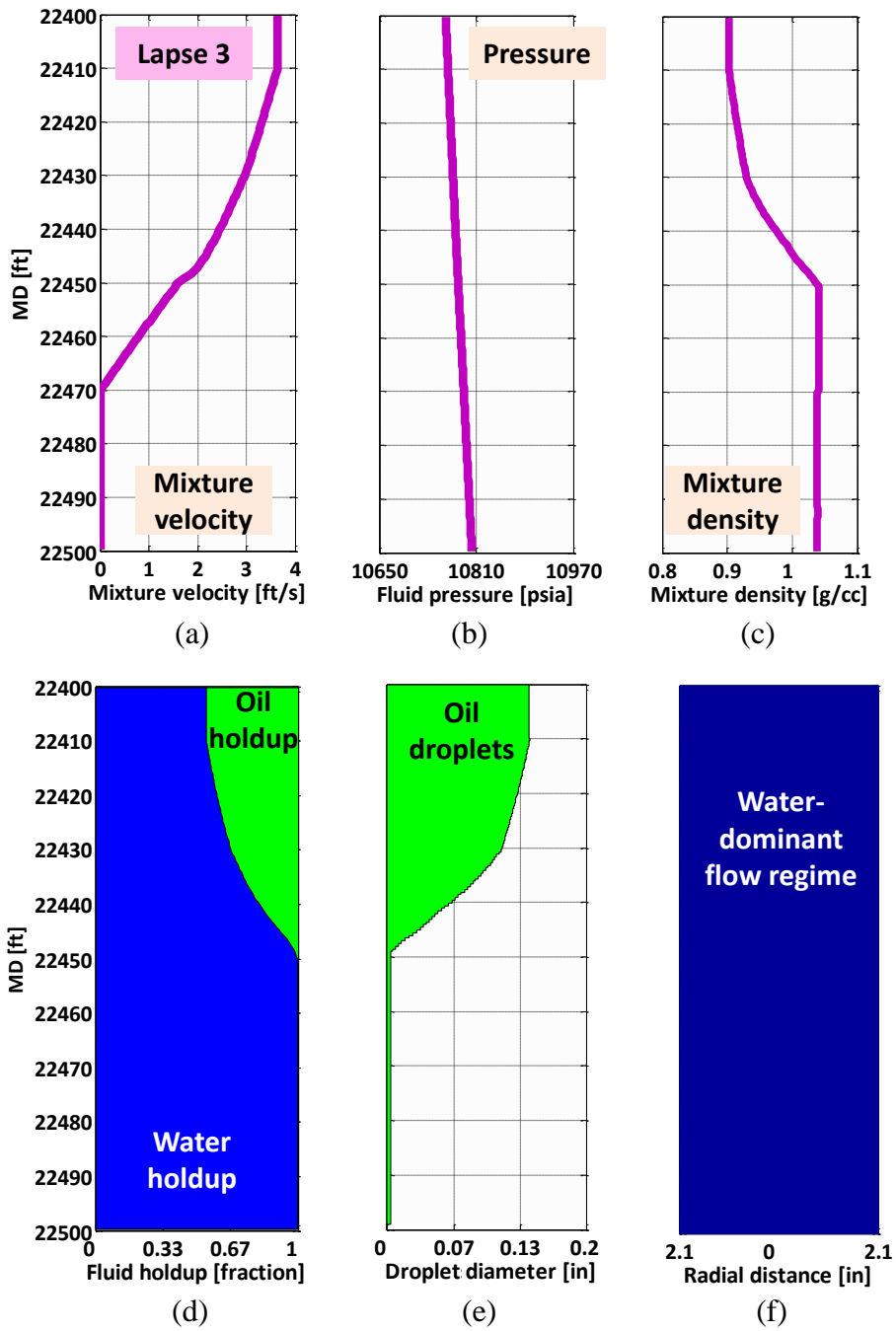


Figure 7.30: Spatial distributions of borehole (a) fluid mixture velocity, (b) fluid pressure, (c) fluid mixture density, (d) fluid holdup, (e) droplet diameter, and (f) fluid flow regime, numerically simulated for the third time lapse. Incremental water production results in higher water production. At this time lapse, flow regime for the entire borehole flowing domain is water-dominant bubbly flow regime.

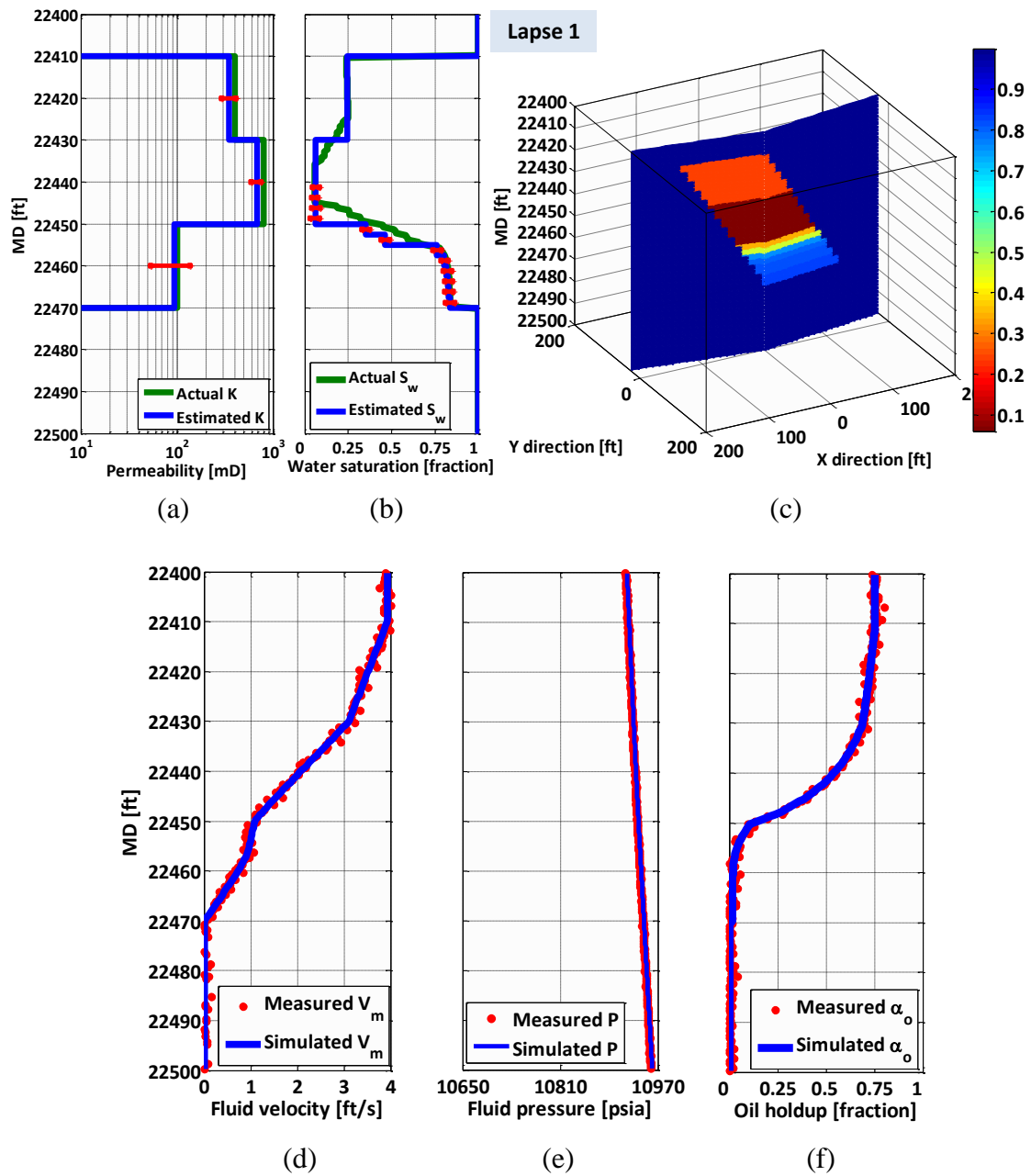


Figure 7.31: Comparison of the estimated and actual values of (a) permeability, and (b) water saturation for the first time lapse. Panel (c) shows the estimated spatial distribution of formation water saturation. The reconstructed borehole fluid mixture velocity (Panel d), fluid pressure (Panel e), and oil-phase holdup (Panel f) show an acceptable match when compared to the corresponding synthetically acquired logs.

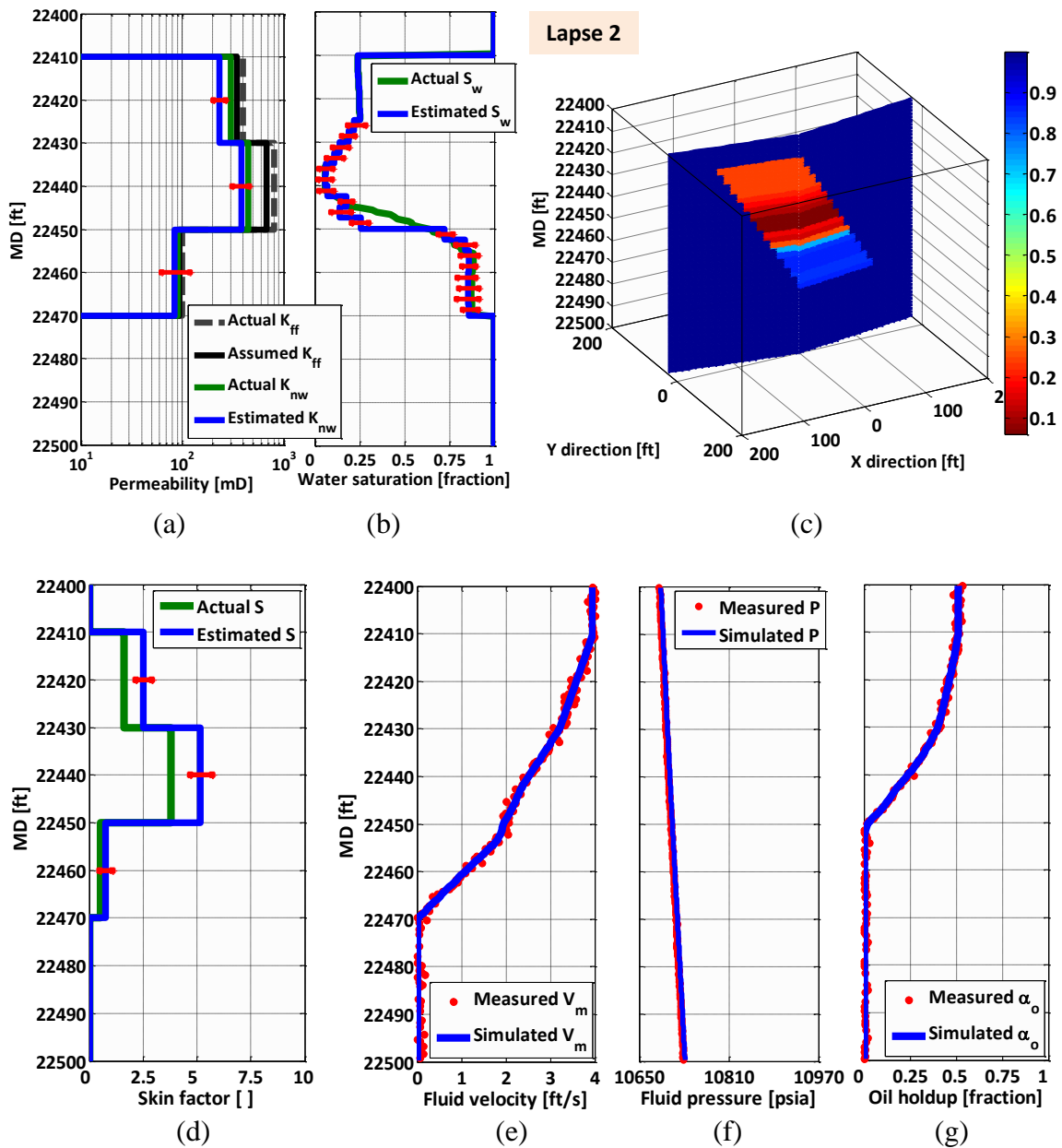


Figure 7.32: Comparison of the estimated and actual values of (a) permeability, and (b) water saturation for the second time lapse. Panel (c) shows the estimated spatial distribution of formation water saturation. Panel (d) compares the estimated near-borehole formation damage with the corresponding actual values. Formation damage was computed by comparing near-borehole and far-field permeabilities using Equation 7.4. The reconstructed borehole fluid mixture velocity (Panel e), fluid pressure (Panel f), and oil-phase holdup (Panel g) show an acceptable match when compared to the corresponding synthetically acquired logs.

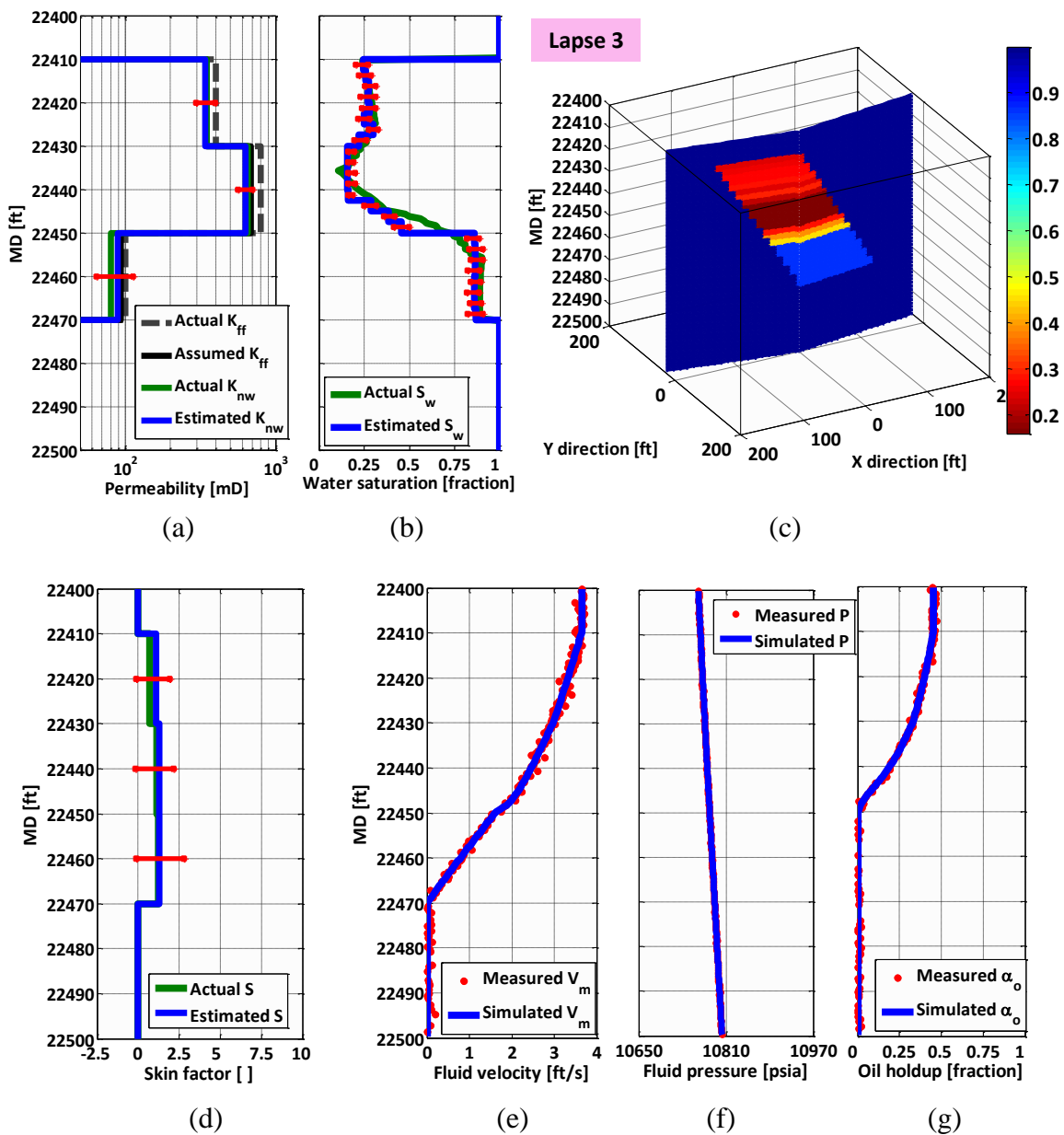


Figure 7.33: Comparison of the estimated and actual values of (a) permeability, and (b) water saturation for the third time lapse. Panel (c) shows the estimated spatial distribution of formation water saturation. Panel (d) compares the estimated near-borehole formation damage with the corresponding actual values. The interpretation algorithm assumes the availability of far-field permeability from PL interpretation of the first time lapse. The reconstructed borehole fluid mixture velocity (Panel e), fluid pressure (Panel f), and oil-phase holdup (Panel g) show an acceptable match when compared to the corresponding synthetically acquired logs.

7.6 FIELD EXAMPLE

7.6.1 General Description

Formations under consideration belong to a sand-shale laminated system originating from a deltaic depositional environment. The sedimentary rocks are composed of medium to coarse grains with a significant portion of micropores. As Figure 7.34 shows, the presence of micropores has increased formation irreducible water saturation up to 41%. The plotted relative permeability and capillary pressure curves are associated with a reference permeability of $K^{\text{ref}}=200$ mD and a porosity of $\phi^{\text{ref}}=25$ pu. To account for depth variations of layer porosity and permeability, capillary pressure is rescaled based on the Leverett-J function, to wit,

$$P_c = P_c^{\text{ref}} \sqrt{\left(\frac{\phi}{K}\right) \left(\frac{K^{\text{ref}}}{\phi^{\text{ref}}}\right)}, \quad (7.5)$$

where superscript "ref" identifies reference values for porosity (ϕ), permeability (K), and capillary pressure (P_c).

The field example includes a multilayer reservoir under commingled production of water and single-component hydrocarbon with PVT properties summarized in Table 7.4. The reservoir is penetrated by a borehole with a radius equal to 3.09 inches, a deviation angle of 12 degrees, and perforated intervals highlighted in Figure 7.35. After producing a significant amount of unwanted water, PLT measurements were acquired to investigate possible workover operations, and to enhance borehole inflow performance. Based on the acquired production logs and available well-log interpretation, I construct a near-borehole formation fluid flow model to identify and diagnose oil- and water-producing intervals. As shown in Figure 7.35, spatial distributions of formation porosity and permeability are generated from well-log interpretation. The plotted permeability is a flow-calibrated permeability that defines formation far-field permeability.

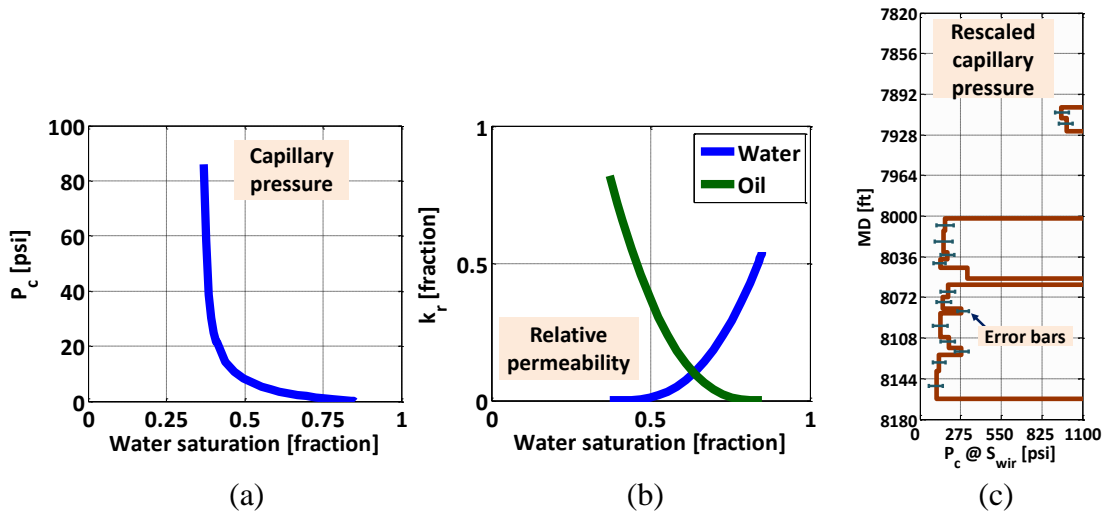


Figure 7.34: Assumed saturation-dependent (a) capillary pressure, and (b) relative permeabilities for PL interpretation of the sand-shale field example. Panel (c) shows the rescaled values of capillary pressure computed (at the irreducible water saturation) from the Leverett-J function.

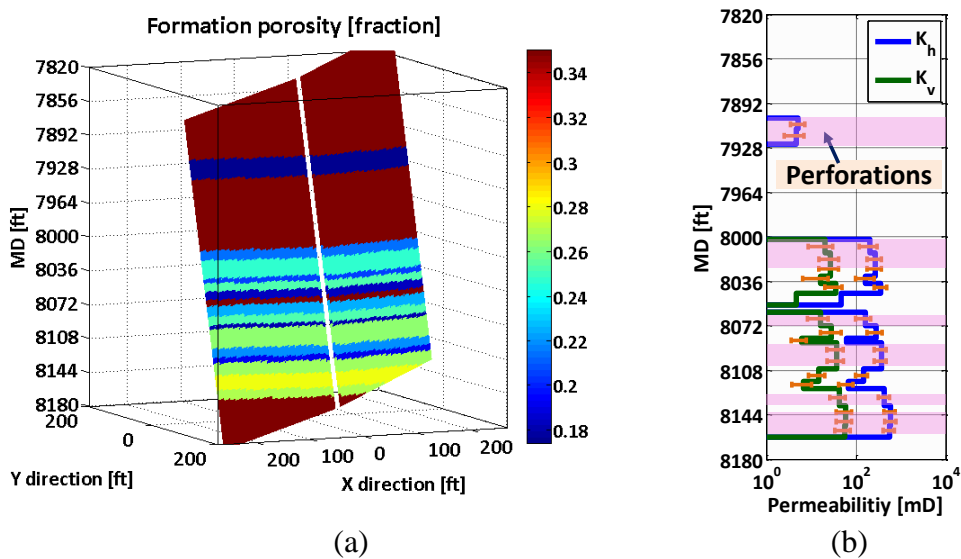


Figure 7.35: Spatial distributions of formation (a) porosity, and (b) far-field permeability derived from well-log interpretation of the sand-shale field example. The highlighted intervals identify perforations. K_h and K_v are horizontal and vertical permeabilities, respectively, with a permeability anisotropy equal to 0.1.

Property	Unit	Component
T_{crit}	$^{\circ}K$	734.5
P_{crit}	atm	17.15
A_c	-	0.683
V_{crit}	$m^3/kgmol$	0.915
MW	g/mol	221

Table 7.4: Summary of properties assumed for the hydrocarbon component used in PL interpretation of the sand-shale field example.

7.6.2 Interpretation of Production Logs

The inversion of production logs is performed by constructing a near-borehole fluid flow model to progressively match fluid mixture velocity, borehole pressure, and oil-phase holdup. Figure 7.36 shows the measured borehole fluid mixture velocity, pressure, holdup, temperature, and oil-phase density. Because of high water volume fractions, the oil and water phases are assumed to flow at the same velocity equal to that of fluid mixture (i.e., no-slip assumption). Under this assumption, borehole fluid-phase volume fraction is linearly related to formation petrophysical properties. In addition, I make explicit an assumption for spatial distribution of the borehole fluid temperature and fluid-phase density to decrease uncertainty of the diagnostic process.

Based on variations of borehole fluid mixture velocity and oil holdup, the near-borehole region is divided into seven spatial windows to perform PL inversion. In contrast to the synthetic example, production measurements are available only at a single time lapse. However, available well-log-derived permeability can be used to quantify near-borehole formation damage with respect to the initial conditions of the reservoir. Inversion results, shown in Figure 7.37, diagnose the lowermost depth interval (i.e.,

interval A) as a highly-damaged formation, exhibiting the highest value of water saturation (i.e., $S_w=68.8\%$). On the other hand, skin factors associated with Intervals B and C are diagnosed as negative values. Results are consistent with a stimulation operation had previously been performed on the borehole to enhance the inflow performance of those intervals. Specifically, Intervals B and C are quantified as layers with -2.76 and -3.54 skin factors, respectively. Because of a low far-field permeability (i.e., 4.7 mD), stimulation of Interval C has enabled that layer to produce oil and water phases at measurable flow rates. Interpretation of production logs additionally quantifies simultaneous production of oil and water across Interval B at approximately identical fluid-phase flow rates. As Figure 7.34 shows, the estimated water saturation for that interval (i.e., $S_w=60\%$) leads to identical water- and oil-phase relative permeability. Interpretation of production logs captures this dynamic property as identical fluid-phase flow rates across Interval B. These results show that the coupled flow algorithm enables the inference of layer fluid saturation and relative permeability based on matching production logs

The uncertainty bounds (shown as error bars in Figure 7.37) are calculated by adding small perturbation to inverted properties associated with each petrophysical layer. I subsequently compare the corresponding perturbed cost function to a threshold value beyond which inverted properties are assumed completely uncertain. Results show that large uncertainties of the estimated properties mainly originate from (i) low-permeability layers, and (ii) conditions of immovable fluid saturation. When produced in commingled mode, a low-permeability layer (e.g., Interval C) contributes low fluid production into the borehole, thereby leading to negligible variations of borehole fluid-phase velocity and holdup across the layer. Therefore, presence of measurement noise across low-permeability layers widens the uncertainty bounds of inverted petrophysical properties.

Furthermore, conditions of immovable fluid saturation (as diagnosed for Interval A) lower the sensitivity of production logs to fluid-phase relative permeability, thus increasing the estimation uncertainty.

Figure 7.38 shows the spatial distributions of estimated water saturation and permeability, and the simulated formation pressure. To generate three-dimensional distribution of layer water saturation, I assume that fluid saturation remains unchanged in the radial direction. This assumption allows one to estimate an average value of layer water saturation within the volume of investigation of PL measurements. Figure 7.39 additionally shows that the reconstructed borehole production measurements match the actual logs within an acceptable range of accuracy.

Simulated fluid flow rates (Figure 7.39d) indicate that Interval A contributes only to water production. However, major water production is from Interval B that is equivalently contributing to hydrocarbon production. Therefore, PL interoperation recommends that an optimum workover operation is the isolation of Interval A to decrease borehole water volume fraction. The PL-calibrated fluid flow model is subsequently invoked to quantify the performance of water shut-off. As quantified in Figure 7.40, performing water shut-off results in approximately 60 psi decrease of borehole pressure, and a 2.3% decrease of downhole water volume fraction. This comparison was carried out under the assumption of equal total fluid flow rates before and after the workover operation (i.e., 6063 bbl/day).

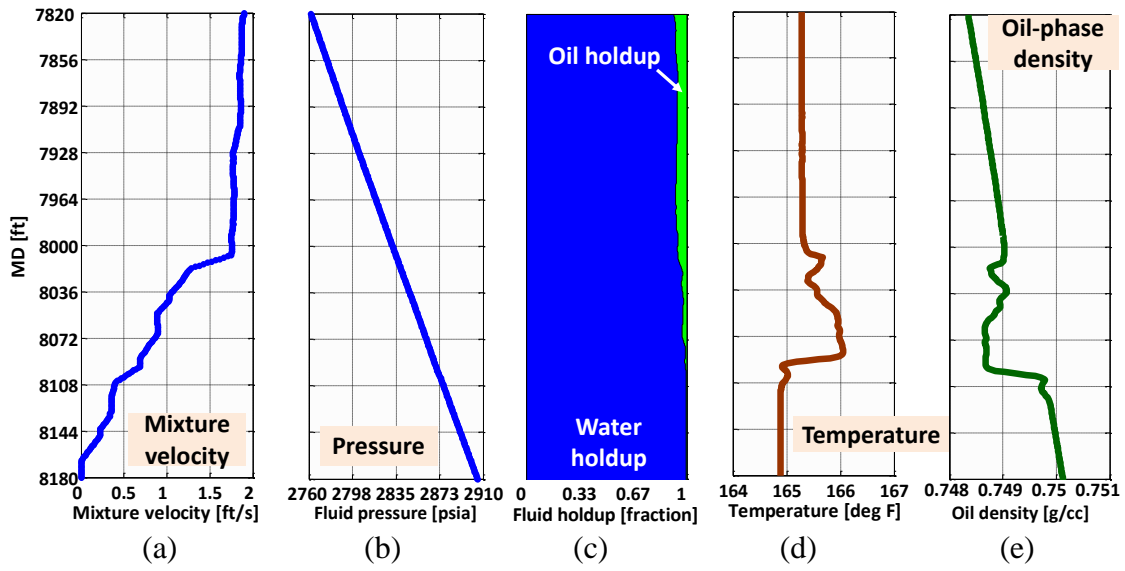


Figure 7.36: Borehole production measurements for (a) fluid mixture velocity, (b) pressure, (c) fluid holdup, (d) temperature, and (e) oil-phase density acquired across the sand-shale reservoir model.

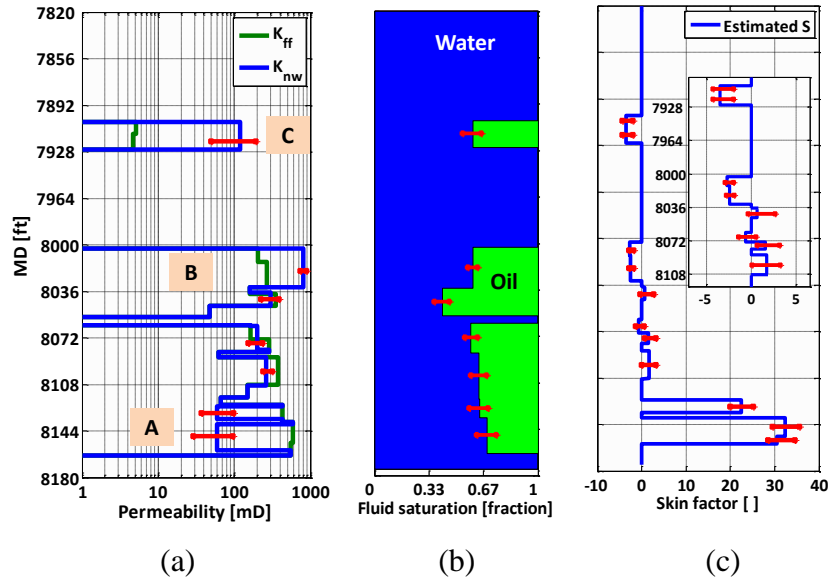


Figure 7.37: Comparison of the estimated and actual values of (a) permeability, and (b) water saturation for the sand-shale field example. Panel (c) compares the estimated near-borehole formation damage (computed from Equation 7.4) with the corresponding actual values. Error bars are calculated by adding small perturbation to inverted properties associated with each layer. Presence of measurement noise across Interval C (as a low-permeability layer) widens uncertainty bounds of the associated inverted properties. In addition, Interval A is at immovable fluid saturation that lowers the sensitivity of production logs to fluid-phase relative permeability, thus increasing estimation uncertainty for that layer. However, estimated permeability and skin factor for Interval B (as a high-permeability layer) are within 23% and 21% accuracy.

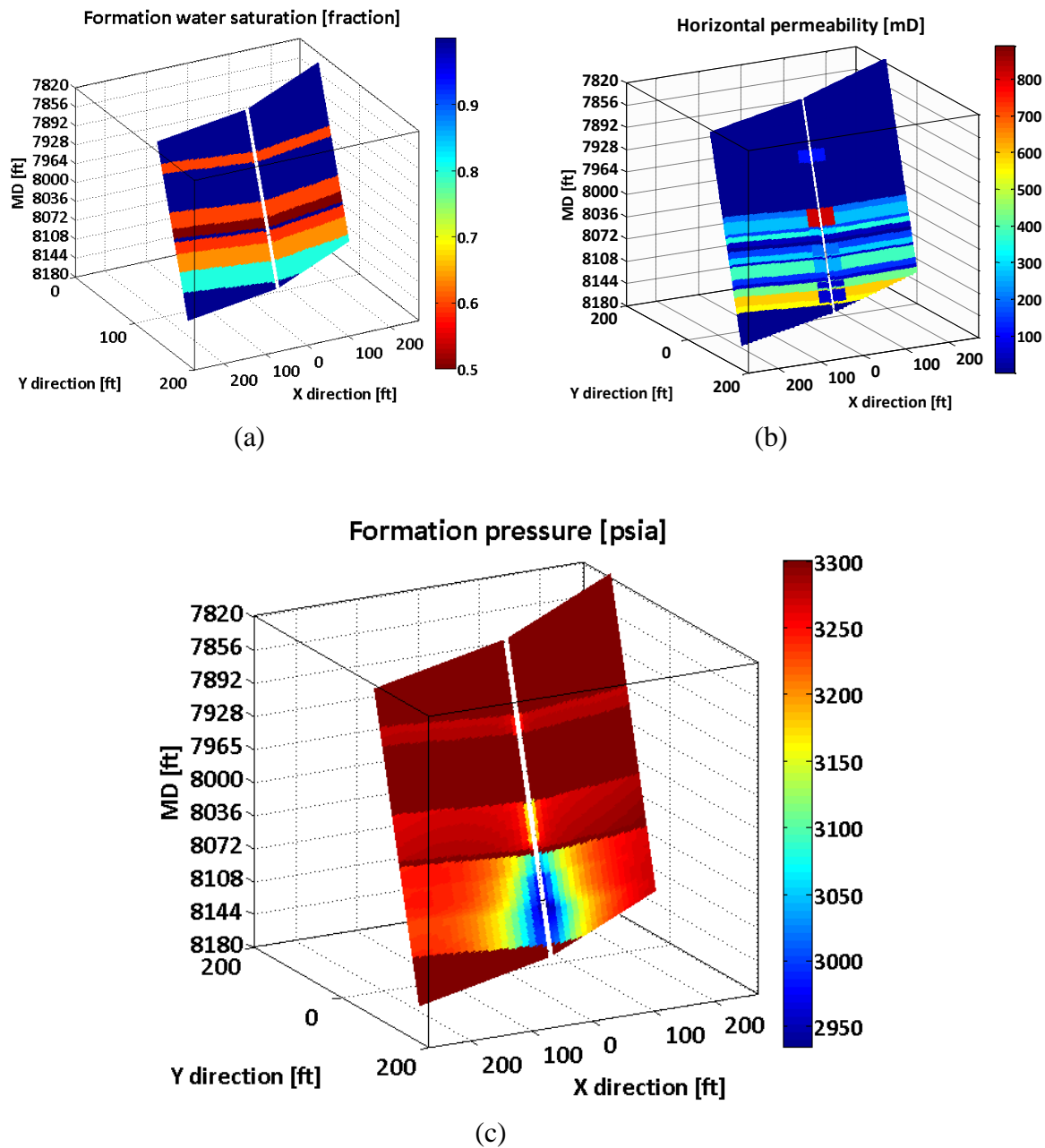


Figure 7.38: Spatial distributions of (a) water saturation, and (b) permeability estimated from PL interpretation of the sand-shale field example. Panel (c) shows the simulated formation pressure distribution. Production logging interpretation is performed by assuming six spatial windows for water saturation, and seven for permeability. Coupled flow algorithm assumes that water saturation remains unchanged radially away from the borehole.

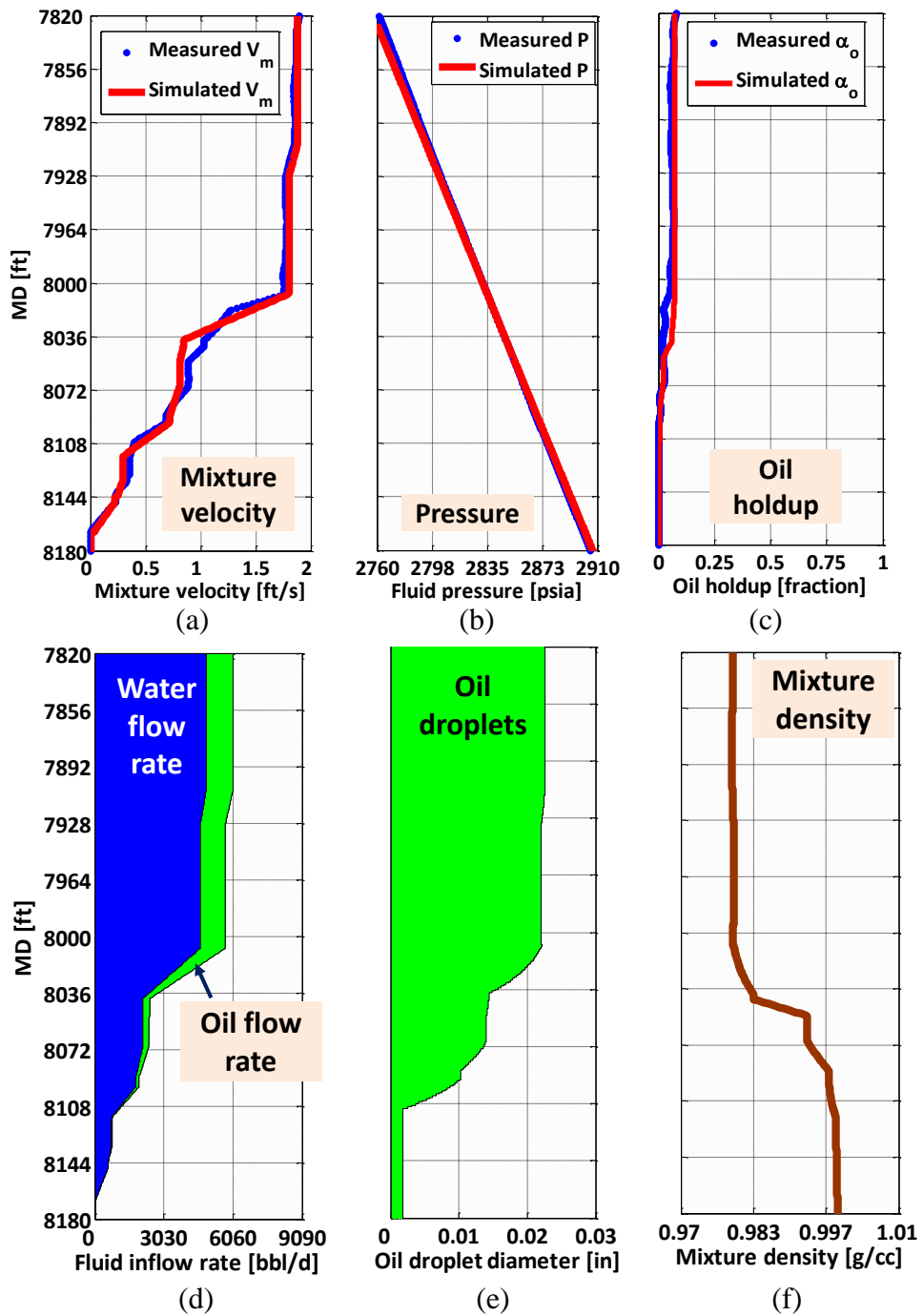


Figure 7.39: Comparison of the actual and reconstructed borehole (a) fluid mixture velocity (b), fluid pressure, and (c) oil-phase holdup for PL interpretation of the sand-shale field example. Panels (d) through (f) show the simulated fluid inflow rate, oil-droplet diameter, and fluid mixture density.

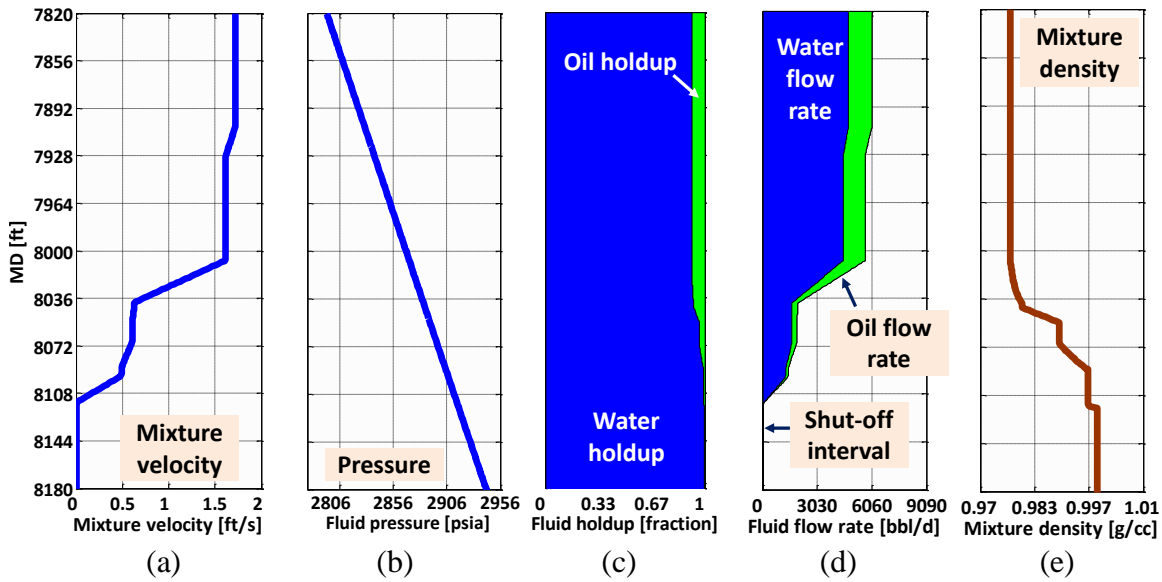


Figure 7.40: Borehole production measurements for (a) fluid mixture velocity, (b) fluid pressure, (c) fluid holdup, (d) fluid temperature, and (e) oil-phase density after performing water shut-off on the lowermost interval of the sand-shale field example. The remedial operation gives rise to 60 psia decrease of borehole pressure, and a 2.3% decrease of downhole water holdup.

7.6.3 Sensitivity Analysis

The reliability of near-borehole permeability and water saturation estimated from production logs significantly depend on the assumptions made on formation properties. Among those, this section quantifies the sensitivity of inverted properties to (i) formation pressure, (ii) permeability anisotropy, (iii) radius of the damaged region, and (iv) the end point of oil-phase relative permeability curve.

7.6.3.1 Formation Pressure

An insufficient shut-in duration prior to measurement acquisition gives rise to an average pressure not necessarily equal to formation stabilized pressure. A lower-than-

actual formation pressure results in overestimation of permeability associated with all the fluid-producing depth intervals. In particular, Figure 7.41a shows more than 17% overestimation of permeability when formation pressure is only 2% lower than the assumed value (i.e., 3200 psia instead of 3275 psia).

7.6.3.2 Permeability Anisotropy

Because borehole axial direction is nearly perpendicular to the sedimentary beds, production measurements are only sensitive to permeability in the horizontal direction. Results show that the estimated permeabilities are almost independent of the assumption made on permeability anisotropy (Figure 7.41b).

7.6.3.3 Radius of Damaged Region

This study implemented near-borehole formation damage based on defining a cylindrical region around the borehole subjected to damage or stimulation. Lack of a direct measuring method for radius of the near-borehole region requires performing sensitivity analyses to quantify the associated uncertainty. Simulation results show that increasing depth of the damaged region causes the estimates of near-borehole permeability become identical to layer average permeability within PLTs' volume of investigation (Figure 7.42). In fact, a considerable increase of damaged radius lowers the sensitivity of borehole measurements to far-field permeability. On the other hand, as Figure 7.42a shows, the interpretation algorithm significantly increases the contrast between near-borehole and far-field permeabilities to account for the reduction of damaged radius. Despite the large sensitivity of near-borehole and far-field permeabilities to radius of the damaged region, the estimated skin factors remain nearly unchanged for

the whole range of damaged radius (Figure 7.42b). Therefore, sensitivity analyses suggest that estimated skin factors are independent of the assumption made on radius of the damaged region.

7.6.3.4 End Point of Relative Permeability

Figure 7.43 describes sensitivity of inverted properties to oil-phase end-point relative permeability associated with four depth intervals. Estimated petrophysical properties at 8150 ft MD (with the highest value of water saturation, i.e., $S_w=68.7\%$) exhibit the lowest sensitivity to oil-phase end-point relative permeability. However, uncertainties of estimated permeability and water saturation continuously increase with decreasing water saturation. In particular, at 8080 ft MD, a 10% increase of end-point relative permeability causes 7% overestimation of permeability, and 4% overestimation of water saturation. In addition, the largest uncertainty is associated with 8040 ft MD, where the layer is at immovable water saturation. These conditions lead to more than 32% overestimation of layer permeability caused by a 10% increase of end-point relative permeability. Because of zero water production, the estimated water saturation remains insensitive to the end point of oil-phase relative permeability at that depth.

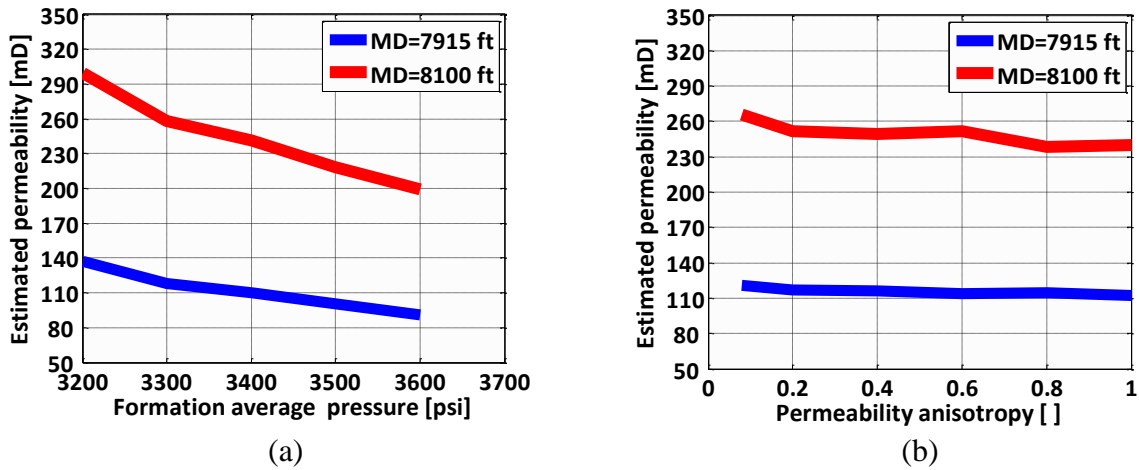


Figure 7.41: Sensitivity of the estimated near-borehole permeability to (a) formation average pressure, and (b) permeability anisotropy for PL interpretation of the sand-shale field example. Uncertainty of the assumed formation pressure is one of the most detrimental parameters that decrease the reliability of estimated layer permeability. On the other hand, permeability estimates are nearly independent of the assumed permeability anisotropy.

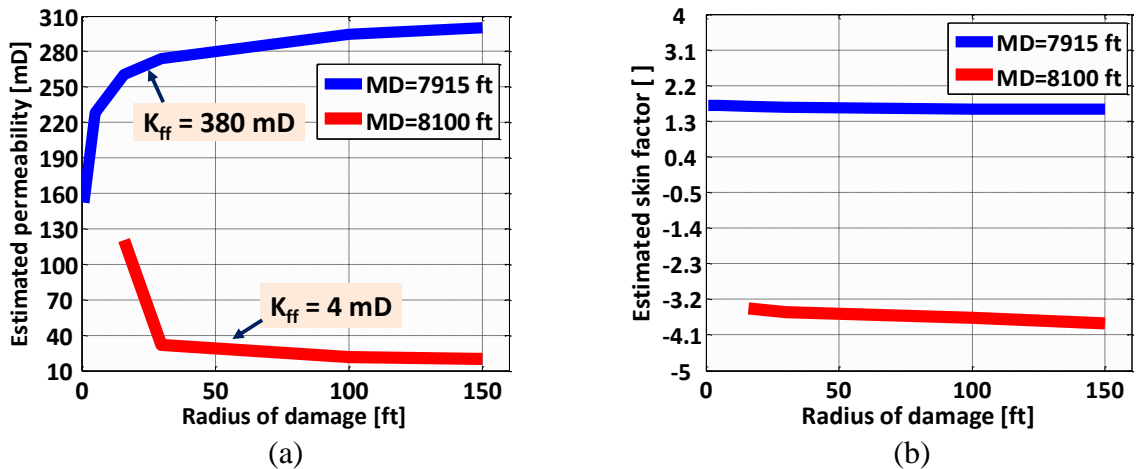


Figure 7.42: Sensitivity of the estimated (a) near-borehole permeability, and (b) skin factor to the assumed radius of damaged region for PL interpretation of the sand-shale field example. When the damaged region becomes thinner, contrasts between near-borehole and far-field permeabilities become larger. On the other hand, a considerable increase of damaged radius lowers the sensitivity of borehole measurements to far-field permeability. However, the estimated skin factor remains independent of the radius of near-borehole region.

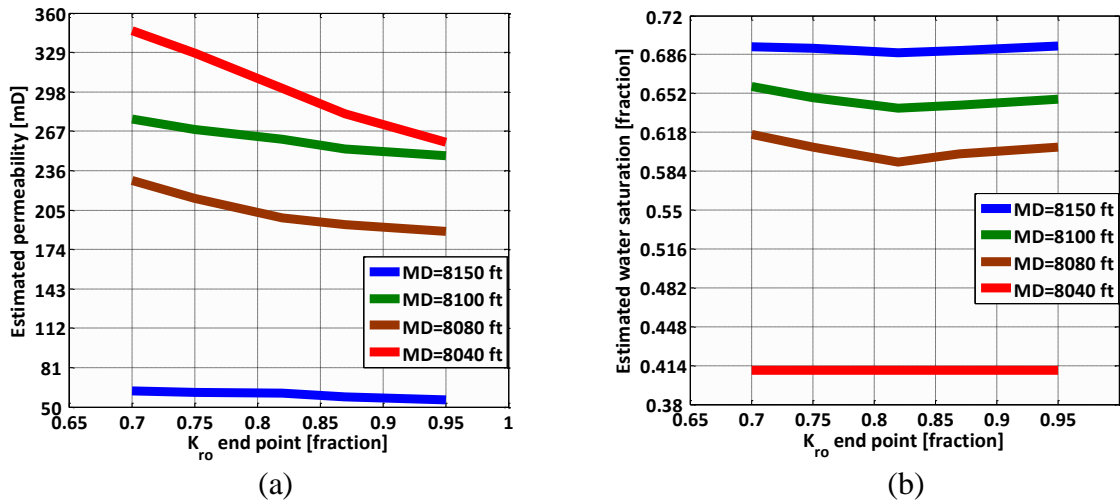


Figure 7.43: Sensitivity of the estimated (a) permeability, and (b) water saturation to oil-phase end-point relative permeability for PL interpretation of the sand-shale field example. Estimates of permeability and water saturation exhibit the lowest sensitivity to oil-phase end-point relative permeability of the unit with the highest water saturation (i.e., the unit centered at 8150 ft MD).

7.7 DISCUSSION

Even though PLTs measure fluid-phase properties in the borehole, interfacing a borehole fluid flow model to a dynamic reservoir model enables the linkage of borehole fluid properties to formation petrophysical properties. A substantial advantage of borehole-formation coupling is to condition the reconstruction of borehole measurements to the physics of fluid flow in porous media. Interpretation of production measurements using this coupled algorithm provides a method to quantify near-borehole formation properties, and to update available dynamic reservoir models.

Petrophysical properties estimated from production logs are field-scale average properties within the volume of investigation associated with PL measurements. A limitation of PL inversion is reliability of the assumptions made on formation and fluid properties within the volume of investigation of the measurements. Because of fluid

movement, formation dynamic properties (such as far-field permeability and average pressure) vary with time, thereby requiring the incorporation of additional independent measurements (e.g., well tests) to decrease estimation uncertainty. In the absence of such measurements, sensitivity of inverted properties to the assumptions made on forward reservoir models should be analyzed to quantify the uncertainty bounds of PL interpretation.

In commingled production of the oil and water phases, presence of fluid-phase slippage leads to accumulation of the heavier phase in the borehole which influences fluid-phase velocity and holdup across reservoir rocks. Therefore, absolute values of production measurements at a certain depth become dependent on petrophysical properties of all the fluid-producing layers. To quantify the sensitivity of borehole measurements to formation properties, the developed inversion algorithm specifies several depth windows in the borehole. Across each depth window, separate cost functions for permeability and water saturation are computed based on variations of borehole fluid-phase velocity and volume fraction. This windowing algorithm, accompanied with an accurate simulation of fluid-phase slip velocity, secures reliable estimates of formation petrophysical properties from production logs. A limitation of this approach originates from the presence of measurement noise that imposes non-physical variations on borehole production measurements. It is therefore recommended to reduce the detrimental noise effects prior to PL inversion to obtain the most reliable estimation.

When production logs are acquired and interpreted separately (as opposed to time-lapse interpretation), no a-priori information is available for spatial distribution of far-field permeability. Therefore, interpretation of production measurements makes it possible to infer an average permeability of each layer. Even though average permeability helps to quantify borehole inflow performance, it is not capable of distinguishing a

damaged layer from a low-permeability layer. However, as shown in the synthetic example, the integration of production logs acquired in time-lapse mode enables the quantification of near-borehole formation damage over the elapsed time. In the absence of time-lapse acquisition, the developed interpretation method makes use of available well-log interpretations to estimate near-borehole formation damage relative to the initial conditions of the reservoir. When applied to highly-heterogeneous rocks, well-log-derived permeability should be calibrated against surface production measurements to obtain reliable estimates of near-borehole formation damage.

A practical application of time-lapse PL interpretation is to evaluate and quantify the performance of stimulation operations performed to enhance borehole productivity. If production measurements are acquired before and after a remedial treatment, the developed diagnostic method helps to evaluate the decrease of positive skin factor associated with individual fluid-producing layers. However, a limitation of time-lapse interpretation is the propagation of error from one lapse to another. I showed that the uncertainty of inverted petrophysical properties in time-lapse mode originates from (i) the uncertainty of production measurements from the current time lapse, and (ii) the uncertainty of far-field permeability estimated from the preceding time lapse.

7.8 SUMMARY AND CONCLUSIONS

This chapter introduced new applications of the developed borehole-formation fluid flow model to simulate and interpret single-phase and two-phase (oil-water) production measurements. The analysis of single-phase flowing systems showed that the estimated layer permeability from production logs quantified directional permeability in the direction of fluid flow. Across anisotropic porous media, production logs acquired from vertical boreholes estimated layer horizontal permeability. While, inclining the

borehole gave rise to estimated permeabilities closer to layer permeability in the vertical direction.

I next showed that PL-derived permeability is influenced by PLTs' volume of investigation. The estimated permeability for a thin-layer reservoir model quantified an average reservoir permeability equivalent to well-test-derived permeability with a relative error less than 4%. Increasing the number of petrophysical layers resulted in an accurate estimation of depth variations of permeability along the borehole. However, results quantified a representative length scale beyond which PL interpretation yielded uncertain permeability estimates due to measurement noise. The largest uncertainty was associated with thinnest layers with lowest permeability where production measurements showed the lowest sensitivity to layer permeability. Additionally, in two-phase flowing systems, a larger number of unknown petrophysical properties led to more uncertainty compared to equivalent single-phase flowing systems.

The use of the 3D multiphase reservoir simulator in time-lapse analysis of the synthetic example enabled the differentiation between skin factors originating from (i) formation damage (or mechanical skin effects), and (ii) presence of the water phase. Therefore, interpretation of borehole measurements in time-lapse mode made it possible to reliably estimate near-borehole mechanical skin of individual rock formations. For a layer with permeability equal to 800 mD and skin factor equal to 5.1, the estimated permeability and skin factor were within 23% and 21% accuracy, respectively. Furthermore, the diagnostic method accurately quantified variations of near-borehole water saturation caused by incremental water production. However, PL interpretation was adversely influenced by conditions of immovable water saturation in formations. Because of zero water production across oil saturated layers, production logs were unable to reliably differentiate any water saturation from irreducible to critical water saturations.

To circumvent this problem, the algorithm made an explicit assumption for water saturation of zero-water-producing depth intervals based on available rock types.

Analysis of the field example was carried out by integrating well logs and production logs. I assumed that far-field permeabilities were equal to flow-calibrated well-log-derived permeabilities to estimate spatial distributions of near-borehole permeability and water saturation. Because of sufficiently low values of borehole oil-phase volume fraction, I made an explicit assumption for fluid flow pattern for the entire borehole flowing domain (i.e., water-dominant bubbly flow regime) to improve the numerical stability of PL inversion. The reconstructed production measurements next verified the validity of that assumption. Production logging interpretation successfully quantified negative and positive skin factors anticipated from historical workover operations. For a layer with near-borehole permeability equal to 845 mD, uncertainties associated with permeability and water saturation were within 17% and 12% of the estimated values, respectively. However, the estimation reliability decreased with decreasing layer fluid-phase inflow rate. It is therefore recommended to acquire precaution logs at highest possible fluid flow rates to increase the sensitivity of PLTs to borehole fluid properties.

The coupled borehole-formation fluid flow model was invoked to perform a sensitivity analysis on the assumptions made on the forward reservoir model. Results showed that formation average pressure and the end points of fluid-phase relative permeability caused the largest uncertainties on the estimated petrophysical properties. For a layer with permeability equal to 265 mD and average pressure equal to 3275 psia, only a 2% increase of layer average pressure resulted in more than 17% overestimation of layer permeability. Furthermore, when a layer was at immovable water saturation (i.e., $S_w=41\%$ with a permeability equal to 302 mD), decreasing oil-phase end-point relative

permeability by a factor of 10% led to an approximately 10% increase of estimated permeability. Sensitivity analyses suggested that independent measurements should be incorporated to PL interpretation to decrease uncertainty bounds associated with formation average pressure and relative permeability curves.

Chapter 8: Estimation of Oil-Water Relative Permeability from Inversion of Time-Lapse Production Logs

Laboratory measurements of saturation-dependent relative permeability are commonly used to construct dynamic reservoir models. However, because of sample size and paucity, their reliability to predict real-time production behavior of heterogeneous rock formations remains questionable. This chapter introduces a new interpretation method to estimate near-wellbore hydrocarbon-water relative permeability from measurements acquired with production logging tools (PLTs). The developed coupled borehole-formation fluid flow model is invoked to simulate hydrocarbon-water production logs (PL) in time-lapse mode. Subsequently, a nonlinear inversion algorithm estimates saturation-dependent relative permeability by minimizing quadratic differences between borehole measurements of velocity, pressure, and holdup of the two phases, and their numerical simulations.

Synthetic examples show that incremental water production from a multilayer reservoir enables inference of fluid-phase relative permeability. However, reliability of the estimation method is limited by the effective water saturation window monitored in the wellbore during the lifetime of producing reservoir.

8.1 INTRODUCTION

Saturation-dependent relative permeability is a dynamic petrophysical property of rock formations that quantifies the effective permeability of immiscible fluid phases in

porous media. A review of relevant documented technical contributions shows that downhole measurements acquired with well testing, well logging, and formation testing have been studied for estimation of saturation-dependent relative permeability (Alpak et al., 2008; Chen et al., 2008; Angeles et al., 2010; Kianinejad, et al. 2014). Alpak et al. (2008) developed a method to estimate relative permeability curves from in-situ measurements acquired with formation-testers. Angeles et al. (2010) extended Alpak et al.'s (2008) work by incorporating resistivity logs to increase the reliability and stability of the estimation. By matching well-test measurements, Chen et al. (2008) additionally introduced a method to calculate relative permeability curves.

This chapter investigates the possibility of estimating oil-water relative permeability curves from inversion of time-lapse production measurements. I develop an inversion-based interpretation algorithm that invokes the coupled fluid flow model described in Chapter 2, and associates variations of production logs to fluid-phase relative permeability. The unknown model parameters considered for PL inversion are relative permeabilities associated with a cylindrical region in the vicinity of borehole. Beyond the near-borehole region, production logs are assumed to be unaffected by relative permeability curves. The inversion method begins with specifying a representative number of petrophysical layers in the near-borehole region. Fluid-phase relative permeability associated with each petrophysical layer is assumed to vary linearly with respect to layer water saturation. Consequently, the inversion method progressively refines fluid-phase relative permeability of each layer to achieve an acceptable match between numerically simulated and synthetically measured borehole production measurements.

8.2 INTERPRETATION METHOD

The inversion-based algorithm described in chapter 5 is modified to enable the estimation of fluid-phase relative permeability from production measurements. I describe the developed formulations and main assumptions made for iterative refinement of near-borehole relative permeability.

8.2.1 General Assumptions

Fluid-phase relative permeabilities associated with the near-borehole region are considered as unknown model parameters for PL inversion. Therefore, explicit assumption is made for remaining static and dynamic formation petrophysical properties such as porosity, permeability, skin factor, bed boundary depths, bed dips, capillary pressure, and relative permeability curves outside the near-borehole region. Production logs considered for inversion process include fluid mixture velocity, fluid pressure, and oil-phase holdup. The oil and water phases are modeled as incompressible fluids with known density and viscosity. I assume that production measurements are acquired at the conditions of stable pressure when formation has reached its average pressure prior to measurement acquisition. Furthermore, the estimation of near-borehole relative permeability requires the availability of near-borehole water saturation distribution. These measurements are assumed to be provided through the concomitant acquisition of cased-hole sigma logs.

8.2.2 Inverse Problem

As Figure 8.1 illustrates, the main inversion loop developed for estimation of relative permeability consists of two iterative inner loops. Both loops minimize a cost

function computed based on quadratic differences between production measurements and corresponding measured values, i.e.,

$$C(\mathbf{x}) = \frac{1}{2} [\|\mathbf{W} \cdot \mathbf{e}(\mathbf{x})\|^2 + \lambda \|\mathbf{x}\|^2], \quad (8.1)$$

where \mathbf{x} is vector of unknown model parameters consisting of fluid-phase end-point relative permeabilities, namely,

$$\mathbf{x} = [\mathbf{k}_{ro}^0, \mathbf{k}_{rw}^0]^T, \quad (8.2)$$

where superscript "0" identifies end-point values of fluid-phase relative permeability associated with near-borehole region, superscript "T" denotes transpose operator, and $\|\cdot\|^2$ designates the 2-norm operation. In Equation 8.1, \mathbf{W} is a data weighting matrix that includes a certain set of unknown properties within each minimization loop, λ is a regularization coefficient that defines the relative importance of end-point relative permeabilities compared to the first additive term, and \mathbf{e} is data mismatch, defined by

$$\mathbf{e}(\mathbf{x}) = \left[\begin{array}{c} \left(\frac{S_v^s(\mathbf{x}) - S_v^m}{S_v^m} \right)_1, \dots, \left(\frac{S_v^s(\mathbf{x}) - S_v^m}{S_v^m} \right)_{N_{wrp}}, \\ \left(\frac{S_\alpha^s(\mathbf{x}) - S_\alpha^m}{S_\alpha^m} \right)_1, \dots, \left(\frac{S_\alpha^s(\mathbf{x}) - S_\alpha^m}{S_\alpha^m} \right)_{N_{wrp}}, \\ \left(\frac{P^s(\mathbf{x}) - P^m}{P^m} \right)_1, \dots, \left(\frac{P^s(\mathbf{x}) - P^m}{P^m} \right)_{N_{mp}} \end{array} \right]^T, \quad (8.3)$$

where subscript " N_{wrp} " is number of petrophysical layers defined in the near-borehole region, subscript " N_{mp} " identifies number of pressure measurements, subscripts "v" and " α " identify fluid mixture velocity and oil-phase holdup in the borehole, respectively, superscripts "s" and "m" denote simulated and measured production logs, respectively,

and S indicates the slope of borehole fluid-phase velocity and holdup across petrophysical layers.

Based on variations of near-borehole water saturation, the developed interpretation algorithm specifies petrophysical layers associated with the near-borehole region. Subsequently, Loop 1 is invoked to estimate layer end-point oil-phase relative permeability assuming fixed values for water-phase relative permeability. Saturation-dependent relative permeability curves are constructed by postulating linear interpolation between water saturation and relative permeability. Iteration within Loop 1 continues until achieving the updated values for near-borehole oil-phase relative permeability. Loop 2 subsequently estimates end-points of water-phase relative permeability by making explicit assumption for oil-phase relative permeability.

8.2.3 Single-Layer Reservoir Example

The developed estimation method is applied to a single-layer reservoir model with relative permeability and capillary pressure curves described in Figure 8.2. Table 8.1 summarizes formation, fluid, and borehole properties. The formation is produced from its transition zone where capillary effects cause a gradual decrease of water saturation from the bottom to the top (Figure 8.3). Therefore, as Figure 8.4 shows, the lower parts of the borehole are mainly contributing into water production while oil phase is mainly produced from the upper portions. Accordingly, the acquired production measurement show that borehole water volume fraction is gradually decreasing from the bottom to the top of the producing interval. As shown in Figure 8.5, non-Gaussian random noises are added to the synthetic measurements of fluid mixture velocity, oil holdup, and borehole pressure to account for tool movements and the chaotic nature of turbulent flow.

The inference of near-borehole relative permeability is carried out by specifying several petrophysical layers around the borehole. Initially, a 4-layer model is invoked to reconstruct borehole production measurements. Figure 8.6 confirms that the simulated measurements for fluid mixture velocity and oil holdup do not accurately match the corresponding simulated values. To improve the accuracy of estimation, I progressively increase the number of near-borehole petrophysical layers to 8, 16, and 32 layers. Figure 8.8 shows an enhancement in the accuracy of fluid-phase relative permeability estimates as more layers are included in PL inversion. However, refining the near-borehole region causes the relative permeability estimates to become adversely influenced by measurement noise. The interpretation shows that 16-layer reservoir model achieves the most accurate results by estimating near-borehole relative permeabilities within 8% of the actual values. The reconstructed borehole measurements from this model additionally show acceptable agreement compared to the (synthetically) measured values (Figure 8.7).

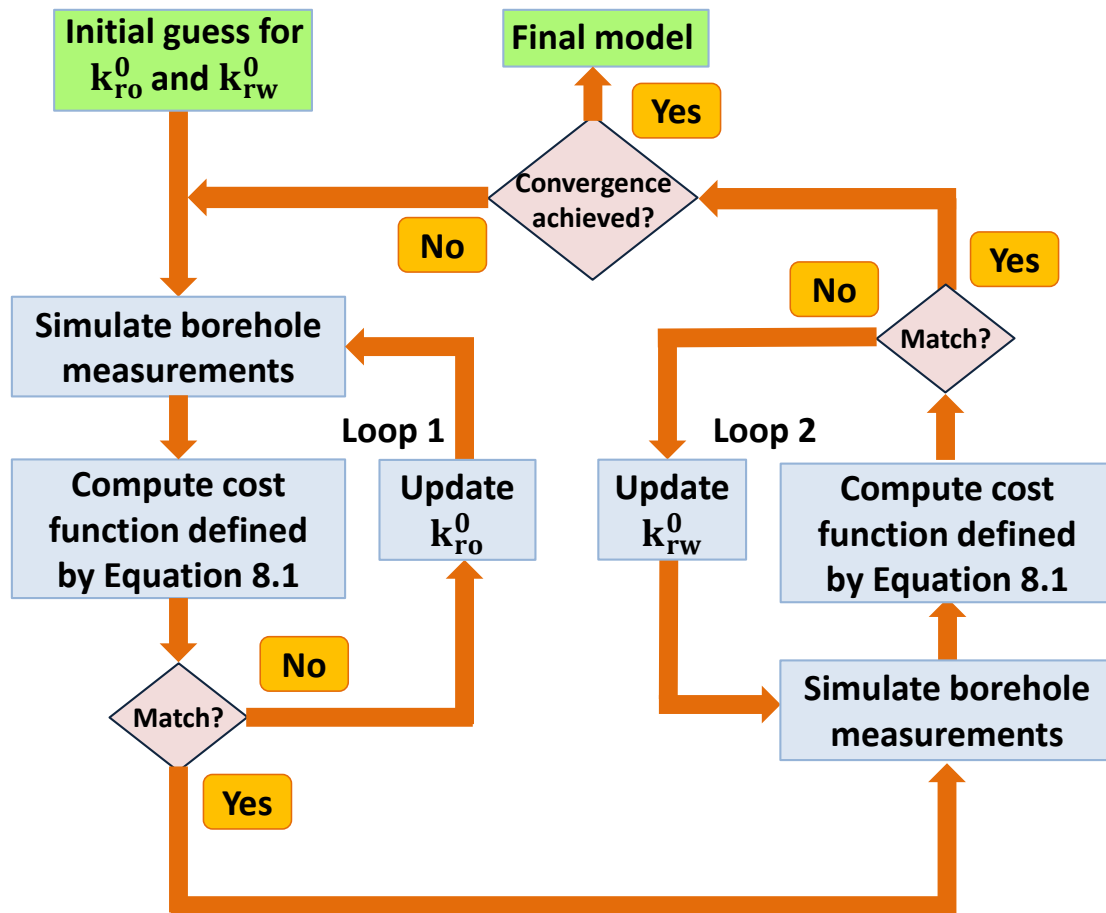


Figure 8.1: Developed iterative workflow to estimate near-borehole fluid-phase relative permeability from inversion of borehole production measurements. Within each minimization loop, end-points of fluid-phase relative permeability are estimated by postulating linear interpolation between water saturation and relative permeability.

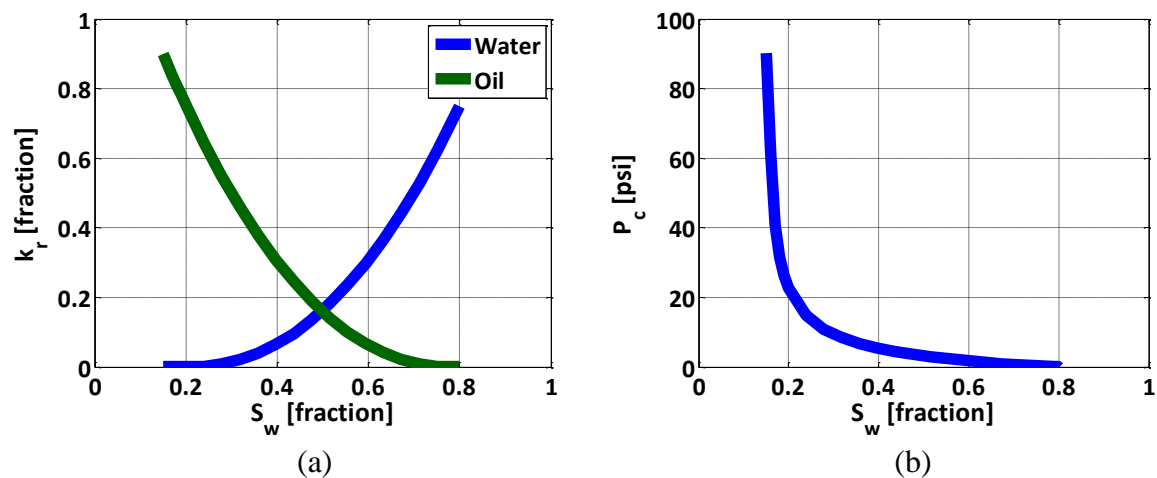


Figure 8.2: Assumed saturation-dependent (a) relative permeability and (b) capillary pressure for the single-layer reservoir model.

Property	Unit	Value
ρ_o	g/cc	0.76
ρ_w	g/cc	1.03
μ_o	cp	0.835
μ_w	cp	1
K	mD	300
ϕ	pu	25
WOC	ft	12200
Q_o	STB/D	6000
P_{avg}	psia	5600
T_{avg}	$^{\circ}$ F	185
r_w	in	2.85

Table 8.1: Assumed fluid-phase, formation, and borehole properties for the single-layer reservoir model.

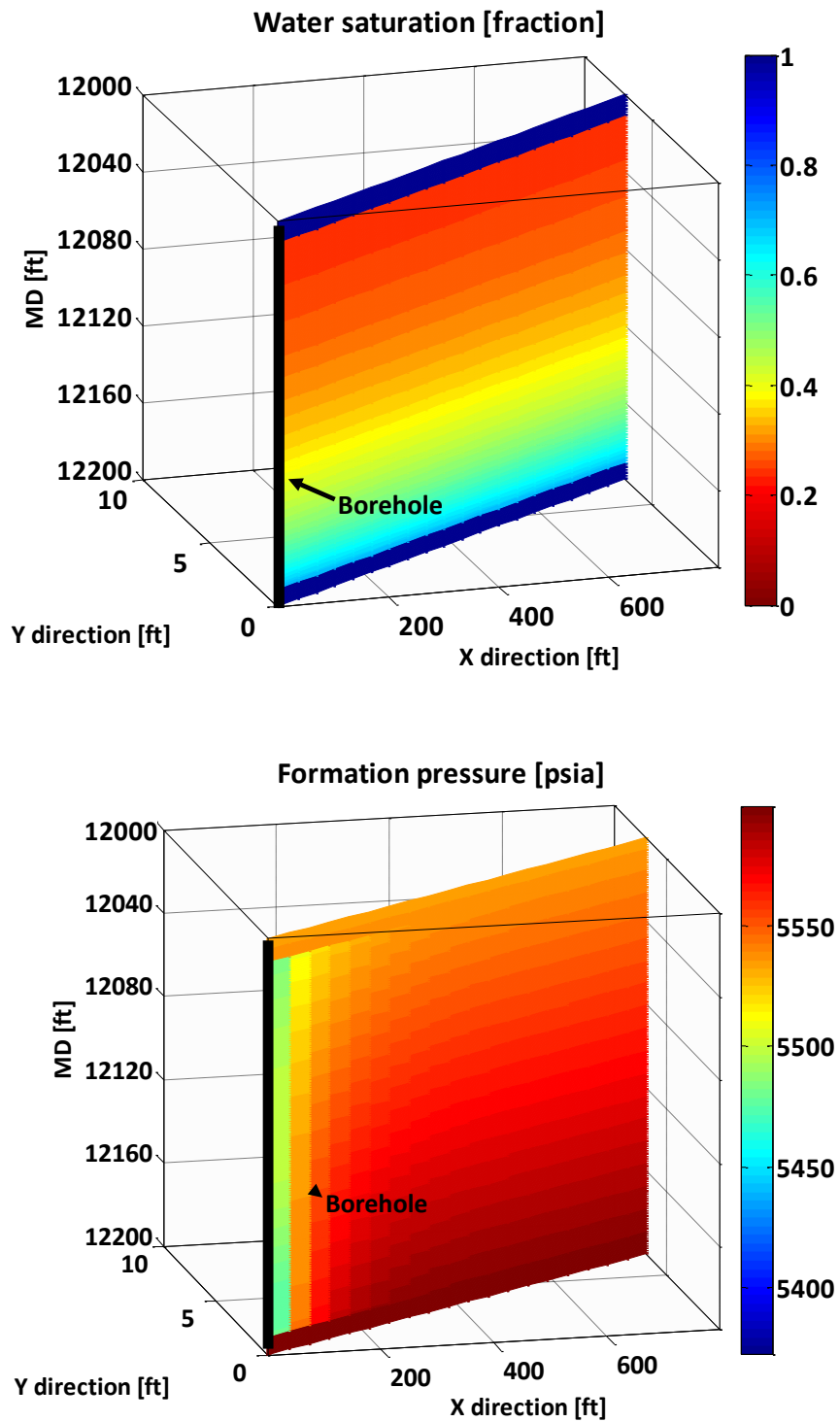


Figure 8.3: Simulated spatial distributions of water saturation (upper panel) and pressure (lower panel) prior to measurement acquisition across the single-layer reservoir model.

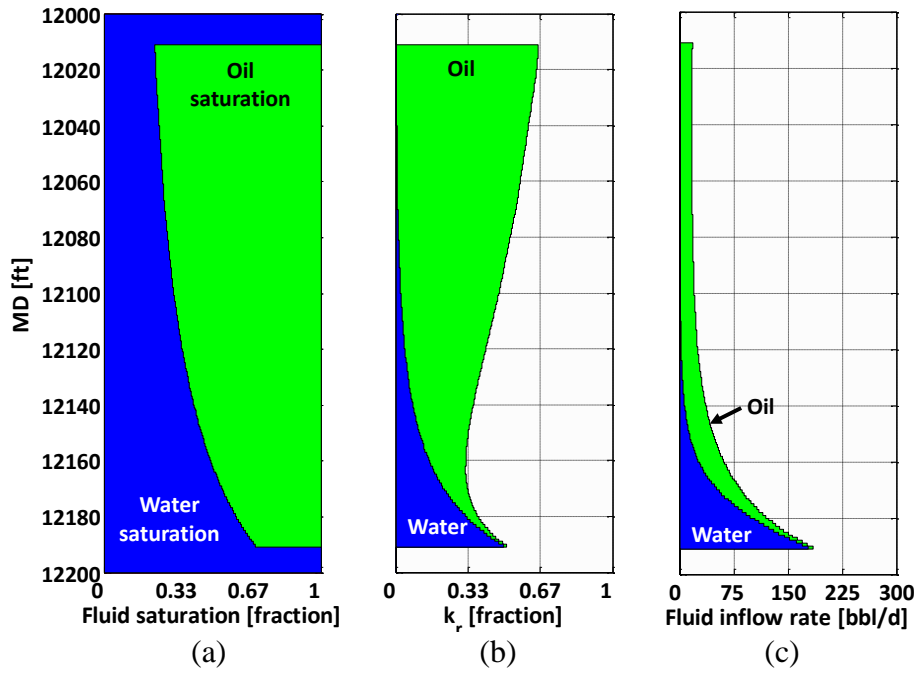


Figure 8.4: Simulated near-borehole fluid-phase (a) saturation, (b) relative permeability, and (c) fluid inflow rate for the single-layer reservoir model.

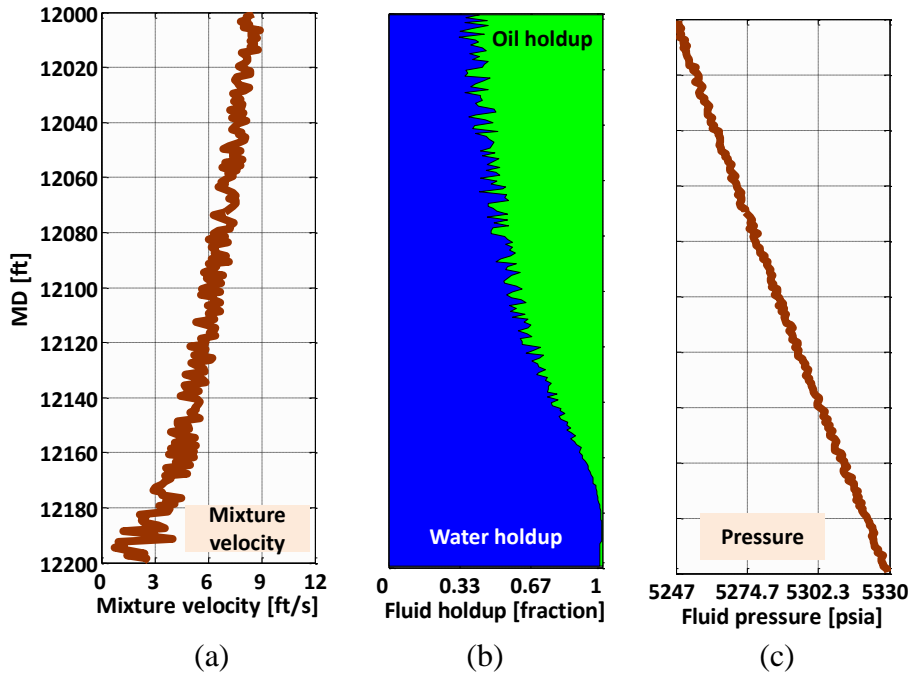


Figure 8.5: Simulated borehole (a) fluid mixture velocity, (b) fluid-phase holdup, and (c) fluid pressure for the single-layer reservoir model.

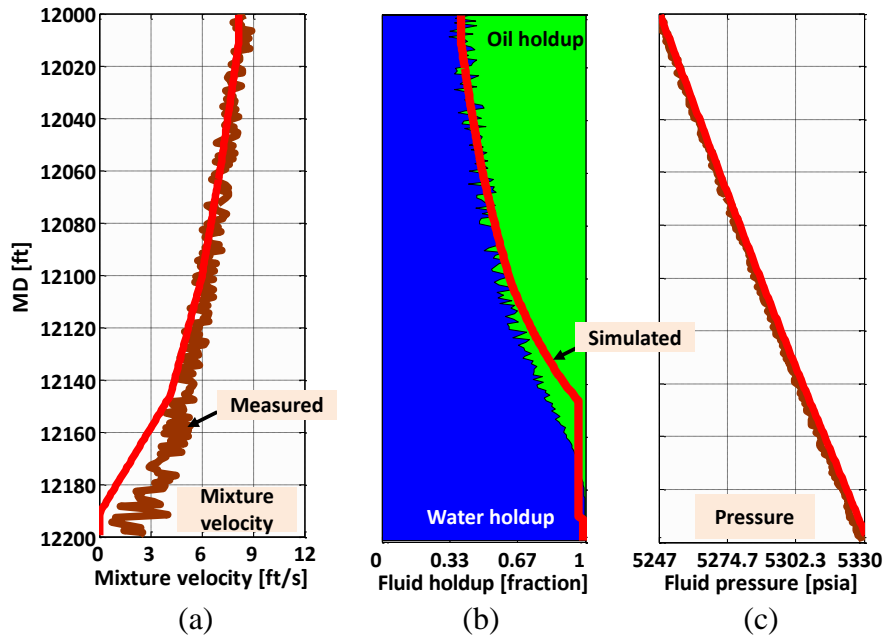


Figure 8.6: Reconstructed production measurements for (a) velocity, (b) holdup, and (c) pressure associated with 4-layer forward reservoir model to estimate relative permeability of the single-layer reservoir model.

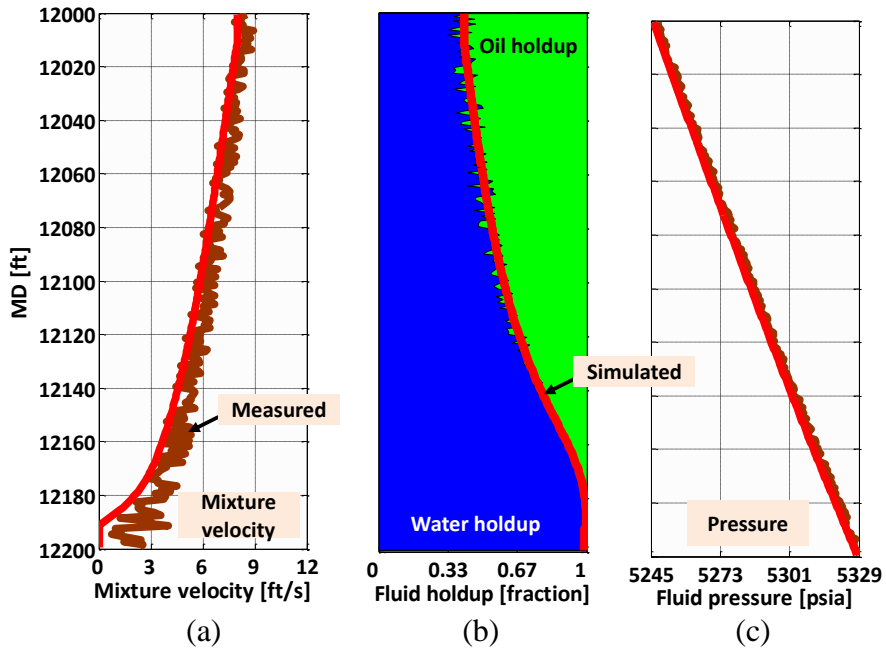


Figure 8.7: Reconstructed production measurements for (a) velocity, (b) holdup, and (c) pressure associated with 16-layer forward reservoir model to estimate relative permeability of the single-layer reservoir model.

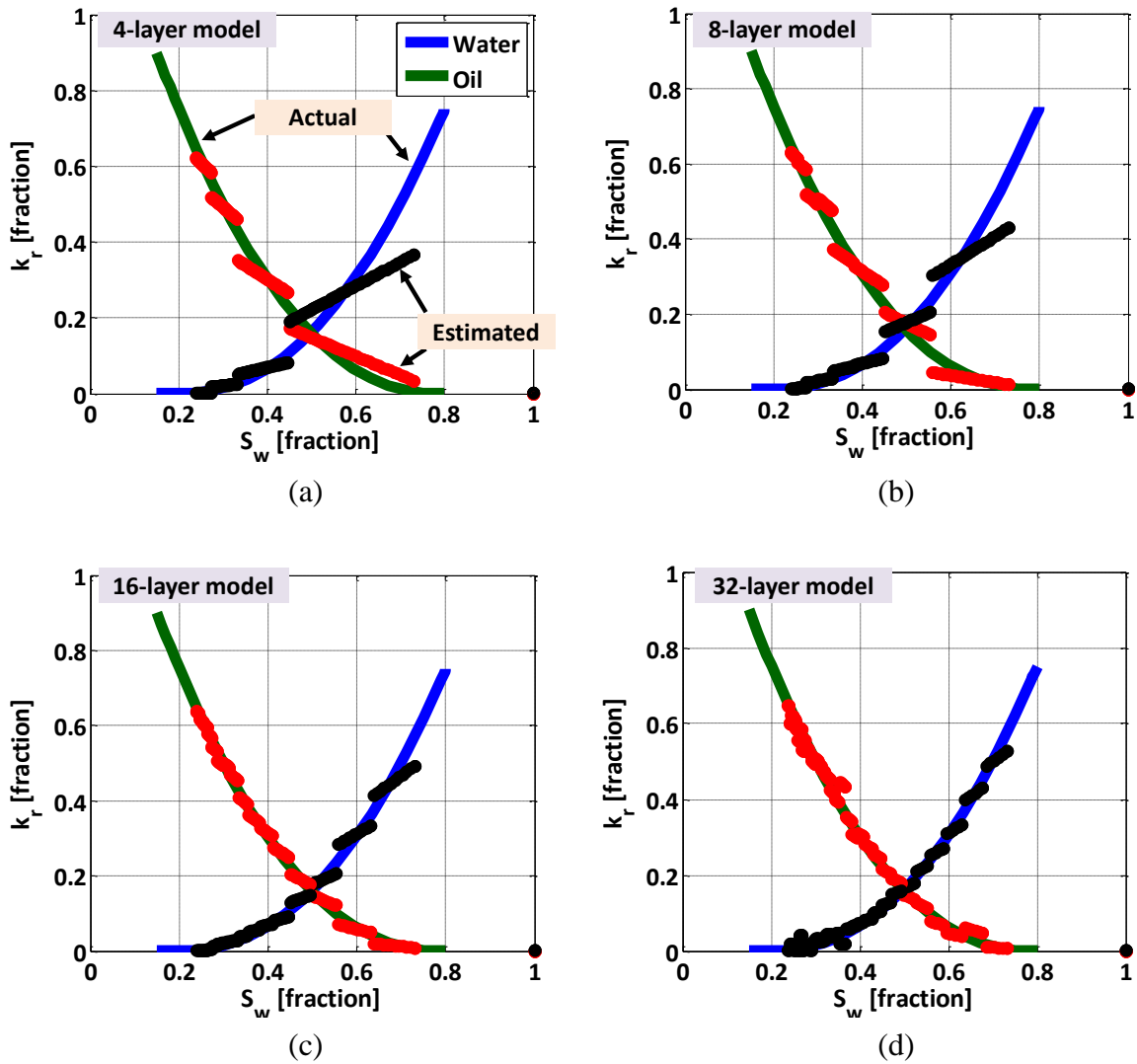


Figure 8.8: Comparison of the estimated fluid-phase relative permeability with the corresponding actual values associated with (a) 4-layer, (b) 8-layer, (c) 16-layer, and (d) 32-layer forward reservoir models for the estimation of relative permeability of the single-layer reservoir model.

8.3 UNCERTAINTY ANALYSIS

Estimation of fluid-phase relative permeability from production logs requires several assumptions on formation static and dynamic petrophysical properties. Uncertainty associated with those assumptions could render erroneous estimation of relative permeability. I construct a multilayer reservoir model to quantify the sensitivity of relative permeability estimates to formation permeability, average pressure, and porosity. The reservoir under consideration consists of three rock formations with relative permeability and capillary pressure curves plotted in Figure 8.9. Borehole and fluid-phase properties are identical to those assumed for the single-layer reservoir model. Table 8.2 additionally summarizes formation petrophysical properties. The simulated spatial distributions of borehole and formation fluid properties are shown in Figures 8.10 and 8.11. In three separate simulations, porosity of Rock 2, average pressure of Rock 2, and permeability of Rock 3 are perturbed with the values shown in Table 8.2 to investigate the uncertainty associated with relative permeability estimates.

Final relative permeability estimates together with their associated uncertainty bounds are shown in Figures 8.12 through 8.14. While uncertainty in porosity does not significantly influence the final estimates, 16% uncertainty in permeability of Rock 3 has caused more than 21% error in the estimated relative permeability of that rock. Furthermore, Figure 8.14 quantifies that when the average pressure of Rock 2 is 4% lower than the actual value, more than 30% error is involved in the estimation of oil-phase relative permeability. In fact, a lower-than-actual value of formation average pressure leads to an overestimation of fluid-phase velocity in the forward model. Thereby, the estimated relative permeabilities associated with both fluid phases become higher than the actual values. However, negligible water production from Rock 2 and 3 decreases the sensitivity of water-phase relative permeability to formation petrophysical

properties. This behavior implies that reliable relative permeability estimates from production logs requires incorporation of additional independent measurements to reduce the deleterious effect of uncertainty associated with formation properties.

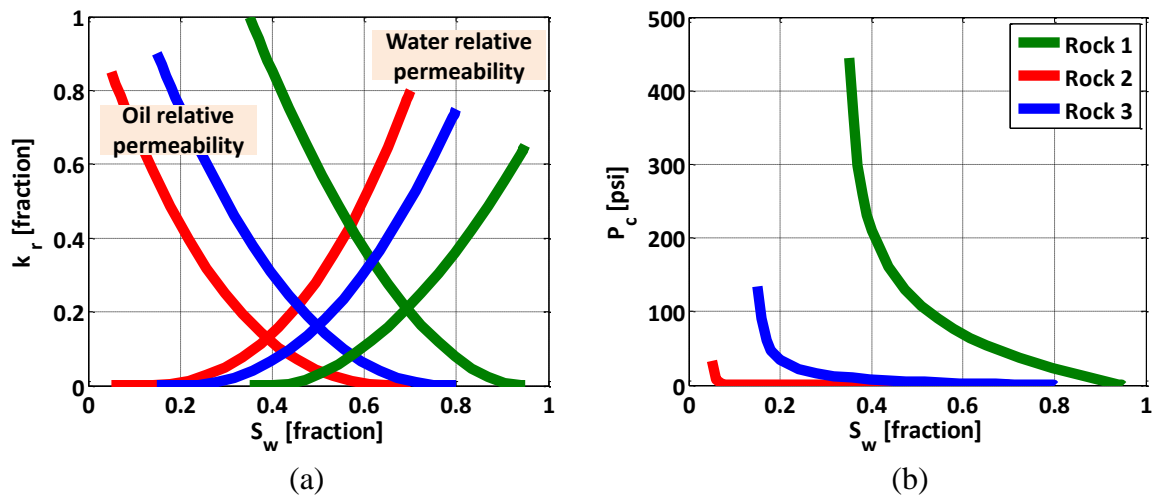


Figure 8.9: Assumed saturation-dependent (a) relative permeability and (b) capillary pressure for the three-layer reservoir model.

Property	K [mD]	ϕ [pu]	P_{avg} [psia]	S []
Rock 1	20	16	5600	0
Rock 2	600	11 \pm 5	5600 \pm 200	0
Rock 3	300 \pm 50	18	5600	0

Table 8.2: Assumed formation petrophysical properties for uncertainty analysis of the three-layer reservoir model.

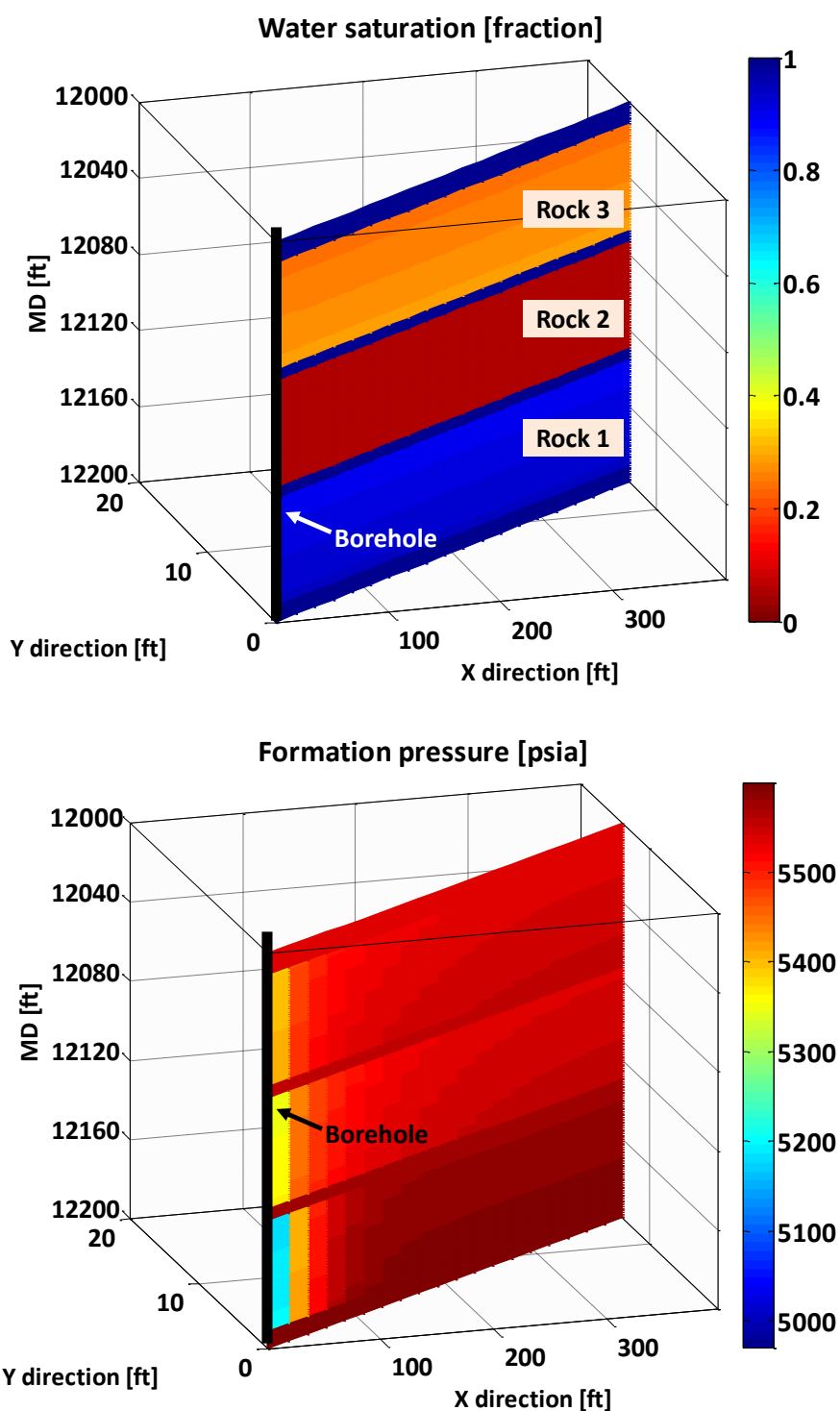


Figure 8.10: Simulated spatial distributions of water saturation (upper panel) and pressure (upper panel) prior to measurements acquisition in the three-layer reservoir model.

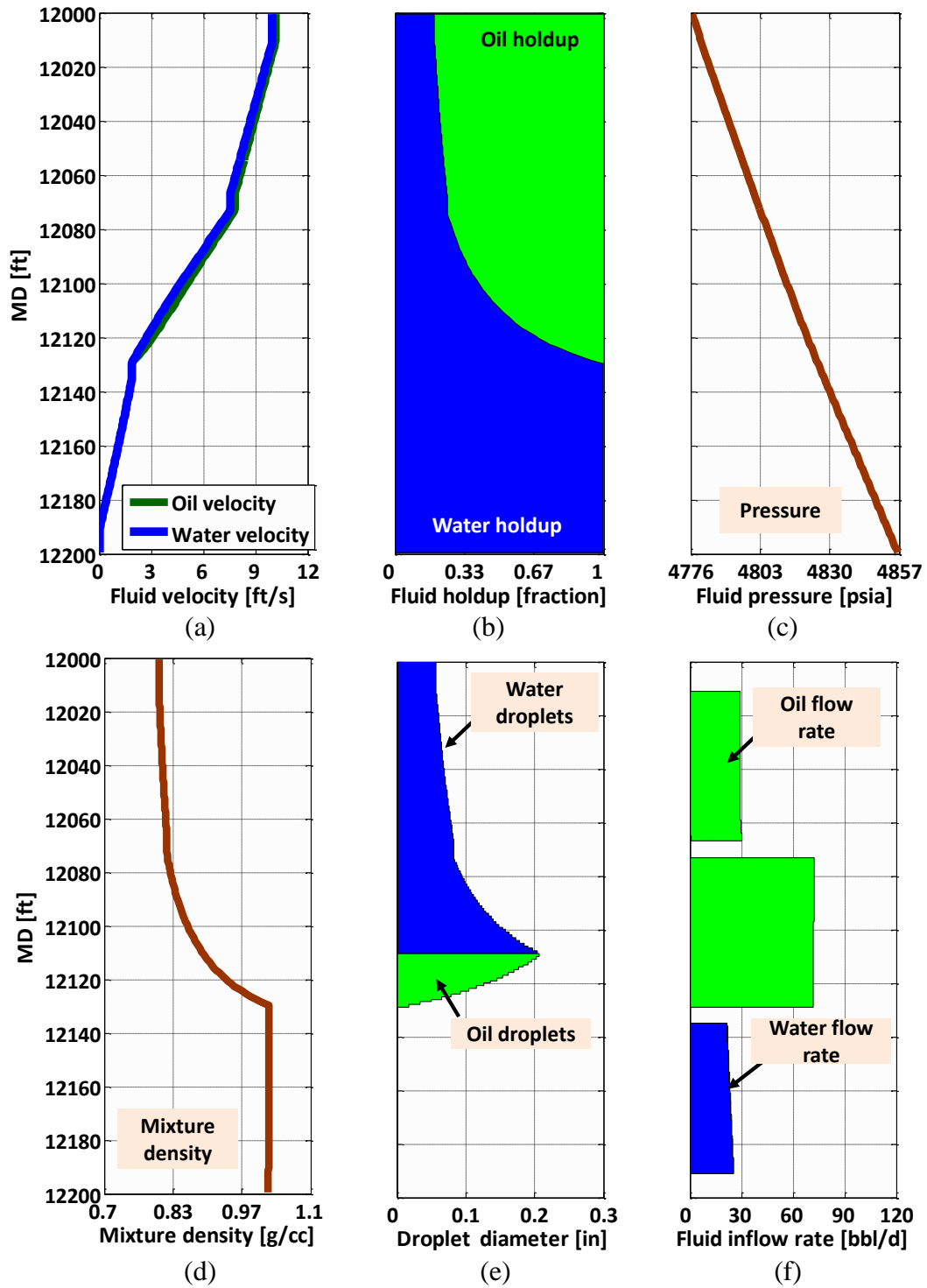


Figure 8.11: Simulated spatial distributions of borehole (a) fluid-phase velocity, (b) fluid-phase holdup, (c) fluid pressure, (d) fluid mixture density, (e) droplet diameter, and (f) fluid-phase inflow rate for the three-layer reservoir model.

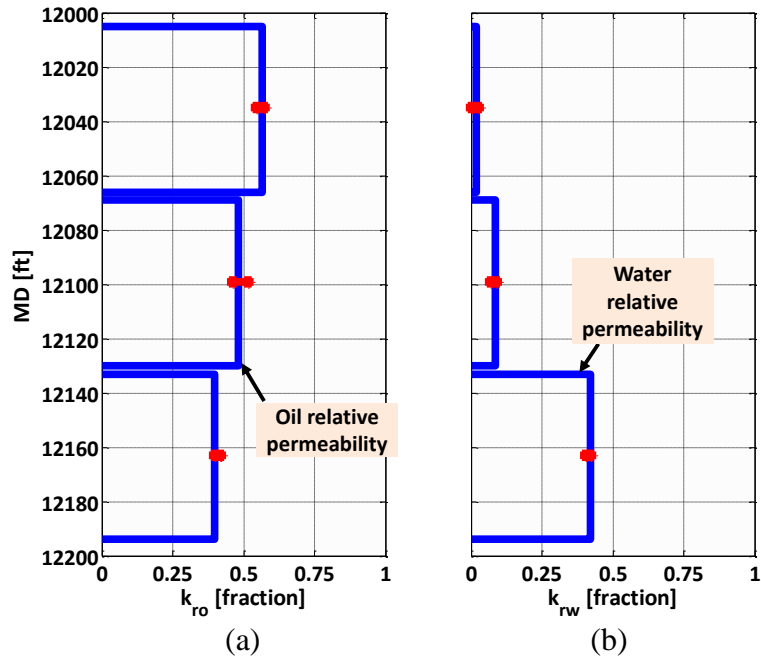


Figure 8.12: Uncertainty analysis for (a) oil-phase and (b) water-phase relative permeabilities due to the uncertainty associated with porosity of Rock 2.

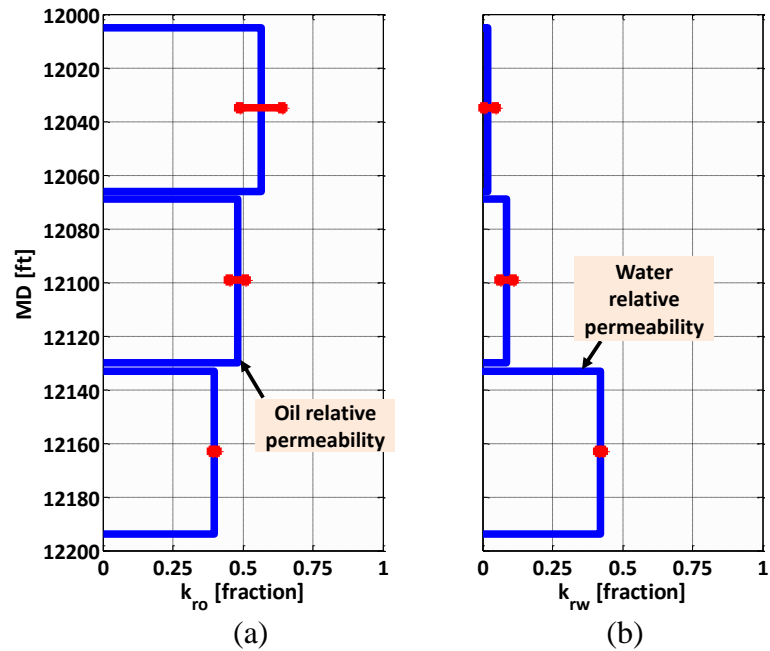


Figure 8.13: Uncertainty analysis for (a) oil-phase and (b) water-phase relative permeabilities due to the uncertainty associated with permeability of Rock 3.

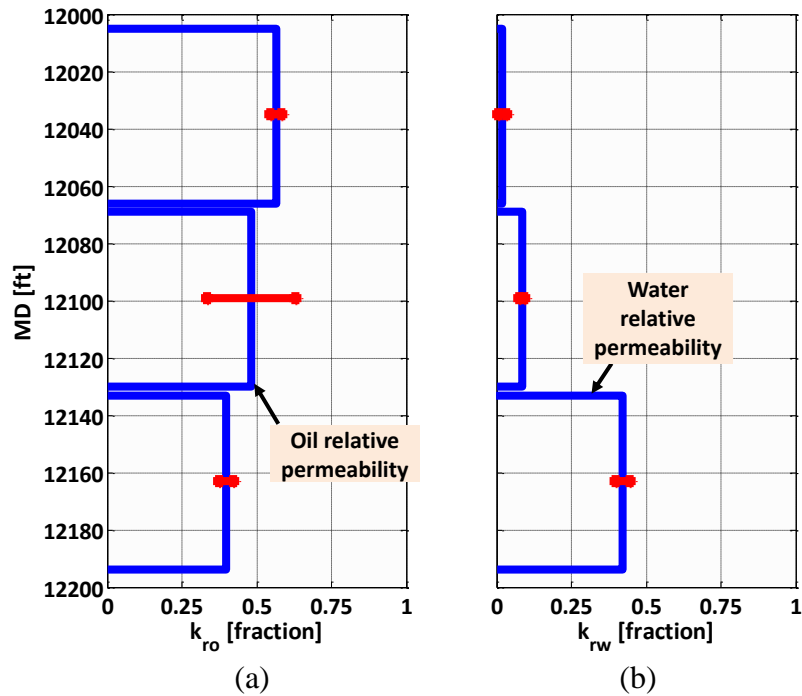


Figure 8.14: Uncertainty analysis for (a) oil-phase and (b) water-phase relative permeabilities due to the uncertainty associated with average pressure of Rock 2.

8.4 TIME-LAPSE ANALYSIS

Production logging is customarily regarded as a method to survey multiphase fluid displacements in the borehole. Acquisition and interpretation of these measurements in time-lapse mode enables the quantification of variations of near-borehole petrophysical properties over time. This section introduces a new application of the developed coupled fluid flow model in combining time-lapse production measurements to estimate near-borehole saturation-dependent relative permeability curves. Oil-water immiscible displacement process in a multilayer reservoir model is simulated to investigate the capabilities and limitations of the new interpretation method. The reservoir consists of three rock formations with capillary pressure and relative permeability curves shown in

Figure 8.9. Remaining formation, borehole, and fluid properties are identical to the three-layer reservoir model described in Section 8.3. In addition, rock formations with a 20-degree dip are supported by an infinite-acting aquifer located at the bottom of the reservoir (i.e., 12200 ft MD). An altered set of relative permeability curves, shown in Figure 8.15, is assumed for a cylindrical region with radius equal to 30 ft around the borehole. Fluid production is simulated with constant fluid flow rate equal to 1500 bbl/day for duration of 2 years while the acquisition of production measurements is scheduled once every 6 months.

Figure 8.16 shows the spatial distributions of formation pressure and water saturation simulated for three time lapses. Initially, near-borehole regions associated with Rocks 2 and 3 are nearly at conditions of irreducible water saturation while Rock 1 exhibits measurable amounts of free oil and water saturations. Over time, aquifer encroachment gives rise to hydrocarbon displacement, thereby continually increasing near-borehole water saturation. Variations of near-borehole water saturation depend on the smoothness and velocity of immiscible displacement front. Rock 2, with a high permeability and low capillary pressure values, exhibits a sharp and fast-moving displacement front. On the other hand, displacement front within Rock 1 is smooth and spread-out that is caused by high capillary pressures associated with that rock. As next section shows, displacing process and the time at which measurements acquisition takes place strongly influence the estimation of near-borehole saturation-dependent relative permeability curves.

Figures 8.17 and 8.18 describe production measurements for borehole fluid velocity, pressure, and oil-phase holdup acquired in 5 time lapses. Production logging interpretation is performed by minimizing quadratic cost function defined in Equation 8.3. The interpretation algorithm constructs a forward reservoir model to attribute

variations of production measurements to near-borehole relative permeability. To decrease uncertainty associated with formation petrophysical properties, the algorithm explicitly assumes availability of (i) relative permeability curves beyond near-wellbore region, and (ii) spatial distribution of near-borehole water saturation.

Figure 8.19 shows final estimate of relative permeabilities. At first time lapse, the estimated values associated with all the formations are limited to a narrow saturation window observed in the borehole. However, as displacement front advances toward the borehole, inversion algorithm obtains additional information about fluid flow, and accurately predicts a wider range of near-borehole relative permeability curves. Specifically, the advancement of displacement front in Rock 3 has made it possible to estimate fluid-phase relative permeabilities associated with water saturations ranging from 38% to 56%. By contrast, because Rock 2 was initially saturated with almost 83% water saturation, time-lapse integration has enabled to estimate only a narrow range of relative permeabilities associated with 83% to 85% water saturations. This analysis shows that the estimation process is passively influenced by the time and spatial variations of near-borehole water saturation. Therefore, depending on the water saturation window observed in the borehole, estimation of a portion or the entire curves of relative permeability is possible. However, as Figure 8.20 shows, the presence of measurements noise inevitably reduces the reliability of inverted estimates.

8.5 SUMMARY AND CONCLUSIONS

I introduced a new method to quantitatively interpret multiphase production logs by effectively coupling time-lapse fluid flow behavior taking place in both borehole and reservoir. The coupling of the two spatial domains via numerical simulation enabled the estimation of dynamic petrophysical properties of hydrocarbon-producing formations.

Specifically, it was shown that time-lapse borehole production measurements can be used to estimate saturation-dependent relative permeability. This estimation was possible in cases where hydrocarbon-producing formations experience measurable variations in water production over time.

Examples of verification with synthetic (numerically simulated) measurements indicated that accurate and reliable estimation of relative permeability from noisy borehole production measurements requires proper selection of the number of petrophysical layers within the depth zone of interest. It was shown that measurement noise and uncertainty in assumed formation petrophysical properties decreases the accuracy of estimated relative permeabilities. Estimations were most sensitive to formation average pressure, where the introduction of 4% perturbations in formation average pressure gave rise to more than 30% error in relative permeability estimates. This analysis confirmed that additional external information and measurements (e.g., well tests and well logs) must be integrated with production logs to reduce uncertainty associated with the estimation of saturation-dependent relative permeability.

The estimation of saturation-dependent relative permeability was next verified for the case of immiscible hydrocarbon displacement in a multilayer reservoir supported by an active aquifer. Simulated time-lapse production logs in this model yielded relative permeability curves within 10% of original values. However, depending on formation petrophysical properties, the accuracy and reliability of estimation results were limited by the effective water saturation window observed in the wellbore during production. The most favorable conditions to estimate relative permeability were observed across hydrocarbon-saturated rock formations exhibiting low capillary pressure. Such favorable conditions of immiscible fluid displacement led to a sufficiently wide window of water saturation over time in the near-wellbore region to reliably estimate complete curves of

relative permeability. Conversely, formations with high initial water saturation exhibited slight fractional flow increments during immiscible displacement thus limiting the estimation of relative permeability curves to a narrower window of water saturation. I additionally showed that the saturation window observed in the wellbore shifts toward higher values of water saturation as water displaces hydrocarbon. On account of this observation, I combined PL measurements acquired at various production times to widen the water saturation window, hence to improve the reliability of relative permeability estimates.

Because the displacement front is not observed in the wellbore prior to breakthrough time, under those conditions the estimation remains restricted to the end-point relative permeability for the displaced phase (i.e., hydrocarbon). On the other hand, at late times, the displacing phase (i.e., water) is the only movable phase in the reservoir, making it possible to only estimate the end-point relative permeability for water. This observation confirms that time-lapse production logs must be acquired during and after fluid breakthrough in the wellbore to secure reliable estimation of relative permeability from production logs.

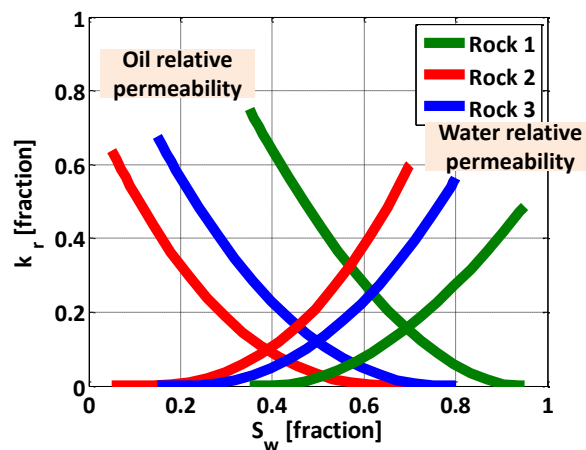


Figure 8.15: Assumed relative permeability curves in near-borehole region of the multilayer reservoir model for time-lapse PL analysis.

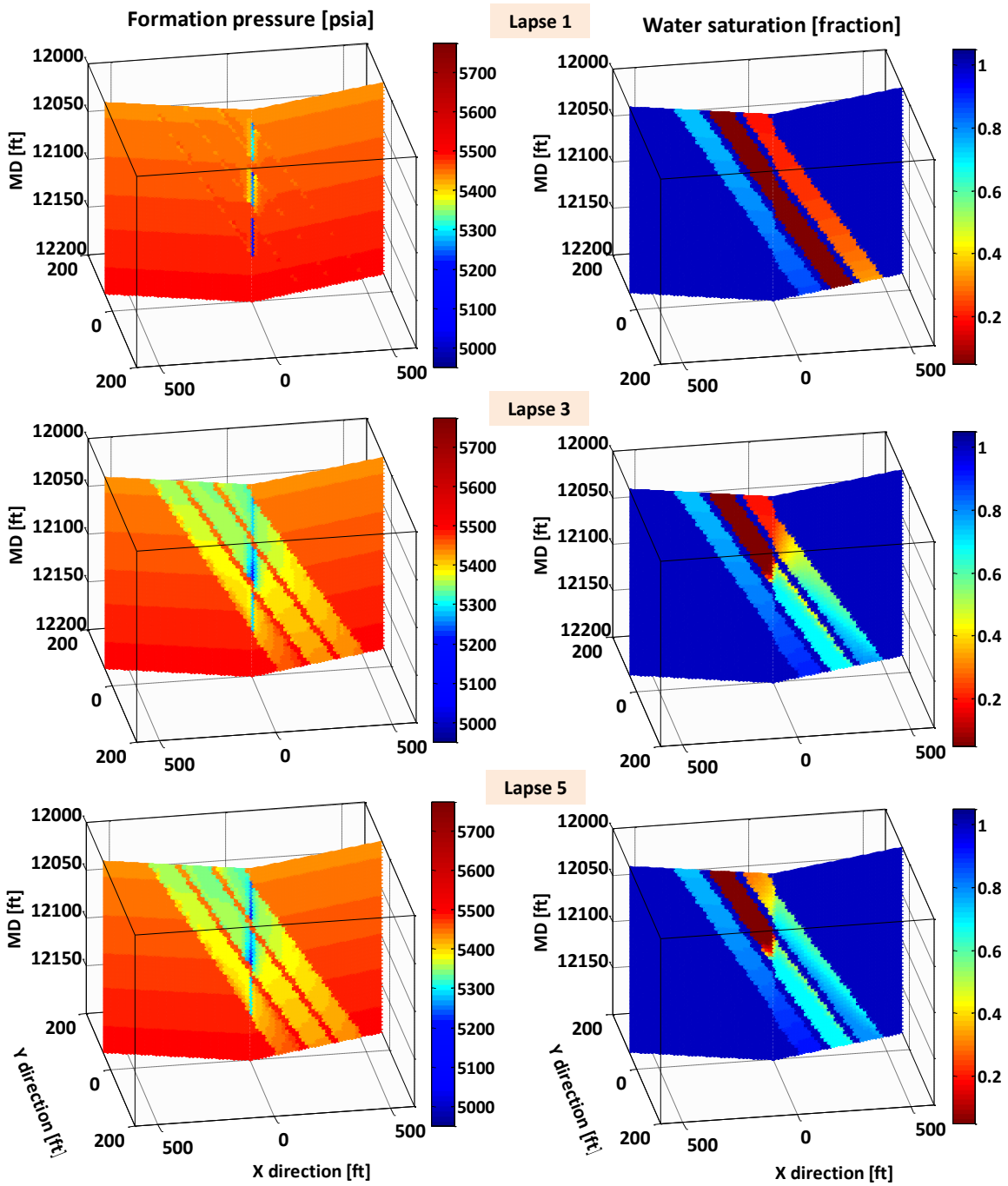


Figure 8.16: Numerically simulated spatial distributions of formation pressure (right column), and water saturation (left column) for time-lapse analysis of the multilayer reservoir model.

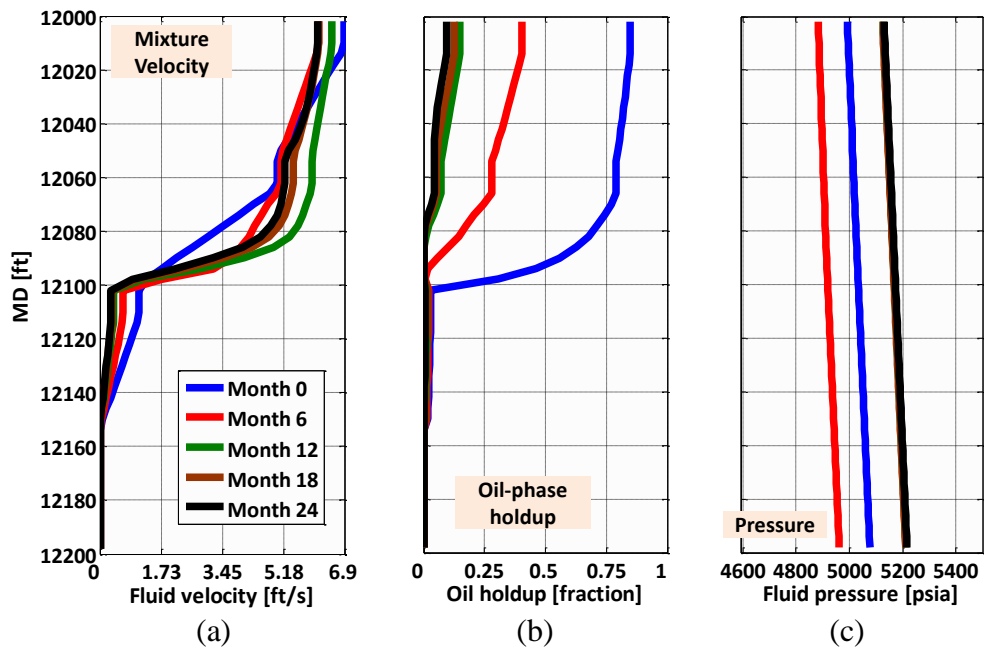


Figure 8.17: Spatial distributions of borehole (a) fluid mixture velocity, (b) oil-phase holdup, and (c) fluid pressure simulated for time-lapse analysis of the multilayer reservoir model.

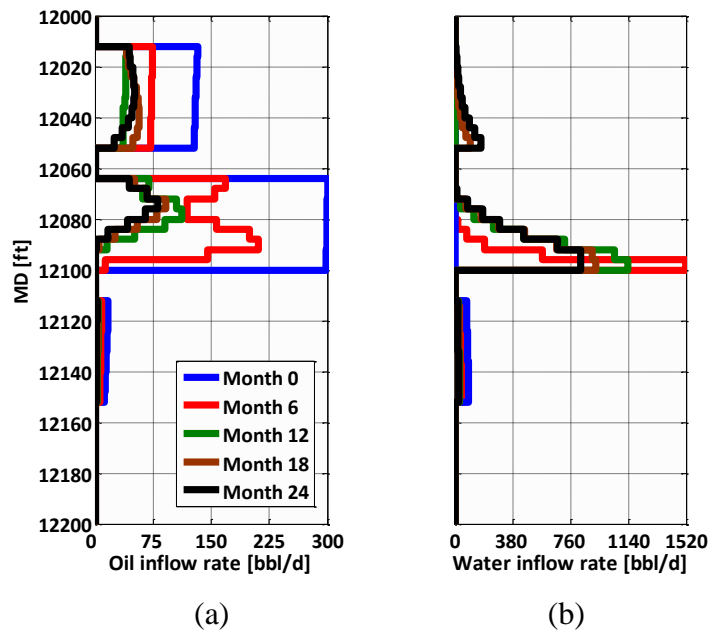


Figure 8.18: Spatial distributions of formation (a) oil-phase, and (b) water-phase incremental inflow rate simulated for time-lapse analysis of the multilayer reservoir model.

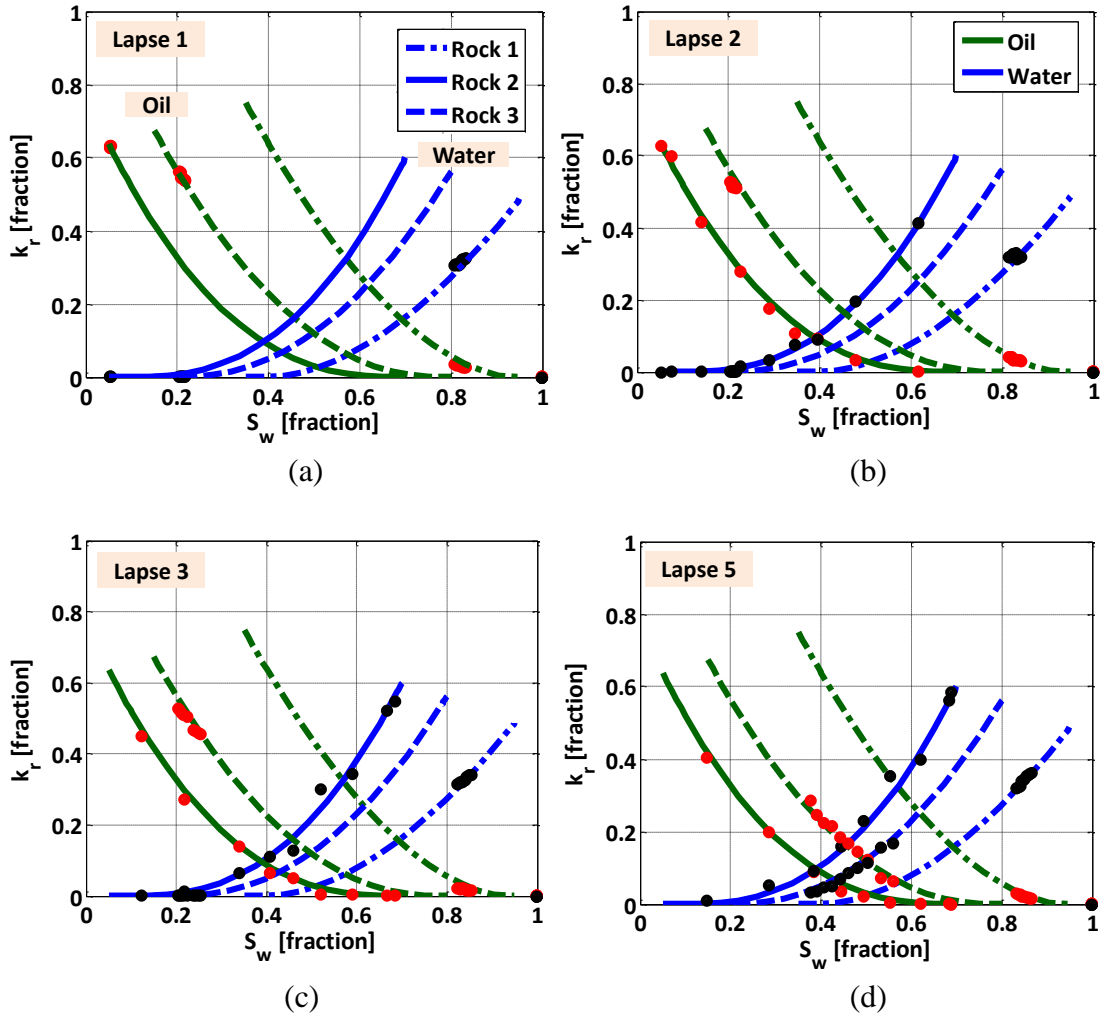


Figure 8.19: Comparison of the estimated and actual fluid-phase relative permeability performed for (a) first, (b) second, (c) third, and (d) fifth time lapses for the multilayer reservoir model.

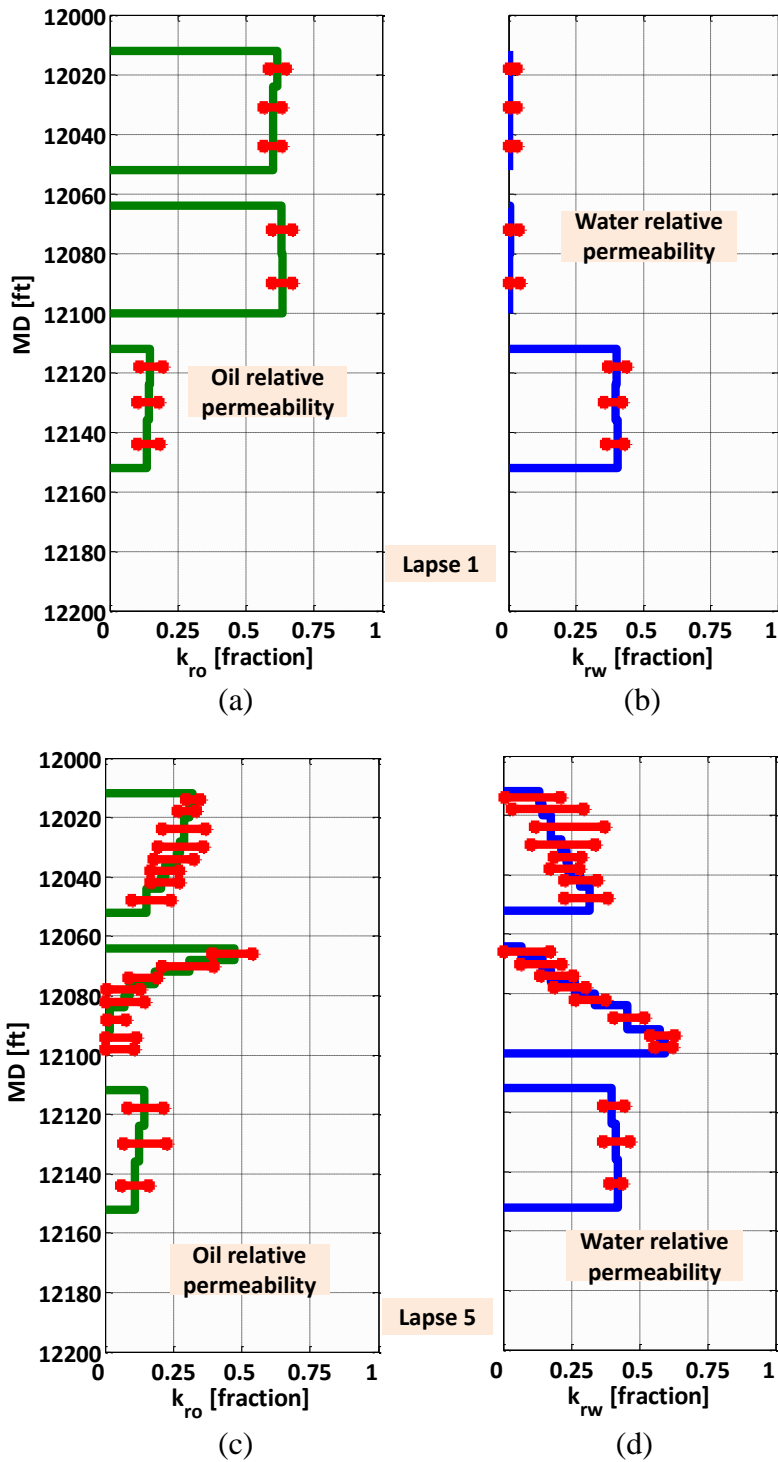


Figure 8.20: Uncertainty associated with the estimated fluid-phase relative permeability for first (Panels a and b) and last (Panels c and d) time lapses in time-lapse analysis of the multilayer reservoir model.

Chapter 9: Summary, Conclusions, and Recommendations

This chapter summarizes the technical contributions achieved in the dissertation, outlines the conclusions stemming from the research, and provides recommendations for future work.

9.1 SUMMARY

This dissertation developed and successfully verified a new borehole-formation fluid flow model to simulate and interpret measurements acquired with production logging tools (PLTs) in vertical and deviated boreholes. The developed borehole fluid flow model was based on an isothermal transient two-fluid formulation in one-dimensional (1D) cylindrical coordinates. The new fluid flow simulator enabled the simulation of time-dependent volume-averaged depth distributions of fluid-phase velocity, pressure, holdup, and density across fluid-producing rock formations. In addition, I developed an inversion-based interpretation method to estimate near-borehole formation petrophysical properties, namely, permeability, fluid-phase relative permeability, and fluid saturation from production logs (PL).

I simulated simultaneous flow of two fluid phases in oil-water, oil-gas, and gas-water flowing systems. Each fluid phase was modelled as an interpenetrating continuum exchanging mass and momentum with the remaining fluid phase. This modelling approach implemented separate mass and momentum conservation equations for each fluid phase, and introduced additional source terms into the conservation equations to

account for interfacial mass and momentum transfers. The mass and momentum conservation equations were numerically solved based on the following assumptions: an isothermal borehole hydraulically coupled to an isothermal reservoir, an identical pressure field shared by the two fluid phases, validity of local thermodynamic equilibrium, buoyant and drag forces as primary sources for momentum transfer, no momentum transfer caused by mass influx from the borehole wall, no mass transfer between the hydrocarbon and water phases, validity of flow-regime maps in pipes for borehole multiphase fluid flow, and borehole deviation angles equal to or less than 70 degrees.

The solution approach for borehole fluid flow equations was based on a guess-and-correct procedure to iteratively solve the partial differential equations arising from discretized fluid flow equations. The discretization was performed with a staggered gridding arrangement where fluid holdup and pressure were defined in the center of a discretized control volume, while fluid velocities were stored at the boundaries of the associated finite volume. I enforced a general mass balance equation to compute a guessed borehole pressure. Following the computation of pressure, fluid-phase momentum equations were implicitly solved to update the guessed fluid-phase velocity. Fluid-phase continuity equation was subsequently invoked to compute the associated fluid-phase holdup with an explicit method. This iterative guess-and-correct procedure continued until satisfying fluid-phase mass and momentum conservation equations.

I invoked an equation-of-state compositional method to model interfacial mass transfer between the oil and gas phases. This method solved $2 \times (n_c - 1)$ convective transport equations (n_c is the number of hydrocarbon components) to compute the overall hydrocarbon molar fraction. Subsequently, an equation-of-state-based compositional method was invoked to compute the associated hydrocarbon density and viscosity.

Following the computation of hydrocarbon properties, I updated interfacial source terms in fluid-phase mass conservation equations to accurately account for the effects of mass transfer on borehole fluid-phase volume fraction.

Separate approaches were taken to model the flow-regime transition for liquid-liquid and liquid-gas flows. In liquid-liquid flowing systems, I introduced oil- and water-dominant bubbly flow regimes with a transition point taking place about oil holdup equal to 0.5. Dispersed fluid phase (namely, oil or water droplets) were modelled as spherical droplets interacting with the continuous fluid phase via drag and buoyant forces. The spatial distribution of droplet diameter was dynamically modified to accurately account for variations of fluid-phase slip velocity along the borehole axial direction. In gas-liquid flowing systems, I identified the following flow regimes: bubbly flow, dispersed-bubbly flow, annular flow, and slug flow. A flow-regime map, originally introduced by Hasan and Kabir 1988a, was implemented to determine the occurrence of each flow regime. Interfacial drag forces were accordingly modified to accurately simulate the associated slip velocity.

A sequential method was developed to interface the borehole fluid flow model to an in-house reservoir simulator developed by Pour (2011). This method introduced additional source terms into borehole mass conservation equations to account for the mass influx from fluid-producing rock formations. At a given time, formation fluid flow equations were numerically solved to calculate fluid-phase and component molar influx. The current time step associated with formation flow equations was used as the time increment required for solving the borehole fluid flow equations. Following the calculation of borehole fluid-phase properties, boundary conditions associated with the formation flow domain was updated to advance the coupled fluid flow simulation to the next time step.

Interpretation of borehole production measurements was carried out by developing an inversion algorithm that minimized quadratic differences between simulated and measured fluid-phase velocity, volume fraction, and pressure. I decoupled the estimation of near-borehole permeability from fluid saturation by implementing three inner iterative refinement loops. The first loop associated variations of borehole fluid velocity and volume fraction across a petrophysical layer to the corresponding layer permeability under an explicit assumption for fluid situation. Following the estimation of layer permeability, variations of borehole fluid-phase holdup were computed to estimate layer fluid saturation (second loop). Subsequently, the entire permeability field was rescaled to honor the measured borehole pressure (third loop). As shown in Chapter 8, the developed iterative refinement was additionally modified to estimate near-borehole fluid-phase relative permeability from inversion of time-lapse oil-water production measurements.

Commingled production of two fluid phases from differentially-depleted rock formations led to borehole cross-flow where fluid phases flowed from the high- into low-pressure rock formations. Quantifying fluid flow behavior in the presence of differential depletion required a coupled transient borehole-formation dynamic model to simulate fluid flow both in the borehole and the near-borehole region. I conducted sensitivity analyses on various parameters governing the development of borehole cross-flow, and quantified their effects on borehole production measurements. I found that fluid-phase density contrast, pressure difference between differentially-depleted rock formations, and borehole deviation angle were the most important parameters that measurably affected the spatial distribution of near-borehole fluid-phase relative permeability of depleted layers.

Estimation of near-borehole fluid saturation and permeability enabled the quantification of pressure-production properties of fluid-producing rock formations. This method constructed near-borehole dynamic reservoir models that explicitly matched borehole production measurements. I showed that reconstructing borehole production measurements enabled the identification of rock formations exhibiting low productivity and those contributing unwanted gas or water production. The developed method was effectively used to evaluate possible workover remedial operations (e.g., gas or water shut-off) to enhance inflow performance of individual rock formations.

I introduced a new application of the developed borehole-formation flow model to estimate near-borehole formation damage from time-lapse production measurements. Production measurements acquired at various times were integrated to estimate depth variations of near-borehole permeability over the elapsed time. In the absence of time-lapse measurements, production logs were integrated with the available well logs to quantify near-borehole formation damage. I showed that the developed interpretation method enabled the differentiation between low-permeable and highly-damaged rock formations.

9.2 CONCLUSIONS

The most important conclusions stemming from this Ph.D. dissertation are summarized as follows:

1. Computational time associated with the simulation of borehole fluid-phase properties was a function of (i) fluid-phase velocity, (ii) fluid-phase density contrast, and (iii) borehole deviation angle. On a computer with 8.00 GB of memory (RAM) and 3.40 GHz of central processing power (CPU), processing times for simulation of single-phase and two-phase fluid properties decoupled

from the reservoir simulator were as follows: (i) 1 day of single-phase fluid flow in a vertical pipe with fluid initially at rest, constant pressure boundary condition at the pipe outlet, constant fluid velocity (equal to 5 ft/s) at the pipe inlet, and 200 finite control volumes, CPU time was less than a minute, (ii) 1 day of simultaneous flow of the hydrocarbon and water phases in a deviated pipe with 35° inclination angle initially filled with water at rest, hydrocarbon and water densities equal to 0.85 and 1 g/cc, respectively, and inlet fluid mixture velocity equal to 5 ft/s, required between 1 to 5 minutes of CPU time, (iii) 1 day of simultaneous flow of gas and oil phases in a deviated pipe with 55° inclination angle initially filled with oil at rest, oil and gas densities equal to 0.85 and 0.15 g/cc, respectively, and inlet fluid mixture velocity equal to 15 ft/s, required between 3 to 15 minutes of CPU time.

2. The new iterative coupling method integrated with the developed borehole fluid flow model allowed dynamic modification of reservoir boundary conditions to accurately simulate transient behavior of borehole cross-flow taking place across differentially-depleted rock formations. In the case of rapid variations of near-borehole properties, frequent borehole-formation communication inevitably increased the computational time required for fluid flow simulation. Despite this limitation, the developed coupling method allowed separate time-step control for borehole and formation fluid flow equations to ensure numerical stability of the solution.
3. The developed borehole fluid flow model accurately simulated phase separation of a homogeneous mixture of hydrocarbon and water with initial water holdup equal to 0.5. Fluid-phase velocity, computed for the undisturbed

middle section of the pipe, was within a 10% difference of the calculated value from the analytical model.

4. Several synthetic and field examples were examined to verify the accuracy of pressure-drop simulation over long pipes. For a gas-oil field example, documented by Hasan and Kabir (2002), results indicated less than 5% error for numerically computed pressure drop when compared to the reported pressure data.
5. Accuracy of the developed borehole fluid flow model to simulate fluid-phase slip velocity was verified against experimental results published by Shi et al. (2005) and Vigneaux et al. (1988). I showed that the simulated fluid-phase holdups for liquid-liquid and gas-liquid steady-state flowing conditions were within 15% of the corresponding measured values.
6. Simulation of production logs across differentially-depleted multilayer reservoirs under shut-in conditions indicated two different time scales: one associated with fluid flow in the borehole, and the other associated with fluid flow in porous media. For a borehole with a length equal to 100ft, and hydrocarbon and water densities equal to 0.85 and 1 g/cc, respectively, the required time for borehole fluids to reach hydrodynamic equilibrium was approximately 90 seconds. Beyond this early time, simulation results showed pressure equilibration between differentially-depleted layers caused by fluid production from high-pressure layers, and fluid injection into low-pressure layers. I quantified that depending on fluid and formation properties, the second time window could last days or months. These results enable petrophysicists to properly filter the effects of early-time hydrodynamic equilibration on borehole fluid properties, thereby reliably associating depth

variations of production measurements with formation petrophysical properties.

7. Fluid-phase density contrast was one of the most important factors controlling the development of two-phase cross-flow. I showed that increasing fluid-phase density contrast led to lower slip velocities, thereby decreasing borehole cross-flow with respect to the lighter fluid phase.
8. Inclining the borehole from the vertical direction caused agglomeration of bubbles toward the borehole's upper wall. I showed that flow-regime change in deviated boreholes gave rise to a considerable increase of fluid-phase slip velocity. For a two-layer reservoir model (with borehole length equal to 100ft, and hydrocarbon and water densities equal to 0.85 and 1 g/cc, respectively), deviation angles more than 15 degrees resulted in vanishing borehole cross-flow with respect to the lighter fluid phase. Therefore, it was necessary to account for depth variations of slip velocity to accurately simulate and interpret two-phase production logs.
9. The developed coupled fluid flow model enabled a new method to simulate two-phase selective-inflow-performance (SIP) analysis. I performed a SIP test on a synthetic four-layer reservoir model to estimate layer average pressure. The test consisted of the acquisition of several production logs at various production rates (including a shut-in test). Following the acquisition of borehole fluid-phase properties, borehole pressure was plotted as a function of incremental fluid flow rates. Borehole pressure associated with zero fluid production was subsequently interpreted as layer average pressure. The method estimated layer average pressure within 10% accuracy compared to actual pressure values.

10. Even though SIP analysis enabled the estimation of layer average pressure, borehole cross-flow across differentially-depleted layers led to change of layer pressure over time. The main advantage of using a coupled fluid flow model in the interpretation of production logs is to estimate time variations of layer pressure during measurement acquisition. When applied to field cases, the coupled flow algorithm lowers uncertainty associated with layer pressure, thus proving reliable information to condition available field-scale reservoir models. The reliability of this approach, however, is limited to the validity of the assumptions made on remaining dynamic properties (e.g., formation permeability and fluid saturation).
11. In the presence of differential depletion, low-pressure intervals were subject to fluid injection that caused the alteration of associated near-borehole fluid-phase saturation and relative permeability. Simulation of SIP tests showed that a reliable estimation of layer average pressure required excluding data points associated with fluid injection during the computation of pressure-production relationships.
12. The most reliable estimation of layer average pressure from SIP analysis was found across high-permeability layers producing single-phase fluid with a known fluid-phase density and viscosity. Reliability of the pressure estimation method was deteriorated by (i) lowering layer permeability, (ii) decreasing layer thickness, (iii) saturating the layer partially with a second fluid phase (that lowered fluid-phase relative permeability), and (iv) depleting layer pressure. The mentioned controlling factors cause a decrease of incremental fluid production rate across a layer, thereby lowering sensitivity of PLTs to layer properties. Therefore, it is highly recommended to acquire production

measurements at highest possible production rates to improve estimation reliability by increasing layer production during PL acquisition.

13. The coupled borehole-formation fluid flow model simulated transient behavior of water backflow in a gas well. Extensive sensitivity analyses were performed to estimate the minimum pressure drawdown required to prevent water backflow. I showed that the occurrence of water backflow was primarily a function of fluid-phase density contrast and borehole deviation angle. For a vertical flowing system with water and gas densities equal to 1 and 0.234 g/cc, respectively, water and gas viscosities equal to 1 and 0.031 cp, respectively, and formation permeability equal to 300 mD, the minimum pressure drawdown necessary to prevent water loading was equal to 1100 psi. Increasing the borehole inclination angle required higher pressure drawdown to lift the produced water.
14. Interpretation of production measurements using the coupled flow algorithm enabled identification of the following reservoir problems accountable for declining fluid production over time: (i) near-borehole formation damage, (ii) excessive gas production (because of gas coning), (iii) excessive water production (because of water encroachment), (iv) presence of depleted layers, and (v) fluid circulation (because of borehole cross-flow). Coupled PL interpretation recommended the following remedial actions to improve borehole inflow performance: (i) selective stimulation of damaged layers to decrease near-borehole skin effects, (ii) isolating gas- or water-producing intervals to prevent unwanted fluid production, (iii) maintaining the bottom-hole pressure above a limit necessary to prevent advancement of the gas or water fronts, and (iv) maintaining layer pressure by including injector wells

into the field. The main advantage of the new interpretation method was quantifying the added value of such remedial operations by constructing flow-calibrated dynamic reservoir models. When applying to field cases, it is highly recommended to incorporate independent measurements to decrease uncertainty associated with borehole, fluid, and formation properties.

15. Interpretation of two-phase production logs consisted of inference of near-bore permeability and fluid saturation. The most favorable conditions leading to reliable estimates of formation properties were across high-permeability layers with measurable incremental fluid-phase production. As fluid-phase saturation became close to end-point values, the dominant fluid phase, even across high-permeability layers, was the only fluid phase detectable by PLTs that gave rise to (wrong) interpretation of single-phase conditions. To circumvent this problem, well-log-derived rock classification should be integrated with PL interpretation to enforce a known end-point fluid saturation (and relative permeability) based on the assumed rock type.
16. The inversion method developed in this dissertation generated several depth windows in the borehole to associate variations of production logs to formation petrophysical properties. Computing variations (slop) of borehole measurements across each depth window (instead of using their absolute values) selectively increased the sensitivity of borehole fluid measurements to a certain unknown petrophysical property. This method increased diagonal dominance of the Jacobian matrix by filtering the effects of adjacent layers on measurements acquired within a certain depth window. Despite its numerical stability, PL inversion using the windowing method increased sensitivity of estimated properties to measurement noise. When applying to noisy data, it is

therefore recommended to process production logs to decrease the detrimental effects of noise prior to PL inversion.

17. Because of low vertical resolutions associated with borehole production measurements, PL interpretation was unable to estimate fine variations of layer permeability across thin layers. As an alternative method, the coupled algorithm is recommended to begin the interpretation with a single-layer reservoir model, and progressively refine the estimated permeability until reaching a certain limit of estimation uncertainty. The advantage of this approach is to secure a reliable initial guess of layer permeability from the results of preceding (less refined) interpretation steps. It is recommended to verify the estimated permeability of the single-layer reservoir model against pressure-transient analyses in order to begin the estimation process with the construction of a reliable flow-calibrated reservoir model.
18. The coupled interpretation algorithm made explicit assumption on reservoir far-field permeability to estimate formation damage from production logs. This method constructed a three-dimensional permeability distribution based on the one-dimensional well-log-derived permeability. However, the reliability of the assumed far-field permeability depends on the degree of rock heterogeneity laterally away from the borehole. When applied to highly-heterogeneous rocks, it is necessary to condition the PL interpretation to available field-scale reservoir models to account for large volume of investigation associated with production logs. An alternative approach was the integration of production logs acquired in time-lapse mode to infer formation damage over the elapsed time. Interpretation of production logs, if available in

time-lapse mode, helps reservoir engineers to identify highly-damaged layers, and plan adequate stimulation operations to enhance borehole productivity.

19. In a synthetic multilayer reservoir model supported by a gas cap, fluid production gave rise to the advancement of the gas front, thus causing the alteration of near-borehole gas saturation. Interpretation of production measurements effectively estimated average near-borehole gas saturations and permeabilities within 20% and 25% accuracy, respectively. For layers at conditions of immovable gas saturation, however, PL interpretation was unable to reliably estimate near-borehole petrophysical properties. A-priori knowledge about immovable gas saturation was included in the interpretation process to decrease the associated uncertainty.
20. While pressure-transient analyses provided no information about depth distributions of formation properties, interpretation of production measurements enabled the quantification of pressure-production behavior of individual rock formations in multilayer reservoirs. For a synthetic model, I quantified the effect of borehole pressure on inflow performance of various fluid-producing rock formations. In the presence of a gas cap, a minimum borehole pressure was determined to prevent the advancement of the gas front from gas saturated layers.
21. Sensitivity analyses showed that production logs exhibited the largest sensitivity across high-permeability layers. Lowering layer permeability led to decreasing fluid influx, thereby decreasing variations of borehole fluid velocity and holdup across the layer. When contaminated with 10% random noise, interpretation of production measurements across a layer with 50 mD

permeability involved more than 100% error into the estimated layer permeability.

22. Uncertainty of the assumed formation average pressure was one the most detrimental parameters that (adversely) influenced the estimated near-borehole permeability. In a four-layer model, increasing formation average pressure by a factor of 8% caused more than 30% underestimation of the associated permeability. To circumvent this problem, independent measurements (e.g., formation testing measurements) should be incorporated into PL interpretation to construct a reliable forward reservoir model.
23. Unaccounted variations of fluid-phase slip velocity across fluid-producing depth intervals gave rise to erroneous estimation of near-borehole fluid saturation. The most unfavorable conditions were found in gas-oil flowing systems where fluid-phase density contrast was considerably high. For a four-layer gas-oil flowing system (with gas and oil densities equal to 0.19 and 0.85 g/cc, respectively), the use of a no-slip model led to 12% error in the estimated near-borehole gas saturation when compared to the corresponding value estimated with the developed coupled model.
24. Interpretation of borehole production measurements in multilayer reservoirs was effectively used to identify layers with high water or gas production. It showed that the estimated near-borehole petrophysical properties enabled evaluation of the performance of remedial operations (e.g., gas shut-off or water shut-off) to decrease unwanted fluid production, thereby enhancing formation productivity.
25. Incremental water production from a multilayer reservoir supported by an infinite-acting aquifer was simulated to synthetically acquire oil-water

production measurements in time-lapse mode. I invoked the developed interpretation method to integrate time-lapse production measurements, and to estimate formation damage over the elapsed time. Results showed that for a layer with permeability equal to 800 mD and skin factor equal to 5.1, the estimated permeability and skin factor were within 23% and 21% accuracy, respectively. An advantage of the new method was to differentiate between mechanical skin and skin due to the presence of a second fluid phase. In addition, the new method enabled quantifying depth variations of formation damage. However, a limitation arose from the validity of assumptions made on formation properties laterally away from the borehole.

26. Simulated production measurements acquired across a multilayer reservoir were interpreted in time-lapse mode to estimate near-borehole fluid-phase relative permeability. For a reservoir supported by an infinite-acting aquifer, the estimated relative permeability curves were within 10% of original values. However, I showed that incremental water production over time caused the estimated near-borehole relative permeability to continually shift toward higher values of water saturation. Therefore, accuracy and reliability of the estimated relative permeabilities were limited by the effective water saturation window measured across fluid-producing rock formations.
27. Sensitivity analyses performed on a synthetic multilayer reservoir model showed that the estimates of fluid-phase relative permeability were most sensitive to formation average pressure. I quantified that introducing only 4% perturbation in formation average pressure gave rise to more than 33% error in fluid-phase relative permeability estimates.

9.3 RECOMMENDATIONS FOR FUTURE STUDIES

The following items summarize my suggestions for potential improvements of the method developed in this dissertation to simulate and interpret borehole production measurements:

1. The two-fluid method developed in this dissertation enabled an accurate simulation of fluid-phase velocity and holdup. However, with slight modifications, the two-fluid computer code can be adapted for homogenous or drift-flux models. I suggest making use of the latter methods to provide an initial estimate of borehole fluid-phase properties for preconditioning the two-fluid simulation. This approach should enhance convergence behavior of the two-fluid algorithm.
2. The coupled borehole-formation fluid flow model in this dissertation was based on the assumption of isothermal conditions. An energy equation can be incorporated into both reservoir and borehole equations to account for depth variations of temperature across fluid-producing rock formations. I suggest a homogeneous approach to simulate fluid mixture temperature along the borehole axial direction. Including a thermal model into the fluid flow simulation enables (i) identifying gas-producing rock formations, and (ii) estimating near-borehole formation damage.
3. The developed borehole-formation fluid flow model included boreholes with inclination angles equal to or less than 70 degrees. The borehole fluid flow model can be extended to horizontal and near-horizontal fluid flows by incorporating the associated flow-regime maps. Because flow regimes are significantly dependent upon borehole deviation angle, I suggest to develop reservoir and borehole fluid flow models capable of accounting for slight

variations of borehole deviation angle along the borehole trajectory. This extension requires implementing a formation fluid flow model based on an unstructured grid arrangement that allows conformity with borehole geometry.

4. The interpretation method developed in this dissertation used measurements acquired with PLTs to estimate near-borehole fluid saturation. As a limitation, this interpretation method was unable to estimate fluid saturation across unperforated depth intervals. I propose the integration of cased-hole production logs (e.g., Sigma logs) with PLT measurements to estimate fluid saturation beyond perforated intervals. Combined interpretation of production logs and Sigma logs should help to quantify the enhancement of oil recovery caused by performing add-perforation operations.
5. Implementation of a fast reservoir simulator such as those based on the streamline tracing methods can reduce the computational time associated with the simulation of two-phase production measurements across complex heterogeneous rocks. I recommend the incorporation of a fast reservoir simulator to compute the Jacobian matrix used in the inversion of borehole production measurements.
6. Quantitative interpretation of borehole production measurements can be extended to fractured reservoirs. I suggest incorporating a suitable fracture model (e.g., discrete fracture network) into the coupled fluid flow simulator to enable the simulation of fluid flow regimes in matrix and fracture networks. Embedding the fracture network into the matrix flow model enables the estimation of near-borehole fracture properties such as fracture permeability.
7. Window-by-window interpretation of borehole production measurements in this dissertation was performed under the assumption of parallel layers

exhibiting constant thickness regardless of their distance from the borehole. Even though borehole fluid velocity and holdup are not sensitive to the lateral extent of layers, (wrong) assumption of constant layer thickness adversely influences measurements of borehole pressure that consequently leads to unreliable estimates of near-borehole permeability. Therefore, I suggest constraining the PL interpretation to available geological maps to account for significant lateral variations of layer thickness (namely, due to funneling effects) within the volume of investigation associated with PL measurements.

Appendix A: Peng-Robinson's Equation of State

The borehole fluid flow model developed in this dissertation invokes a compositional PVT model that uses Peng-Robinson's equation of state (PR-EOS) to compute hydrocarbon-phase compressibility factors. The cubic form of PR-EOS is written as (Firoozabadi, 1999)

$$Z_h^3 + (-1 + B)Z_h^2 + (A - 3B^2 - 2B)Z_h - (AB - B^2 - B^3) = 0, \quad (\text{A.1})$$

where Z is fluid-phase compressibility factor, given by

$$Z_h = \frac{P\hat{V}_h}{RT}, \quad (\text{A.2})$$

where P and T are borehole pressure and temperature, respectively, \hat{v} is hydrocarbon molar volume, R is the gas universal constant defined by Equation 2.36. Coefficients A and B in Equation A.1 are computed as follows:

$$A = \frac{aP}{(RT)^2}, \quad (\text{A.3})$$

and

$$B = \frac{bP}{RT}, \quad (\text{A.4})$$

where a and b are functions of hydrocarbon-component properties as

$$a = \sum_{j_1=1}^{n_c} \sum_{j_2=1}^{n_c} \hat{x}_{j_1} \hat{x}_{j_2} a_{j_1 j_2}, \quad \text{and} \quad b = \sum_{j_1=1}^{n_c} \hat{x}_{j_1} b_{j_1}, \quad (\text{A.5})$$

where coefficient $a_{j_1 j_2}$ is calculated by

$$a_{j_1 j_2} = (1 - \delta_{j_1 j_2}) \sqrt{a_{j_1} a_{j_2}}. \quad (\text{A.6})$$

In Equations A.5 and A.6, superscripts "j₁" and "j₂" identify hydrocarbon components, n_c is the number of hydrocarbon components, δ_{j₁j₂} is binary interaction coefficient between components j₁ and j₂, x̂ is component molar fraction, and a_j and b_j are given by

$$a_j = \Omega_a \frac{\alpha (RT_{j,\text{crit}})^2}{P_{j,\text{crit}}}, \quad \text{and} \quad b_j = \Omega_b \frac{RT_{j,\text{crit}}}{P_{j,\text{crit}}}, \quad (\text{A.7})$$

where T_{j,crit} and P_{j,crit} are component critical temperature and pressure, respectively, and Ω_a, Ω_b, and α are defined as

$$\Omega_a = 0.45724, \quad \Omega_b = 0.0778, \quad \text{and} \quad (\text{A.8})$$

$$\alpha = \left\{ 1 + (1 + 0.37464 + 1.54226 A_{C,j} - 0.26992 A_{C,j}^2) \left[1 - \sqrt{\frac{T}{T_{j,\text{crit}}}} \right] \right\}^2. \quad (\text{A.9})$$

where A_{C,j} is component acentric factor.

List of Symbols

a	Constant in PR-EOS
a_{ik}	Interfacial area concentration for k-th fluid phase, 1/ft
\hat{a}_{ik}	Dimensionless interfacial area concentration for k-th fluid phase
A	Parameter of PR-EOS
A_c	Acentric factor
A_{cv}	Area of the faces of a finite control volume, ft ²
$A_{i_s, x_{jk}}$	Coefficients of discretized component-based mass conservation equation, lb _m /s/ft ³
$A_{i_s, PC}$	Coefficients of discretized two-phase pressure-correction equation, lb _m /ft ³ /s/psi
$A_{i_s, PC}^S$	Coefficients of discretized single-phase pressure-correction equation, lb _m /ft ³ /s/psi
A_{i_s, α_k}	Coefficients of discretized fluid-phase mass conservation equation, lb _m /s/ft ³
$A_{i_v, P}$	Pressure coefficients for discretized single-phase momentum conservation equation, 1/ft
A_{i_v, P_k}	Pressure coefficients for discretized fluid-phase momentum conservation equation, 1/ft
$A_{i_v, V}$	Velocity coefficients for discretized single-phase momentum

	conservation equation, $\text{lb}_m/\text{s}/\text{ft}^3$
A_{i_v, V_k}	Velocity coefficients for discretized fluid-phase momentum conservation equation, $\text{lb}_m/\text{s}/\text{ft}^3$
$A_{i_v, V_{lk}}$	Interfacial velocity coefficients for discretized fluid-phase momentum conservation equation, $\text{lb}_m/\text{s}/\text{ft}^3$
$A_{i_v, \rho}$	Coefficients of discretized single-phase mass conservation equation, lb_m/ft^4
A_{i_v, ρ_k}	Coefficients of discretized overall mass conservation equation, $1/\text{ft}$
A_k	Projected area of a droplet perpendicular to flow direction, in^2
A_{perf}	Perforated area available for fluid phases to flow into the borehole, in^2
$A_{p,r}$	Radially-projected area of the interface shared by two adjacent petrophysical layers in a formation grid block, ft^2
$A_{p,z}$	Vertically-projected area of the interface shared by two adjacent petrophysical layers in a formation grid block, ft^2
$A_{p,\theta}$	Azimuthally-projected area of the interface shared by two adjacent petrophysical layers in a formation grid block, ft^2
$A_{v,r}$	Radially-projected area of the portion of a formation grid block occupied by a petrophysical layer, ft^2
$A_{v,z}$	Vertically-projected area of the portion of a formation grid block occupied by a petrophysical layer, ft^2
$A_{v,\theta}$	Azimuthally-projected area of the portion of a formation grid block

	occupied by a petrophysical layer, ft^2
b	Constant in PR-EOS
B	Parameter of PR-EOS
$B_{i_s, x_{jk}}$	Source terms of discretized component-based mass conservation equation, $\text{lb}_m/\text{s}/\text{ft}^3$
$B_{i_s, PC}$	Source terms of discretized two-phase pressure-correction equation, $\text{lb}_m/\text{s}/\text{ft}^3$
$B_{i_s, PC}^S$	Source terms of discretized single-phase pressure-correction equation, $\text{lb}_m/\text{s}/\text{ft}^3$
B_{i_s, α_k}	Source terms of discretized fluid-phase mass conservation equation, $\text{lb}_m/\text{s}/\text{ft}^3$
$B_{i_v, V}$	Source terms of discretized single-phase momentum conservation equation, lb_f/ft^3
B_{i_v, V_k}	Source terms of discretized fluid-phase momentum conservation equation, lb_f/ft^3
$B_{i_v, \rho}$	Source terms of discretized single-phase mass conservation equation, $\text{lb}_m/\text{s}/\text{ft}^3$
B_{i_v, ρ_k}	Source terms of discretized overall mass conservation equation, $1/\text{s}$
C	Fluid isothermal compressibility, μsip
C_D	Drag coefficient
C_L	Cost function, fraction

C_o	Distribution parameter
C_{perf}	Perforation shape factor
\mathbf{d}	Vector of production measurements
d_{CD}	Critical bubble diameter for bubble deformation, in
d_{stable}	Stable bubble diameter in dispersed-bubbly flow regime, in
D	Borehole diameter, in
D_b	Bubble diameter, in
D_h	Pipe hydraulic diameter, in
D_{hk}	Pipe hydraulic diameter with respect to k-th fluid phase, in
D_h^{int}	Interfacial shape factor, in
D_{min}	Minimum pipe diameter for the occurrence of bubbly flow regime, in
e_L	Data residual, fraction
f^{int}	Interfacial friction coefficient for annular flow regime
f_{Dlk}	Interfacial friction coefficient for k-th fluid phase from l th fluid phase
f_k	Wall friction factor for k-th fluid phase
f_m	Wall friction factor for fluid mixture
$F_{B,r}$	Radial component of buoyant force on a droplet, lb_f/ft^3
\vec{F}_D	Vector of interfacial drag force, lb_f/ft^3
F_D	Interfacial drag force, lb_f/ft^3
F_{Dlk}	Drag force on k-th fluid phase from l-kh fluid phase, lb_f/ft^3
F_{Dk}	Drag force on k-th fluid phase, lb_f/ft^3

$F_{D,r}$	Radial component of interfacial drag force on a droplet, lb_f/ft^3
F_{Da}	Interfacial drag force associated with annular flow regime, lb_f/ft^3
F_{Db}	Interfacial drag force associated with bubbly flow regime, lb_f/ft^3
F_{Ds}	Interfacial drag force associated with segregated flow regime, lb_f/ft^3
F_{Dsl}	Interfacial drag force associated with slug flow regime, lb_f/ft^3
F_{Du}	Interfacial drag force associated with uniformly-distributed flow regime, lb_f/ft^3
$F_{T,r}$	Radial component of turbulent-induced force on a droplet, lb_f/ft^3
$\bar{F}_{T,r}$	Volume-averaged radial component of turbulent-induced force on a droplet, lb_f/ft^3
F_{Wk}	Wall friction force acting on k-th fluid phase, lb_f/ft^3
\vec{F}_{Wk}	Vector of wall friction force acting on k-th fluid phase, lb_f/ft^3
\vec{F}_{Wm}	Wall friction force acting on fluid mixture, lb_f/ft^3
g	Gravitational acceleration, ft/s^2
h	Formation thickness, ft
$H_{i_v,P}$	Pressure-velocity correction coefficient for single-phase flow, $\text{ft}/\text{s}/\text{psi}$
$H_{i_v,Pk}$	Implicit form of pressure-velocity correction coefficient for two-phase flow, $\text{ft}/\text{s}/\text{psi}$
$G_{i_v,Pk}$	Explicit form of velocity-correction coefficient for two-phase flow, $\text{ft}/\text{s}/\text{psi}$
$H_{i_v,Vlk}$	Implicit form of velocity-velocity correction coefficient for two-phase

	flow
I	Identity matrix
J	Jacobian matrix
K	Unknown layer permeability vector, mD
k_r	Fluid-phase relative permeability, fraction
k_{rk}	Fluid-phase relative permeability, fraction
k_{rk}^0	Fluid-phase end-point relative permeability, fraction
K_r	Permeability of a formation grid block in radial direction, mD
K	Formation permeability, mD
K^{ref}	Reference permeability, mD
K_d	Directional permeability, mD
K_{ff}	Far-field permeability, mD
K_h	Horizontal permeability, mD
K_{nw}	Near-borehole permeability, mD
K_{Parallel}	Average permeability of layers in parallel arrangement, mD
K_s	Permeability of near-borehole damaged region, mD
K_{Series}	Average permeability of layers in series arrangement, mD
K_v	Vertical permeability, mD
K_z	Permeability of a formation grid block in vertical direction, mD
K_θ	Permeability of a formation grid block in azimuthal direction, mD
L_p	Laplace length, in

\hat{L}_p	Dimensionless Laplace length
m	Slope of borehole pressure as a function of time in pressure-time semi-log plot
\vec{M}_k^{int}	Interfacial forces acting on k-th fluid phase, lb_f/ft^3
MW_h	Hydrocarbon-phase molar mass, $\text{lb}_m/\text{lb}_m \text{ mole}$
MW_j	Molar mass of j-th hydrocarbon component, $\text{lb}_m/\text{lb}_m \text{ mole}$
n	North face of a control volume
\hat{n}	Unit vector perpendicular to the surface of a control volume
n_c	Number of hydrocarbon components
n_d	Drift-velocity exponent
n_p	Number of fluid phase
N_m	Number of borehole measurements
N_{mp}	Number of measured borehole pressure
N_p	Number of formation unknown properties
N_s	Number of SCVs
N_v	Number of VCVs
N_{wp}	Number of permeability windows for inversion of production logs
N_{wrp}	Number of relative permeability windows for inversion of production logs
N_{ws}	Number of fluid-saturation windows for inversion of production logs
P	Borehole pressure, psia

p^m	Measured borehole pressure, psia
p^s	Simulated borehole pressure, psia
P_{avg}	Formation average pressure, psia
P_{bh}	Bottom-hole pressure, psia
P_c	Capillary pressure, psi
P_{crit}	Critical pressure, atm
P_k	Fluid-phase pressure, psia
P_k^{int}	Fluid-phase pressure at interface, psia
Q_g	Gas flow rate from formation, MMSCFPD
Q_o	Oil flow rate from formation, STBPD
Q_t	Total fluid flow rate from formation, ft ³ /s
r	Radial distance from borehole centerline, in
r_s	Radius of near-borehole damaged region, in
r_w	Borehole radius, in
R	Gas universal constant, 10.73159 ft ³ psi/ °R /lb _m mole
R_d	Droplet radius, in
Re_m	Reynolds number with respect to fluid mixture velocity
Re_s	Reynolds number with respect to slip velocity
s	South face of a control volume
S	Skin factor
S^{int}	Interfacial area, in ²

S_k	Fluid-phase saturation, fraction
\mathbf{S}_k	Unknown fluid-phase saturation vector, fraction
S_v^m	Variations of measured fluid velocity across a layer, 1/s
S_v^s	Variations of simulated fluid velocity across a layer, 1/s
S_α^m	Variations of measured fluid holdup across a layer, 1/ft
S_α^s	Variations of simulated fluid holdup across a layer, 1/ft
S_{wir}	Irreducible water saturation, fraction
sign	Sign function
t	Time, s
t_n	Discretized time, s
T	Borehole temperature, °F
T_{avg}	Formation average temperature, °F
T_{crit}	Critical temperature, °K
v	Volume of a finite control volume in the borehole, ft ³
v'	Radial velocity fluctuations, ft/s
$\overline{v'^2}$	Root mean square of radial velocity fluctuations, ft/s
v_b	Volume of a formation grid block, ft ³
v_{bi}	Volume of a formation grid block occupied by i-th layer, ft ³
\hat{v}_h	Hydrocarbon molar volume, ft ³ /mole
V	Fluid velocity in single-phase flow, ft/s
V_{crit}	Critical volume, m ³ /kgmole

V_d	Drift velocity, ft/s
V_h	Hydrocarbon-phase velocity, ft/s
V_k	Fluid-phase velocity, ft/s
\vec{V}_k	Fluid-phase velocity vector, ft/s
\vec{V}_k^{int}	Fluid-phase velocity at interface, ft/s
V_{ks}	Fluid-phase superficial velocity, ft/s
\vec{V}_m	Fluid mixture velocity vector, ft/s
$V_{m,r}$	Radial component of fluid mixture velocity, ft/s
V_∞	Bubble terminal rise velocity, ft/s
$V_{\infty\theta}$	Modified bubble terminal rise velocity, ft/s
\mathbf{W}_L	Data weighing matrix
W_e	Eccentricity factor
W_{sl}	Interpolation weighting factor for computation of drag force associated with slug flow regime
\mathbf{x}^c	Vector of unknown petrophysical properties
\hat{x}_j	Molar fraction of j-th component in first hydrocarbon phase, fraction
x_{jk}	Mass fraction of j-th component in k-th fluid phase, fraction
\hat{y}_j	Molar fraction of j-th component in gas phase, fraction
z	Borehole axial position, ft
z_{is}	Axial position of the center-point of a SCV, ft

z_{i_v}	Axial position the center-point of a VCV, ft
\hat{z}_j	Overall molar fraction of j-th component in hydrocarbon phase, fraction
Z_h	Hydrocarbon-phase compressibility factor

Subscript

D	Drag force
g	Gas phase
h	Hydrocarbon phase
i_m	Index of borehole production measurements
i_p	Index of formation unknown properties
i_s	Index of scalar-property control volumes
i_v	Index of velocity control volumes
j	Hydrocarbon-component index
k	Index of fluid phases (i.e., oil, gas, and water)
l	Index of fluid phases (i.e., oil, gas, and water)
L	Index of minimization loops for PL inversion
l_q	Liquid phase
m	Fluid mixture
o	Oil phase
r	Radial direction

v	Fluid velocity
w	Water phase
W	Borehole wall
z	Vertical direction

Superscript

c	Index of iterations in a minimization loop
c_n	Index of current solutions for fluid-phase properties
c'_n	Index of corrective values to be applied to fluid-phase properties
c_n^*	Index of trial solutions for fluid-phase properties
c_n^{**}	Index of guessed values of fluid-phase properties
c_p	Index of previous solutions for fluid-phase properties
for	Fluid-producing rock formation
int	Fluid-phase interface
m	Index of measured fluid-phase properties
n	Index of discretized times
s	Index of simulated fluid-phase properties
T	Transpose operator

List of Greek Symbols

α	Constant in PR-EOS
α_{ag}	Gas volume fraction associated with slug-to-annual transition criterion, fraction
α_{bg}	Gas volume fraction associated with bubbly-to-slug transition criterion, fraction
α_h	Hydrocarbon-phase volume fraction, fraction
α_h^*	Hydrocarbon-phase volume fraction at thermodynamic equilibrium, fraction
α_k	Fluid-phase volume fraction, fraction
γ	Permeability rescaling factor
Γ^{for}	Mass influx from formation in single-phase flow, $lb_m/s/ft^3$
$\hat{\Gamma}_{jh}^{for}$	Molar influx of j-th component from formation into hydrocarbon phase, $lb_m\text{mole}/s/ft^3$
Γ_{jk}^{for}	Mass influx of j-th component from formation into k-th fluid phase, $lb_m/s/ft^3$
$\hat{\Gamma}_{jk}^{for}$	Molar influx of j-th component from formation into k-th fluid phase, $lb_m\text{mole}/s/ft^3$
$\hat{\Gamma}_{jo}^g$	Molar influx of j-th component from gas phase into oil phase, $lb_m\text{mole}/s/ft^3$

$\hat{\Gamma}_{jg}^o$	Molar influx of j-th component from oil phase into gas phase, lb _m mole/s/ ft ³
Γ_k^{for}	Mass influx of k-th fluid phase from formation, lb _m /s/ ft ³
Γ_k^{int}	Mass influx of k-th fluid phase through interface, lb _m /s/ ft ³
Γ_{lk}^{int}	Mass influx of k-th fluid phase from l-th fluid phase, lb _m /s/ ft ³
Γ_{ψ_k}	Source terms of generic transport property
$(\Gamma_{V_k})_{i_v}$	Volume-averaged momentum source terms in a VCV
$\delta_{j_1j_2}$	Binary interaction coefficient between components j ₁ and j ₂
ΔP_{lim}	Maximum acceptable variation of fluid pressure, psi
ΔP_{max}	Maximum variation of fluid pressure, psi
Δt^{new}	Next finite time step, s
Δt^{old}	Previous finite time step, s
Δt_{CFL}	Time step limit with respect to CFL condition, s
Δt_n	Finite time step, s
Δt_p	Time step limit with respect to relative variations of fluid pressure , s
Δt_{pv}	Minimum of Δt_p and Δt_v , s
Δt_v	Time step limit with respect to relative variations of fluid velocity , s
ΔV	Fluid-phase slip velocity, ft/s
ΔV_{lim}	Maximum acceptable variations of fluid velocity, ft/s
ΔV_{max}	Maximum variations of fluid velocity, ft/s

Δz_{i_s}	length of a SCV in z direction, ft
Δz_{i_v}	length of a VCV in z direction, ft
ε	Borehole roughness, in
ε_m	Energy dissipation rate of fluid mixture per unit mass, ft^2/s^3
$\hat{\varepsilon}_m$	Dimensionless energy dissipation rate of fluid mixture per unit mass
η_{ψ_k}	Diffusion coefficient of a generic transport property
θ	Borehole deviation angle, degrees
λ_1	Regularization multiplier for first optimization loop, $1/\text{mD}^2$
λ_2	Regularization multiplier for second optimization loop, fraction
μ	Fluid viscosity in single-phase flow, cp
μ_h	Hydrocarbon-phase viscosity, cp
μ_j	Viscosity of j-th hydrocarbon component, cp
μ_k	Fluid-phase viscosity, cp
μ_m	Fluid mixture viscosity, cp
ρ	Fluid density in single-phase flow, g/cc
$\hat{\rho}_h$	Hydrocarbon-phase molar density, gmole/cc
ρ_h^*	Hydrocarbon-phase molar density at thermodynamic equilibrium, gmole/cc
ρ_j	Density of j-th hydrocarbon component, g/cc
ρ_k	Fluid-phase density, g/cc
ρ_m	Fluid mixture density, g/cc

σ_{kl}	Surface tension of k-th fluid phase with respect to l-th fluid phase, dynes/cm
$\bar{\bar{\tau}}_k$	Fluid-phase viscous shear stress tensor, psia
$\bar{\bar{\tau}}_k^{\text{Re}}$	Fluid-phase Reynolds shear stress tensor, psia
φ	Generic fluid-phase property
ϕ	Porosity of a formation grid block, pu
ϕ^{ref}	Reference porosity, pu
ϕ_i	Porosity of i-th layer, pu
ψ_k	Generic transport property (e.g., fluid-phase velocity or holdup)
Ψ_k	Intermediary variable defining fluid-phase pressure-velocity linkage in two-phase flow, ft/s/psi
Ω_a	Constant in PR-EOS
Ω_b	Constant in PR-EOS

Subscript

α	Fluid holdup
θ	Azimuthal direction

List of Acronyms

1D	One dimensional
3D	Three dimensional
AN	Annular
bbbl	Barrel
BL	Bubbly
bfpd	Barrels of fluid per day
bopd	Barrels of oil per day
CPU	Central processing unit
CFL	Courant Friedrichs Lewy
DB	Dispersed bubbly
EOS	Equation of state
GOR	Gas oil ratio, scf/STB
IPR	Inflow performance relationship
IPSA	Inter-phase slip algorithm
IPSA-C	Inter-phase slip algorithm, coupled
MBEUB	Material balance error upper bound
MBELB	Material balance error lower bound
MD	Measured depth
MMSCFPD	Million million standard cubic feet per day

PCE	Pressure correction error, psi
PL	Production log
PLT	Production logging tool
PR-EOS	Peng-Robinson's equation of state
pu	Porosity unit
PVT	Pressure volume temperature
RAM	Random access memory
rcf	Reservoir cubic feet
RCFPD	Reservoir cubic feet per day
scf	Standard cubic feet
SCV	Scalar control volume
SIMPLE	Semi implicit method for pressure linkage equations
SIMPLE-C	Semi implicit method for pressure linkage equations consistent
SIP	Selective inflow performance
SL	Slug
STB	Standard barrel
STBPD	Standard barrel per day
TVD	True vertical depth
VCV	Velocity control volume
WOC	Water oil contact

References

- Abdel-Ghani, R., Krinis, D., and Camargo, N. 2011. Incorporating PLT-Distributed Dynamic Permeability into Reservoir Simulation Models Improves and Accelerates the History Matching Process. Paper SPE 145416 presented at the Society of Petroleum Engineers Reservoir Characterization and Simulation Conference and Exhibition, Abu Dhabi, UAE, 9-11 October.
- Alpak, F.O., Torres-Verdín, C., Habashy, T.M., and Sepehrnoori, K. 2008. Estimation of In-Situ Petrophysical Properties from Wireline Formation Tester and Induction Logging Measurements: A Joint Inversion Approach. *Journal of Petroleum Science and Engineering* **63** (2008): 1-17.
- Angeles, R., Torres-Verdín, C., Hadibeik, H., and Sepehrnoori, K. 2010. Estimation of Capillary Pressure and Relative Permeability from Formation-Tester Measurements Using Design of Experiment and Data-Weighing Inversion: Synthetic and Field Examples. *Journal of Petroleum Science and Engineering* **75** (2010): 19-32.
- Ansari, A.M., Sylvester, N.D., Sarica, C., Shoham, O., and Brill, J.P. 1994. A Comprehensive Mechanistic Model for Upward Two-Phase Flow in Wellbores. *SPE Production and Facilities Journal* **9** (2): 143-151.
- Aster, R.C., Borchers, B., and Thurber, C.H. 2005. *Parameter Estimation and Inverse Problems*. Burlington, Massachusetts: Elsevier Academic Press.
- Bahonar, M., Azaiez, J., and Chen Z. 2011. Transient Non-Isothermal Fully-Coupled Wellbore-Reservoir Model, Part I: Model Development. *Journal of Canadian Petroleum Technology* **50** (9), 37-50.
- Bahonar, M., Azaiez, J., and Chen Z. 2011. Transient Non-Isothermal Fully-Coupled Wellbore-Reservoir Model, Part II: Applications in Gas Well Testing. *Journal of Canadian Petroleum Technology* **50** (9), 51-70.
- Barnea, D., Shoham, O., and Taitel, Y. 1982. Flow Pattern Transition for Vertical Downward Two Phase Flow. *Chemical Engineering Science Journal* **37** (5): 741-744.

- Barnea, D. 1985. Transition from Annular Flow and from Dispersed Bubbly - Unified Models for the Whole Range of Pipe Inclinations. *International Journal of Multiphase Flow* **12** (5): 733-744.
- Barnea, D. 1987. A Unified Model for Predicting Flow-Pattern Transitions for the Whole Range of Pipe Inclinations. *International Journal of Multiphase Flow* **13** (1): 1-12.
- Bendiksen, K.H., Malnes, D., Moe, R., and Nuland, S. 1991. The Dynamic Two-Fluid Model OLGA: Theory and Application. *SPE Production Engineering Journal* **6** (2): 171-180.
- Bird, R.B., Stewart, W., and Lightfoot, E.N. 2002. *Transport Phenomena*. 2nd Edition, Hoboken, New Jersey: John Wiley and Sons.
- Bonizzi, M. and Issa, R.I. 2003. On the Simulation of Three-Phase Slug Flow in Nearly Horizontal Pipes Using the Multi-Fluid Model. *International Journal of Multiphase Flow* **29** (11): 1719-1747.
- Cebeci, T., Shao, J.P., Kafyeke, F., and Laurendeau, E. 2005. *Computational Fluid Dynamics for Engineers*. Long Beach, California: Horizons Publishing.
- Chang, Y. 1990. *Development and Application of an Equation of State Compositional Simulator*. Ph.D. Dissertation, The University of Texas at Austin, Austin, Texas.
- Chang, Y.B., Pope, G.A., and Sepehrnoori K. 1990. A Higher-Order Finite Difference Compositional Simulator. *Journal of Petroleum Science and Engineering* **5** (1): 35-50.
- Chen, S., Li, G., Peres, A., and Reynolds, A.C. 2008. A Well Test for In-Situ Determination of Relative Permeability Curves. *SPE Reservoir Evaluation and Engineering Journal* **11** (1): 95-107.
- Connolly, E.T. 1965. Production Logging, a Resume and Current Status of the Use of Logs in Production. Paper presented at the SPWLA 6th Annual Logging Symposium, Dallas, Texas, 4-7 May.
- Courant, R., Friedrichs, K., and Lewy, H. 1967. On the Partial Difference Equations of Mathematical Physics. *IBM Journal of Research and Development* **11** (2): 215-234.

- Boyle, K., Ayan, O., and Bustani, A. 1996. Applications of a New Production Logging Tool to Locate Fluid Entries and Borehole Flow Imaging. Paper SPE 36221 presented at the Abu Dhabi International Petroleum Exhibition and Conference, Abu Dhabi, UAE, 13-16 October.
- Colebrook, C.F. 1939. Turbulent Flow in Pipes, with Particular Reference to the Transition Region between Smooth and Rough Pipe Laws. *Journal of the Institution of Civil Engineers* **11** (4): 133 –156.
- Cortez, O.D. and Corbett P.W.M. 2005. Time-lapse Production Logging and the Concept of Flowing Units. Paper SPE 94436-MS presented at the Society of Petroleum Engineers Europec/EAGE Annual Conference, Madrid, Spain, 13-16 June.
- Davarzani, M.J. and Miller, A.A. 1983. Investigation of the Flow of Oil and Water Mixtures in Large Diameter Vertical Pipes. Paper presented at the SPWLA 24th Annual Logging Symposium, Calgary, Alberta, Canada, 27-30 June.
- Drew, D.A. and Lahey, R.T. 1979. Application of General Constitutive Principles to the Derivation of Multidimensional Two-Flow Equations. *International Journal of Multiphase Flow* **5** (4): 243-264.
- Drew, D.A. and Passman, S.L. 1999. *Theory of Multicomponent Fluids*. New York City, New York: Springer.
- Elshahawi, H. and Mostafa, H. 2002. Advanced Production Logging Technology for More Accurate Flow Profiling - Case Studies from the Gulf of Suez. Paper SPE 77839 presented at the Society of Petroleum Engineers Asia Pacific Oil and Gas Conference and Exhibition, Melbourne, Australia, 8-10 October.
- Firoozabadi, A. 1999. *Thermodynamics of Hydrocarbon Reservoirs*. New York City, New York: McGraw-Hill.
- Flores, J.G., Sarica, C., Chen, T.X., and Brill, J.P. 1998. Investigation of Holdup and Pressure Drop Behavior for Oil-Water Flow in Vertical and Deviated Wells. *Journal of Energy Resources Technology* **120** (1): 8-14.
- Flores, J.G., Sarica, C., Chen, T.X., and Brill, J.P. 1999. Characterization of Oil–Water Flow Patterns in Vertical and Deviated Wells. *SPE Production and Facilities Journal* **14** (2): 102-109.

- Frooqnia, A., A-Pour, R., Torres-Verdín, C., and Sepehrnoori, K. 2011. Numerical Simulation and Interpretation of Production Logging Measurements Using a New Coupled Wellbore-Reservoir Model. Paper VV presented at the SPWLA 52nd Annual Logging Symposium, Colorado Springs, Colorado, 14-18 May.
- Frooqnia, A., Torres-Verdín, C., A-Pour, R., Sepehrnoori, K., and Mohebbinia, S. 2013. Estimation of Near-Wellbore Relative Permeability from Numerical Simulation and Inversion of Time-Lapse Multi-Phase Production Logs. Paper VVV presented at the SPWLA 54th Annual Logging Symposium, New Orleans, Louisiana, 22-26 June.
- Govier, G.W. and Aziz K. 1972. *The Flow of Complex Mixtures in Pipes*. New York, New York City: Van Nostrand Reinhold.
- Gysen, A., Gysen, M., Zett, A., Webster, M., and Calero, G.H.Y. 2010. Production Logging in Highly Deviated and Horizontal Wells: Moving from Qualitative to Quantitative Answers. Paper SPE 133479 presented at the Society of Petroleum Engineers Annual Technical Conference and Exhibition, Florence, Italy, 19-22 September.
- Hadibeik, H., Proett, M., Chen, D., Eyuboglu, A.S.S., Torres-Verdín, C., and A-Pour, R. 2012a. Formation-Tester Pulse Testing in Tight Formations (Shales and Heavy Oil): Where Wellbore Storage Effects Favor the Determination of Reservoir Pressure. Paper SPE 155037 presented at the Society of Petroleum Engineers Americas Unconventional Resources, Pittsburgh, Pennsylvania, 5-7 June.
- Hadibeik, H., Chen, D., Proett, M., Eyuboglu, A.S.S., and Torres-Verdín, C. 2012b. Petrophysical Properties of Unconventional Low-Mobility Reservoirs (Shale Gas and Heavy Oil) by Using Newly Developed Adaptive Testing Approach. Paper SPE 159172 presented at the Society of Petroleum Engineers Annual Technical Conference and Exhibition, San Antonio, Texas, 8-10 October.
- Harmathy, T.Z. 1960. Velocity of Large Drops and Bubbles in Media of Infinite or Restricted Extent. *AIChE Journal* **6** (2): 281-288.
- Hasan, A.R. and Kabir, C.S. 1988a. A Study of Multiphase Flow Behavior in Vertical Wells. *SPE Production Engineering Journal* **3** (2): 263–272.
- Hasan, A.R. and Kabir, C.S. 1988b. Predicting Multiphase Flow Behavior in Deviated Wells. *SPE Production Engineering Journal* **3** (4): 474–482.

- Hasan, A.R. and Kabir, C.S. 1990. A New Model for Two-Phase Oil/Water Flow: Production Log Interpretation and Tubular Calculations. *SPE Production Engineering Journal* **5** (2): 193-199.
- Hasan, A.R., Kabir, C.S., and Wang, X. 1998. Wellbore Two-Phase Flow and Heat Transfer During Transient Testing. *SPE Journal*, **3** (2): 174-180.
- Hasan, A.R. and Kabir, C.S. 1999. A Simplified Model for Oil/Water Flow in Vertical and Deviated Wellbores. *SPE Production and Facilities Journal* **14** (1): 56-62.
- Hasan, A.R. and Kabir, C.S. 2002. *Fluid Flow and Heat Transfer in Wellbores*. Richardson, Texas: SPE Textbook Series.
- Hasan, A.R., Kabir, C.S., and Sayarpour, M. 2007. A Basic Approach to Wellbore Two-Phase Flow Modeling. Paper SPE 109868 Presented at the Society of Petroleum Engineers Annual Technical Conference and Exhibition, Anaheim, California, 11-14 November.
- Hawkins, J.M. 1956. A Note on the Skin Effect. *Journal of Petroleum Technology* **8** (12): 65-66.
- Hibiki, T. and Ishii, M. 1977. One-Dimensional Drift-Flux Model and Constitutive Equations for Relative Motion between Phases in Various Two-Phase Regimes. *International Journal of Heat and Mass Transfer* **46** (25): 4935-4948.
- Hibiki, T., Ishii, M., and Xiao, Z. 2001. Axial Interfacial Area Transport of Vertical Bubbly Flows. *International Journal of Heat and Mass Transfer* **44** (10): 1869-1888.
- Hibiki, T. and Ishii, M. 2002. Development of One-Group Interfacial Area Transport Equation in Bubbly Flow Systems. *International Journal of Heat and Mass Transfer* **45** (11): 2351-2372.
- Hibiki, T., Lee, T.H., Lee, J.Y., and Ishii, M. 2006. Interfacial Area Concentration in Boiling Bubbly Flow Systems. *Chemical Engineering Science Journal* **61** (24): 7979-7990.
- Hill, A.D. 1990. *Production Logging-Theoretical and Interpretive Elements*. Richardson, Texas: SPE Textbook Series.

- Hill, A.D. and Oolman, T. 1982. Production Logging Tool Behavior in Two-Phase Inclined Flow. *Journal of Petroleum Technology* **34** (10): 2432-2440.
- Hoffmann, K. and Chiang, S.T. 2000. *Computational Fluid Dynamics*. Volume 1, 4th Edition, Wichita, Kansas: Engineering Education System.
- Holmes, J.A., Barkve, T., and Lund, Ø. 1998. Application of a Multisegment Well Model to Simulate Flow in Advanced Wells. Paper SPE 50646 presented at the Society of Petroleum Engineers European Petroleum Conference, Hague, Netherlands, 20-22 October.
- Hughes, W.F. and Brighton, J.A. 1991. *Schaum's Outline of Fluid Dynamics*. 2nd Edition, New York City, New York: McGraw-Hill.
- Ishii, M. 1975. *Thermo-Fluid Dynamic Theory of Two-Phase Flow*. Paris, France: Evrolles.
- Ishii, M. and Hibiki, T. 2011. *Thermo-fluid Dynamics of Two-Phase Flow*. 2nd edition, London, England: Springer Dordrecht Heidelberg.
- Kaya, A.S., Sarica, C., and Brill, J.P. 1999. Comprehensive Mechanistic Modeling of Two-Phase Flow in Deviated Wells. Paper SPE 56522 presented at the Society of Petroleum Engineers Annual Technical Conference and Exhibition, Houston, Texas, 3-6 October.
- Khor, S.H., Mendes-Tatsis, M.A., and Hewitt, G.F. 1997. One-Dimensional Modelling of Phase Holdups in Three-Phase Stratified Flow. *International Journal of Multiphase Flow* **23** (5): 885-897.
- Kianinejad, A., Aminzadeh, B., Chen, X, and Dicarolo, D.A. 2014. Three-Phase Relative Permeabilities as a Function of Flow History. Paper SPE 169083 presented at the Society of Petroleum Engineers Improved Oil Recovery Symposium, Tulsa, Oklahoma, 12-16 April.
- Kim, J., Moin, P., and Moser, R.D. 1987. Turbulence Statistics in Fully Developed Channel Flow at Low Reynolds Number. *Journal of Fluid Mechanics* **177** (1): 133-166.
- Kleinstreuer, C. 2003. *Two-Phase Flow: Theory and Application*. London, England: Taylor and Francis Book Inc.

- Kobori, T. and Terada, M. 1978. Application of the Needle-Type Void Meter to Blow-Down Tests. Paper presented at the 2nd CSNI Specialist Meeting on Transient Two-phase Flow, Paris, France, 12-14 June.
- Kolev, N.I. 2007. *Multiphase flow dynamics 1: Fundamentals*. New York City, New York: Springer.
- Lahey, R.T. 2005. The Simulation of Multi-Dimensional Multi-Phase Flows. *Nuclear Engineering Design Journal* **235** (10): 1043-1060.
- Leverett, M. 1941. Capillary Behavior in Porous Solids. *Transactions of the American Institute of Mining Metallurgical and Petroleum Engineers* **142** (1): 152-169.
- Levich, V.G. 1962. *Physicochemical Hydrodynamics*. Englewood Cliffs, New Jersey: Prentice-Hall.
- Livescu, S., Durlofsky, L.J., and Aziz, K. 2009. Development and Application of a Fully-coupled Thermal Compositional Wellbore Flow Model. Paper SPE 121306 presented at the Society of Petroleum Engineers Western Regional Meeting, San Jose, California, 24-26 March.
- Moody, L.F. 1944. Friction Factors for Pipe Flow. *Transactions of the American Society of Mechanical Engineers* **66** (8): 671-684.
- Ouyang, L.B. and Aziz K. 1999. A Mechanistic Model for Gas-Liquid Flow in Pipes with Radial Influx or Outflux. Paper SPE 56525 presented at the Society of Petroleum Engineers Annual Technical Conference and Exhibition, Houston, Texas, 3-6 October.
- Patankar, S.V. and Spalding, D.B. 1972. A Calculation Procedure for Heat, Mass and Momentum Transfer in Three-Dimensional Parabolic Flows. *International Journal of Heat and Mass Transfer* **15** (10): 1787-1806.
- Peng, D. and Robinson, D. 1976. A New Two-Constant Equation of State. *Industrial and Engineering Chemistry Fundamentals Journal* **15** (1): 59-64.
- Peters, E.J. 2012. *Advanced Petrophysics: Volume 1: Geology, Porosity, Absolute Permeability, Heterogeneity, and Geostatistics*. Austin, Texas: The Live Oak Press.

- Pour, R. 2011. *Development and Application of a 3D Equation-Of-State Compositional Fluid-Flow Simulator in Cylindrical Coordinates for Near-Wellbore Phenomena*. Ph.D. Dissertation, The University of Texas at Austin, Austin, Texas.
- Pourafshary, P. 2007. *A Coupled Wellbore/Reservoir Simulator to Model Multiphase Flow and Temperature Distribution*. Ph.D. Dissertation, The University of Texas at Austin, Austin, Texas.
- Pourafshary, P., Varavei, A., Sepehrnoori, K., and Podio, A.L. 2009. A Compositional Wellbore/Reservoir Simulator to Model Multiphase Flow and Temperature Distribution. *Journal of Petroleum Science and Engineering* **69** (1-2): 40–52.
- Prosperetti, A. and Tryggvason, G. 2007. *Computational Methods for Multiphase Flow*. Cambridge, England: Cambridge University Press.
- Radovich, N.A. and Moissis, R. 1962. The Transition from Two Phase Bubble Flow to Slug Flow. Report Number 7-7673-22, Department of Mechanical Engineering, Massachusetts Institute of Technology, Cambridge, Massachusetts.
- Rey, A.C., Peres, A.M., Junior, A.B., Almeida, S.R., and Sombra, C.L. 2009. Direct Permeability Estimation Using Production Logging. Paper WWW presented at the SPWLA 50th Annual Logging Symposium, Houston, Texas, 21-24 June.
- Rezaveisi, M., Sepehrnoori K., and Johns, R.T. 2014. Tie-Simplex-Based Phase-Behavior Modeling in an IMPEC Reservoir Simulator. *SPE Journal* **19** (02): 327-339.
- Rezaveisi, M., Johns, R.T., and Sepehrnoori K. 2014. Application of Multiple Mixing-Cell Method to Improve Speed and Robustness of Compositional Simulation. Paper SPE 169063 presented at the Society of Petroleum Engineers Improved Oil Recovery Symposium, Tulsa, Oklahoma, 12-16 April.
- Satta, F., Simoni, D., Ubaldi, M., and Zunino, P. 2006. Velocity and Turbulence Measurements in a Separating Boundary Layer with Laser Doppler Velocimetry. Paper presented at the AIVELA XIV Annual Meeting, Rome, Italy, 6-7 November.
- Schlumberger, 1973. *Production Log Interpretation*. Houston, Texas: Schlumberger.
- Schnorr, D.R. 1996. More Answers from Production Logging Than Just Flow Profiles. Paper KK presented at the SPWLA 37th Annual Logging Symposium, New Orleans, Louisiana, 16-19 June.

- Sharma, R., Nghiem, A., Siu A., Collins, D.A., Mourits, F.M. 1996. Efficient Modelling of Wellbore Backflow. *Journal of Canadian Petroleum Technology* **35** (06): 34-41.
- Shi, H., Holmes, J.A., Durlofsky, L.J., Aziz, K., Diaz, L., and Alkaya, B. 2005. Drift-Flux Modeling of Two-Phase Flow in Wellbores. *SPE Journal* **10** (1): 24-33.
- Shirdel, M. and Sepehrnoori, K. 2012. Development of a Transient Mechanistic Two-Phase Flow Model for Wellbores. *SPE Journal* **17**(3): 942-955.
- Shirdel, M. 2013. *Development of a Coupled Wellbore-Reservoir Compositional Simulator for Damage Prediction and Remediation*. Ph.D. Dissertation, The University of Texas at Austin, Austin, Texas.
- Smith, J. and Van Ness, H. 2004. *Introduction to Chemical Engineering Thermodynamics*. New York City, New York: McGraw-Hill.
- Sommerfeld, M., Bourloutski, E., and Broeder, D. 2003. Euler/Lagrange Calculations of Bubbly Flows with Consideration of Bubble Coalescence. *Canadian Journal of Chemical Engineering* **81** (3-4): 508-518.
- Spalding, D.B. 1980. Mathematical Methods in Nuclear-Reactor Thermal Hydraulics. Keynote Paper, ANS Meeting on Nuclear-Reactor Thermal Hydraulics, Saratoga, New York.
- Stadtke, T. 2006. *Gasdynamic Aspects of Two-Phase Flow: Hyperbolicity, Wave Propagation Phenomena and Related Numerical Methods*. Weinheim, Germany: Wiley-VCH.
- Steward, J. 2008. *Multivariable Calculus, Early Transcendentals*, 6th Edition, Belmont California: Thomson Brooks/Cole.
- Stone, T.W., Edmund, N.R., and Kristoff, B.J. 1989. A Comprehensive Wellbore/Reservoir Simulator. Paper SPE 18419 presented at the Society of Petroleum Engineers Reservoir Simulation Symposium, Houston, Texas, 6-8 February.
- Sullivan, M.J., Belanger, D., and Skalinski, M. 2006. A New Method for Deriving Flow-Calibrated Permeability from Production Logs. Paper K presented at the SPWLA 47th Annual Logging Symposium, Veracruz, Mexico, 4-7 June.

- Sullivan, M.J. 2007. Permeability from Production Logs - Method and Application. *Journal of Petroleum Technology* **59** (7): 80-87.
- Sun, X., Kim, S., Ishii, M., and Beus, S.G. 2003. Model Evaluation of Two-Group Interfacial Area Transport Equation for Confined Upward Flow. *Nuclear Engineering and Design* **230** (1-3): 27-47.
- Taitel, Y. and Dukler, A.E. 1976. A Model for Predicting Flow Regime Transition in Horizontal and Near Horizontal Gas-Liquid Flow. *AIChE Journal* **22** (1): 47-57.
- Taitel, Y., Barnea, D., and Dukler, A.E. 1980. Modeling Multi-Pattern Transitions for Steady Upward Gas-Liquid Flow in Vertical Tubes. *AIChE Journal* **26** (3): 345-354.
- Taitel, Y., Barnea, D., and Brill, J.P. 1995. Stratified Three Phase Flow in Pipes. *International Journal of Multiphase Flow* **21** (1): 53-60.
- Takacs, G. and Guffey, C.G. 1989. Prediction of Flowing Bottomhole Pressures in Gas Wells. Paper SPE 19107 presented at the Society of Petroleum Engineers Gas Technology Symposium, Dallas, Texas, 7-9 June.
- Truesdell, C. and Toupin, R. 1960. *The Classical Field Theories*. Berlin, Germany: Springer-Verlag OHG.
- Van Doormaal, J.P. and Raithby, G.D. 1984. Enhancements of the SIMPLE Method for Predicting Incompressible Fluid Flows. *Numerical Heat Transfer* **7** (2): 147-163.
- Versteeg, H.K. and Malalasekera, W. 1995. *An Introduction to Computational Fluid Dynamics, the Finite Volume Method*. New York City, New York: Longman Scientific and Technical.
- Vigneaux, P., Chenais, P., and Hulin, J.P. 1988. Liquid-Liquid Flows in an Inclined Pipe. *AIChE Journal* **34** (5): 781-789.
- Viswanath, D.S., Ghosh, T., Prasad, D.H.L., Dutt, N.V.K., and Rani, K.Y. 2007. *Viscosity of Liquids: Theory, Estimation, Experiment, and Data*. New York City, New York: Springer.
- Wallis, G.B. 1969. *One-Dimensional Two-Phase Flow*. New York City, New York: McGraw-Hill Book Inc.

- Winterfeld, P.H. 1989. Simulation of Pressure Buildup in a Multiphase Wellbore Reservoir System. *SPE Formation Evaluation Journal* **4** (2): 247-252.
- Yeoh, G.H. and Tu, J. 2010. *Computational Techniques for Multi-Phase Flows*. Burlington, Massachusetts: Butterworth-Heinemann.
- Zavareh, F., Hill, A.D., and Podio, A. 1988. Flow Regimes in Vertical and Inclined Oil/Water Flow in Pipes. Paper SPE 18215 presented at the Society of Petroleum Engineers Annual Technical Conference and Exhibition, Houston, Texas, 2-5 October.
- Zett, A., Webster, M., Seccombe, J., Colbert, C., Ansari, R.Z., and Chace, D. 2011. Extending Production Petrophysics Applications in Monitoring Complex Recovery Mechanisms. Paper SPE 146662 presented at the Society of Petroleum Engineers Annual Technical Conference and Exhibition, Denver, Colorado, 30 October - 2 November.
- Zuber, N. and Findlay, J.A. 1965. Average Volumetric Concentration in Two-Phase Flow Systems. *Journal of Heat Transfer* **87** (4): 435-468.